SYNTHESIS OF HYDROCARBONS AND FLUOROCARBONS IN A TIP-TIP ARC DISCHARGE REACTOR AT HIGH PRESSURE

by

SAMUEL A. IWARERE

MScEng (Chemical)

University of KwaZulu-Natal

Submitted in fulfilment of the academic requirements for the degree of Doctor of Philosophy in Engineering (Chemical) to the School of Engineering, College of Agriculture, Engineering and Science, University of KwaZulu-Natal, Durban, South Africa.

July 2013

Supervisor: Professor D. Ramjugernath

Co-supervisor: Professor L. Fulcheri

ABSTRACT

In the field of nonthermal plasma physics, the term “high pressure” refers to pressures ranging from 0.01 to 0.5 MPa, while “very high pressure” refers to pressures ≥ 1 MPa. Generating and sustaining a nonthermal plasma at those pressures using a low current is a virgin area of research, especially in the field of organic and inorganic synthesis. This can be attributed to the instability of the electric discharge at conditions of high pressure and low current.

The main objective of this project was to investigate the potential for hydrocarbons and fluorocarbons synthesis in a high-pressure arc discharge reactor. Experimental equipment was set up and commissioned to this effect. The tip-tip electrical arc discharge reactor used in this project has a pressure limit of 20 MPa. The arc discharge generated in the reactor chamber could be viewed through two pairs of borosilicate windows. A video camera was used to capture the discharge image. The plasma was generated using a high voltage direct current (HVDC) power supply operating at low current (< 1 A); and a high frequency pulse power supply operating between 1 to 6 kHz. Quantitative and qualitative analyses of the gas products were carried out in a gas chromatograph (GC) and a gas chromatograph mass spectrometer.

Preliminary experiments were conducted at a pressure of 2.2 MPa and a current of 0.35 A for hydrocarbon synthesis via the Fischer-Tropsch (FT) process using three different treatment modes, a continuous treatment mode and two intermittent modes with a relaxation time between successive discharges. This was carried out using a high voltage power supply that operates on the principle of double resonance technology at high frequencies up to 50 kHz. Significant amounts of CH_4 and smaller amounts of C_2H_4 and C_2H_6 were formed. The continuous mode was found to favour CH_4 synthesis. The intermittent modes showed better kinetics for the syntheses of C_2H_4 and C_2H_6.

Preliminary experiments on hydrogenation of CO were conducted at pressures ranging from 0.5 to 15 MPa, and current ranging from 0.20 to 0.40 A using a HVDC power supply. The results from the preliminary studies indicated that the main synthesized molecules are CH_4, C_2H_4, C_2H_6, C_3H_6, and C_3H_8 over the entire pressure range investigated. C_2H_2 was obtained at pressures of 0.5 and 1 MPa only.

Experiments conducted on the dry reforming process at pressures up to 7.8 MPa showed the production of H_2, CO, C_2H_2, C_2H_4, C_2H_6, with low concentrations of C_3H_6, and C_3H_8. The carbon deposit formed in this process was observed to decrease as the pressure increases. A good H_2/CO ratio of 2.1 to 2.6, which is desirable for the production of synthetic fuels in FT process were obtained between the pressures of 0.5 and 4 MPa.

Experimental measurements performed using two different treatment modes, a continuous and an intermittent mode at a pressure of 2 MPa, a current of 0.35 A, and an interelectrode gap of 0.4 mm revealed that C_2F_6 and C_3F_8 production from CF_4 is favoured by the intermittent mode than the continuous mode.

The dissociation of CF_4 in the tip-tip plasma reactor were investigated at pressures from 1 to 9 MPa, with varying parameters such as current and interelectrode gap.

The experimental results indicated that the high operating pressures together with the input power influence the conversion of CF_4 into higher fluorocarbons.

The experimental results obtained by varying the operating currents from 0.3 to 0.45 A at a pressure of 1 MPa, and an interelectrode gap of 0.4 mm, showed that the conversion of the CF_4 into higher fluorocarbons was influenced by a strong decrease of the reduced electric field in the discharge zone.

The influence of varying the interelectrode gap at a pressure of 1 MPa, and a current of 0.35 A was found to be of a little significance in the fluorocarbon formation process.

Theoretical studies carried out on the dissociation of CF_4 revealed that the nonthermal plasma process via electron impact resulted in higher energy efficiency than the thermal plasma process.

Thermodynamic and kinetic analyses were carried out for the dry reforming process at high pressure. High conversions were obtained for the CH_4 and CO_2 using thermodynamic calculations. The conversions were observed to decrease with pressure.

Modelling of the dry reforming were undertaken using the perfectly stirred reactor (PSR) and SENKIN (0-D homogeneous model for closed system) modules of the CHEMKIN II Package. The kinetic model with all the four different methane oxidation mechanisms showed good agreement with the experimental data in terms of the chemical reaction performance of the nonthermal plasma reactor at high pressure. The conversion of CH_4 and CO_2 was revealed to depend strongly on the residence time.

A three-dimensional time dependent magneto hydrodynamics (MHD) model of the arc discharge was set up with Code_Saturne. The assumption of local thermal equilibrium (LTE) made for the low current high-voltage arc discharge was studied for pressure ranges of 2 to 10 MPa at 0.35 A and for current ranges of 0.25 to 0.40 A at a pressure of 8 MPa with helium. A typical reference case at a pressure of 8 MPa and a current of 0.35 A was also studied. Good agreement with experimental data was obtained.

DECLARATION

This thesis constitutes my doctoral research work under the Thermodynamic Research Unit in the School of Engineering at the University of KwaZulu-Natal, Durban and the Plasma Group of the Centre for Energy and Processes, MINES ParisTech, Sophia Antipolis, France from April 2010 to November 2012 under the supervision of Professor D. Ramjugernath and Professor L. Fulcheri.

I declare that:

(i) This thesis except where otherwise indicated is my original work.

(ii) Some part of my experimental results has been published, while some have been submitted for publication in collaboration between the Plasma Group and the Thermodynamic Research Unit.

(iii) The written expressions are in my own words, and where other written sources have been quoted, then:

a) their words have been re-written but the general information attributed to them has been referenced;

b) where their exact words have been used, their writing has been placed inside quotation marks, and referenced.

_____

S.A. Iwarere

As the candidate's supervisors, we approved this thesis for submission.

_____ _____

Professor L. Fulcheri Professor D. Ramjugernath

ACKNOWLEDGEMENTS

The successfully completion of this work would not have been possible without the direct and indirect contributions of several individuals and groups. However, space would not permit me to list everyone who made this a reality. Therefore, I kindly apologize to those whose names might not be mentioned in this acknowledgement. Please kindly accept my apologies in good faith. I love and appreciate you all.

- Jesus Christ, my Lord and Personal Saviour, the Pillar that holds my life. I will not have gone this far without you. I love you Lord!
- Professor D. Ramjugernath and Professor L. Fulcheri, this will not have happened without your professional support and guidance. Your knowledge, ideas, and experience are unquantifiable.
- The Plasma team at Sophia Antipolis and administration unit under the CEP in France. You are awesome!
- Ken Jack, Leon, and team, I really appreciate your technical assistance.
- All my colleagues in TRU, you are the best!
- Dr P. Naidoo, you are an asset to the group.
- Alex, you made MHD modelling possible. Thanks a lot.
- NECSA; National Research Foundation (NRF) of South Africa; South African Research Chair Initiative; University of KwaZulu-Natal Scholarships office and CEP in France, thanks for the financial support.
- My spiritual family (His People Christian Church, Durban), I am short of words to describe your love!
- The Bible study unit at Chem. Eng. We had great times together in God's presence.
- Professor E.O. Odebunmi (my undergraduate project supervisor), you have been a father.
- My biological parents, Mr & Mrs F.O. Iwarere, you are the best and I love you both!
- My wife's parents, Elder & Mrs L.O. Oni, thank you for your prayers and support.
- Babs Iwarere, I could not have asked for a better brother. You remain my hero!
- Buky Iwarere, Titi Oni, Bosede Oni, Sanmi Oni, I love you all.
- Margareth, Letsabisa, One, Sister Gbonju, Edison, you are far but near.
- Finally, my two girls (my wife-Funsho and daughter-Ifeoluwa), you both make my world special. Thank you sweetheart for all your understanding, support, encouragement, motivation, and prayers. I love you and I will always do.

Table of Contents

LIST OF FIGURES

Chapter 1

Chapter 2

Chapter 3

Chapter 4

Chapter 5

Appendix A

Appendix B

Appendix E

LIST OF PHOTOGRAPHS

Chapter 4

Chapter 5

Chapter 6

LIST OF TABLES

Chapter 1

Chapter 2

Chapter 3

Chapter 4

Chapter 5

Chapter 6

Appendix A

Appendix C

Appendix E

Appendix F

NOMENCLATURE

List of symbols

A	angular impulse or magnetic vector potential: $V.s.m^{-1}$
A_i	pre-exponential factor in the rate constant of the i th reaction: mol.cm.s.K
B	magnetic field or (magnetic flux density): $V.s.m^{-2}$
D	electric displacement field; $C.m^{-2}$
E	electric field: $V.m^{-1}$
e	electron
E_e	electronic excitation
E_i	activation energy in the rate constant of the i th reaction: $cal.mol^{-1}$
G	generation ionization rate
H	magnetizing field or (magnetic field intensity): $A.m^{-1}$
I	ionization
J	total electric current density: $A.m^{-2}$
jq_e	positive ionic charge: C
k	Boltzmann's constant: $eV.K^{-1}$
L	characteristics dimensions of the discharge chamber
m_e	mass of the electron: kg
n_e	electron density: m^{-3}
n_i	positive ion density: m^{-3}
q_e	charge of an electron: C
R	recombination rate of particle
T_e	temperature of the electrons: eV
T_i	temperature of the ions: K
V	voltage: V
v(v)	velocity dependent collision frequency: Hz
v_{me}	averaged momentum loss frequency: Hz

Abbreviations

CCD	Charge-coupled Device
CFCs	Chlorofluorocarbons
CMOS	Complementary Metal Oxide Semiconductor
DC	Direct Current
e-Trans.	electronic to translational energy
e-Vib.	electron to vibrational energy
EEDF	Electron Energy Distribution Function
EAMS	Electron Attachment Mass Spectrometer
FEI	Fluorine Expansion Initiative
GAT	Glow to Arc Discharge Transition

GCMS	Gas Chromatograph Mass Spectrometer
GEC Cell	Gaseous Electronic Conference Cell
HCFCs	Chlorohydrofluorocarbons
HFCs	Hydrofluorocarbons
IEDF	Ion Energy Distribution Function
IRLAS	Infrared Laser Absorption Spectroscopy
Kn	Knudsen number
kTe	energy of the electron
LIF	Laser induced fluorescence
NECSA	South African Nuclear Energy Corporation
OES	Optical Emission Spectroscopy
PECVD	Plasma Enhanced Chemical Vapor Deposition
PELCHEM	Pelindaba Chemical
PFCs	Perfluorocarbons
QMS	Quadrupole Mass Spectrometer
Rot.	Rotational energy
Trans.	Translational
TRU	Thermodynamic Research Unit
UKZN	University of KwaZulu-Natal
Vib.	Vibrational
V-Trans.	vibrational to translational energy
IUPAC	International Union of Pure and Applied Chemistry

IUPAC Nomenclature for Some Organic Compounds

CF_4	Tetrafluoromethane
CCl_2F_2	Dichlorodifluoromethane
CH_2F_2	Difluoromethane
CH_3F	Fluoromethane
C_2F_4	Tetrafluoroethene
C_2F_6	Hexafluoroethane (R116))
C_2H_2	Acetylene
C_2H_4	Ethene
C_2H_6	Ethane
C_2HF_5	1,1,1,2,2-pentafluoroethane
C_3H_6	Propene
C_3H_8	Propane
C_3F_6	Hexafluoropropene (R1216)
C_3F_8	Octafluoropropane (R218)
HF	Hydrogen fluoride

Greek Alphabets

$\nabla\cdot$	divergence operator : m^{-1}
$\nabla\times$	curl operator: m^{-1}
λ	mean free path: m
Λ	discharge volume: m^3
ε_0	permittivity of free space: $\mu F.m^{-1}$
β_i	temperature exponent in the rate constant of the i th reaction
λ_D	Debye length: m
ρ	total charge density: $C.m^{-3}$
ϕ	electric potential: V

Constants used in the work

Avogadro's number, n_A, 6.02×10^{23} mol^{-1} at NTP (normal temperature and pressure, 20^oC and 760 Torr)

Boltzmann's constant, $k = R_0/n_A$, 1.38×10^{-23} J K^{-1} = 8.617 x 10^{-5} $eV.K^{-1}$

Charge of electron, e, 1.6×10^{-19} C

Electron volt, eV, 1.6×10^{-19} J

Mass of electron, m_e, 9.11×10^{-31} kg

Permittivity of free space ε_0, 8.85×10^{-12} $F.m^{-1}$

Universal gas constant based on energy units, R_0, 8.31447 J $K^{-1}.mol^{-1}$

Universal gas constant based on volume and pressure units, R_0, 8.31447 $cm^3.MPa.K^{-1}.mol^{-1}$

1 bar = 0.9869 atm = 750 Torr = 100 kPa = 0.1 MPa

Chapter 1

INTRODUCTION

1.1 Background to the Research

In Raizer's book on gas discharge physics [1], the term *low pressure* refers to pressures ranging from approximately 10^{-3} to 10^{0} torr (~ 10^{-7} to 10^{-3} MPa) where the positive column of the arc is believed to be nonequilibrium, while *high pressure* refers to pressures above the range of 0.01 to 0.5 MPa. However, unlike the low pressure discharge, the positive column of the arc is generally in equilibrium and collisions are mostly believed to be elastic [2], with a low likelihood of negative ions been formed at those pressure conditions. Discharges generated at pressures ≥ 1 MPa has been described as *very high pressure* in relation to the field of nonthermal physics [1, 3-5].

This research work is focused on the application of high pressure and very high pressure plasma for hydrocarbon and fluorocarbon synthesis. For example, researchers have recently embraced the use of nonthermal plasma as a technological tool for synthesizing organic compounds. This is mainly attributed to the fact that plasmas are capable of producing chemically active species such as electrons, ions, radicals as well as ionized and neutral species. These species can participate in plasma-chemical reactions, and thus lead to the creation of new products. Therefore, plasma technology is seen as a 21st century tool to help with the synthesis of hydrocarbons via the reforming processes.

For example, the application of plasma technology in the synthesis of hydrocarbons via the historical Fischer-Tropsch (F-T) process is quite an interesting field to explore especially above atmospheric pressure conditions and at low current. It is expected that the use of plasma as against the conventional catalytic process should help to solve some problems such as coking, catalyst deactivation, catalyst poisoning, and cost associated with catalyst regeneration. Moreover, plasma, on the environment point of view is seen as a tool for producing clean and environmental friendly gas-to-liquid downstream products.

Therefore, over the years, there has been extensive research into alternative technologies such as plasma to successfully replace the use of catalyst for synthesis gas production from natural gas, as well as the catalytic conversion of syngas into synthetic liquid fuels [6-20]. However, all this research is at sub-atmospheric and atmospheric pressure conditions.

On the other hand, fluorine chemistry is one of the most researched fields in chemistry considering industrial and global contributions. According to Schofield [21], fluorine based compounds have drawn more attention or interest within the organic and inorganic chemistry research communities than any other elements going by the high rate of journal publications between the 1980s and 1990s. However, despite the wide applications of fluorochemicals in the world at large, the issues of the environmental impact of some fluorine-containing compound such as the second and third generations of refrigerants namely CFCs and HCFCs respectively have reduced the sales of fluorocarbons in a way. Thus, one of the current challenges is to achieve a better compromise between the individual usefulness of the fluorochemicals especially the hydrofluorocarbons (HFC) and perfluorocarbons (PFCs) and their possible environmental ramifications.

Furthermore, current methods for the commercial production of fluorocarbons involve direct fluorination of hydrocarbons with elemental fluorine as well as electrochemical fluorination. For instance, Pelchem, a South African company and the chemical division of NECSA is focused on improving the quality and sales of existing fluorochemicals as well as synthesizing new ones. Some of their commonly used products include xenon difluoride, which is in high commercial demand within the micro electro mechanical systems (MEMS) in the semiconductor industries as well as other high value commercial products such as hydrofluoric acid (HF) and hexafluoropropylene (HFP). However, the production of these products is currently via the direct fluorination processes. One major problem associated with direct fluorination using elemental fluorine is the high health and safety risk of handling elemental fluorine. In addition, the high operating temperature of the process can result in the degradation of some desired products.

1.2 Research Problem and Question

1.2.1 Fluorocarbon Synthesis

Fluorspar, the commercial name for calcium fluoride (CaF_2), a mineral fluorite, accounts for the fluorides used in the production of all fluorine-based products worldwide. It is a mineral having long history in its use as a flux in metallurgical operations [22]. However, most of its current market amongst others is in the area of fluorochemicals as well as the production of UF_6, which is used in nuclear fuel enrichment.

The grading of fluorspar is divided into two categories: Acidspar, which has a CaF_2 purity greater than 97 percent, and metspar, which is the metallurgical grade and has a CaF_2 with purity of less than 97 percent. As of the year 2008, the world's production of fluorspar was approximately 6 million tonnes per year; it was estimated to exceed 6.8 million tonnes by end of 2012. The bulk of this production is acidspar, which accounts for up to 70 percent of production.

In the late 1970s, fluorspar production was led by the defunct Soviet Union, Mexico, and South Africa [23]. However, the world production and consumption of fluorspar has been influenced by China since the latter part of 1990s. According to the report from NECSA [24], while South Africa, which has the second largest reserves of fluorspar in the world, occupies the third position in terms of production, approximately only 5 percent of its production is consumed within the country (by way of sales to industry) earning less than 0.1 percent of its value as revenue [24]. This makes it difficult for the country to benefit sufficiently from its own resources.

Therefore, the conversion of fluorspar into value-added products with a wide range of applications in industries such as chemical and steel manufacturing, ceramic and glass industries to mention a few in a country like South Africa will be of a great benefit to the country's economic growth. Figure 1.1 gives a summarised fluorspar supply chain.

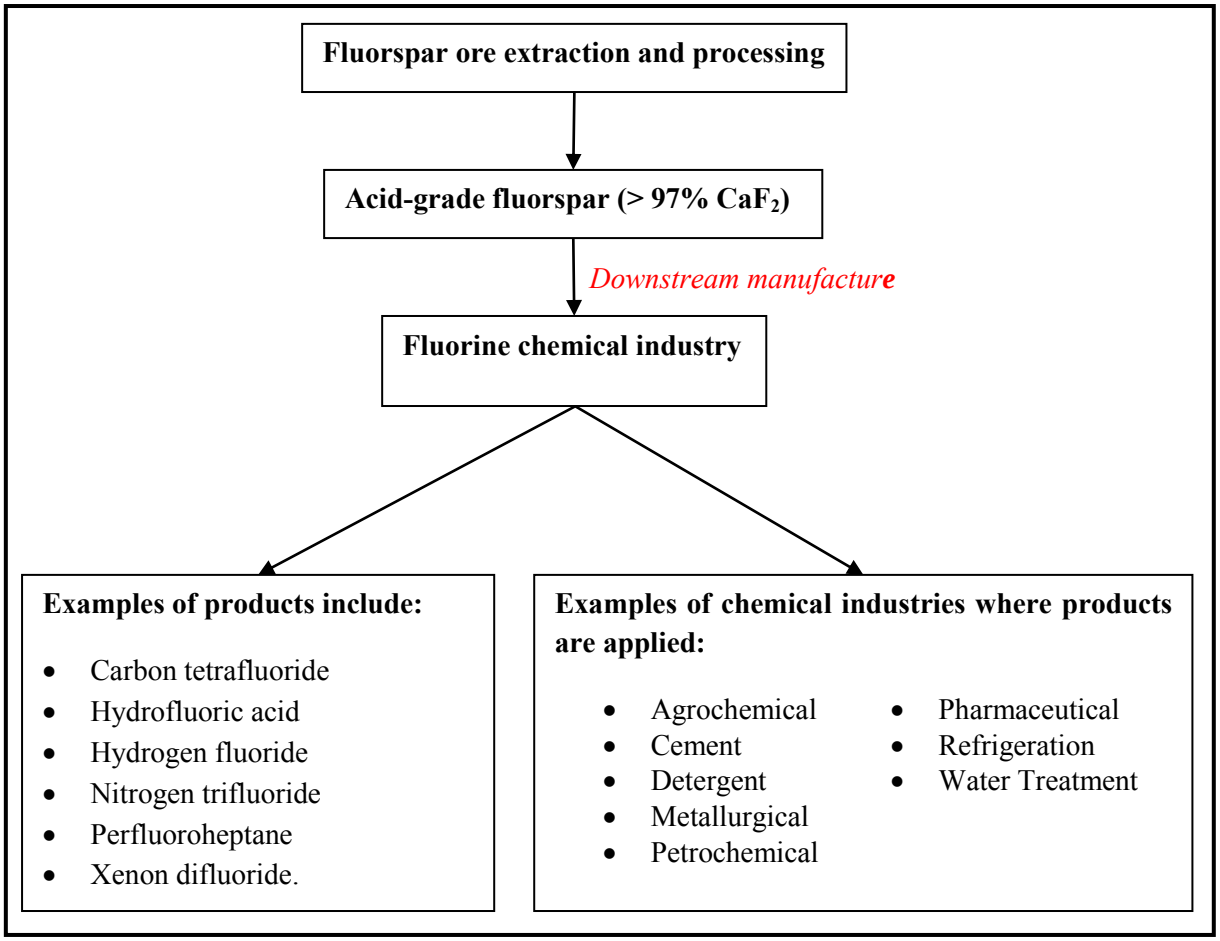

Figure 1.1: A summarized fluorspar supply chain

However, conversion of CaF_2 with carbon to gaseous products such as C_1 to C_4 fluorocarbons is not favoured thermodynamically because of the high temperature and energy required to dissociate such compounds. To this end, plasma technology, which has been researched at NECSA for about three

decades is seen as a viable tool. Over the years, NECSA for instance, has developed and implemented different plasma devices, which operate at input powers as high as 30 kW on laboratory scale and 450 kW on industrial scale. In addition, dielectric barrier discharge and microwave discharge with input power up to 0.5 and 1.5 kW respectively have also been used. However, all these plasma devices work at sub-atmospheric and atmospheric pressure.

For organic synthesis, thermal plasma at low pressure is capable of causing production constraints in terms of the formation of some unwanted by-products. For example, tetrafluoroethylene (C_2F_4) will easily decompose under very high temperature, and recovery is only possible by rapid quenching method of the process. Moreover, the very high temperature of the thermal process leads to erosion of the tip of the electrodes. Kalra et al. [25] pointed out that the need for fast quenching in thermal plasma chemical processes coupled with extensive erosion of the electrodes places limitations on the energy efficiency of the system. Thus, such technological challenges limit its application for high-value fluorochemical products. In addition, high costs are incurred in order to maintain the quenching unit and constantly replace the eroded electrodes. High temperature also places limitations on the selectivity to the desired products.

Conversely, nonthermal plasma systems, where the electron temperature is higher than the translational gas temperature, offer high selectivity and energy efficiency for plasma chemical reactions. The low gas temperature also allows the system to effectively operate without the need for any special quenching unit. However, reseachers such as Fridman and Kennedy [26] have mentioned that large scale industrial production of organic molecules have not been possible due to the relatively low operating pressures and power levels of the nonthermal discharges.

Therefore, the research questions are: *Is fluorochemicals production possible via non-direct fluorination methods using plasma technology? Can the design and operation of high pressure plasma reactor at low current favour the formation of fluorochemicals and hydrocarbons? Can the investigation of the effect of adjustable parameters in the reactor lead to a good selectivity and a good yield of products which are energy efficient, and commercially viable*?

In conclusion, the successful demonstration of the influence of high pressure plasma on fluorocarbon synthesis via non-direct fluorination methods in this research could open up new perspective into organic synthesis.

1.2.2 Hydrocarbon Synthesis

The historical Fischer-Tropsch synthesis (F-T), which is a catalytic thermochemical process, is one of the most common routes for hydrocarbons synthesis whereby syngas is converted into liquid fuels. As mentioned in section 1.1, extensive research are being carried out that involves the use of plasma as

an alternative technology to the conventional catalytic processes for synthesis gas production from natural gas, and the catalytic conversion of syngas into synthetic liquid fuels [6-20]. One area of interest has been the conversion of natural gas (mainly methane) into other value-added chemicals such as acetylene, ethylene, and hydrogen, amongst a few other gaseous hydrocarbons [27].

Historically, research into hydrocarbons synthesis started with the use of high temperature and high energy consumption processes with the commercial production of acetylene from crude oil, coal, and natural gas using an electric arc furnace dating back to over seven decades ago [28]. Commercial electric arc processes such as the Hüls plasma process for converting natural gas, coal, or even crude oil to acetylene as well as ethylene operates at very high voltage, current, and power of 7 kV, 1150 A and 8000 kW respectively [29]. High-energy consumption, issues of catalyst deactivation, coking and high cost associated with catalyst regeneration unit has created the drive for researchers to search for commercial catalysts that are capable of operating without carbon formation [30-31].

Some researchers have shifted their focus to the application of nonthermal plasma for hydrocarbon synthesis in the last two decades [20, 32-47]. According to Brock et al. [39], the indirect conversion of natural gas into synthesis gas using a nonthermal electrical discharge is interesting to researchers because of the characteristics of this type of discharge, i.e. ability to operate at high electron temperature (1 to 10 eV) while the bulk gas temperature remains as low as the ambient temperature. This type of discharge should favour chemical selectivity of syngas to longer chain hydrocarbons in contrast to thermal plasma processes [48].

As for the case of fluorocarbon synthesis, most of the studies undertaken to date in relation to hydrocarbon synthesis using plasma have been at sub-atmospheric and atmospheric pressure conditions. This lack of experimental and theoretical exploration in the field of high and very high pressure plasma using low current (< 1 A) can be attributed to operational and technological difficulties faced in sustaining electric discharges at pressures higher than 1 MPa. In addition, there are other challenges associated with experimental analyses and plasma diagnostics at high pressure because of high plasma frequency and possible instability of the discharges. Nonetheless, application of high pressure plasma in natural gas and syngas conversion is expected to increase carbon chain growth as well as reduce or eliminate problems associated with carbon formation while leading to higher energy efficiency.

1.3 Plasma Technology

Plasma technology has a long history from Davy's invention of the electric arc to one of the first applications of the arc in chemical process, namely, the synthesis of nitric oxide by Birkeland and

Eyde [49] at the beginning of the 20th century. However, it is now seen as one of the 21st century's scientific tools with more researchers looking at extending its application into a broad field of science.

While plasma is commonly referred to as the fourth state of matter [50], a recent publication by Burm [51] presents an argument that plasma should not be referred to as the fourth state of matter as it does not follow the first-order phase transitions observed for solid, liquid and gas. In spite of these differences, plasma is universally agreed to contain positive, negative, and neutral particles that are electrically conductive. In addition, its quasineutrality, whereby negatively charged particles (electrons) are balanced with the positively charged particles in the plasma column, is a distinct characteristic of plasma.

1.4 Plasma Applications

Plasma research has brought great development in the area of semiconductor manufacture over the last few years. However, as the Earth is under great threat in relation to the depletion of the ozone layers as well as global warming due to large emission of carbon dioxide and other greenhouse gases, researchers are beginning to look at exploring the application of plasma even more. Table 1.1 shows some of the few areas where plasma technology has been applied.

Table 1.1: Some application of plasma as it affects our environment and manufacturing sectors

Diverse Areas of Plasma Application		
Application of plasma in relation to the environment	Plasma application in manufacturing	Other areas of application of plasma
• Air pollution control [52] • Purification of water [53] • Waste treatment using high-temperature plasma arc furnaces[54] • Treatment of flue gas [55]	• Computer hard drives and electronics [56] • Magnetic recording media [56] • Microchips and some integrated circuits used in computers [56].	• Surface treatments [57] • Chemical synthesis [58] • Nanoparticles Production [59] • Sterilization of medical/ hospital instrument [60] • Treatment of textile materials [61]

It can be said that plasma is a technological tool with great potential to positively influence every area of our manufacturing sectors as well as our daily lives even though it is in an exploratory stage with respect to organic synthesis of new and environmentally friendly compounds.

1.5 Application of High Pressure Plasma Technology

The majority of experiments conducted at high pressures have been studied under conditions of very high currents (i.e. currents greater than 10 A). This according to Fulcheri et al. [4], could be attributed to the complex technologies involved in generating as well as sustaining electrical discharge coupled with the unavailability of published literature on the electrical behaviour of plasma properties at high pressure and low current. Some of the areas in literature regarding the use of high pressure (up to 10 MPa) and high current (>> 10 A) plasma technologies are:

- Underwater construction and repairs of offshore structures [62]
- Underwater welding and cutting using an oxy-hydrogen flame [63]
- Arc discharge lamps and plasma heaters [63]
- Porous carbon film synthesis [64]
- Analysing the electrical as well as optical properties of landfills and their behavior [64-66]

In addition, researchers such as Lock et al. [67-68] have reported plasma generation in supercritical fluid CO_2 at high pressures with Goto et al. [69] showing the potential of plasma generated at very high pressures to induce chemical reactions in supercritical carbon dioxide. It is therefore seen that the current technological challenge is the development of an energy efficient plasma reactor that will operate at low current and very high pressure.

1.6 Objectives of the Research

The main objectives of this research work were:

- Set up and commissioning of a very high pressure plasma reactor
- Investigation of the influence of pressure, current, and interelectrode gap on hydrocarbon and fluorocarbon synthesis
- Study of the chemical reaction mechanism for the synthesis of hydrocarbons and fluorocarbons
- Identification of the various species formed during the production process and how these species and other reactor operating parameters affect the process
- Comparing the experimental data obtained with theoretical models to explain the behaviour of the plasma process at high pressure conditions

In conclusion, this is a preliminary study aimed at contributing to the very little knowledge available on the application of high and very high pressure in organic synthesis given the few publications at

pressures above atmosphere. It is an exploratory study with respect to hydrocarbon and fluorocarbon synthesis using very high pressure electrical discharge.

Chapter 2

REVIEW OF PLASMA DISCHARGES AND DEVICES

Plasma reactors are devices inside which an electric discharge or plasma is generated.The plasma is generally classified as either a thermal or nonthermal plasma. One of the characteristics of the thermal plasma is their ability to operate at high temperature. Thus, electrons, ions, and neutral atoms are in thermal equilibrium. However, for nonthermal plasma, there is a difference in the temperature of the electrons and the ambient gas particles. While most thermal plasma reactors are operated under vacuum, the nonthermal plasma reactors can be operated up to atmospheric pressure.

Different plasma devices have been used and are being developed for plasma generation on a laboratory scale. The generation of an electric discharge requires a power source. Power sources range from alternating and direct current, to radio frequency and microwave power. The operating condition can determine the regime in which the generated plasma falls. The reactor geometry and configuration can also be a strong determinant of the type of plasma obtained.

The operating pressure in the reactor is seen as one of the parameters capable of influencing plasma behaviour. Thus, researchers are employing the use of atmospheric pressure plasmas as a potential means for a continuous and cost effective solution to vacuum plasma systems. The success of the atmospheric pressure plasmas was viewed as a way of overcoming the poor manufacturability hurdle of low-pressure plasmas by offering a continuous process as well as avoiding the production of unwanted by-products. For detailed information on industrialized atmospheric plasma sources, the reader is referred to the publication of Tendero et al. [70].

2.1 Introduction to Plasma Discharges

Plasma discharges at low-pressure have been researched extensively [71]. However, in this chapter, a brief review will be made of the commonly used plasma devices reported in literature for a general perspective.

The term *electrical arc discharge* is usually used to refer to the phenomenon where inert and nonconductive gases such as air, argon, and helium become conductive because of current flowing

through it at a particular voltage. Practically speaking, when two electrode materials (anode and cathode) depending on the chosen electrode configuration (i.e. axial or parallel) are connected to a high voltage power supply, the passage of a nonconductive gas through the gap or spacing (in millimetres) between the electrodes will lead to the electrical breakdown of the gas, thereby leading to the gas becoming conductive. This electrical breakdown of the gas leads to the generation of electric discharges.

There are various electrical discharge devices that are used for generating plasmas. Some of these include: arc discharge reactor, atmospheric pressure glow discharge (APGD), atmospheric pressure plasma jet (APPJ), corona discharge reactor, dielectric barrier discharge reactor (DBD), gliding-arc discharge reactor, microwave discharge reactor, plasma torch reactor, radio frequency (RF) capacitive discharges, and RF inductively coupled plasmas to mention a few. Usually, plasma discharges can be generated at low-pressure, atmospheric pressure through the more *traditional method*, novel atmospheric pressure and very high-pressure (above atmospheric pressure conditions).

Table 2.1 lists some of the commonly used discharges categorized based on operating pressure and their application in the plasma processing field. A further review of plasma devices used for fluorocarbons and hydrocarbons synthesis is presented in subsequent sections.

Table 2.1: Examples of various discharges and their application in the field of plasma processing

	Low-pressure discharge	**Atmospheric pressure discharge**
Operating Pressure	$10^{-5} < P \approx 10^{-3}$ bar	1 bar or 0.1 MPa
Examples	Capacitively coupled plasma, Glow discharge plasma, Inductively coupled plasma, and Microwave heated plasma.	Arc discharge, Corona discharge, Capacitive discharge, Dielectric barrier discharge and Gliding arc discharge
Industrial Applications	Capacitively coupled plasmas (CCP) are also non-thermal plasma like the glow discharge except that it is generated at a high radio frequency (13.56 MHz). Commonly applied in The semiconductor manufacturing industry for plasma etching and plasma enhanced chemical vapour deposition (PECVD) [72]. Capacitive discharge can be operated at low-pressure (under vacuum) or atmospheric pressure. It is called capacitive because one of the electrodes in the reactor is grounded while the other one is connected to a power supply, thus having the configuration of a capacitor.	Arc discharge is an example of thermal plasma discharge that usually operates at temperatures as high as (10,000 K). It has found application in metallurgical processes, electric arc furnaces, welding, etc. It operates at atmospheric pressure. Gliding arc discharge is an example of non-equilibrium discharge usually operated at atmospheric pressure conditions. It has been applied in the steam reforming process of hydrocarbons.
	Glow discharge plasmas are non-thermal plasmas. It is the type generated in fluorescent lamp, plasma lamp, etc. It is usually generated by direct current or a low radio frequency (< 100 kHz) electric field. Generally, the glow discharge is the most commonly used discharge especially in the semiconductor manufacturing industries. There are normal and abnormal types of glow discharge.	Corona discharge is commonly used for disinfecting water in a swimming pool, photocopying (electrostatic copying), cleaning of the atmosphere through the removal of harmful volatile chemicals, i.e. pesticides. It is generated when high voltage is applied to the tip of an electrode. Thus, it usually involves two asymmetrical electrodes (with one having a curved needle-like point capable of introducing a high potential gradient) and the other can be a low curvature point like a plate. It is also an example of a non-thermal plasma discharge.
	Inductively coupled plasma (ICP) is similar to the CCP except that for CCP, the electrodes are usually placed inside the reactor while for ICP, the electrodes are placed outside the chamber of the reactors. This makes them free from possible contamination that may result from the chemically reactive species. It is generated by electromagnetic induction.	The dielectric barrier discharge can simply be described as a discharge generated between two electrodes with one grounded and the other powered either by DC or RF but bridged by a non-conducting material (dielectric barrier).This is the most common configuration for the generation of a dielectric barrier discharge. It is applied in web treatment of fabrics [73], with major application in the area of water treatment and the production of ozone.

2.2 Thermodynamics of Plasmas

Laboratory and industrial plasmas can be classified using several factors [74] amongst which are:

- Chemical composition
- Degree of ionization (i.e. fully and partially ionized)
- Power source (i.e. direct current, radio frequency, and microwave)
- Pressure (i.e. low pressure, high pressure/atmospheric pressure)
- Temperature (i.e. thermal and non-thermal)
- The presence of an external electric/ magnetic fields (i.e. magnetized and non-magnetized)

Some researchers have tried to generalize thermal plasma to be those operating at atmospheric pressure conditions, and the non-thermal plasma as those operating at low pressure (sub-atmospheric or vacuum conditions). Therefore, the common school of thought is that plasmas become thermal as the pressure tend towards the atmospheric pressure region [26, 71]. Thus, there is a transition from a glow discharge to the arc discharge regime. However, researchers such as Schutze et al. [75], Schoenbach et al. [76], and Staack et al. [77] have shown that it is possible to generate discharges that possess non-thermal, non-equilibrium characteristics at atmospheric pressure and above atmospheric pressure [4].

As mentioned earlier, plasma processing at low pressure has received a lot of attention in the past four to five decades; however, because of the high capital and maintenance costs incurred as a result of employing vacuum facilities, more researchers are beginning to look at the prospect of atmospheric pressure plasma discharges. This was viewed as a good step in the future of plasma as it will open up possible applications to high pressure favoured material science and plasma processes [78]. Many of the current plasma processes in industry requires non-thermal plasma. One of the reasons is that there is a non-equilibrium distribution of energy in non-thermal plasmas. This implies that energies between degrees of freedom are different [79]. According to Staack et al.[77], when dealing with molecular gases used during generation of non-thermal plasmas by applying direct current (DC), it is assumed that the temperature of the electron (T_e) is greater than the electronic excitation ($T_{elex.}$), vibrational (T_{vib}), rotational ($T_{rot.}$),and translational temperatures (T_{trans}) [77]. In addition, the non-equilibrium nature of the non-thermal plasmas allows the possibility of creating some active species without generating excessive heat capable of damaging substrates. It is therefore seen, that non-thermal, non-equilibrium plasmas provide opportunities for wider application in chemical processing or syntheses of some organic compounds, which naturally would have been destroyed under thermal energy conditions.

Therefore, to further understand the dynamics of the behaviour of plasma discharges at low and high pressure, two of the commonly generated discharges: the glow and the arc discharge will be briefly discussed. In addition, a brief review will be given on low and high temperature plasmas together with the various devices that have been designed over the years for these types of plasmas. Greater detail is available in the publications of Tendero et al. [70], and Conrads and Schmidt [80].

2.2.1 The Glow Discharge

The name 'glow' is used to describe this type of discharge because of the luminosity of the discharge. Practically, all discharges carry a degree of luminescence. The glow discharge exists in a regime characterised by higher current than it is required to sufficiently sustain and keep a discharge in the Townsend discharge regime. Hence, it is the discharge regime between the Townsend breakdown regime and arc discharge.

As stated earlier, electrical breakdown occurs when the current flowing through the electrodes in the presence of a strong electric field is high enough at a certain voltage to cause electrons to be freely emitted from the cathode. These electrons then collide with the gas particles in the chamber as it is continuously being accelerated by the electric field until sufficient energy is gained by the electrons, which leads to the neutral gas atoms becoming ionized. The ionized gas becomes an electrically conducting fluid. The de-exicitation of atoms of the gas, going back to lower state of excitation, free their energy by emitting a visible light. This visible light is called the glow discharge. Figure 2.1 shows a simple scheme of the electric circuit for generating a DC glow discharge.

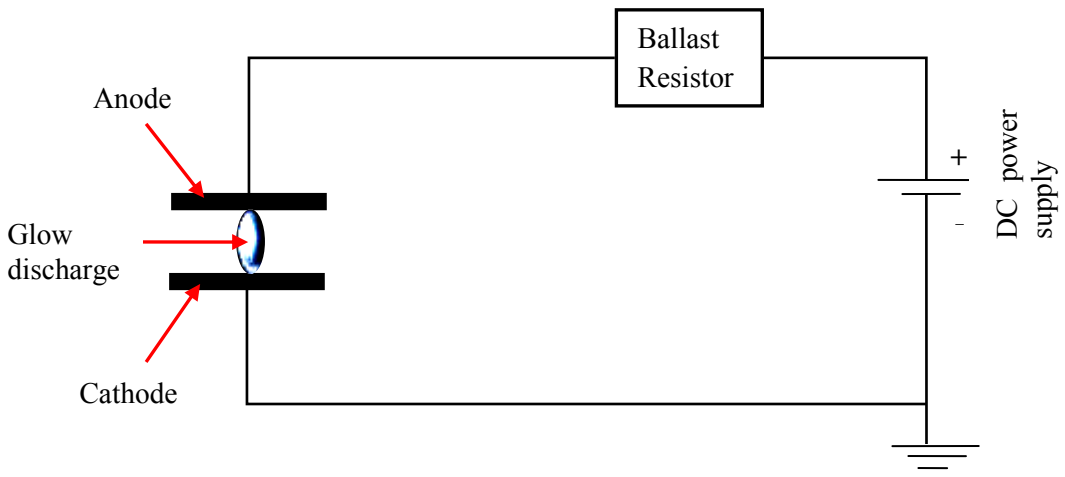

Figure 2.1: A simple electric circuit diagram showing the generation of a DC glow discharge [79]

A glow discharge can be generated using different sources of power supply, but the two commonly used power supply sources are direct current (DC) and radio frequency (RF).

To investigate the characteristics of DC discharges, parameters such as current, pressure, and voltage can be adjusted in order to monitor and control the discharge source. These three parameters are adjusted in such a way that a simple expression that shows the relationship between them can be established. This is obtained by keeping two of the parameters constant while varying one until the whole plasma process is completed.

In contrast to direct current, radio frequency uses applied power, applied voltage, applied blank power, DC bias voltage, and pressure to monitor and control the generation of plasma discharges. However, it must be mentioned that despite the wider range of adjustable plasma parameters available in the use of RF, several research studies have revealed that there is no major difference between RF and DC glow discharges. Researchers such as Winchester et al. [81] have referred to the RF glow discharge as a DC discharge with a superimposed high-frequency field. However, with similarities such as ion and atom bombardment of possible samples by plasma gases, excitation of the sputtered atoms by more energetic electrons and metastable atoms, de-excitation and photon emission; the capability of the RF to be used in the analysis of both conductor and non-conductor materials while DC cannot, is a major difference between the two.

2.2.1.1 The Structure of the Glow Discharge

Although, the focus of this research is the application of a low-current DC arc discharge in hydrocarbons and fluorocarbon synthesis at high pressure, understanding of the extensively studied structure for low-pressure DC glow discharge operation is essential. According to the study of Staack [79], some of the structures that are well documented in textbooks [1-2] for low-pressure glow discharges were also observed for DC microplasma systems at atmospheric pressure. The structures that were observed at atmospheric pressure include the negative glow, faraday dark space, and positive column as seen in Figure 2.2. Hence, a summarized note is presented on the cathode, positive column, and the anode in a glow discharge reactor.

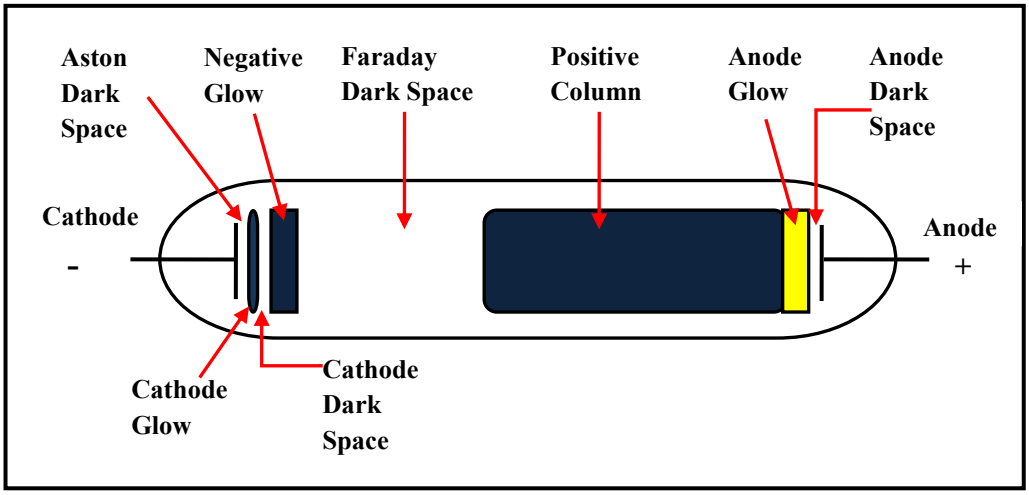

Figure 2.2: Structure of a DC glow discharge [1]

Cathode

In the field of electronics and physics, the electrode from which free electrons are emitted into a discharge tube is referred to as the cathode. Electrons can be emitted from the surface of a cathode by either secondary electron emission or thermionic emission. These two are the most common ways to sustain a discharge. While secondary electron emission is caused by applying a strong electric field to the cathode, thermionic emission is the result of a continuous direct heating of the electrode either through a DC or through RF power supply.

Positive Column

This is a luminous region characterized by low net space charges, but has an electric field strength that is capable of maintaining the degree of ionization required to reach the length of the anode. This region is sometimes known as the positive glow. It extends between the Faraday space and the anode. It has a relatively high electron density as well as high electron temperature even at very low pressure. Generally, the length of the positive column increases as the length of the discharge tube increases when the pressure is constant [80], thus forming a long glow region that is usually striated.

Anode

Although, it is an established fact that in all electrochemical devices, the electrode in which direction the negatively charged anions move is the anode while the cathode is the opposite. The type of device and the operational mode affects the polarity of the electrodes. Thus, in a power-consuming device, the positive side is the anode but the opposite is true in a device which provides power. Therefore, the function of the electrodes is determined largely by the direction in which the current flows, with diodes as an exception (because electrode is named based on the forward current direction). According to Harry [82], the anode serves as the sink to the plasma column in an electric discharge device.

2.2.2 The Arc Discharge

Not only has the arc discharge been categorized as an example of a high temperature plasma that is usually generated at atmospheric pressure, it has also been identified as a type of discharge characterized by low voltage and high current. It has also been said to be an example of discharges that are in thermal equilibrium. However, some research journals and published books by authors such as Raizer [1] on gas discharge physics and Meek and Craggs [2] on electrical breakdown of gases have revealed that the operating gas pressure could determine if an arc discharge will be at thermal or non-thermal equilibrium. Hence, according to Raizer [1], while all discharges that are in thermal equilibrium could be of an arc type, nonthermal equilibrium discharges could also be of an arc type especially at low pressure.

However, it is interesting to point out that a recent research by Fulcheri et al. [4] involving the use of a low-current DC discharge microreactor capable of working pressures up to 20 MPa has shown that it is possible to generate a nonthermal nonequilibrium arc discharge at low-current and very high pressure. Thus, the statement is not conclusive that arc discharges can only be generated at high current, high temperature and low voltage. It also becomes difficult to generalize all arc discharges as an example of thermal equilibrium plasma. However, it remains a fact that the arc discharges are generated at a higher current than the glow discharges as most arc discharges have been a result of glow discharge transition. Greater detail on electrical breakdown of gases and glow-arc transitions is available in Meek and Craggs [2] as well as in the publication of Druyvesteyn and Penning [83]. A simple schematic diagram of the arc discharge method is presented in Figure 2.3.

It is also important to mention that most plasma textbooks and published journal articles on arc discharges are restricted to the area of thermal plasmas with currents ranging from 10 to 2000 A and voltages as low as 15 V with DC depending on the application, especially in metal fabrication processes [82]. Common industrial applications are in the area of arc welding (where the high temperature gradient of the electrode regions are employed) [82], plasma touch (where the high temperature of arc column is transferred for gas heating purpose), and high-pressure discharge lamps (operating at current $\geq$ 1 A and pressure close to 0.1 MPa) amongst others. For further information on arc discharge and its various types, readers are referred to the textbook of Raizer [1] and the journal article of Druyvesteyn and Penning [83]. However, it is important to point out that while most of the previous applications of arc discharge have been at very high temperatures, even with the recent production of carbon nanostructures such as fullerenes and highly graphitized carbon nanotubes, this work focuses on the application of a low-current arc discharge at very high pressure and a low gas temperature.

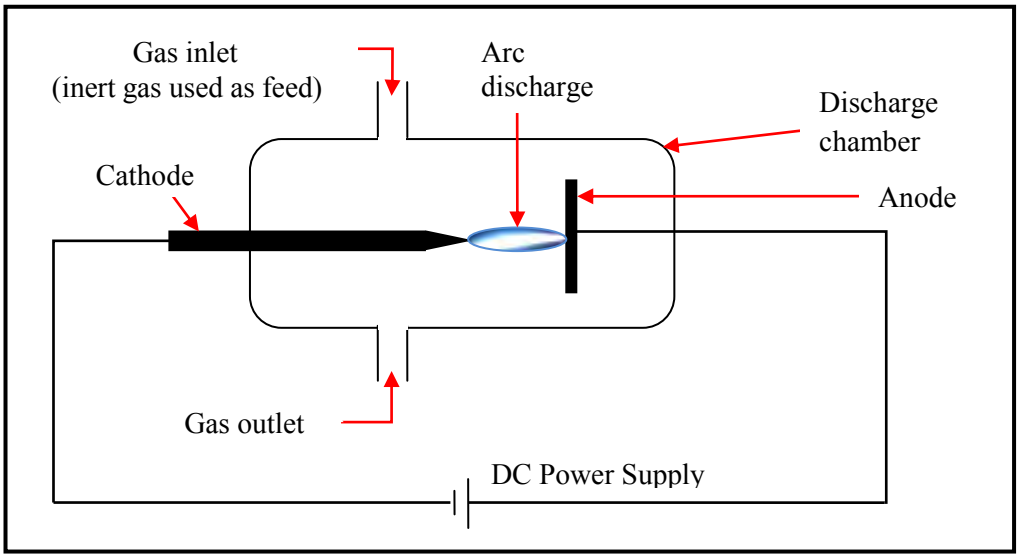

Figure 2.3: A simple electric circuit diagram showing the generation of a DC atmospheric arc discharge

2.2.2.1 The Structure of Arc Discharge

Every type of discharge has similarities in that free ions and electrons are involved in all atomic or molecular gases at low and atmospheric pressure. Most discharges have three basic identifiable potential distribution regions namely; the near-cathode region, the positive column, and the near-anode region [4]. Although, the structures at the near-cathode and near-anode regions may differ for the various discharges based on the operating pressure and the current applied in generating and sustaining the discharge, literature has revealed that these three basic zones or regions are common to most of the discharges at low pressure [84], atmospheric pressure [77], and above atmospheric pressure [4].

A schematic diagram of the structure of an arc discharge as well as the scheme showing the axial variation of associated drop in voltage at the various zones is shown in Figure 2.4, while Figure 2.5 gives the nonthermal and thermal classification of plasma based on the electron and gas temperature variation with pressure.

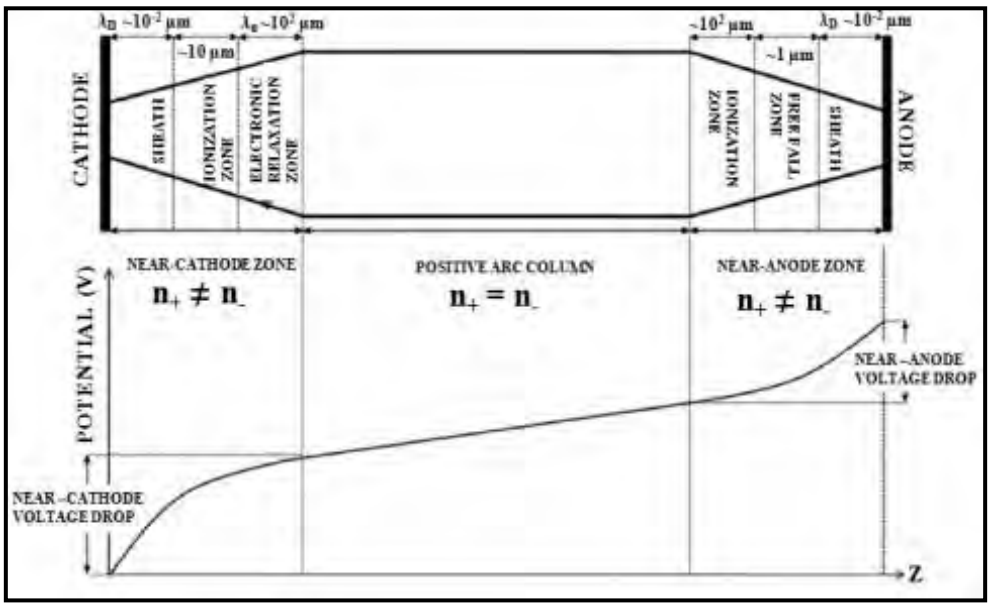

Figure 2.4: Schematic representation of an arc discharge and the potential distribution in the arc in terms of voltage drop [4, 85]

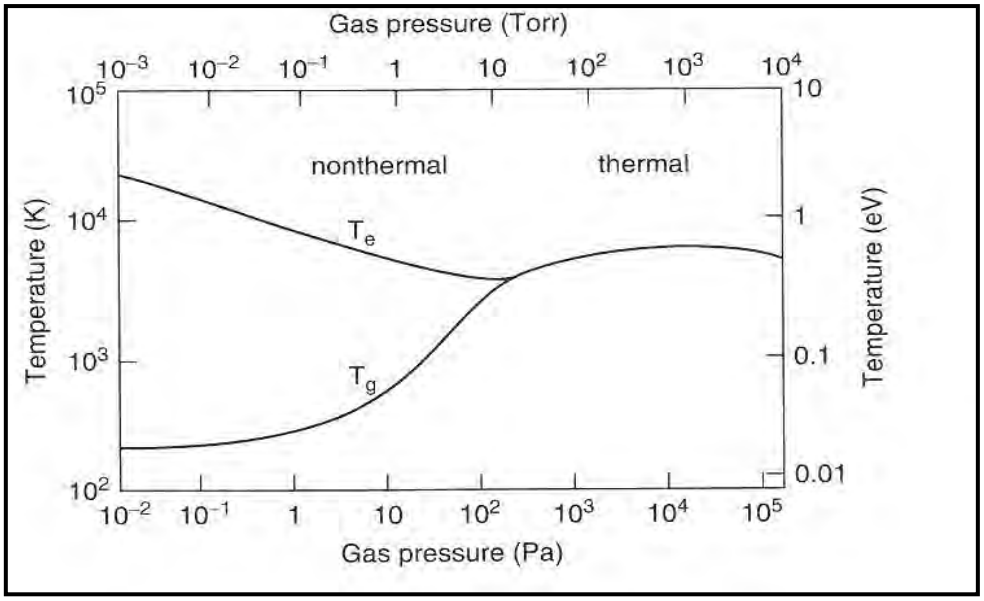

Figure 2.5: Graphical representation of the variation of electron and gas temperatures with gas pressure for an arc discharge up to atmospheric pressure (extracted from Brown [86])

The Near-Cathode Zone

More attention has been given to the near-cathode zone in published literature as it is seen to be more crucial in the performance of arc devices than the near-anode zone [87]. This zone is usually characterized by a strong nonlinear voltage drop. The strong difference in electrical behaviour in this zone can be attributed to the difference in the densities of the negative and positive charges. Hence, as the plasma approaches the near-cathode and near-anode zones, the characteristics become more nonequilibrium [4]. This zone usually has a higher cathode fall in voltage in comparison to the anode fall in the near-anode zone.

The Positive Arc Column

This zone has a balance of negative and positive charges respectively (quasi-neutral) [88] and thus the particle densities in this zone are in equilibrium. Therefore, the axial variation of the voltage drop in this zone can be said to be quasilinear [4]. Another characteristic of this zone is the low electric field and high temperature, which is of importance in heating the gas.

The Near-Anode Zone

This zone has different densities for the negative and positive charges. In addition, the temperature gradient is high with a relatively high electric field for the positive and negative charges in this zone. Researchers such as Benilov [87] report that the temperature is higher at the near-anode zone than the near-cathode zone for high-current arc discharges, but lower than the near-cathode zone for low-current arc discharges.

2.2.3 Discharge Regimes

One of the most accurate ways to distinguish between discharges is by using their observed current-voltage characteristics, the current density, and the particle energy density. These characteristics are dependent on the applied voltage, discharge current, electrode material, gas, geometry of the electrodes, pressure, temperature, and the dimension of the discharge tube [85]. Thus, transition from one type of discharge to another can be observed from the current-voltage characteristics curve of a DC electric discharge of a gas as shown in Figure 2.6.

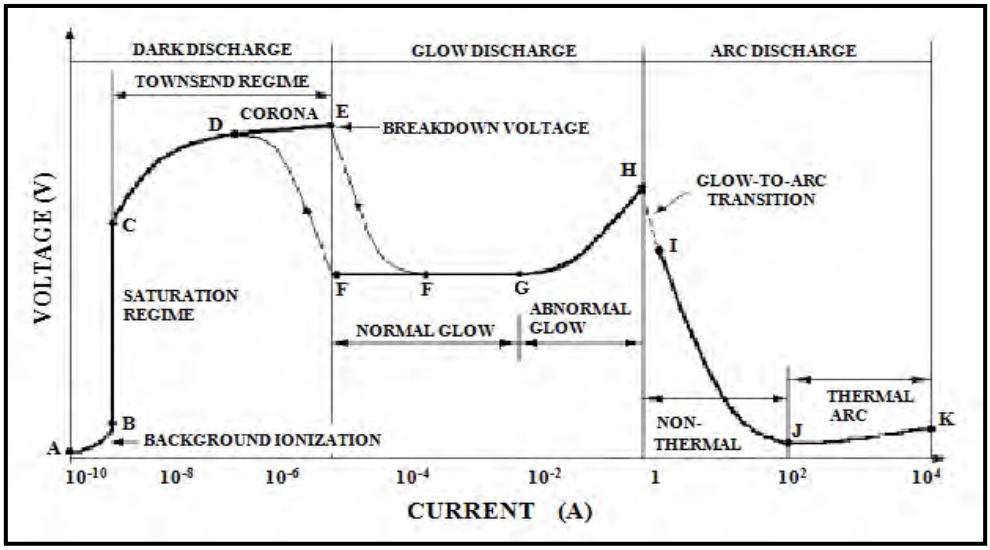

Figure 2.6: Generalized voltage - current characteristics of discharges showing the transition from the dark discharge to the glow discharge and finally to the arc discharge regime at low pressure [85]

At a relatively low current (less than a microampere), the electric field strength is not sufficiently high to generate self-sustained discharges, thus at point A, only naturally free electrons are ionized with a low charge density. This stage (A-B) as indicated in Figure 2.6 is referred to as the background ionization stage because the ions and the electrons are ionized by background radiation. However, as the voltage is increased across the discharge tube, the electric field becomes sufficient to energize the electrons, which consequently ionizes the gas until a point (B-C) is attained where current becomes saturated and thus, the current becomes constant while the voltage continues to increase. The gas becomes more ionized at point (B-C) because the electric field becomes higher and therefore more electrons are energized. However, point (C-D) is the point before the corona discharge (D-E) where the density of the electrons is still unable to generate a self-sustained discharge. As observed in Figure 2.6, the current begins to increase exponentially from point C-D through to E. Hence, a corona discharge is generated due to the strong electric field at the pointed tip of the electrodes. It must be mentioned that at a sufficiently high current, the discharge generated at point (D-E) can be luminous enough that it is often confused as a glow discharge. However, as seen in Figure 2.6, the current is

still low, hence the corona discharge in this region is dark and in the Townsend regime. It is important to note that the corona discharge generated at point (D-E) is influenced more by the strong electric field around the sharp point or tip of the electrodes than the electrical potential across the electrodes. In the Townsend regime as shown in Figure 2.6, electrical breakdown occurs as more ions bombard the surface of the cathode resulting in the generation of secondary electron emissions, which helps to self-sustain the discharge. Thus, a glow discharge is observed (F-H) at low current. The glow discharge observed from point F-H is of two types; F-G being the normal glow and G-H being the abnormal glow.

A constant voltage with a continuous increase in current over several magnitudes characterizes the normal glow discharge. This also leads to an increase in the diameter of the discharge. As the current continues to increase, a stage is reached where the discharge covers the entire surface of the cathode. At this stage, the current density of the discharge needs to be increased in order to increase the total current further. As more energy is added to the system, the minimum Paschen value required to keep the discharge as a normal glow is exceeded, hence, an abnormal discharge is observed as in (G-H). This region is characterized by an increase in the cathode fall potential and it is brighter than the normal glow.

As the voltage as well as the current increases, the ions bombarding the cathode also increase. Hence, an increase in the cathode current density is expected. This eventually leads to the overheating of the cathode, and electrons become emitted thermionically. At this stage, the current is observed to greatly increase, leading to a glow to arc discharge transition (GAT) identified as H-J in Figure 2.6.

Besides thermionic emission, which is the result of overheating of the cathode leading to the transition from abnormal glow to arc discharge, it is also possible to have a transition from the normal glow to arc discharge. According to Yahya and Harry [84], the transition from glow to arc discharge is a cathode effect. Therefore, a transition occurs from the abnormal glow region to the arc when the cathode is relatively small, but when the cathode is sufficiently large, a continuous increase in current leads to the contraction of the positive glow column and finally a direct transition from the normal glow region to the arc region is experienced. In conclusion, Fan [89] suggest that increasing current while keeping gas pressure constant or increasing gas pressure under constant current are common ways of experiencing glow-to-arc transition.

Table 2.2: Comparison of cathode, anode, and plasma column properties of low-pressure glow and atmospheric pressure arc discharges [82]

Discharge Regime	**Representative values**	
	Glow	**Arc**
Cathode process	*Secondary emission*	*Thermionic / field emission*
Fall voltage (V)	300	8 - 15
Fall thickness (mm)	10	0.1 - 10
Current density (A mm^{-2})	0.1	10 - 10^4
Anode		
Fall voltage (V)	20- 30	3 - 12
Fall thickness (mm)	10	0.1
Current density (A mm^{-2})	0.1	10
Plasma Column		
Voltage gradient (V mm^{-1})	1- 10	1
Current density (A mm^{-2})	2×10^{-3}	10
Mean temperature of neutral particles (K)	Close to ambient	6000
Number density (electrons m^{-3})	5×10^{15}	-

2.2.4 Stability of Plasma Discharges

Overcoming the instabilities of plasma discharges in high-pressure nonthermal plasmas has been a general challenge during experimental investigations into the application of discharges in surface treatment and plasma enhanced chemical vapor deposition (PECVD) amongst others [1,77]. According to researchers such as Kunhardt [78], to sustain glow discharges at pressures higher than 0.1 MPa is difficult. This is because the current density increases with the pressure until a maximum point where instabilities are experienced which leads to glow-arc transition [4]. Thus, Kunhardt [78] describes glow-to- arc transition as the transition from a nonthermal to a thermal discharge.

Authors such as Staack et al. [90] have attributed this instability to the onset of the ionization overheating instability and some other instabilities in the electrical behaviour or characteristics of DC discharges at higher pressures which has led to transition from the glow discharge to arc discharge regime as reported by some researchers [4,77].

While there are various suggestions as to how to overcome these challenges, it is inappropriate to generalize all these suggestions for all issues relating to instabilities of the plasma discharges. Some of the recommendations include; wall cooling for low-pressure systems as this helps to prevent the

increase in gas temperature, which can lead to instabilities. However, this recommendation has been reported to be ineffective for DC microplasma discharges at atmospheric pressure [90].

According to the investigation of Staack et al. [77] on DC glow discharges of helium, hydrogen, argon, and nitrogen at atmospheric pressure, it was observed that these gases though nonthermal, become "warm" when the temperatures of the gases are in the range of 300 to 1500 K depending on the discharge power and the gas [90]. Thus, instability in microplasma discharge was observed at the temperature range between 300 and 1500 K.

In addition, Fulcheri et al. [4] reported the glow-to-arc transition at nonequilibrium conditions for low-current DC discharge at very high pressures. Investigations by Fulcheri et al. [4] show that the glow discharge was observed to be stable at low pressures ranging from 0.1 to 1 MPa. They reported an observed transition to the arc discharge region at moderately high pressure, specifically from 1 to 5 MPa where they stated that the fluctuation in the root mean square (rms) voltage value was observed to be higher than 10%. They further stated that stability was observed between the pressure range of 5 and 7 MPa while the discharge still remains in the arc region. Thus, from the investigations of Fulcheri et al. [4], the instability sometimes observed between the pressures ranges of 5 to 7 MPa could be explained by an arc jump phenomenon (taking down the arc from its initial hitching point during the discharge and hanging it to a more stable point). However, Fulcheri et al. [4] concluded that the process would not have any significant change on the behaviour of the rms voltage curve since the arc jump is irreversible.

2.2.5 Low-Temperature (Nonthermal) Plasmas

Low-temperature plasma is a term used to refer to electrical discharges in which the gas temperature is very low even down to its surrounding temperature while the electron temperature is high enough to break molecular bonds. This is assumed to happen when the gas temperature and the electron temperature are not at equilibrium. This is also generally classified as a nonthermal plasma. Glow discharge is a common example of low-temperature and low-pressure phenomenon.

Low-temperature plasma has been applied over the years to applications such as surface modification (e.g. photography, printing, semiconductors, textiles, etc.) and organic synthesis. Although, literature surveys reveal that there has been extensive research into the industrial applications of low-temperature plasmas for more than four decades ago, the industrial application of low-temperature plasma in the area of chemical synthesis has only been successful for the synthesis of ozone, along with a few other compounds [74]. However, on-going research has witnessed the application of low-temperature plasma technology to the production of new materials such as fullerenes [91].

One of the major differences between thermal and nonthermal plasma lies in the dependence of a thermal plasma on the equilibrium temperature of the system as a function of the energy density of the discharge, while a nonthermal discharge is dependent on the strong effect of the electric field. This feature in a nonthermal discharge makes it possible to maintain its nonequilibrium nature. Thus, in nonthermal plasmas, the energy supplied into the system mostly has direct impact on the electrons and ions in what is referred to as partial ionization of the plasma rather than full interactions with all particles within the system. Therefore, the neutral atoms essentially do not feel the electric field whereas the charged particles are accelerated by it.

2.2.5.1 Low-Temperature Plasma Discharge Apparatus

While different apparati have been developed in various fields of applications of plasmas, only a brief review is presented in Table 2.3. Since the focus of this research is on the synthesis of organic chemicals, most of the reviews are on plasma discharge generating devices that are specifically used for chemical synthesis.

Table 2.3: US patents of some electric discharge apparati used for organic synthesis and other applications at low temperature

Patent Number	Date of Issue	Inventor/s	Assignee	Title
2,191,797	27/02/1940	G.L.Matheson		Apparatus for treating material with silent electric discharge.
2,689,217	14/09/1954	W.J.Cotton	Mattieson Chemical Corp., Virginia	Production of chlorine oxides by Electric Discharge
3,205,162	07/09/1965	A.F.MacLean	Celanese Corp. of America, New York, NY	Electrical discharge process and apparatus. Applicable at atmospheric pressure for chemical reaction such as hydrogenation of organic compounds such as aliphatic hydrocarbons.
3,475,308	28/10/1969	J.C.Burleson, W.F.Yates.	Monsanto Co. St. Louis, MO	Preparation of Alkylene Oxides in a Silent Electric Discharge.
3,954,585	05/04/1977	R.J.Lagow, L.L.Gerchman, R.A.Jacob	Massachusetts Institute of Technology Cambridge, MA	Synthesis of Trifluoromethyl-Substituted Compounds.

Table 2.3 (continued): US patents of some electric discharge apparati used for organic synthesis and other applications at low temperature

Patent Number	Date of Issue	Inventor/s	Assignee	Title
4,016,448	04/05/1977	W.L.Nighan, W.J.Wiegand	United Technologies Corp., Hartford, CT	High-Power electric discharge method and apparatus for laser chemical synthesis.
5,314,539	24/05/1994	R.W.Brown, I.H.Coopes, J. Fusca, K.J. Gifkins, J.A. Irvin.	Eastman Kodak Company. Rochester, NY	Apparatus for plasma treatment of continuous material
5,698,164	16/12/1997	T. Kishioka, K.Nagata, N.Nishida, M.Nieda.	Takashi Kishioka, Osaka; Okayama-Ken; Ohnit Co; Ltd. Japan	Low-Temperature plasma generator for removing an offensive odour, sterilizing bacteria & water purification.
5,908,539	01/06/1999	A.Y. Raymond, S.D. Ferencz, H. Zhong-Quiang.	Wisconsin Alumni Research Foundation, Madison, Wis.	Method for reactions in dense-medium plasmas and products formed thereby.

Table 2.4: Some other non-US patents used in low-temperature plasma applications

Patent Number	Date of Issue	Inventor/s	Assignee	Title
05/52102	08/07/2005	F. Boudjemaa, E. Duval-Brunel, N. Huon, L. Fulcheri, T. Planas, Jean-Damien Rollier,	Renault SAS, France.	Device generating plasma for a multi-fuel reformer.
05/09731	23/09/2005	F. Boudjemaa, E. Duval-Brunel, T. Planas, N. Huon, L. Fulcheri, Jean-Damien Rollier	Renault SAS, France.	Plasma generator and hydrocarbon reforming device.
20100187999	29/07/2010	A. Agneray, M. Pariente	Renault SAS, France.	Radiofrequency plasma generation device.

2.2.6 High-Temperature (Thermal) Plasmas

Plasma technology is a prospective research field where extensive research has been carried out. Previous research has revealed the applications of high-temperature plasma reactors in the area of extractive metallurgy such as the production of molybdenum metal from its ore (molybdenum disulfide) [92], the synthesis of ceramic powders [93] as well as the synthesis of inorganic compounds such as the synthesis of tungsten and tantalum carbide [94]. The production of acetylene and hydrocyanic acid using high-temperature plasma [95] is viewed as a success in the area of synthesizing organic compounds. Another area in organic synthesis where high-temperature plasma has been applied is the synthesis of carbon-fluorine reactions exemplified by the production of tetrafluoroethylene through the reaction of carbon and tetrafluoromethane [96]. Other areas include the preparation of high-purity fused silica [97], production of mullite glass ceramics [98], and production of cement [99].

In summary, a review of published textbooks and journals shows that very few organic products such as acetylene have been produced on a commercial scale using high-temperature plasma, while no organic product is reported to have been successfully produced using very high-pressure plasma. Thus, this research is a big step towards the production of important organic products on a laboratory scale using very high-pressure plasma.

Literature surveys for some high-temperature plasma generating devices that has been used in organic reactions are presented in Table 2.5, while Figure 2.7 (A-B) shows some thermal plasma devices that have been employed in plasma chemical processes. Additional information is available in Iberrson and Thring [100].

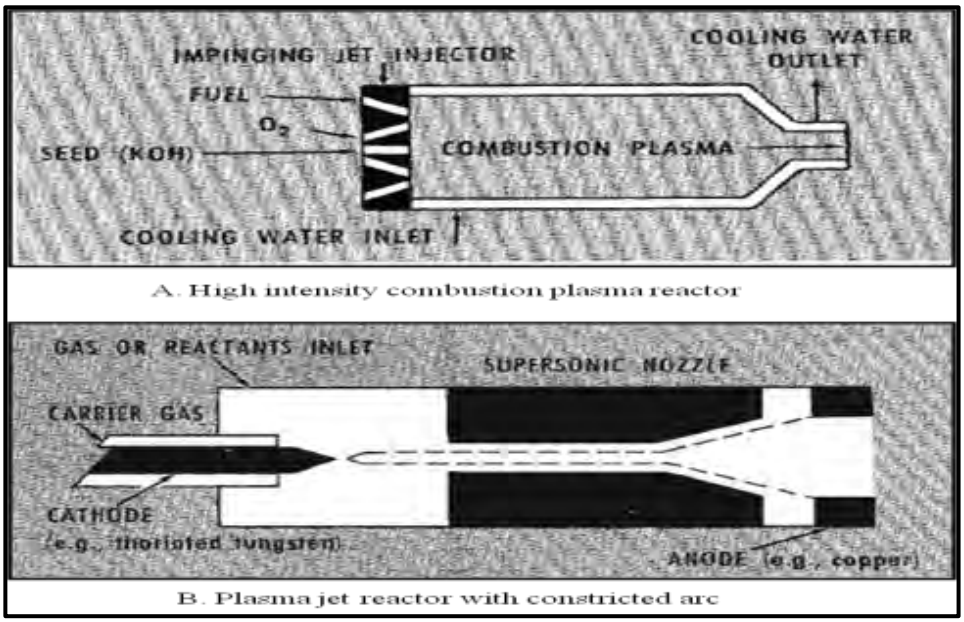

Figure 2.7: Examples of thermal plasma generating devices (extracted from Iberrson and Thring [100])

Table 2.5: US patents of some electric discharge apparati used for organic reactions at high temperature

Patent Number	Date of Issue	Inventor/s	Assignee	Title
3,516,921	23/06/1970	J.P.Manion, D.J. Davies.	Allis-Chalmers Mfg. Co. Milwaukee, WI	Apparatus for magnetic stirring of discharge plasma in chemical synthesis.
3,658,673	15/04/1972	T Kugler Sins, J.Silbigier Basel.	Lonza Ltd. Gampel/Valais, Switzerland.	Process for carrying out chemical reactions under the thermal action of an arc discharge.
3,895,796	21/03/1972	R.Bainbridge.	Ionarc Smelters Ltd. Vancouver, BC, Canada.	Chemical process in high enthalpy thermal environment.
3,840,750	08/10/1974	R.D.Davies, T.N. Meyer, R.L. Blizzard.	Plasmachem Inc. Santa Ana, CA.	Plasma apparatus for carrying out high-temperature chemical reactions.
3,904,501	09/09/1975	R.J.Lagow, R.F. Bassour, D.K.Lam, L.A. Shimp.	Massachusetts Institute of Technology, MA.	Fluorine plasma synthesis for carbon monofluorides.
3,954,954	04/05/1976	R.D. Davies, T.N. Meyer, R.L. Blizzard.	Plasmachem Inc. Santa Ana, CA.	Plasma method and apparatus for carrying out high-temperature chemical reactions.
4,472,172	18/09/1984	T.J. Dougherty, S. Korman, C. Sheer.		Arc gasification of coal. (An arc discharge that converts reactive material made up of mixtures of pulverized coal and steam to gaseous products consisting hydrogen, carbon monoxide and carbon dioxide).
4,566,961	28/01/1986	H. Diaz, P. Jorgensen, P. Vernet.	The British Petroleum Company P.L.C (London, GB2).	Electric arc conversion process.
5, 409,584	25/04/1995	W.M.Sackinger	University of Alaska, Fairbanks, Ak.	Electrical method for the conversion of molecular weights of particulates. (An electrical apparatus that converts mixtures in particulate form into new compounds)

Table 2.6: Comparison between some of the plasma process parameters for low and high temperature plasma [101]

Type of Plasmas	High-Temperature Plasma	Low-Temperature Plasma
Frequency (MHz)	-	2 - 40
Temperature (K)	1- 4 × 10^4	77 - 1300
Pressure (Bar)	1.013	(0.0013 - 1.33) ×10^{-2}
Discharge current density (A/cm^2)	10 - 10^5	0.001 - 1
Degree of ionization	≈ 1	10^{-8} - 0.8
Applications	ammonia synthesis	Surface modification
Remarks	Electrons, ions, and species are in thermodynamic equilibrium	Species are not in thermodynamic equilibrium since the temperature of ions and neutral particles is significantly lower than the electron temperature.

2.3 Review on the Production of Fluorochemicals

The history of the fluorochemical industry spans from the time of the successful isolation of elemental fluorine by Moissan's in 1886 through what is called the first attempt at producing organic fluorides via the conversion of chlorocarbons to chlorofluorocarbons (CFCs) with the aid of antimony trifluoride (SbF_3) by Swarts in 1892, and the interesting synthesis of dichlorodifluoromethane (Freon-12®) in 1931 [102]. The history is filled with some of the notable contributions to the field of fluorine chemistry with a few being honoured with the prestigious "Nobel Prize". However, one of the discoveries that cannot go unmentioned with regards to this research work is the production of fluorocarbons and some derivatives from hydrogen fluoride by applying external voltage as reported by Simons in 1949 [103]. This discovery has gone a long way in influencing the production of fluorochemicals.

Therefore, the aim of this section is to give a summary on the fluorine chemistry from an industrial perspective. This is important in order to know the historical trend of the fluorine chemical industry, and the future prospect of this gigantic industry. Figure 2.8 below gives a summary of the fluorine chemical industry in an organisational way.

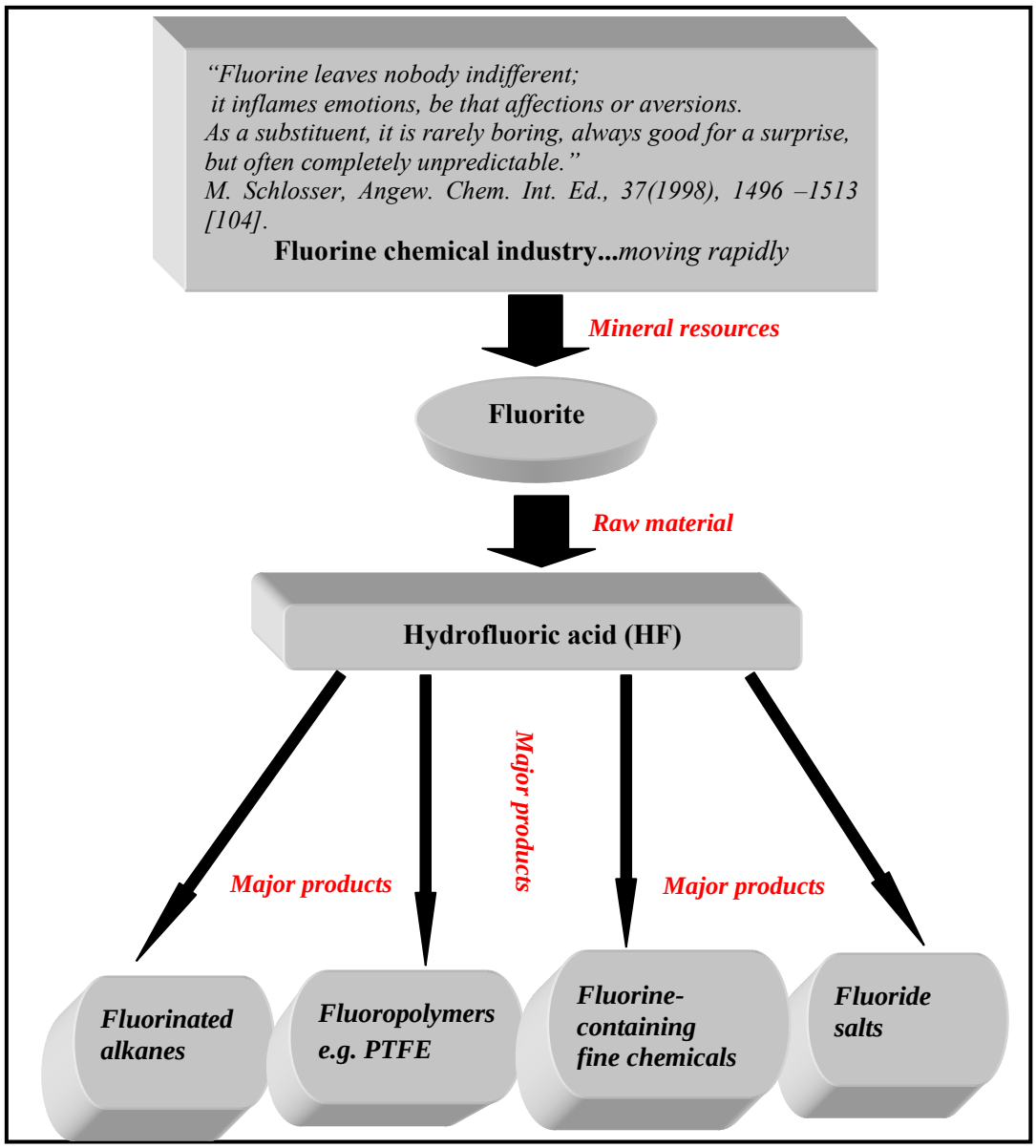

Figure 2.8: A descriptive chart of the fluorine chemical industry with its major products

The field of fluorine chemistry has brought with it many surprises such as the "unintentional" discovery of polytetrafluoroethylene (PTFE) by Plunkett [105], while many more are yet to be *unravelled* (*unravelled* in this contest speaks of more surprises to come from the fluorine chemical industry). According to Dolbier [106], the 21st century may witness what would probably be referred to as the "renaissance" of the fluorine chemistry field. This view is supported by the recent need for more environmentally friendly refrigerants, modern exploratory research in the area of medicinal and pharmaceutical chemistry which shows fluorinated pharmaceutical products to increase above 18% at the beginning of year 2000 from a previous 2% as at the 1970s [107]. In addition, some fluorinated compounds have been identified as anticancer and antiviral agents. Additional information about some of the biological roles of fluorinated compounds can be found in Isanbor and O'Hagan [107] and Kirk [108].

It is interesting to know that while some researchers are striving to improve on the generation of new environmental friendly fluorocarbon gases, some researchers are also looking at the possibilities of extending low-temperature plasma into more applications at atmospheric pressure conditions. Thus, this research is unique in its contributions to the field of high-pressure plasma chemistry and plasma processing, as well as the generation of environmental friendly synthetic fuels and fluorochemicals along with areas such as renewable energies.

2.3.1 Review of Electrical Discharge Devices used for the Production of Fluorochemicals

Literature review shows that there are few plasma technologies that have and are still being employed in the organic synthesis of fluorochemicals. However, researchers like Baddour and associates [109] have published some works on fluorine reactions in plasma. One of these articles was on the conversion of tetrafluoroethane (CF_4) into tetrafluoroethylene (C_2F_4) in a high-intensity carbon arc reactor [96]. Figure 2.10 is a picture of the high-intensity carbon arc reactor employed by Baddour and Bronfin [96].

As mentioned in section 1.2, fluorspar has the potential for great industrial and economic benefit to South Africa and the world at large. In the organic syntheses of fluorocarbons, one of the commonly used household products from fluorspar is polytetrafluoroethylene resin generally known as "Teflon®". Different plasma discharge techniques and devices are reported in literature to have been used for the synthesis of fluorocarbons amongst which are: the carbon arc reactor, the plasma-jet reactor, and the high-voltage discharge. A summarized table of the various reactor designs are presented in section 2.4, while a review of the carbon arc reactor, plasma-jet reactor and the high voltage, low current discharge is discussed in sections 2.3.2 to 2.3.4.

According to Bronfin [110], every chemical reaction leading to the synthesis of organic compounds in thermal plasma reactors are expected to follow a commonly used scheme. In this scheme, the first stage in the chemical syntheses process in the plasma reactor is the generation of the plasma. This is followed by the chemical combination stage. This stage involves the introduction of the second reagent B in post-generator mixing. Post-generator mixing refers to a stage where reagent B is only introduced after reagent A, which is the first feed gas, has generated highly reactive plasma streams [110], and thus capable of initiating A-B combination reactions leading to the formation of intermediate species. According to this reaction scheme, the third stage is the quenching of the intermediate products. Several researchers have proposed different methods for quenching; amongst these are the cold surface method of Timmins and Ammann [111], the Fluidized bed method adopted by Goldberger and Oxley [112], and the cold gas entrainment technique used by Grey and Jacobs [113]. Figure 2.9 gives a description of the scheme as reported by Bronfin [110].

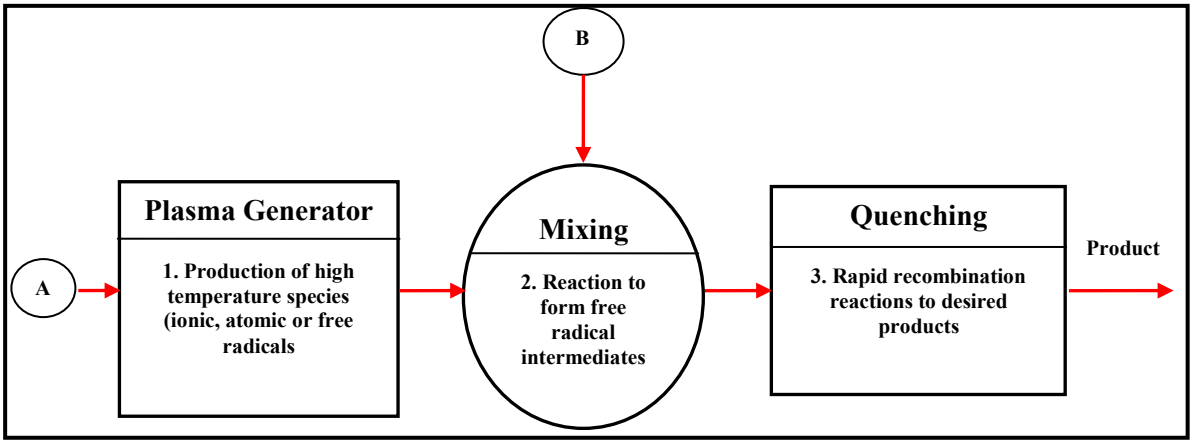

Figure 2.9: The over-all thermal plasma reaction process in the electric discharge reactor [110]

2.3.2 The High-Intensity Carbon Arc Reactor

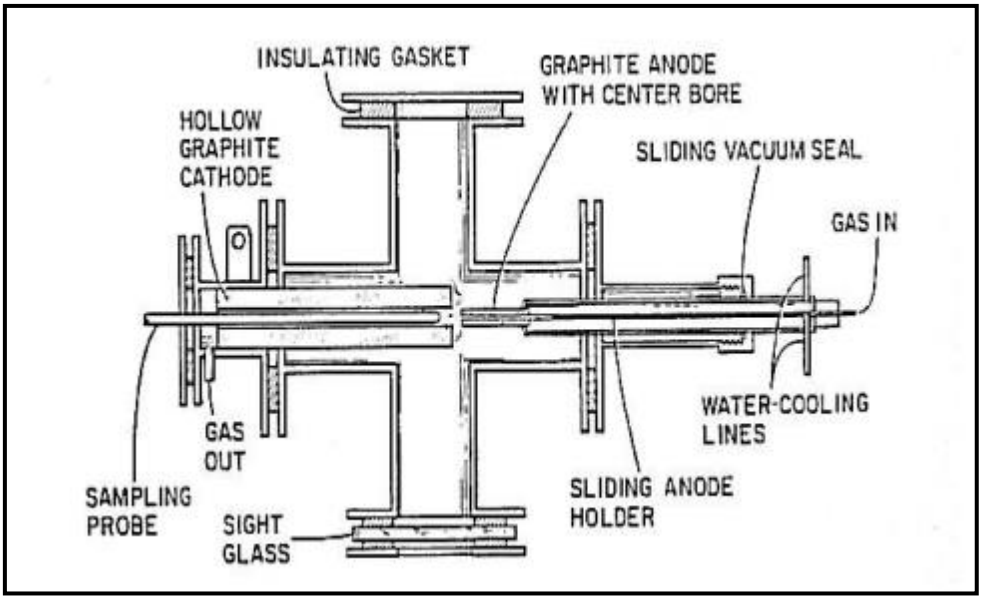

Figure 2.10: High-intensity carbon arc reactor (extracted from Baddour and Bronfin [96])

The name "high-intensity arc" was given because of the high current density at the anode, which eventually leads to the corrosion of the electrode at the anode in the arc reactor at high voltage. Baddour and Bronfin [96] employed this high-intensity carbon arc reactor for the syntheses of tetrafluoroethylene (C_2F_4) by reacting tetrafluoromethane (CF_4) with carbon (C) at high-temperature conditions ranging between 2000 and 10000 K. This was achieved by introducing the gas feed into the high-temperature luminous region of the arc discharge. However, this was only after the high-intensity reactor was considered suitable as a chemical reactor. According to Baddour and Bronfin [96], some of the features of the high-intensity arc reactor that have made it suitable for consideration as a chemical synthesizing reactor include:

- The extremely high temperature range (2000 to 10000 K) observed in the reaction zone of the reactor;

- The various reactive species observed to be produced in high concentration at the high temperature range of 2000 to 10000 K;
- The reactor was small and versatile (not limited to fluorochemical synthesis). Thus, the reactor was characterised by short response times to energy input as well as fast rates of reaction.

The arc reactor has electrically insulated ports with the reaction chamber having a of diameter of 76.2 mm at the cross centre port. The plasma source was a direct current (DC) power supply unit connected to the electrodes in an axial configuration. The hollow graphite cathode of 50.8 mm outer diameter was fixed at one end of the port while the anode made of graphite rod is centred-bored with an outer diameter of 12.7 mm. The hole in the graphite anode allows for the free flow of the feed gas directly into the plasma formed across the gap between the cathode and the anode electrodes. A sight glass was placed, as in Figure 2.10, at a port close to the electrode ports to allow for the viewing of the arc discharge formed. The reactor has gas inlet and outlet points through which the reactant gas is fed and exits respectively. The metal parts of the reactor are cooled with water to prevent overheating of the inside of the reactor. In addition, a water-cooled sampling probe through which the gas sample is taken for analysis in the gas chromatography was placed at the last port of the reactor. The arc discharge was initiated by allowing current to flow across the small gap between the electrodes leading to the ionization of the interrupting gas at high voltage.

Baddour and Bronfin [96] further comment that the process described for the formation C_2F_4 using the high intensity carbon arc reactor should be taken as a representative route for synthesizing all fluorocarbon systems in the pressure range of 0.01 to 0.10 MPa via thermal plasma. Additional information is available in Baddour and Bronfin [96].

2.3.3 The Plasma-Jet Reactor

Bronfin and Hazlett [114] employed the plasma-jet reactor for the synthesis of nitrogen trifluoride gas (NF_3) by mixing fluorides such as CF_4 or SF_6 with the nitrogen plasma-jet. The plasma-jet is similar to the high-intensity arc reactor. However, the plasma-jet as shown in Figure 2.11 used the stick and cylinder electrode configuration. This configuration has been commonly employed where tungsten is used as one of the electrode material. Thus, the stationary electrode is the cathode while the anode is a movable cylinder made of copper. The stick and cylinder configuration is presented in Figure 2.12.

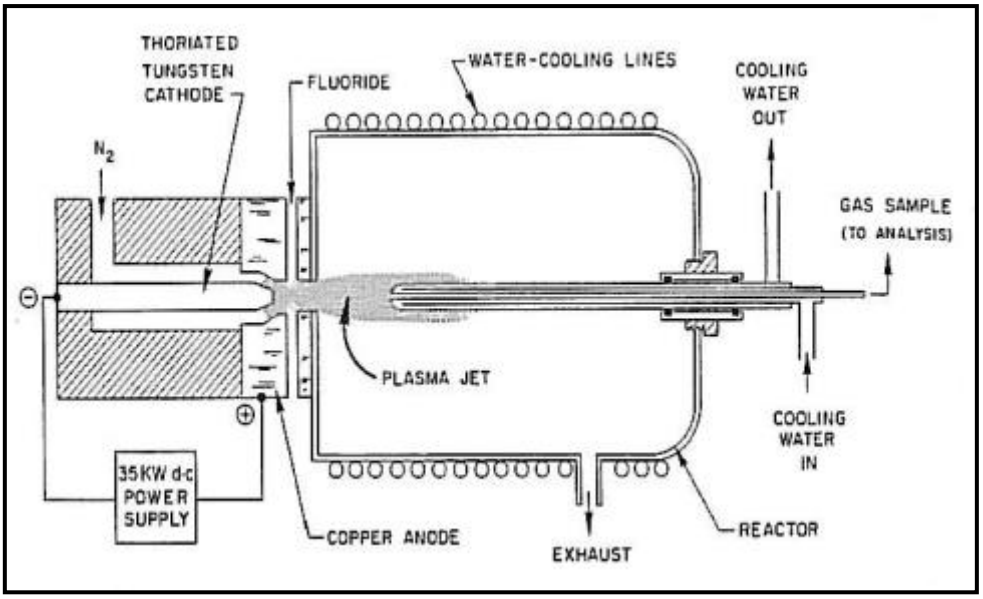

Figure 2.11: Plasma-jet reactor (extracted from Bronfin and Hazlett [114])

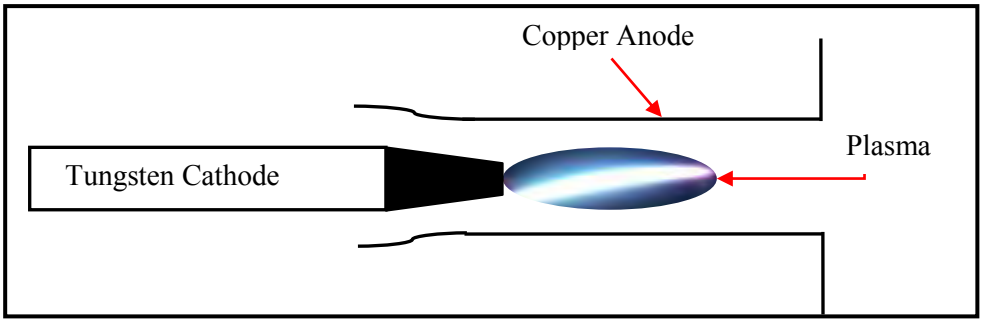

Figure 2.12: The stick and cylinder type of electrode configuration [115]

A high voltage direct current (DC) power supply unit powers the plasma generator. As in Figure 2.11, a direct connection to the cathode tungsten electrode was made from the power supply unit. A small gap exists at the top of the cathode rod through which one of the reactants was fed into the reactor. The reactants used in the syntheses of fluorocarbons were dry nitrogen gas and fluoride. The nozzle of the copper anode, with an internal diameter of about 7.95 mm, was placed close to the tip of the cathode as shown in Figure 2.11. The plasma-jet generated between the inter-electrode distances (gap) was passed into the water-cooled cylinder for the quenching process. The water-cooled cylinder has an internal diameter of about 1.2 mm, and a volume capacity of about 2.8 litres with both inlet and outlet points. The cylinder was properly sealed to prevent leakage of gases. A sight window was fitted into the design, as was the case with the high-intensity arc reactor. This was to make it possible for the visualization of the discharge via a camera, as it was dangerous to look directly into the discharge chamber. More details on the procedure for this reactor can be obtained in the publication of Bronfin and Hazlett [114]. The use of plasma-jet reactor is also an example of fluorochemical

syntheses via thermal plasmas, and has also been used for the synthesis of sulphur hexafluoride (SF_6) gas [96].

2.3.4 The High –Voltage Discharge Reaction Tube

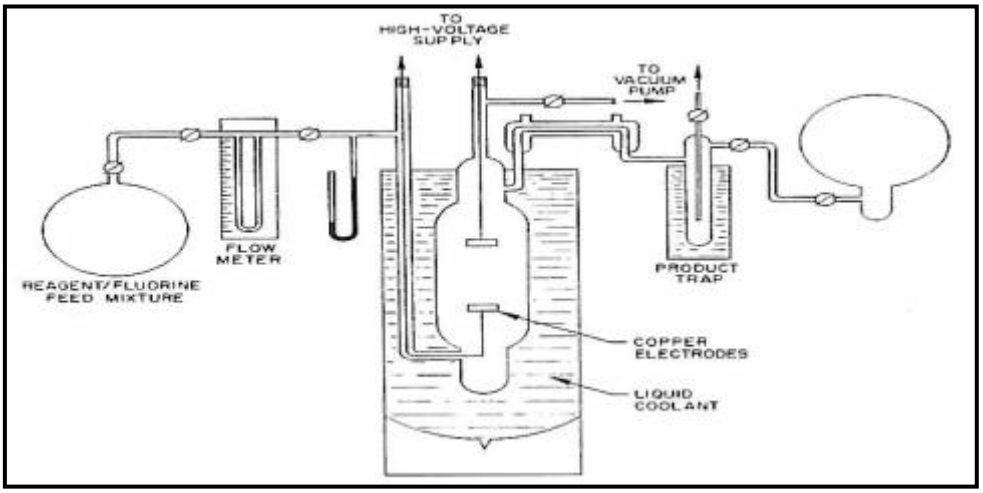

Figure 2.13: High voltage, low-current discharge apparatus (extracted from [116])

Ruff and Menzel [116] employed a high-voltage, low-current discharge tube apparatus made of Pyrex glass for the syntheses of oxygen fluoride compounds. This discharge works at low-pressure conditions and the products are formed in the walls of the discharge tube which is immersed in a coolant with a low temperature range of 333.15 to 363.15 K. This type of device has also been used in the synthesis of fluorides of rare gases such as krypton and xenon.

2.3.5 Other Related Plasma Devices for the Production of Fluorochemicals

Other methods and devices reported in literature for producing various fluorochemicals include: the production of trifluoroacetonitrile by the pyrolysis of fluoroform (trifluoromethane) using a nitrogen plasma jet [117] as well as tetrafluoroethylene and other higher fluorocarbons from tetrafluoromethane using a carbon arc [118-120]. In addition, tetrafluoroethylene has been produced from hot argon plasma gas brought into contact with pentafluoroethane or fluoroform [121]. Other researchers have reported patents relating to the formation of other by-products, which include tetrafluoromethane, hexafluoroethane, hexafluoropropene, and other fluoroolefins in small quantities using a plasma touch at high current and input power [122-125].

However, all these patents involve operations at sub-atmospheric pressure conditions and a few at atmospheric pressure condition in a thermal arc generator ranging from tens to hundreds of amperes of current. In addition, the general scheme followed in most cases involves the description in Figure 2.9. Hence, these processes are plagued with high power consumption, high cost associated with the vacuum maintenance, production of some undesirable by-products as well as the need to operate at

high temperatures above 1900 K to bring about decomposition, but subsequently quenching the products at temperatures lower than 800 K in less than 1 second (<< 1 sec.) in order to obtain good yields of the desired products. Some reports of the formation of fluorocarbons such as tetrafluoroethylene are still characterized by long and complex synthesising routes [123] as shown in Figure 2.14 below. Hence, there is a need for more economically viable synthesizing routes for some fluorochemical compounds.

As a conclusion, it is important to mention that some organic compounds have been synthesized using low intensity arcs as well as low pressure and low current glow discharges at nonequilibrium conditions. Thus, the review is admittedly a summary of the application of plasmas in fluorine reactions and organic synthesis as a whole. However, it gives an insight into the objectives of this research and the use of electric discharges in organic synthesis. Additional information in excellent texts like "Plasma Chemistry" authored by Fridman [126] and "The Application of Plasmas to Chemical Processing" edited by Baddour and Timmins [127] is available for detailed understanding of plasma applications in organic synthesis.

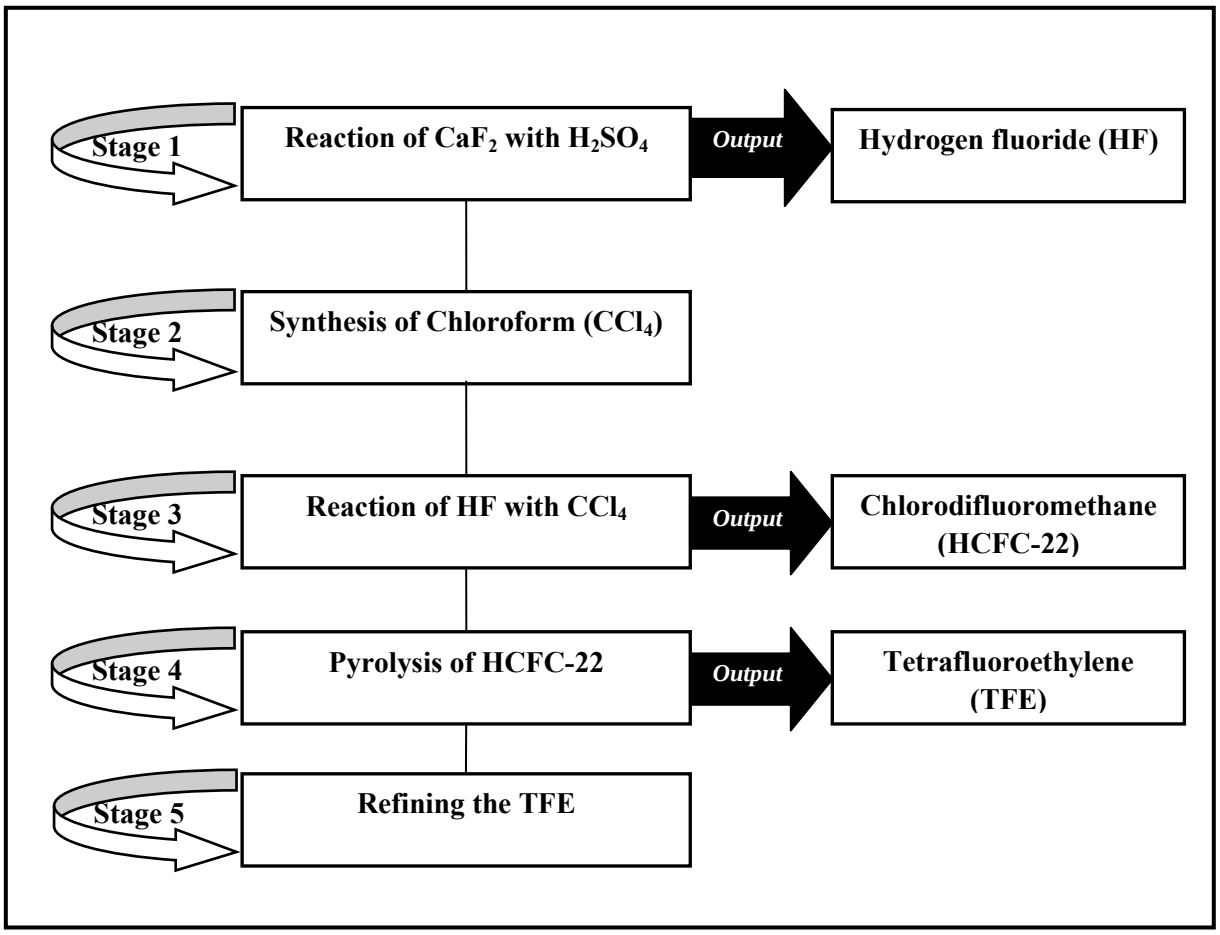

Figure 2.14: Scheme for the commercial routes for producing tetrafluoroethylene (TFE) worldwide since 1950s

2.3.6 Summary on Fluorocarbons Synthesis Studies Using Different Plasma Devices

In addition to the devices briefly discussed in Section 2.3.2 to 2.3.4, Table 2.7 presents some of the different devices that have been employed in the syntheses of fluorocarbons along with the operating conditions. All the apparatus mentioned under section 2.4 were operated at a maximum pressure of 0.1 MPa, and the minimum temperature at which the yield for the desired products were obtain was about 800 K using a very high power and current input. However, it must be mentioned that the devices of Malone [121] for the production of tetrafluoroethylene as well as that of Swanepoel and Lombaard [125] for the production of fluorocarbon compounds has a pressure capacity higher than 0.1 MPa. A more detailed list could be found in the textbook of Baddour and Timmins [127].

Truesdale and Smolinsky [128] have detailed work on pure C_1 to C_2 fluorocarbon plasmas as well as their mixture with hydrogen with a follow up experiment involving C_2F_6 and acetylene (C_2H_2) mixtures [127]. All the experiments reported by Truesdale and Smolinsky et al. [128-129] were conducted in an alumina flow-tube reactor with RF discharge at pressures less than 1 torr.

Table 2.7: Summary of the synthesis of some fluorocarbons using different devices

Power (kW)	Pressure (MPa)	Reactants	Feed rate (moles/sec.)	Reported Products	Discharge Device	References
25	0.101	CF_4	1.0×10^{-3}	C_2F_4, CF_4, C_2F_6, C_3F_6	High-intensity arc with cold-wall quench	[96]
28.5	0.01	CF_4	3.7×10^{-3}	C_2F_4, CF_4, C_2F_6, C_3F_6	High-intensity arc with carbon-bed quench	[130]
7.6	0.0047	CF_4	1.05×10^{-2}	C_2F_4, CF_4, C_2F_6	Carbon arc with carbon-bed quench	[118,120]
0.16	0.087	CF_4	2.0×10^{-5}	C_2F_4, C_2F_6, C_3F_6, CF_4	Carbon arc with carbon-bed quench	[118,120]
0.4	0.0043	C_3F_8	9.8×10^{-4}	C_2F_4, CF_4, C_3F_8, C_2F_6, C_3F_6	Carbon arc with quench	[118,120]
0.4	0.0053	C_3F_6	1.4×10^{-3}	C_2F_4, CF_4, C_3F_6, C_2F_6, C_3F_8	Carbon arc with quench	[118,120]
0.87	0.0047	CF_4	4.0×10^{-5}	CF_4, C_2F_4, C_2F_6,	Glow discharge between carbon electrodes	[131]
0.1	0.101	liquid HF coke granules	batch	CF_4, CF_2H_2, CF_3H, CFH_3,C_2F_5H, C_2H_2	Transient arcs pulsing through liq. HF/coke mixtures at 19^oC	[122]
20	0.101	N_2 mixture + CF_4	3.5×10^{-2} 1.8×10^{-2}	NF_3, CF_3NF_2, N_2F_4, C_2F_6, N_2F_2, C_2F_4	N_2 plasma jet injected with fluoride	[115]
12	0.101	Ar mixture + C_2HF_5	2.98×10^{-2} 1.25×10^{-3}	CF_4, C_2F_6, CHF_3, C_2F_4, $CClF_3$, C_3F_6	Heating of C_2HF_5 with hot argon gas	[121]
13.3	0.01	C_2F_6	4.6×10^{-3}	CF_4, C_2F_4, C_2F_6, C_3F_6	Plasma torch	[125]

2.4 Review of Electrical Discharge Devices for the Hydrocarbon Synthesis

The synthesis of hydrocarbons using plasma reactors have been studied extensively by different research groups around the world. According to Petitpas et al. [132], the last two decades has witnessed the development of different plasma reactors to investigate hydrocarbon production paths with regards to conversion, product yield and energy efficiency. The designs and construction were based primarily on the desired condition of operation, the reactants to be used, and the desired products. To this end, different plasma devices have been reported for the conversion of reactants such as methane to syngas and higher hydrocarbons amongst which are the corona discharge [9, 44]; microwave discharge [43]; pulsed glow discharge [45]; pulsed discharge [12, 34, 35, 37]; pulsed spark discharge [20, 27]; silent discharge [6, 39]; arc-jet discharge [16]; gliding-arc [47, 133] and mini gliding-arc [19]. In the next subsections, a brief description will be presented on devices such as the corona discharge reactor, dielectric barrier discharge reactor, gliding-arc reactor, microwave discharge reactor, and the plasmatron of Bromberg et al. [48].

2.4.1 Corona Discharge Reactor

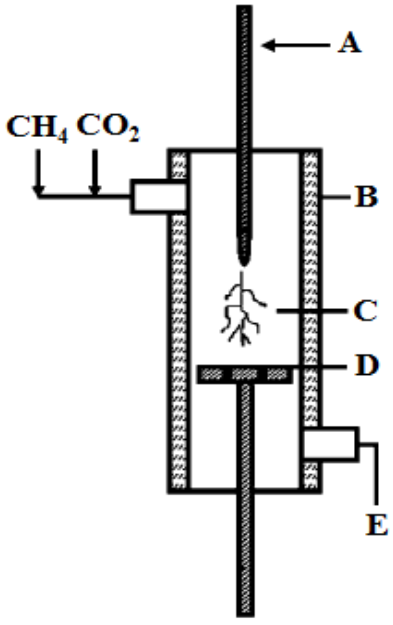

Figure 2.15: Schematic diagram of a corona discharge reactor [44]

Figure 2.15 is a schematic diagram of a DC corona discharge used for hydrocarbon synthesis using CH_4 and CO_2 reforming [44]. The corona discharge reactor is capable of generating a positive or negative discharge depending on the polarity of the power source, connected to the wire electrode (A) in Figure 2.15. The electrodes are enclosed within a quartz tube (B) in a coaxial configuration with the discharge (C) generated in the interelectrode gap of 10 mm between the high voltage wire electrode

and the grounded plate electrode (D). The internal diameter of the quartz tubular reactor is 13.2 mm. The discharge voltage and current can be measured on a digital oscilloscope and the electrical power supplied to generate the discharge can then be calculated. The discharge products collected from the outlet point (E) is sampled on a gas chromatograph either by direct injection or by an online sampling technique.

The corona discharge is capable of operating at atmospheric pressure, but its inhomogeneous nature does not allow for large volume of the gas to be treated.

2.4.2 Dielectric Barrier Discharge Reactor

The dielectric barrier discharge (DBD) reactor which is sometimes called "silent discharge reactor" operates mainly at atmospheric pressure. It is a discharge reactor type popular for its commercial use in the generation of ozone. This reactor according to Kogelschatz et al. [49] was first used by Siemens in 1857 for 'ozonizing air'. It is one of the most widely used reactors due to its large treatment volume and has been employed in surface treatment, pollution control, and flat plasma displays.

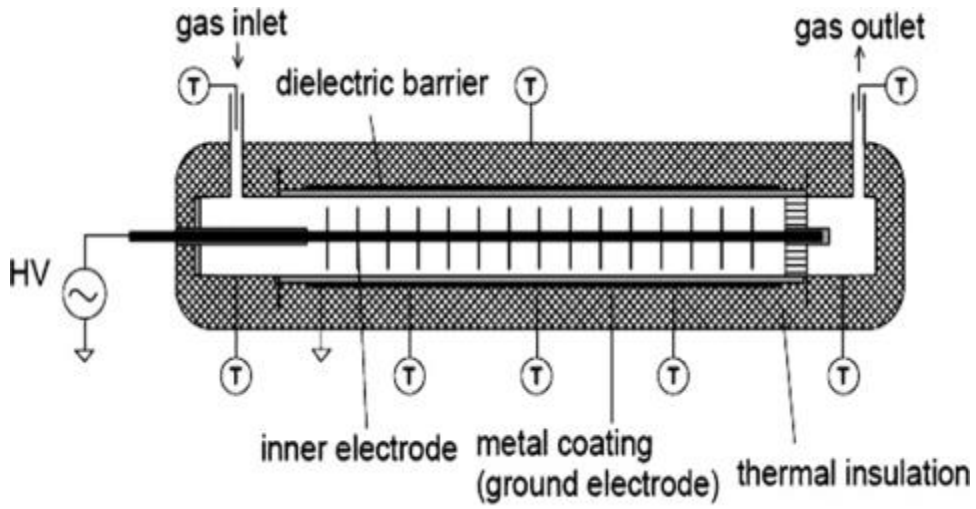

Figure 2.16: Schematic diagram of a dielectric barrier discharge reactor [132]

The DBD reactor consists of two planar electrodes placed in a parallel configuration several millimetres apart. The alumina ceramics (Al_2O_3) serves as the dielectric material covering one of the electrodes. The grounded electrode serves as the anode. The discharge contains many microdischarge channels shown in Figure 2.16. These microdischarge channels are where the activation of the reactants takes place at high electron temperature (up to 10 eV) and gas temperature at few hundreds K. Thus, it is a nonthermal plasma. This discharge is inhomogeneous discharge and mainly operated using alternating voltages.

According to Tao et al. [133], some researchers have used the DBD reactor for hydrocarbon synthesis with methane and carbon dioxide as reactants [36, 38, 42]. However, the results in term of conversion, product selectivity, and product yield were low. The use of different types of catalyst in combination with plasma in a DBD has also been reported [134-139]. Nonetheless, no significant improvement in the reaction performance was observed.

2.4.3 Gliding-Arc Discharge Reactor

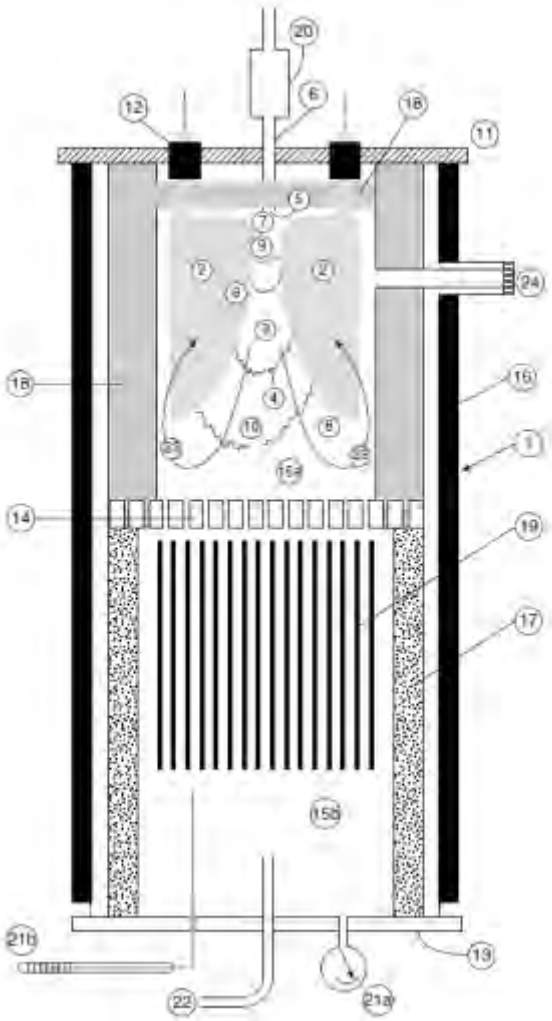

Figure 2.17: Schematic diagram of the glidarc-I reactor (extracted from [140])

Some authors such as Petitpas et al. [132] and Tao et al. [133] in their review of hydrocarbon synthesis through reforming processes have ascribed the invention of the gliding arc discharge reactor to Czernichowski [140]. The gliding arc, which is unique due to its ability to generate a thermal or nonthermal plasma depending on the input energy and gas flow rate, has been widely tested for hydrocarbon synthesis using different feed gases. According to Czernichowski [140], the reactor was tested on a laboratory scale for partial oxidation of methane, dry reforming, and steam reforming. Different synthetic fuels are reported by [140] to have been produced.

A gliding arc reactor can have two or more diverging electrodes. For example, the GlidArc-I reactor (1) consist of six electrodes (2) (although only two is shown on Figure 2.17 in a symmetrical arrangement) with each having a thickness of 0.2 cm. These electrodes are of dimension 8 cm by 25 cm. The reactor has a large volume of 1900 cm^3 and pressure capacity up to 0.6 MPa. The gliding arc discharge (4) is developed in the nozzle-shaped volume (3) created by the electrodes. This discharge (4), which is initially formed at the closest gap between the electrodes, is gradually pushed up in response to the flow rate of the feed gas and discharge power. The operating principle of the glidarc provides for greater volume of gas to be treated by the discharge as a preheated fluid mixture is introduced into the reactor through the nozzle (5). The premixed fluid (6) is then blown in to the space (7) where it is converted between the electrodes. The converted fluid is allowed to flow freely in a continuous motion along the central part of the electrodes, hence exposing it to the discharges for further treatment within the reactor volume.

Other researchers such as Rusu and Cormier [141] and Indarto et al. [142] have employed a gliding arc reactor for the direct conversion of methane as well as steam reforming of methane. While, results reported with the use of a gliding arc discharge reactors are still low in reaction performance, their ability to work in a thermal or nonthermal regime coupled with high pressure (up to 0.6 MPa) and homogeneous treatment of the gas in large volumes gives it an advantage over the corona and DBD reactors.

2.4.4 Microwave Discharge Reactor

Microwave discharges are usually induced by a microwave generator operating at very high frequency, generally greater than 2.45 GHz and atmospheric pressure. The microwave discharge reactor shown in Figure 2.18(a) consists of an internal conductor, a resonance cavity, and a microwave generator. Figure 2.18(b) shows a quartz tubular reactor covered with a quartz jacket (13). The tube is packed with a porous plate (14) and a catalyst and microwave receptor (15). Microwave radiation (16) is applied to the gas mixture as it flows into the reactor through the porous plate (14). The discharge products are collected at the top as shown in Figure 2.18(b).

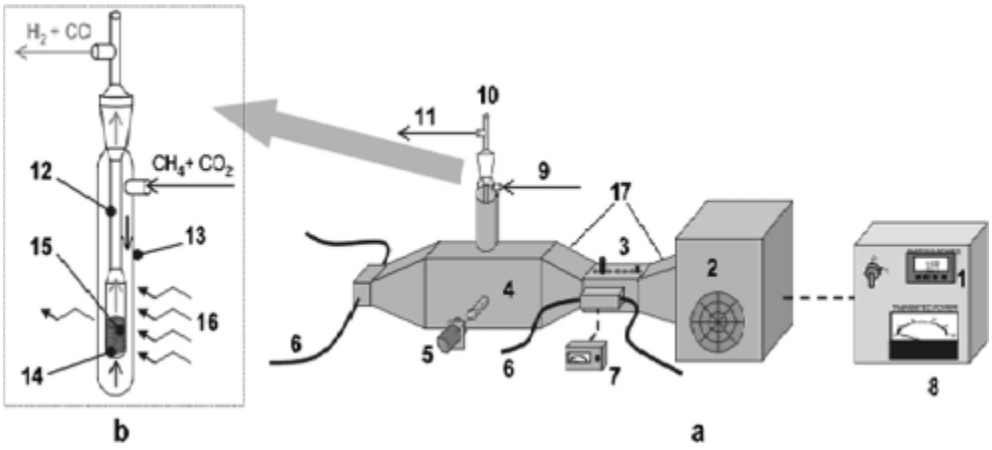

Figure 2.18: Schematic of a microwave discharge reactor in (b) with the entire setup in (a) [143]

On laboratory scale, good conversions, product selectivity, and product yield have been reported for CO_2 reforming of methane in a microwave discharge reactor [43]. The large discharge volume and homogeneous nature of the discharge in a microwave discharge reactor is an advantage it possesses over the corona discharge and DBD. However, the complexity and bulkiness of the equipment required to generate a microwave discharge is still a disadvantage for meeting industrial requirements.

2.4.5 Plasmatron Reformer

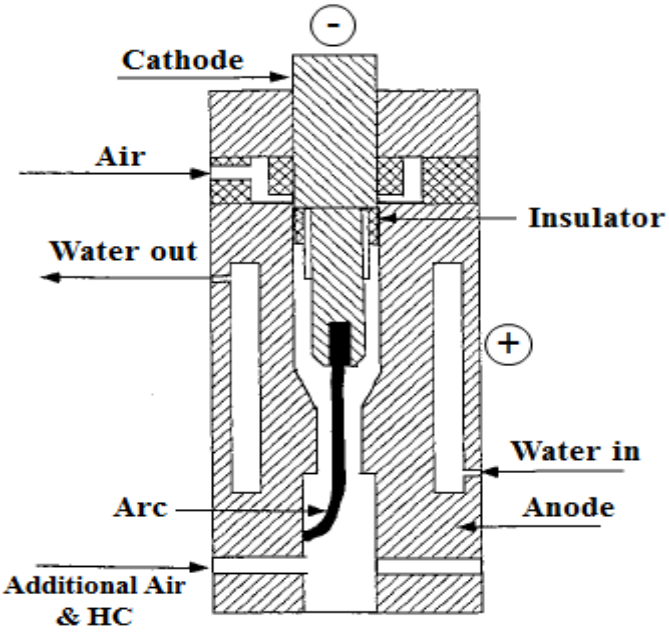

Figure 2.19: Schematic diagram of a plasmatron reformer (extracted from [48])

This laboratory scale plasmatron developed by Bromberg and co-workers at the Plasma Science and Fusion Center (PSFC) group in Massachusetts Institute of Technology (MIT) is a thermal plasma

reformer. Although, they have shifted their research into the use of nonthermal plasma reactors, this reformer shown in Figure 2.19 was used for the reforming of methane [48].

The reactor is a steel tube that is 20 cm long with an outer diameter of 9 cm. It is lined internally with a ceramic material acting as an insulator to the cathode tip. The plasmatron, which can be described as a fuel reformer with a length of 7.5 cm and an outer diameter of 4 cm is connected to the top of the reactor. The electrodes are located within the plasmatron. The cathode is made of a zirconium tip, while the anode is made of copper. Water circulates around the plasmatron to help in cooling the electrodes. Hydrocarbons such as methane are introduced from the anode root of the arc as shown in Figure 2.19. Bromberg et al. [48] reported that at currents less than 100 A, the plasmatron has a lifespan of between 1000-2000 h.

2.4.6 Summary on Some Hydrocarbon Synthesis Using Different Discharges

In addition to the devices briefly discussed in Sections 2.4.1 to 2.4.5, Table 2.8 presents selected plasma-assisted hydrocarbon synthesis along with the operating conditions. All the apparatus mentioned are laboratory scale and operate at 0.1 MPa.

Table 2.8: Hydrocarbon synthesis from dry reforming processes using different devices

Power (kW)	Pressure (MPa)	Reactants ratio	Feed rate (moles/sec.)	Reported Products	Discharge Device	Reference
0.023	0.10	CH_4/CO_2=1/1	8.93×10^{-5}	H_2, CO, C_2H_2, C_2H_4, C_2H_6,C	Pulsed glow discharge	[12]
0.065	0.10	CH_4/CO_2=1.5	1.49×10^{-4}	H_2, CO, C_2H_2, C_2H_4, CH_4,CO_2	Pulsed microwave discharge	[43]
0.063	0.10	CH_4/CO_2=1/2	4.46×10^{-5}	H_2, CO,CH_4,CO_2,C	DC corona discharge	[44]
0.50	0.10	CH_4/CO_2=2/1	1.11×10^{-4}	H_2, CO, C_2H_2, C_2H_4, C_2H_6, C_3H_6, C_3H_8, C_{4+}, CH_4,CO_2	Dielectric barrier discharge	[36]
18.0	0.10	CH_4/CO_2=4/6	5.45×10^{-2}	H_2, CO,CH_4,CO_2,C	Binode thermal plasma	[143]
0.770	0.10	CH_4/CO_2=4/6	6.20×10^{-3}	H_2, CO,CH_4,CO_2,C	Cold plasma jet	[144]
0.190	0.10	CH_4/CO_2=1/1	7.44×10^{-4}	H_2, CO, C_2H_2, CH_4,CO_2	Gliding arc discharge	[145]
0.204	0.10	CH_4/CO_2=1/1	7.44×10^{-5}	H_2, CO, CH_4,CO_2,C	DC arc discharge	[146]
0.0884	0.10	CH_4/CO_2=4/6	7.44×10^{-4}	H_2, CO, CH_4,CO_2,C	Atmospheric pressure plasma jet	[14]

Chapter 3

REVIEW OF ANALYTICAL AND NUMERICAL MODELLING APPROACHES FOR PLASMA PROCESSES

3.1 Introduction

In the development of a simple model for the behaviour of electrical discharge at very high pressure, there needs to be an understanding of the different theories on the development of discharges at low pressure, high pressure, and very high pressure. The literature shows that three categorizes of modelling approach have commonly been employed for the modelling and simulation of plasma discharges, especially at low pressure and low-temperature. These three modelling approaches are classified as:

- The Fluid modelling approach;
- The Particle-In-Cell and Monte-Carlo Collisions modelling approach;
- The Hybrid modelling approach [147].

While one of the focuses and objectives of this research work is to successfully model the behaviour of plasma in a very high-pressure electric discharge reactor, it must be mentioned that most of the published works on the modelling of plasma discharge is for the modelling of low-pressure discharges. Generally, this could be attributed to the fact that low-pressure plasma has gained significant applications in the field of semi-conductors and flat panel display electronics such as the plasma television. Low-pressure and temperature discharges are also applied in plasma-enhanced chemical vapour deposition and plasma etching. Thus, the need for modelling and simulation of plasma discharges, at low pressure, in order to understand its behaviour have been seen as important. This is because modelling and simulation provides us with information about the internal parameters, which usually could not be obtained by rigorous experimental effort [148].

In this chapter, a brief review of the various plasma models will be discussed. Additional information is available in the textbooks and published journal articles of Birdsall and Langdon [148-149].

3.2 Fundamental Principles in Plasma

Generation of an electric arc discharge will always result in the formation of various species, which can be influenced by different adjustable plasma parameters during the process. The formation of the different class of species (which could be atoms, free radicals, ions, and molecules) in a reactor occurs when there is a transfer of energy to neutral gas molecules by free electrons that have been initially energized by an imposed electric field but lost the energies when in collision with the neutral gas molecules. Thus, plasmas are sometimes referred to as a neutral body that has a smaller Debye length (λ_D) in comparison to its discharge volume (Λ) [150]. The Debye length in plasma is given by:

$$\lambda_D = \sqrt{\frac{\varepsilon_O k / e^2}{n_e / T_e + \sum_{i\,j} j^2 n_{ij} / T_i}} \tag{3.1}$$

where ε_O is the permittivity of free space; k is the Boltzmann constant; T_e is the temperature of electrons; T_i is the temperature of ions; n_e is the electron density; n_{ij} is the density of atomic species i, with positive ionic charge jq_e; and e is the charge of an electron. Figure 3.1 shows a plot of the density of the electrons (n_e) against the energy of the electron (kT_e) for the various plasma regimes. However, when the mobility (a property that relates the drift velocity to the electric field) of the ions is relatively small in comparison to the process timescale [151], the ion term is neglected and the expression becomes:

$$\lambda_D = \left(\frac{\varepsilon_O k T_e}{n_e e^2} \right)^{1/2} \tag{3.2}$$

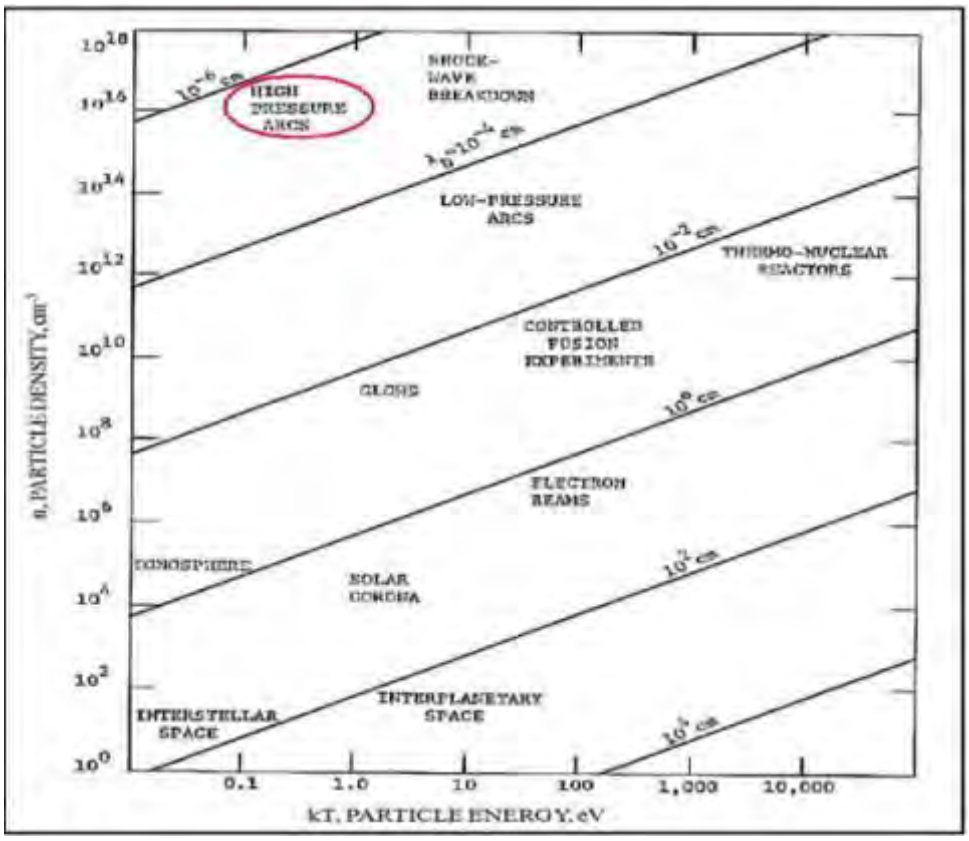

Figure 3.1: Energy-Density diagram showing the various particle kinetics of space and laboratory plasmas. The red cycled region shows the high-pressure arc discharge (extracted from [151])

3.3 Plasma Modelling Approach

Modelling plasma discharges requires the solving of mathematical equations for the conservation of mass, momentum and energy for each species i.e. electrons, ions and neutrals present in plasma discharges. Ideally, the most accurate method of modelling plasma will employ the calculation of each individual particle involved in the plasma-chemical reaction while taking into account the possible effect of the electromagnetic field on the plasma physics. However, due to the numerous steps in the kinetic mechanisms of plasma chemistry, which usually leads to a more complex model and long computational time, researchers such as Meyyappan and Kreskovsky [152] modelled glow discharge in a simplified approach using three-moment and two-moment one-dimensional simulation for the electron and ions respectively [153]. Since transport kinetics as well as Maxwell's equations are important in solving the conservation equations, a specific approach for modelling plasma discharge must be considered. This is necessary because when employing direct current: where the magnetic field is static and only effects from the strong electric field are considered, the Maxwell's equation reduce to the Poisson's equation. This is also feasible where low current (<< 1 A) is employed, and thus the strength of the magnetic field will be low. This approach is also valid for low-temperature plasma modelling.

Generally, the Maxwell equations describe the relationship of the electric and magnetic fields to the charge and current densities using a partial differential equation of the form:

$$\mathrm{E} = -\nabla\phi - \frac{\partial \mathrm{A}}{\partial t} \tag{3.3}$$

$$\mathrm{B} = \nabla \times \mathrm{A} \tag{3.4}$$

$$\nabla \cdot D = \rho \tag{3.5}$$

$$\nabla \times H - \frac{\partial D}{\partial t} = J. \tag{3.6}$$

Equation (3.3) gives the relationship between the electric field (E) in $V.m^{-1}$ and the electric potential (ϕ) given in volts where $\partial/\partial t$ is the partial derivative with respect to time per second. Equation (3.4) shows the link between the magnetic field (B) in tesla (T) and magnetic vector potential (A) given in $V.s.m^{-1}$. The electric displacement field (D) given in $C.m^{-2}$ is related to the total charge density (ρ) given in $C.m^{-3}$ by equation (3.5). H in equation (3.6) is the magnetic field intensity given in $A.m^{-1}$ and J is the current density given in $A.m^{-2}$.The divergence and curl operator are denoted with the symbol $\nabla\cdot$ and $\nabla\times$ respectively.

Equations 3.5 and 3.6 are generally referred to as Gauss's law for electricity and Ampere's law. The Poisson's equation gives an expression that relates electric potential to the charge density. Hence, the electric field (E) can be related to the charge density (ρ) through divergence relationship of the form:

$$\nabla \cdot \mathrm{E} = \frac{\rho}{\varepsilon_0} \tag{3.7}$$

given that, ε_0 is permittivity or dielectric constant of vacuum with a value 8.85×10^{-12} $CV^{-1}m^{-1}$. The divergence theorem explains that when an electric field diverges at a point in space, it is equal to the ratio of the total charge density to the permittivity in space. Using the gradient relationship, an expression relating electric field to electric potential in a vector form is obtained:

$$\mathrm{E} = i\mathrm{E}_x + j\mathrm{E}_y + k\mathrm{E}_z = -i\frac{\partial\phi}{\partial x} - j\frac{\partial\phi}{\partial y} - k\frac{\partial\phi}{\partial z} = -\left[i\frac{\partial}{\partial x} + j\frac{\partial}{\partial y} + k\frac{\partial}{\partial z} \right]\phi \tag{3.8}$$

where $-\left[i\frac{\partial}{\partial x} + j\frac{\partial}{\partial y} + k\frac{\partial}{\partial z} \right]$ in equation 3.8 is referred to as the gradient which is represented with the symbol (∇).The electric field in a substituted form becomes:

$$\mathrm{E} = -\nabla\phi \tag{3.9}$$

Therefore, Poisson's equation is given in a form that makes it easy to calculate the electric potential.

$$\nabla \cdot \nabla\phi = \nabla^2\phi = -\frac{\rho}{\varepsilon_0} \tag{3.10}$$

It is important to mention that, the right approach to be employed in the modelling of plasma should be based on the operating regime of the discharges. This is because each approach generally has its advantages as well as its limitations. In addition, each discharge regime is characterized based on certain features such that it would be inappropriate to generalize plasma behaviour with a particular model. Smirnov [154] suggest that in modelling gas discharge plasma, it is inconvenient to attempt to use a universal approach. Hence, it is advised that only processes that are important in describing the properties of the discharge should be included in models. However, in a homogeneous gas discharge, it is necessary to take into account the equation of the ionization balance, equation for the current - voltage characteristic i.e. electrical characteristics of the discharge and the discharge mode as well as the energy balance equation for a gas discharge in describing the properties of plasmas.

3.3.1 The Fluid Model Approach

This model links the moments of the Boltzmann equation to Poisson's equation in order to effectively calculate the charge density, drift velocity, the energy of the charged species as well as the electric field. It is an approach that generally considers the various generated plasma species i.e. electrons, free radicals and ions as a group of individual particles [155] while making some possible assumptions. For example, the distance between the electrodes is assumed to be greater than the mean free path (λ), which is the average distance between an electron-neutral collision. Three categories have been identified for the fluid models, which are based on the number of moments used [147]. The one-moment is a simplified model for describing the electron transport in low-pressure and low-temperature plasmas, while the two-moment is a more accurate model that takes into consideration the conservation of mass and momentum equations in describing the motion of electrons for low-pressure and low-temperature plasmas. The three-moment approximation is a more robust model that takes into account the momentum of the species together with the conservation of energy equation. Table 3.1 gives the comparison between all three categorises of the fluid theory.

Table 3.1: Comparison of the three different categorizes of the fluid theory model

Categorizes of fluid theory	One-moment	Two-moment	Three-moment
	Drift-diffusion approximation is employed while the momentum conservation equations are neglected [147].	The electron inertia is given strong consideration in this model.	The momentum balance equation is employed [158].
	A local field approximation is employed instead of the electron energy balance equation.	An electron energy balance equation is employed instead of the local field approximation [156-157].	Density and energy continuity equation is employed [158].

It must be mentioned that while there may be few publications on the application of the fluid theory approach in the field of high-pressure plasma discharges, numerous works have been published on the successfully implementation of the fluid theory in the area of low-pressure, low-temperature DC and RF discharges by various researchers [155-161]. However, most of the simulations are in the area of semi-conductor devices, plasma panel displays and other material processing applications. Therefore, details will not be given into the application of the fluid theory in low-pressure DC and RF discharges since this is not the aim of this research work. Additional information is available in the textbook of Iza et al. [162] and published journal articles of Kortshagen et al. [163], Kolobov et al. [164], and Degond et al. [165].

3.3.2 The Particle-In-Cell (PIC) and Monte-Carlo Collisions Model Approach (MCC)

The particle-in-cell method and Monte-Carlo collision model are amongst the most common examples of kinetic models in plasma processing of materials and plasma physics. While it proposes a more detailed and accurate representation for the description of particle collisions in the discharge chamber to the physical reality [149], the long computational time required in stepwise solving of the equation of motion for every single particle involved in the collision process has given the partial differential equations preference over it amongst researchers [149]. However, the particle-in-cell and Monte-Carlo collisions approaches are still the most reliable when modelling systems that exhibit a non-Maxwellian electron and ion distribution function. It is also the best choice when dealing with large Knudsen numbers, i.e. when the mean free path for the collisions between electron and neutral particles are of a comparable value to the characteristics dimension of the discharge chamber. Thus, the fluid theory is not accurate when the Knudsen number is greater or equal to 1. The Knudsen number (Kn) is the ratio of the mean free path (λ) to the characteristic dimension of the discharge chamber (L). Therefore, the operating regime of the discharge is a determinant in the choice of a suitable model i.e. the fluid theory approach will be more suitable when the discharges are in the

continuum region but the kinetic models is more suitable for plasma discharges in the non-continuum regions [147].

It is important to mention that despite the long computational time associated with Monte-Carlo collision models, researchers such as Birdsall [149] and Surendra and Graves [166] have effectively coupled the particle-in-cell approach with the Monte-Carlo techniques. In addition, some researchers [167-170] have performed one-dimensional particle-in-cell Monte-Carlo simulations on capacitively coupled radio frequency discharges at low-pressure. However, it must be mentioned that long computational time has limited the use of the PIC method to low-pressure plasmas: characterised by low plasma densities ($< 10^{17}$ m^{-3}). More detailed information on the modelling of plasma discharges using the particle-in-cell are available in Birdsall and Langdon [148,149].

3.3.3 The Hybrid Model Approach

A hybrid model is a term used to refer to models that combine the functionality of the fluid theory and the Monte-Carlo collision model (an example of kinetic models). The hybrid model though a bit complex, is effective due to its ability to model plasma discharges using the fluid theory approach as well as the Monte-Carlo collisions model approach. Thus, it has the advantage of faster computational time in comparison to the Monte-Carlo collisions model approach (an example of kinetic models) while still maintaining the effective application of the Monte-Carlo collisions model approach over the fluid theory [147]. However, the need to have the fluid module separate from the Monte-Carlo collision module means that this approach is not self-consistent and simultaneous in implementation but rather requires the iterative solution of the different modules until steady-state is achieved [162].

Researchers in recent times have applied this model to modelling DC glow discharges at low-pressure [171]. Some researchers such as Cartwright [172] have employed a hybrid electrostatic particle-in-cell to investigate ion acoustic waves and other low-frequency phenomenon by modelling electrons with low energy using the Maxwell-Boltzmann (MB) distribution function, and electrons with high energy using the particle-in-cell method. In addition, Porteous and Graves [173] developed a hybrid electron fluid-particle ion model, which treated electrons using the fluid approach, and ions as particles using the kinetic approach in magnetically confined low-pressure plasmas. Other researchers like Sommerer and Kushner [174] have equally employed a Monte-Carlo fluid hybrid model (MCFH) for low-pressure radio-frequency discharge that involve plasma etching of semi-conductors using chlorine chemistry. In the MCFH model, the electrons were treated using the Monte-Carlo approach while ions were treated using a self-consistent fluid model (SCFM). Kolobov [175] has successfully employed the hybrid models developed by researchers such as Sommerer and Kushner [174] as well as Arslanbekov and Kolobov [176-177] for low-pressure DC argon glow discharges. The fluid theory approach was utilized in this hybrid models to obtain the electron and ion densities, the electron mean

energy and local electric field while Poisson's equation was used to obtain the electric field. The Boltzmann equation was solved in a chemical kinetic model in order to obtain the electron energy distribution function (EEDF). The EEDF value was further used in the Boltzmann equation to obtain the electron transport coefficient as well as the electron induced reaction rates while the electron density was then evaluated from the electron transport coefficient and the reaction rate using the continuity equation [147].

In concluding this section, it should be mentioned with reference to Iza et al. [162], the main limitation with hybrid models lies on its dependency on the chosen scheme as well as properties of the discharge. This means that to effectively implement a hybrid model, the fluid module should be used to describe species in local equilibrium while particles affected by non-local effects (i.e. not in local equilibrium) must be described using a PIC module. Thus, there is on-going research aimed at improving existing kinetic and fluid models.

3.4 Comparison of the Three Plasma Discharge Models

All the plasma discharge models discussed above are good. However, each model has major disadvantages and advantages that are capable of influencing the decision of the researchers in employing them. Table 3.2 gives a basic comparison of the three plasma discharge models that have been successfully used at low-pressure (sub-atmospheric pressure conditions).

Table 3.2: Comparison of the Fluid Theory, Monte-Carlo Collisions, and Hybrid Model

	The Fluid Theory Model	**The Monte-Carlo Collisions Model**	**The Hybrid Model**
Ability to resolve electron energy distribution function (EEDF) as well as the ion energy distribution function (IEDF)	EEDF – NO IEDF – N/A	EEDF – YES IEDF – YES	EEDF – YES IEDF – YES
Ability to predict collective plasma characteristics effect.	YES	YES	YES
Approximation of velocity distribution function for particles	YES	NO	N/A
Computational time	very fast	long	fast

3.5 Guidelines for Selecting the Correct Plasma Model

Selection of the correct physical model and modelling approach to use for electric discharge is essential. As mentioned earlier in section 3.3 by Smirnov [154], generalizing models for different discharges would lead to an error as each model has its assumptions outside which it would not give adequate and meaningful understanding to the process. Hence, following the suggestion of Kolobov [175] as shown in Figure 3.2 for DC discharge for pressures greater than 760 torr and reactor scale between 10^0 and 10^1 cm, it is evidence that only the fluid model would be suitable. Furthermore, the plasma in this case is considered as a single continuous fluid for which the fluid model is the most suitable. Finally, while glow discharge has been observed in this tip-tip discharge reactor at pressures between 0.1 and 1 MPa [4], the most predominant discharge regime is the arc regime. In this regime, high current density and high collision frequency is prevalent because of the operating pressure. Therefore, the fluid model approach was considered for this work.

In conclusion, calculation of plasma parameters should be based on the type of discharge or the discharge regime. Thus, it will be inappropriate to use the same model for dielectric barrier discharge as with glow, corona, gliding arc and arc discharge. It is also not applicable to use the same model for low temperature plasma at low pressure as well as low temperature plasma at very high pressure. These are some of the challenges with accurately modelling plasma because the behaviour of plasma under high pressure is as yet to be established.

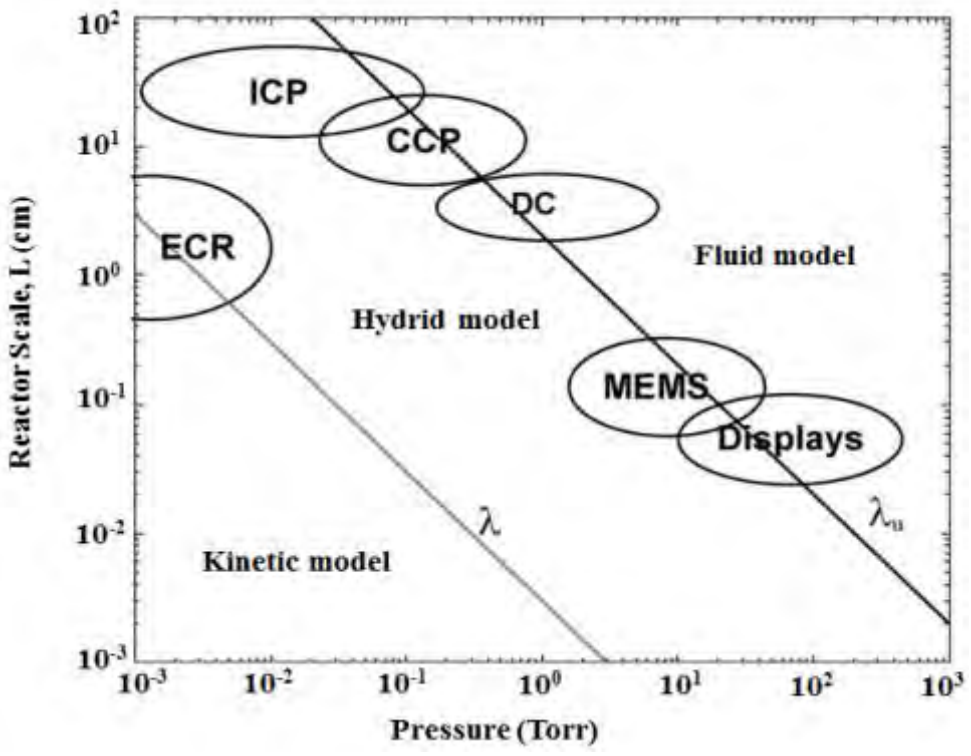

Figure 3.2: Guidelines for choosing the right plasma model (extracted from [175])

3.6 High Pressure Arc DischargeModelling

As mentioned in section 1.5, most investigations done at pressure above 1 MPa relates to high current (I >> 10 A) operations involving AC or DC thermal arc.To put it in the words of Fulcheri et al. [4] and Rohani et al. [178], discharges employing the use of low-current (I << 1 A) above 1 MPa "remains almost unexplored".

Therefore, it is an acceptable fact that insufficient literature on plasma-chemical reaction mechanisms has led to the poor understanding of plasma behaviour and subsequently made modelling electrical discharges difficult. While plasma modelling in itself is a challenge due to the complexity in reaction mechanisms; modelling such reactions in a high pressure electric discharge chamber is more difficult. This according to some researchers has been attributed to the high collision frequency experienced with discharges as the pressure increases up to and above the atmospheric pressure.

In addition, plasma discharges at pressure ≥ 1 MPa are often observed to transition from one discharge regime to another discharge regime [4]. Moreover, low current (< 1 A) operation makes it more difficult. In fact, Lebouvier et al. [179] comment that the high level of physical instabilities within the discharge which leads to instabilities in the numerical values as well as difficulties with plasma diagnostics makes plasma modelling at low-current very challenging. This problem, amongst others such as the limited understanding of such discharges, has led many researchers, including Lebouvier et al. [179] into modelling plasma at low-current using local thermodynamic equilibrium (LTE); a hypothesis which is usually far from reality. Hence, this section aims at giving a summary of the present understanding of the behaviour of plasma generated by low current at pressure above 1 MPa.

3.5.1 Current Knowledge on Modelling High Pressure Plasmas

Most models reviewed in literature for plasma processing have been in the field of plasma-etching, sputtering, deposition of thin films, and plasma display panels where the basic operating pressures are sub-atmospheric [154, 165, 180-186]. While some have been applied at atmospheric pressure, especially the dielectric barrier discharge [185], researchers such as Donko et al. [186], mentioned other areas where plasma modelling have been focused with specific references.

According to Benilov [87], reliable experimental data alongside theoretical models for understanding plasma behaviour at high pressure and low current were lacking until the 1990s. Indeed, his review on theoretical models and methods of simulation at high pressure is the most substantial review that has been published on low current arc discharges at high pressure to date. In particular, his review only gives insight to the modelling of plasma-cathode plasma-anode interaction for low current arc

discharges at pressures up to 3 MPa. A more detailed information on plasma-electrode interaction modelling for low-current arc discharges at high pressure is available in published journal articles of Benilov [87], as well as Benilov and Naidis [187].

3.5.2 Current Knowledge: Analysis and Modelling of Fluorocarbons and Hydrocarbons Plasma

This section provides information about the diagnostic approach to plasma properties, analysis of synthesized products as well as the modelling approach for plasma-chemical reactions involving hydrocarbons and fluorocarbons. Thus, a subsection on the plasma diagnostic approach, analysis of products, and plasma-chemical reaction model will be presented.

3.5.2.1 Diagnostic Approach

Parameters such as the temperature of electrons and ions, electron and ion densities as well as the densities of excited particles are useful in understanding the energy levels of electrons and ions in the plasma. However, direct measurements of such parameters are difficult due to the possibilities of electrical interference and disturbance of the plasma because of the various regimes in which plasma can operate within. Thus, the use of non-intrusive methods like optical absorption techniques, optical emission spectroscopy (OES), and laser-induced fluorescence (LIF) [188] amongst others has been preferred to the Langmuir probes. According to Harry [82], while the complexity involved in measurement and interpretation together with the high cost of purchasing OES, LIF, as well as infrared laser absorption spectroscopy (IRLAS) may be a limitation to its use, the use of absorption spectroscopy and OES has helped to improve the current knowledge of plasma physics and chemistry. In addition, most of the current knowledge about the absolute densities of radicals commonly observed in dissociated products of fluorocarbon plasmas can be attributed to the success of non-intrusive methods like the IRLAS. However, each of the non-intrusive techniques has its advantages and disadvantages, which will not be discussed in this thesis, but additional information is available from Bonitz et al. [189] and other textbooks that focus on plasma diagnostics.

The use of electrical instruments such as a digital oscilloscope is useful in measuring the current and voltage of the discharges via connection with hall-effect current and high voltage probes. These measured properties are useful in calculating the power consumed in generating the plasma. Other properties like the gas temperature can be measured using temperature probes such as a k-type thermocouple insulated in order to avoid the disruption of the plasma.

3.5.2.2 Analytical Approach

Some of the instruments commonly employed in the quantitative analysis of the outlet gas species include the gas phase chromatograph analyser [189]. In most of the cases, the gas chromatograph has been equipped with at least two detectors, namely one thermal conductivity and one flame ionization detector. This is primarily because of the difference in sensitivity of each of the detectors to gases, especially hydrocarbon gases.

The use of a Fourier transform infrared (FTIR) spectrometer has been employed in certain cases to identify and quantitatively analyse products from plasma-chemical reactions [190-191] that involve hydrocarbons. Cruden et al. [192] mentioned the application of FTIR for 'in situ' concentration measurement of neutrals, radicals and charged species in a designed standard reference reactor (the GEC cell) for a low temperature tetrafluoromethane (CF_4) plasma. More information about the GEC cell can be obtained in the publication of Olthoff and Greenberg [193].

Spectroscopic instruments such as infrared laser adsorption spectroscopy has been used in combustion technology for determining the ground and excited states concentration of species as well as using the spectra information to estimate the temperature profile and densities of the various species that are active in the infrared region. Other instruments such as the electron attachment mass spectrometer (EAMS) and the quadrupole mass spectrometer (QMS) have been found to be useful at detecting negative ions formed as a result of low energy electrons in electrical discharges. Nevertheless, the use of the classical gas chromatograph (GC) and mass spectrometry (MS) technique has been the most common, easiest, and cheapest means of identifying and analysing the gas-phase species.

3.5.2.3 Numerical Approach for Modelling Fluorocarbon Plasmas

Fluorocarbons have received great attention due to their use as plasma-etch gases in semiconductor devices. This has led to the development of chemical reaction mechanisms aimed at bringing an understanding to their role in the etching and polymerization process. However, all these various models and simulation tools are mainly useful at low pressure for glow discharges. Indeed, the reported working pressure in various literature ranges from approximately 66 to 133 Pa [194-203] with some going as low as 1.29 Pa [194].

Specific literature related to the modelling of fluorocarbons and development of transport and thermodynamic properties for fluorocarbons from the 1970s to 2012 shows 90% of the work to have been done in microelectronic related studies. Some of the fluid models have also been done using a non-Maxwellian approach by solving for the electron energy distribution function (EEDF) using programs such as BOLSIG+ [204] and one-dimensional simulation tools such as SIGLO-RF [205]. In addition, the only thermodynamic and transport properties available and reliable up to date is that of

Wang et al. [199] which is limited to a pressure of 1MPa for a temperatures range of 300 to 30000 K. Thus, the only reliable modelling approach for fluorocarbons plasma, which could be compared to gas species obtained as products, are thermodynamic models.

In conclusion, while modern modelling tools such as CHEMKIN 4.1and COMSOL Multiphysics 3.5 exist with a plasma module, the available mechanisms are still those dedicated to plasma etch studies taking into account gas phase and surface reaction.

3.5.2.4 Numerical Approach for Modelling Plasma-Assisted Hydrocarbon Synthesis

Petitpas et al. [132] in their comparative review of plasma-assisted reforming processes, mentioned that different research groups in the field of plasma have employed the use of thermodynamic, kinetics and fluid models. According to Benilov and Naidis [206], the use of a thermodynamic model can be justified in arc discharges where temperatures are greater than 2000 K in the plasma zone. Literature reviews actually show that, plasma reforming of methane has been modelled mostly using the thermodynamic models and chemical kinetic models [48, 141-142]. Bromberg et al. [48] mentioned that thermodynamic models are capable of providing information on the optimum operating conditions for an ideal plasma process and the main species that can be obtained under that condition. However, chemical kinetic models, which take into account more parameters such as the residence time or flow rates together with the input power are capable of providing results closer to reality.

One of the challenges associated with kinetic modelling is the need to get the appropriate mechanism with temperature and pressure in the range of operation. In addition, for reaction mechanisms to be relevant, it has to be up to date. The most used methane oxidation mechanisms are GRI-Mech 3.0 [207], Konnov's [208], and the Leeds methane oxidation mechanism version 1.5 [209]. However, validation of the mechanisms is essentially a difficult task to perform.Thus, it is highly uncertain to get validated mechanisms for oxidative reforming of methane and syngas conversion at very high pressure and temperature higher than 2000 K. For example, the validity range for GRI-Mech 3.0 with respect to temperature and pressure are 1000 to 2500 K and 0.001 to 1 MPa respectively. Another issue is that most of the commonly used mechanisms for combustion of natural gas such as GRI-Mech 3.0 do not take into account soot formation. However, if the kinetic mechanisms are based on elementary reaction rate theory, it might still be acceptable for use above the optimization and validation ranges.

In conclusion, commercial computational fluid dynamic (CFD) model such as Fluent can be coupled with kinetics. These however require the mechanisms to be in reduced form. Nonetheless, researchers such as De Bie et al. [210] have used a 1D fluid model coupled with kinetics to successfully describe

plasma chemistry for pure methane, partial oxidation of methane, and CO_2 reforming of methane in a dielectric barrier discharge (DBD) at 0.1 MPa. In addition, Machrafi et al. [211] using a 2D and 3D COMSOL model coupled with kinetic mechanism have described the reforming of methane with CO_2 in a DBD at 0.1 MPa.

Chapter 4

ASSEMBLY AND COMMISSIONING OF A HIGH PRESSURE PLASMA REACTOR

This research work was carried out at two different locations namely; the Plasma Group at MINES ParisTech Sophia-Antipolis, France and the Thermodynamic Research Unit in Chemical Engineering at the University of KwaZulu-Natal (UKZN), South Africa. To this end, photographs of the two experimental setups will be presented but one process flow diagram will be shown since the experimental procedures are the same.

4.1 The High Pressure Plasma Reactor

The design and construction of a high pressure plasma reactor was initiated about a decade ago in the Plasma Group at the Center for Energy and Processes. However, the first two designs had several technical issues that affected the operational process of the first and second prototypes. This has led to the design and construction of the current prototype with pressure capacity of 20 MPa. The first and second prototype is fully detailed in the PhD thesis of Izquierdo [212], and thus, only a brief review will be presented on them in the next subsections.

4.1.1 The First Prototype of the High Pressure Plasma Reactor

The first prototype of the plasma reactor was designed to bear a pressure capacity as high as 10 MPa and temperature of 530 K. This reactor has an outer diameter of 6 cm with a reactor volume of 2.65 cm^3.

According to Izquierdo [212], after some preliminary experimental runs, it was observed that the reactor has the following limitations:

- The working pressure of 3 MPa could not be exceeded due to the sealing problems observed at the metal-ceramic assembling point.
- The interelectrode gap could not be measured precisely because of effects resulting from the erosion of the tip of the electrodes.

- The aluminium material used to construct the base of the electrodes was observed to melt during most experiments.

Hence, it became necessary to rectify these limitations in a second prototype.

A schematic diagram and photograph of the first prototype of the high pressure plasma reactor is presented in Figure 4.1

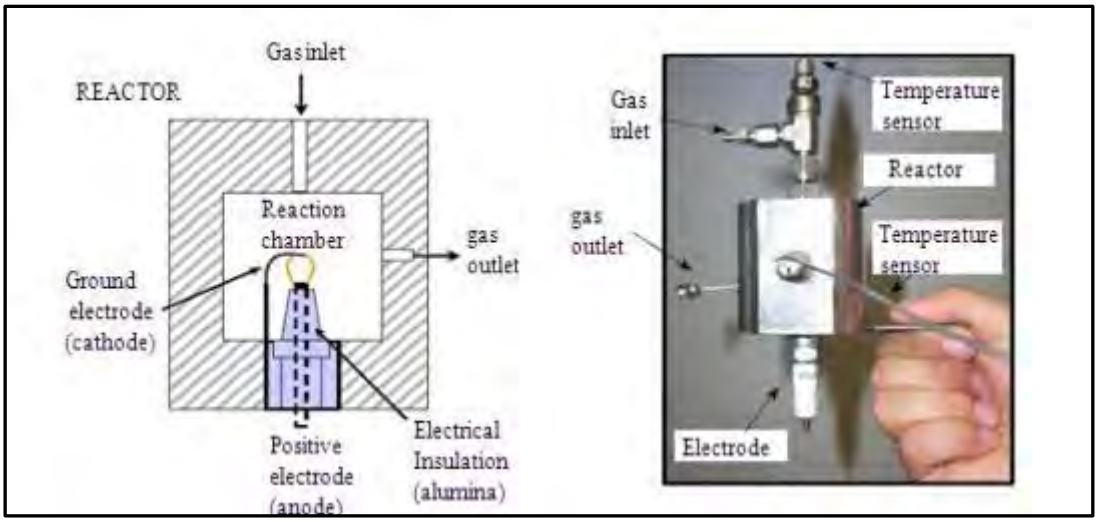

Figure 4.1: Photograph on the right and schematic diagram on the left showing the first prototype of the high pressure plasma reactor (extracted from [212])

4.1.2 The Second Prototype of the High Pressure Plasma Reactor

The second design, which addressed the limitations of the first prototype, was used by Izquierdo [212] to conduct experiments at pressure ranging between 0.1 to 15 MPa for Ar/H_2 gas mixtures [3]. In this second prototype, the interelectrode gap could be varied between 0.5 and 1.5 mm and the operating current range was 0.1 to 0.35 A.

The reactor chamber of this second design has a length of 2 cm with an outer and inner diameter of 2.54 cm and 1.27 cm respectively. The volume of the reactor was 2.53 cm^3. Figure 4.2 presents a schematic and photograph of the second prototype.

Although, the second design was able to overcome the sealing problem, which brought a limitation on the working pressure for the first design, as well as other issues observed during preliminary runs, it does not integrate a sight-glass through which the discharge generated could be physically observed. Thus, it was not possible to capture images of the discharge and estimate the volume of the discharge. Nonetheless, the second design was a big step forward in providing an understanding of the electrical characterization of argon gas at very high pressure in a low current arc discharge [3]. In addition, the second design provided for the successful measurement of discharge voltage and current through which the discharge power could be estimated.

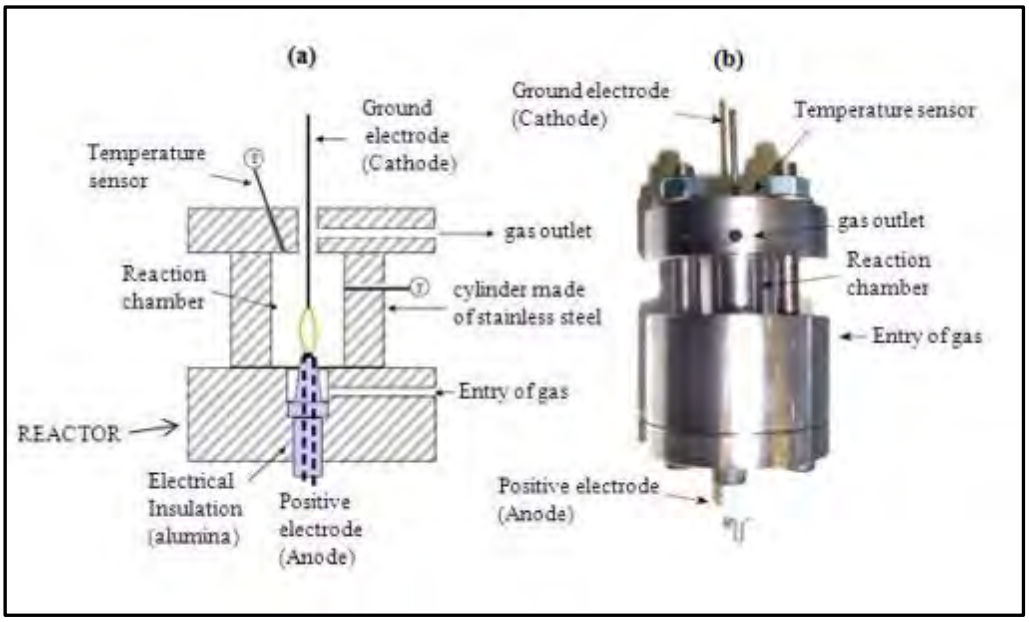

Figure 4.2: Schematic diagram (a) and Photograph (b) showing the second prototype of the high pressure plasma reactor (extracted from [212])

4.1.3 The High Pressure Plasma Reactor used in this Project

The high pressure plasma reactor was designed by the Plasma Group at MINES ParisTech Sophia-Antipolis, and has allowed for the electrical characterization of helium at an interelectrode gap between 0.25 and 2.5 mm, pressure up to 20 MPa and operating current up to 0.6 A [4]. Hence, the current experimental setup at the Plasma Group in MINES ParisTech, Sophia Antipolis, France and at the Thermodynamic Research Unit, University of KwaZulu-Natal, South Africa will be presented.

4.2 Experimental Set-up

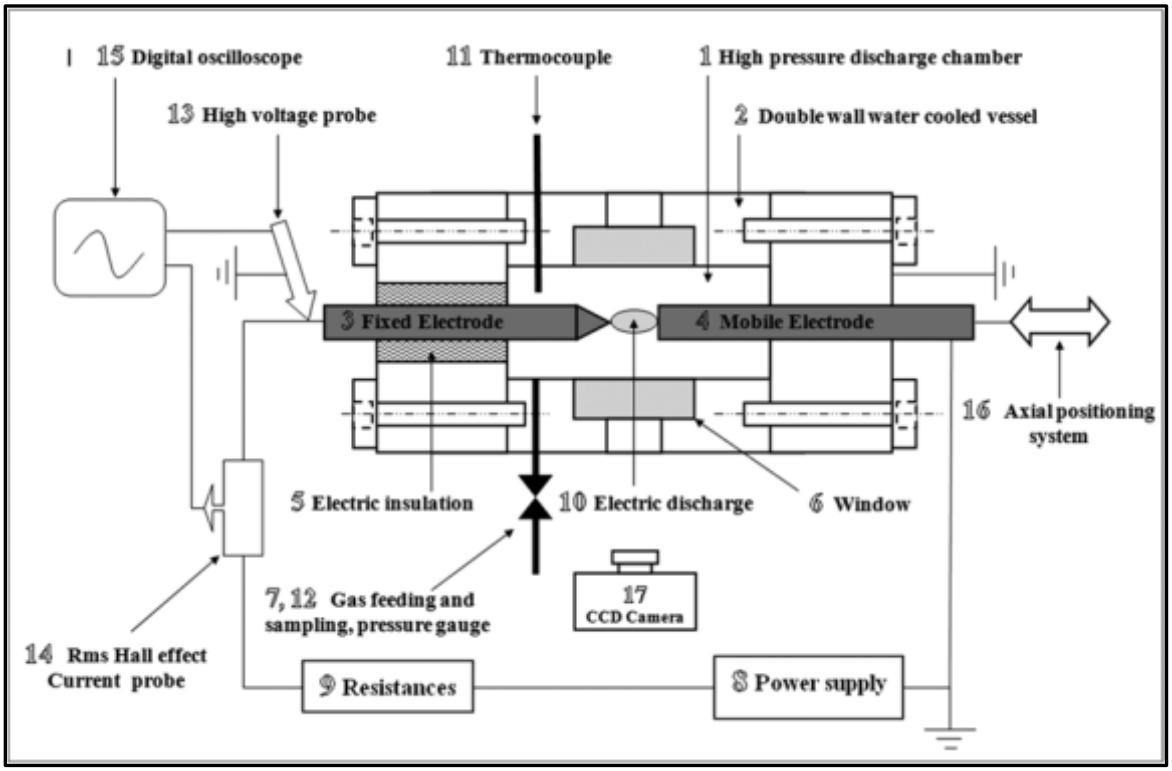

Figure 4.3: Schematic diagram of the of the tip-tip arc discharge reactor [4]

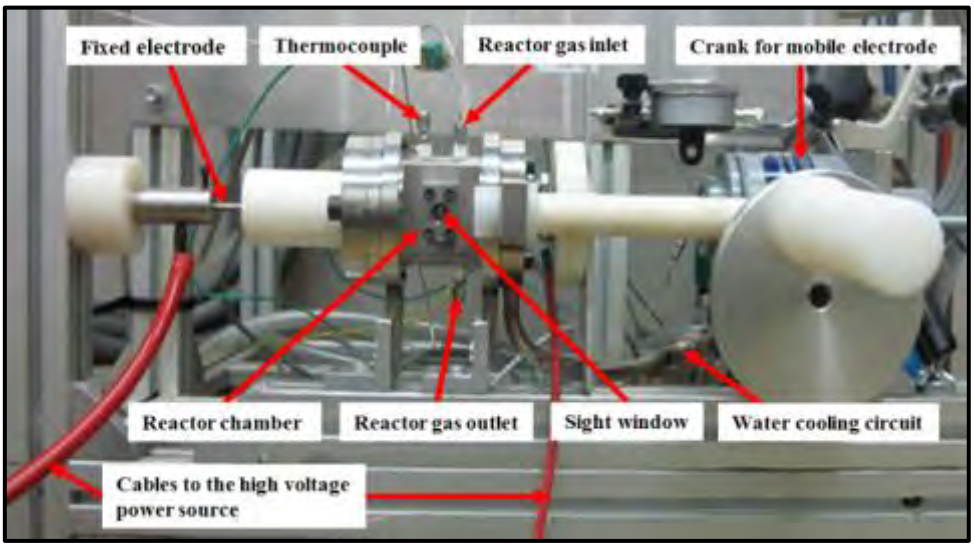

Photograph 4.1: Picture of the tip-tip arc discharge reactor

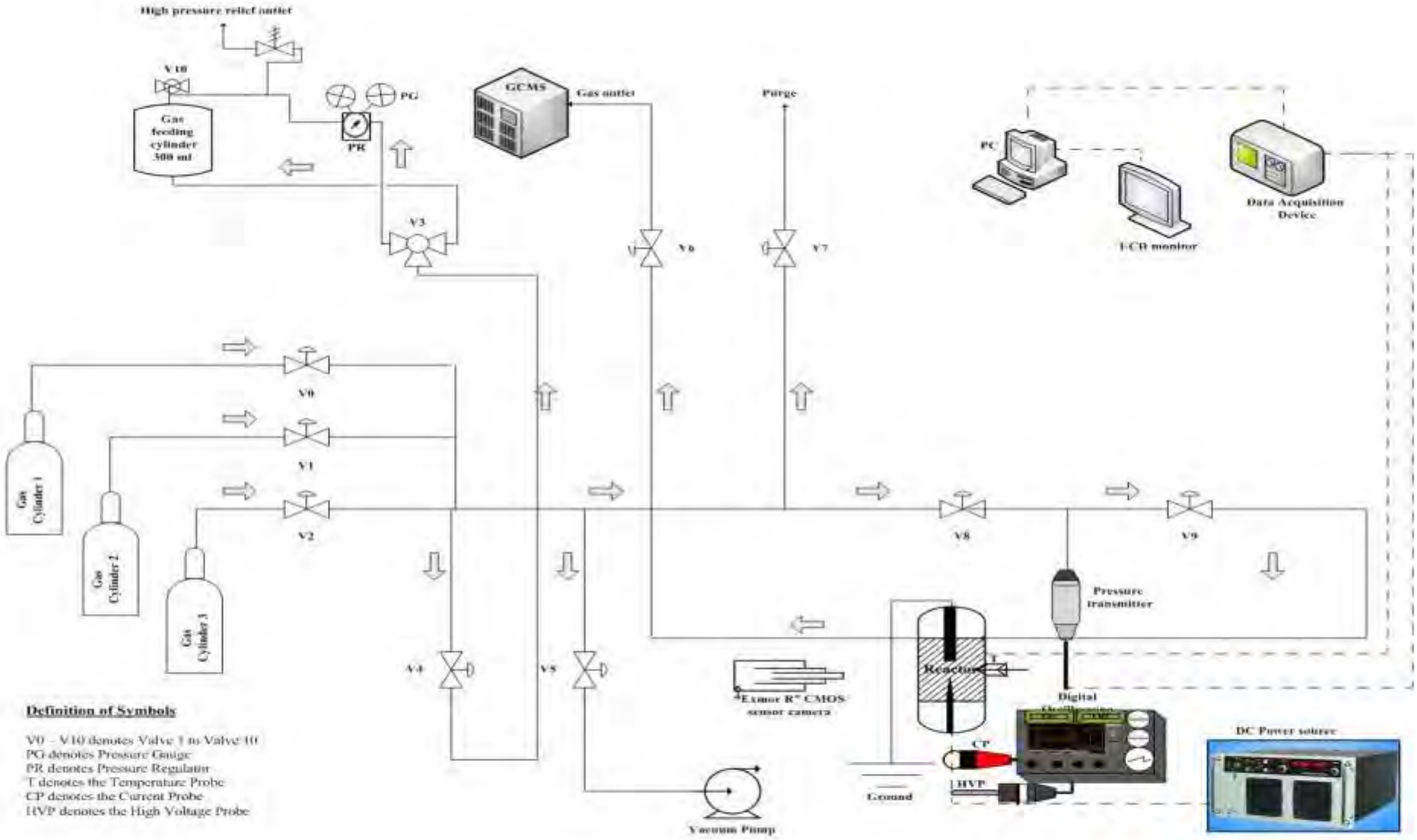

Figure 4.4: Process flow diagram of the entire experimental setup

Figure 4.3 is a schematic representation of the tip-tip arc discharge reactor. A photo image of the reactor is provided in Photograph 4.1. Figure 4.4 is a process flow diagram showing the entire setup with all the electrical measuring devices included.

The discharge chamber is of total dimension 70 x 60 mm and made of 316 L stainless steel with two face-to-face borosilicate Pyrex™ sight windows to allow visualization and spectroscopic studies of the arc discharge. The reactor has a volume of 2.56 cm^3 with an interelectrode gap of 1 mm. The discharge chamber is well sealed in terms of gas tightness to prevent leakage of air into the system as well as the introduction of impurities into the discharge chamber. The cathode electrode is a tungsten rod of length 150 mm and 4 mm in diameter, while the anode electrode is a tungsten rod of length 19 mm, 4 mm in diameter with a plane tip (flat edge) of diameter 3.80 mm and length 2.50 mm. The cathode has a conical-like tip which is at a geometrical angle of 60^o with the edge of the rod. One of the electrodes (cathode) is fixed while the other electrode (anode) is mobile. The mobile electrode is connected to an axial positioning system which has a resolution of ± 10 μm. This allows adjustment of the gap width between the two electrodes by the use of a handwheel.

The circuit used to generate the arc discharge consist of a DC power supply, which was connected in series to two ballast resistors of one (1) KiloOhms each and the discharge reactor. The primary function of the ballast resistors is to stabilize and limit the discharge current going into the electric circuit. A Chauvin-Arnoux E3N Clamp Hall-effect current probe with bandwidth from 0 to 100 kHz was used for measuring the current. The discharge voltage was measured using a HX0027 high-voltage probe, which measures up to 20 kV with bandwidth up to 30 MHz. The high-voltage probe and the current probe were connected to the fixed electrode on one end while the BNC connector was connected to the digital oscilloscope. An Agilent DSO 1004A digital oscilloscope with bandwidth of 60 MHz was used at CEP in Sophia Antipolis, while a LeCroy WJ354A with bandwidth of 500 MHz was used at the Thermodynamic Research Unit laboratory in UKZN. The oscilloscope with a sampling time of 1nanoseconds could capture and output up to 200001 data points on the oscilloscope used. The ballast resistor was placed physically close to the discharge reactor in order to reduce the stray capacitance of the circuit and to improve the stability of the discharge.

For visualization, a Sony HDR-XR150 video camera with 25x optical zoom capacity was used. This camera was placed on a stand 1 m away from the reactor with a double optical filter on the lens focused on the discharge generated in the reactor chamber. The digital camera is equipped with the Exmor R™ CMOS image sensor capable of 1920×1080 active imaging pixels and three megapixel still images. The generator consists of a DC high voltage power supply operating on current regulation mode (Technix: SR-15-R-10000 and Technix: SR-10-R-5000). The maximum output voltage and current were 15 kV and 660 mA for the Technix: SR-15-R-10000 and 10 kV and 500 mA

for the Technix: SR-10-R-5000 respectively. The errors in the electrode spacing could be neglected as operation is at low current, and thus the possibility of thermal expansion or erosion of the electrodes is negligible within the operating time. The offset from the current probe and voltage probe are 0.3 mV/A for 100 mV/A and 0.2 mV respectively.

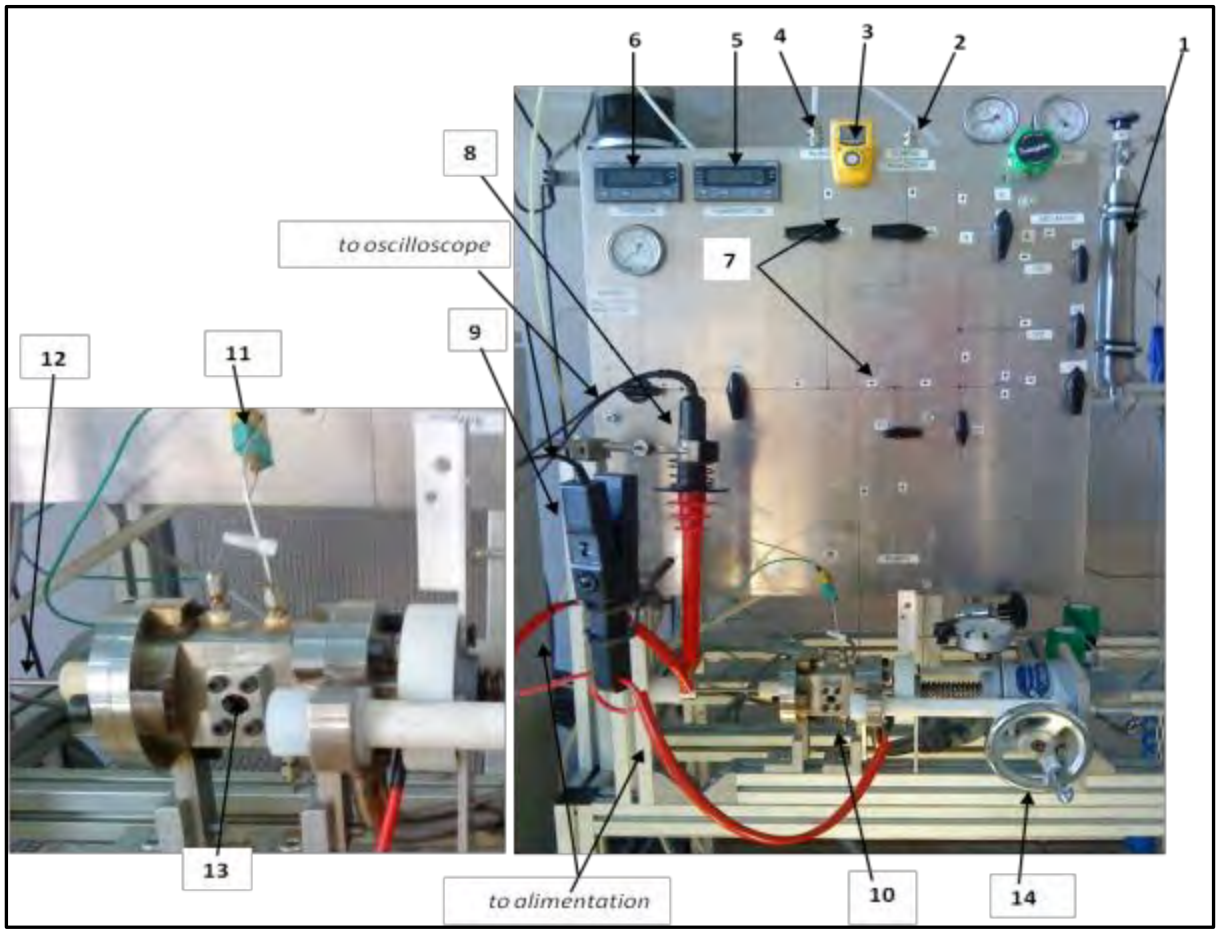

Photograph 4.2: The experimental and analytical set-up of the tip-tip arc discharge reactor

1: The Cylinder for the mixture gas (Reservoir). 2: Location of sampling syringe. 3: CO detector. 4: Gas purging point. 5: Temperature Digital Display Unit. 6: Pressure Digital Display Unit. 7: Gas supply valves. 8: High Voltage Probe. 9: E3N Clamp Current Probe. 10: Reactor. 11: Thermocouple. 12: electrode. 13: sight window. 14: Hand Wheel for regulating the distance between electrodes

4.3 Power Supply Sources

A plasma arc can be generated using different power or energy sources. Some of these sources include alternating current (AC), direct current (DC), microwave frequency, and radio frequency (RF). The use of direct current has been linked to the fact that it allows the behaviour of the discharge as a function of current to be observed [213]. It also makes the control of the current as well as other adjustable plasma parameters more easy. During the course of this research, two different power

supply source was employed; a continuous high voltage (HV) dc power supply, and a high frequency pulse power supply to generate the discharge.

4.3.1 The High Voltage Generator

A Technix-SR model with adjustable output voltage from 0 to a maximum of 15 kV and 10 kW power was employed as the power supply for all experiments conducted at the Plasma Group in MINES ParisTech. A Technix-SR model with adjustable voltage from 0 to a maximum of 10 kV and 5 kW was employed for all the experimental works conducted at the Thermodynamic Research Unit laboratory at UKZN. Both high voltage dc power supplies are the same with the difference linked only to the maximum set voltage and current.

This power source operates on double resonance technology. The power supply unit consists of an inductor-capacitor (LC) resonant circuit, which acts as a filter and thus makes it possible for smooth control of the current flowing to the load. The electrical power flowing through the high voltage transformer is regulated by the filter impedance, which directly depends on the signal frequency. The HVDC is connected to two resistors 1kΩ each, which are in series. These resistors help to protect the power supply by limiting the current. Therefore, the general operating principle of the HVDC power supply starts with the primary rectifier, which provides continuous voltage at a regulated current to the inverter. The inverter comprises of an insulated gate bipolar transistor (IGBT) bridge. The inverter produces a square waveform voltage at high output frequency up to 50 kHz. This high frequency voltage waveform is controlled by the LC resonant circuit with its primary function been the control of electrical power into the high voltage transformer. The alternate current high voltage from the transformer is rectified and the final output current is made to fit within the set current in the display panel of the power supply by the mean current controller system. A photograph and schematic diagram of this unit is presented in Photograph 4.3 and Figure 4.5.

Photograph 4.3: Picture of the high voltage resonance-type generator

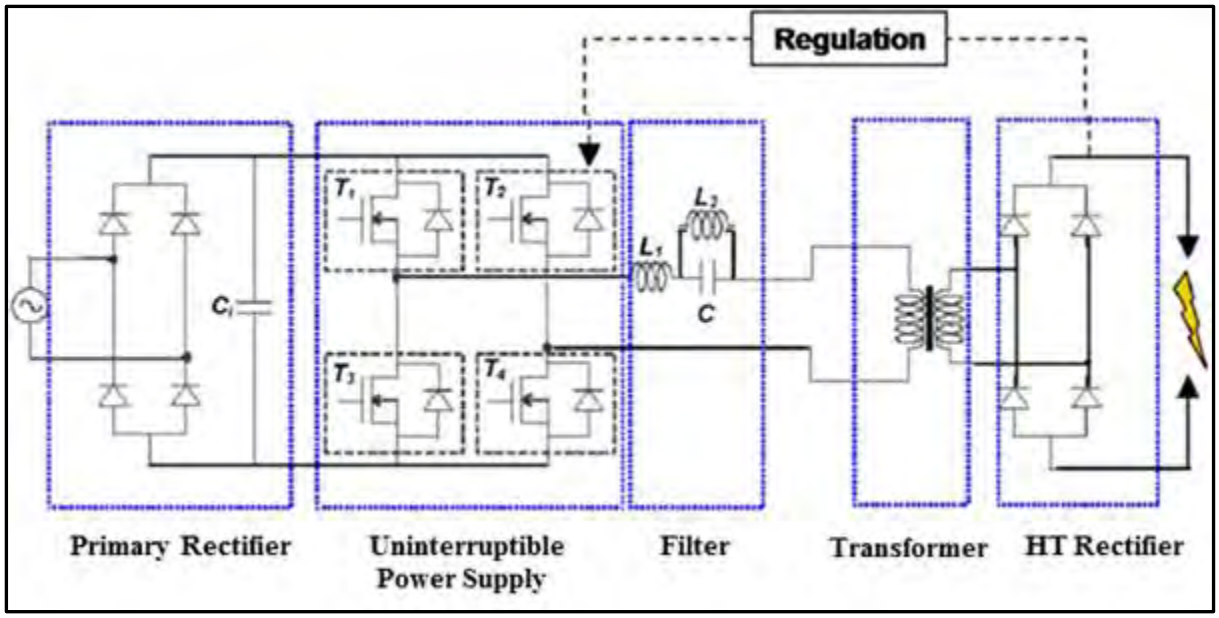

Figure 4.5: Schematic diagram of the high voltage generator [4]

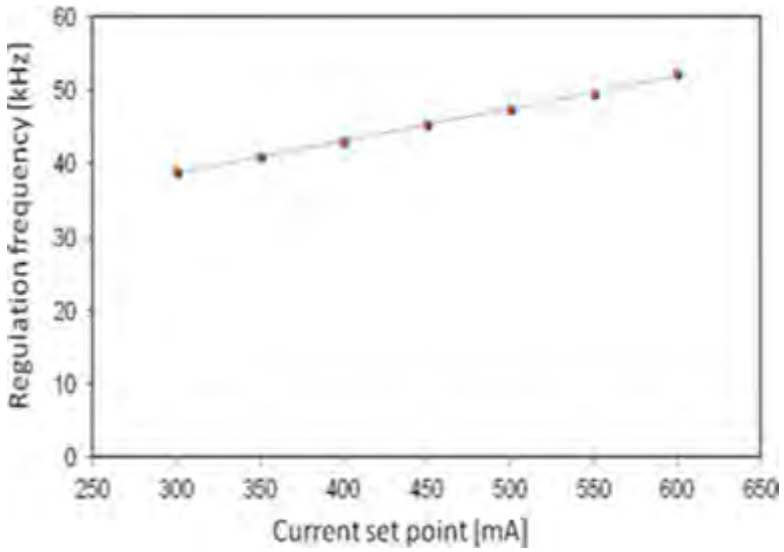

Figure 4.6: Regulation frequency versus setting current for resonance-type generator [4]

4.3.2 The High Frequency Pulse Power Supply

The high frequency pulse power supply unit used consists of a QSC audio RMX 2450 professional power amplifier connected to an Agilent 33210A 10 MHz function waveform generator. The operating principle of the pulse power supply is briefly summarized hereafter: a function generator delivers a sine waveform signal at a set and controlled pulse frequency and peak-to-peak driving voltage. The delivered waveform is taken as input to a stepper motor controller. This controller acts as an integrator circuit by generating direction signals for the power amplifier as well as the function generator. It further controls the peak current per amplification and thus reduces power loss to the amplifier by reducing the current during pulses.The power amplifier, which uses a high-current

toroidal transformer and ample filter capacitance then picks up the AC power signal and outputs it as clean DC, thus reducing the electrical power supplied into the reactor for generating a pulse discharge. A photograph and block diagram of this unit is presented in Photograph 4.4 and Figure 4.7.

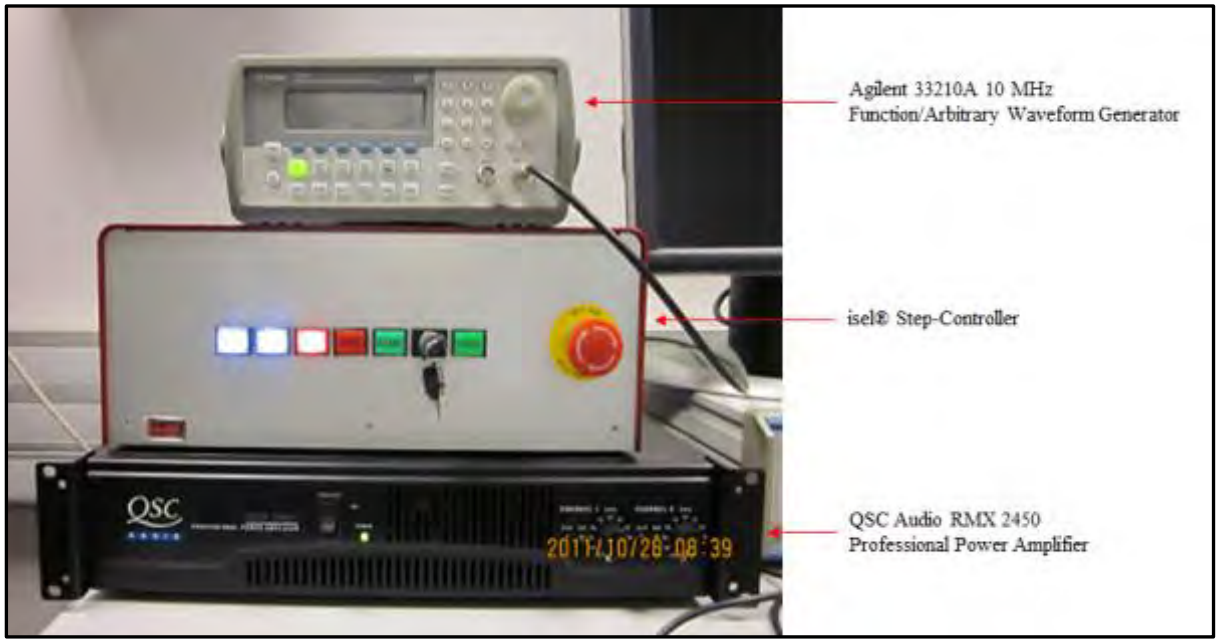

Photograph 4.4: Picture of the high frequency pulse power supply unit

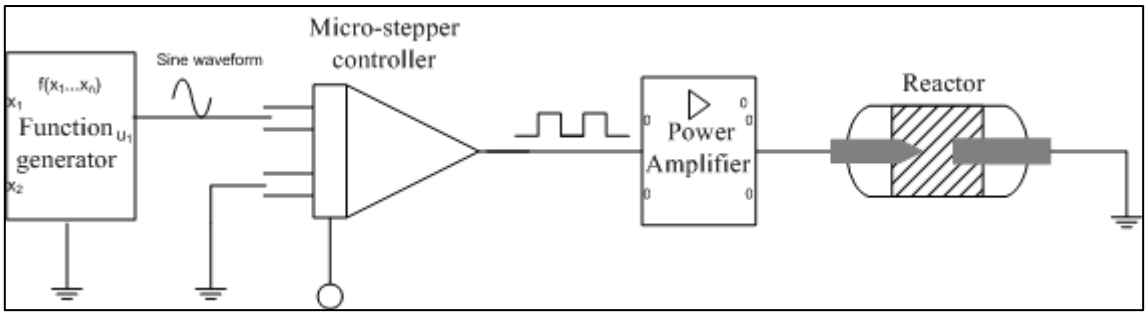

Figure 4.7: Block diagram of the high frequency pulse power supply unit

4.4 Experimental Procedure

The experimental procedure consists mainly of the procedure for treating the reactants with the discharge generated and the procedure for sampling and analysing the gas products obtained after the discharge. A detailed procedure for calibrating the detector of the GC for the various gases used, pressure transducer, and temperature probe used are presented in Appendix A and B respectively.

A summarized procedure that does not include the start-up and shutdown procedure is therefore presented below.

4.4.1 Procedure for the Electrical Characterization of a Non-reactive Gas (Helium)

Step1: The discharge chamber of the reactor is filled with helium gas at the required pressure using a pressure-regulator to control the pressure. This was done while the two electrodes are in contact.
Step 2: The power supply is switched on, and the current is set to a selected set point.
Step 3: After the discharge is observed to be ignited, the mobile electrode is then gradually moved backwards to the desired interelectrode gap.
Step 4: After step 3, the discharge is observed until it is stabilized. Then the root mean square value for the current and the voltage is measured on the digital oscilloscope.

The same measurement procedure was repeated by varying the current, the inter-electrode gap, and the pressure. By varying the three parameters, measurements were made for each run several times. These was done in order to eliminate any possible time lag that may be experienced as an effect of the adjustment of the current, inter-electrode gas spacing, and the increase or decrease in the pressure.

4.4.2 Procedure for Reactive Gas Mixtures in the Electric Discharge at High Pressure

According to the experimental setup and the process flow diagram shown in Figure 4.4, the reactants are fed into a gas-mixing cylinder based on their partial pressures. The gases are allowed to mix, and the gas mixture is then fed into the reaction chamber of the reactor. Since the gases are not reactive enough to initiate a chemical reaction spontaneously, the energy supplied into the system by the power generator brings about the generation of the plasma which through dissociation and ionization processes produces more reactive atomic species and new free radicals. The recombination process leading to the synthesis of new products then finally follows this. The experimental procedures described below have been used for the synthesis of hydrocarbon systems at high pressure and has been published by Rohani et al. [178] and it is the best suitable procedure for now.

Several experiments were carried out using carbon monoxide, hydrogen, and helium gas mixtures; methane and carbon dioxide gas mixtures; and tetrafluoromethane and helium gas mixtures.

At the start of an experiment, the reactor chamber is purged twice using an inert gas (helium) in order to evacuate gas impurities that may be in the system from the previous experiments. Taking as an example, the experiments involving syngas (mixture of H_2 and CO), CO was first supplied through an input valve into a stainless steel mixing cylinder which has a capacity 300 cm^3. The gas was filled to a desired pressure measured as the partial pressure of the gas. Then H_2 was supplied as the second reactant gas into the same mixing cylinder and filled to the desired pressure based on the reaction stoichiometry molar ratio of the gas mixtures. All this stage has been completed; samples are taken in triplicate from the reactor in order to analytically verify the composition ratio of the gas mixtures

using a classical GC. After verification was deemed satisfactory, the gas mixtures were introduced into the reactor chamber via a three-way valve and the chamber was pressurized up to the desired operating or working pressure. The pressure in the reactor is monitored using a pressure transducer and a pressure gauge.

Before generating the electric arc discharge within the reactor chamber, a worm gear actuator is used to bring the mobile electrode into contact with the fixed electrode. After both electrodes are in contact, the water circuit is turned on and water which acts as a cooling fluid is allowed to continuously circulate through the stainless steel jacket around the reactor chamber. The power supply is switched on, and the mobile electrode is gradually adjusted as the arc discharge is ignited and generated between the mobile and fixed electrodes at the required operating conditions. Although, the velocity at which the gear actuator rotates is not constant during the stretching of the discharge, a stopwatch used to monitor the duration of the discharge is only activated after the desired interelectrode gap is reached. The discharge is sustained by the power source during the duration allowed for each experiment and then turned off. This experimental sequence was repeated for all of the experiments carried out in the reactor under different experimental conditions with the CO_2 introduced first and CH_4 introduced as the second reactant in the experiment using the CH_4 and CO_2 gas mixtures. After each experiment, a gaseous sample is taken for GC analyses.

4.4.3 GC Analysis Procedure

For the analysis of the gas sample, a classical gas chromatograph was used as well as a gas chromatography mass spectrometer. For the hydrocarbon synthesis experiments, a Perichrom-2100 gas chromatograph was used, while for the fluorocarbon synthesis experiments; a Shimadzu GC-2010 gas chromatograph was employed. A brief description of the sampling procedure on the two classical gas chromatographs is presented in the next subsections.

4.4.3.1 Perichrom-2100 Gas Chromatograph

The analysis of the hydrocarbon systems was carried out on a Perichrom PR2100 GC model. One of the important features of the PR2100 GC is that it allows three detectors (2 TCD with an FID) to operate simultaneously.

The gas mixtures in the reactor were sampled before and after discharge using a 60 ml syringe fitted with a manual valve. The gas collected was then injected into a PR2100 gas chromatograph and the respective peaks obtained are integrated for qualitative purposes while the compositions are analysed quantitatively to determine the concentration of each species based on calibrated gas standards for the C_1, C_2, C_3, and C_4 species. One flame ionization detector (FID) and two thermal conductivity

detectors (TCD) using helium and nitrogen as carrier gas were operated concurrently on the PR2100 gas chromatograph. A FID/methanizer was also employed in order to improve the detection of the CO and CO_2 gases.

The PR2100 GC was used for the purpose of quantitative and qualitative analyses of the outlet gas phase products while a QP2010S GCMS with a Supel-Q™ PLOT column and helium as carrier gas was employed for the confirmation of some species and identification of unknown synthesis species. The PR2100 GC used was configured with two parallel analysis circuits that allows for the use of two different carrier gases namely; nitrogen and helium for the separation process. The GC's parameters are monitored and control on a graphical interface chromatography workstation software (Winlab III) via the use of a timed event switching method. Figure 4.8 gives a layout configuration of the PR2100 GC. Details of the program setting and configuration for the PR2100 are presented in Appendix E.

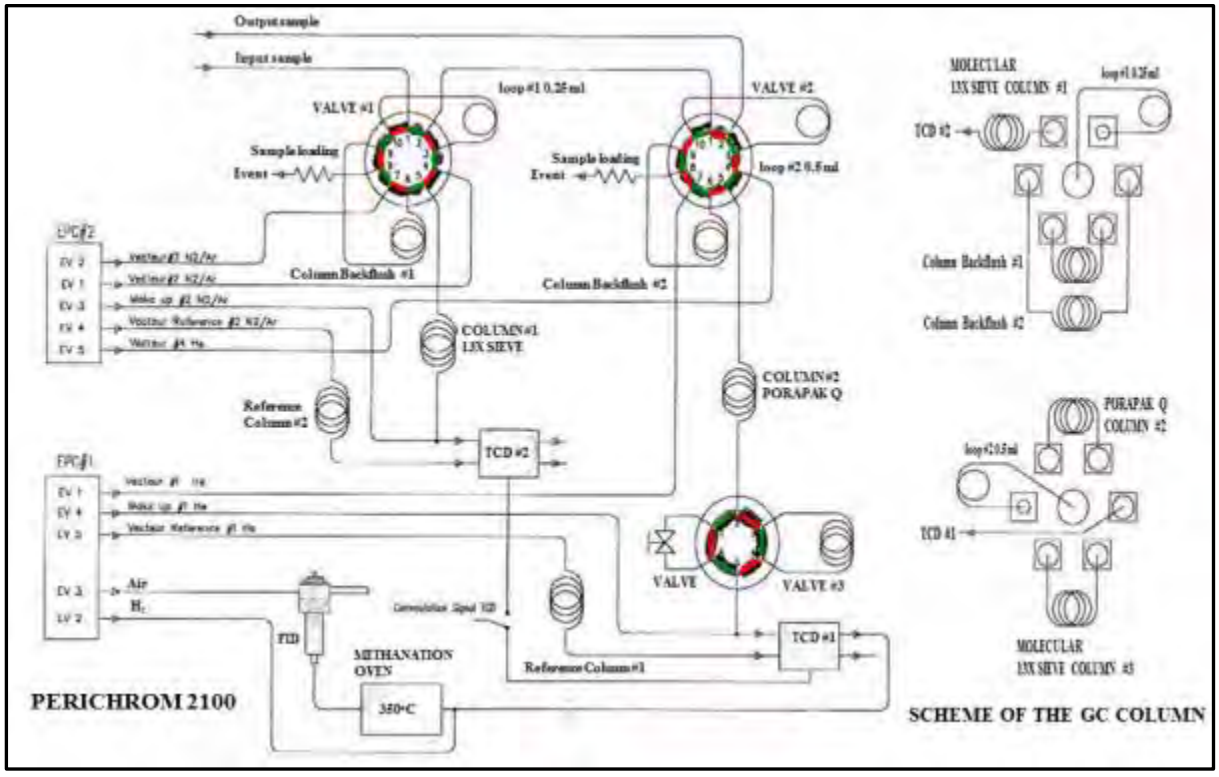

Figure 4.8: Schematic diagram showing the principle of setup for the PR2100 gas chromatograph

Two molecular sieves 13X and a Porapak Q column were used in the GC analyses. The first molecular sieve column completely separates the He and H_2 gas and is connected to a TCD with nitrogen as the carrier gas. The GC event then switches after the first 3 min, and the Porapak Q together with the second molecular sieve column then enables the separation of O_2, N_2, CO, CO_2, saturated C_1 to C_4 and the unsaturated C_2 to C_4 hydrocarbons with helium as the carrier gas and is passed through the second TCD. Nitrogen was used as the carrier gas in the first TCD because of its low thermal conductivity in relation to helium and hydrogen, while helium was used as carrier gas for

the second TCD because of its high thermal conductivity in relation to the remaining gases as well as its wide range of application in gas chromatography separation process. The FID, which is more sensitive to the hydrocarbons, was relied upon for detection of saturated C_1 to C_4 and the unsaturated C_2 to C_4 hydrocarbons at low ppm levels.

An optimum oven temperature of 200 ^oC was used in the PR2100 GC. Starting with an initial temperature of 40 ^oC with an isothermal delay of 17 min, an increasing ramp rate of 15.0 $^oC.min^{-1}$was used until the optimum temperature was attained and held constant for 12.5 min. TCD 1 and 2 were set to a temperature of 150 ^oC each, while the FID was set to a temperature of 255 ^oC. The temperatures of the injector 1 and 2 were 150 and 350 ^oC respectively. An injection volume and sampling rate of 1 μL and 25 $samples.s^{-1}$ respectively were specified for the GC analysis of each sample, and a carrier gas flow rate of 30 $ml.min^{-1}$ and pressure of 0.1 MPa.

4.4.3.2 Shimadzu Gas Chromatograph-2010

A Shimadzu GC-2010 used for the analysis of fluorocarbons was equipped with a capillary column (HP Al_2O_3PLOT column), injection ports, and a flame ionization detector. The column was able to separate each fluorocarbon gas distinctively. The calibration results for the fluorocarbons are presented in Appendix A.

The Shimadzu GCsolution® software interface installed on a personal computer was used for the purpose of data acquisition and control of the gas chromatograph parameters. The GC solution software interface allows the creation of a method file on which parameters such as the column, injector, and detector temperatures can be set. The column flow rate, make-up gas flow can also be set and loaded into the method file. The acquired data during sample analysis is stored and can be opened afterward for post-run analysis of the results. Figure 4.9 is an output file for a post-run analysis for CF_4 dissociation.

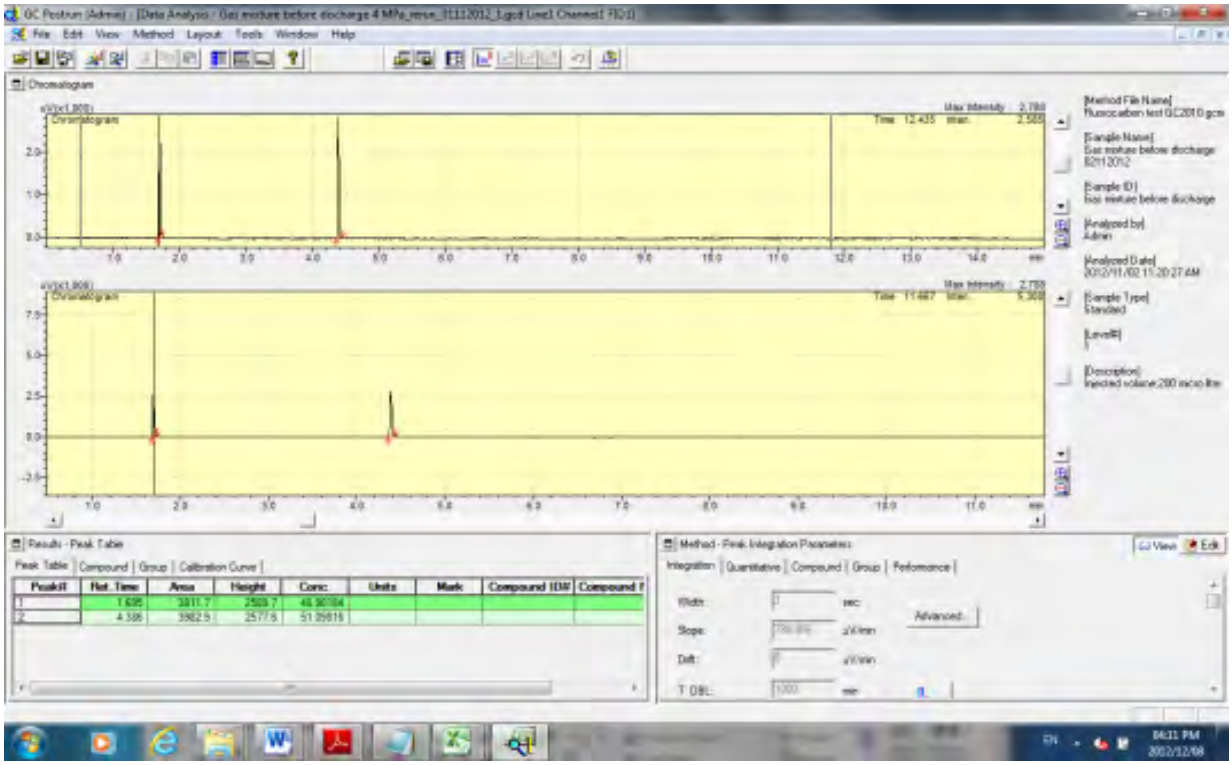

Figure 4.9: Post-run analysis of the chromatograms on the Shimadzu GC solution software

Table 4.1 present the specifications of the GC column used, while Table 4.2 present the settings for parameters used for both the calibration and the analysis of the fluorocarbons on the Shimadzu GC-2010.

Table 4.1: Specifications of the GC column used on the Shimadzu GC for fluorocarbons

Column	**Specified value**
HP-PLOT/Al_2O_3	
Serial #: 19095P-M23	
Length (m)	30
Film thickness (µm)	15
Inner diameter (mm)	0.53
Maximum usable temperature (^oC)	250

Table 4.2: Method file settings and parameters used on the Shimadzu GC for fluorocarbons

Parameters	**Settings**
Makeup Gas	He
Inlet pressure (kPa)	100
Primary pressure (kPa)	300-500
Detector temperature (^{o}C)	250
Injector temperature (^{o}C)	250
Column temperature (^{o}C)	50
Split ratio	50
Total flow (mL/min)	181.1
Linear velocity (cm/sec)	28.8
Column flow (mL/min)	3.49
Pressure (kPa)	23.0
Hold Time (min)	20

Chapter 5

RESULTS AND DISCUSSION

The aim of this project was to investigate the effect of certain adjustable parameters on the synthesis of hydrocarbons and fluorocarbons in a tip-tip discharge reactor at high pressure. To this effect, preliminary studies have been conducted under certain experimental conditions with helium used as a diluent in order to ensure the ignition and stabilization of the discharge for high pressure operation for the following reactive gas mixtures:

- mixtures of hydrogen and carbon monoxide with helium as diluent for the Fischer-Tropsch Process;
- synthesis gas (mixtures of hydrogen and carbon monoxide) for the Fischer-Tropsch Process;
- methane and carbon dioxide mixtures for the dry reforming process;
- tetrafluoromethane and helium mixtures for fluorocarbons synthesis

In addition, electrical characterization experiments were carried out for a non-reactive gas (helium) at the following conditions in order to be able to compare the results to 3D MHD modelling.

- pure helium at 8 MPa, 1 mm interelectrode gap, and varying current from 0.25 to 0.4 A;
- pure helium at 0.35 A, 1 mm interelectrode gap, and varying pressure from 1 to 8 MPa;
- pure helium at 8 MPa, 0.35 A, and varying interelectrode gap of 1, 1.25, 1.50 and 2 mm.

The results presented are from experiments carried out at the Center for Energy and Processes, MINES ParisTech, France and the Thermodynamic Research Unit laboratory in the School of Engineering at the UKZN, South Africa. The sets of experimental results presented in section 5.1 have been published [178], while the three others are in preparation for submission.

For the purpose of clarifications, a set of experimental results will be presented in a subsection with every analysis and comments relating to the results presented as well under the same heading. The specifications of the gases used for the hydrocarbon synthesis experiments are presented in Table 5.1, with all results obtained following the experimental procedure explained in section 4.4 of Chapter four.

Table 5.1: Specifications of the gases used in investigations with the maximum concentrations of impurities

Hydrogen	Carbon Monoxide	Carbon Dioxide	Methane	Helium
H_2O < 0.5 ppm	Ar < 2 ppm	H_2O < 10 ppm	C_2H_6< 200 ppm	H_2O < 3 ppm
O_2< 0.1 ppm	O_2< 20 ppm	O_2< 10 ppm	CO_2< 10 ppm	O_2< 2 ppm
CO < 0.1 ppm	N_2< 9 ppm		C_nH_m< 50 ppm	CH_4 < 0.5 ppm
CO_2< 0.1 ppm	H_2< 8 ppm		O_2< 10 ppm	
CH_4≤ 0.1 ppm	CH_4< 5 ppm		N_2< 200 ppm	
			H_2O ≤ 5 ppm	
			H_2< 20 ppm	

5.1 Hydrocarbon Synthesis from Syngas through Three Modes of Treatment

Experiments were conducted for He/H_2/CO gas mixtures in percentage mole fraction ratios of 40/48/12 respectively. These experiments served to demonstrate the influence of the different treatment mode on the synthesis of longer chained hydrocarbons from syngas. Helium was added to the syngas mixture to stabilize and ensure the ignition of the discharge for high pressure operation. The experimental operating conditions for this work are presented in Table 5.2 below.

Table 5.2: Operating conditions for hydrocarbon synthesis from syngas according to the mode of treatment

Operating conditions	Continuous mode	Cycle mode 1c = 9s	Cycle mode 1c = 1s
Current	0.35A	0.35 A	0.35 A
Ignition Voltage	8 kV	8 kV	8 kV
Pressure	2.2 MPa	2.2 MPa	2.2 MPa
Syngas / Helium	3 / 2	3 / 2	3 / 2
H_2 / CO	4 / 1	4 / 1	4 / 1
Inter-electrode gap	1.25 mm (constant)	0→1.25 mm (variable)	0.25 mm (constant)
Discharge duration	0→100 s	0→180 s	0→20 s
Treatment time	0→100 s	0→750 s (0→20 cycles)	0→590 s (0→20 cycles)
Graphical results	Figure 5.1	Figure 5.2	Figure 5.3

These experiments further investigate the effect of the three different treatment modes (one continuous and two intermittent modes with a relaxation time between successive discharges). The continuous mode implies that the gas mixture is exposed to treatment by the discharge over a

continuous extended period referred to as the "discharge duration". For the first cyclic mode, the gas mixture was treated by generating the discharge in successive cycles characterized by a duration of 9 s, which is separated by a relaxation period of 30 s. The second cyclic mode is similar to the first cyclic mode except that the discharge duration for a cycle is 1 s, which is then followed by a relaxation period of 30 s. The results show that significant amounts of C_1 and very low amounts of C_2 hydrocarbons were obtained. Graphical representations of the results are presented in Figures 5.1 to 5.3.

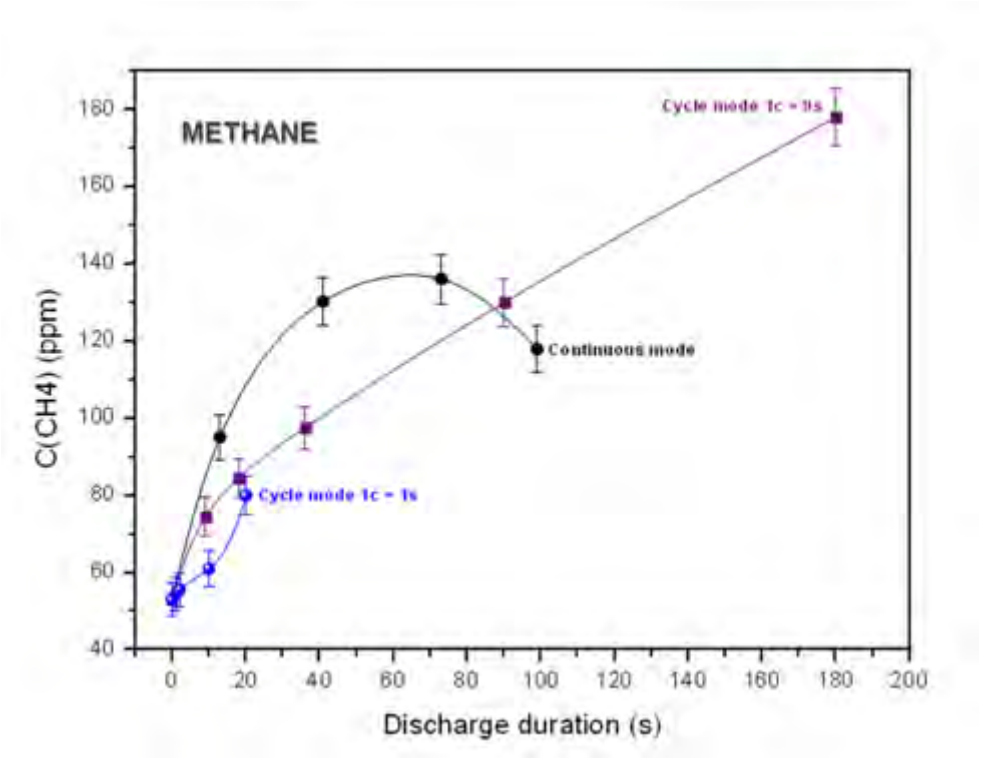

Figure 5.1: Concentration of CH_4 produced versus discharge duration for the three modes of treatment

For each of the quantitative analyses, errors were estimated based on the repeatability of the measured sample (R_{SM}) and the accuracy of the calibrated gas standards(A_{CGS}), while taking into account the background noise (BN) in both case. Thus, the sample measurement error (SME) and the calibration error (CE) for individual analysis are given by the equations:

$$SME(ppm) = R_{SM}(\pm 3\%) + BN(\pm 0.05\,ppm) \tag{5.1}$$

$$CE(ppm) = A_{CGS}(\pm 5\%) + BN(\pm 0.05\,ppm) \tag{5.2}$$

Hence, an approximated total error of ± 8 % for concentration was included for each synthesized product. This is indicated in the graphical results in the form of a representative error bar for each data point.

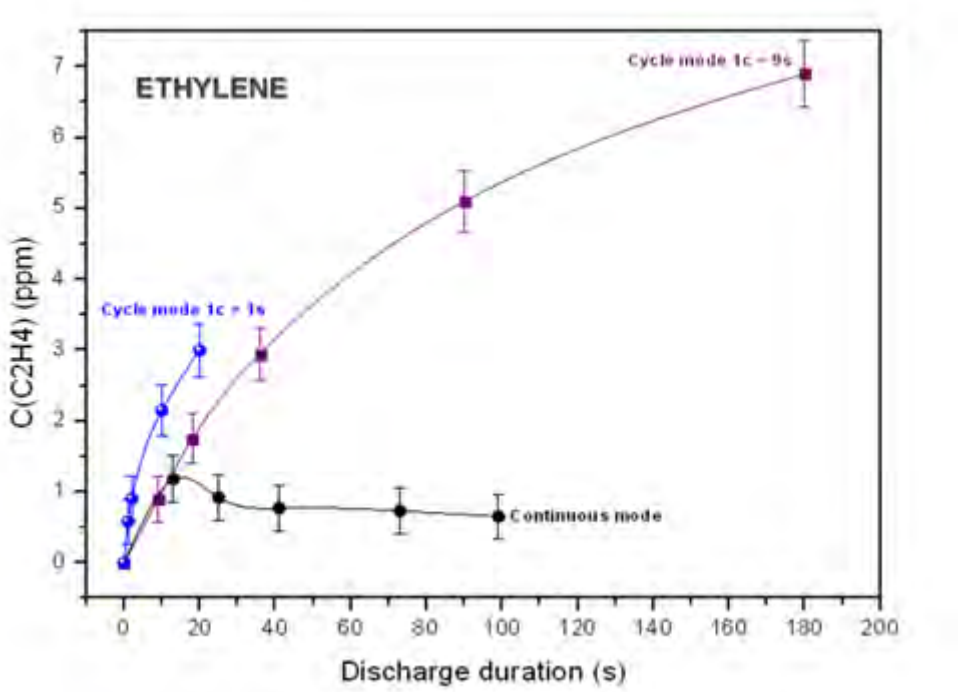

Figure 5.2: Concentration of C_2H_4 produced versus discharge duration for the three modes of treatment

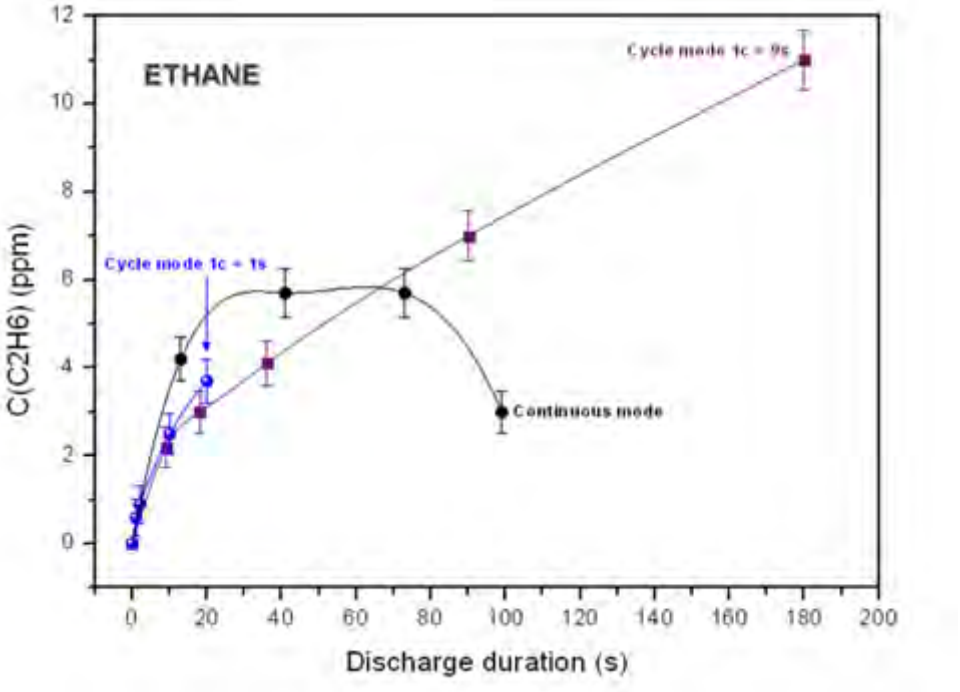

Figure 5.3: Concentration of C_2H_4 produced versus discharge duration for the three modes of treatment

5.1.1 Comments on the Results from theThree Treatment Modes

As mentioned in the published version of this work [180], CH_4, C_2H_4 and C_2H_6 were observed to be produced for all the treatment modes investigated. From the graphical results shown in Figures 5.1 to 5.3, the produced species were observed to be influenced by the treatment mode used. While high production rate was observed for the species in the continuous mode under 20 s, the production rate decreased rapidly after a discharge time between 60 and 70 s for CH_4; 15 s for C_2H_4; and after 60 s for C_2H_6. Thus, under the continuous discharge mode regime, the discharge generated seems to destroy the species produced after a certain time is reached. This mode of operation thus put a limitation on the species that can be produced based on the discharge duration.

For the cyclic mode 1c = 9s, a continuously increasing trend of the species produced was observed as a function of the discharge duration. This result shows that by generating the discharge intermittently after a relaxation period, the kinetic inversion observed for the continuous mode could be prevented.

By comparing the continuous mode and the first cyclic mode in Figure 5.1, it was observed that CH_4 has the highest production rate of approximately 2.5 ppm/s between discharge duration of 0 and 9 s. However, the production rate decreases slowly after 65 s. On the other hand, CH_4 production under the first cyclic mode shows similar trends to that of the continuous mode during the 0 to 9 s interval, but increases more slowly after 9 s in comparison to the continuous mode. While the CH_4 production rate for the first cyclic mode becomes constant with a value of approximately 0.55 ppm/s after 40 s, it surpasses the continuous mode after 90 s with respect to the amount to CH_4 produced.

The second cyclic mode 1c = 1 s shown in Figure 5.1 shows the different CH_4 production kinetic rates from the two modes discussed above. While the CH_4 production rate is lower for this cyclic mode, between discharge duration of 0 and 20 s in comparison to the other 2 modes, an exponential trend was observed, which implies that the production rate increases as a function of the discharge duration.

The concentration of C_2 hydrocarbons produced, as shown in Figures 5.2 and 5.3, are low in comparison to the CH_4 produced by the three modes in Figure 5.1. From Figure 5.2, it can be seen that the curve for C_2H_4 production follows the same trend for the continuous mode and the first cyclic mode 1c = 9 s in the discharge duration of under 20 s. However, the continuous mode is observed to reach a maximum at approximately 17 s, while the cyclic mode 1c = 9 s increases monotonically as a function of the discharge duration. Interestingly, the cyclic mode 1c = 1 s shows the highest production rate for C_2H_4 as can be seen in Figure 5.2. This could mean that the second cyclic mode 1c = 1 s is suitable for C_2 hydrocarbon production.

A look at Figure 5.3 for C_2H_6 production reveals a trend similar as for CH_4 produced by the continuous mode and the cyclic mode 1c = 9 s. The concentration of C_2H_6 produced by the continuous

mode was observed to increase between the time intervals of 0 to 30 s to a maximum value of 5.5 ppm, and then decrease after 60 s. With the continuous mode, the destruction rate of the C_2H_6 was estimated to reach 0.1 ppm/s at 100 s with a continuously decreasing production rate as a function of the discharge duration. Again, as in the case with CH_4, the cyclic mode shows prospects for the production of C_2H_6 following the same trend as observed for its production of CH_4.
In this mode, the production rate of C_2H_6 was observed to decrease quickly between the discharge duration of 0 and 40 s, but becomes relatively stable after 40 s before decreasing slowly again. Thus, the synthesis of C_2H_6 with the cyclic mode 1c = 9 s can be said to ease with time. Unlike in the production of CH_4 where the cyclic mode 1c = 1 s shows an acceleration in CH_4 production rate, Figure 5.3 shows a decreasing production rate for C_2H_6, like the other two modes.

In conclusion, it must be said that despite the low CH_4 concentration obtained in the second cyclic mode (1c = 1s) in comparison with the other two other treatment modes,the concentration of the C_2 hydrocarbons is higher with this mode in the time intervals of 0 and 20 s than the continuous and first cyclic mode 1c = 9 s. Thus, the second cyclic mode (1c = 1s) shows the best kinetics for the synthesis of C_2H_4 and C_2H_6.

5.1.2 Analysis and Discussion

For an interelectrode gap of 0.25 and 1.25 mm, the ratio of the discharge volume to the volume of the reaction chamber can be as low as 10^{-6} and 10^{-5} respectively. Based on this understanding, it is important to estimate the maximum value of concentration that can be obtained for the products under instantaneous treatment mode for 1s. This approach will help to explain the reason why the production rates for C_2 did not exceed 1 ppm/s with the treatment mode. In order to carry out, a global species balancing of the synthesized reaction equation occurring within the active volume of the reactor during the 1c = 1s treatment mode, the following assumptions are made;

- That mass transfer between the discharge volume and the other parts of the reaction chamber is strongly limited during discharge duration of 1 s;
- That the hydrodynamic transport within the reaction chamber can be neglected based on the first assumption.
- That all the synthesis reactions occurred in an active volume (V_A), which includes the discharge volume and its direct surroundings.

Hence, with the concentrations of species before and after the 1s treatment in the cyclic mode (1c = 1s) as well as the volume of the reactor (V_R) known, the volume (V_X^P) of each species (X) produced in V_A during one second of treatment can be calculate using the formula:

$$V_X^P = \left(C_m^f(X) - C_m^i(X)\right) \times V_R \tag{5.3}$$

Where $C^i_m(X)$ and $C^f_m(X)$ are the initial and final concentrations of the species (X) measured by GC. Using this formula, the volume of each hydrocarbon species produced in V_A during 1s is:

$$V^P_{CH_4} = 3.84\times10^{-3}\,mm^3 \quad ; \quad V^P_{C_2H_6} = 1.536\times10^{-3}\,mm^3 \quad ; \quad V^P_{C_2H_4} = 1.485\times10^{-3}\,mm^3$$

From GC measurements, no CO_2 was produced, which implies $V^P_{CO2} = 0$. Based on a case of 100% conversion of CO, the initial volume V^A_{CO} of CO in the active volume (V_A) required for the production of C_1 and C_2 hydrocarbons quantities during 1s can be estimated to be:

$$V^A_{CO} = V^P_{CH_4} + 2\times(V^P_{C_2H_4} + V^P_{C_2H_6}) = 9.88\times10^{-3}\,mm^3 \tag{5.4}$$

Since the initial gas mixture contains 12% of CO, the required active volume V_A will be

$$V_A = \frac{V^A_{CO}}{0.12} = 8.235\times10^{-2}\,mm^3 = 32\times10^{-6}\times V_R \tag{5.5}$$

The result obtained in equation (5.5) implies that the active volume corresponds to 32 ppm of the reactor volume in a total CO conversion to CH_4, C_2H_6, C_2H_4 and H_2O. Hence, for a cylindrical form discharge of length equal to the interelectrode gap of 0.25 mm, the active radius will be 0.32 mm. The analysis of the discharge image shown in Photograph 5.1, as captured with the help of a video camera and an optical filter with an extenuation of 25% gives the averaged discharge radius to be between 0.15 and 0.16 mm. However, the discharge radius based on 100% CO conversion is approximately twice the discharge radius estimated by imaging.

The difference between the discharge radius calculated based on 100% CO conversion and the one estimated from the image in Photograph 5.1is a confirmation of the fact that the CO conversion is quasi-complete in the discharge volume [178]. It equally means that the discharge volume is certainly larger than the luminous volume visually determined with the video camera and, thus there is significant amount of mass transfer between the discharge volume and its immediate surroundings because of hydrodynamic transport.

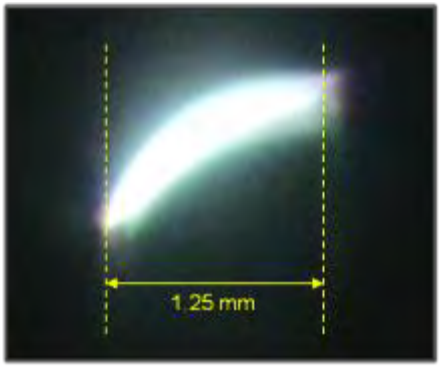

Photograph 5.1: Photo image of the discharge for an inter-electrode distance of 1.25 mm, obtained with a video camera and an optical filter (-25%) [178]

Thus in view of the assumptions made, the synthesis reaction for 1 s instantaneous treatment is:

$$CO + 4H_2 \xrightarrow{d} xCH_4 + yC_2H_6 + zC_2H_4 + tH_2 + wH_20 \tag{5.6}$$

Using ratio calculus, the coefficients for the hydrocarbon species are estimated, while the coefficients of H_2O and H_2 are obtained by the conservation of hydrogen and oxygen in the chemical equation:

$$x = \frac{V_{CH_4}^P}{V_{CO}^A} = 0.39 \quad ; \quad y = \frac{V_{C_2H_6}^P}{V_{CO}^A} = 0.155 \quad ; \quad z = \frac{V_{C_2H_4}^P}{V_{CO}^A} = 0.15 \quad ; \quad t = 1.45 \quad ; \quad w = 1$$

Thus, the global synthesis equation operating in the active volume during one second of treatment is:

$$CO + 4H_2 \xrightarrow{d} 0.39CH_4 + 0.155C_2H_6 + 0.15C_2H_4 + 1.45H_2 + H_20 \tag{5.7}$$

This result is important for improving the treatment efficiency. Following the results of this analysis, it can be seen that an increase in the discharge volume will lead to a significant improvement of the synthesis process. In addition, the intermittent treatment mode with short discharge durations and large discharge volumes should promote hydrocarbon chain growth.

5.2 Hydrocarbon Synthesis from Syngas using a High Voltage Direct Current

This set of experiments was conducted with the use of a high voltage direct current power supply. The influence of two parameters, viz. operating pressure and current on syngas conversion to higher hydrocarbons was studied. The operating conditions for the experiments are presented in Table 5.3.

Table 5.3: Operating conditions for hydrocarbon synthesis from syngas at different pressures and currents using the continuous high voltage DC power supply

Operating Conditions	Pressure variation	Current variation
Current/ A	0.35	0.20, 0.30, 0.35, 0.40
Ignition voltage / kV	8	8
Interelectrode gap / mm	1.0	0.4
Pressure / MPa	0.5, 1.0, 2.0, 4.0, 6.0, 8.0, 10.1, 11.9 , 14.7	0.5
Ratio of H_2:CO	2.2:1	2.2:1
Discharge time / s	60	120

5.2.1 Influence of Operating Pressure Range 0.5 to 15 MPa on Hydrocarbons Synthesis

The effect of pressure is rarely investigated in most plasma processes as most experiments are conducted at fixed pressure (sub-atmospheric or atmospheric). In the tip-tip arc discharge reactor used in this study, the influence of pressure on hydrocarbon synthesis was studied. The operating condition for these experiments is listed in Table 5.3 under the heading "pressure variation". The results showing the concentration of the hydrocarbons produced as a function of the operating pressure are presented in Figures 5.4 and 5.5. The inability to generate a discharge at a pressure of 2 MPa and currents lower than 0.3 A is due to insufficient input power and results in the use of a fixed current of 0.35A. This fixed current of 0.35 A is the minimum current required in order to generate discharge at pressures up to 15 MPa at the interelectrode gaps considered.

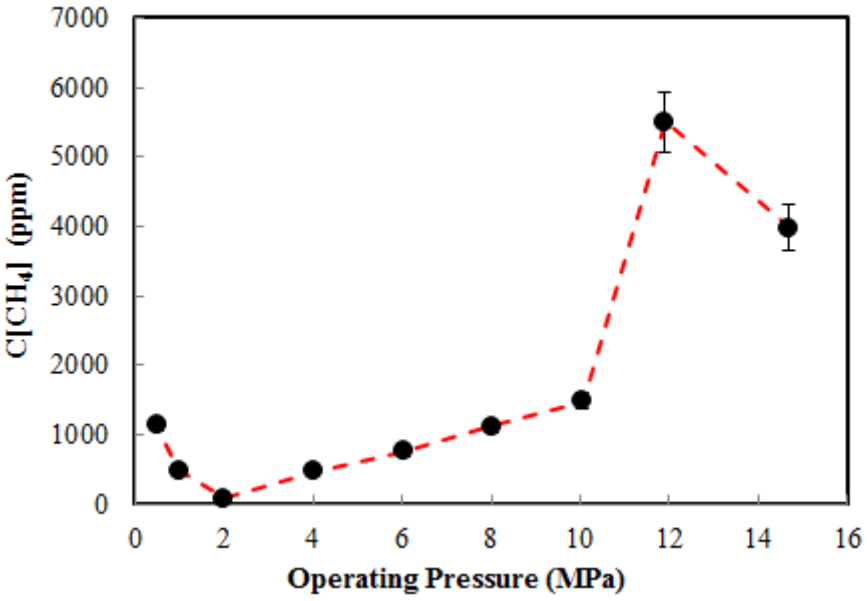

Figure 5.4: Concentration of CH_4 produced as a function of the operating pressure for H_2/CO ratio of 2.2 at a current (I) of 0.35 A, interelectrode gap (d) of 1 mm and discharge duration (t) of 60 s

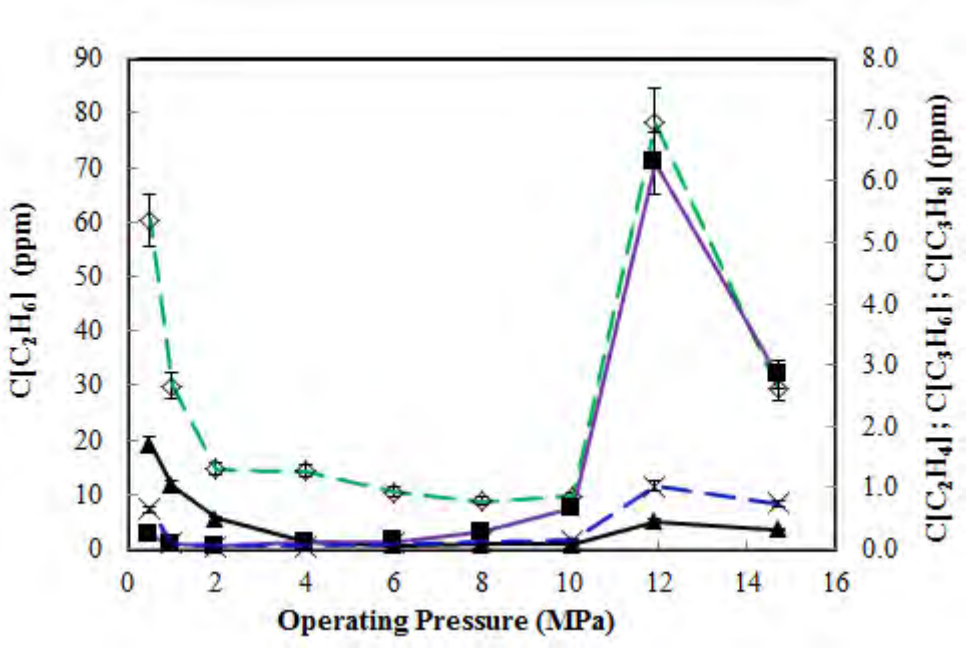

Figure 5.5: Concentration of the C_2 and C_3 hydrocarbons produced as a function of the operating pressure for H_2/CO ratio of 2.2 at a current of 0.35 A, d= 1 mm and t = 60 s.◊ with dotted green line (C_2H_6); ▲ with solid black line (C_2H_4); X with dotted blue line (C_3H_6); ■ with solid purple line (C_3H_8)

Figure 5.4 shows that the concentration of CH_4 produced initially decreases with an increase in pressure between 0.5 and 2 MPa. However, a gradual increase in the concentration of CH_4 produced was observed as the operating pressure increases after 2 MPa until a maximum was reached at 12 MPa. This indicates that CH_4 production can be increased by increasing the operating pressure up to 12 MPa in reference to the operating conditions investigated. As seen in Figure 5.5, the concentrations of the C_2 and C_3 hydrocarbons decreases between 0.5 and 2 MPa as observed for the CH_4. However, the positive contribution of the pressure increases is significant between 4 and 10 MPa considering that there was an increase of approximately 76%, 82%, 95% and 98% for C_2H_4, C_2H_6, C_3H_6, and C_3H_8 respectively between 4 MPa and 12 MPa. This again confirms the influence of operating pressure on the synthesis of hydrocarbons from syngas. This is further illustrated with the reaction performance calculations.

Explaining the influence of operating pressure is a complex concept in the light of multi-fluid gas. Since it is known that plasma consist of radicals, ions, electrons and molecules which can each possess its own temperature, it therefore means that an increase in pressure will increase the collision of particles within the reactor. In addition, the rate of natural convection is expected to increase with pressure. Following the equation of state for ideal multi-fluid gas, an increase in pressure will lead to a corresponding increase in the number of moles of the gas at constant temperature and volume. Furthermore, in a batch configuration with fixed reactor volume and nominal residence time or

discharge duration, the mass flow rate of the reactant gases strongly depend on the mass density of the gases. This mass density at a constant temperature will depend primarily on the pressure. Hence, to explain the influence of pressure in this experiment, the specific energy input of the reactant as well as the volume of the gas treated by the discharge within the discharge duration must be estimated.

In order to analysis the electrical performance of the plasma for the process in terms of energy input, energy requirements and efficiency, precise and accurate measurement of the root mean square voltage (V_{rms}) and current (I_{rms}) using an oscilloscope was made. For this purpose, a high voltage probe Elditest GE3830 with bandwidth between 0 and 100 kHz and a Chauvin Arnoux E3N Hall-effect current probe with bandwidth up to 100 kHz were connected to an Agilent DSO 1004A digital oscilloscope. The bandwidth of the oscilloscope is 60 MHz.

The input power (P) was calculated as shown in equation (5.8). From the obtained input power, the electrical energy (E) consumed by the process could be estimated as given below with t being the discharge duration:

$$P(W) = V_{rms} * I_{rms} \tag{5.8}$$

$$E(J) = P(W) * t(s) \tag{5.9}$$

The specific energy input (SEI), which is the amount of electrical energy deposited in the reactor divided by the moles of reactants fed, is shown in Figure 5.7. From this calculation, it was observed that the SEI decreases as the operating pressure increases. A high SEI is an indication that the process is close to thermal plasma and most of the energy goes into gas heating. Hence, it can be seen that the discharge is primarily by electron impact above 4 MPa and therefore nonthermal in nature. Furthermore, the specific energy requirement (SER) is calculated for CH_4, since it is the product obtained with the highest concentrations. From the calculations and the plot presented for SER as a function of the operating pressure in Figure 5.8, it can be observed that the specific energy required to produce a mole of CH_4 increases as the pressure increases between 0.5 amd 2 MPa. This again is an indication that the process requires very high specific energy for syngas conversion between 0.5 and 2 MPa and this may be attributed to possible thermal losses at those pressure conditions. However, above 2 MPa, the specific energy required to produced CH_4 decreases as the operating pressure increases. This leads to better plasma efficiency at very high pressure which implies that very high pressure will help to minimize the thermal losses and allow an improved energy utilization efficiency.

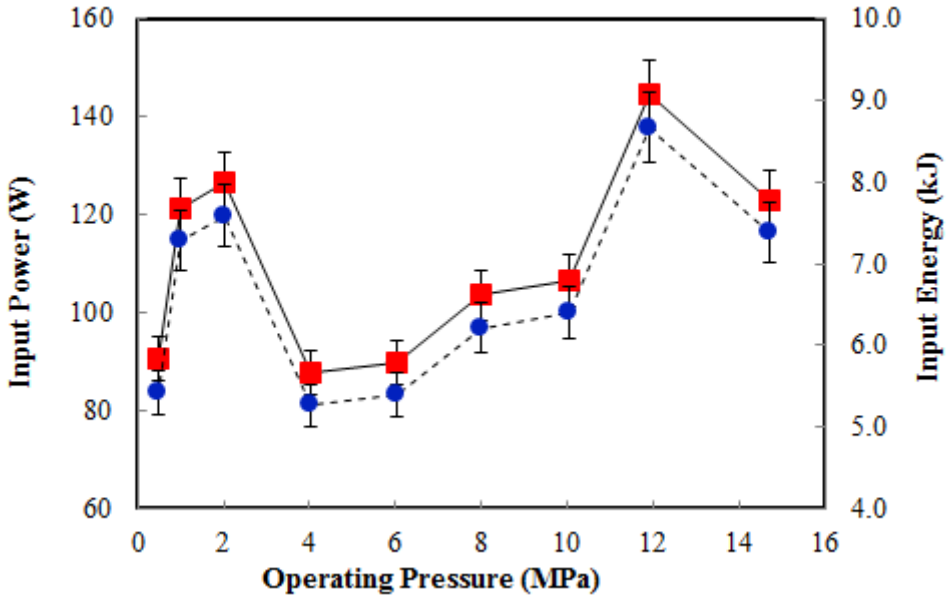

Figure 5.6: Input power and input energy for syngas conversion as a function of the operating pressure for a H_2/CO ratio of 2.2 at a current of 0.35 A, d = 1 mm and t = 60 s.■with solid black line (Input power); ●with dotted black line (Input energy)

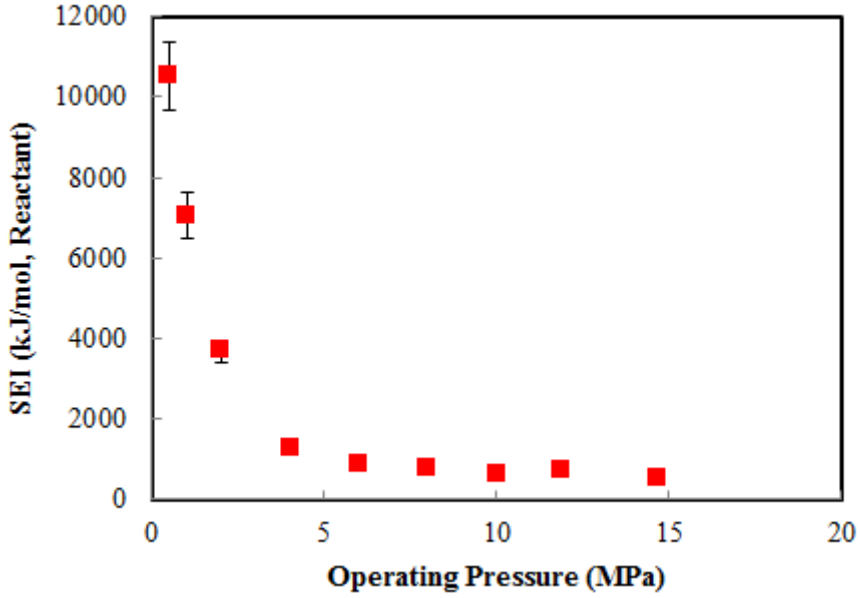

Figure 5.7: Specific energy input versus the operating pressure for a H_2: CO ratio of 2.2:1 at a current of 0.35 A, d = 1 mm and t = 60 s

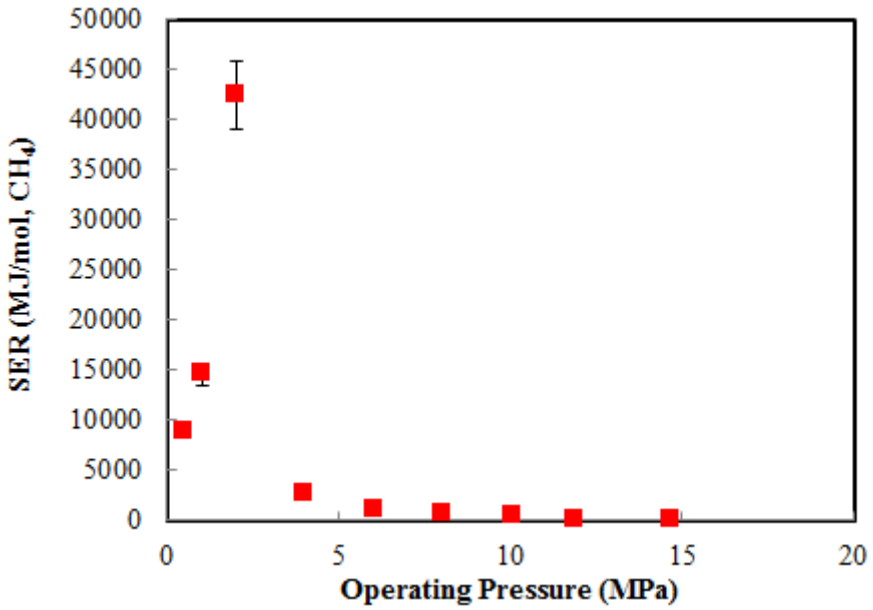

Figure 5.8: Specific energy required per mole of CH_4 produced versus the operating pressure for a H_2: CO ratio of 2.2:1 at a current of 0.35 A, d = 1 mm and t = 60 s

Furthermore, preliminary CFD calculations carried out on the batch reactor at high pressure shows that the velocity field in the arc increases as the operating pressure increases from a value of approximately 0.32 ms^{-1} at 4.0 MPa up to 0.43 ms^{-1} at 10 MPa. The CFD calculations also reveal that the arc was not constrained by high pressure and has a constant radius of approximately 0.16 mm. Thus for an interlectrode gap of 1.0 mm, the cross-section of the arc was found to be 3.2×10^{-3} cm^2. Therefore, by applying the continuity equation for a 1D flame, the volume of the gas treated by the arc was observed to increase with the operating pressure. The calculation further shows that the volume of the gas that will be treated by the arc in a discharge duration of 1 min is 6.14 cm^3 at 4 MPa and 8.26 cm^3 at 10 MPa. This implies that the high pressure operation favours a larger treatment of the gas in the arc discharge.

5.2.1.1 Reactor Performance Analysis

In order to better understand the performance of the reactor with respect to syngas conversion, the percentage conversions as well as the product selectivities towards CH_4, C_2 and C_3 hydrocarbons was calculated based on the carbon balance following the approach of [132].

The percentage conversion (χ) of the reactants (H_2 and CO) is the amount of the reactant that was converted divided by the amount of reactant fed into the reactor. This was calculated using the equation below:

$$\chi_{H2}(\%) = \frac{n(H_2)_{in} - n(H_2)_{out}}{n(H_2)_{in}} \times 100 \quad (5.10)$$

where $n(H_2)_{in}$ is the initial amount of hydrogen gas fed into the reactor before discharge and $n(H_2)_{out}$ is the final amount of hydrogen gas that exits the reactor after discharge. This same approach was used in calculating the conversion of CO.

$$\chi_{CO}(\%) = \frac{n(CO)_{in} - n(CO)_{out}}{n(CO)_{in}} \times 100 \quad (5.11)$$

Selectivity and yield are two terms that must be carefully defined. Generally, selectivity is considered as a performance indicator that measures the effectiveness of a reaction or process in producing the desired product relative to undesired products. In this study, product selectivity is defined as the amount of carbon atoms in the desired product formed, divided by the amount of carbon atoms in all the products. Hence, the selectivities (S) to CH_4, $C_2$and C_3 hydrocarbons were calculated on a carbon basis using equation (5.12):

$$\mathrm{S(CH_4)}\ (\%) = \frac{\text{Number of moles of C atoms in the formed } CH_4}{\text{Total number of moles of C atoms in the formed products}} \times 100 \quad (5.12)$$

Yield on the other hand is a reaction performance indicator that measures the effectiveness of a reaction or process in converting the reactants to the desired products. Thus, the yield (Y) for CH_4 was calculated on carbon basis using equation (5.11).

$$\mathrm{Y(CH_4)} = \frac{\text{Number of moles of C atoms in the formed } CH_4}{\text{Total number of moles of C atoms injected}} \quad (5.13)$$

The plasma efficiencies (η) for H_2 and CO conversion were calculated following equation (5.14 and 5.15) below:

For H_2: $$\eta_{H_2}(\%/W) = \frac{\chi_{H_2}(\%)}{P(W)} * 100 \quad (5.14)$$

For CO: $$\eta_{CO}(\%/W) = \frac{\chi_{CO}(\%)}{P(W)} * 100 \quad (5.15)$$

5.2.1.2 Performance Analysis for the Process in terms of Pressure and Power

As can be observed in Figure 5.6, there exist a nonlinear relationship between the operating pressure, and the input power . In view of this, a plot of the specific energy input and the volume of gas treated

by the arc in the entire discharge duration versus the operating pressure is presented in Figure 5.8. Based on theoretical calculations, it was revealed that the volume of the gas that passes through the arc zone in a 60 s discharge time is about 2.4 times more than the reactor volume at 4.0 MPa and approximately 3.2 times the reactor volume at 10 MPa.

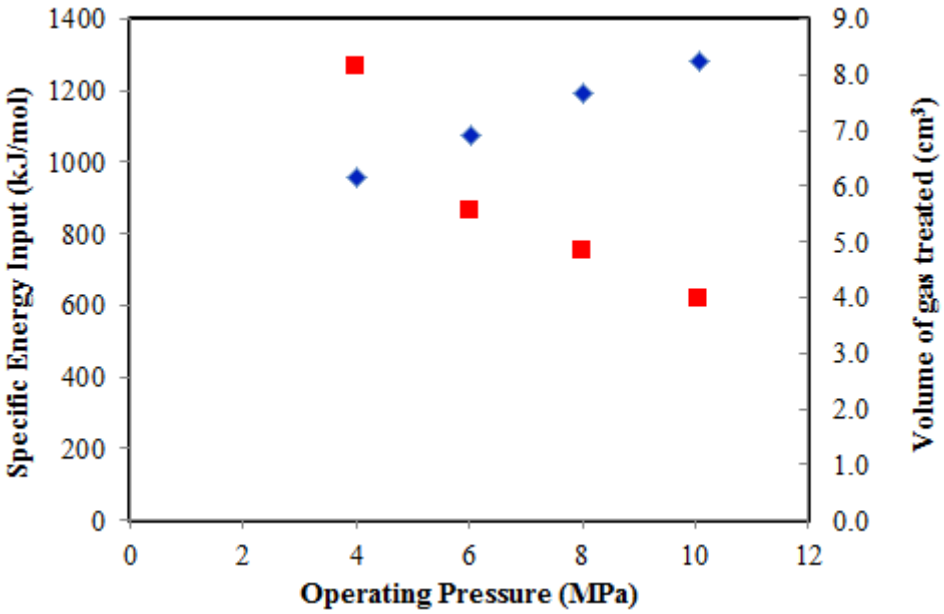

Figure 5.9: Specific energy input and volume of gas treated by the discharge versus the operating pressure ■ specific energy input; ♦volume of gas treated by discharge in 60 s

From Figure 5.9, it can be seen that the volume of the gas treated increases with an increasing pressure. In addition, the SEI decreases as the pressure increases, indicating that the process consumes less energy at higher pressure and thus has the higher energy efficiency. However, the lower amount of available energy does not allow for a good conversion.

In order to explain the results obtained in reference to the input power, input energy and operating pressure, calculation of the conversion, selectivity, and yields was carried out for all the major species obtained according to the equations given in (5.10 to 5.14). From the calculations, the highest amount of syngas converted was obtained at 12 MPa, which also relates to the highest conversion for H_2 and CO. The plot showing the conversion for H_2 and CO is presented in Figure 5.10. From Figure 5.10, it is observed that product distributions were in the order CH_4>C_2H_2>C_2H_6>C_2H_4>C_3H_6>C_3H_8 between 0.5 to 2 MPa, while the order was CH_4>C_2H_6>C_2H_2~C_2H_4>>C_3H_8>C_3H_6 at 4 MPa, with the disappearance of C_2H_2. The new order for product distribution was then found to be CH_4>C_2H_6>C_2H_4>>C_3H_8>C_3H_6 between 4 to 15 MPa. This indicates that production of saturated hydrocarbons is higher at a higher pressure, i.e. above 4 MPa, but the production of acetylene is favoured at pressures below 2 MPa.

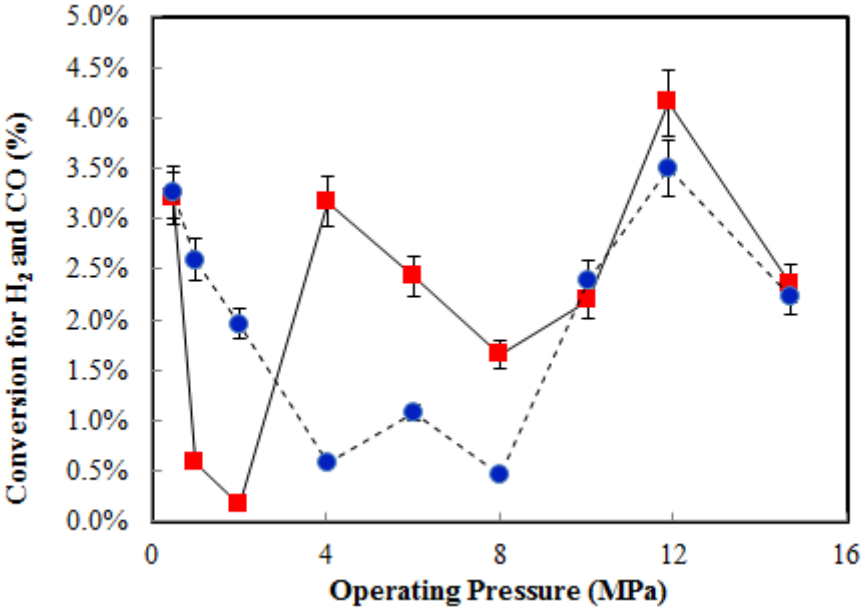

Figure 5.10: Conversion for H_2 and CO as a function of the operating pressure for a H_2/CO ratio of 2.2 at a current of 0.35 A, d = 1 mm and t = 60 s. ■ with solid black line (H_2); ● with dotted black line (CO)

Furthermore, the selectivity to the C_2 and C_3 hydrocarbons were observed to be at its highest value at a pressure of 12 MPa, in a trend similar to that presented for methane in Figure 5.11. In addition, all the yields calculated for CH_4, C_2 and C_3 hydrocarbons were highest at 12 and 15 MPa.

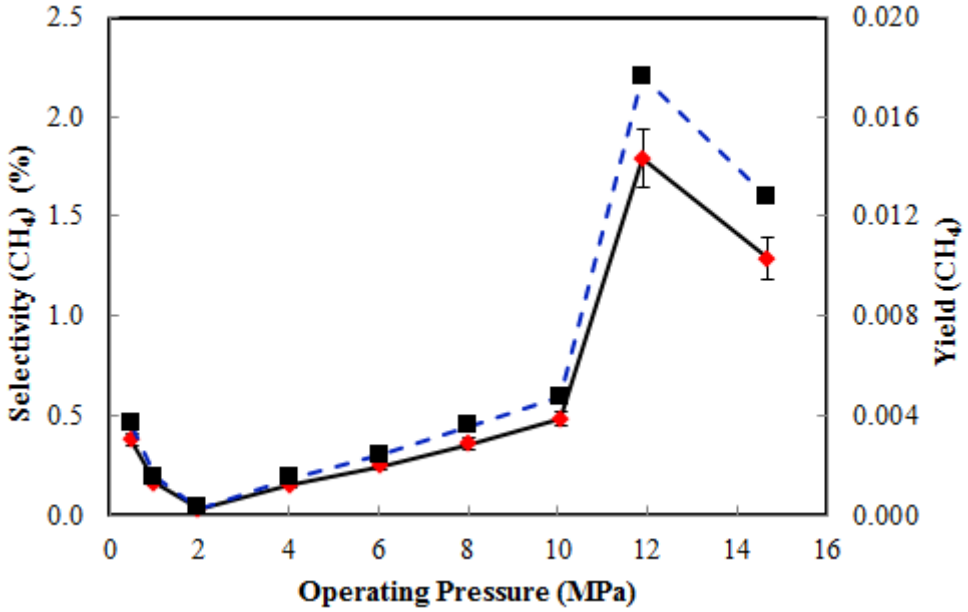

Figure 5.11: Selectivity and Yield for CH_4 as a function of the operating current for a H_2/CO ratio of 2.2 at a current of 0.35 A, d = 1 mm and t = 60 s. ■ with solid black line (Selectivity CH_4); ■ with dotted blue line (Yield CH_4)

In conclusion, the inversion of the curve for the input power and input energy (Figure 5.6) in comparison with the conversion versus the operating pressure plot shows that the conversion of H_2 (Figure 5.10) decreases as the input power and energy increases between 0.5 and 2 MPa. Moreover, while the pressure increases by a factor of 2 between these intervals, the input power and energy increases by a factor of 1.0 and 1.3 for all the products obtained in the same pressure intervals. The decrease in concentration of hydrocarbons produced between 0.5 and 2 MPa could mean that the increase in power does not lead to an increase in the production of hydrocarbons on one hand. On the other hand, it could mean that high input power at pressures ≤ 2 MPa results in thermal losses and a decrease in conversion for CO and H_2. It is important to mention that this pressure interval of 0.5 to 2 MPa results in the formation of acetylene which is a major product of thermal plasma direct conversion of methane. This interval could possibly lead to the formation of carbon after a prolong discharge duration. Hence, the product distribution trend was found to be CH_4>C_2H_2>C_2H_6>C_2H_4>C_3H_6>C_3H_8 in the interval between 0.5 and 2 MPa. At pressures of 2 and 4 MPa, the conversion of H_2 was found to increase significantly showing that the formation of saturated hydrocarbons was favoured and the order of the product distribution changes to follow the trend; CH_4>C_2H_6>C_2H_4>C_3H_8>C_3H_6 with the disappearance of acetylene. This shows that this condition might be suitable if acetylene production is not desired. While the conversion of H_2 is observed to decrease between 4 and 8 MPa, the conversion of CO remains relatively stable within this pressure interval with the trend remaining stable. The conversion was observed to have a similar trend with respect to input power, input energy, and concentrations of hydrocarbons produced between 10 and 15 MPa. Further analysis of the results revealed that the input energy increased by a factor of 1.4 at pressure between 10 MPa to 12 MPa while the conversion (%) increases by 1.9 and 1.5 for H_2 and CO between those two pressures. In addition, the selectivity (%) to C_2 and C_3 were found to be 7.9 and 9.1 in this interval respectively. The yield increased by 13.2 and 13.3 for C_2 and C_3 hydrocarbons respectively between 10 and 12 MPa. This trend was observed for all the species obtained. Thus, it can be concluded that the increase in the products concentration for the higher hydrocarbons is influenced by pressure as well as the input energy. The performance analysis calculations for the reactor under the operating pressures of 0.5 to 15 MPa are presented in Table 5.4 for all the experimental results obtained.

Table 5.4 Performance of the tip-tip arc discharge reactor for syngas conversion at operating pressure between 4 to 15 MPa

Process Description	Reactor type	Batch								
	Plasma type	Low Current Arc Discharge								
	Plasma source	High Voltage DC Power Supply								
	Reactor Volume (cm^3)	2.56								
	Discharge Volume (cm^3)	8.04×10^{-05}								
Process Conditions	Current (A)	0.35								
	Interelectrode gap (mm)	1								
	Discharge duration (s)	60								
	Initial Gas Temperature (K)	298.15								
	Process Pressure (MPa)	0.5	1.0	2.0	4.0	6.0	8.0	10.1	11.9	14.7
Calculated Reaction Performance	Input Power (W)	90.5	121.4	126.4	87.7	89.8	103.5	106.7	144.5	122.9
	Input Energy (kJ)	5.43	7.28	7.58	5.26	5.39	6.21	6.40	8.67	7.38
	Specific Energy Input (kJ/mol reactant)	10518	7053	3672	1267	865	752	616	705	486
	Plasma efficiency (%/W) for H_2	0.035	0.005	0.001	0.036	0.027	0.016	0.02	0.029	0.019
	Plasma efficiency (%/W) for CO	0.036	0.021	0.015	0.007	0.012	0.004	0.022	0.024	0.018
	CO conversion (%)	3.25	2.59	1.96	0.58	1.08	0.46	2.39	3.49	2.23
	H_2 conversion (%)	3.19	0.58	0.17	3.17	2.43	1.66	2.19	4.15	2.35
	Power density (MW/cm^3) per Discharge Volume	1.13	1.51	1.57	1.09	1.12	1.29	1.33	1.80	1.53
	Selectivity to CH_4 (%)	0.38	0.16	0.03	0.15	0.24	0.36	0.48	1.79	1.29
	Selectivity to ($C_2H_4 + C_2H_6$) (%)	0.05	0.03	0.01	0.01	0.01	0.01	0.01	0.05	0.02
	Yield (CH_4) $\times 10^{-2}$	0.36	0.15	0.028	0.15	0.24	0.36	0.47	1.8	1.3

5.2.2 Influence of Operating Current on Hydrocarbons Synthesis

The graphical representation of the results obtained by varying the operating current with other parameters fixed as listed in Table 5.3 is presented in Figure 5.12. The results show the production of saturated C_1 to C_3 hydrocarbons, as well as unsaturated C_1 to C_3 hydrocarbons at all the operating currents. At an operating current of 0.2 A, additional discharge products such as propyne (C_3H_4); 1,3-butadiyne (C_4H_2); 1,2-butadiene (C_4H_6); 1-butene (C_4H_8); 1-buten-3-yne (C_4H_4); and benzene (C_6H_6) were identified using the PR2100 GC.

The concentrations of the hydrocarbons produced were observed to decrease gradually with an increase in the operating current. This trend is characteristic of the voltage-current curve for nonthermal arc discharges. In addition, the input power was observed to decrease with an increase in the operating current with a minimum observed at 0.35 A. The voltage and power versus current curve is presented in Figure 5.13. While there is a decrease of input power as the current increases as shown in Figure 5.13, the voltage decreases strongly in comparison with the current increase. This

leads to a strong decrease of the electric field in the discharge. The decrease of the reduced electric field results in a strong deviation from thermodynamic equilibrium within the arc. The reduced electric field thus plays a role in the conversion of syngas to higher hydrocarbons.

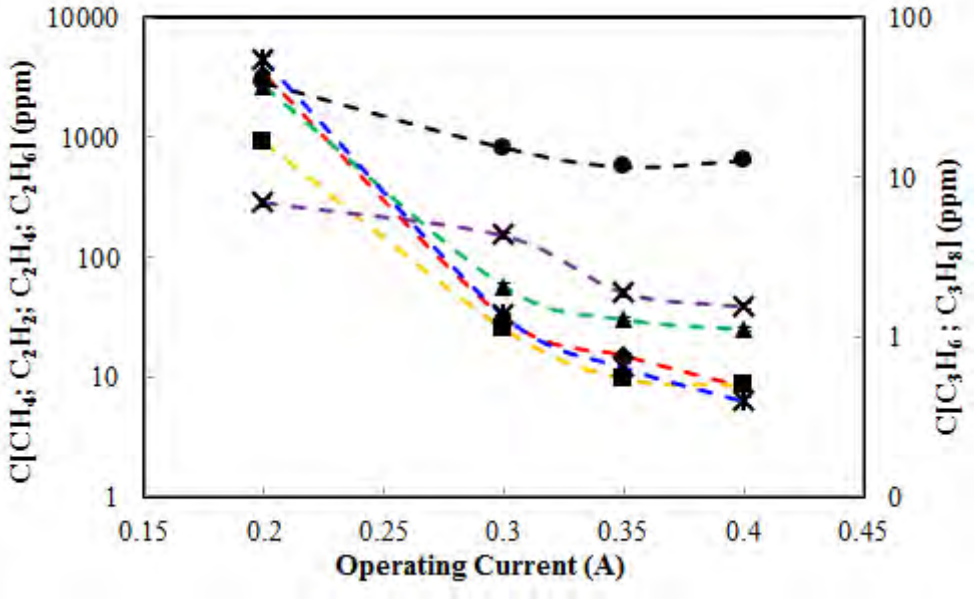

Figure 5.12: Concentrations of the main gas phase hydrocarbons produced as a function of the operating current for a H_2/CO ratio of 2.2 at 0.5 MPa, d = 0.4 mm, and t = 120 s. ♦ with dotted red line (C_2H_2); ■ with dotted orange line (C_2H_4); ▲ with dotted green line (C_2H_6); ● with dotted black line (CH_4); X with dotted blue line (C_3H_6); X with dotted purple line (C_3H_8)

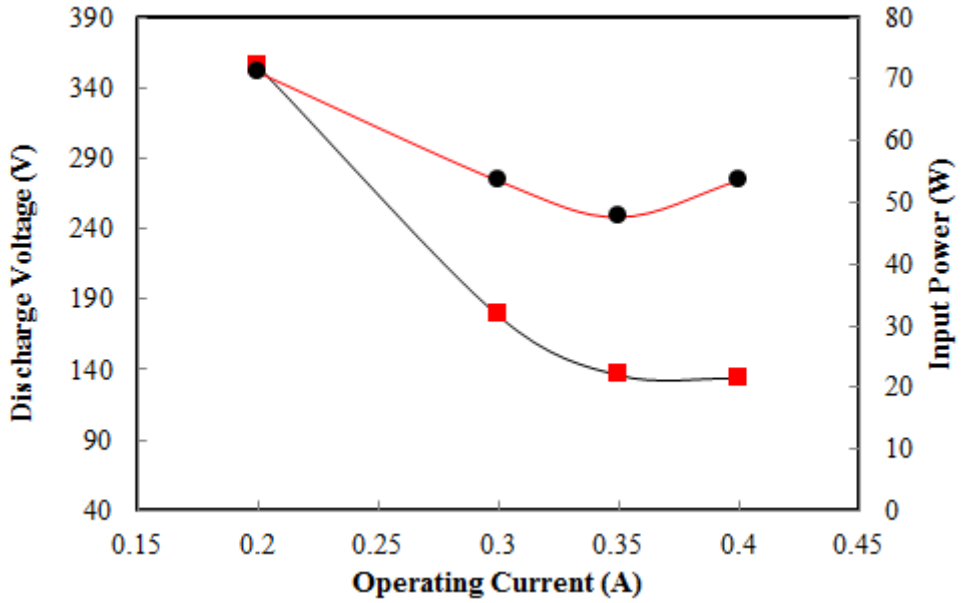

Figure 5.13: Discharge voltage and input power versus the operating current for a H_2/CO ratio of 2.2 at 0.5 MPa, d = 0.4 mm, and t = 120 s.■with solid black line (Discharge voltage); ● with solid red line (Input power)

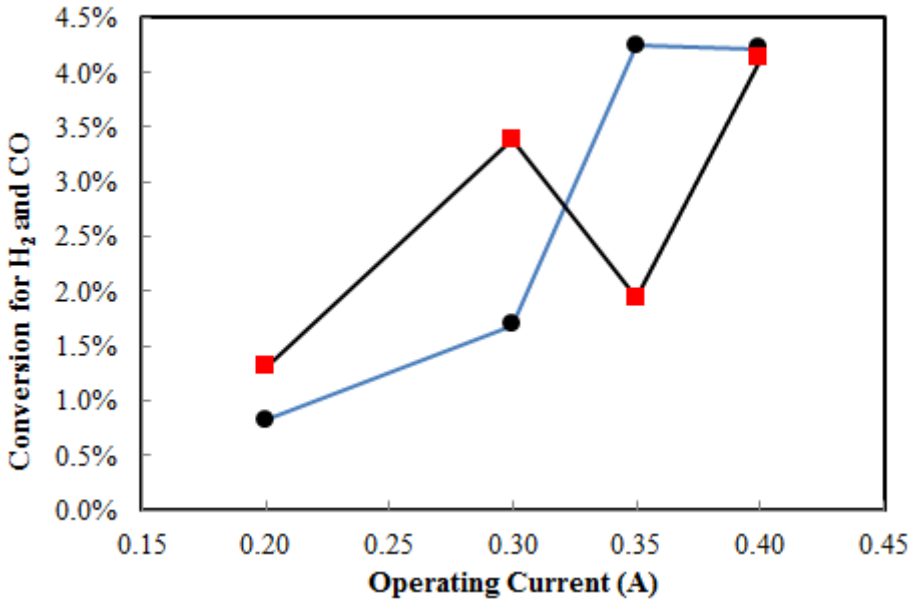

Figure 5.14: Conversion versus the operating current for hydrocarbon synthesis■ with solid black line (CO); ● with solid blue line (H_2)

In Figure 5.14, the conversion for hydrogen (H_2) was observed to increase gradually as the operating current increases between 0.2 and 0.35 A, after which it became stable at 0.4 A. In contrast, Figure 5.13 shows the input power to decrease with an increase in the operating current up to a minimum found at 0.35 A before increasing steadily again at 0.4 A. This shows that the operating current influences the conversion of H_2 and CO. The plasma efficiency calculated from equation (5.17) and plotted as a function of the operating current in Figure 5.15 was found to show the same trend with the conversion. This parameter reveals that the efficiency of the plasma for converting H_2 and CO to higher hydrocarbons increases as the operating current increases and the power decreases.

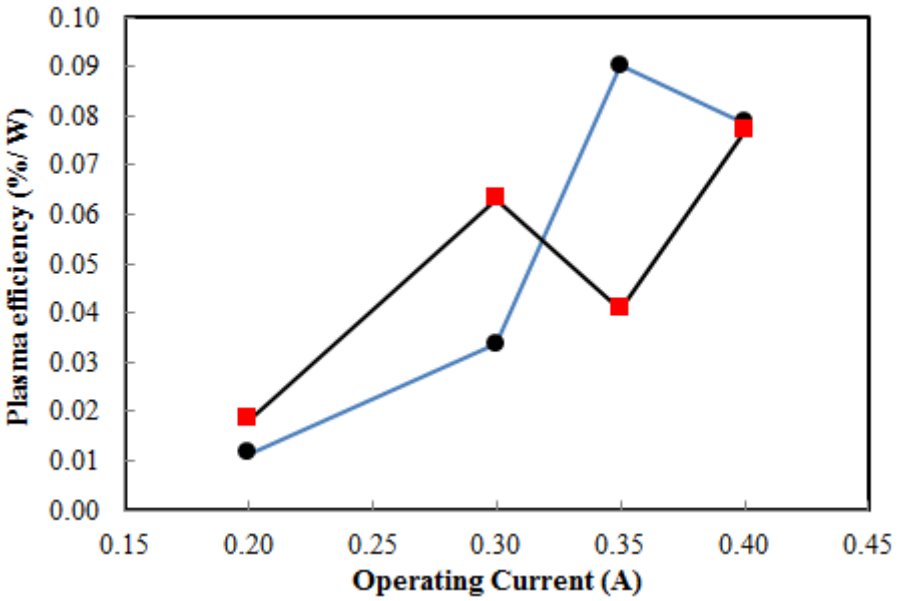

Figure 5.15: Plasma efficiency versus the operating current for hydrocarbon synthesis ■ with solid black line (CO); ● with solid blue line (H_2)

In terms of reaction performance analysis, the input energy, specific energy input, power density and specific energy requirement were calculated. These parameters are presented in Table 5.5. The results show the specific energy input (SEI) to decrease as the operating current increases. This is an indication that the concentration trend observed for the hydrocarbons produced in Figure 5.12 strongly depends on the energy fed into the system. In addition, the high power density observed at 0.2 A and the high SEI is an indication that the surrounding gases were probably heated up at this operating condition. Furthermore, the specific energy required to produce 1 mole of CH_4 versus the operating current is presented in Figure 5.16.

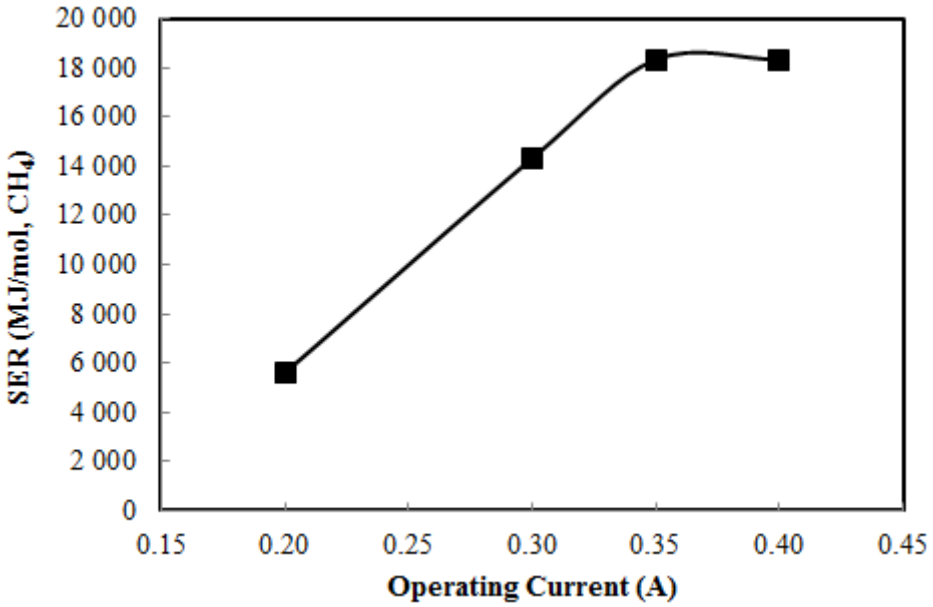

Figure 5.16: Specific energy required per mole of CH_4 produced versus the operating current for a H_2: CO ratio of 2.2:1 at a pressure of 0.5 MPa, d = 0.4 mm and t = 120 s

Table 5.5: Performance of the high pressure tip-tip arc discharge reactor for sngas conversion at varying operating current using the high voltage DC power supply

Process Description	Reactor type	Batch			
	Plasma type	Low Current Arc Discharge			
	Plasma source	High Voltage DC Power Supply			
	Reactor Volume (cm^3)	2.56			
	Discharge Volume (cm^3)	3.22×10^{-05}			
Process Conditions	Process Pressure (MPa)	0.5			
	Interelectrode gap (mm)	0.4			
	Discharge duration (s)	120			
	Initial Gas Temperature (K)	298.15			
	Current (A)	0.2	0.3	0.35	0.4
Calculated Reaction Performance	Input Power (W)	71.1	53.5	47.6	53.6
	Input Energy (kJ)	8.53	6.42	5.72	6.43
	Specific Energy Input (kJ/mol reactant)	16526	12439	11071	12451
	Plasma efficiency (%/W) for H_2	0.01	0.03	0.09	0.08
	CO conversion (%)	1.3	3.38	1.94	4.13
	H_2 conversion (%)	0.82	1.69	4.25	4.22
	Power density (MW/cm^3) per Discharge Volume	2.21	1.66	1.48	1.67

5.2.3 Conclusions on Hydrocarbon Synthesis at High Pressure and Low Current

The aim of the work was to demonstrate the influence of high pressure operation on hydrocarbon synthesis from syngas in a tip-tip arc discharge reactor. New experimental results has been obtained regarding the influence of operating pressure on hydrocarbon synthesis from syngas for pressures ranging from 0.5 to15 MPa for which experimental data are very scarce in literature. The results from the preliminary studies indicate that the main molecules synthesized were CH_4, C_2H_6, C_2H_4,C_3H_6, and C_3H_8 at all the investigated conditions with C_2H_2 obtained at pressures of 0.5 and 1 MPa only. In addition, the influence of varying the operating current ranging from 0.20 to 0.40 A was studied. The combined effect of input power and reduced electric field was found to play a role in the behavior of the discharge at varying current. The increase of operating pressure between 4 and 10 MPa was found to result in a gradual increase of the concentrations of the species produced. A significant increase of the products was observed between 10 and 12 MPa.

Given that this technology is in its infancy and considering the volume ratio of the discharge to the total reactor volume, which shows the discharge volume to be 10^{-5} times smaller than the total reactor volume, it is clear that very high pressure arc discharge has the potential for syngas conversion with good energy efficiency. This can be supported by the results obtained from the computational fluid dynamic model which shows the volume of the gas treated by the discharge to increase as the operating pressure increases. Secondly, from the work of Xiang et al. [14] where syngas was produced using a novel atmospheric pressure plasma jet, it was observed that the increase of the interelectrode gap from 6 to 9 mm led to a significant increase of CH_4 and CO_2 conversion from approximately 65% and 52% to 93% and 85% respectively. Furthermore, an increase of the interelectrode gap was observed to lead to an increase in the volume of the discharge generated, and thus an increase in the selectivity to H_2 and CO. Therefore, a reactor configured with a large active discharge volume (V_A) to the total reactor volume (V_R) as observed in the GlidArc of Czernichowski [140] would improve the volume of the gas treated in the plasma zone at pressures > 0.1 MPa.

5.3 Hydrocarbon Synthesis from Syngas using a Pulse Power Supply

The influence of operating pulse frequency on hydrocarbon synthesis from syngas at high pressure was investigated using a high frequency pulsed power supply. This was followed by investigating the influence of discharge time based on the number of discharges generated on the species produced at high pressure condition. This experiment was conducted at 0.5 MPa due to the inability to operate at higher pressures with pure H_2 and CO mixtures. The high frequency pulse power supply used here has been described in section 4.3.2 in chapter 4. The operating condition used in this study is presented in Table 5.6.

Table 5.6: Operating conditions for hydrocarbon synthesis from syngas at different frequencies using the pulsed power supply

Operating Conditions	Pulse frequency variation	Time variation
Frequency/ kHz	1.0, 2.0, 2.5, 3.0, 4.0, 6.0	3.0
Peak to Peak driving voltage / Vpp	2	2
Power amplification gain	26	26
Interelectrode gap / mm	0.4	0.4
Pressure / MPa	0.5	0.5
Ratio of H_2:CO	2.5:1	2.5:1
Discharge time / s	120	120

For the experiments involving time variation at a fixed pulse frequency, a continuous treatment with discharge duration of 60 s was applied, followed by a cyclic mode (1c = 120 s) consisting of a succession of treatment cycles characterized by duration of 120 s separated by a relaxation period of 60 s. This was conducted for 1, 5, 10, and 20 cycles respectively. Hence, the total considered discharge duration does not involve the total relaxation period between each cycle. Relaxation in this context means that the power supply was switched off for a particular duration before the next discharge was initiated. Figure 5.17 gives a graphical description of the terms used in the time variation experiment. Graphical representations of the results in terms of concentration of the species obtained for pulse frequency variation is presented in Figure 5.18.

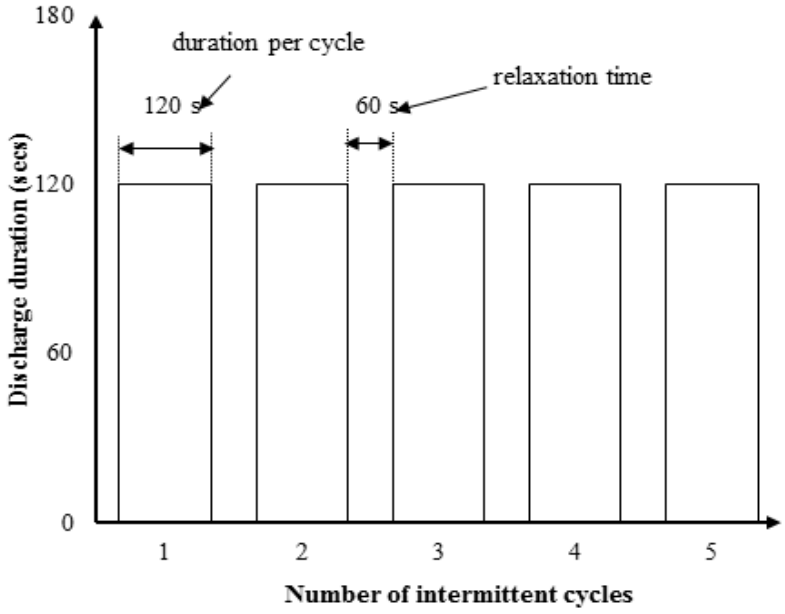

Figure 5.17: Graphical description of intermittent time variation using the pulsed power supply

It must be mentioned that the pulsed power supply unit used in this study caused some major drawbacks on the operating conditions of the reactor. Amongst these was the inability to ignite and sustain a discharge for gas mixtures of H_2 and CO only at pressures higher than 4.5 MPa and an interelectrode gap of 0.1 mm without the addition of up to 80% helium as diluents gas. In addition, the discharge could not be sustained for more than 40 s at high pressure and pulsed frequencies higher than 8 kHz, even with as short an interelectrode gap of 0.15 mm. These difficulties support the reason for scarcity of experimental data in the field of high-pressure plasma chemistry.

5.3.1 Reactor Performance Analysis

In order to understand the performance of the reactor with respect to H_2 and CO conversion using the high frequency pulsed power supply unit, the conversion as well as the product selectivity towards C_2 hydrocarbons was calculated using equations (5.10 to 5.13).

The selectivity (S) for the C_2 and C_3 hydrocarbons can be calculated using the equation (5.16):

$$S_{CxHy}(\%) = \frac{x \times n_{C_xH_y}}{(n_{(H_2)i} - n_{(H_2)f}) + (n_{(CO)i} - n_{(CO)f})} \times 100 \tag{5.16}$$

where x is the carbon number of the product in question, $n_{(CxHy)}$ denotes the number of moles of C_2 and C_3 hydrocarbons in the products after discharge, while $n_{(H2)i}$, $n_{(CO)i}$,$n_{(H2)f}$and $n_{(CO)f}$ denotes the number of moles of H_2, CO before and after discharge respectively. From the calculated conversion and selectivity, the yield (Y) for C_2 and C_3 hydrocarbons was calculated.

For the electrical performance calculation, given that *V(t)* and *I(t)* denotes voltage and current as a function of time respectively and *f* is the pulse frequency for a single period power considered in the pulse power supply application, a mathematical expression was employed to calculate the energy injected into the plasma per pulse (P_e). From the obtained pulse energy, the input power was estimated as given below:

$$Pe(J) = \int_{t_1}^{t_2} V(t)I(t)dt \tag{5.17}$$

$$P(W) = Pe * f \tag{5.18}$$

The plasma efficiency (η) for hydrogen (H_2) and carbon monoxide (CO) conversion was calculated using equations (5.14 and 5.15) in section 5.2.1.2.

5.3.2 Influence of the Pulse Frequency on the Synthesis of Hydrocarbons

From the plot of the results in Figure 5.18 showing the concentrations of the hydrocarbon species produced as a function of the pulse frequency, it can be seen that all the main species produced in the reactor after the treatment process follows a similar trend with the maximum concentrations lying between 2.5 and 3.0 kHz.

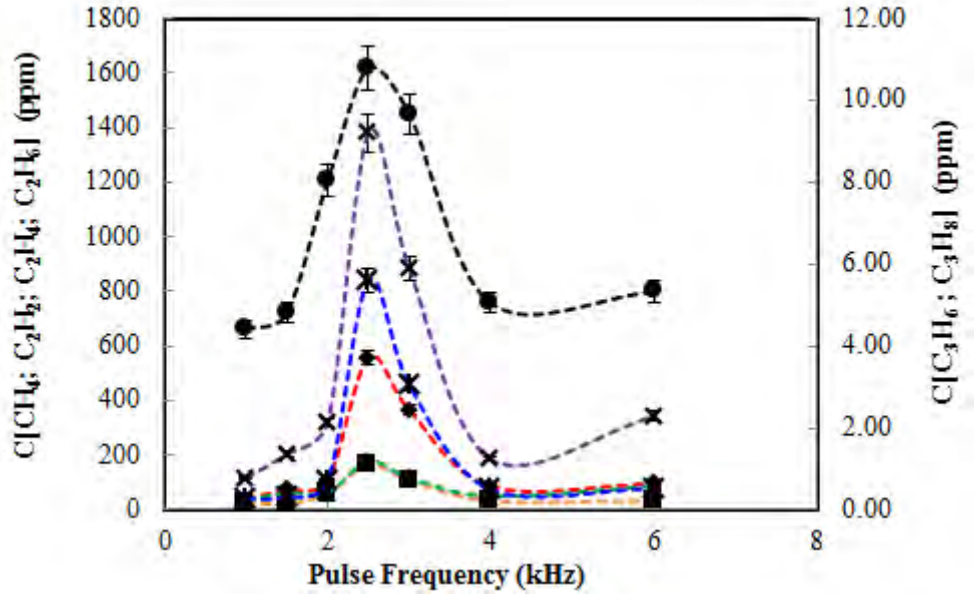

Figure 5.18: Concentration of the main gas phase hydrocarbons produced as a function of the operating frequency using a pulsed power supply for a H_2/CO ratio of 2.5. ♦ with dotted red line (C_2H_2); ■ with dotted orange line (C_2H_4); ▲ with dotted green line (C_2H_6); ● with dotted black line (CH_4); X with dotted blue line (C_3H_6); X with dotted purple line (C_3H_8)

The effect of the pulse frequency on the reaction performance was investigated using equations (5.8 to 5.15). From the calculations, the syngas conversion was found to be at maximum at a pulse frequency of 2.5 kHz. A plot showing the conversion of CO as a function of the pulse frequency is shown in Figure 5.19. From Figure 5.19, the conversion of CO was observed to decrease slightly between a pulse frequency of 1 and 2 kHz. This is in contrast to the trend observed for CO produced within these frequencies in Figure 5.18. According to Figure 5.18, the concentration of hydrocarbon species produced increase gradually as the pulse frequency increases up to 2.5 kHz after which the curve begins to descend. Thus, it is essential to investigate the electrical performance of the reactor by considering the plot of the input power, which is the electrical power consumed to convert syngas to the various hydrocarbons.

From the plot of the input power in Figure 5.20, it was observed that the input power increases with an increase in the pulse frequency between 1 and 3 kHz. Hence, the highest input power was found at

a pulse frequency of 3 kHz. Thus, calculation of the plasma efficiency for syngas conversion was employed in order to relate the chemical performance to electrical performance. A detailed Table showing the performance of the reactor at high pressure for syngas conversion under this condition is presented in Table 5.7.

Table 5.7: Performance of the high pressure tip-tip arc discharge reactor for syngas conversion using high pulse frequency

Process Description	Reactor type	Batch			
	Plasma type	Pulse Arc Discharge			
	Plasma source	High Frequency Pulse Power Supply			
	Reactor Volume (cm^3)	2.56			
	Discharge Volume (cm^3)	3.22×10^{-05}			
Process Conditions	Process Pressure (MPa)	0.5			
	Interelectrode gap (mm)	0.4			
	Discharge duration (s)	120			
	Initial Gas Temperature (K)	298.15			
	Pulse Frequency (kHz)	2.0	2.5	3.0	4.0
Calculated Reaction Performance	Input Power (W)	9.37	23.83	48.13	35.24
	Energy per pulse injected into plasma (mJ)	4.68	9.72	15.98	8.46
	Specific Energy Input (kJ/mol reactant)	6.59	4.28	37.37	6.52
	Plasma efficiency (%/W) for H_2	0.01	0.03	0.09	0.08
	Plasma efficiency (%/W) for CO	0.27	0.29	0.03	0.04
	CO conversion (%)	2.53	6.95	1.28	1.44
	H_2 conversion (%)	0.80	2.97	0.57	2.66
	Power density (MW/cm^3) per Discharge Volume	0.303	0.789	1.45	1.33
	Power density (W/cm^3) based on Reactor Volume	3.66	9.31	18.80	13.77

From Table 5.7, the reactor was observed to increase in efficiency between 1 and 2.5 kHz and has the lowest efficiency at 3 kHz. This implies that working at a pulse frequency between 1 and 2.5 kHz would probably be desirable for syngas conversion.

On the other hand, investigation of the influence of the pulse frequency on the product selectivity and yield based on H_2 and CO conversion given by equation (5.11) reveals that the product selectivity increases gradually as the pulse frequency and input power increases until a maximum was attained at 3 kHz. This trend, which is similar to the trend of the input power and energy versus the pulse frequency, indicate that unlike for the case of conversion, the input power plays a significant role in the product selectivity to C_2 and C_3 hydrocarbons between 1 and 3 kHz. It could be concluded that a pulse frequency above 3 kHz does not present any interesting observations with respect to the reaction performance and thus suggests that a higher frequency than 3 kHz might not be necessary for this process using the pulsed power supply.

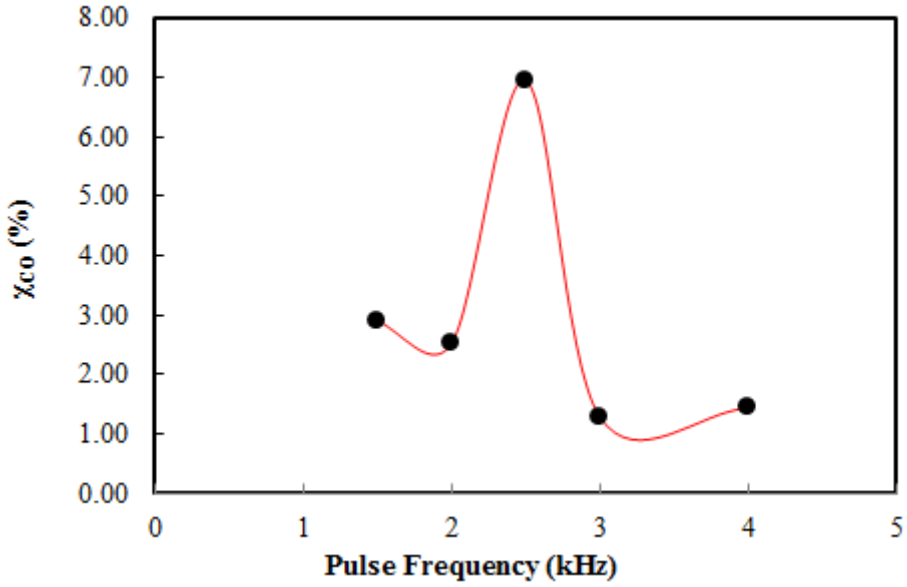

Figure 5.19: CO conversion versus the pulse operating frequency

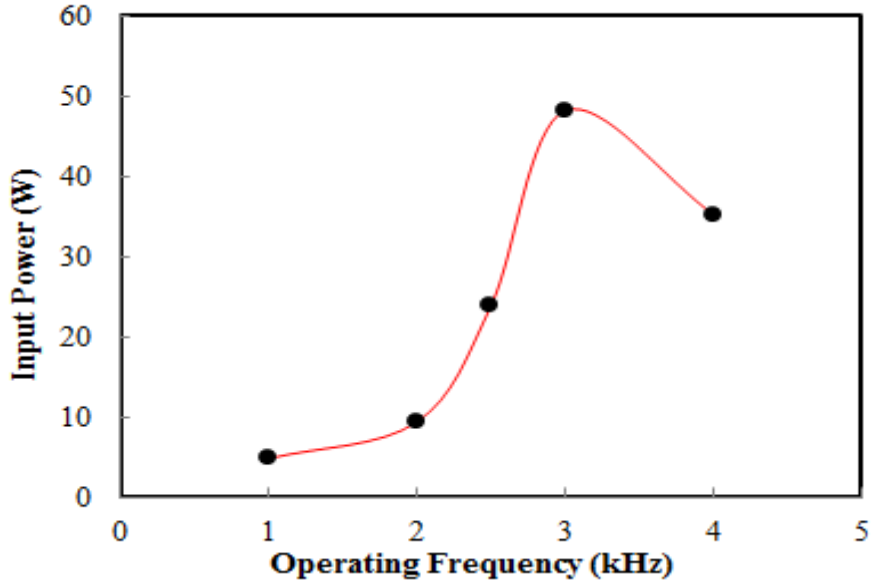

Figure 5.20: Input power versus the operating pulse frequency for hydrocarbon synthesis

5.3.3 Influence of the Discharge Duration on the Synthesis of Hydrocarbons

As shown in Figure 5.17, the influence of the discharge duration based on the number of discharges generated in cyclic mode (1c = 120 s) was investigated. For this experiment with the operating conditions listed in Table 5.6, the graphical representation of the result is shown in Figure 5.21.

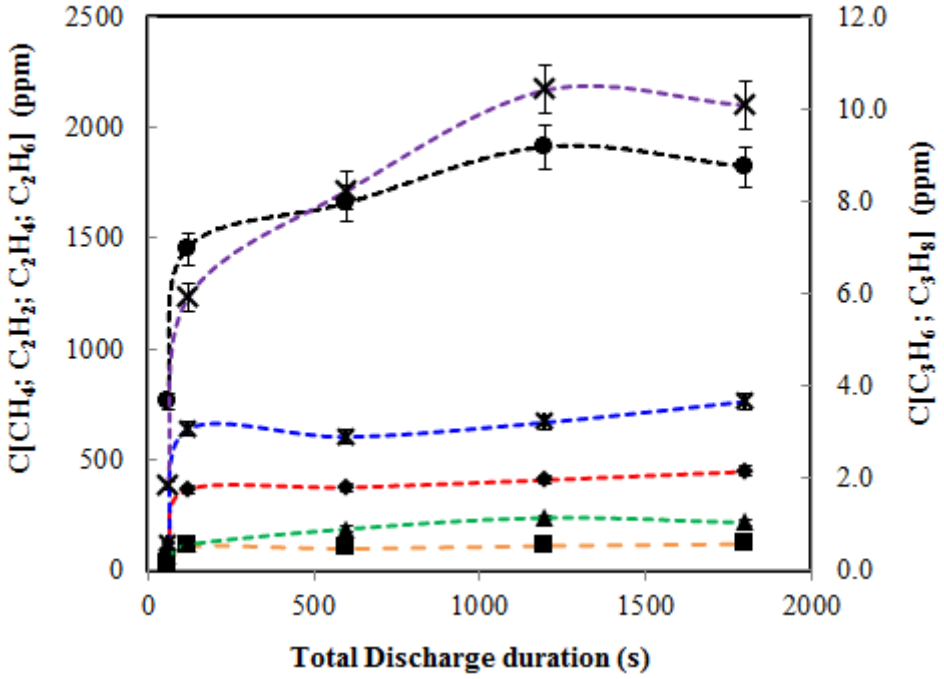

Figure 5.21: Concentration of the main gas phase hydrocarbons produced as a function of the discharge duration using a pulsed power supply for a H_2/CO ratio of 2.5. ♦ with dotted red line (C_2H_2); ■ with dotted orange line (C_2H_4); ▲ with dotted green line (C_2H_6); ● with dotted black line (CH_4); X with dotted blue line (C_3H_6); X with dotted purple line (C_3H_8)

The influence of discharge duration on the concentration of the products serves to provide information as to whether or not it would be necessary to have the plasma ignited for a long duration i.e. 30 min. In addition, by calculating the production rate, the production or decay of a particular species can be observed as a function of the discharge duration. Furthermore, a global balancing of the synthesis equation could be presented based on discharge duration. As shown in Figure 5.21, it was observed that the concentration of the saturated C_1 to C_3 hydrocarbons shows the same tendencies, while the unsaturated C_1 to C_3 also follows a similar trend. From Figure 5.21, the amount of CH_4 produced was observed to increase gradually between discharge intervals of 60 and 1200 s. It then became relatively constant between 1200 and 1800 s. This trend was also observed for C_2H_6 and C_3H_8. Contrary to the trend observed for the saturated hydrocarbons, the amount of C_2H_2, C_2H_4 and C_3H_6 produced increased quickly between the 60 and 120 s time intervals. This was followed by a slow increase in the concentration of those species as the number of cycle's increases.

The production rate was calculated using the ordinary differential equation in computing the first derivative of concentration (C) with time (t). From the calculations, the highest production rate was revealed to be during the first cycle of 120 s for C_2H_2, C_2H_4, C_3H_6 and C_3H_8 with the exception of CH_4 and C_2H_6 which has its highest production rate in half a cycle (60 s). It was further observed that the

production rate was highest for CH_4 (~12.7 ppm.s^{-1}) followed by C_2H_2 (~ 4.6 ppm.s^{-1}), C_2H_4 (~1.4 ppm.s^{-1}) and C_2H_6 (~1.1 ppm.s^{-1}) in the first cyclic mode. The production rate was observed to decrease in a slow but steady trend after the first cycle and became relatively constant between 10 and 15 cyclic modes for the unsaturated hydrocarbons, with the saturated hydrocarbons (CH_4 , C_2H_6 and C_3H_8) showing a gradual and continuous destruction of the species with time. For CH_4 and C_2H_6 which shows an exception to the trend for the other species, the production rate decreases continuously with the discharge duration until it became negative after 10 cycles which equates to 1200 s. Thus, overall the discharge duration of 120 s seems to provide the best kinetics for C_2H_2, C_2H_4, C_3H_6 and C_3H_8 and perhaps favors the production of the other species over CH_4.

Therefore, certain assumptions were made in order to estimate the volume of the individual species produced within the active zone of the reactor. These assumptions consider that the entire synthesis reactions took place within the "active discharge"; which is the volume inclusive of the discharge zone as well as its surrounding regions, and that there is little transport of fluid between the discharge zone and its periphery. Hence, calculations were made taking the 1 cycle of 120 s as a basis by employing the same approach given in section (5.1).

$$V_X^P = \left(C_m^f(X) - C_m^i(X)\right) \times V_R \tag{5.3}$$

where V^P_X is the volume of individual organic species produced in the reactor after discharge, V_R is the volume of the reactor, which is taken to be 2560 mm^3, and $C^f_m(X)$ and $C^i_m(X)$ are the final and initial concentration of the all species obtained from the outlet of the reactor as measured on the GC. Based on these calculations, the respective volumes of CH_4, C_2H_2, C_2H_4, C_2H_6, C_3H_6, and C_3H_8 in cubic millimetres were 3.717, 0.937, 0.280, 0.302, 0.008, and 0.015. Furthermore, by taking CO as the limiting reactant, the active volume (V^A_{CO}) required to produce the C_1-C_3 hydrocarbons was estimated to be 6.8230 mm^3 for a case of complete conversion of CO. Since the initial gas mixture before discharge contains 28 per cent of CO, the calculated active volume required for the process is approximately 0.95 per cent of the entire volume of the reactor (V_R) for an interelectrode gap of 0.4 mm. Hence, the mole balance based on the complete conversion of CO to CH_4, C_2H_2, C_2H_4, C_2H_6, C_3H_6, C_3H_8 and H_2O was made using the conservation of oxygen for water and the ratio calculus for the hydrocarbon products. From the material balance, the calculated stoichiometric coefficients for all the species produced within the active volume were obtained for the following reaction equation:

$$CO + 2.5H_2 \rightarrow uCH_4 + vC_2H_2 + wC_2H_4 + xC_2H_6 + yC_3H_6 + zC_3H_8 + tH_2 + sH_2O \tag{5.19}$$

$$u = \frac{V_{CH_4}^P}{V_{CO}^A} = 0.545;\ v = \frac{V_{C_2H_2}^P}{V_{CO}^A} = 0.137;\ w = \frac{V_{C_2H_4}^P}{V_{CO}^A} = 0.041;\ x = \frac{V_{C_2H_6}^P}{V_{CO}^A} = 0.044;$$

$$y = \frac{V_{C_3H_6}^P}{V_{CO}^A} = 0.0011;\ z = \frac{V_{C_3H_8}^P}{V_{CO}^A} = 0.0022; \qquad t = 0.046;\ s = 1$$

Therefore, the overall synthesis equation in the active volume during one cycle of 120 s assuming a complete conversion of CO can be written by inserting the estimated value of *s,t, u,v,w,x,y,z* respectively into equation (5.19) above.

From this global synthesis equation, it can be deduced that the calculated active volume of the plasma-chemical reactions was much more than what was observed visibly via a video camera and an optical filter (-25 %) for an interelectrode gap of 0.4 mm, and thus there is a significant interaction between the species generated in the discharge and its boundary. The result for this process does not produce carbon dioxide (CO_2) which is expected for a H_2/CO ratio > 2 as mentioned in a previous publication [178] and seems to favour C_{2+} hydrocarbons, which could probably be improved by a high discharge volume to total reactor volume ratio. In addition, the global balance shows more reactants than products which is expected for hydrogenation of CO.

The chemical and electrical performance of the plasma reactor based on equation (5.10) to (5.18) was carried out. Based on the calculated values, it was observed that the selectivity for all the main products obtained increases marginally with the total discharge duration, which is a function of the number of cycles as shown in Figure 5.17. Although the syngas conversion is lower at 120 s, conversion of CO increases with the discharge time. The calculated yields and product selectivity along with the syngas conversion based on the experimental results are presented in Tables 5.8 and 5.9. Considering that the desired products are the C_2 and C_3 hydrocarbons, the yields are presented as a function of the total discharge duration in Figure 5.22 and 5.23. From Figures 5.22 and 5.23, the yield can be observed to increase as the total discharge duration increases.

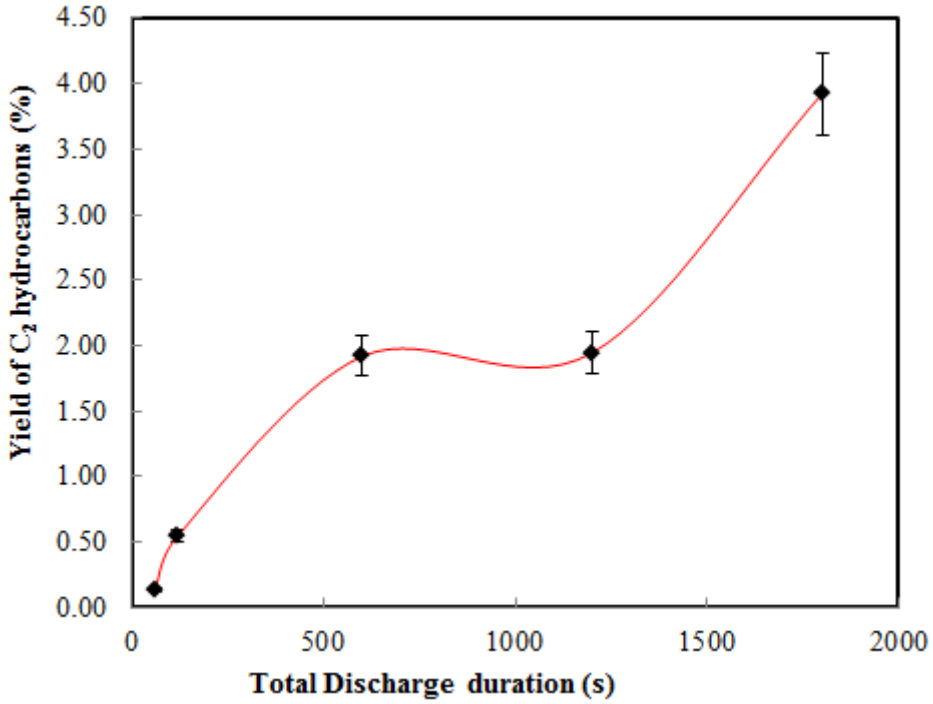

Figure 5.22: Yield of C_2 hydrocarbons as a function of the total discharge duration for a H_2: CO ratio of 2.5:1, pulse frequency of 3 kHz and an interelectrode gap of 0.4 mm at 0.5 MPa

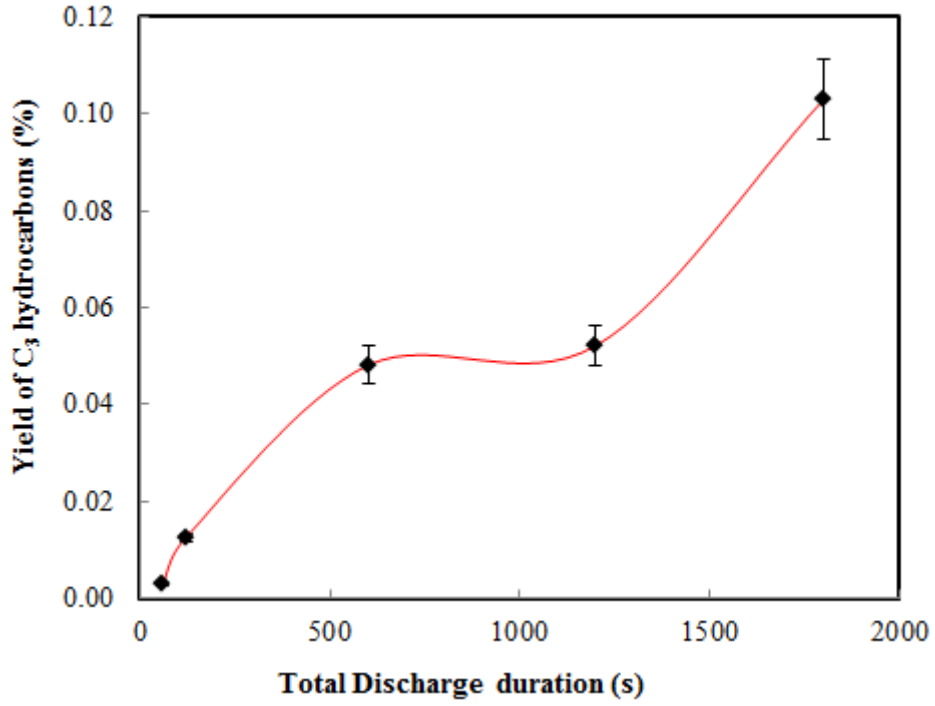

Figure 5.23: Yield of C_3 hydrocarbons as a function of the total discharge duration for a H_2: CO ratio of 2.5:1, pulse frequency of 3 kHz and an interelectrode gap of 0.4 mm at 0.5 MPa

Table 5.8: Influence of total discharge duration variation on product selectivity for a H_2/CO of 2.5/1; Pulse frequency at 3 kHz; Interelectrode gap of 0.4 mm)

Time (s)	S_{CH4} (%)	S_{C2H2} (%)	S_{C2H4} (%)	S_{C2H6} (%)	S_{C3H6} (%)	S_{C3H8} (%)
60	0.28	0.07	0.02	0.05	0.001	0.002
120	0.53	0.26	0.08	0.09	0.003	0.006
600	0.62	0.28	0.80	0.14	0.003	0.009
1200	0.72	0.31	0.09	0.18	0.004	0.012
1800	0.70	0.35	0.09	0.17	0.004	0.012

Table 5.9: Influence of total discharge duration variation on conversion, yields and C_2 and C_3 selectivity for a H_2/CO ratio of 2.5/1; Pulse frequency at 3 kHz; Interelectrode gap of 0.4 mm

Time (s)	$S_{C2H2+ C2H4 + C2H6}$ (%)	$S_{C3H6 + C3H8}$ (%)	X_{CO} (%)	Y_{C2}(%)	Y_{C3}(%)	Y_{CH4} (%)
60	0.13	0.003	1.02	0.14	0.003	0.29
120	0.43	0.010	1.28	0.55	0.012	0.67
600	0.50	0.013	3.83	1.92	0.048	2.38
1200	0.58	0.015	3.38	1.94	0.052	2.44
1800	0.61	0.016	6.45	3.92	0.103	4.55

5.3.4 Influence of Interelectrode Gap on Hydrocarbons Synthesis

Table 5.10: Operating conditions for hydrocarbon synthesis from syngas at different interelectrode gaps

Operating Conditions	Pressure Variation
Current / A	0.35
Ignition voltage / kV	8
Interelectrode gap / mm	0.4, 1.0, 2.0
Pressure / MPa	4.02
Ratio of H_2:CO	2.2:1
Discharge time / s	60
Power Source	High voltage direct current

The effect of increasing the interelectrode gap was investigated for hydrocarbon synthesis at 4 MPa, a fixed current of 0.35 A, and a discharge duration of 60 s for a H_2/CO ratio 2.2. From the result obtained at an interelectrode gap of 0.4, 1, and 2 mm, it was observed that the discharge voltage and input power increases as the interelectrode gap increases in a linear trend as shown in Figure 5.24.

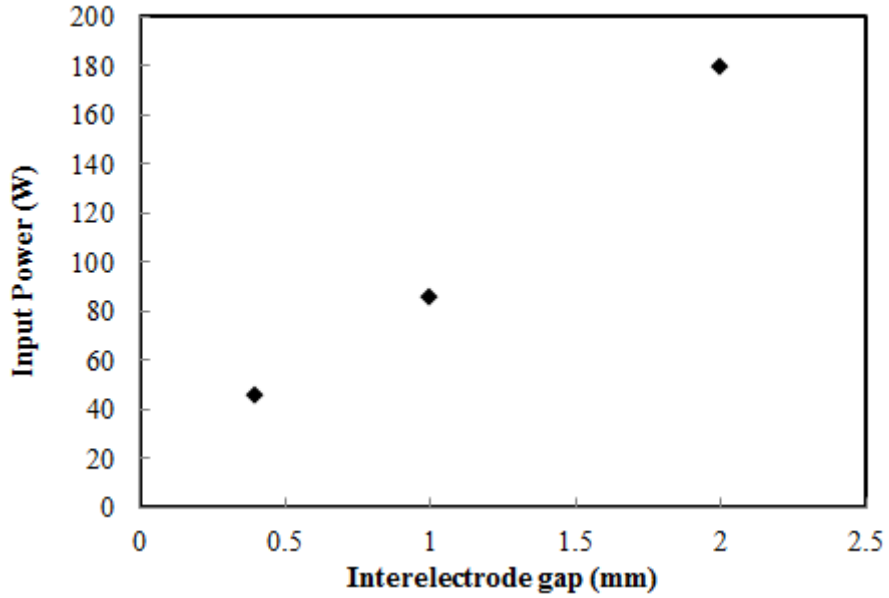

Figure 5.24: Input power versus interelectrode gap variation for a H_2/CO ratio of 2.2 at a pressure of 4 MPa and current of 0.35 A

This trend led to an increase in the concentration of hydrocarbon species produced. The calculation of the power density (input energy per volume of the discharge) as shown in Figure 5.25 reveals that the volumetric power is the same for an interelectrode gap of 1 mm and 2 mm, but slightly higher for 0.4 mm. This goes to show that an increase of the interelectrode gap will lead to corresponding increase of the discharge volume (V_D), and of the volume ratio (V_D/V_R) by a value of $1.1x10^{-5}$, $2.7x10^{-5}$, and $5.2x10^{-5}$ for 0.4, 1 and 2 mm respectively. Hence, the obtained species in the discharge zone will be diluted to a lesser volume at a gap of 2 mm, than at 1 mm and 0.4 mm.

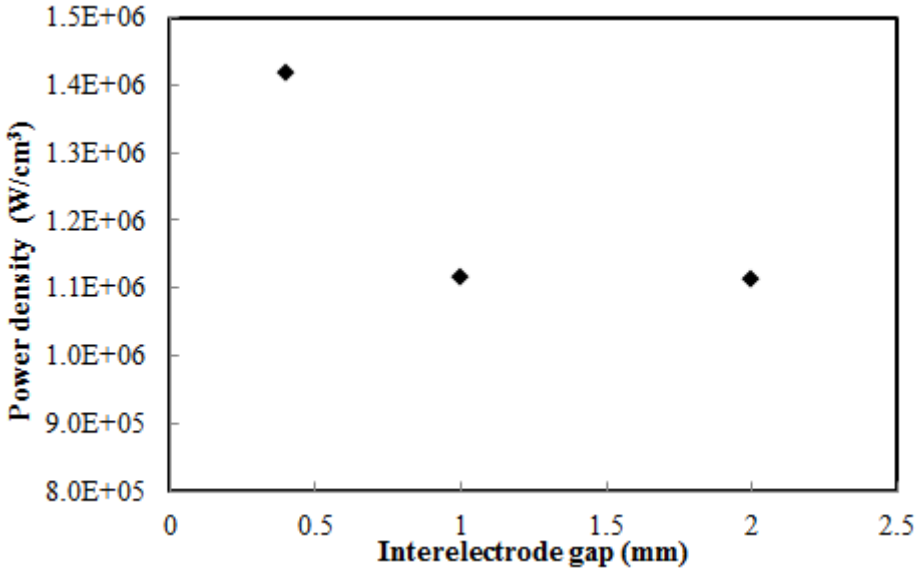

Figure 5.25: Power density versus interelectrode gap for a H_2/CO ratio of 2.2 at a pressure of 4 MPa and current of 0.35 A

In conclusion, it must be mentioned that the voltage-current characteristic curve for a H_2/CO ratio of 2.2 at 4 MPa, interelectrode gap of 1 mm and current ranging from 0.3 to 0.5 (Figure 5.26) shows a trend that is characteristic of nonthermal arc discharge already reported for a nonreactive gas. The MHD model that will be presented later in chapter 6 confirms this experimental result. Hence, it is clear that the discharge generated at 4 MPa and above are nonthermal and in the arc regime.

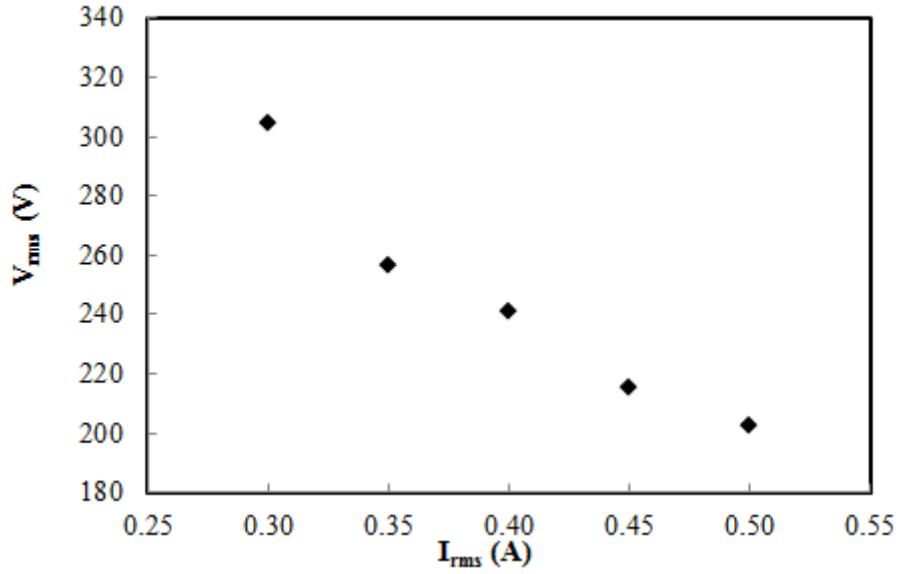

Figure 5.26: Voltage-Current curve for a reactive gas (H_2/CO = 2.2), pressure of 4 MPa and an interelectrode gap of 1 mm

5.4 CO_2 Reforming of Methane in a Tip-Tip Reactor at High Pressure

Table 5.11: Operating conditions for dry reforming at high pressures using the continuous high voltage DC power supply

Operating Conditions	Pressure Variation
Current / A	0.35
Ignition voltage / kV	8
Interelectrode gap / mm	0.4
Pressure / MPa	0.5, 1.0, 4.0, 7.8
Ratio of CH_4:CO_2	1.8:1
Discharge time / s	60
Graphical representation	Figures 5.27, 5.28

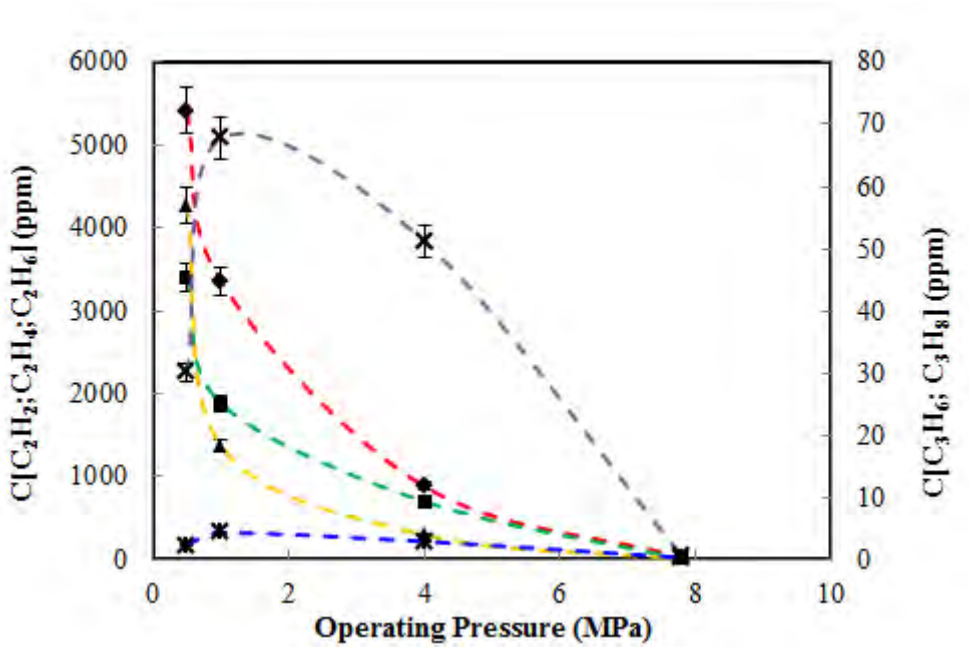

Figure 5.27: Concentration of the main gas phase hydrocarbons produced as a function of the operating pressure using a high voltage DC power supply for dry reforming (CH_4/CO_2 ratio of 1.8). ♦ with dotted red line (C_2H_2); ■ with dotted orange line (C_2H_4); ▲ with dotted green line (C_2H_6); X with dotted blue line (C_3H_6); X with dotted purple line (C_3H_8)

5.4.1 Comments on the result of dry reforming

As mentioned in the introduction (section 1.0), there is a growing interest amongst researchers in exploring CH_4 and CO_2 gas mixture processes. The results obtained in this study as shown in Figure 5.27, indicate a high concentration of C_2 hydrocarbons formed, and syngas produced (Figure 5.28) with H_2/CO ratios between 2.1 and 2.6. This study also indicates the formation of higher hydrocarbons C_4+ even for pressures as high as 4 MPa. However, the drawback in this process is the formation of carbon deposits, which usually leads to the discharge being generated between the movable electrode and the carbon deposits close to the reactor wall. Increasing the operating pressure (7.8 MPa) resulted in very low carbon deposits formed but also a reduction in the concentration as well as disappearance of some of the previous products obtained at a pressure of 1 MPa. At 4 MPa, the experiment was run first for a discharge duration of 60 s where carbon deposits were observed to be formed. However, when the same experiment at 4 MPa was run for discharge duration of 5 s, the amount of carbon deposits formed decreased significantly while the concentration of the products obtained in both cases were fairly similar. In addition, the mass of the carbon black deposit obtained from the reactor using a gravimetric analysis were 0.218 mg at an operating pressure of 1 MPa, 0.141 mg and 0.202 mg for discharge durations of 5 and 60 s respectively, at an operating pressure of 4 MPa. These observations further support the postulation that increasing the operating pressure would help to reduce formation of carbon black. Also, considering the large difference in the mass of carbon

black formed at 4 MPa with different discharge durations, i.e. 0.141 mg for 5 s and 0.202 mg for 60 s, it could be further suggested that reducing residence time or discharge duration to about 2 s would also help to prevent formation of carbon black.

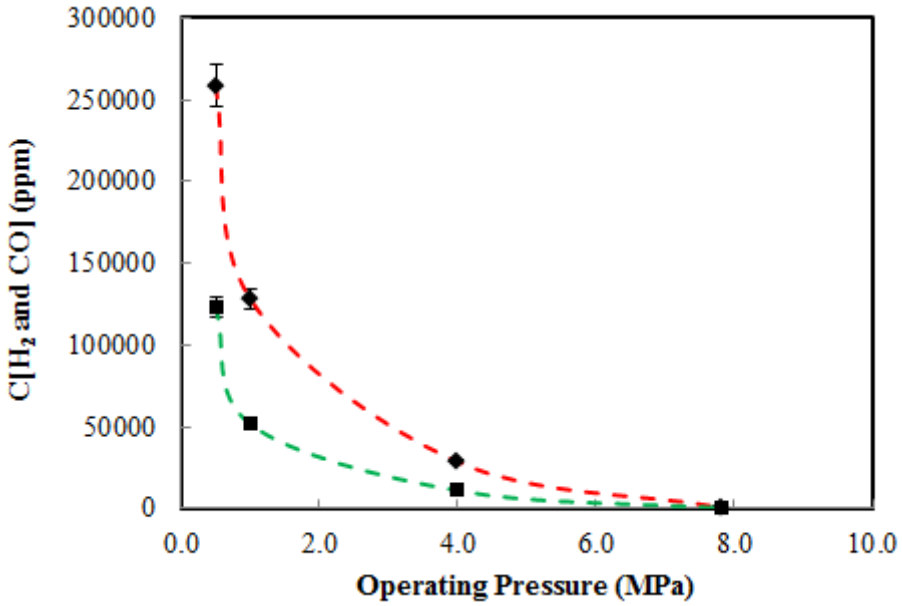

Figure 5.28: Concentration of the synthesis gas (H_2 and CO) produced as a function of the operating pressure using a high voltage DC power supply for dry reforming (CH_4/CO_2 ratio of 1.8). ♦ with dotted red line (H_2); ■ with dotted green line (CO)

The conversion of CH_4 and CO_2 decreases with an increase in pressure, as can be observed in Figure 5.29. However, the calculated input energy to generate the discharge shows that lower power was utilized at the higher pressure condition than at pressures of 0.5 and 1 MPa. It can be concluded that the operating pressure as well as the specific energy input of the reactant as shown in Figure 5.30 influence the conversion of the reactant. It can also be deduced that the observed increase of pressure (6 to 12 %) inside the reactor after the discharge is the result of cracking of methane as presented in reaction equation 8 or probably the cracking of acetylene as observed by the reaction mechanism. In addition, the observed product trend shows that C_2H_6 might have been the first converted product of CH_4 and CO_2 alongside CO and H_2O. Thus, C_2H_6 might subsequently have been cracked to produce C_2H_4 and H_2, with the C_2H_4 also further decomposed to give C_2H_2 and more H_2. This assumption was made when the successive decrease of concentration from C_2H_6 to C_2H_4 to C_2H_2 was taken into account. This is further shown by the observed selectivity trend for the C_2 hydrocarbons.

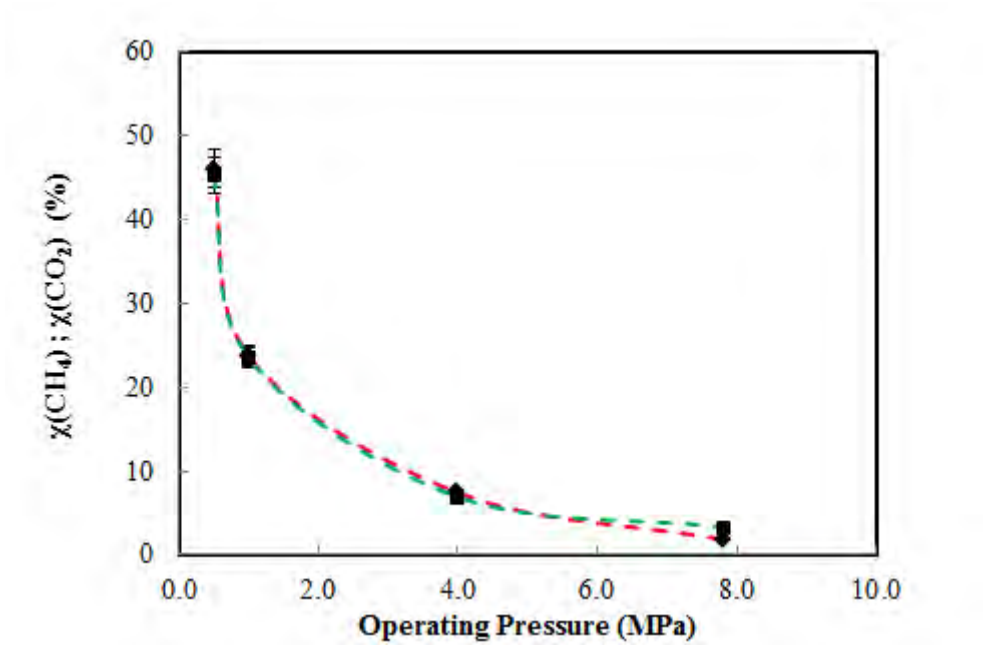

Figure 5.29: CH_4 and CO_2 conversion as a function of the operating pressure using a high voltage DC power supply for dry reforming (CH_4/CO_2 ratio of 1.8). ♦ with dotted red line (CH_4); ■ with dotted green line (CO_2)

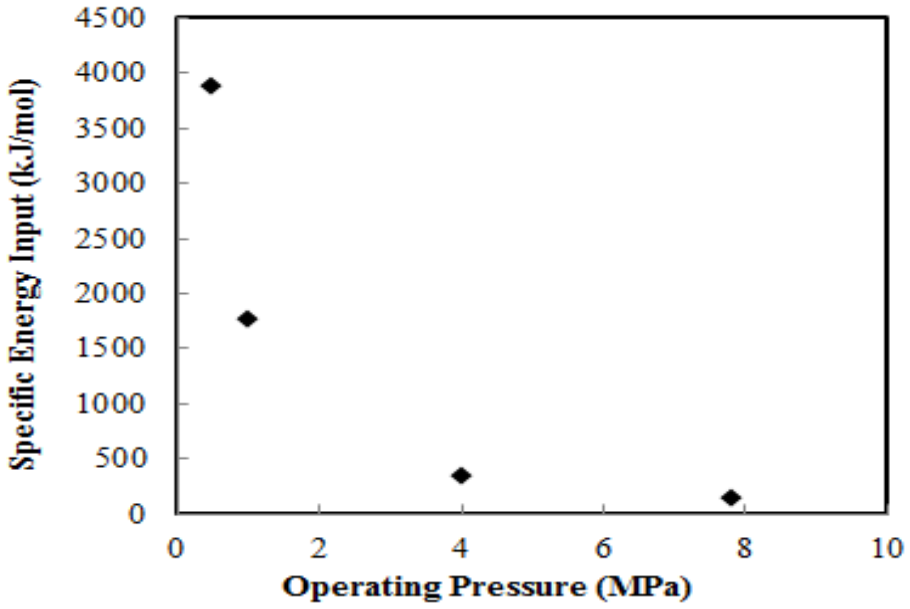

Figure 5.30: Plot of the specific energy input versus the operating pressure in a tip-tip arc discharge reactor for CH_4/CO_2 ratio of 1.8, current of 0.35 A and an interelectrode gap of 0.4 mm

5.4.2 Performance Analysis of the Tip-Tip Plasma Reactor for the Dry Reforming Process

In order to better understand the performance of the reactor with respect to the reforming of methane and carbon dioxide, the conversion of the reactants, the product selectivity, and the yields were

calculated following the standard approach found in literature i.e. Xiang et al. [14], Tao et al. [145], Yan et al. [148].

The conversions (χ) of the reactants (CH_4 and CO_2) for the reforming process were calculated using the equation below:

$$\chi_{CH_4}(\%) = \frac{n_{(CH_4)_{in}} - n_{(CH_4)out}}{n_{(CH_4)in}} \times 100 \tag{5.20}$$

Given that $n_{(CH4)in}$is the initial number of moles of methane gas in the reaction chamber before discharge and $n_{(CH4)out}$ is the final number of moles of methane gas in the reaction chamber after discharge. This same approach was used in calculating the conversion of CO_2.

$$\chi_{CO_2}(\%) = \frac{n_{(CO_2)_{in}} - n_{(CO_2)out}}{n_{(CO_2)_{in}}} \times 100 \tag{5.21}$$

From the conversion plot in Figure 5.29, there are indications to suggest that CH_4 and CO_2 reforming might proceed in an equilibrium stoichiometric ratio and thus the limiting reactant in this reaction will be CO_2.

Furthermore, the selectivity (S) for each of the discharge products H_2, CO, C_2H_2, C_2H_4, C_2H_6, C_3H_6 and C_3H_8 analyzed quantitatively on the gas chromatograph were calculated using the following equations:

$$S_{H_2}(\%) = \frac{1}{2} \times \frac{n_{H_2}}{n_{(CH_4)_{in}} - n_{(CH_4)_{out}}} \times 100 \tag{5.22}$$

$$S_{CO}(\%) = \frac{n_{CO}}{(n_{(CH_4)in} - n_{(CH_4)out}) + (n_{(CO_2)in} - n_{(CO_2)out})} \times 100 \tag{5.23}$$

$$S_{CO^*}(\%) = \frac{n_{CO}}{(n_{(CO_2)_{in}} - n_{(CO_2)_{out}})} \times 100 \tag{5.24}$$

$$S_{CnHm}(\%) = \frac{x \times n_{C_xH_y}}{(n_{(CH_4)in} - n_{(CH_4)out}) + (n_{(CO_2)in} - n_{(CO_2)out})} \times 100 \tag{5.25}$$

where n_{H2},n_{CO}, n_{CxHy} denotes the number of moles of H_2, CO and C_1 to C_3 hydrocarbons analysed on the gas chromatograph after discharge respectively. From the calculations, it was observed that the selectivity to H_2, CO and C_2H_6 decreases with the operating pressure, while the selectivity to C_2H_2 increased to a maximum value at 1 MPa before decreasing steadily between 4 and 7.8 MPa. In

addition, it was observed that the selectivity to C_2H_4, C_3H_6, and C_3H_8 increased gradually from 0.5 to 4 MPa before decreasing very significantly. Figure 5.31 gives the selectivity plot for syngas (the major products) and Figure 5.32 gives the selectivity plot for the other hydrocarbon products. The selectivity for the entire list of hydrocarbon products at each operating pressure is presented in Table 5.11.

The product yields (Y) of H_2, CO, C_2 and C_3 hydrocarbons were calculated using the equation (5.26) to (5.29) respectively.

$$\mathrm{Y}_{H_2}(\%) = \frac{\chi_{CH_4} \times S_{H_2}}{100} \tag{5.26}$$

$$\mathrm{Y}_{CO}(\%) = \frac{\left[\sum(\chi_{CH_4}, \chi_{CO_2})\right] \times S_{CO}}{100} \tag{5.27}$$

$$\mathrm{Y}_{C_2}(\%) = \frac{\left[\sum(\chi_{CH_4}, \chi_{CO_2})\right] \times \left[\sum(S_{(C_2H_2, C_2H_4, C_2H_6)}\right]}{100} \tag{5.28}$$

$$\mathrm{Y}_{C_3}(\%) = \frac{\left[\sum(\chi_{CH_4}, \chi_{CO_2})\right] \times \left[\sum(S_{(C_3H_6, C_3H_8)}\right]}{100} \tag{5.29}$$

The carbon balance (B_C) is given as the ratio of the carbon in the products analysed to the carbon in the reactants as shown in equation (5.30):

$$B_C = 100 \times \left[1 - \frac{n_{CH_4out} + n_{CO_2out} + x \times n_{C_xH_yout}}{n_{CH_4in} + n_{CO_2in}}\right] \tag{5.30}$$

The H_2/CO ratio is the ratio of hydrogen produced to the carbon monoxide produced according equation (15) given below:

$$\frac{H_2}{CO} = \frac{n_{H_2}}{n_{CO}} \tag{5.31}$$

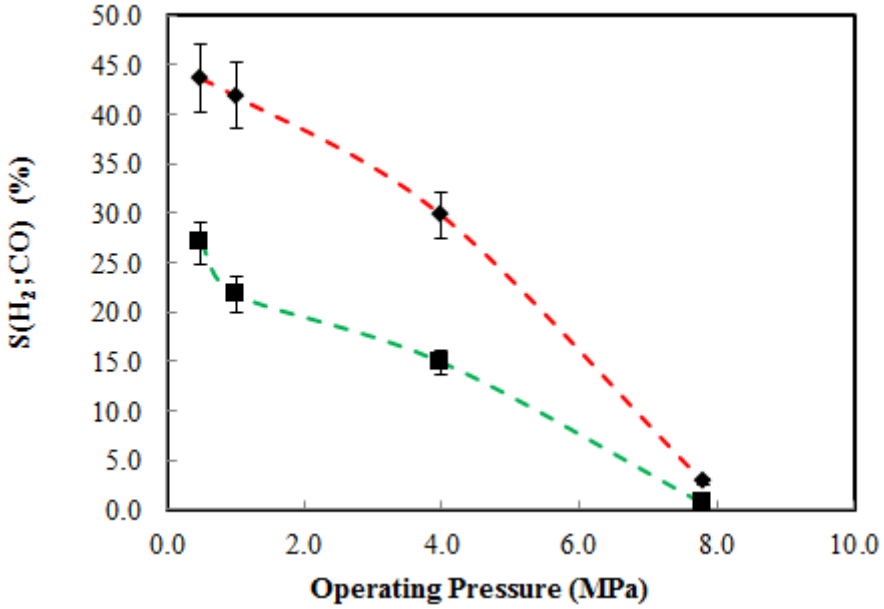

Figure 5.31: Selectivity of H_2 and CO produced via dry reforming in a tip-tip arc discharge reactor at very high pressure; ♦ (H_2); ■(CO)

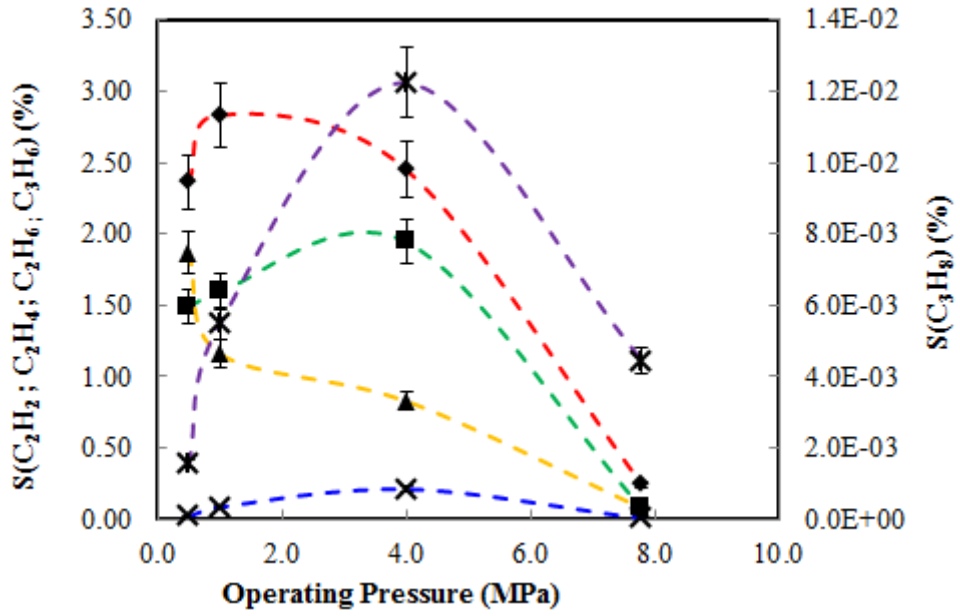

Figure 5.32: Selectivity of C_2H_2, C_2H_4, C_2H_6, C_3H_6 and C_3H_8 CO produced via dry reforming in a tip-tip arc discharge reactor at very high pressure. ♦ (C_2H_2); ■(C_2H_4); ▲(C_2H_6); X with dotted blue line (C_3H_6); X with dotted purple line (C_3H_8)

For a better understanding of the selectivity to discharge products, a CO_2-based selectivity to CO was defined based on the assumption that all CO produced is as a result of CO_2 decomposition using equation (5.24). Hence, no CO was from CH_4. When the calculated total carbon-based CO selectivity

is compared to solely CO_2-based CO selectivity, the ratio of CO selectivity based on CO_2 conversion alone is approximately three times more than that from a total carbon-based conversion for pressures ranging from 0.5 to 4 MPa, and exactly twice more for a pressure of 7.8 MPa. This indicates that the CH_4 contribution is much higher than CO_2 and decreasing the ratio of CH_4/CO_2 might have a significant effect on the selectivities to the C_2 and C_3's hydrocarbons as well as the product yield. In addition, the formation of carbon deposits could be attributed to methane cracking rather than the reversed Boudouard CO disproportionation reaction. This was based on the observed increase in pressure (by about 15 and 8 % at pressures of 0.5 and 1 MPa respectively) within the reactor during and after discharge. Hence, using a CO_2/CH_4 ratio > 1 might help to eliminate carbon deposit. However, this is likely to reduce selectivities to H_2, C_2, C_3 as well as CO. The H_2/CO ratio ≥ 4.5 at 7.8 MPa may be an indication that CO involvement for production of higher hydrocarbons is not enhanced at that pressure.

The calculated product yields for H_2, CO, C_2 and C_3 hydrocarbons based on equations (5.26 to 5.29) shows the decreasing yield for H_2, CO, and C_2 from 0.5 to 7.8 MPa, while the C_3 yield was observed to increase between 0.5 to 1 MPa before decreasing steadily between 1 to 7.8 MPa. A plot of the product yield for H_2, CO and C_2 hydrocarbons is presented in Figure 5.33. The yields for the C_3 hydrocarbons have not been presented in Figure 5.33 due to its low concentration over the pressure range (less than 0.5%). The calculated carbon balance was observed to decrease with an increase in the operating pressure. Thus, confirming the suggestion that very high pressure could reduce carbon deposit formation.

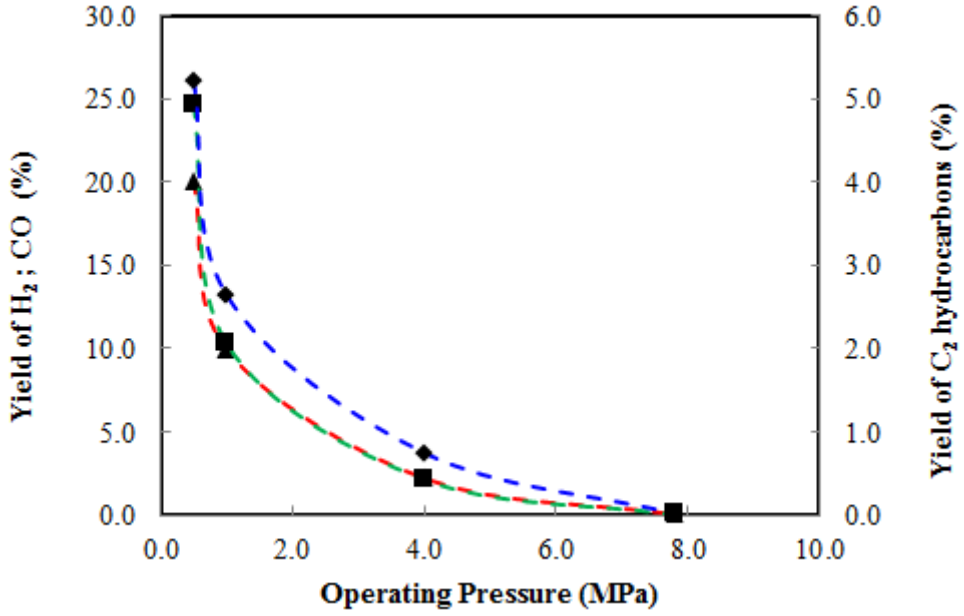

Figure 5.33: Yield of H_2, CO and C_2 hydrocarbons produced via dry reforming in a tip-tip arc discharge reactor at very high pressure; ▲ (H_2); ■(CO); ♦ (C_2hydrocarbons)

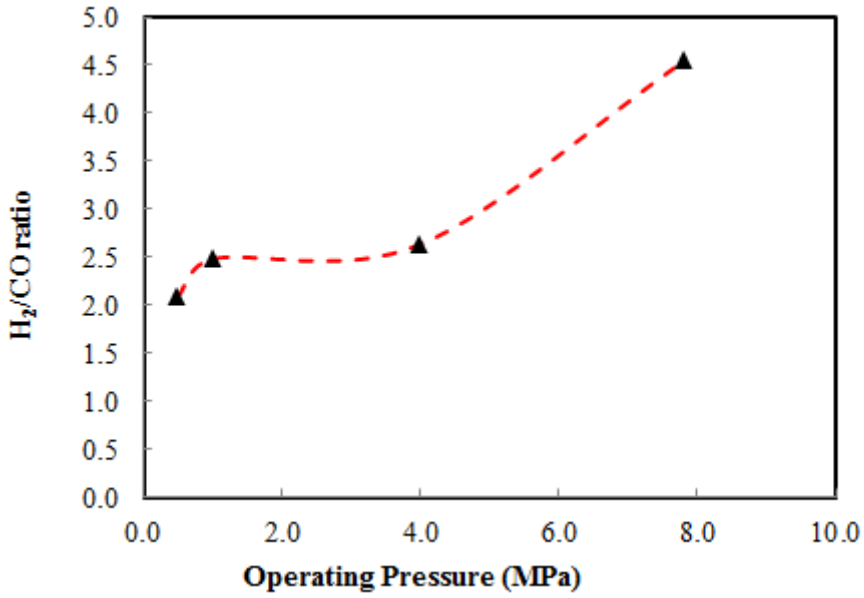

Figure 5.34: H_2/CO ratio versus the operating pressure for dry reforming process in a tip-tip arc discharge reactor

Table 5.12: Influence of operating pressure on conversion and product selectivity (Discharge duration, 60 sec; Initial feed of CH_4/CO_2, 1.8/1; Current, 0.350 A; Interelectrode gap, 0.4 mm)

Pressure (MPa)	$\chi_{(CH4)}$	$\chi_{(CO2)}$	$S_{(C2H2)}$	$S_{(C2H4)}$	$S_{(C2H6)}$	$S_{(C3H6)}$	$S_{(C3H8)}$	$S_{(H2)}$	$S_{(CO)}$	$S_{(CO*)}$	H_2/CO
0.5	46.00	45.22	2.37	1.49	1.87	0.020	1.5E-03	43.63	26.99	76.73	2.1
1.0	23.72	23.49	2.84	1.60	1.16	0.086	5.5E-03	41.86	21.79	61.65	2.5
4.0	7.39	6.90	2.45	1.95	0.83	0.213	1.2E-02	29.78	14.92	43.87	2.6
7.8	1.84	3.31	0.24	0.08	0.08	0.007	4.4E-03	2.82	0.62	1.25	4.5

CO* denotes CO_2-based selectivity to CO

Considering the high importance of ethylene in chemical processes, the ethylene/ethane as well as propylene/propane ratio was calculated and observed to increase between the pressure range of 0.5 to 4 MPa and then decreases thereafter. The H_2/CO ratio was observed to increase slightly from 0.5 to 1 MPa and become relatively constant from 1 to 4 MPa before a sharp and steady increase was observed thereafter. Thus, it might be interesting to subsequently try to understand the mechanism and reaction kinetics between the pressure ranges of 0.5 to 4 MPa as this could possibly be an alternative way to produce ethylene and propylene. Furthermore, the observed product trend and distribution from the experimental data for the dry reforming process is $C_2H_6 < C_2H_4 < C_2H_2$ along with carbon deposit.

The identified synthesized molecules in the carbon dioxide and methane reforming process where carbon formation is considered are H_2, CO, C_2H_2, C_2H_4, C_2H_6, C_3H_6, C_3H_8, C, H_2O, with C_4 hydrocarbons and benzene (C_6H_6) in addition to unconverted CH_4 and CO_2.

5.4.3 Comparative Review and Discussion on Some Dry Reforming Plasma Reactors

Petitpas et al. [132] in their comparative study on the performances of non-thermal plasma used three indicators namely: conversion, efficiency, and specific energy requirement to explain the performance of the fuel reforming processes. Tao et al. [133] in evaluating and comparing the performance of different plasma technologies for dry reforming process used the following indicators: energy conversion efficiency, specific energy, conversion (χ), and selectivity (S). In this study, product selectivity (S) and product yield (Y) of syngas were included in addition to the indicators given by Petitpas et al. [132]. Hence, in addition to conversion, selectivity and yield define by equations (5.21 to 5.28), the specific energy input (SEI), specific energy requirement (SER) and energy efficiency were calculated.

The specific energy input is the ratio of the input energy (E) for the reforming process in relation to the number of moles of the injected reactants (n_{reac}) calculated based on ideal gas law for a batch reactor as given by equation (5.32).

$$SEI(kJ/mol) = \frac{E}{n_{reac}} \tag{5.32}$$

The specific energy requirement is the input electrical energy used by the plasma and required to produce one mole of syngas (H_2 and CO) as given by equation (5.33) in line with Petitpas et al. [134]:

$$SER(kJ/mol) = \frac{P}{[H_2 + CO]_{produced}} \tag{5.33}$$

where P is the input plasma power in kW, $[H_2+CO]_{produced}$ is the moles of syngas (H_2+CO) produced per second. Large SEI and SER values indicate high energy consumption of that plasma system for the dry reforming process. Hence, it is necessary to calculate the energy efficiency.

According to Parvulescu et al. [214], reformer efficiency is generally defined in twofold: fuel production efficiency and chemical energy efficiency.The fuel production efficiency of the reforming process (η_{fp}) expresses the lower heating value (LHV) of synthesis gas produced in the reforming process divided by the input power of plasma and the LHV of methane injected. The chemical energy efficiency, which is calculated as the enthalpy of the reaction (ΔH_r) divided by the electrical power consumed (E_p) by the reactant in kJ/mol, is also a good indicator of how efficient the process is with respect to energy consumption.

$$\eta_{fp} = \frac{n_{H_2} \times LHV_{H_2} + n_{CO} \times LHV_{CO}}{P + n_{CH_4 in} \times LHV_{CH_4}} \tag{5.34}$$

where n_{H2}, n_{CO} are the moles of H_2 and CO produced; n_{CH4in} is the moles of CH_4 injected; LHV_{H2}, LHV_{CO} are the lower heating values of the H_2 and CO produced in kJ/mol respectively; LHV_{CH4} is the lower heating value of CH_4 in kJ/mol.

The chemical energy efficiency for the dry reforming processes compared was calculated using equation (5.35):

$$\eta_{ce}(\%) = \frac{\Delta H_{reaction}}{E_P} \times 100 \tag{5.35}$$

From the comparative study, a full comparison is presented in Table 5.13 based on reaction performance and energy performance of the dry reforming from experimental data for best conversion and product selectivity. By comparing the results obtained for the reaction performances (i.e., conversion, selectivity and yield), the DC arc plasma of Yan et al. [146] gave the best results. However, the specific energy requirement for the DC arc plasma is very high at 2742 kJ/mol and chemical energy efficiency is the lowest at 2%. Since the specific energy requirement as presented in Figure 5.35 on a logarithmic based scale is an indication of the energy consumed in producing 1 mol of syngas, high SER could be an indication of thermal losses in the DC arc plasma.

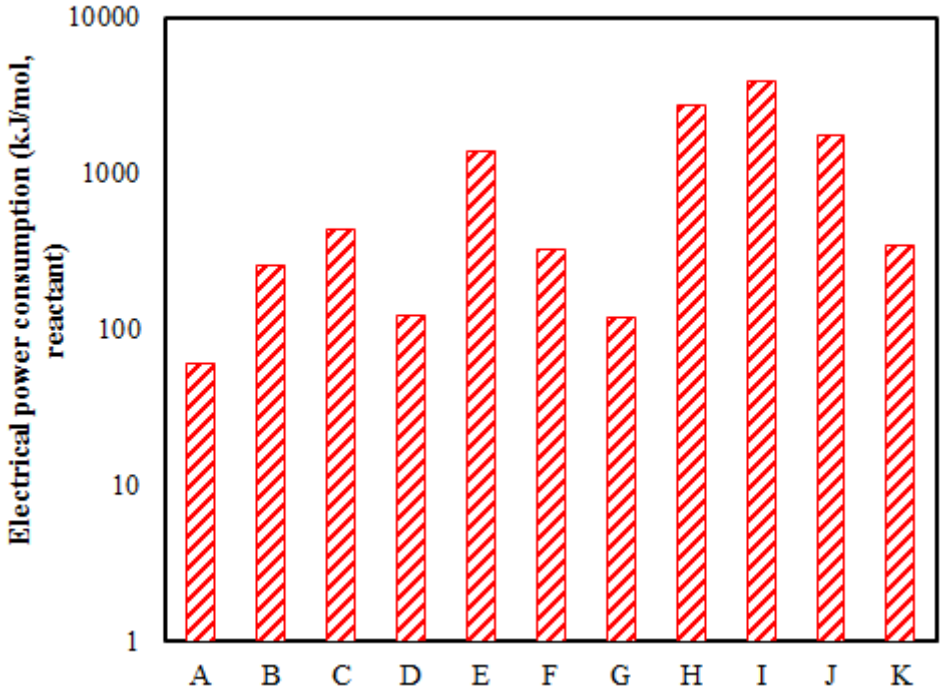

Figure 5.35: Specific energy requirement for production of 1 mol syngas through different plasma dry reforming processes. **A**: Dry reforming– Ideal plasma. **B**: Dry reforming – Pulsed Glow Discharge [12].**C**: Dry reforming – Pulsed Microwave Discharge [43]. **D**: Dry reforming – Cold Plasma Jet [144]. **E**: Dry reforming – (Positive) DC Corona Discharge [44]. **F**: Dry reforming – Binode Thermal Plasma [143]. **G**: Dry reforming – Atmospheric Pressure Plasma Jet [14]. **H**: Dry reforming – DC Arc Plasma [146]. **I**: Dry reforming – High Pressure Tip-Tip DC Arc Discharge [This work at 0.5 MPa]. **J**: Dry reforming – High Pressure Tip-Tip DC Arc Discharge [This work at 1.0 MPa]. **K**: Dry reforming – High Pressure Tip-Tip DC Arc Discharge [This work at 4.0 MPa]

Figure 5.36 gives the conversion and chemical energy efficiency of the ten dry reforming system compared using a perfect dry reforming based on theoretical calculations as a basis. With the exception of the experimental results reported by the atmospheric pressure plasma jet of Xiang et al. [14] which gave a high efficiency of 93% despite the high conversion, selectivity and yield, every other process showed a trade-off between energy efficiency and conversion. Thus, the reactor configuration of Xiang et al. [14] seems to be very suitable for the dry reforming process considering the low power density for a large interelectrode gap of 9 mm.

While the tip-tip DC arc discharge used in this study gave a lower conversion for CH_4 and CO_2 respectively in comparison to the reviewed literature data, it is the only plasma reactor with results above atmospheric pressure and a short interelectrode gap of 0.4 mm.

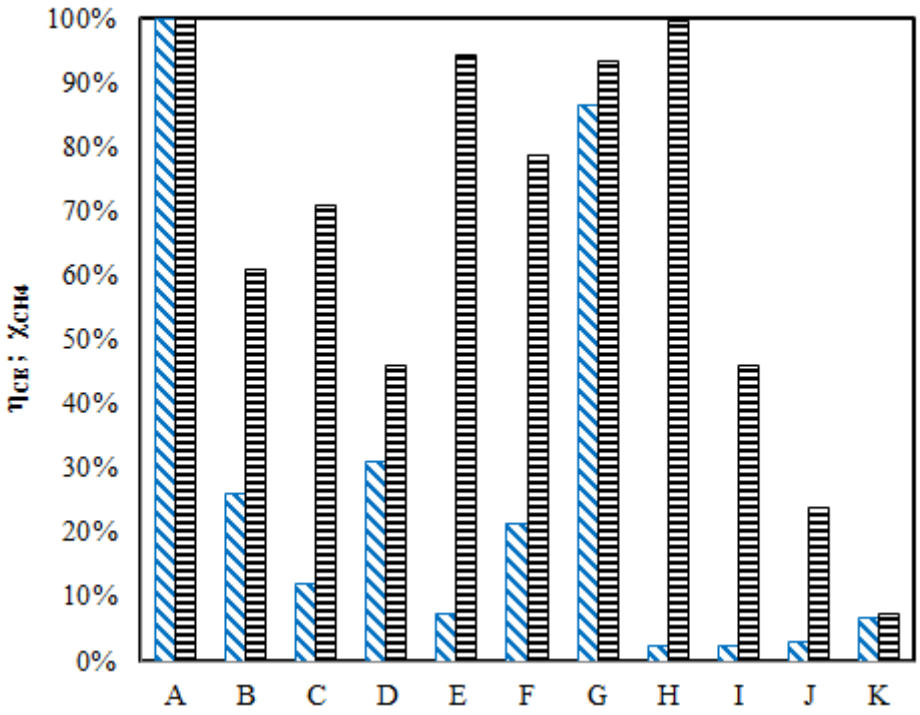

Figure 5.36: CH_4 conversion (χ_{CH4}) and energy efficiency (η_{CE}) for production of 1 mol syngas through different plasma dry reforming processes. **A**: Dry reforming– Ideal plasma. **B**: Dry reforming – Pulsed Arc Discharge [12].**C**: Dry reforming – Pulsed Microwave Discharge [43]. **D**: Dry reforming – Cold Plasma Jet [144]. **E**: Dry reforming – (Positive) DC Corona Discharge [44]. **F**: Dry reforming – Binode Thermal Plasma [143]. **G**: Dry reforming – Atmospheric Pressure Plasma Jet [14]. **H**: Dry reforming – DC Arc Plasma [146]. **I**: Dry reforming – High Pressure Tip-Tip DC Arc Discharge [This work at 0.5 MPa]. **J**: Dry reforming – High Pressure Tip-Tip DC Arc Discharge [This work at 1.0 MPa]. **K**: Dry reforming – High Pressure Tip-Tip DC Arc Discharge [This work at 4.0 MPa]

With respect to other plasma technologies (Table 5.13), all the results obtained in the tip-tip plasma reactor led to high and low values for SER and production yields respectively. These results are not surprising considering the very poor mass exchange between the active volume (arc) and the non-active volume (cold gas) in batch configuration. Indeed, in this configuration, the mass exchange between the gas and the arc zone takes place only under the effect of natural convection with approximately 0.1 m/s maximum velocity in a thin layer at the fringe of the arc core. Preliminary CFD calculations carried out on this reactor at 0.5 MPa shows that the effective gas volume treated by the discharge during 60 s is approximately half the reactor volume. As a result, one can reasonably estimate that at 0.5 MPa, the SER and production yields related to the gas that has really passed through the arc zone could be reduced and increased by a factor 2 respectively. At higher pressure, CFD modeling reveals that the volume of gas treated increases. The first aim of this work is the study of the influence of pressure on dry reforming. Obviously, in the perspective of process optimization, it will be necessary to switch from a batch configuration to a forced flow configuration similar to a DC plasma torch.

Therefore, it could be concluded that this tip-tip arc discharge has the potential for high CH_4 and CO_2 conversion and product selectivity to higher hydrocarbons and syngas at high pressures between 0.5 and 4 MPa if the interelectrode gap could be increased. In addition, high pressure can help to reduce problem associated with carbon deposit, which is the major cause of catalyst deactivation in dry reforming processes. Furthermore, this plasma reactor gave a H_2/CO ratio of 2.1to 2.6 at pressures of 0.5 to 4 MPa, which is suitable for the Fischer-Tropsch process compared to the low H_2/CO ratio less than 2 given by the other reactors indicating some energy will be used to adjust the H_2/CO ratio in those processes.

Table 5.13: Comparison of reaction and energy performance for different dry reforming plasma reactors

Plasma form	Feed flow rate (mL/min)	CH_4/CO_2	P (W)	$X(CH_4)$ (%)	$X(CO_2)$ (%)	S(CO) (%)	$S(H_2)$ (%)	$S(C_2H_2)$ (%)	$S(C_2H_4)$ (%)	$S(C_2H_6)$ (%)	$Y(H_2)$ (%)	H_2/CO	SER (kJ/mol)	η_{CE} (%)
Pulsed Glow Discharge [12]	120	1	23	61	50	65	77	14	7.6	0.9	47.0	1.3	258	26.0
Pulsed Microwave Discharge [43]	200	1.5	65	70.8	68.8	75	92.6	17.8	4.1	NR	65.6	1.5	437	12.0
Cold Jet Plasma [144]	0.8330×10^4	4/6	770	46	34	85	78	NR	NR	NR	35.88	0.8	124	31.0
Binode Thermal Plasma [143]	7.3300×10^4	4/6	18000	78.71	64.8	96.79	82.85	NR	NR	NR	65.21	0.8	330	21.0
DC Corona Discharge [44]	60	0.5	63	94.1	77.9	97.1	69.4	NR	NR	NR	65.31	0.54	1411	7.0
Atmospheric Pressure Plasma Jet [14]	1000	4/6	88.4	93.28	84.97	83.51	79.23	NR	NR	NR	73.9	0.8	119	86.0
DC Arc Plasma [146]	100	1	204	99.6	99.3	100	99.6	NR	NR	NR	99.2	1	2742	2.0
This work at 0.5 MPa		1.8/1	38.85	46.0	45.2	26.99	43.63	2.37	1.49	1.87	20.07	2.1	3884	2.3
This work at 1.0 MPa		1.8/1	35.35	23.72	23.49	21.79	41.86	2.84	1.60	1.16	9.93	2.5	1767	3.0
This work at 4.0 MPa		1.8/1	28.0	7.39	6.90	14.92	29.78	2.45	1.95	0.83	2.20	2.6	350	6.5

5.4.4 Conclusions on the Dry Reforming Study

Experimental studies on dry reforming at pressures up to 7.8 MPa indicate that the main molecules synthesized were H_2, CO, C_2H_6, C_2H_4, C_2H_2 with low amounts of C_3H_6, and C_3H_8. This study, which is aimed at demonstrating the influence of very high pressure on dry reforming, has shown a decrease in carbon deposit formation with increasing working pressure. While low conversions were obtained in comparison to the best dry reforming results reported in literature, the positive influence of very high pressures from 0.5 to 4 MPa on the energy efficiency is ascertained. Considering the good H_2/CO ratio of 2.1 to 2.6, which is desirable for production of synthetic fuels in F-T process compared to the low H_2/CO ratio of other reviewed dry reforming process, the energy required for adjusting H_2/CO will be reduced.

From the comparative study, a trade-off is observed to exist between energy efficiency and conversion. An improvement in the conversion could possibly be obtained by increasing the treatment zone of the arc discharge in a batch configuration or creating a plasma jet in a flow configuration at high pressure.

From this work, plasma-assisted dry reforming at very high pressure exhibits interesting results in terms of energy efficiency, and low carbon deposit formation. More knowledge on convection effect can be obtained by CFD modeling. Thus, the production of synthesis gas via dry reforming can have an environmental benefit as it utilizes CO_2 as the second reactant.

5.5 Fluorocarbon Synthesis using Tip-Tip Arc Discharge Reactor at High Pressure

Experiments relating to the formation of fluorocarbons using an electric arc discharge were conducted using CF_4/He mixtures as the reacting gas. Helium gas was introduced to help stabilize the discharge and allow for ignition of the discharge at high pressure condition, as pure CF_4 could not be ignited above 0.3 MPa. Investigations were made to understand the effect of working under a continuous mode and an intermittent (cyclic) mode. Further experiments were conducted to investigate the influence of pressure variation, current variation, and interelectrode gap variation.

5.5.1 Fluorocarbon Synthesis Using Two Different Treatment Modes at High Pressure

Experiment was conducted for a CF_4/He gas mixture with a percentage mole fraction of 40/60 respectively. This experiment serves to demonstrate the influence of the different treatment modes on the synthesis of higher fluorocarbons from CF_4. Helium was added to CF_4 to stabilize the discharge for high pressure operation. The experimental operating conditions for this work are presented in Table 5.14 below.

Table 5.14: Operating conditions for fluorocarbon synthesis from CF_4 according to the mode of treatment

Operating conditions	Continuous mode	Cycle mode 1c = 8 s
Current	0.35 A	0.35 A
Ignition Voltage	8 kV	8 kV
Pressure	2.0 MPa	2.0 MPa
CF_4 / Helium	2 / 3	2 / 3
Interelectrode gap	0.4 mm (constant)	0→0.4 mm (variable)
Discharge duration	0→80 s	0→160 s
Treatment time	0→80 s	0→730 s (0→20 cycles)
Graphical results	Figure 5.37	Figure 5.38

These experiments further investigated the effect of two different treatment modes (one continuous and one intermittent mode with a relaxation time between successive discharges). The continuous mode implies that the gas mixture was exposed to treatment by the discharge over a continuous extended period referred to as the "discharge duration". For the cyclic mode, the gas mixture was treated by generating the discharge in successive cycles characterized by a duration of 8 s, which is

separated by a relaxation period of 30 s. The results showed the production of hexafluoroethane (C_2F_6) and octafluoropropane (C_3F_8) in very low concentrations. From the calibration curves, C_2F_4, C_2F_6, and C_3F_8 have their approximated peak areas as 2292262, 25509, and 3138970 for an injected volume of 20 µL. These peak areas correspond to a concentration value of 8.192×10^{-7}, 8.279×10^{-7}, and 8.023×10^{-7} moles of C_2F_4, C_2F_6, and C_3F_8 respectively. If a linear response factor is assumed over the entire injected volume range of 20 to 200 µL, then the concentrations that correspond to the highest peak area obtained for the C_2F_6 and C_3F_8 as the gaseous products will be 5.12×10^{-7} and 8.34×10^{-7} respectively. These values obtained for the C_2 and C_3 fluorocarbons produced were below the calibration range, and therefore the gaseous fluorocarbon products were not quantified. However, a graphical representation using the peak areas obtained from the chromatogram are shown in Figures 5.37 and 5.38.

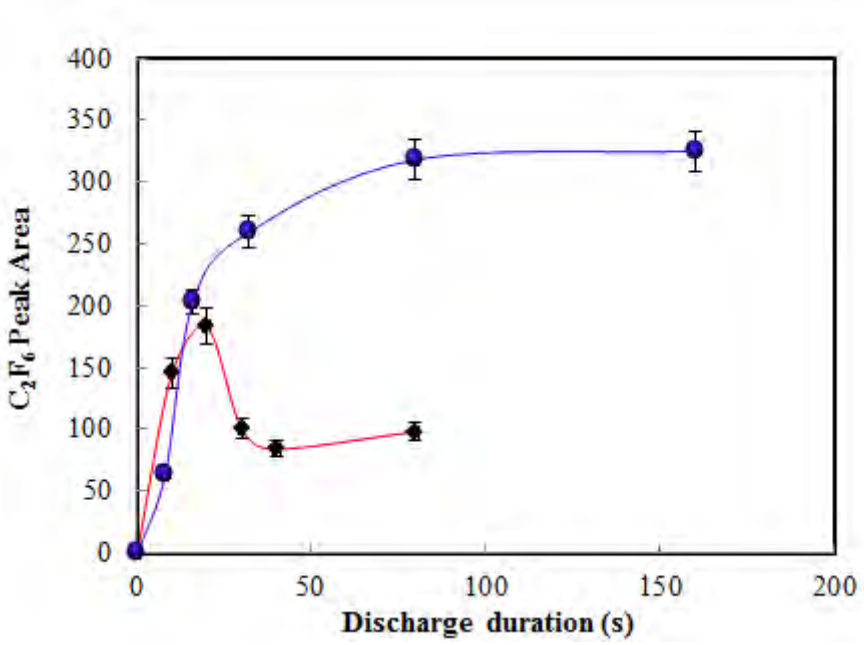

Figure 5.37: Concentration of C_2F_6 produced versus discharge duration for the two modes of treatment; ♦ continuous mode; ●cyclic mode

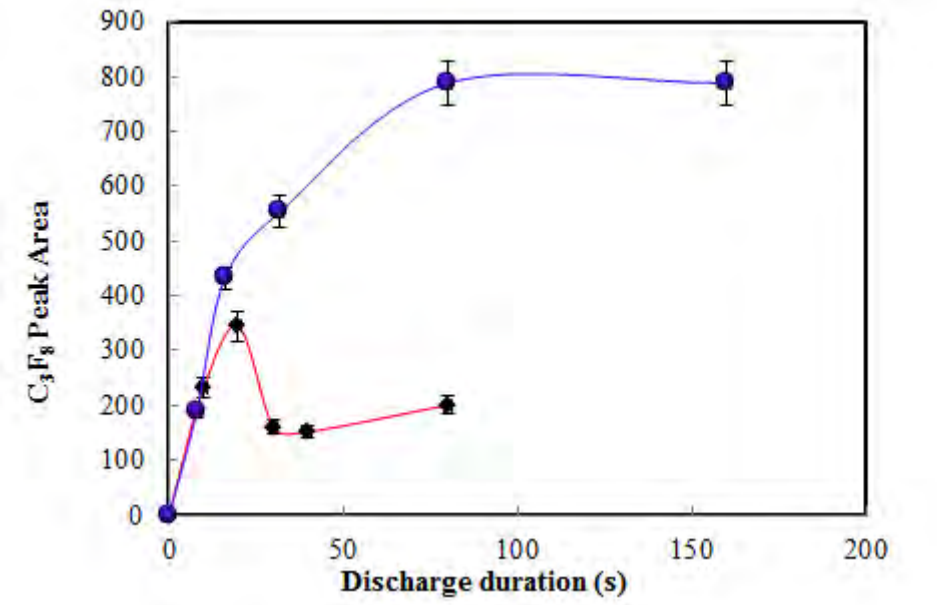

Figure 5.38: Concentration of C_3F_8 produced versus discharge duration for the two modes of treatment; ♦ continuous mode; ●cyclic mode

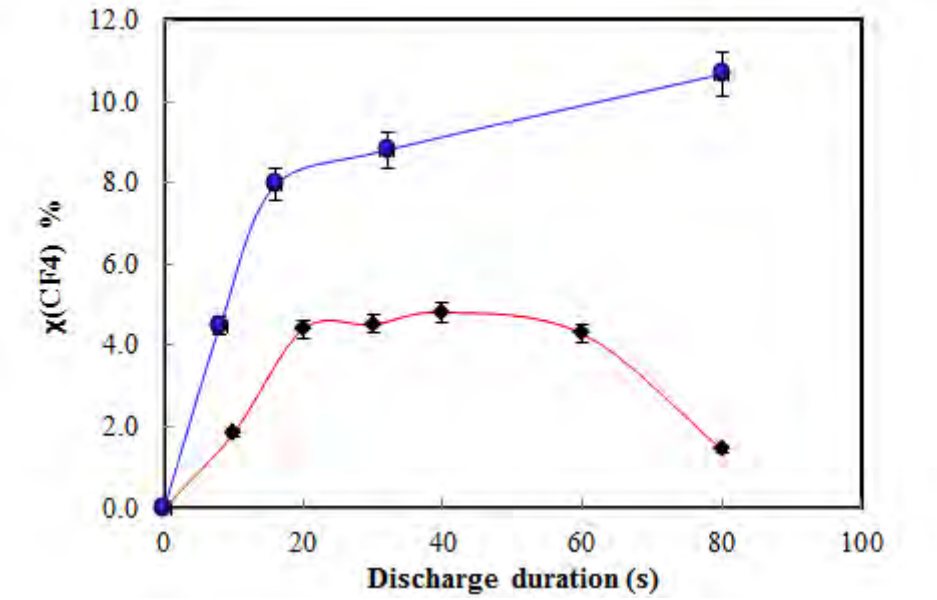

Figure 5.39: Conversion of CF_4 through the two different modes of treatment versus discharge duration; ♦ continuous mode; ●cyclic mode

5.5.1.1Comments and Discussion on the Results from theTwoTreatment Modes

The results show the production of C_2F_6 and C_3F_8 from CF_4 at 2 MPa for the two modes of treatment. From graphical results in Figures 5.37 and 5.38, the species produced were observed to be influenced by the treatment mode used. The production rates were observed to increase for the C_2F_6 and C_3F_8 species in the continuous mode under 20 s. However, the production rates decreased quickly after

discharge duration of 30 s for both species under the continuous mode. This shows that under the continuous discharge mode, the discharge generated seems to destroy the species produced after a certain time is reached. This mode of operation thus puts a limitation on the species that can be produced based on the discharge duration.

For the cyclic mode, a continuously increasing trend of the species produced was observed as a function of the discharge duration. This result shows that by generating the discharge intermittently after a relaxation period, the kinetic inversion observed for the continuous mode could be prevented.

By comparing the continuous mode and the cyclic mode in Figure 5.37, it was observed that C_2F_6 has the highest production rate between a discharge duration of 0 and 20 s. However, the production rate decreases slowly after 20 s before becoming relatively constant after 40 s. On the other hand, C_2F_6 production under the cyclic mode shows a similar trend to that of the continuous mode during the 0 to 20 s interval, but increases more slowly after 20 s in comparison to the continuous mode. While C_2F_6 production for the cyclic mode gave lower values than the continuous mode for a discharge duration less than 10 s, it surpasses the continuous mode after 20 s with respect to the peak area of C_2F_6 produced.

The concentration of C_3F_8 produced as shown in Figure 5.38 is high in comparison to C_2F_6 produced by the two modes in Figure 5.37. From Figure 5.38, it can be seen that the curve for C_3F_8 production follows the same trend as for the continuous mode and the cyclic mode in the discharge duration of under 20 s. However, the continuous mode is observed to reach a maximum at approximately 20 s, while the cyclic mode increases monotonously as a function of the discharge duration. Thus, as in the case with C_2F_6, the cyclic mode shows prospects for the production of C_3F_8 following the same trend as observed for the production of C_2F_6. This could mean that the cyclic mode is suitable for C_2 and C_3 fluorocarbon production.

In Figure 5.39, the conversion of CF_4 to higher fluorocarbons was observed to increase gradually within the 0 and 20 s interval in the continuous mode. However, the conversion became constant between 20 and 40 s before slowly decreasing afterward in a continuous trend. This again further supports the understanding that the continuous mode operation of discharge duration exceeding 30 s might not be suitable for the formation of the higher fluorocarbons under a batch configuration. In contrast to the continuous mode, the cyclic mode again seems to provide a new prospect for the dissociation of CF_4 under electric arc discharge by generating the discharges intermittently. This approach perhaps supports the treatment of a larger quantity of the gas than the continuous mode.

Based on the understanding that the CF_4 used is 40% of the total gas mixture of CF_4/He, and that helium is one of the two gases that does not react with fluorine, the dissociation of CF_4 under an

electric arc discharge leads to the formation of C_2F_6 and C_3F_8. In addition, the presence of helium in high quantity is expected to lower the conversion tendency of CF_4 under a nonequilibrium plasma condition. To support this, a theoretical study will be presented to show the possible influence of helium on the conversion process. This approach will help to explain the reason why the production for C_2F_6 and C_3F_8 is very low in this study.

In conclusion, the possibility of formation of higher fluorocarbons (C_2 to C_3) from CF_4 through electric arc discharge operating at high pressures has been demonstrated in this study. The two treatment modes were investigated under similar experimental conditions of CF_4/He composition, discharge current, and working pressure. While both modes of treatment led to the production of small amounts of C_2F_6 and C_3F_8, the cyclic modes shows better results for the synthesized species than the continuous mode. Furthermore, from the specific treatment duration under the continuous mode, negative production rates were observed, which is an unfavorable kinetics of synthesis for the process. On the other hand, the intermittent (cyclic) mode of treatment, which includes a relaxation time between two successive periods of discharge results in a progressive trend. Thus, the use of the intermittent treatment mode might be essential for a continuous fluorocarbon synthesis process. However, a short discharge duration, less than 30 s, might be suitable for operation under the continuous treatment mode.

5.5.2 Influence of Operating Pressure on Fluorocarbons Synthesis

One of the novel contributions about this research work involves studying the effect of high pressure plasma on the synthesis of fluorocarbons. Until now, there is no report of any experimental work carried out above 1 MPa for the synthesis of fluorocarbons using electric arc discharges at low current. Thus, to this effect, the influence of pressure variation on fluorocarbon formation has been studied with the operating condition presented in Table 5.15. The results show the production of C_2F_6 and C_3F_8 over the entire operating pressure range from 1 to 9 MPa, while C_2F_4 and C_4F_{10} were observed to be produced at specific operating pressures.

Table 5.15: Operating conditions for fluorocarbon synthesis from CF_4 at varying operating pressures

Operating conditions	Pressure Variation
Current	0.35 A
Ignition Voltage	8 kV
Pressure	1.0, 2.0, 3.0, 3.5, 3.75, 4.0, 4.5, 5.0, 5.5, 6.0, 6.2, 6.7, 7.0, 8.0, 9.0 MPa
CF_4: Helium	30% : 70%
Inter-electrode gap	0.4 mm
Discharge duration	0→30 s
Treatment time	0→30 s

Figure 5.40 shows the peak areas of the main species produced in the operating pressure range of 1 to 5 MPa. This plot indicates that the measured peak area of C_2F_6 and C_3F_8 tends to decrease as the operating pressure increases. This is contrary to the trend observed in the operating pressure range of 6 to 9 MPa, where the measured peak area of these species was observed to increase as the operating pressure increases. This is shown in Figure 5.41. Interestingly, the species produced in the highest concentration at 1, 3 to 5 MPa was C_2F_4. This indicates that the best operating pressure range for C_2F_4 production is from 3 to 5 MPa.

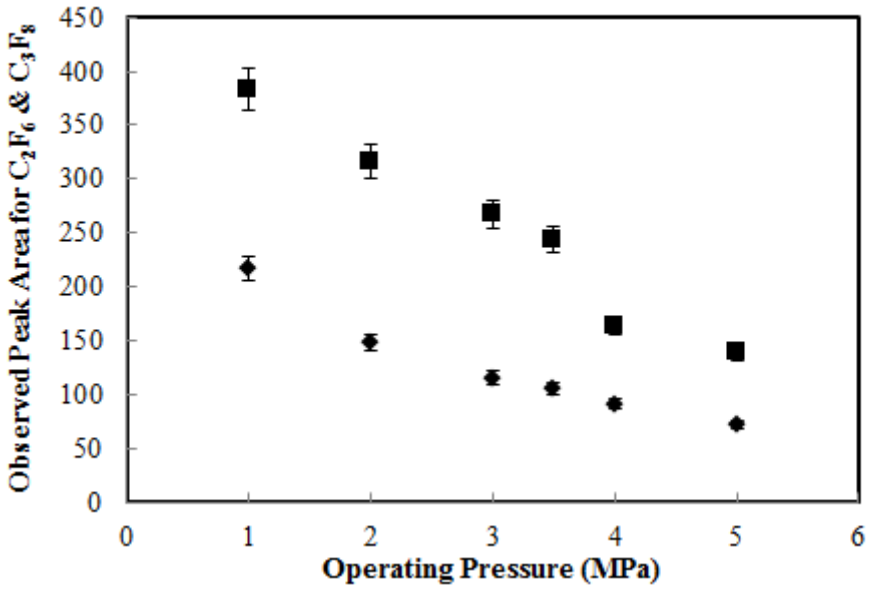

Figure 5.40: Measured peak areas of C_2F_6 and C_3F_8 produced as a function of the operating pressure of 1 to 5 MPa for a CF_4/He ratio of 3:7 at a current of 0.35 A, d = 0.4 mm and t = 30 s. ♦(C_2F_6); ■(C_3F_8)

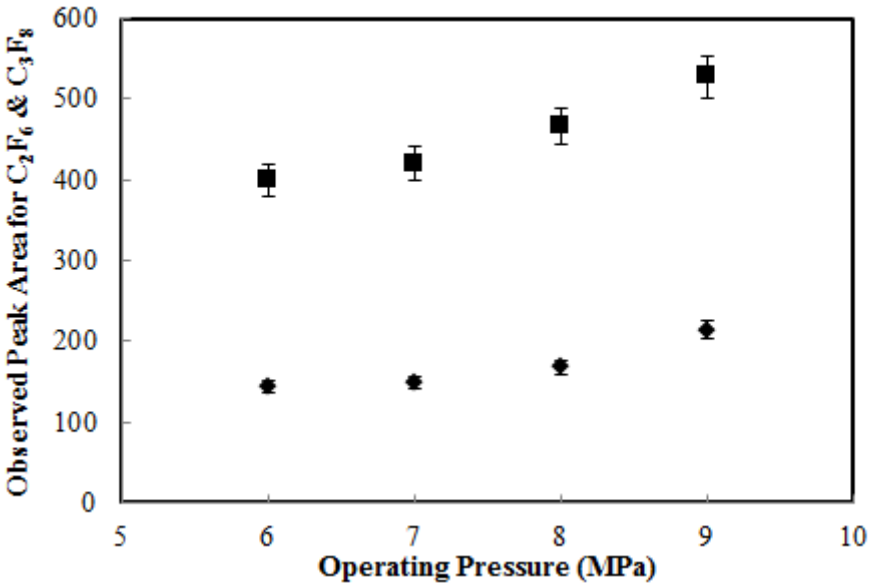

Figure 5.41: Measured peak areas of C_2F_6 and C_3F_8 produced as a function of the operating pressure of 6 to 9 MPa for a CF_4/He ratio of 3:7 at a current of 0.35 A, d = 0.4 mm and t = 30 s. ♦(C_2F_6); ■(C_3F_8)

A plot showing the trend of the species produced over the entire range of operating pressures investigated is in Figure 5.42. This Figure shows that the amount of species produced decreases gradually as the pressure increases until a minimum was obtained at 5 MPa. Afterwards, the increase in the operating pressure was observed to increase the species produced from 6 to 9 MPa.

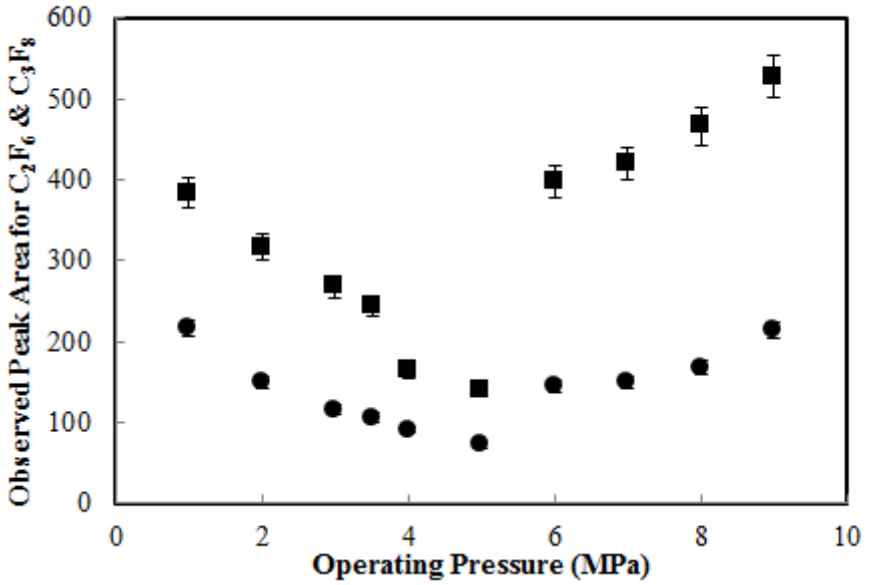

Figure 5.42: Measured peak areas of C_2F_6 and C_3F_8 produced as a function of the operating pressure of 1-9 MPa for a CF_4/He ratio of 3:7 at a current of 0.35 A, d = 0.4 mm and t = 30 s. ♦(C_2F_6); ■(C_3F_8)

As mentioned in section 5.2.1, explaining the influence of operating pressure on plasma-chemical processes can be a very complex concept depending on the gas used. Moreover, the influence of high pressure ranging from 1 to 9 MPa on transport properties such as electrical conductivity, thermal conductivity, and enthalpy can be very significant at very high temperature (above 1 eV) which is common under nonequilibrium discharge. In addition, since it is known that plasma consists of radicals, ions, electrons, and molecules which can each possess its own temperature, it therefore means that an increase in pressure will increase the collision of particles within the reactor. Thus, the density of the gas changes significantly at high pressure and temperature. More so, the rate of natural convection is expected to increase with pressure. Hence, to explain the influence of pressure in this experiment, the input power, the specific energy input of the reactant as well as the conversion of CF_4 is presented in Figures 5.43 to 5.45 respectively.

As mentioned in previous sections relating to hydrocarbon synthesis, electrical performance analysis of the plasma process involves accurate and precise measurement of the root mean square voltage (V_{rms}) and current (I_{rms}) using an oscilloscope. This was done using a high voltage probe Chauvin Arnoux HX0027 with bandwidth up to 30 MHz and a Chauvin Arnoux E3N Hall-effect current probe with bandwidth up to 100 kHz both connected to a LeCroyWaveJet 354A digital oscilloscope. The bandwidth of the oscilloscope is 500 MHz.

The input power (P) and electrical energy (E) consumed by the process were calculated following equations (5.8 to 5.9) previously given under section 5.2.1.

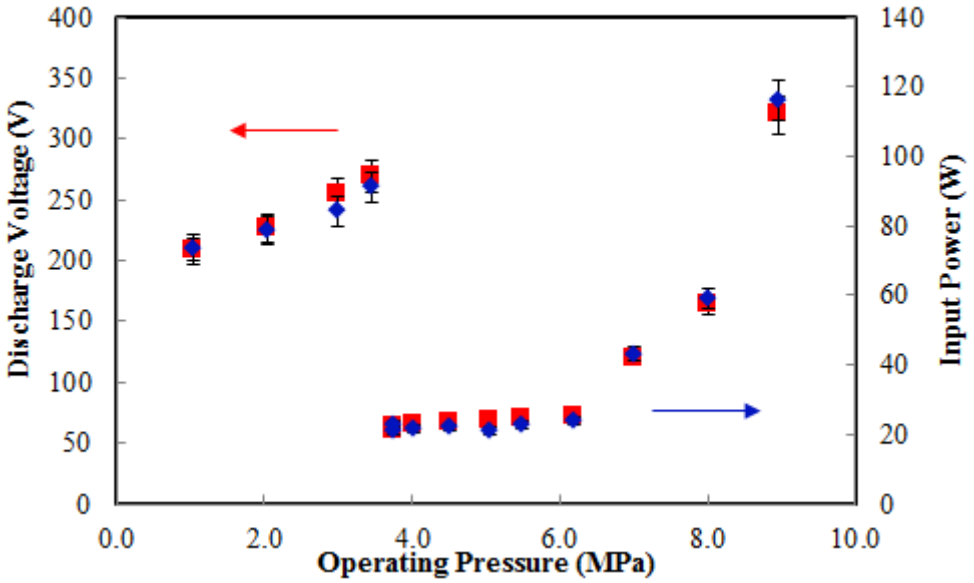

Figure 5.43: Input power and discharge voltage for CF_4 conversion as a function of the operating pressure for a CF_4/He ratio of 3:7 at a current of 0.35 A, d = 0.4 mm and t = 30 s. ■ (discharge voltage); ♦ (Input power)

From the plot of the input power versus the operating pressure in Figure 5.43, it can be seen that the discharge voltage and power increases as the pressure increases from 1 to 3.5 MPa. This voltage-current curve is characteristic of a glow-type discharge. In this pressure range, the discharge was observed to be relatively stable with the standard deviation of the rms voltage less than 5%. While the discharge voltage was observed to be relatively constant between 3.7 and 5.5 MPa, the discharge was also stable with fluctuations in rms voltage lower than 5%. However, between pressures of 6 to 8 MPa the fluctuations in the rms voltage was higher than 10% with an arc -type discharge observed from 3.7 to 9 MPa. Interestingly, this result is an indication that by adjusting the gas pressure at a fixed current and interelectrode gap, the energy transferred into the plasma could influence the products formed as well as the type of discharges generated. Moreover, considering the CF_4 conversion and distribution of the fluorocarbons produced under electric discharge, it can be seen that a high amount of C_2F_4 can be produced in the pressure range of 3.7 to 5 MPa while subsequently reducing the production of C_2F_6 and C_3F_8. Equally, the production of C_2F_4 can be avoided at pressures between 6 to 9 MPa while increasing the amount of saturated fluorocarbons (C_2F_6 and C_3F_8).

For the specific energy input (SEI), which was defined in section 5.2.1 as the amount of electrical energy deposited in the reactor divided by the moles of reactants fed, the plot is shown in Figure 5.45. From this calculation and Figure 5.45, the SEI is observed to decrease as the operating pressure increases between 1 and 3.5 MPa. However, the value is relatively constant between 3.7 and 5.5 MPa, with a slow increase observed from 6 to 9 MPa. Thus, the SEI value is highest at lower pressure which is an indication that the process is close to thermal and most of the energy probably goes into gas heating, while the low SEI at 3.7 MPa up to 9 MPa implies that the discharge is more by electron impact.

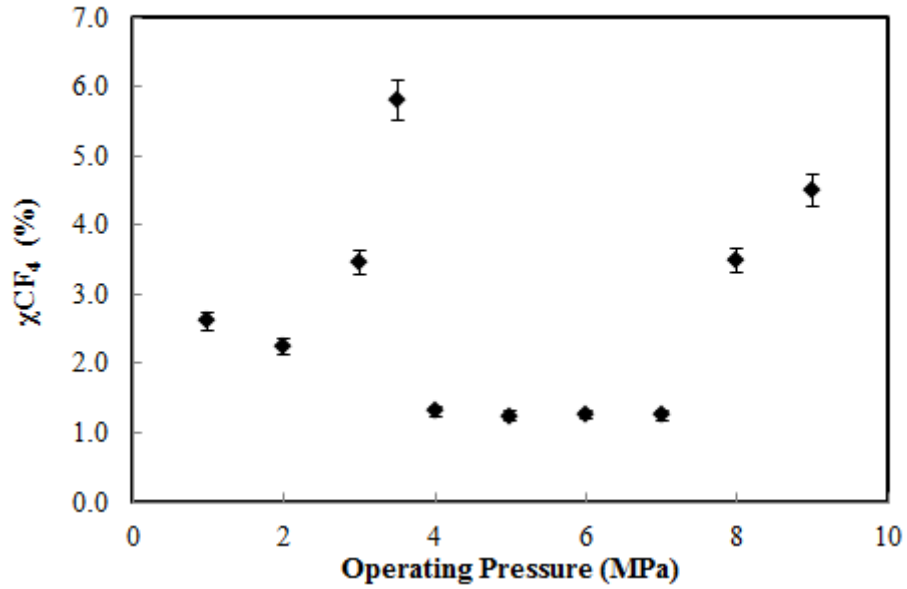

Figure 5.44: Conversion for CF_4 as a function of the operating pressure for a CF_4/He ratio of 3:7 at a current of 0.35 A, d = 0.4 mm and t = 30 s

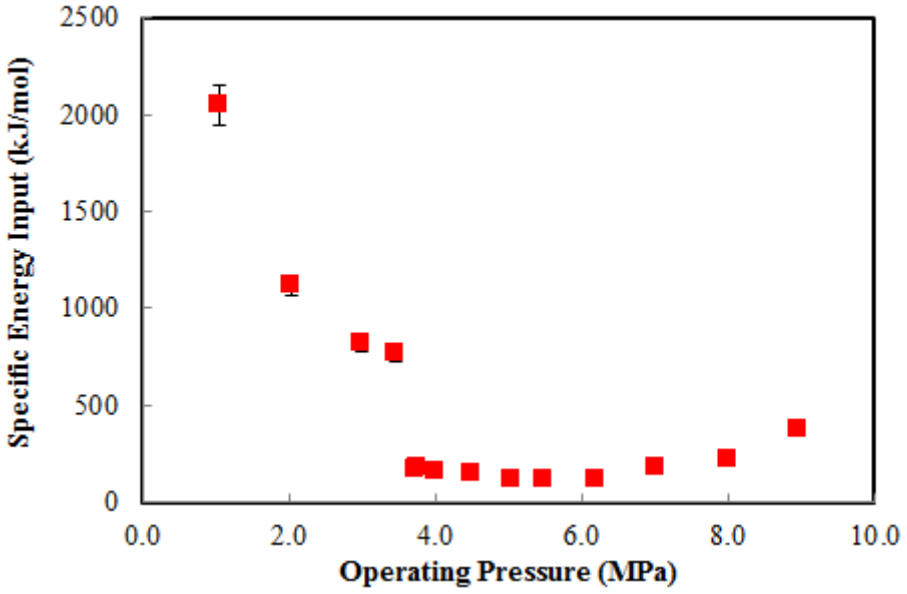

Figure 5.45: Specific energy input versus the operating pressure for a CF_4: He ratio of 3:7 at a current of 0.35 A, d = 0.4 mm and t = 30 s

In conclusion, as demonstrated in Figure 5.9 under section 5.2.1.2, the volume of the gas treated by the discharge increases as the working pressure increases. Again, the SEI was observed to decrease as the operating pressure increases. This is an indication that the process consumes less energy at higher

pressure and thus gives the best performance in terms of energy efficiency, but the low amount of available energy does not enable a good conversion.

Although, the input power shows a non-linear trend and may not have a directly proportional relationship with the amount of product formed, the overall results show that the operating pressure and input power plays a major role in the conversion process and formation of the higher fluorocarbons. On the other hand, it could mean that high input power at pressures from 2 to 3.5 MPa and 6 to 9 MPa were the driving force for the high conversion witnessed at those pressures. The low input power between 3.7 and 5.5 MPa is also an indication that C_2F_4 production could be more energy efficient that the saturated hydrocarbons at lower pressure.

5.5.3 Influence of Operating Current on Fluorocarbons Synthesis

Table 5.16: Operating conditions for fluorocarbon synthesis from CF_4 at varying operating current

Operating conditions	Current Variation
Current	0.30, 0.35, 0.40, 0.45 A
Ignition Voltage	8 kV
Pressure	1.0 MPa
CF_4 : Helium	30% : 70%
Inter-electrode gap	0.4 mm
Discharge duration	0→30 s
Treatment time	0→30 s

The graphical representation of the results obtained by varying the operating current with other parameters fixed as listed in Table 5.16 is presented in Figure 5.46. The results show the production of saturated fluorocarbons C_2F_6, C_3F_8 and unsaturated C_2F_4 as the main products synthesized by the electric discharge for all the operating currents investigated in this study.

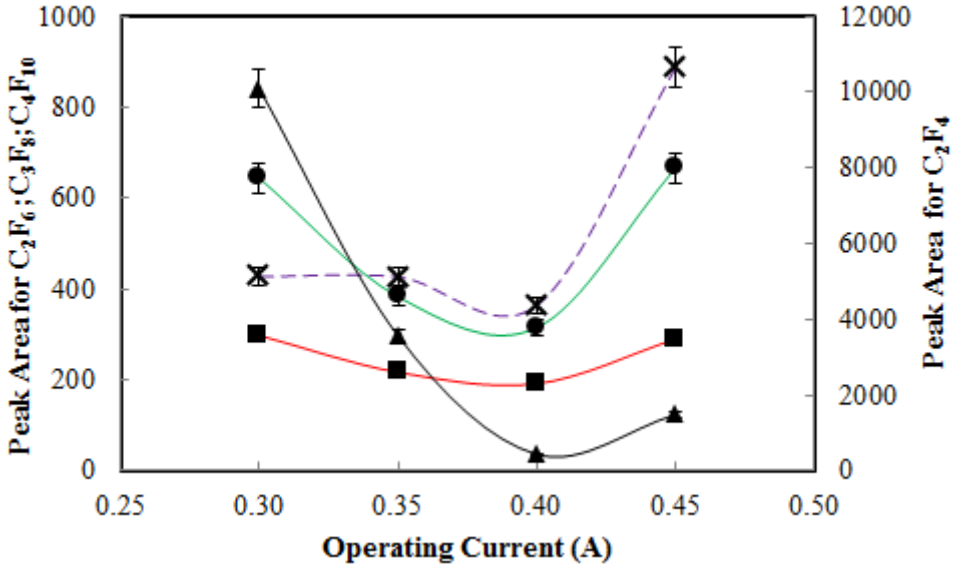

Figure 5.46: Measured peak areas of the main gas phase fluorocarbons produced as a function of the operating current for a CF_4/He ratio of 3:7 at 1 MPa, d = 0.4 mm, and t = 30 s. ■ with solid red line (C_2F_6); ▲ with solid black line (C_2F_4); ● with solid green line (C_3F_8); X with dotted purple line (C_4F_{10})

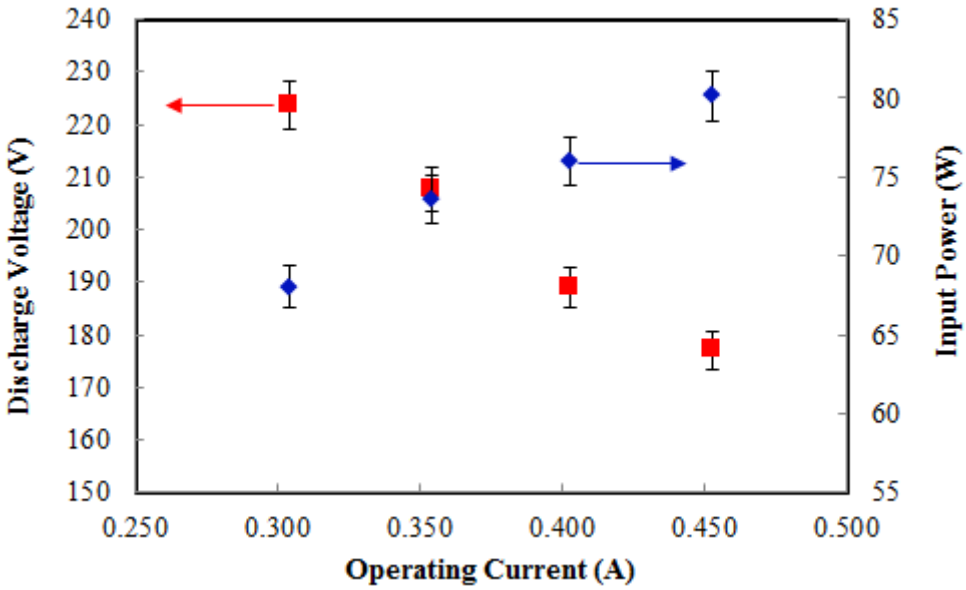

Figure 5.47: Discharge voltage and input power versus the operating current for a CF_4/He ratio of 3:7 at 1 MPa, d = 0.4 mm, and t = 30 s.■ with solid black line (Discharge voltage); ♦ with solid blue line (Input power)

From Figure 5.46, the measured peak areas of the main fluorocarbons produced were observed to decrease gradually with an increase in the operating current up to a minimum at 0.4 A before an increase was observed at 0.45 A. In addition, C_4F_{10} was identified to be formed with the measured peak area found to be relatively constant at 0.3 and 0.35 A and decreased at 0.4 A before increasing at 0.45 A. This trend is characteristics of the voltage-current curve for nonthermal arc discharges for the fluorocarbons at those operating conditions as displayed in Figure 5.47. Thus, the root mean square voltage was observed to decrease as the operating current increases, while the input power was found to increase with a decrease in the operating current. The voltage and power versus operating current curve is presented in Figure 5.47.

The strong decrease of the discharge voltage will lead to a decrease of the reduced electric field in the discharge in comparison with the current increase. As mentioned earlier in section 5.2.2, the decrease of the reduced electric field will result in a strong deviation from thermodynamic equilibrium within the arc. The reduced electric field thus plays a role in the conversion process of the CF_4 into higher fluorocarbons. A plot representing the conversion of CF_4 to higher fluorocarbons is presented in Figure 5.48 below.

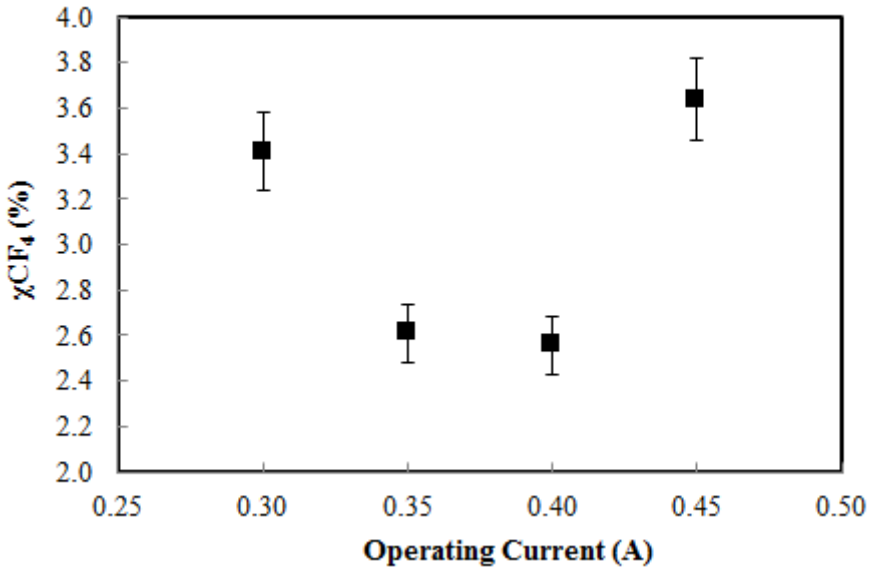

Figure 5.48: Conversion versus the operating current for fluorocarbon synthesis from CF_4

In Figure 5.48, the conversion for tetrafluoromethane (CF_4) was observed to decrease gradually as the operating current increases between 0.3 A and 0.35 A, after which it became stable at 0.4 A. This is in contrast to the observed trend of the input power versus operating plot in Figure 5.47 where the power increases with a corresponding increase in the operating current. This shows that the reduced electric field could have an influence on the conversion process. However, the presence of helium in high concentration could also have influenced the electric conductivity and specific heat of the gas mixture.

The electronic excitation and vibrational excitation of the CF_4 gas could equally be influenced by the high helium concentration in the mixture, and thus lowered the conversion of the process under nonequilibrium condition. This will be illustrated further in the theoretical study section of CF_4 dissociation under electric arc discharge.

The specific input energy (SEI) versus operating current plot shows an increasing trend of the SEI with a corresponding increase in the current as in Figure 5.49. This is an indication that the product trends as well as the conversion of CF_4 do not directly depend on the energy fed into the system, as an increase in conversion would have been expected. Thus there is a high probability that there are radiation losses at lower currents of 0.3 to 0.4 A.

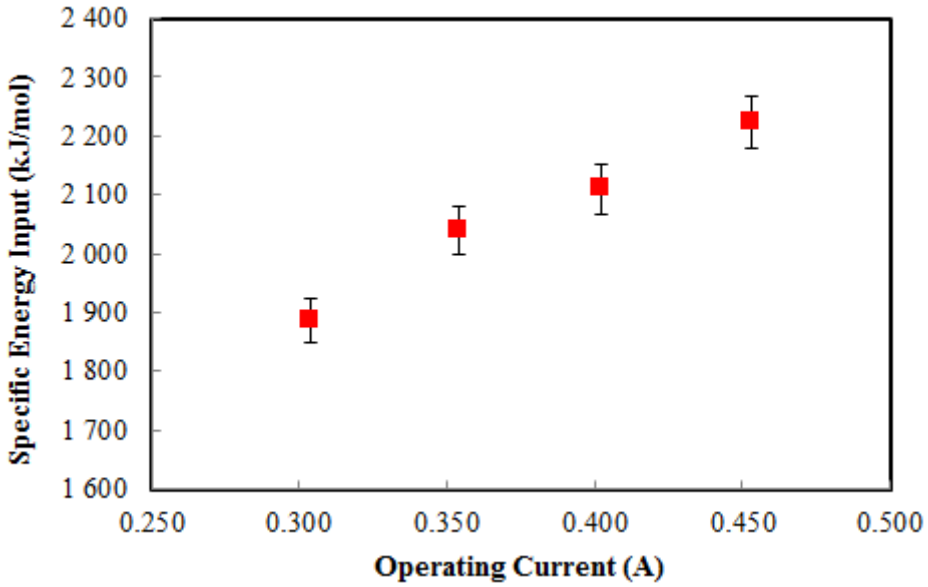

Figure 5.49: Specific energy input per mole of reactant injected versus the operating current for a CF_4: He ratio of 3:7 at a pressure of 1 MPa, d = 0.4 mm and t = 30 s

5.5.4 Influence of Interelectrode Gap on Fluorocarbons Synthesis

The effect of increasing the interelectrode gap was investigated for fluorocarbon synthesis at 1 MPa, a fixed current of 0.35 A, and a discharge duration of 30 s for a CF_4/He ratio of 3:7. From the result obtained at an interelectrode gap of 0.4, 0.6, 0.8 and 1 mm, the measured peak areas of the main products is shown in Figure 5.50 for the experimental operating condition listed in Table 5.17.

Table 5.17: Operating conditions for fluorocarbon synthesis from CF_4 at varying interelectrode gap

Operating conditions	Interelectrode gap Variation
Current	0.35 A
Ignition Voltage	8 kV
Pressure	1.0 MPa
CF_4 : Helium	30% : 70%
Inter-electrode gap	0.4, 0.6, 0.8, 1.0 mm
Discharge duration	0→30 s
Treatment time	0→30 s

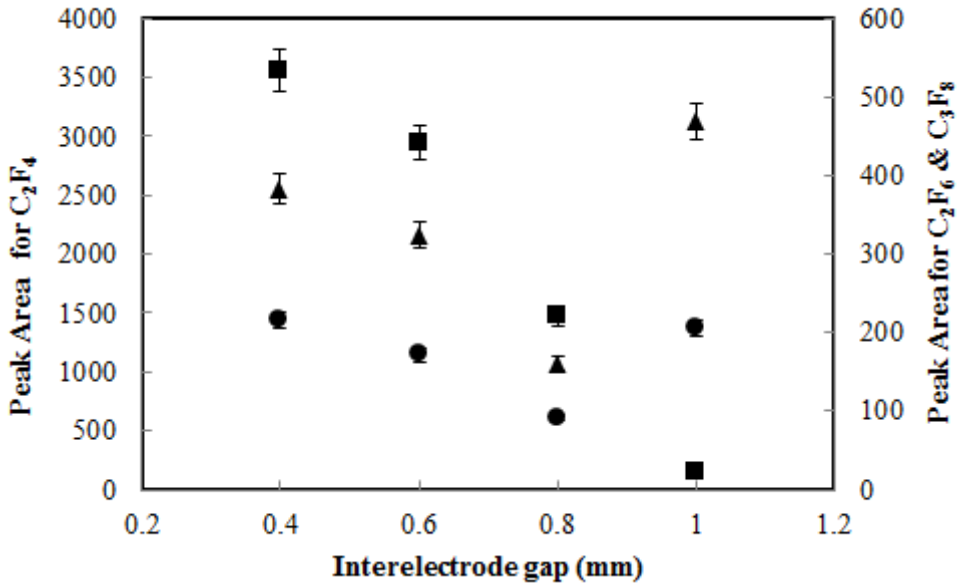

Figure 5.50: Measured peak areas of the main gas phase fluorocarbons produced as a function of the interelectrode gap for a CF_4/He ratio of 3:7 at 1 MPa, d = 0.4 mm, and t = 30 s. ■ (C_2F_4); ● (C_2F_6); ▲ (C_3F_8)

As can be seen in Figure 5.50, the measured peak area of C_2F_4 produced decreases as the interelectrode gap increases. This trend was initially observed for C_2F_6 and C_3F_8 production at 0.4, 0.6, and 0.8 mm respectively with an increase observed at 1 mm. This trend was unexpected, i.e. it was expected that the production of the higher fluorocarbons would increase with a corresponding increase in the interelectrode gap. However, the calculation of the volume power density (input energy per volume of the discharge) as shown in Figure 5.51 reveals that the volumetric power is relatively of the same magnitude for an interelectrode gap of 0.4 to 1 mm. This shows that the power supplied to each discharge volume is the same and that there may be radiation losses as the interelectrode gap decreases.

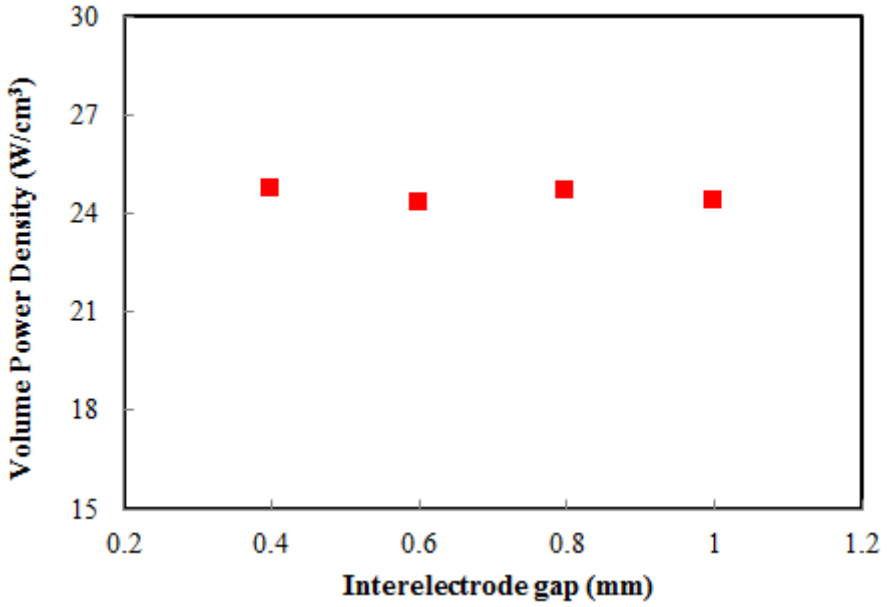

Figure 5.51: Power density versus interelectrode gap for a CF_4/He ratio of 3:7 at a pressure of 1 MPa and a current of 0.35 A

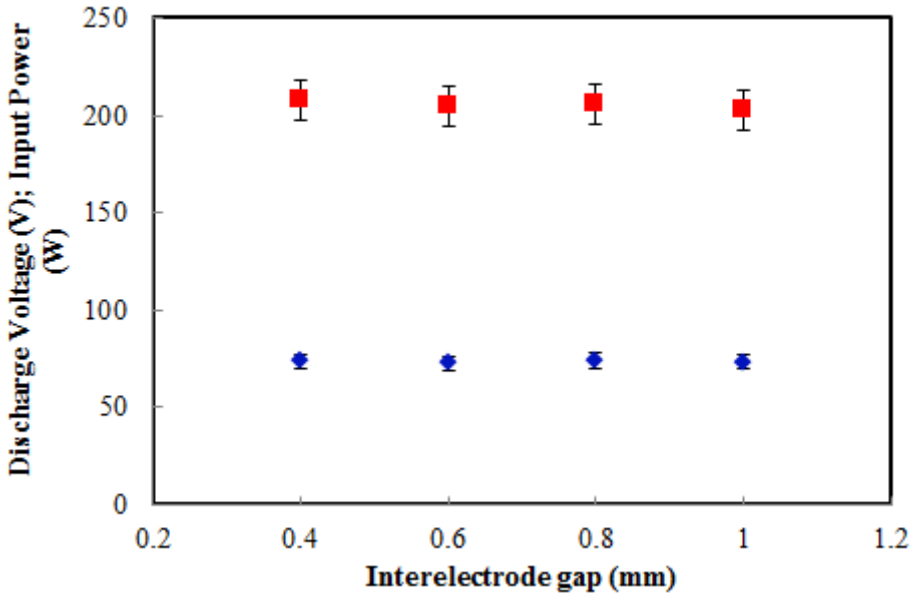

Figure 5.52: Discharge voltage and input power versus the operating current for a CF_4/He ratio of 3:7 at 1 MPa, I = 0.35 A, and t = 30 s.■ with solid black line (Discharge voltage); ♦ with solid blue line (Input power)

Furthermore, the discharge voltage and input power were found to be relatively constant over the entire interelectrode gap investigated. This indicates that the dissociation of CF_4 does not directly depend on the input power or discharge voltage. This can be seen through the conversion versus interelectrode gap plot in Figure 5.53. From Figure 5.53, the CF_4 conversion can be observed to

increase from 0.4 mm to 0.6 mm. However, considering the error bar of ± 5%, the conversion rate is within the same statistical confidence interval between 0.6 and 1 mm.

In conclusion, while the influence of interelectrode gap might be significant for a pure CF_4 gas, the influence of helium as a diluent at high concentration cannot be ruled out. Nevertheless, the results obtained show that the increase of interelectrode gap for the gas mixtures considered does not play a major role in the process.

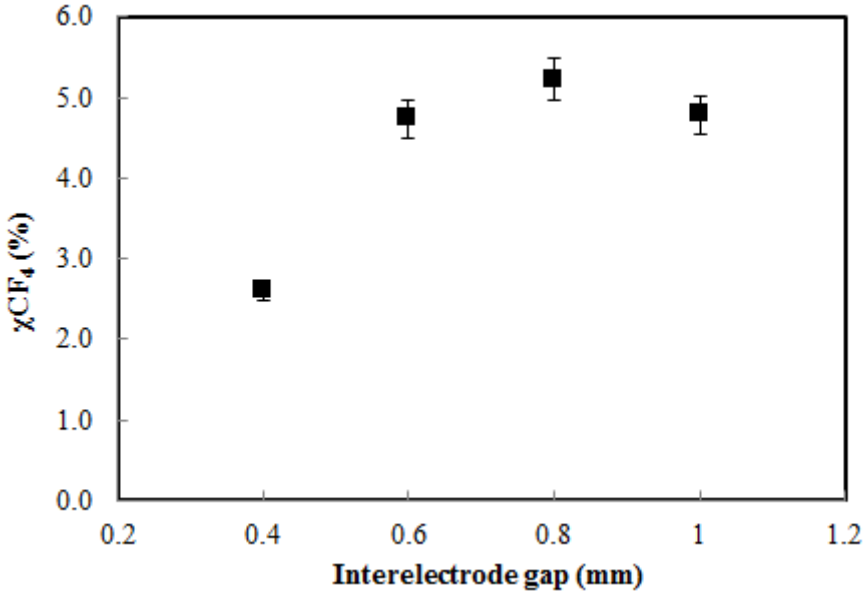

Figure 5.53: Conversion of CF_4 versus interelectrode gap for a CF_4/He ratio of 3:7, a pressure of 1 MPa and a current of 0.35 A

5.6 Theoretical Study of CF_4 Dissociation through Electrical Discharges

Fluorocarbon plasma processes are studied in a wide range of applications from plasma etching to surface modifications. As mentioned in the current review of fluorocarbon modelling, the main categories of CF_4 dissociation into higher fluorocarbons (mainly the C_2 to C_4) is through thermal plasma based processes. Swanepoel and Lombaard [125] have demonstrated the use of thermal plasma in their patent for pressures of 0.001, 0.01, 0.05, and 0.1 MPa respectively. However, the aim of this theoretical study is to demonstrate the thermal dissociation of CF_4 under thermodynamic equilibrium condition at pressures of 0.1, 1 and 10 MPa, and high temperature using T&Twinner software [215]. Furthermore, dissociation of CF_4 by electron impact is also demonstrated within the context of fractional energy losses and the influence of helium on the process under nonequilibrium conditions.

5.6.1 Thermal Dissociation of CF_4

Thermal dissociation of CF_4 was studied using a thermodynamic model for the calculations. The T&Twinner software used for the thermodynamic calculations considers the equilibrium composition calculations and the temperature variations at a fixed pressure. Thus, the equilibrium compositions are evaluated as a function of temperature. This modelling approach assumes the residence or discharge time to be infinite. It is a model based on global minimization of the Gibbs free energy algorithm. The atomic and ionic species considered and the temperature range for which the thermodynamic properties were available in the National Institute of Standards and Technology (NIST) database are presented in Table 5.18.

Table 5.18: List of species with their thermodynamic proprieties considered in the calculations

Species Considered	Nomenclature	Phase	Temperature range (K)
e	electron	Gas	298-100000
C^-	Carbon anion	Gas	298-20000
C_2^-	Dicarbon anion	Gas	298-20000
F^-	Fluorine atom anion	Gas	298-10000
C^+	Carbon cation	Gas	298-30000
CF^+	Fluoromethylidyne cation	Gas	298-3000
CF_2^+	Carbon difluoride cation	Gas	298-3000
CF_3^+	Trifluoromethyl cation	Gas	298-3000
C_2^+	Dicarbon cation	Gas	298-20000
F^+	Fluorine atom cation	Gas	298-20000
He	Helium atom cation	Gas	298-30000
He	Helium dimer cation	Gas	298-30000
C	Carbon	Gas	298-30000
CF	Fluoromethylidyne	Gas	298-2000
CF	Fluoromethylidyne	Gas	298-3000
CF_2	Carbon difluoride	Gas	298-2000
CF_2	Carbon difluoride	Gas	298-3000

Table 5.18 (continued): List of species with their thermodynamic proprieties considered in the calculations

Species Considered	Nomenclature	Phase	Temperature range (K)
CF_3	Trifluoromethyl	Gas	298-3000
CF_3	Trifluoromethyl	Gas	298-6000
CF_4	Tetrafluoromethane	Gas	298-6000
C_2	Bicarbon	Gas	298-20000
C_2F_2	Difluoroethyne	Gas	298-3000
C_2F_4	Perfluoroethylene	Gas	298-3000
C_2F_6	Hexafluoroethane	Gas	298-3000
C_3	Tricarbon	Gas	298-20000
C_3F_6	Hexafluoropropylene	Gas	298-1500
C_3F_8	Octafluoropropane	Gas	298-1500
C_4	Tetracarbon	Gas	298-20000
C_4F_{10}	Decafluorobutane	Gas	298-1500
C_4F_8	Perfluorocyclobutane	Gas	298-1500
C_4F_8	Octafluoro-2-butene	Gas	298-1500
F	Fluorine atom	Gas	298-10000
F_2	Fluorine	Gas	298-10000
He	Helium	Gas	298-30000
C	Graphite	Solid	298-4000

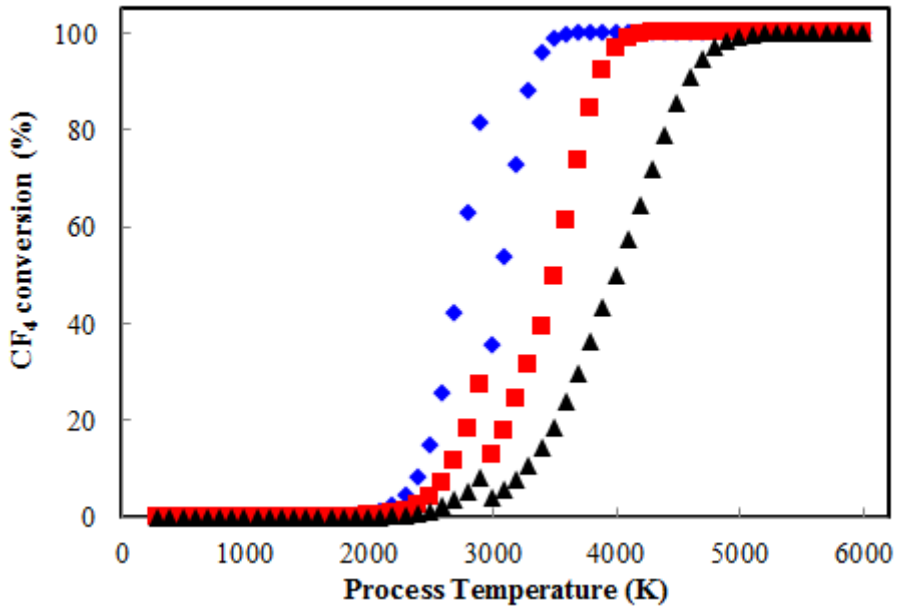

Figure 5.54: Conversion of CF_4 as a function of the temperature via thermodynamic model calculations at three different pressures. ♦ (0.1 MPa); ■ (1.0 MPa); ▲ (10 MPa)

Thermal plasma processes can be employed to dissociate CF_4 into other species at high temperature. From the plot in Figure 5.54, it was observed that the thermal dissociation of CF_4 up to 1% begins at 2100, 2300, and 2500 K for pressures of 0.1, 1.0, and 10 MPa respectively. Thus, high conversions will only be attained at temperatures above 3000 K for high pressure operations above 1 MPa.

Moreover, from Figure 5.54, it can be seen that at a fixed temperature at total pressures of 0.1, 1, and 10 MPa, CF_4 conversion is higher at lower operating pressures than at higher operating pressures. For example, at a pressure of 0.1 MPa, a conversion of 80% can be obtained between 2800 and 2900 K. This same CF_4 conversion of 80% at 1 MPa will be attained between 3700 and 3800 K, while at 10 MPa the conversion only reaches 80% between 4400 and 4500 K. In addition, under these thermal conditions, the main products will be radicals (as seen in Figure 5.55) which can only recombine to the desired molecular products by fast quenching to low temperature.

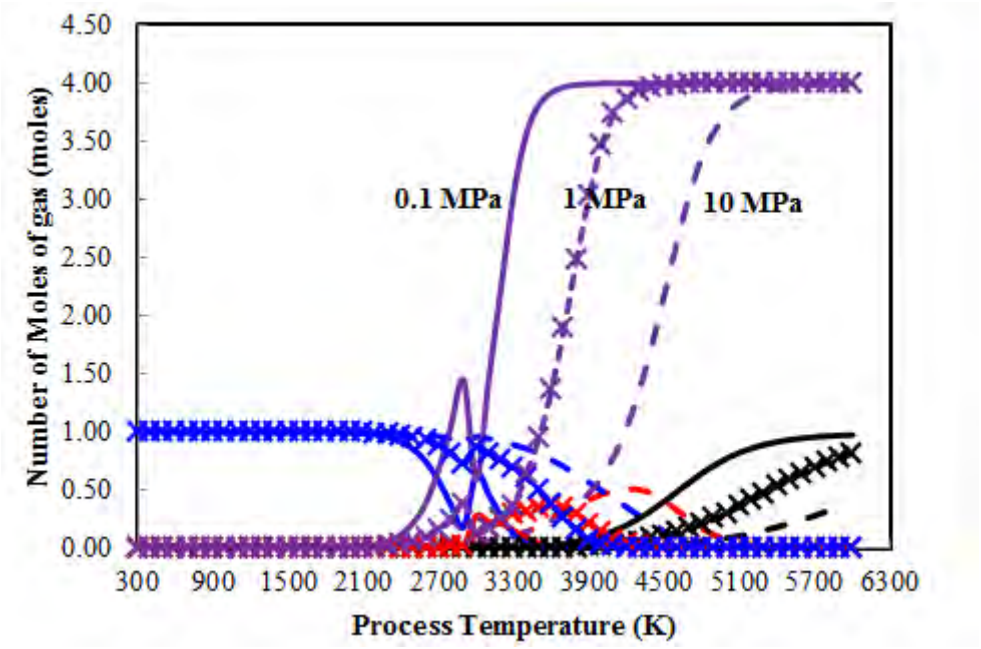

Figure 5.55: Equilibrium molar composition of CF_4 dissociation in thermal plasma as a function of the temperature via thermodynamic model calculations at three different pressures. All solid lines are for pressure of 0.1 MPa ─ (C); (─F); ─ (CF_3); ─ (CF_4), All dotted lines with X are for pressure of 1.0 MPa ─x─ (C); (─x─ F); ─x─ (CF_3); ─x─ (CF_4), All dashed lines are for pressure of 10 MPa - - - - (C); (- - - - F); - - - - (CF_3); - - - -(CF_4)

One of the main limitations of this process based on thermodynamic calculations can be explained in relation to the production of desired species such as C_2F_4, C_2F_6, C_3F_6, and C_3F_8. For example at 0.1 MPa, the production of C_2F_4 under thermodynamic equilibrium starts at 2500 K and stops at 2900 K in low quantity, while C_2F_6 starts at 1700 K and stops at 2900 K. However, the production of C_3F_6, C_3F_8, and C_4F_{10} cannot be accessed under this high temperature conditions due to unavailability of thermodynamic data for the species above 1500 K. This also shows that the energy efficiency of the thermal process would also be low for a high conversion to be obtained for CF_4.

It is interesting to mention that despite the low production of the desired products and the high temperatures required for high conversion of CF_4, Figure 5.56 shows that a high selectivity of approximately 40% can be obtained for C_2F_6 at 10 MPa and temperature of 1800 K, while C_2F_4 is not

produced at that temperature and pressure conditions. Hence, the production of higher fluorocarbons tends to be favoured by high pressure operation. This is in agreement with the experimental results obtained which also shows that C_2F_4 was not produced as the pressure increased. This is shown in Figure 5.57. The plot showing the conversion of CF_4 at different operating pressures and temperature of 2500 K is presented in Figure 5.58. The temperature of 2500 K is the temperature at which C_2F_4 production begins.

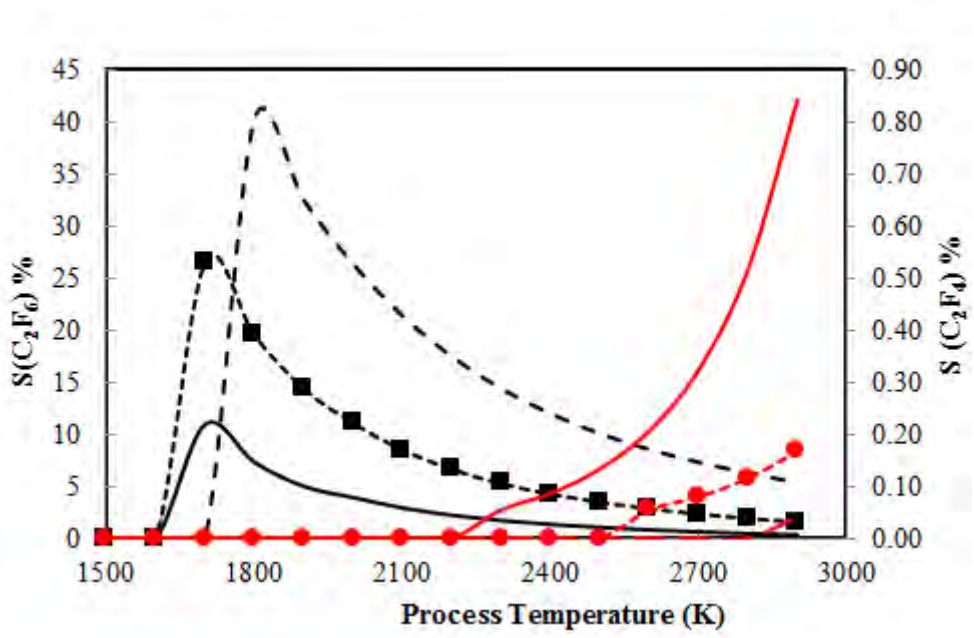

Figure 5.56: Selectivity of desired fluorocarbons produced via thermal dissociation of CF_4 as a function of the temperature at three different pressures. ─ (C_2F_6) at 0.1 MPa; ─ (C_2F_4) at 0.1 MPa; ─■─ (C_2F_6) at 1 MPa; ─●─ (C_2F_4) at 1 MPa; - - - - (C_2F_6) at 10 MPa; - - - - (C_2F_4) at 10 MPa

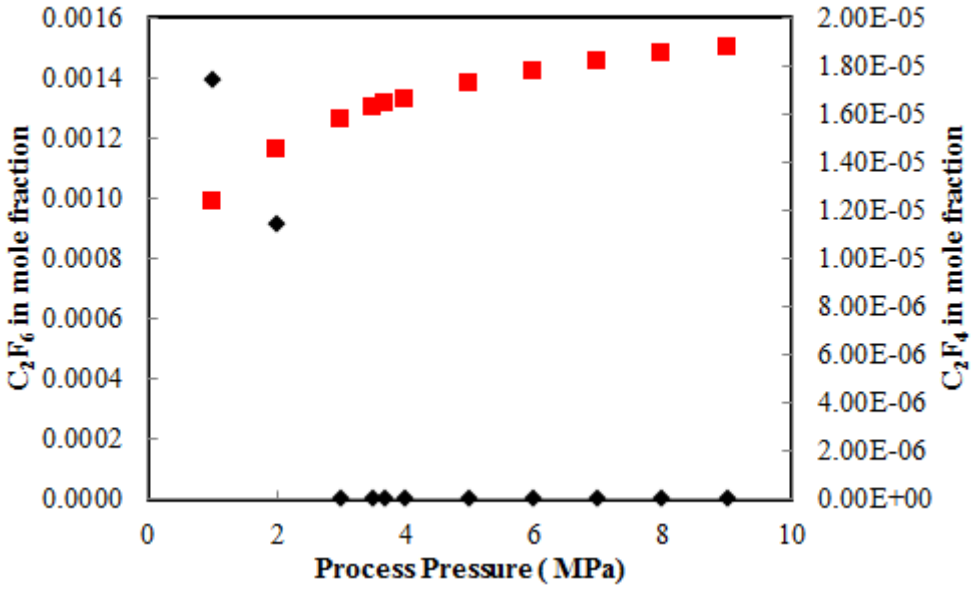

Figure 5.57: Equilibrium molar composition of desired fluorocarbons produced via thermal dissociation of CF_4 at 2500 K at pressures ranging from 1 to 9 MPa. ♦ (C_2F_4); ■ (C_2F_6)

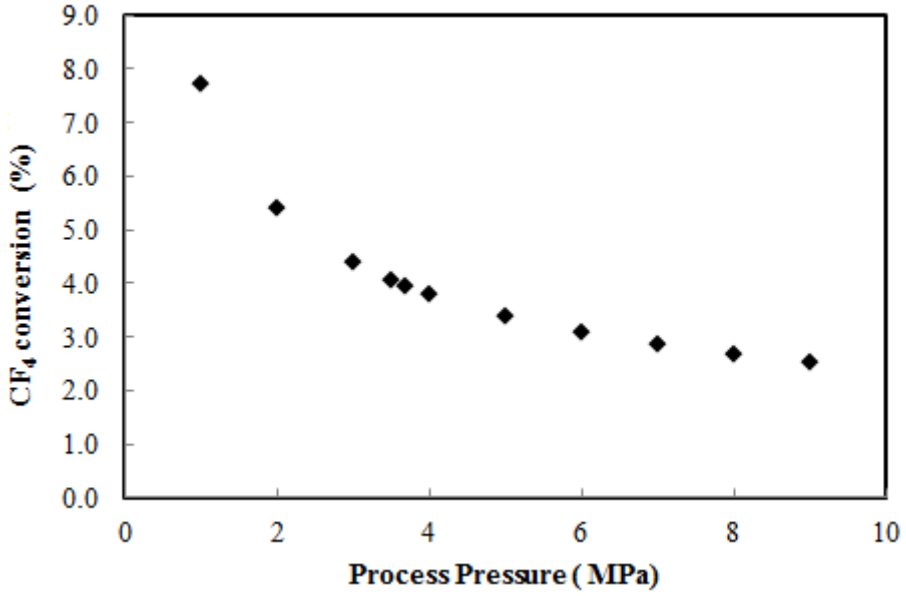

Figure 5.58: Conversion of CF_4 at operating pressures ranging from 1 to 9 MPa via thermal plasma at a temperature of 2500 K

5.6.2 Dissociation of CF_4 in Nonthermal Plasma Conditions

Nonthermal plasma processes provide more mechanisms through which CF_4 dissociation can be effectively carried out with high energy efficiency. Description of this process in plasma modelling requires the collision cross sections and the electron energy distribution function (EEDF) data. Due to difficulties in obtaining these values via experimental measurements, software such as Bolsig+ [204] has been employed to numerically determine the EEDF.

Bolsig+ is a time-dependent two-term Boltzmann equation solver. It uses the electron collision cross-sections of CF_4 taken from literature as input data. The CF_4 data used were published by Nakamura [216]. It can be employed for weakly ionized gases in a low-temperature plasma involving electron collision impact by using the balance between electric acceleration and momentum loss and energy loss in collisions with neutral gas particles to determine the EEDF. Bolsig+ is also used for obtaining other parameters such as diffusion coefficients, mean energy, mobility, energy mobility, energy diffusion coefficients, total collision frequency, rate coefficients as well as energy loss coefficients and fractions. All these calculations can be done as a function of the electron energy or of the reduced electric field strength. Further details on the solution process and capability of Bolsig+ can be found in literature [204].

In Figure 5.59, a plot showing the dissociative rate coefficients (on a logarithmic scale) for CF_4 is presented as a function of the reduced electric field (E/n). From the plot, it can be observed that the dissociation rate coefficients increase as the reduced electric field increases.

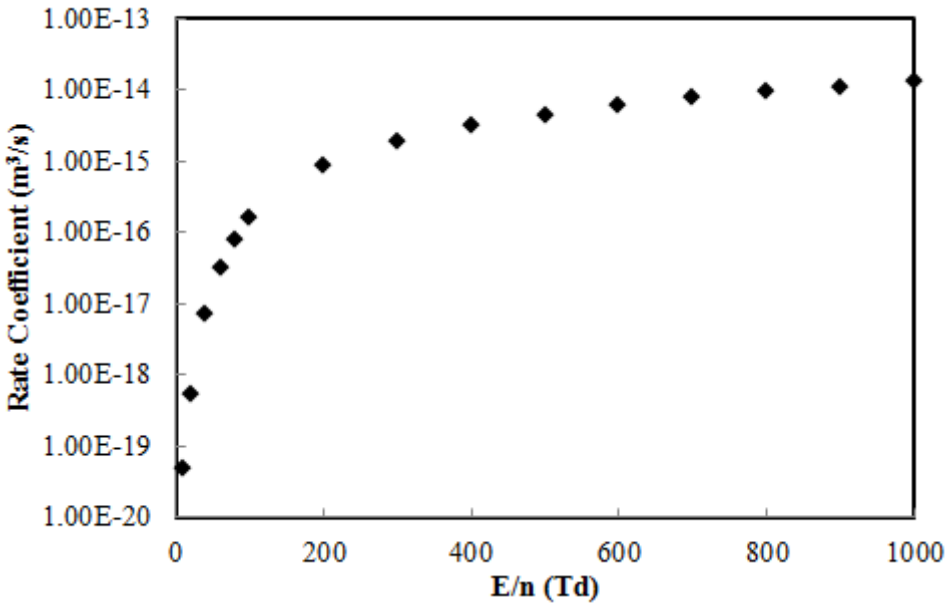

Figure 5.59: Dissociation rate coefficients for CF_4 at gas temperature of 300 K, ionization degree of $1.0x10^{-4}$, and electron density of $1.0x^{18}$ m^{-3}

In the model, under electron-collision processes, the different channels through which CF_4 can be dissociated include vibrational excitation, electronic excitation, dissociative excitation, total ionization, and dissociative attachment. The different channels through which the discharge energy can be transferred from the electron during collision with neutral particles are shown in Figure 5.60.

From Figure 5.60, the efficiency of the different excitation processes can be observed. This plot demonstrates that the dissociation of CF_4 by electron impact is more efficient through electronic excitation if the reduced electric field is in the range of 10 and 100 Td. Hence, an efficiency of up to 88% can be obtained between 20 to 60 Td. This range corresponds to mean electron energies of about 3.485 to 4.861 eV. Furthermore, this indicates that between 83 and 88% of the electron energy can be used for CF_4 dissociation under favourable nonthermal plasma conditions.

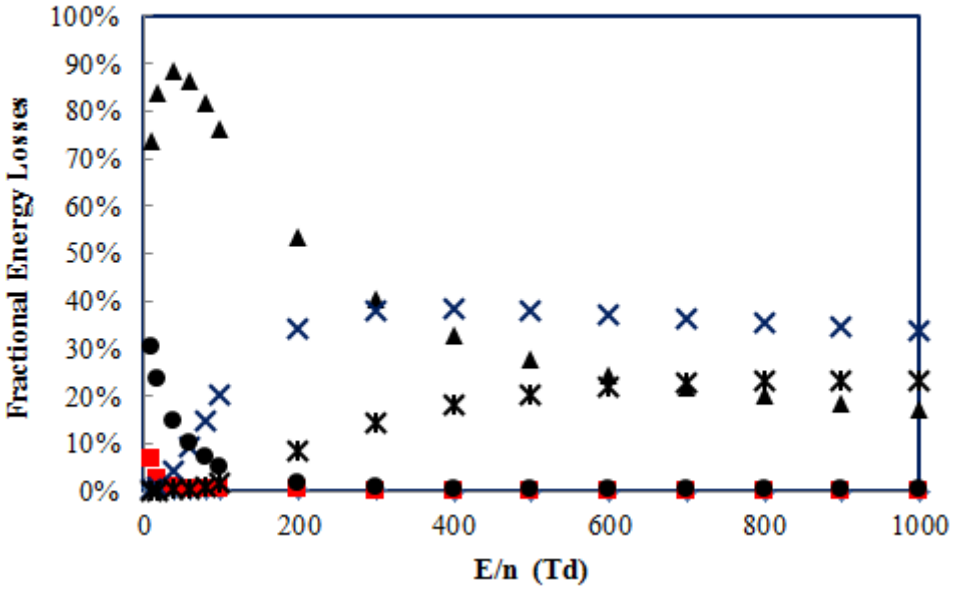

Figure 5.60: Fractions of nonthermal CF_4 discharge energy that is transferred from the plasma during electron impact into different channels of excitation for the effective and efficient dissociation of CF_4 ▲ (Electronic excitation); ■ (Vibrational Excitation); ● (Dissociative attachment); X (Dissociative excitation); ♦ (Elastic); X (Ionization)

5.6.2.1 Dissociation of CF_4 in Plasma by Electronic Excitation of Molecules

As mentioned, based on the observation from Figure 5.60, dissociation of CF_4 was studied for an ionization degree of $1.0x10^{-4}$, gas temperature of 300 K and an electron density of $1.0x10^{18}$ m^{-3}. For the calculation of the rate coefficients for the different energy transfer processes through which CF_4 dissociation can occur, the collision cross section for electron impact is important. In this study, it was observed through the plot of the rate coefficients versus the reduced electric field in Figure 5.61, that the electronic excitation channel depends on the reduced electric field (E/n). Hence, the dissociation of CF_4 through electronic excitation can play a very significant role in nonthermal plasma at high values of reduced electric field at 0.1 MPa. However, the main limitation of this process lies in the high threshold energy of 7.57 eV for CF_4 dissociation through electronic excitation which leads to loss of electron energy at high values of E/n. Nonetheless, the process can be optimized for high energy efficient under the electronic excitation by operating at low E/n values between 20 to 60 Td which correspond to mean electron energy lower than the threshold energy.

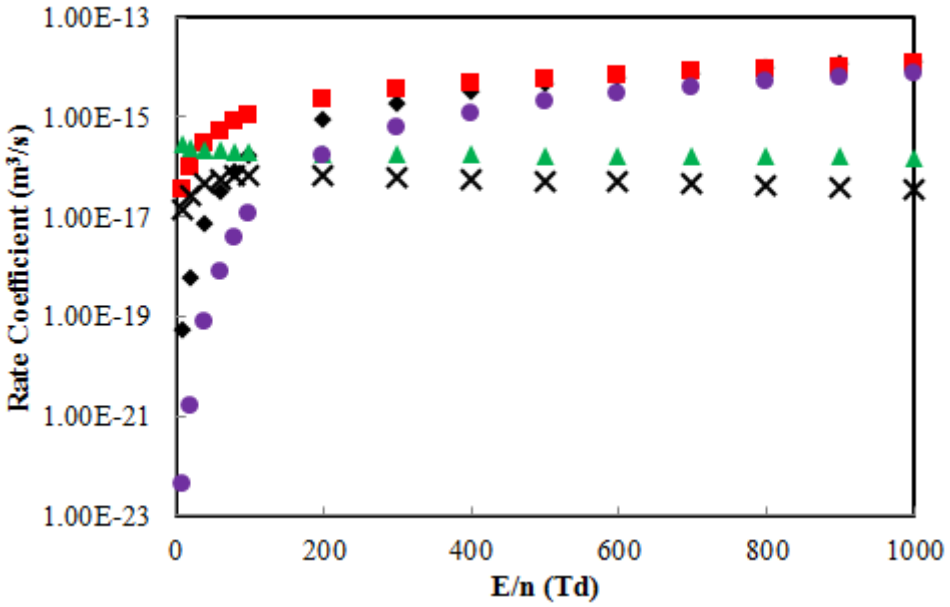

Figure 5.61: Rate coefficients for the electron-impact dissociation of CF_4 via the different channels as a function of the reduced electric field *E*/*n*. (■) Electronic excitation; (♦) Dissociative excitation; (▲) Vibrational excitation; (●) Total ionization; (X) Dissociative attachment

5.6.2.2 Dissociation of CF_4 in Plasma by Dissociative Excitation of Molecules

Dissociative excitation is the process whereby the discharge energy is transferred into the CF_4 molecules and thus leads to its dissociation into CF_2 or CF radicals and other products such as F_2. From Figure 5.60, it can be seen that only about 38% of the electron energy can be used for the CF_4 dissociation process under favourable conditions. This value can only be attained at high E/n values between 300 to 500 Td. Again, this process has a high threshold energy of 12.7 eV and requires a mean electron energy between 8.734 to 11.19 eV in the E/n range. Thus, the efficiency of this process will depend on the electron collision cross section coefficient as well as the EEDF.

$$e + CF_4 \rightarrow e + CF_2 + F_2 \tag{5.36}$$

The limitation in this process lies in its high threshold energy, which means that effective collision can only take place when the electron energy is sufficiently high. This would lead to losses of electron energy in the process and thus lowering of the energy efficiency of the system. Nonetheless, this information is useful in determining the different pathways for CF_4 dissociation by electron impact.

5.6.2.3 Dissociation of CF_4 in Plasma by Dissociative Attachment of Electrons

In the dissociation of CF_4 by electron impact, it is important to investigate the contribution of the dissociative attachment process. The production of ions such as F^-, CF_3^- can also be initiated at this stage.

$$e + CF_4 \rightarrow e + CF_2^- + F_2 \tag{5.37}$$

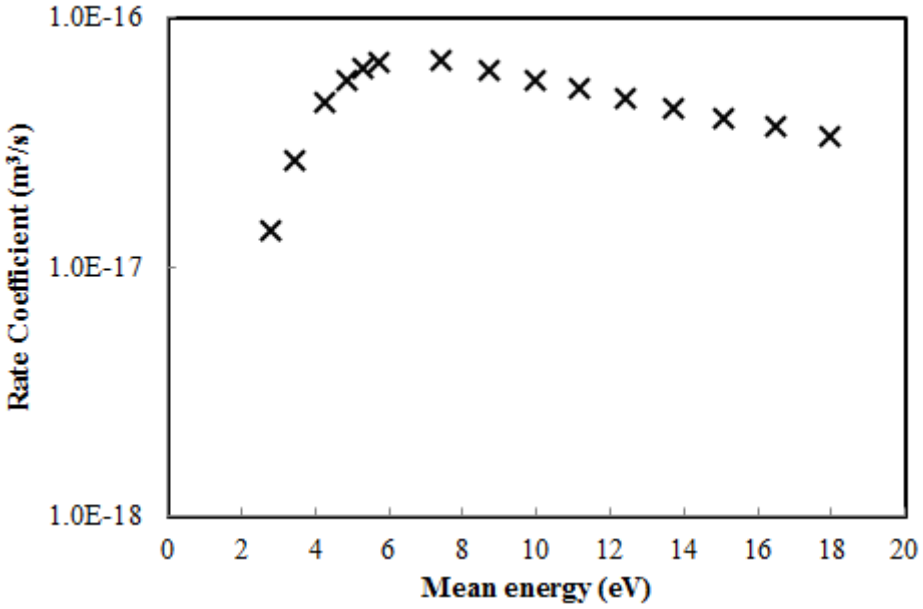

Figure 5.62: Dissociative attachment rate coefficients for the electron-impact dissociation of CF_4 as a function of the mean electron energy

The energy threshold for this process is 6.42 eV with the electron energy lying between 5 to 8 eV which is lower than that of the electronic and dissociative excitation. However, the maximum value of the rate coefficients for dissociative attachment is not high (~ 10^{-17} m^3/s) which implies that it is a slow process and its contribution towards the overall kinetics is not significant. This could also be observed in Figure 5.60 where the energy loss of the process under dissociative attachment is shown to be high.

5.6.2.4 Influence of Helium on the Dissociation Efficiency of CF_4 in Nonthermal Plasma

The influence of helium on the energy efficiency for the dissociation of CF_4 was studied. By comparing Figures 5.63 (A to D), the maximum energy efficiency can be observed.

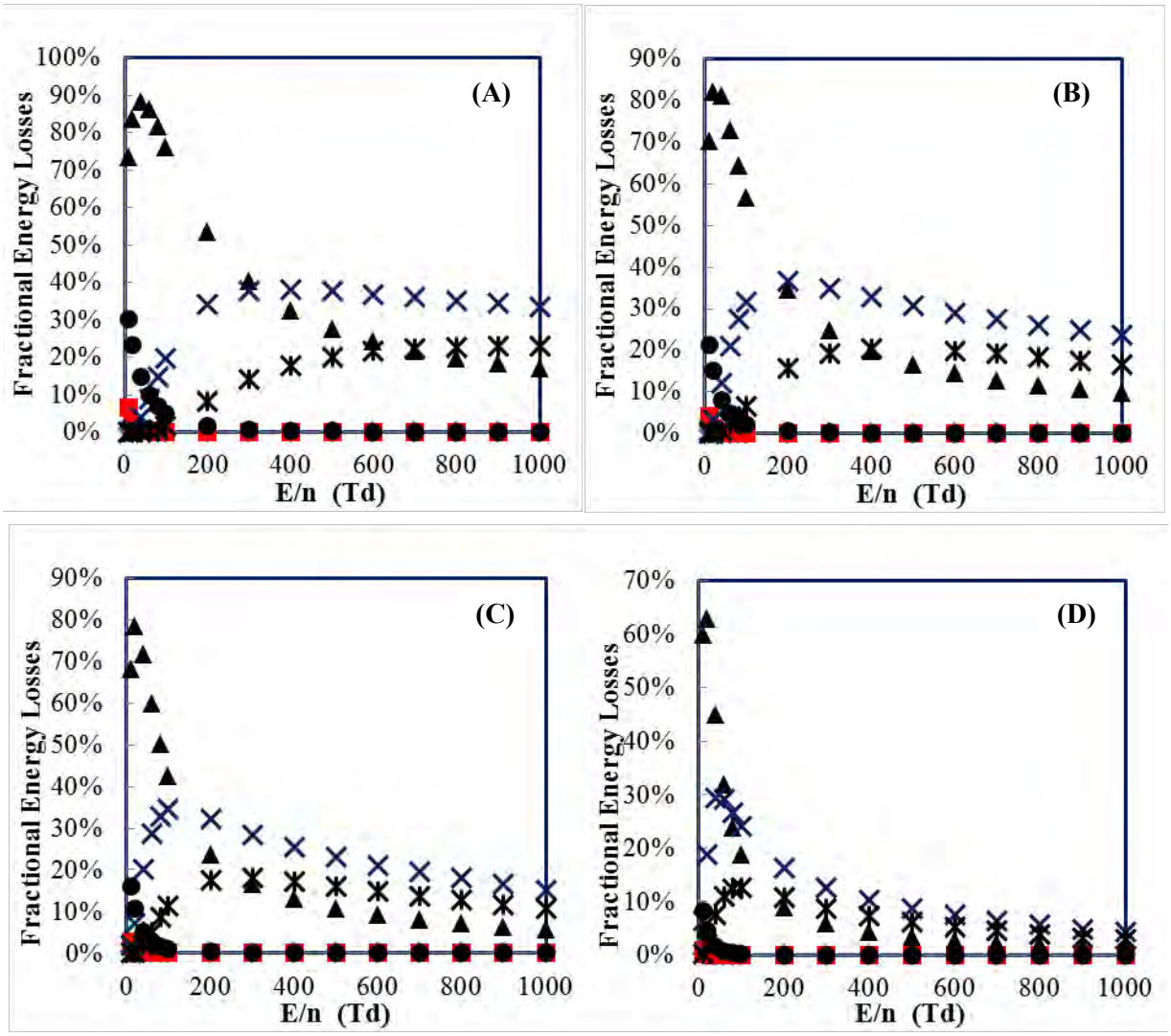

Figure 5.63: Fractions of nonthermal CF_4 discharge energy that is transferred from the plasma during electron impact into different channels of excitation for the dissociation of CF_4. ▲ (Electronic excitation); ■ (Vibrational Excitation);● (Dissociative attachment); X (Dissociative excitation); X (Ionization). (A) CF_4 with mole fraction of 1; (B) CF_4 + He with mole fraction ratio of 0.5:0.5; (C) CF_4 + He with mole fraction ratio of 0.3:0.7; (D) CF_4 + He with mole fraction ratio of 0.1:0.9

Figure 5.63A is a plot of the fractional energy losses in CF_4 with a mole fraction of 1. Under a gas temperature of 300 K, ionization degree of $1.0x10^{-4}$, and electron density of $1.0x10^{18}$ m^{-3}, it was observed that the fractional energy losses which represent the portion of the electron energy that can be used for the dissociation of the molecule, while the remaining energy is converted into heat, can

reach 88%. However, on the addition of an equal molar fraction of helium, the energy efficiency is reduced to 82% at an E/n value of 20 Td. This is an indication that some of the energy from the plasma was transferred into the helium. Although, at this stage the energy transferred into the helium is not sufficient to excite the helium atom. On the addition of CF_4-He mole fraction ratio of 0.3:0.7, the energy efficiency in dissociating the CF_4 was further reduced to ~79% at an E/n value of 20 Td. Contrary to when an equal molar fraction of helium and CF_4 was used, the influence of the discharge energy is beginning to show via electronic excitation of the helium. Finally, on the addition of more helium to change the CF_4-He mole fraction ratio to 0.1:0.9, the maximum energy efficiency that can be obtained for CF_4 dissociation via electronic excitation was reduced to approximately 63%. Thus, at this stage, sufficient discharge energy has been transferred to the helium which leads to the electronic excitation as well as partial ionization of helium.

These results therefore show the effect of using helium as a diluent gas in CF_4 dissociation under nonthermal plasma condition to be contrary to a thermal process.

In conclusion, it can be seen that the nonthermal plasma process of dissociating CF_4 into higher fluorocarbons holds more interesting potential, depending on the energy efficiency of the process. It also has the tendency to improve the selectivity if more control of the input power can be achieved. Moreover, the very high gas temperature required for the dissociation of CF_4 under thermal conditions will generally lead to the formation of unwanted species. Nonetheless, the thermodynamic model provides insight into the influence of high pressure operation on the selectivity and yield of the C_2 and C_3 fluorocarbons. Thus, this study demonstrate that by controlling the input energy which is linked to gas temperature under thermal conditions, pressure is capable of influencing the product distribution in fluorocarbon formation.

5.7 Modelling of Plasma-Assisted Dry Reforming Process

The focus of the dry reforming experiment was to produce syngas and other higher hydrocarbons. In order to better understand the performance of the high pressure plasma reactor, numerical modelling has been employed. In this study, two modelling approaches are used for describing the chemical performance of the reaction process. The two approaches are a thermodynamic model, and a chemical kinetic model.

5.7.1 Thermodynamic Modelling Approach

The dry reforming process is one of the natural gas-to-liquid routes (GTL) usually investigated for synthesis gas production from which synthetic fuels can be further synthesized via the Fischer-Tropsch process. While this route is yet to be commercialized, its utilization of methane (CH_4) and carbon dioxide (CO_2) which are two greenhouse gases is important for the future of green economy. Dry reforming is a hydrocarbon reforming process in which CO_2 plays a role of an oxidant. Thus, it could also be referred to as the oxidative reforming of methane using CO_2. However, this is not the only oxidative reforming route for methane as there are also partial oxidation processes using oxygen (O_2) and methane steam reforming using water (H_2O).

The global balance equation for the dry reforming process is represented below in reaction equation (1):

1. $CH_4 + CO_2 \rightarrow 2CO + 2H_2$ $\Delta H^{O}_{298\ K} = +246.9\ kJ.mol^{-1}$

Reactions (2) and (3) commonly referred to as the oxidative coupling of methane with carbon dioxide is another possible reaction that could be considered in dry reforming;

2. $2CH_4 + CO_2 \rightarrow C_2H_6 + CO + H_2O$ $\Delta H^{O}_{298\ K} = +106\ kJ.mol^{-1}$
3. $2CH_4 + 2CO_2 \rightarrow C_2H_4 + 2CO + 2H_2O$ $\Delta H^{O}_{298\ K} = +284\ kJ.mol^{-1}$

The thermodynamic calculations are taken as a preliminary modeling approach for understanding the chemical reaction performance of the process under thermal equilibrium conditions. For the thermodynamic calculations, the T&Twinner software [215] was utilised. The calculation approach used by the software is based on global minimization of the Gibbs free energy algorithm.

From the thermodynamic calculations, it was observed that the main species between temperatures of 300 and 5000 K were H, H_2, H_2O, CO, and solid carbon at pressures of 0.5, 1, 4 and 7.8 MPa. Low amounts of C_2H_2, C_2H_4, and C_2H_6 were predicted at temperatures between 1500 to 5000 K, 1200 to

4000 K, and 700 to 1100 K respectively. The predicted species are in line with those obtained from GC analysis after the arc discharge process. Therefore, to analyze the chemical reaction performance in terms of conversion, a conversion temperature was defined arbitrarily as the temperature at which about 99% of the maximum number of moles of syngas (H_2 and CO) has been attained. Thus, 2000 K was taken as the temperature under which the reaction was studied and compared with the experimental results in terms of conversion of the reactant, product selectivity, and yield. While this model shows a trend similar to that obtained in the experiment, the prediction in terms of performance was much higher in value compared to those obtained in the experiment. Therefore, the results clearly indicate that the model is far from the reality, and inaccurate in describing the chemical behavior and performance of the experimental study.

5.7.2 Chemical Kinetic Modelling Approach

Kinetic models are useful tools in understanding chemical reaction processes going on inside a reactor. Kinetic models can be represented in the form of global reaction mechanisms that are reduced or it can be in a more detailed form showing the reaction rate constant for every elementary reaction steps available. As mentioned under the review section for plasma modeling of hydrocarbon processes, chemical reaction mechanisms available in literature are usually validated for certain temperature and pressure ranges. For this study, three commonly reaction mechanism that have been developed for methane oxidation were used. The experimental work was studied at the operating pressures of 0.5, 1, 4 and 7.8 MPa.

The Leeds methane oxidation mechanism version 1.5 [209] used are valid in temperatures ranging between 500 and 2000 K. This mechanism consists of 175 elementary reactions of 37 species. The detailed mechanisms are presented in Table F.2 in Appendix F. The GRI-Mech version 3.0 [207] is another commonly used mechanism for the oxidation of methane. This mechanism consists of 325 elementary reactions for 53 considered species. The condition under which this mechanism is valid is within a temperature range of 1000 to 2000 K and sub-atmospheric pressure up to 1 MPa for premixed systems with an equivalence ratio between 0.1 and 5. The third mechanism used in this study for the oxidative reforming of methane was developed by Konnov [208]. It consists of 1207 elementary reactions for 127 considered species. The temperature validity range of this mechanism is 950 to 2700 K, while the valid pressure ranges from subatmospheric up to 8.8 MPa. A list of the reaction mechanisms are presented in Table F.6 in Appendix F. Finally, in order to take into account the effect of ionized species, a reaction mechanism developed by Pedersen and Brown [217] for simulating the effect of electric field in a premixed methane flame was used. The mechanism developed by Pedersen and Brown [217] consists of 86 reactions for 31 species out of which five are positive ions, one for excited species, and electrons. The use of these four different mechanisms

allows the model results to be compared with the experimental results. In addition, the use of different kinetic models helps us to observe the model results closest to the experimental data.

To simulate this process, a two-stage reactor approach was employed. This approach entails considering the arc discharge zone; this is the zone between the fixed and the mobile electrodes. From experimental observations and energy estimations, the electric arc initiates the reactions by heating the gas in the discharge volume and thus results in the production of more active species such as radicals, electrons, excited species, atomic species, and molecules. During this process, there is limited heat and mass transfer to the surroundings i.e. global heating of the bulk gas. This assumption was made by considering that the volume of the discharge for an interelectrode gap of 0.4 mm (3.217×10^{-5} cm^3) is approximately 1.25×10^5 times smaller than reactor volume of 2.56 cm^3. This is approximately 0.00125% of the total reactor volume. Furthermore, it was considered that there is an instantaneous mixing between the hot plasma zone and the cold gas after the discharge is extinguished, in which recombination occurs and some of the unstable radicals and other species generated within the arc zone forms new molecules or products.

Therefore, to perform kinetic modelling, it is assumed that the products from the plasma-assisted oxidative reforming of methane are primarily a result of gas phase reactions. The elementary reactions used involve radical production. Thus, the model can be termed a homogenous 0-D model for a closed adiabatic system at constant pressure. This approach is expected to give useful information relating to the discharge chemistry.

The following assumptions were made for the implementation of the model:
(1) Only a fraction of the reactants actually passes through the arc discharge, with the remaining fraction being deviated from the arc zone;
(2) Radicals are produced within the arc zone;
(3) Radicals once produced are uniformly distributed within the whole volume after discharge i.e. a zero-dimensional model;
(4) Chemistry of the process depends mainly on the behaviour of the radicals formed during discharge;
(5) There is no mass transfer between the arc zone and the bulk gas fraction in the reactor during discharge;
(6) Thermal decomposition at the conditions of the experiment for the bulk gas (T = 298 to 308K) is negligible.

The chemical kinetics occurring in the arc discharge zone was modelled based on the discharge volume, the input power, the residence time, gas pressure, and initial gas temperature as available in the perfectly stirred reactor (PSR). The outlet gases are then considered to be perfectly and

instantaneously mix after discharge in a closed batch reactor. The model was implemented in FORTRAN code using PSR and SENKIN (a 0-D homogeneous gas-phase chemical kinetic model for closed system) modules of the CHEMKIN II package [218]. A schematic diagram of the kinetic modelling approach is presented in Figure 5.64.

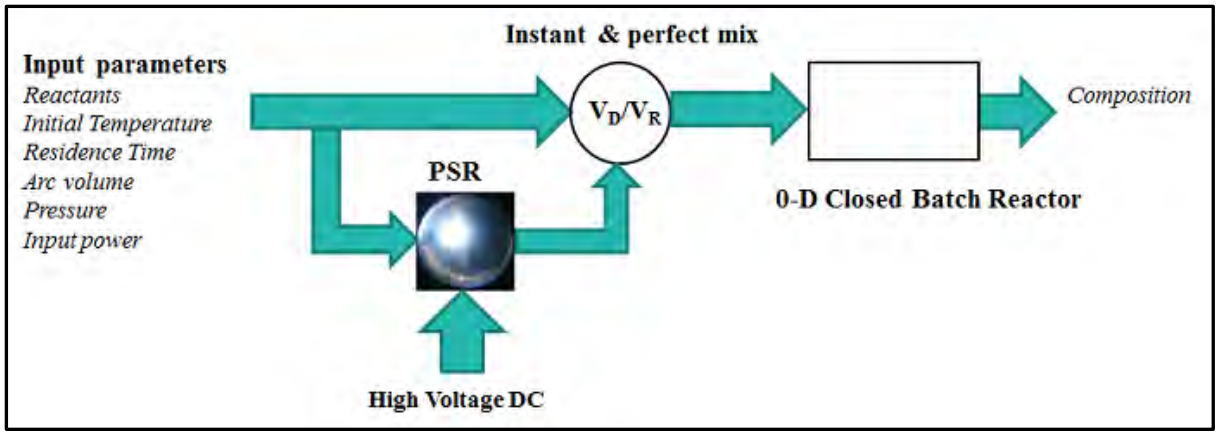

Figure 5.64: Schematic diagram of the two-stage kinetic model describing the low current plasma-assisted dry reforming process at high pressure

5.7.3 Comparison of Modelling Results with Experimental Results

A comparison of the models with the experimental data was done based on the reaction performance of the high pressure plasma reactor.The input power was not kept constant for the kinetic model as it is observed from Figure 5.65 that the input power changes with the operating pressure for a fixed current and discharge volume under experimental conditions.

Three indicators used in measuring the performance of the reactor are the conversion for CH_4 and CO_2; the product selectivity for syngas (H_2 and CO); and the product yield for H_2. These performance indicators were calculated using equations 5.20 to 5.23, and 5.26. The plots are presented in Figures 5.66 to 5.70.

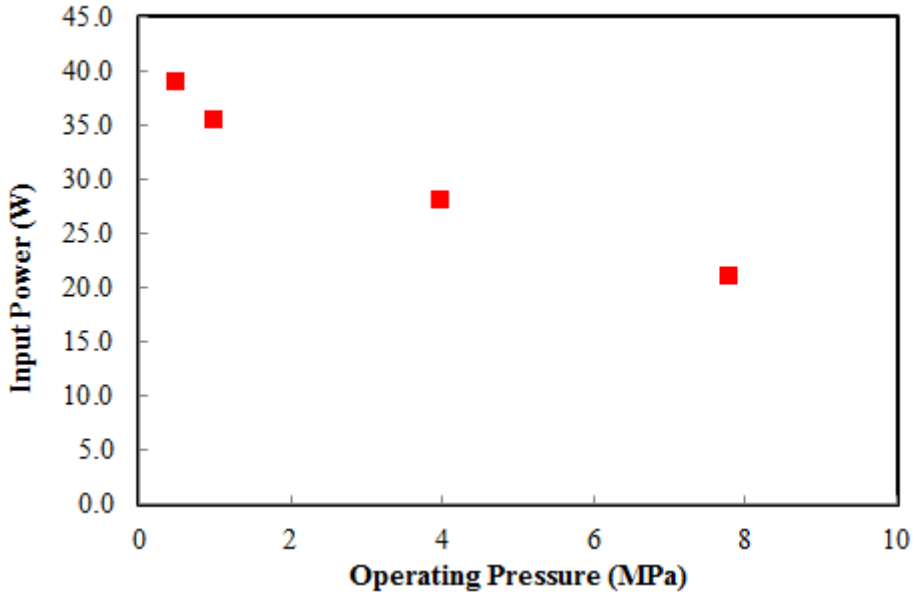

Figure 5.65: Input power versus operating pressure for the dry reforming process with a CH_4/CO_2 ratio of 1.8, a current of 0.35 A, an interelectrode gap of 0.4 mm, and a discharge time of 60 s

The conversion for CH_4 and CO_2 were observed to be much higher in the thermodynamic model than in the experimental measurements or kinetic model. This may be due to the residence time, which is infinite for the thermodynamic model. Another possible reason might be the power loss from the reactor which was accounted for by the kinetic model but not taken into account for the thermodynamic model.

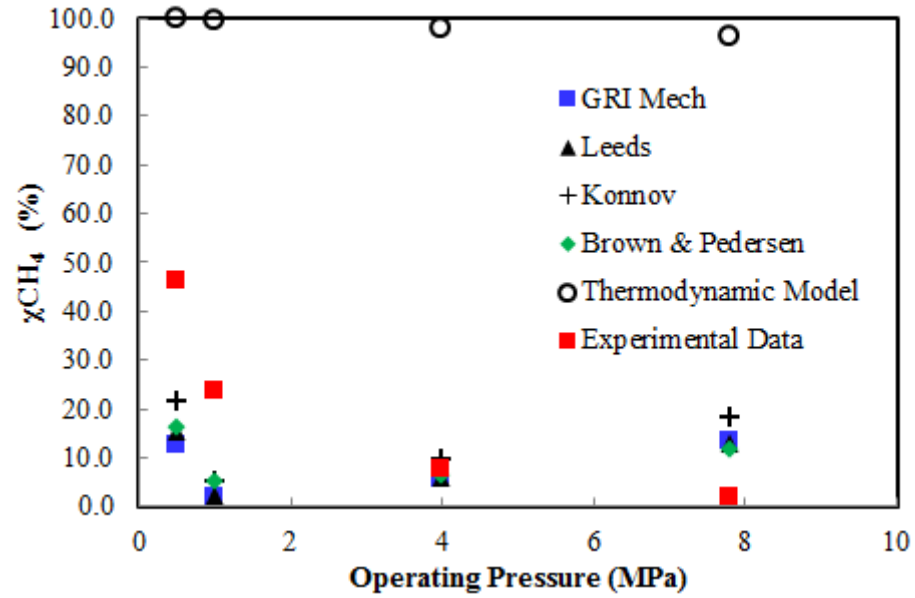

Figure 5.66: Conversion for CH_4 in the dry reforming process: kinetic model, thermodynamic model, and experimental results as a function of operating pressure

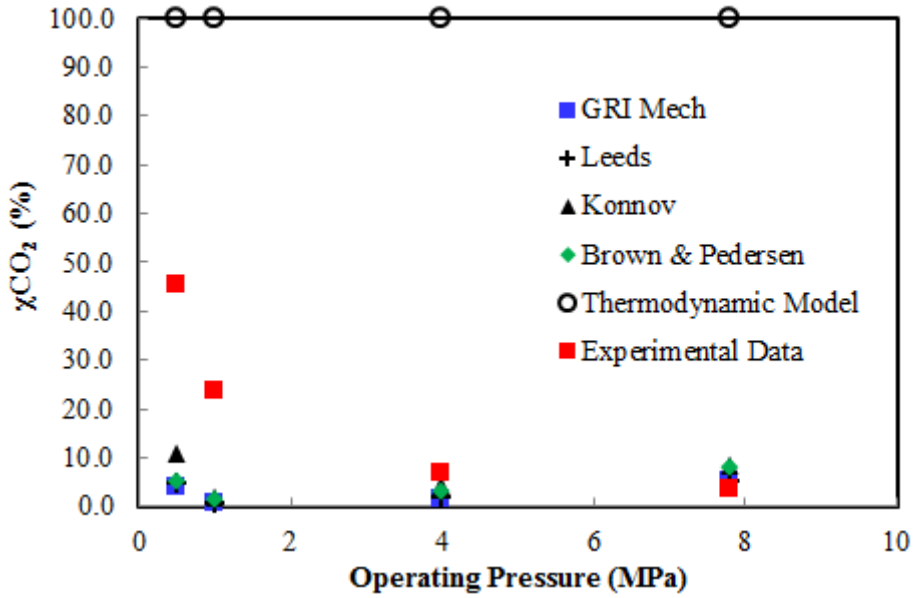

Figure 5.67: Conversion for CO_2 in the dry reforming process: kinetic model, thermodynamic model, and experimental results as a function of operating pressure

From Figures 5.66 and 5.67, the conversion of CH_4 and CO_2 were observed to decrease as the operating pressure increases. This trend which was observed experimentally is similarly observed from the thermodynamic model. However, all four mechanisms used for the kinetic model show that the conversion for CH_4 and CO_2 decreases between 0.5 and 1 MPa, but increase afterward between 4 and 7.8 MPa. Further calculations of the product selectivity for H_2 and CO as presented in Figures 5.68 and 5.69 show agreement between all chemical reaction mechanisms used for the kinetic model.

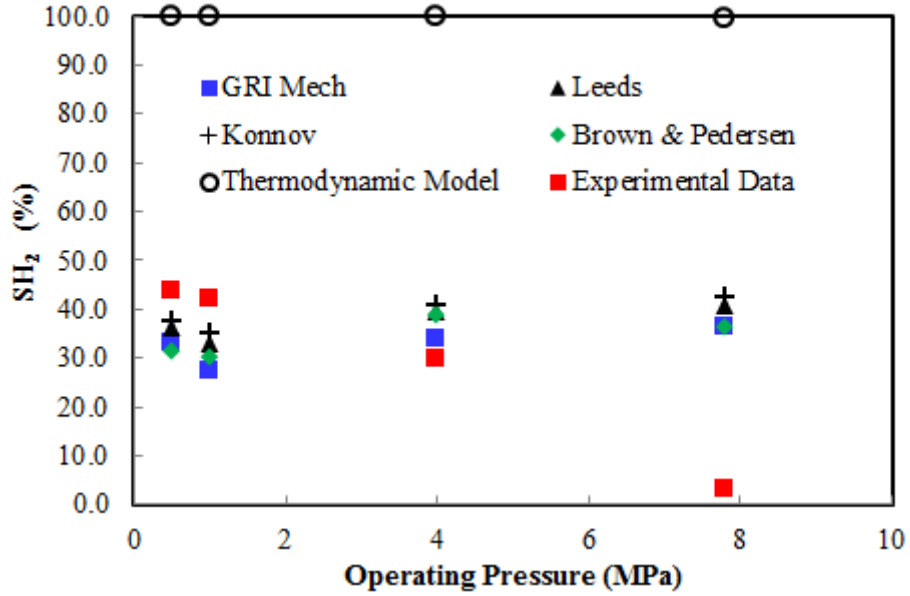

Figure 5.68: Product selectivity for H_2 in the dry reforming process: kinetic model, thermodynamic model, and experimental results as a function of operating pressure

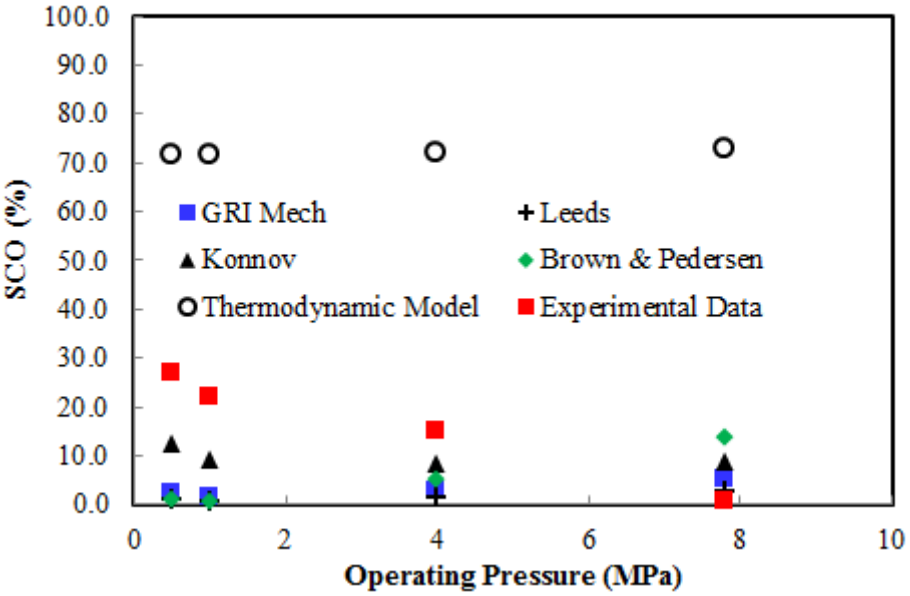

Figure 5.69: Product selectivity for CO in the dry reforming process: kinetic model, thermodynamic model, and experimental results as a function of operating pressure

From the thermodynamic calculations, the energy efficiency was observed to increase slightly with pressure. In accordance with Le Chatelier's principle, the gas mixture is inclined to shift its equilibrium position to counteract the effects of pressure. Thus, the increase in pressure is balanced by an increase in the number of moles. Therefore, the forward reaction is promoted with respect to the

reverse reaction leading to an increase in the energy efficiency. This is also supported by a decrease in the enthalpy of the reaction as the process pressure increases under thermodynamic calculations.On the other hand, from kinetic analysis, an increase in pressure will promote the kinetics of the reaction for a specified volume and residence time since the mass flow rate of the gas is increased along with the mass density.

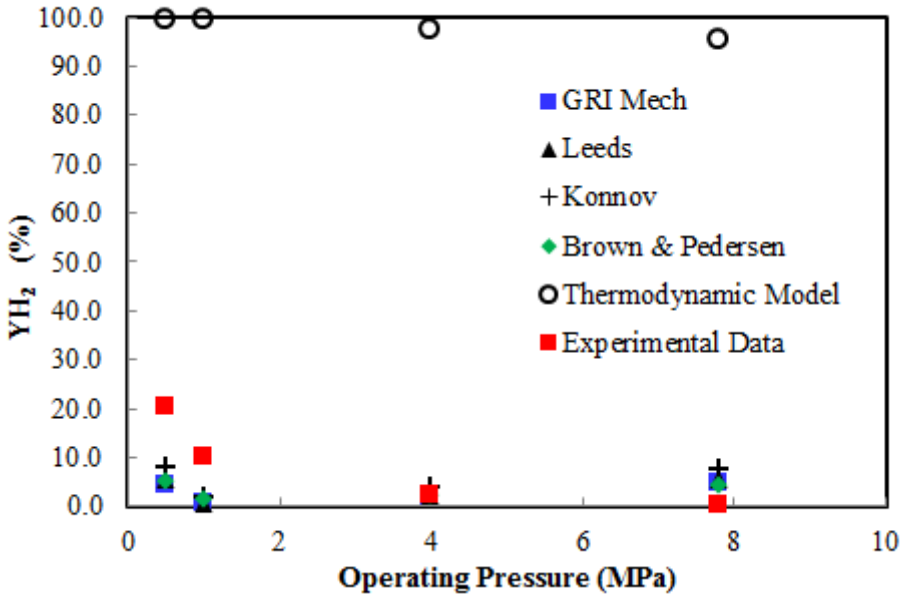

Figure 5.70: Yield of H_2 in the dry reforming process: kinetic model, thermodynamic model, and experimental results as a function of operating pressure

Comparison with experimental data indicates that the thermodynamic model overestimates the performance of the electric arc discharge reactor. The results obtained from the kinetic model are closer to the experimental results. The results from the kinetic analysis are more reliable considering that input parameters such as the volume of the discharge, residence time, and discharge power loss from the reactor were taken into account. Therefore, it could be said that the discrepancy observed between the kinetic model and the experimental data especially at pressures between 0.5 and 1 MPa probably imply that there are large heat losses at these pressures which shows higher input power and hence, higher reactor temperature. Another explanation might be linked to the fact that the chemical mechanisms used were specifically developed for the case of methane oxidation such as partial oxidation where O_2 is a reactant and therefore has some important but unconsidered chemical reactions for CO_2 conversion. This could be the reason for the low CO_2 conversion.

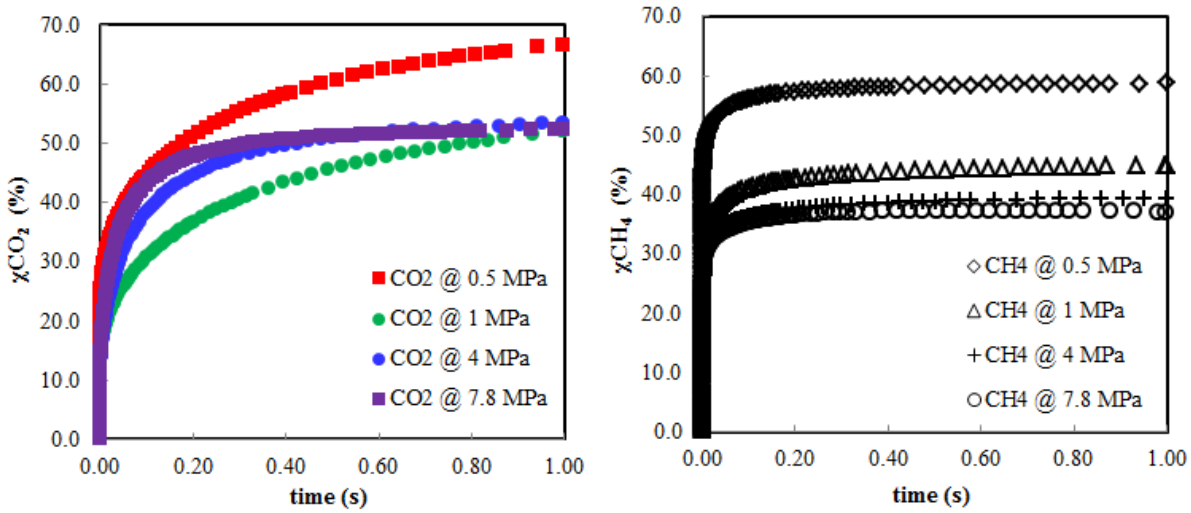

Figure 5.71: Conversion of CH_4 and CO_2 versus the time of methane reforming using the Gas Research Institute Methane Oxidation Mechanism 3.0 at process pressures of 0.5, 1.0, 4.0, and 7.8 MPa

5.7.4 Conclusions on the Thermodynamic and Kinetic Modelling Results

Electric arc discharges at low current and high pressure consist of different active species such as radicals, ions (positive and negative), electron, excited species, atomic, and molecular species which makes its behaviour far from thermodynamic equilibrium. Thus, the modelling of an arc discharge assisted dry reforming process is a complex phenomenon.

In this work, a systematic model was used for describing the chemical reaction performance of the nonthermal plasma reactor for dry reforming at high pressure. The model made it possible to use input parameters such as discharge power, residence time, inlet gas temperature, as well as pressure in order to analyse the performance of the plasma-assisted dry reforming process with respect to CH_4 and CO_2 conversion, selectivity to syngas production (H_2 and CO), as well as yield of H_2 and CO.

Overall, the kinetic model with the different methane oxidation mechanisms shows good agreement with the experimental results. While thermodynamic calculations indicate a high conversion for CH_4 and CO_2 at the pressures studied, kinetics analysis performed using the code SENKIN from the CHEMKIN-II package and the GRI-Mech 3.0 scheme reveals that the conversion of CH_4 and CO_2 is strongly dependent on the residence time.

Chapter 6

LOW CURRENT MHD MODELLING OF A HIGH PRESSURE BATCH REACTOR WITH HELIUM

Numerical modelling is essential for a better understanding of all plasma-assisted processes. As mentioned in Chapter 3, Petitpas et al. [132] in their review mentioned modelling approaches that have been reported by different research groups around the world for plasma-assisted reforming. Two common approaches for plasma modelling involve using a computational fluid dynamics model (CFD) and a gas phase kinetic model. In this chapter, a magnetohydrodynamics model using the code_saturne open source code was employed. The magnetohydrodynamics model considers the plasma as a single hydrodynamic fluid while taking into account the effects of Lorentz forces, as well as the Maxwell equations for the electromagnetic fields.

Literature review shows that most of the works relating to MHD arc modelling have been focused on sub-atmospheric pressure and atmospheric conditions at high current (≥ 1 A) [219-220] because of the lack of data and existing applications at very high pressure. Besides Lebouvier et al. [179, 221], there are no reports of the successful three dimensional MHD modelling under low-current (< 1 A), high voltage conditions at atmospheric pressure. Hence, this mathematical model is based on the 3D MHD model developed by Lebouvier et al. [179, 221] for a low-current, high voltage non-transfer flow plasma torch with air and has been modified to work at very high pressure in a batch reactor using nonreactive helium. The results from this MHD modelling have recently been published [222].

6.1 Mathematical Model

A three dimensional thermal arc model was developed based on the open source CFD software Code_saturne. In the generation of an electric arc discharge, a magnetic field is induced within the interelectrode gap as the electric current passes between the electrodes. As the magnetic flux density of the magnetic field interacts with the current density, Lorentz forces are produced. This force is of great importance in the momentum equations governing plasma behaviour in the arc zone. The direction of this force is highly dependent on the electrode configuration in the reactor chamber. In addition, as the interelectrode gap increases between the cathode and the anode, the intensity of the electromagnetic force decreases. A pressure gradient can be created in the arc column depending on

the variation in the strength of the Lorentz force.This results in a high-velocity plasma being directed from the cathode towards the anode surface.

Coupling reaction kinetics with 3D MHD model is currently impractical due to the huge computational time required and the lack of kinetic mechanisms for plasma application. Another challenge with high pressure plasma modelling is the unavailability of transport coefficients and thermodynamic properties of gas molecules at very high pressure and temperature up to 20000 K. Thus, since helium is a nonreactivegas which is stable at very high pressure and temperature due to its high ionization energy, data are available for very high pressure conditions. Electrical characterization of the plasma reactor was studied between a working pressure of 1 to 8 MPa and compared with the results from the MHD simulation.

In the next subsections, a detailed description of the assumptions, governing equations, boundary conditions and parameters of the model at very high pressure will be presented using a case of the generated arc discharge at a pressure of 8 MPa and a current of 0.35 A.The simulation results are then compared with the experimental data.

6.1.1 Assumptions

The low current arc discharges are usually nonequilibrium in nature considering the high difference in electron temperature and bulk gas temperature. However, the use of a model that assumes LTE, which is appropriate for high power density plasmas has been employed in order to overcome numerical issues associated with the low current and very high pressure modelling. Moreover, at the time of this write-up, the work of Lebouvier et al. [179, 221] were the only literature available on three-dimensional MHD time-dependent problem involving low-current arc discharge at atmospheric pressure. Both works relate to the use of a dc plasma torch in a flow configuration. Thus, it is considered that the LTE is sufficient for preliminary understanding of plasma behaviour at very high pressure and low current.

Therefore, the three-dimensional MHD modelling was implemented based on the following assumptions:

- The plasma is a Newtonian fluid and considered as a single continuous fluid (helium).
- The plasma column is considered to be at Local Thermodynamic Equilibrium (LTE). This means that the electron temperature is equal to the heavy particles temperature in the arc column

- The gas is treated as mechanically incompressible, but thermally expandable. Thus, thermodynamic properties and transport coefficients of the gas depend only on the temperature, the pressure effects are neglected.
- Gravitational effects are taken into account in the –x direction.
- The fluid domain simulates a batch adiabatic reactor.

6.1.2 Governing Equations

The modelling of the arc column can be defined by the Navier–Stokes (conservation of mass, momentum, and energy) set of equations and Maxwell electromagnetic equations for fluid dynamics. The conservation of mass equation is given by:

$$\frac{\partial \rho}{\partial t} + \vec{\nabla} \cdot (\rho \vec{v}) = 0 \tag{6.1}$$

where $\vec{v}$ is the velocity vector of the flow, ρ is the mass density and its temperature dependent.
For the conservation of momentum equation;

$$\frac{\partial \rho h}{\partial t} + \vec{\nabla} \cdot \rho h \, \vec{v} - \vec{\nabla} \cdot \frac{\lambda}{C_p} \vec{\nabla} h = \vec{J} \cdot \vec{E} - S_{rad} \tag{6.2}$$

where h, λ,C_p, $\vec{J}$, $\vec{E}$,S_{rad} are the gas enthalpy, thermal conductivity, the specific heat, the current density vector , the electric field and the radiation losses respectively.
The energy transport with the arc column is represented by the enthalpy conservation equation as:

$$\frac{\partial \rho \vec{v}}{\partial t} + \vec{\nabla} \cdot (\rho \vec{v} \otimes \vec{v}) = -\vec{\nabla} p + \vec{\nabla} \cdot \vec{\tau} + \vec{J} \times \vec{B} + \rho \vec{g} \tag{6.3}$$

where $\vec{\tau}$, $\vec{B}$, and $\vec{g}$ are the shear stress tensor, the magnetic field vector and the gravity acceleration respectively.

The Lorenz force acting on the flow is represented as:

$$\vec{F}_L = \vec{J} \times \vec{B} \tag{6.4}$$

From equation (6.2), $\vec{J} \cdot \vec{\mathrm{E}}$ represent the Joule heating, the radiation losses (S_{rad}) is further expressed by the equation:

$$S_{rad} = 4\pi\varepsilon_{\mathrm{N}} \tag{6.5}$$

where ε_{N} is the net emission coefficient.
In considering the electromagnetic phenomena occurring within the arc zone, the Maxwell's equations are employed. These Maxwell's equations (consisting of Faraday's law, Ampere's law, and Gauss' electric and magnetic laws) can be presented in a simplified form following assumptions such as; electro-neutrality for each volume element in the mesh cell on a macroscopic scale; quasi-steady state,

which considers the convection current to be negligible in comparison to the conduction current. The former assumption leads to a reduced form of Gauss's electric law, while the latter assumption results in a reduced form of the Ampere's law. Hence, the reduced forms of the electromagnetic equations are presented in sets of equations below.

The reduced form of Gauss' electric law is given as:

$$\vec{\nabla} \cdot \vec{E} = 0 \tag{6.6}$$

Gauss' magnetic law:

$$\vec{\nabla} \cdot \vec{\mathrm{B}} = 0 \tag{6.7}$$

$$\vec{\nabla} \cdot \vec{J} = 0 \tag{6.8}$$

Faraday's law:

$$\vec{\nabla} \times \vec{E} = 0 \tag{6.9}$$

Ampere's law:

$$\vec{\nabla} \times \vec{B} = \mu_0 \vec{J} \tag{6.9}$$

Ohm's law:

$$\vec{J} = \sigma \vec{E} \tag{6.10}$$

where μ_0 is the vacuum permeability. The scalar electric potential (φ) and the vector potential $(\vec{\mathrm{A}})$ can be derived by the combination of equations (6.6) to (6.10) above. Thus, the scalar electric potential is given by equation (6.11):

$$\vec{E} = -\vec{\nabla}\varphi \tag{6.11}$$

With the Gauss' magnetic law relating the magnetic field (B) to the vector potential by (6.12),

$$\vec{B} = \vec{\nabla} \times \vec{\mathrm{A}} \tag{6.12}$$

The Maxwell's equations relating the two potentials $(\varphi \text{ and } \vec{\mathrm{A}})$ are presented in reduced form:

$$-\vec{\nabla} \cdot (\sigma \vec{\nabla}\varphi) = 0 \tag{6.13}$$

$$-\vec{\nabla} \cdot (\vec{\nabla}\vec{A}) = \mu_0 \vec{\mathrm{J}} \tag{6.14}$$

The CFD software *Code_Saturne*® V2.2.1 is used to solve the coupled Navier-Stokes and Maxwell's set of equations by employing the SIMPLEC algorithm to obtain a fully implicit solution.

6.1.3 Transport Coefficients and Thermodynamic Properties

In fluid dynamic simulations of plasma, the accuracy of results of the mass, momentum, and energy equations solved, in conjunction with the electromagnetic field equations strongly depend on the transport coefficients and thermodynamic properties used. While transport coefficients and thermodynamic properties are readily available at 0.1 MPa and temperatures up to 2,000 K, data above 1 MPa and at very high temperatures up to 20,000 K are hardly available in published literature. The high temperature conditions are common in the arc discharge fluid modelling approach, while the high-pressure operation of the reactor used in this study necessitates the need for data up to 10 MPa. To this effect, T&TWinner software [215] was used to calculate and generate all the transport and thermodynamic properties for helium with the exception of the net emission coefficient, which is not available in the software calculation module and only available in literature at 0.1 MPa. T&TWinner software is a chemical equilibrium model based on minimization of Gibbs free energies calculation of the gas composition. The transport properties are calculated by resolving the Boltzmann's integro-differential equation using the Chapman- Enskog method. The calculated data is considered to depend mainly on temperature. Plots of the various properties are presented as a function of temperature at different pressures in Figures 6.1 to 6.6.

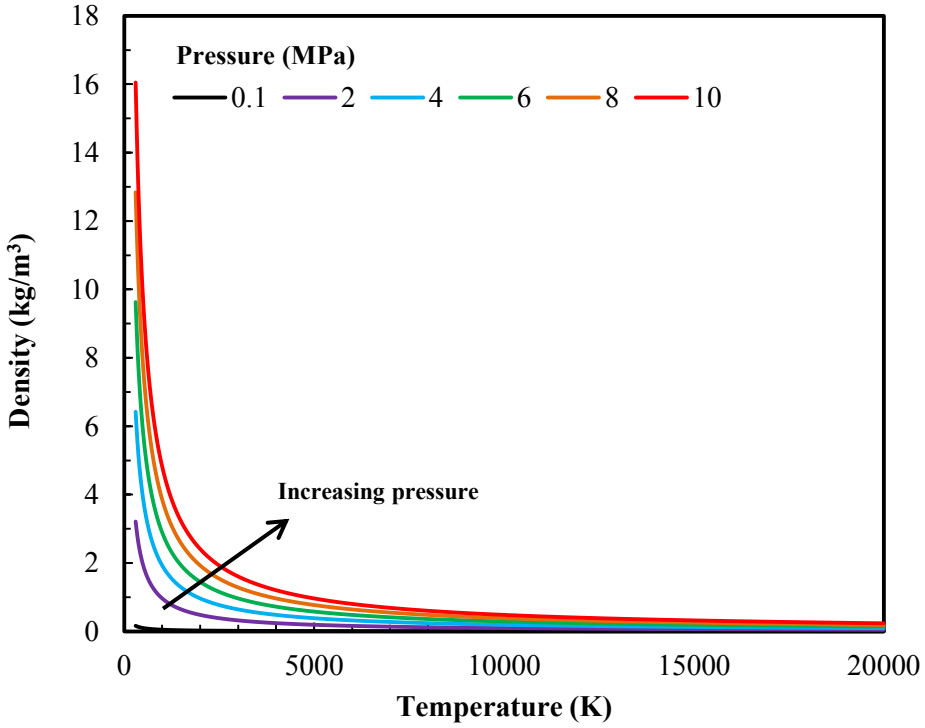

Figure 6.1: Density of helium gas versus temperature at pressures of 0.1 to 10 MPa

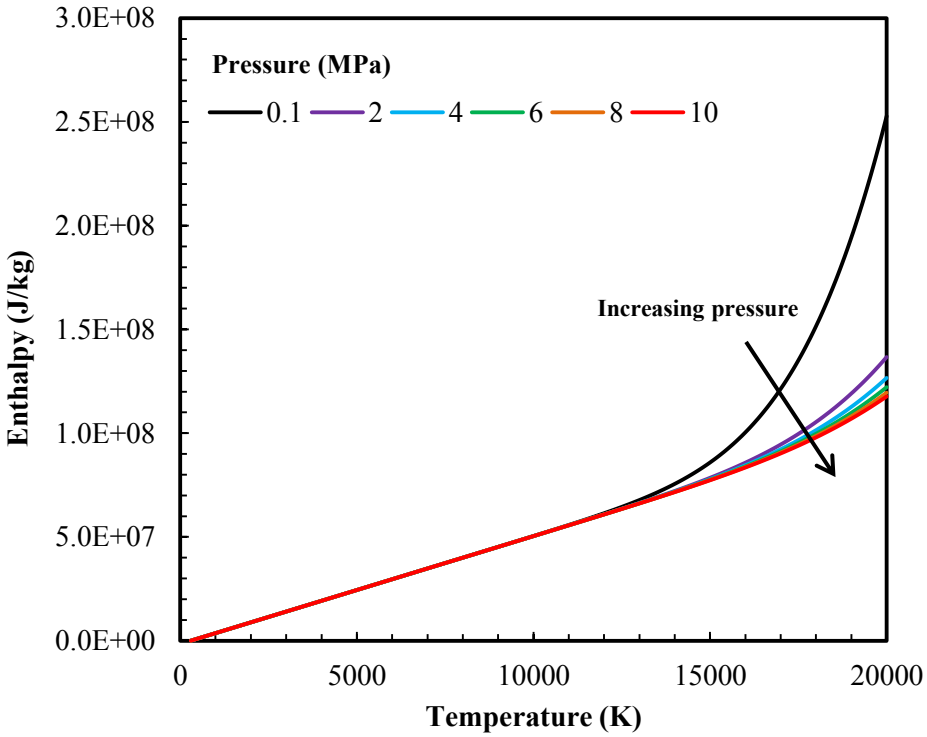

Figure 6.2: Enthalpy of helium gas versus temperature at pressures of 0.1 to 10 MPa

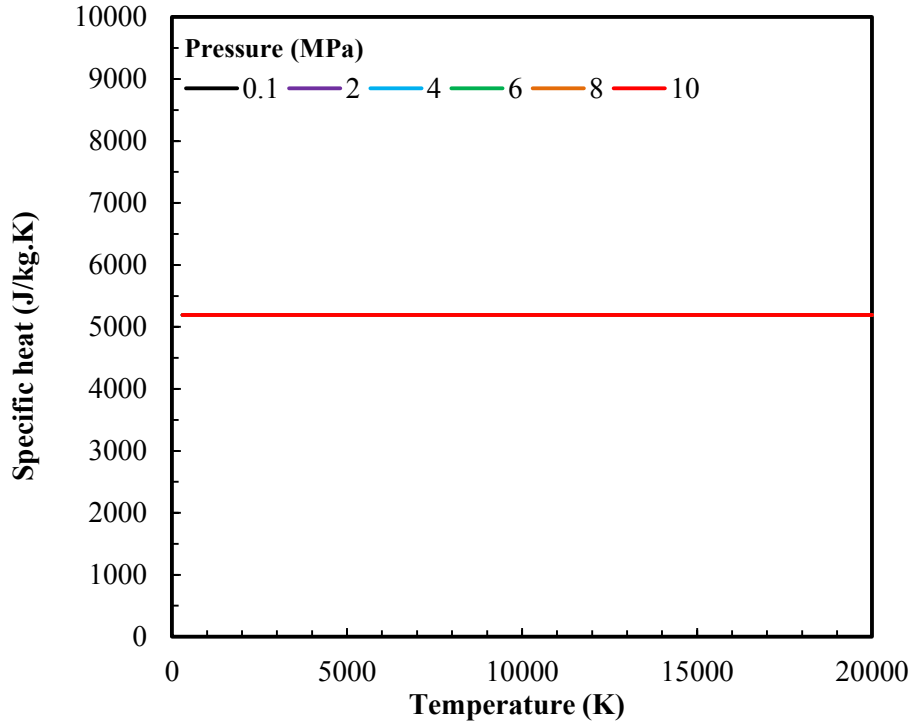

Figure 6.3: Specific heat of helium gas versus temperature at pressures of 0.1 to 10 MPa

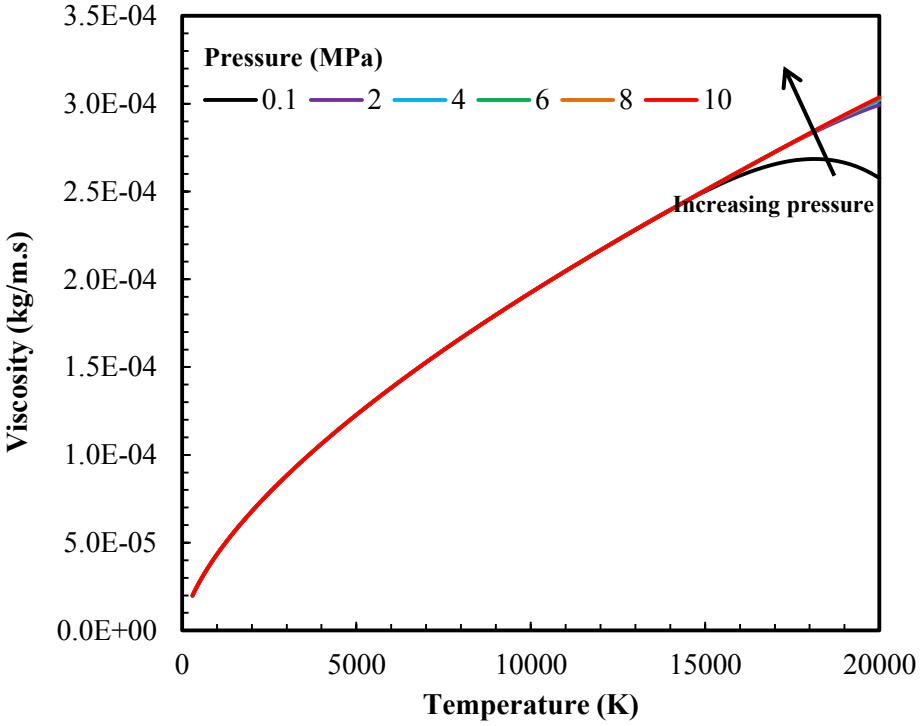

Figure 6.4: Viscosity of helium gas versus temperature at pressures of 0.1 to 10 MPa

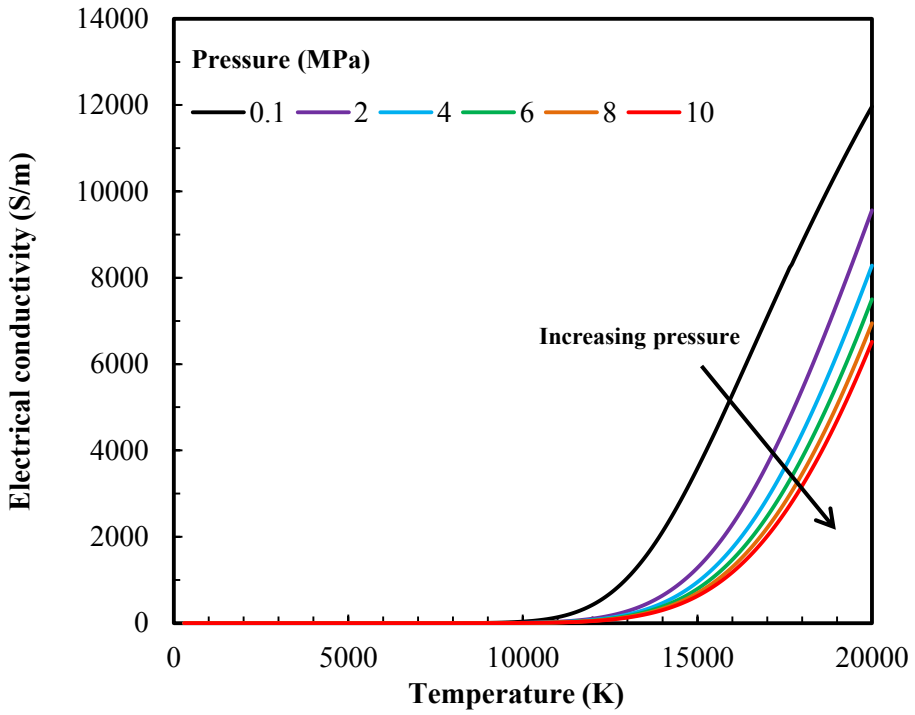

Figure 6.5: Electrical conductivity of helium gas versus temperature at pressures of 0.1 to 10 MPa

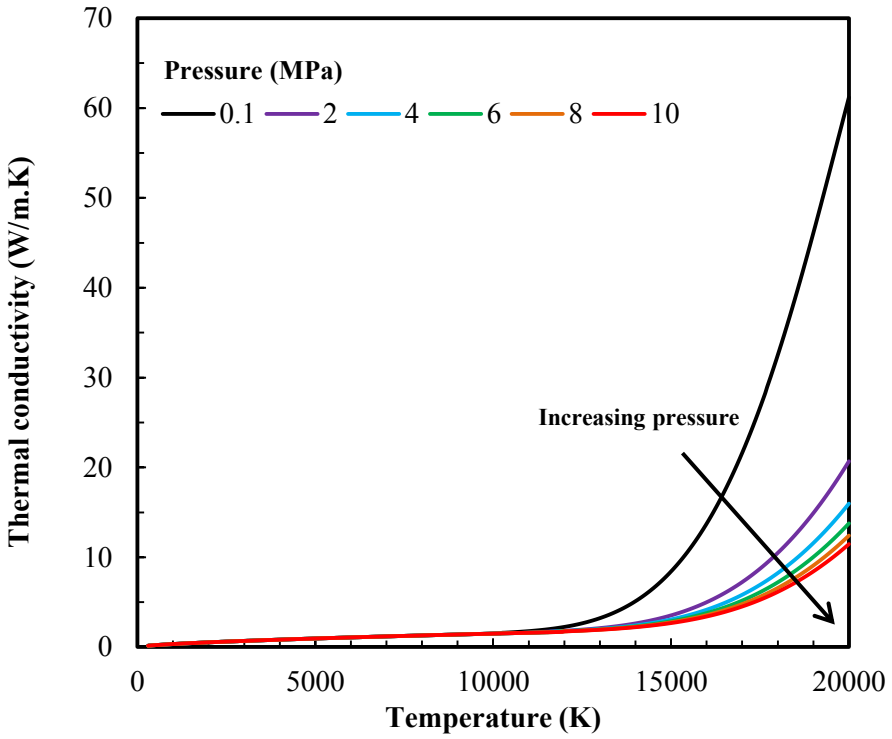

Figure 6.6: Thermal conductivity of helium gas versus temperature at pressures of 0.1 to 10 MPa

As it can be seen from the various plots, the transport coefficients and thermodynamic properties are similar at different pressures up to 12,000 K. However, the density (Figure 6.1) and specific heat (Figure 6.3) were an exception to the trend as the specific heat of helium was found to be relatively constant over the temperature and pressure range studied.

6.1.4 Computational Grid and Boundary Conditions

Computational fluid dynamics solution of transport equations requires the computational grid and initial boundary conditions to be specified. The initial conditions are necessary parameters for the time-dependent calculations as it gives the initial state of the reactor under consideration. A schematic diagram of this high-pressure tip-tip arc discharge reactor is shown in Figure 6.7. For an interelectrode gap of 1 mm, the volume of the simulated reactor is 2.56 cm^3. In the experimental study, the cathode is the fixed electrode, which is connected to the negative polarity of the high voltage direct current power supply. The anode is the movable grounded electrode, which allows the arc discharge to be generated by contact, needed at very high pressure. In this MHD model, the anode is fixed at an interelectrode gap of 1 mm. The pressure is set to the operating pressure in the whole reactor domain with the temperature in the surroundings of the arc region set to 300 K. However, due to the non-dynamic mesh used in the model, the ignition is simulated by applying a 0.1 mm radius initial hot channel of 11 000 K (σ = 16.26 S/m at 8 MPa) between the two electrodes at the first time step.

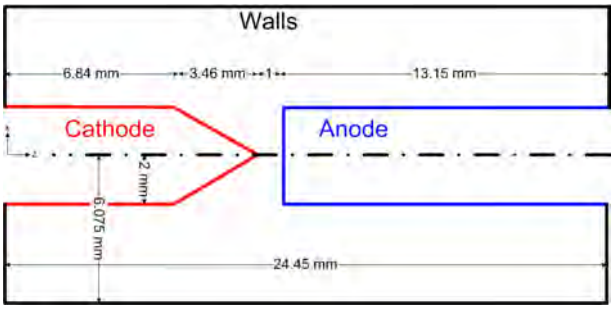

Figure 6.7: Schematic diagram of the tip-tip plasma reactor

The computational grid mesh is presented on Figure 6.8. This structured grid mesh contains 188550 hexa-cells, which is refined in the interelectrode zone where the gradients are the highest. The mean axial spacing grid in the interelectrode zone is 33 µm, with a radial spacing between 3.3 and 33 µm.

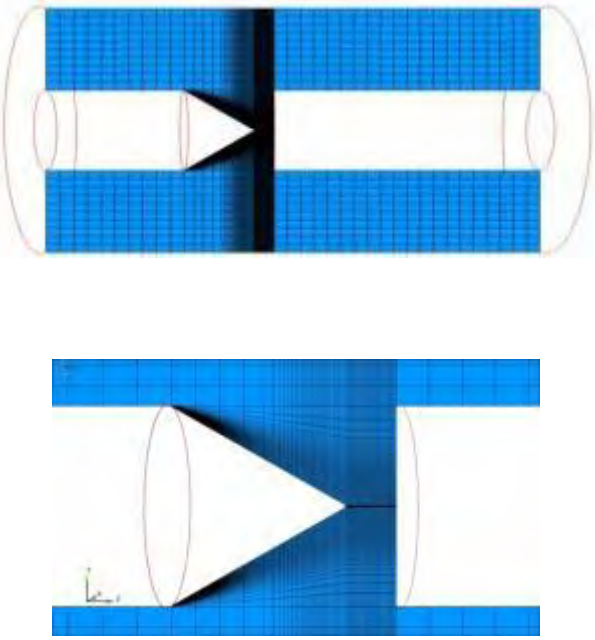

Figure 6.8: Computational grid mesh of the tip-tip plasma reactor (top) and zoom in the interelectrode zone (bottom)

In this study, the boundary conditions are presented in Table 6.1. This model does not include a sheath model because of the difficulty to estimate a voltage drop for low-current arcs, which is usually between 3 and 10 V for high current arcs. Thus, the total voltage drop results are only that which occurred in the arc column. Since this is a reactor of batch configuration, there are no inlet and outlet boundary conditions to be specified.

Table 6.1: Boundary conditions of the 3D MHD model

	Walls	**Cathode**	**Anode**
V_i (ms^{-1})	0	0	0
T (K)	$\frac{\partial T}{\partial \vec{n}} = 0$	$\frac{\partial T}{\partial \vec{n}} = 0$	$\frac{\partial T}{\partial \vec{n}} = 0$
φ (V)	$\frac{\partial \varphi}{\partial \vec{n}} = 0$	$\varphi^{(n)}$	0
P (Pa)	$\frac{\partial P}{\partial \vec{n}} = 0$	$\frac{\partial P}{\partial \vec{n}} = 0$	$\frac{\partial P}{\partial \vec{n}} = 0$
A_i (T.m)	0	$\frac{\partial A_i}{\partial \vec{n}} = 0$	$\frac{\partial A_i}{\partial \vec{n}} = 0$

6.1.5 Simulation Parameters

To prevent divergence of the calculations and instability in the arc zone, a small time-step of 0.25μs was set for the first 10000 time steps. Then, the time step was set to 1 μs for 47500 time steps (50 ms) While the time-step used here is lower than the typical 5 μs time-step used for plasma modelling found in some literature [223, 224], it is the largest possible time-step for convergence of the model calculations at the pressure and current investigated.

The calculations were carried out using an eight processor HP Pavilion DV6 computer with total calculation time of around 80 h. For the typical case with pressure of 8 MPa and a current of 0.35 A, a time-step of 2.5 μs was set after 57500 time steps. The calculation was run for a longer time (100 ms) in order to be able to observe the convection effects. The long computation time of this study can be attributed to the difference between the time constants of a plasma flow reactor and the natural convection predominating under a batch reactor.

6.2 Results, Analysis, and Comparison with Experimental Results

The simulated results are presented for a reference case of the high-pressure arc reactor at 8 MPa and a set current of 0.35 A for a non-reactive gas (helium) at an interelectrode gap of 1 mm. The results are compared to experimentally measured data obtained in the tip-tip arc discharge reactor for pure helium. In the subsequent section 6.2.2 and 6.2.3 results from simulation relating to the influence of pressure at a fixed current of 0.35 A and influence of current at a fixed pressure of 8 MPa are

presented. In each case, the results of the simulation are compared with the experimentally obtained results.

6.2.1 Results for Pressure = 8 MPa and Current = 0.35 A

The evolution of the arc temperature during the transient period is shown in Figure 6.9. From Figure 6.9 (a), the cathodic arc root could be observed to remain attached to the tip of the electrode while the anodic arc root starts sliding along the anode after 2 ms. The continuous sliding of the anodic arc root along the anode could be observed to increase with the time-step until the anodic arc root reaches its final position at approximately 32 ms.

From Figure 6.10, the evolution of the voltage with time at a steady current of 0.35 A is observed. The voltage is observed to drop to -102 V at 20 ms before becoming stable afterwards at -104 V. This voltage drop is a response to the increase in temperature of the surrounding gas which results in a corresponding increase of the electrical conductivity, and thus a lower voltage. The voltage drop speed decreases and then increases with the increase of the arc bend, and thus of the arc length, leading to a higher voltage.

The model takes into account the acceleration of gravity in the –x-axis direction (-9.8 m/s^2). Hydrodynamics and electromagnetic forces can be said to influence the arc root movement along the anode as observed in Figure 6.9 (a-c). The bending of the arc is a phenomenon observed in the experimental reactor for syngas and helium mixtures at a pressure of 2.2 MPa [178] as shown on Photograph 6.1. This bending arc phenomenon could be attributed to the effect of the high temperature in the arc and density gradient between the arc column and the surrounding gas which pushes the arc up at high pressure. These high temperatures will lead to the natural convection of the gas to the top of the reactor (see Figure 6.11). Therefore, the observed arc shape can be linked to the combined effects of natural convection, electromagnetic forces, and gravity. While it is very difficult to obtain a clear picture of the arc at distances less than 1 mm due to the very small size of the arc and the high light emissions, the arc shape is similar to the one observed experimentally.

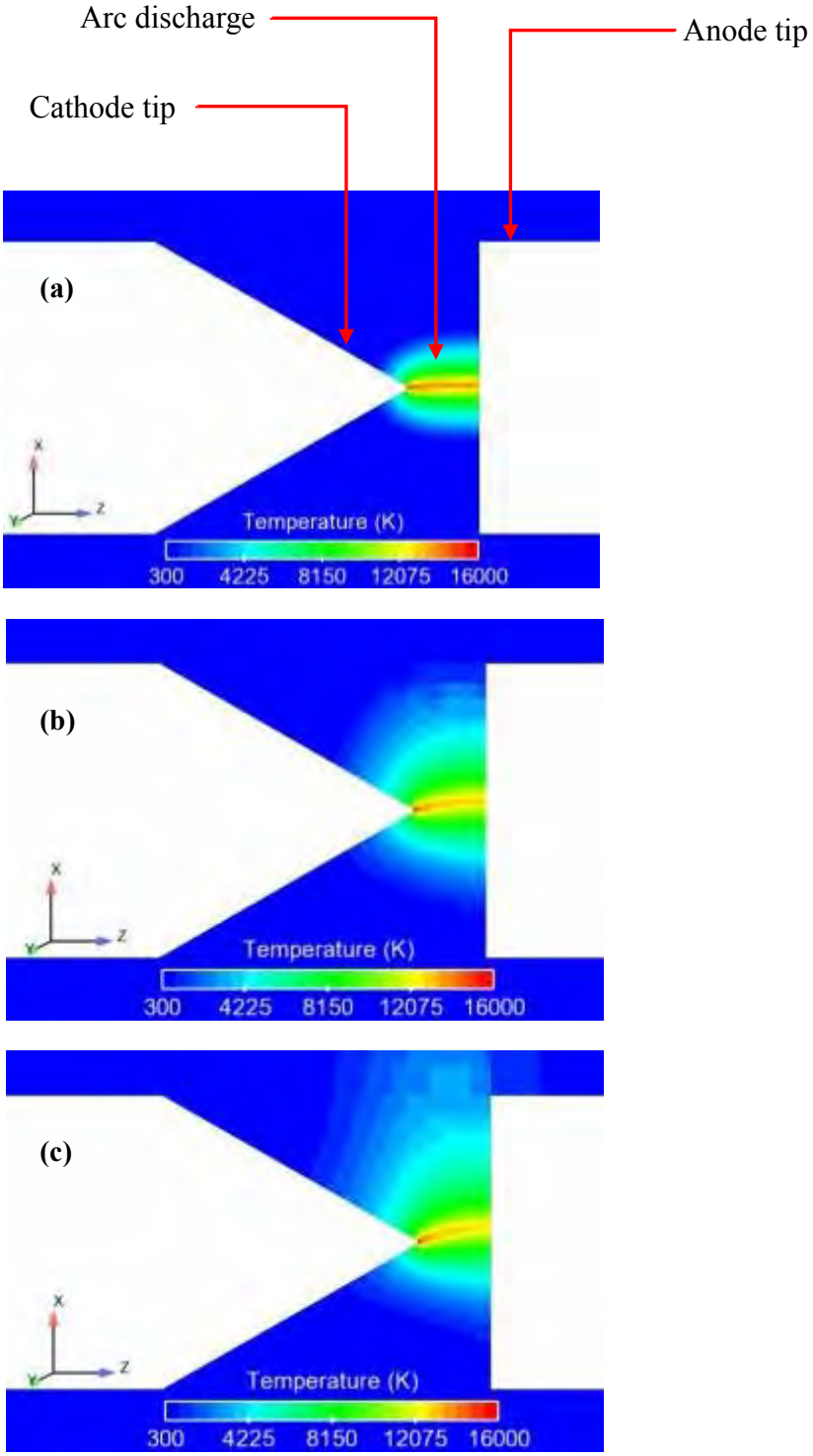

Figure 6.9: Evolution of the arc shape for (a) 2, (b) 15, and (c) 50 ms at P = 8 MPa, I = 0.35 A

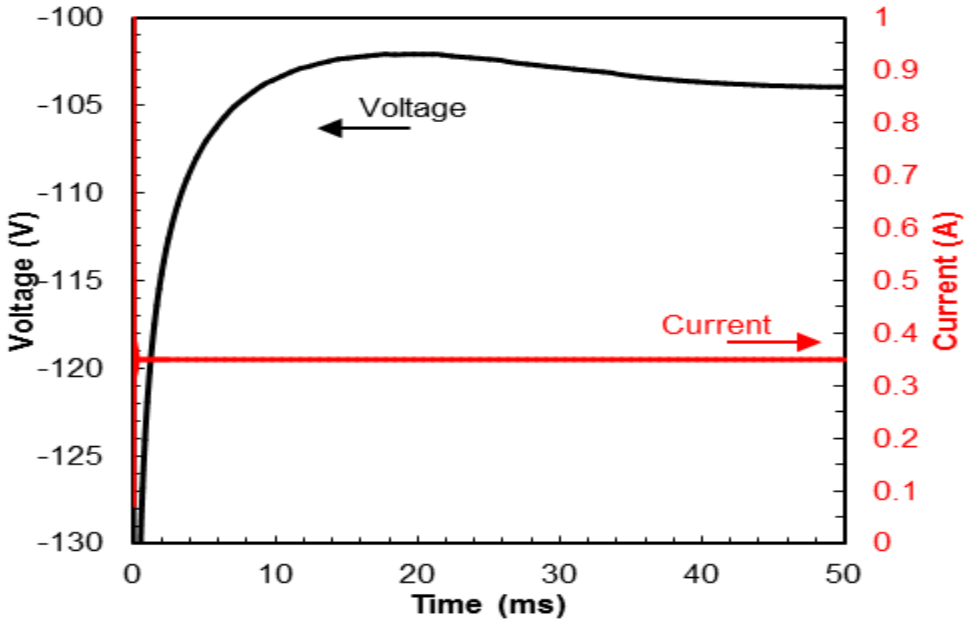

Figure 6.10: Voltage and current versus time of the discharge at P = 8 MPa, I = 0.35 A

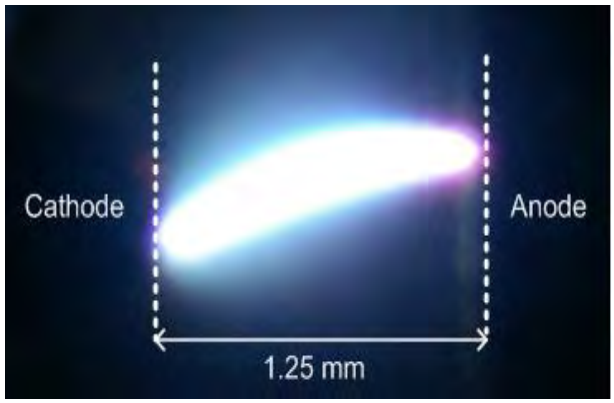

Photograph 6.1: Picture of the arc discharge for an interelectrode gap of 1.25 mm at a current of 0.35 A and a pressure of 2.2 MPa for a mixture of $He/H_2/CO$ (40/48/12%)

The temperature field profile at a time of 0.1 s is presented in Figure 6.11. The arc core temperature is around 16200 K at the cathode tip and 12700 K at the anode. The electrode tip effect increases the value of every variable near the tip compared to the rest of the arc. The hot gas is moving towards the top of the reactor due to the natural convection effects. The reactor chamber is water-cooled during the experiments but this property is not taken into account in the model since understanding the behaviour of the arc column is the primary focus here. However, in 0.1 s, it is assumed that heat transfer occurs slightly between the hot, the cold gas, and the wall of the reactor. The temperature gradient is shown on Figure 6.12. From Figure 6.12, it can be seen that the gas temperature reaching the wall can quickly attain a couple of thousands Kelvins. The temperature gradient reaches 12200 K/mm in the arc.

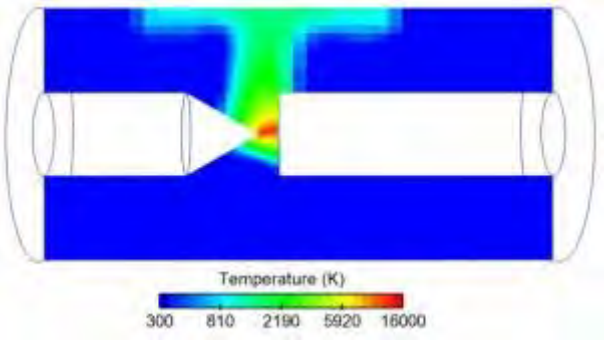

Figure 6.11: Representation of the temperature field at the last time step (0.1 s) in the whole reactor, logarithmic scale at P = 8 MPa, I = 0.35 A

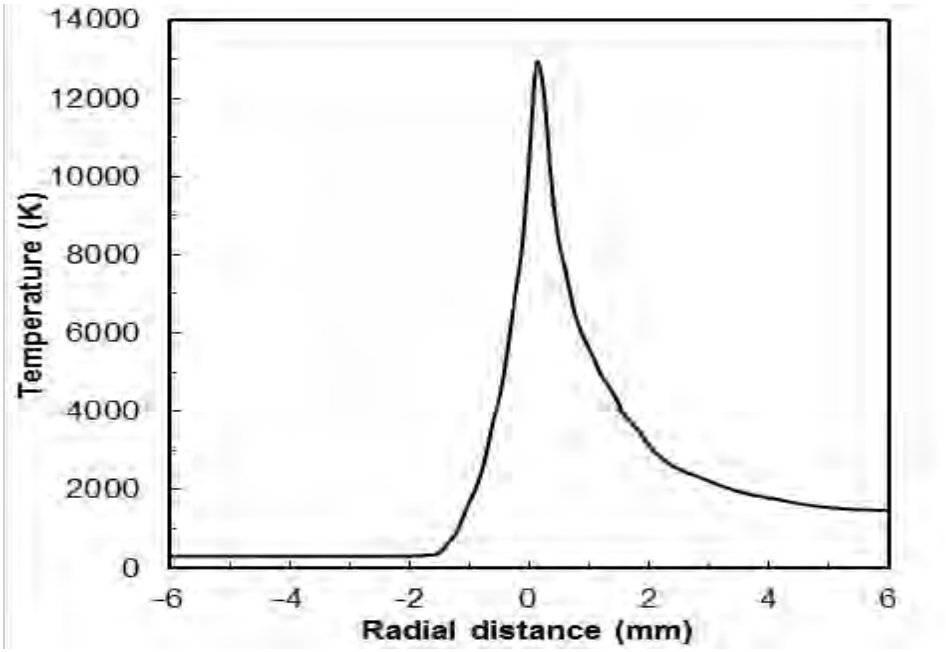

Figure 6.12: Temperature gradient along the x-axis in the middle of the interelectrode region at P = 8 MPa, and I = 0.35 A

The pressure displayed in Figure 6.13 is the relative pressure to the working pressure, which means that a relative pressure of 0 Pa corresponds to an absolute pressure of 8 MPa. It could be seen from Figure 6.13 that the pressure inside the arc is around 4.3 Pa higher than the operating pressure of 8 MPa at the cathode tip. This creates a depression zone near the cathodic arc root (up to 1 Pa above the tip). It can be observed from Figure 6.14 that the pressure gradient in the arc is thus very low (0.38 Pa at the middle of the interelectrode region).

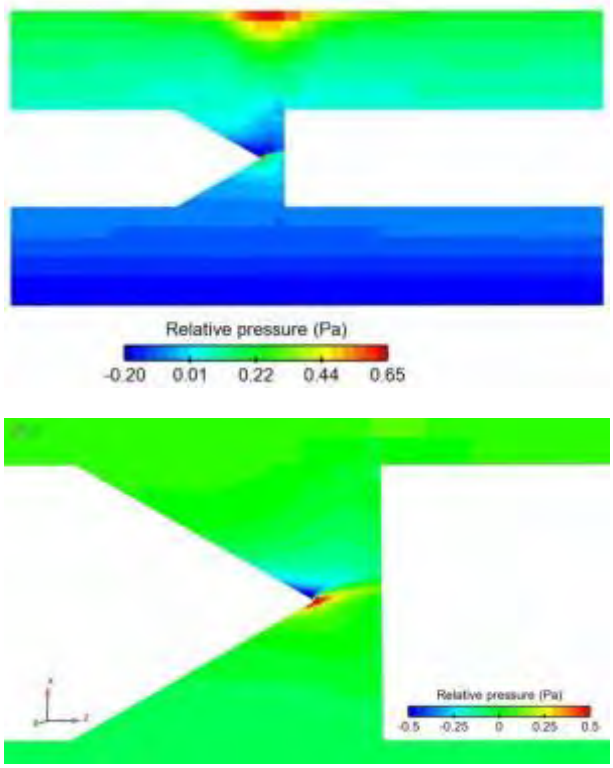

Figure 6.13: Relative pressure (ref 8 MPa) in the reactor (top) and zoom-in in the interelectrode zone (bottom) at P = 8 MPa, and I = 0.35 A

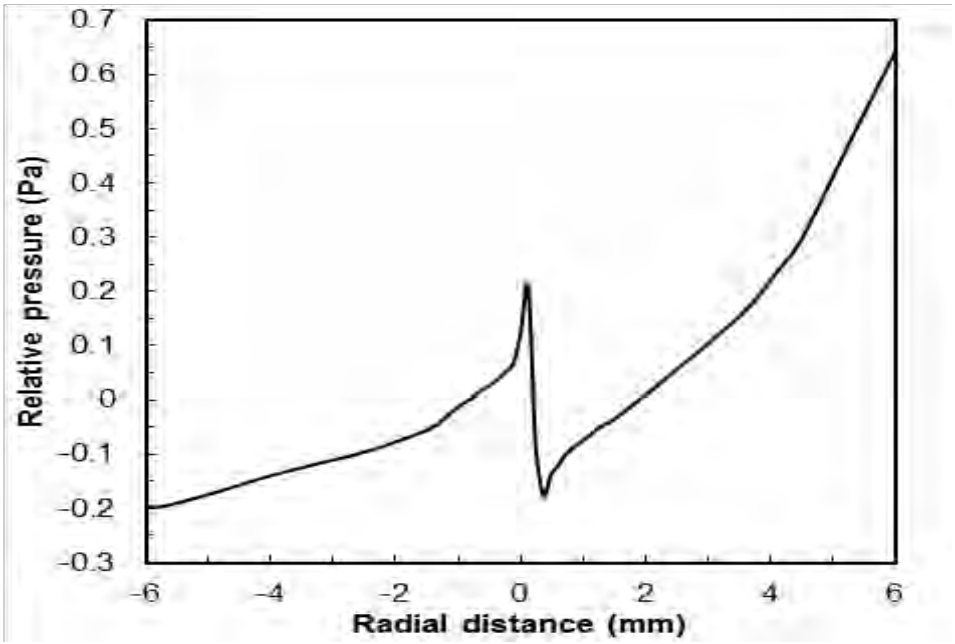

Figure 6.14: Pressure gradient along the x-axis in the middle of the interelectrode regionat P = 8 MPa, and I = 0.35 A

A pressure gradient of 0.85 Pa is also observed in the reactor between the top and the bottom. This phenomenon is due to the convection effect pushing the hot gas up and the high temperature expanding the gas, creating a depression in the bottom of the reactor. An average pressure increase of 0.1 MPa was measured experimentally by the pressure transducer located at the top of reactor during discharge for pure helium.

The low current used leads to a low magnetic field and Lorentz forces (0.45 mT and 2.8 kN/m^3, respectively at the middle of the interelectrode gap) which are not able to constraint the arc. Thus, the typical arc "bell-shape" constraint observed in high plasma torch is not observed in this case study.

The voltage value of -104 V approximately 36.6% relative to the RMS (root mean square) value of -164 V measured experimentally. This deviation can be explained by the lack of a sheath model, which may be emphasized by the very high pressure. The cathode and anode sheaths are usually modeled by imposing boundary conditions to the electrodes.This involves fixing the cathode enthalpy at a temperature (≈ 3200 K) while the anode enthalpy is defined as a function of a fixed voltage drop, electron condensation, temperature and current density. Benilov [87] in his review of plasma-electrode interaction phenomenon at high pressure mentioned that deposition of additional electrical energy is essential at the cathodic space-charge sheath but it is not significant at the anodic space-charge sheath at high pressure. This explains the deviation in the voltage drop between the experimental and the model value which does not take into account the sheaths.

Thus, the dissipated power from the simulation was 36.7 W instead of 57.4 W obtained from experimental measurement. Figure 6.15 shows the representation of the electrical potential in the arc domain. The electrical potential drop along the z-axis in the middle of the reactor showed a linear trend as can be seen in Figure 6.16. This linearity is in line with magneto-resistive model used (generalized Ohm's law).

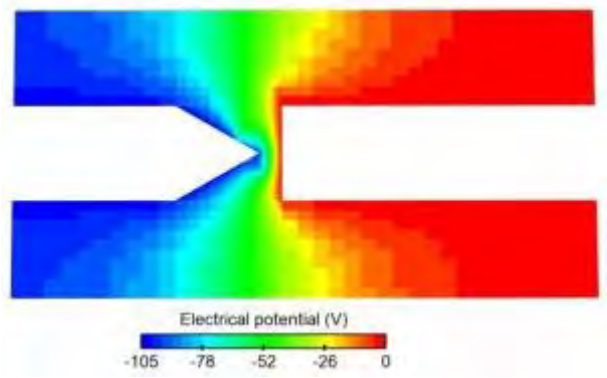

Figure 6.15: Electrical potential field at P = 8 MPa and I = 0.35 A

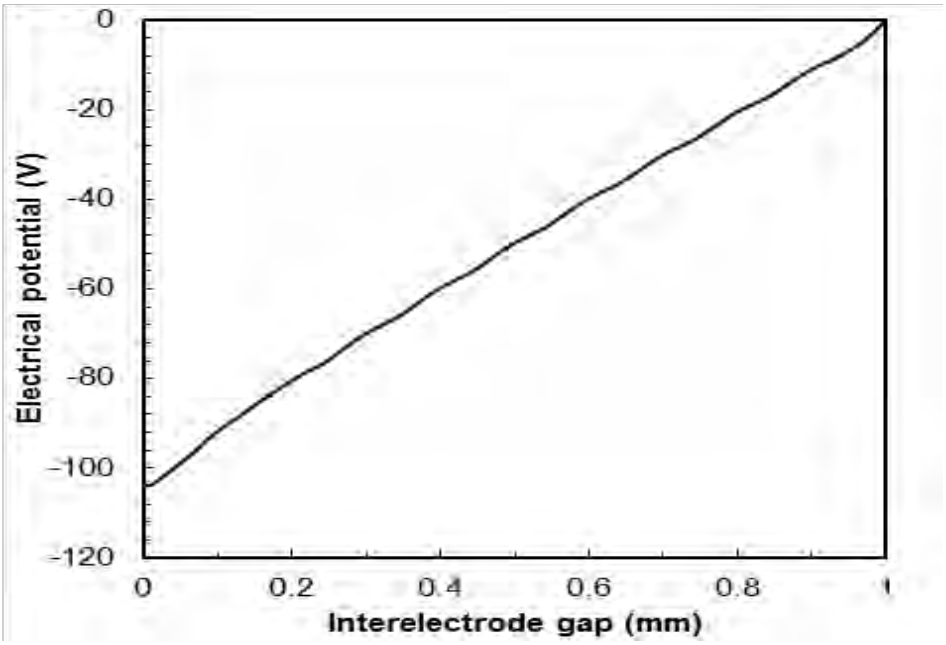

Figure 6.16: Electrical potential along the z-axis centered on the tip of the cathode at P = 8 MPa and I = 0.35 A

The velocity field is shown in Figure 6.17. In the high pressure batch reactor configuration studied, the mass exchange between the gas and the arc zone takes place only under the effect of natural convection with a maximum velocity of 0.44 m/s at the fringe of the arc core. This implies that a long time is required for the entire gas in the reactor to flow through the arc zone due to the very slow velocity of the gas. Moreover, the high current density of around 3×10^8 A/m^2 near the cathodic arc root leads to a maximum value of the Lorentz force near the cathode. The Lorentz force induces the movement of the gas from the bottom to the top of the reactor improving the amount of gas treated by the arc discharge.This recirculation phenomenon observed in the reactor is shown in Figure 6.18. This phenomenon referred to as the "Maecker's effect" [225] is responsible for the convection in the arc column as well as the pumping of the cold surrounding gas in the reactor.

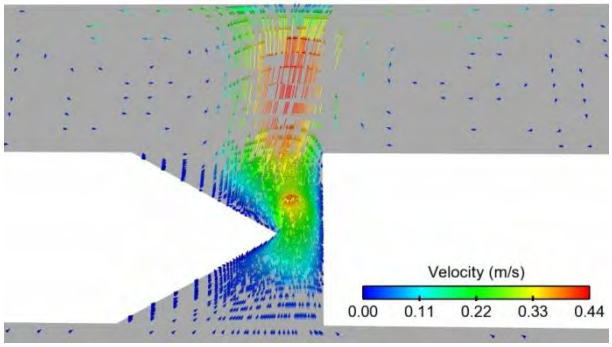

Figure 6.17: Velocity arrows coloured by velocity magnitude field at P = 8 MPa and I = 0.35 A

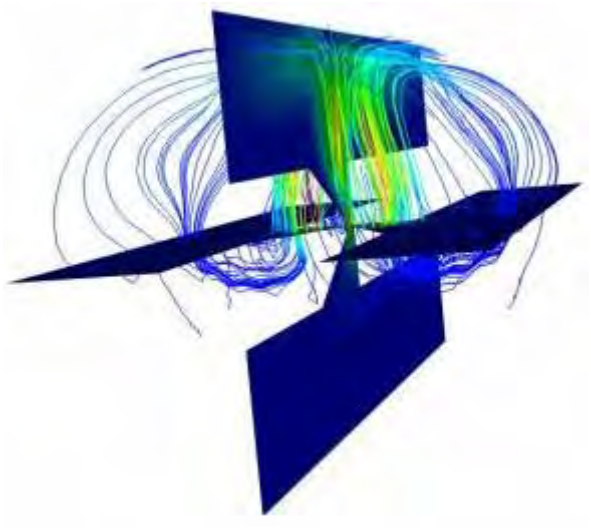

Figure 6.18: Velocity streamlines in the reactor at P = 8 MPa and I = 0.35 A

In a previous publication [178] involving an experimental study of syngas conversion at high pressure in the same reactor, the arc core radius was calculated based on conversion results to be equal to 0.322 mm, but the measured arc core radius obtained using a video camera with an optical filter (-25%) was between 0.15 and 0.16 mm. It was therefore concluded in the publication, that the active discharge volume in which the reaction took place is certainly bigger than the luminous volume visibly determined with the video camera.

From the simulation, the maximum current density obtained was 3×10^8 A/m^2 near the cathode tip as can be seen on Figure 6.19. According to Selvan et al. [226], the arc core radius can be estimated from the current density. To implement this approach, the arc core radius is defined as the radial distance between the arc centreline and the point where the current density is equal to 0. However, due to the arc shape obtained in the simulation, the arc radius was defined as the radial distance between the 2 points where the current density reaches 10% of the maximum value, divided by 2. Following this approach, (see Figure 6.20), the radius of the arc core in the middle of the interelectrode gap was estimated to be 0.168 mm, which is in line with the previously published value of 0.16 mm obtained experimentally [178].

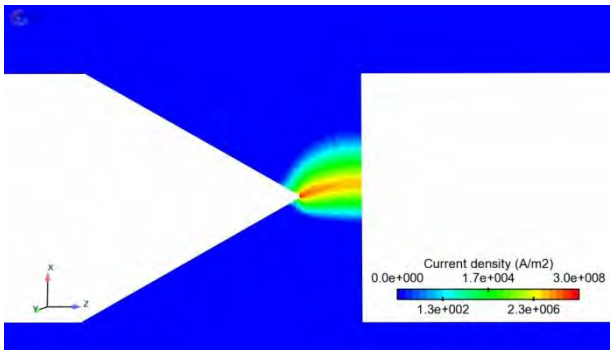

Figure 6.19: Current density field on a logarithmic scale at P = 8 MPa and I = 0.35 A

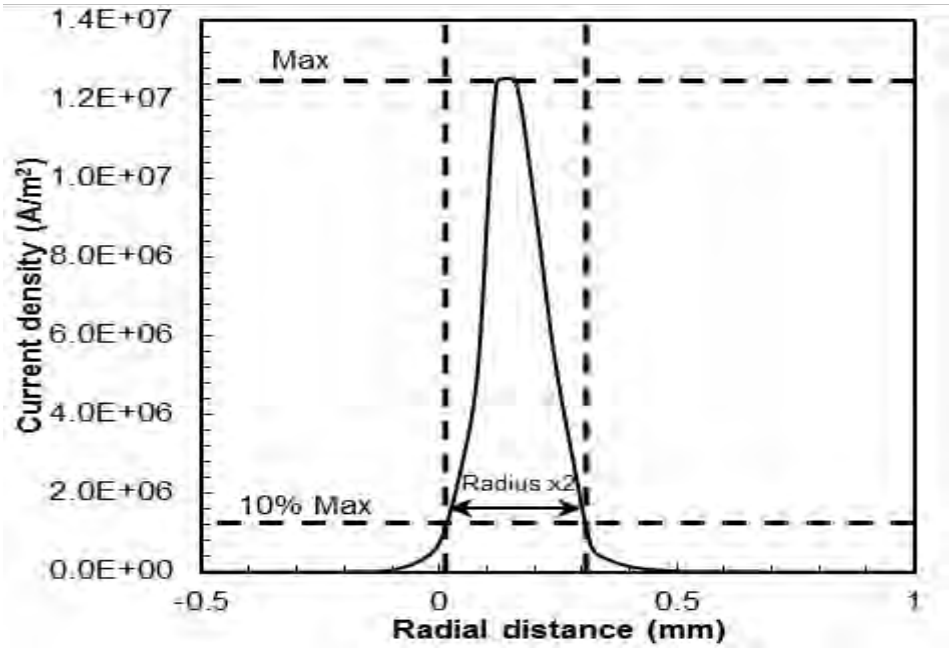

Figure 6.20: The radial current density profile in the middle of the interelectrode gap as a function of the radial distance

In a batch reactor, information regarding the mass transfer within the arc discharge is essential in order to be able to estimate the amount of the gas treated during the discharge duration. From the estimated radius of 0.16 mm, the volume of the arc for an interelectrode gap of 1 mm was calculated to be 8×10^{-5} cm^3. This is about 3.14×10^5 times smaller than the volume of the reactor of 2.56 cm^3. From the simulation result, the average velocity of the gas going through the arc section of 3.2×10^{-4} mm^2 was estimated to be 0.4 m/s. Thus, by calculation, volumetric flow rate of the gas treated by the arc is 0.128 cm^3/s. Therefore, for a discharge duration of 60 s, the volume of gas treated is 7.68 cm^3. This corresponds to 3 times the volume of the reactor.

6.2.2 Influence of Pressure (I = 0.35 A)

The influence of operating pressure on the voltage was studied for pressures ranging between 2 and 10 MPa at a fixed current of 0.35 A. From Figure 6.21, it can be observed that the higher the pressure, the higher the voltage. The experimental voltage corresponds to a rms value. As mentioned in section 6.2.1, the deviation between the experimental and model value can be attributed to the lack of space-charge sheaths by the model as well as the LTE assumption made for the model.

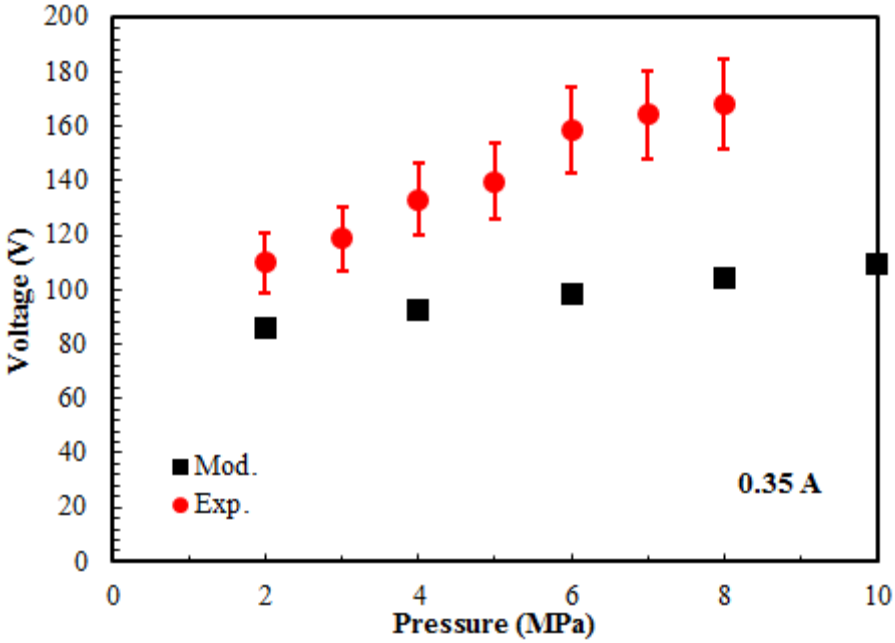

Figure 6.21: Simulated voltage as a function of pressure in comparison with experimental data

Figure 6.22 presents the variation of the velocity magnitude as a function of the working pressure along the radial cross section in the middle of the interelectrode gap. From this plot, it can be noticed that the higher the pressure, the higher the velocity of the gas, and thus the higher the volumetric flow rate of gas treated by the discharge. Hence, the molar flow rate of the treated gas is 2.5×10^{-4} and 5.11×10^{-4} mol/s at 6 and 10 MPa respectively.

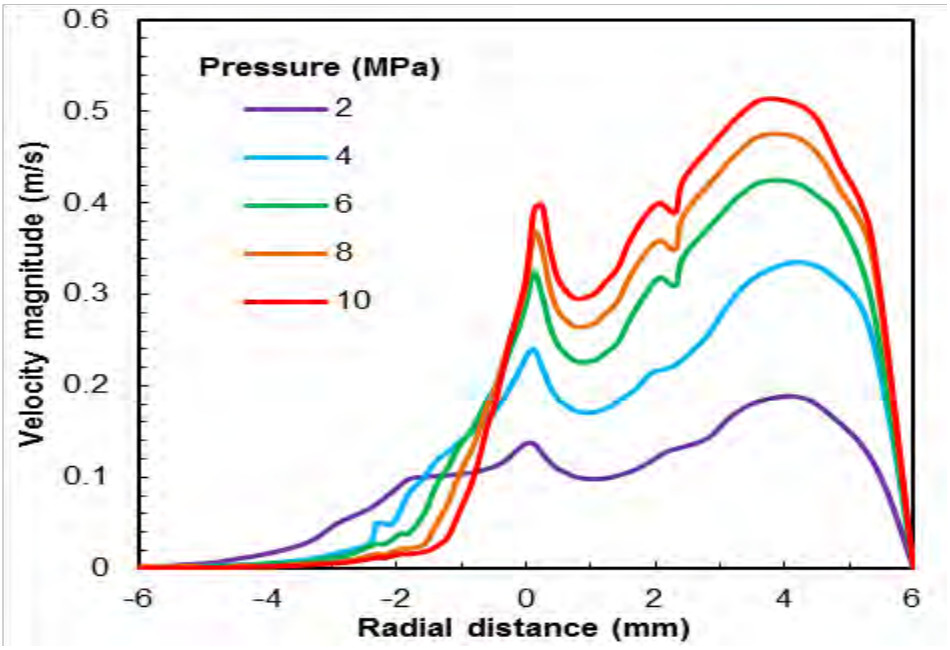

Figure 6.22: Evolution of the velocity along the radial cross section as a function of the working pressure at I = 0.35 A and time step = 50 ms

The temperature of the arc is almost equal at the pressures studied (2,4, 6, 8 and 10 MPa), but the velocity varies. This variation in velocity is attributed to the high density gradients between the hot and cold gas at high pressure as shown in Figure 6.23 given that the temperature difference and the viscosity are similar at high pressure. This phenomenon is the main driving force for the natural convection in the reactor under gravitational effect. Generally, the Rayleigh number, which governs the onset of the natural convection, depends mainly on the density, the viscosity and the temperature differentials.

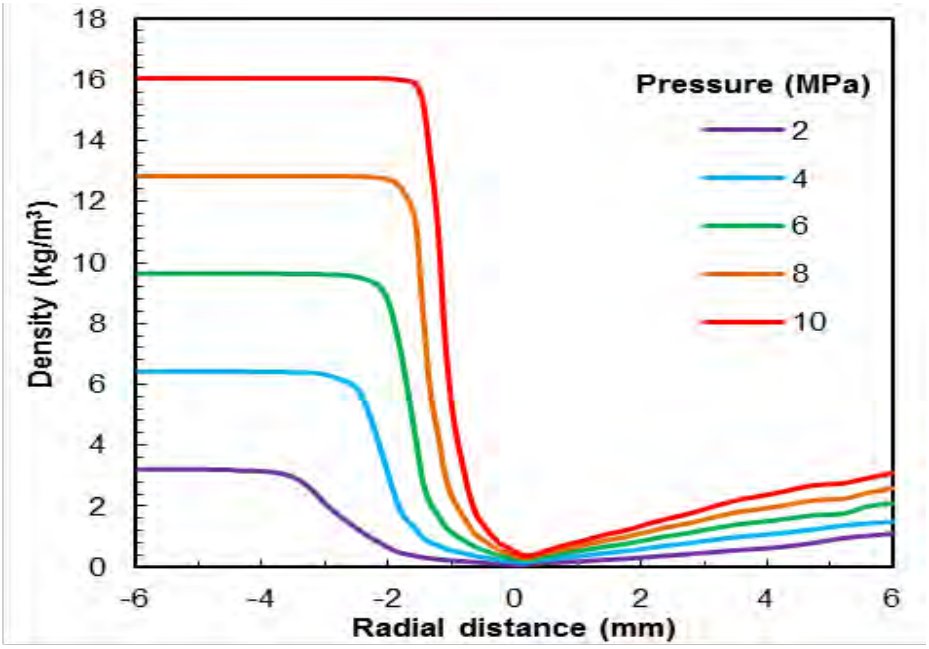

Figure 6.23: Evolution of the density along the radial cross section as a function of the working pressure at I = 0.35 A and a time step = 50 ms

It can be seen from Figure 6.24 that a pressure increase results in a higher displacement of the arc core and the anodic arc root towards the top of the reactor. This is due to the above-mentioned higher convective motion of the gas at higher pressure. The arc radius is between 0.153 and 0.168 mm for the five working pressures studied which means that no constraint of the arc core by the surrounding pressure is observed. Although, the arc radius is constant over the varying pressure, the maximum current density is observed to increase with a corresponding increase in the working pressure. This is because the electric field and the voltage increase with increasing pressure while the electrical conductivity slightly decreases.

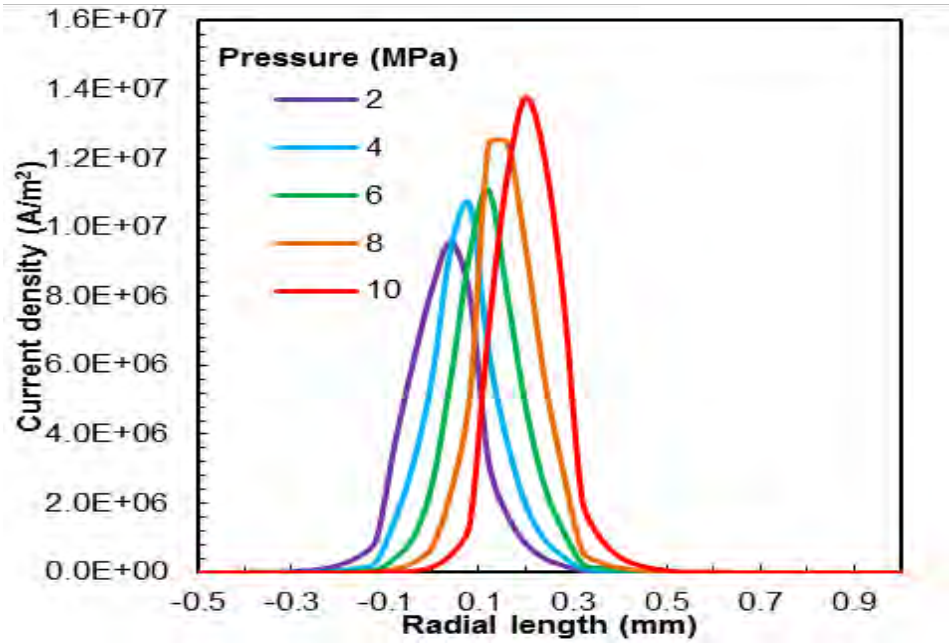

Figure 6.24: Evolution of the current density as a function of the working pressure at I = 0.35 A and time step = 50 ms

6.2.3 Influence of Current (P = 8 MPa)

The effect of current variation was studied between the current range of 0.25 to 0.4 A for a pressure of 8 MPa and the simulated results were compared to the ones obtained at the same experimental operating conditions. Figure 6.24 shows a negative V-I characteristic commonly observed for a nonthermal plasma arc. The experimental and simulated characteristics present similar trends with a discrepancy of 65 V due to the assumptions made in the model. The variation of the operating current is observed to have a very slight influence on parameters such as temperature, velocity, pressure or arc core radius. This is in contrast to the study of the arc discharge behaviour under the influence of pressure variations, where parameters such as velocity, current density were observed to be significantly influenced by varying the working pressure.

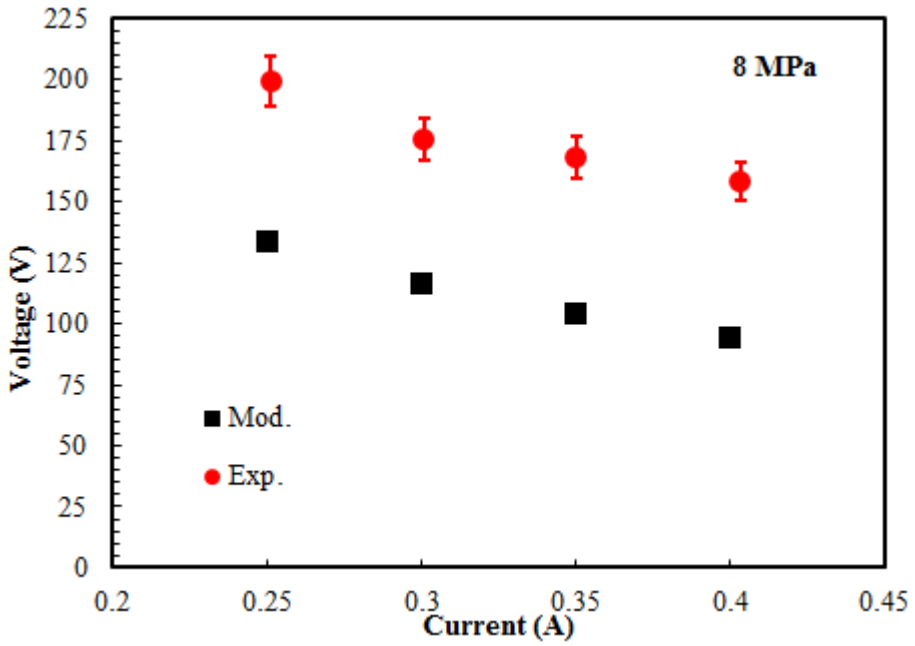

Figure 6.24: Simulated voltage as a function of current and comparison with experimental data

6.3 Conclusions on MHD modelling

The low current and high pressure conditions leads to instabilities and makes the MHD model difficult to converge. However, the use of a very small time step allows stabilization of the model. The thermodynamics and transport properties are also scarce for very high pressure and temperature. Nonetheless, a CFD MHD model of a batch reactor working with high pressure of helium and in low current conditions has been successfully implemented, assuming the LTE.

A detailed case for a pressure of 8 MPa and a current of 0.35 A has been studied. The results show a bending of the arc shape and a motion of the anodic arc root towards the top of the reactor, as observed experimentally due to the electromagnetic forces and convection effects. Gas recirculation takes place in the reactor. The hot gas moves towards the top of the reactor, cools down, mixes with the cold surrounding gas, and is then driven to the sides and the bottom of the reactor, leading to a small pressure gradient inside the reactor. The temperature of the arc column obtained from the simulation is about 12700 K, at the anode, and 16200 K at the cathode. The cathode is indeed subjected to the tip effect, which increases the value of all the variables. The model also reveals that the pressure gradient inside the arc is negligible. The arc core radius has been estimated to be between 0.153 and 0.168 mm for the five pressures cases investigated, and thus corresponds to the one observed experimentally. The volumetric flow rate of the gas treated in the arc was estimated to be 0.128 cm^3/s. Furthermore, from the current range investigated, the voltage shows similar trends to the measured voltage, although the values from the model are lower. The observed voltage-current curve

is typical of that of a nonthermal arc discharge. In addition, the results of the MHD model shows that an increase of the pressure has no effect on the arc radius, but leads to an increase of the convective forces and thus a higher displacement of the arc root towards the top of the reactor.

Chapter 7

CONCLUSIONS

The main objective of this research project was to investigate the potential for hydrocarbons and fluorocarbons synthesis in a high pressure plasma reactor at low current.

A tip-tip high pressure arc discharge reactor was set up and commissioned for this research project. It has a maximum operating pressure limit of 20 MPa. The high pressure plasma apparatus is equipped with two pairs of borosilicate sight windows that permit the viewing of the arc discharge generated in the reactor chamber. The image of the arc discharge can be captured by the use of a video camera fitted with optical filters. The reactor has a worm gear actuator attached to the movable electrode for varying the interelectrode gap. The discharge was generated using a high voltage direct current (HVDC) power supply, and a high frequency pulse power supply. The sampling of the gaseous products was carried out 5 min after the power supply has been turned off. This allowed the recombination process to occur, and the gas temperature to return to ambient temperature. The sampling method involves the use of a gas tight syringe to draw the gas products from a small volume gas tank used to collect the gas at the reactor outlet. Analyses of the samples were done on a classical gas chromatograph (GC) and a gas chromatograph mass spectrometer (GCMS).

Preliminary experiments were conducted for hydrocarbon synthesis via the Fischer-Tropsch (FT) process at a fixed pressure of 2.2 MPa, and a current of 0.35 A using three different treatment modes: a continuous treatment mode, and two intermittent modes with a relaxation time between successive discharges. This was carried out using a high voltage power supply that operates on the principle of double resonance technology at high frequencies (50 kHz). This work which is related to the Fischer-Tropsch synthesis of hydrocarbons showed that significant amount of C_1 and smaller amounts of C_2 hydrocarbons can be synthesized by plasma reaction. Furthermore, the results obtained indicated that the continuous mode gave better result for C_1 synthesis, while the intermittent modes showed better kinetics for C_2 synthesis. The concentrations of CH_4, C_2H_4, and C_2H_6 were observed to increase in a progressive trend in the cyclic modes, while concentration reached a maximum for species in the continuous mode. Overall, the kinetics of organic synthesis was found to depend strongly on the treatment mode, for which the intermittent mode showed a better performance than the continuous mode.

A series of preliminary experiments were conducted for syngas conversion to higher hydrocarbons at varying pressures ranging from 0.5 to 15 MPa using a HVDC power supply. The results from these preliminary studies revealed the main synthesized molecules to be CH_4, C_2H_4, C_2H_6, C_3H_6, and C_3H_8 over the entire pressure ranges investigated. C_2H_2 was obtained at pressures of 0.5 and 1 MPa only. In addition, the influence of varying the operating current from 0.20 to 0.40 A was studied. The combined effect of input power and reduced electric field was found to play a significant role in the behaviour of the discharge at the currents investigated. The increase of the operating pressure between 4 and 10 MPa was found to result in a gradual increase of the concentrations of the species produced. A significant increase of the products was observed between 10 and 12 MPa.

The dry reforming process was investigated at pressures up to 7.8 MPa. From this study, H_2, CO, C_2H_2, C_2H_4, C_2H_6, with low amounts of C_3H_6, and C_3H_8 were obtained as the main synthesized molecules. This study also showed a decrease in carbon deposit formation as the working pressure increases. A comparative study with the best dry reforming results reported in literature indicated lower conversions for this high pressure arc discharge reactor. However, the positive influence of very high pressures from 0.5 to 7.8 MPa on the energy efficiency which has not been previously reported was observed. In addition, a good H_2/CO ratio of 2.1 to 2.6, which is desirable for the production of synthetic fuels in FT process, compared to the low H_2/CO ratio of other reviewed dry reforming process was obtained.

Preliminary experiments on the formation of higher fluorocarbons from CF_4 was performed using two different treatment modes at a pressure of 2 MPa, a current of 0.35 A, and an interelectrode gap of 0.4 mm. The results revealed a similarity with those observed in the case of hydrocarbon synthesis. While very low concentrations of C_2F_6 and C_3F_8 were produced in the continuous and intermittent treatment modes, again the intermittent treatment mode showed better results and favourable kinetics for the synthesized species than the continuous mode.

The dissociation of CF_4 in the tip-tip plasma reactor was investigated at high pressures in the range of 1 to 9 MPa, with varying parameters such as current and interelectrode gap. The experimental results revealed that pressure variation together with the input power plays a major role in the conversion process and the formation of higher fluorocarbons. Furthermore, high conversion of CF_4 was observed at pressures from 2 to 3.5 MPa, and 6 to 9 MPa where the input power was high. The low input power between 3.7 and 5.5 MPa was found to favour the production of C_2F_4 within this pressure ranges.

The variations of the operating current from 0.3 to 0.45 A at a pressure of 1 MPa, and an interelectrode gap of 0.4 mm showed a strong decrease of the discharge voltage. This voltage trend was found to lead to a strong decrease of the reduced electric field in the discharge, which resulted in

a strong deviation from thermodynamic equilibrium within the arc zone. Thus, the conversion of the CF_4 into higher fluorocarbons is influenced by the reduced electric field.

In the synthesis of higher fluorocarbons from CF_4, the influence of varying the interelectrode gap at a pressure of 1 MPa and a current of 0.35 A for a discharge duration of 30 s was found to be of a little significance in the fluorocarbon formation process.

Theoretical studies carried out on the dissociation of CF_4 indicated that the nonthermal plasma process would result in higher energy efficiency than the thermal plasma process. Furthermore, the addition of helium to CF_4 under electron impact process resulted in a decrease of the energy conversion efficiency of the process as the molar concentration of helium increases.

Thermodynamic analysis was performed for the plasma-assisted fluorocarbons and hydrocarbons processes. The thermodynamic calculations indicated a high conversion for the dry reforming process at the investigated pressures. A zero-dimensional (0-D) kinetic modelling approach was implemented in the perfectly stirred reactor (PSR) and SENKIN (0-D homogeneous model for closed system) modules of the CHEMKIN II Package. Four different methane oxidation mechanisms were used in the kinetic modelling approach to describe the chemical reaction performance of the nonthermal plasma reactor for dry reforming at high pressure. Overall, the kinetic model with the different methane oxidation mechanisms gave good agreement with the experimental results. Kinetics analysis performed using the code SENKIN from the CHEMKIN-II package and the GRI-Mech 3.0 scheme showed the conversion of CH_4 and CO_2 to depend strongly on the residence time.

A three-dimensional time dependent magneto hydrodynamics (MHD) model of the arc discharge was set up with Code_Saturne. The low current high-voltage arc discharge was studied for pressure ranges of 2 to 10 MPa at a current of 0.35 A and for current ranges of 0.25 to 0.40 A at a pressure of 8 MPa with helium using the assumption of local thermal equilibrium (LTE) in the model. A typical reference case at a pressure of 8 MPa and a current of 0.35 A was also studied for helium. Good agreement with experimental data was obtained. From the MHD results, a bending of the arc shape and a motion of the anodic arc root towards the top of the reactor was observed. This phenomenon was also observed in the experimental study with helium. In addition, the results of the MHD model showed that the increase of the working pressure has no effect on the arc radius, but leads to an increase in the volume of the gas treated by the arc discharge subject to natural convection.

In conclusion, the potential of the high pressure arc discharge in the synthesis of fluorocarbons and hydrocarbons was demonstrated in this research project. In addition, a relevant knowledge base has been created with respect to high pressure and very high pressure arc discharge, products distribution, and plasma chemistry understanding for fluorocarbons and hydrocarbons synthesis.

Chapter 8

RECOMMENDATIONS

The study of high pressure electric arc discharge was found to be highly challenging considering the difficulty encountered in igniting and sustaining the discharge at pressures above 0.1 MPa using a low current and a high voltage power supply. Hence, the following recommendations have been made to allow for proper and smooth operation of the high pressure plasma reactor for future research work.

(1) In order to successfully operate at pressures ranging from 1 to 17 MPa for any planned experiment, the current of 0.35 A should be used as this was found to be the minimum current possible to ignite and sustain the discharge as the pressure exceed 2 MPa for gas mixtures and reactive gases.
(2) When working with electronegative gases especially CO_2 and CF_4 as observed in the course of this study, it is necessary to dilute the gases with high ratio of helium in percent as this helps to stabilise and sustained the discharge at high pressure above 1 MPa.
(3) Before generating electric discharge under any experimental conditions, it is essential to purge the reactor twice with the new mixture and sample the gas mixture afterwards in order to verify the absence of heavy molecule gases from previous experiment as well as reconfirm the new gas mixture ratio.
(4) Sampling the gas at high pressure with the current setup needs to be carefully carried out. Thus, the possibility of an online sampling system using the ROLSI™ for example is recommended for future ease in sampling.

As mentioned in the introduction section of the MHD modelling and possibly kinetic modelling, the following recommendations are made:

(5) A two-temperature modelling of low current discharge at high pressure should be looked at in future work especially since such conditions usually lead to deviation from thermodynamic equilibrium within the discharge.
(6) Development of a nonequilibrium model (chemical and thermal nonequilibrium) in future work could support the treatment of the sheath regions, which was not accounted for by the current MHD model, used in this study for very high pressure modelling.

(7) For future work, computational fluid dynamic (CFD) modelling that integrates reaction kinetics and mechanism for the dry reforming process within the discharge volume at very high pressure should be explored. This will provide better understanding of the plasma process and importance at such pressures.

(8) Future experimental studies regarding the synthesis of fluorochemicals other than the carbon-fluoride compounds can be investigated using high pressure arc discharge. This would increase the existing knowledge of high pressure application in the formation of fluorochemicals.

(9) The current reactor configuration does not allow for the sampling of liquid products without opening up the entire reactor chamber. Thus, future modifications should be carried out on the reactor to enable its usage in experiments involving liquid reactants and products.

Additional recommendations are mentioned below for successfully running of the high pressure plasma reactor.

(10) In the course of the study on fluorocarbon formation, it was observed that the highly reactive nature of fluorine in the perfluorcarbons causes it to attack most of the materials used as insulator for the fixed electrode as well as the mobile electrode holder. While this was not experienced at all in the hydrocarbon studied, it is recommended that for a tungsten electrode, aluminium and titanium should be used as the electrode holder. Only ceramics made of alumina was found to resist the overall mechanical and chemical challenges associated with the use of a fluorocarbon gas (CF_4) during this study. Thus, overall for high pressure operation, alumina should be used as the insulator for the fixed electrode.

(11) The elaboration of a new reactor configuration in order to increase the ratio of the active discharge volume to the reactor volume without necessarily studying the effect of interelectrode gap as a parameter should be considered as this could probably improve the synthesis kinetics of $C_n>2$ hydrocarbons and fluorocarbons.

REFERENCES

[1] Raizer YP (1991) Gas Discharge Physics. Springer-Verlag, Berlin Heidelberg

[2] Meek JM, Craggs JD (1953) Electrical Breakdown of Gases. The Clarendon Press, Oxford

[3] Izquierdo E, Gonzalez-Aguilar J, Fulcheri L (2009) Electrical characterization of very high pressure Ar/H_2 low-current arc discharge, J High Temp Mater Process 13:71–76

[4] Fulcheri L, Rohani V, Fabry F, Traisnel N (2010) Experimental electrical characterization of a low-current tip–tip arc discharge in helium atmosphere at very high pressure. Plasma Sources Sci Technol 19:045010

[5] Arkhipenko V, Kirillov AA, Safronau YA, Simonchik LV , Zgirouski SM (2009) Self-sustained dc atmospheric pressure normal glow discharge in helium: from microamps to amps Plasma Sources Sci Technol 18:045013

[6] Gesser HD, Hunter NR, Probawono D (1998) The CO_2 Reforming of Natural Gas in a Silent Discharge Reactor. Plasma Chem Plasma Process 18: 241-245

[7] Zhou LM, Xue B, Kogelschatz U, Eliasson B (1998) Nonequilibrium Plasma Reforming of Greenhouse Gases to Synthesis Gas. Energ Fuel 12:1191-1199

[8] Thanyachotpaiboon K, Chavadej S, Caldwell TA, Lobban LL, Mallinson RG (1998) Conversion of Methane to Higher Hydrocarbons in AC Nonequilibrium Plasmas. AIChE J 44:2252-2257

[9] Malik MA, Jiang XZ (1999) The CO_2 Reforming of Natural Gas in a Pulsed Corona Discharge Reactor. Plasma Chem Plasma Process 19:505-512

[10] Liu C-J, Xu G-H, Wang T (1999) Non-thermal plasma approaches in CO utilization. Fuel Process Technol 58:119-134

[11] Goujard V, Tatibouet J-M, Batiot-Dupeyrat C (2009) Use of a non-thermal plasma for the production of synthesis gas from biogas. Appl Catal A Gen 353:228-235

[12] Ghorbanzadeh AM, Lotfalipour R, Rezaei S (2009) Carbon dioxide reforming of methane at near room temperature in low energy pulsed plasma. Int J Hydrogen Energy 34:293-298

[13] Wang Q, Yan B-H, Jin Y, Cheng Y (2009) Investigation of Dry Reforming of Methane in a Dielectric Barrier Discharge Reactor. Plasma Chem Plasma Process 29:217-228

[14] Xiang L, Mei-gui B, Xu-mei T, Shu-yong S, Yong-xiang Y, Xiao-yan D (2010) Carbon dioxide reforming of methane to synthesis gas by an atmospheric pressure plasma jet. J Fuel Chem Technol 38:195-200

[15] Matin NS, Jalili AH, Jenab MH, Zekordi SM, Afzali A, Rasouli C, Zamaniyan A (2010) DC-Pulsed Plasma for Dry Reforming of Methane to Synthesis Gas. Plasma Chem Plasma Process 30:333-347

[16] Hwang N, Song Y-H, Cha MS (2010) Efficient Use of CO_2 Reforming of Methane With an Arc-Jet Plasma. IEEE Trans Plasma Sci 38:3291-3299

[17] Goujard V, Nozaki T, Yuzawa S, Ağiral A, Okazaki K (2011) Plasma-assisted partial oxidation of methane at low temperatures: numerical analysis of gas-phase chemical mechanism. J Phys D Appl Phys 44:274011

[18] Pinhão NR, Janeco A , Branco JB (2011) Influence of Helium on the Conversion of Methane and Carbon dioxide in a Dielectric Barrier Discharge. Plasma Chem Plasma Process 31:427-439

[19] Rueangjitt N, Sreethawong T, Chavadej S, Sekiguchi H (2011) Non-Oxidative Reforming of Methane in a Mini-Gliding Arc Discharge Reactor: Effects of Feed Methane Concentration, Feed Flow Rate, Electrode Gap Distance, Residence Time, and Catalyst Distance. Plasma Chem Plasma Process 31:517-534

[20] Li X-S, Zhu B, Shi C, Xu Y, Zhu A-M (2011) Carbon Dioxide Reforming of Methane in Kilohertz Spark-Discharge Plasma at Atmospheric Pressure. AIChE J 57:2854-2860

[21] Schofield H (1999) Fluorine chemistry statistics: numbers of organofluorine compounds and publications associated with fluorine chemistry. J Fluorine Chem 100:7-11

[22] Schwerin L (1940) Fluorspar-Its chemical and industrial applications. J Chem Edu 17:160-165

[23] Rotberg RI (1980) Suffer the future: Policy Choices in Southern Africa, Economic Strength and Vulnerabilities. Harvard University Press

[24] Media Release from NECSA by C. Janneker and E. Mulane, 23 March 2009, available online at http://www.necsa.co.za/Press-Room/Press-Releases [Accessed 19.03.2010]

[25] Kalra CS, Gutsol AF, Fridman AA (2005) Gliding Arc Discharges as a Source of Intermediate Plasma for Methane Partial Oxidation. IEEE Trans Plasma Sci 33:32-41

[26] Fridman A, Kennedy LA (2004) Plasma Physics and Engineering. Taylor & Francis Books Inc. New York

[27] Kado S, Urasaki K, Sekine Y, Fujimoto K (2003) Direct conversion of methane to acetylene or syngas at room temperature using non-equilibrium pulsed discharge. Fuel 82:1377-1385

[28] Anderson RP, Fincke JR, Taylor CE (2002) Conversion of natural gas to liquids via acetylene as an intermediate. Fuel 81:909-925

[29] Gannon RE (2000) Acetylene from Hydrocarbons. Kirk-Othmer Encyclopedia of Chemical Technology, Wiley & Sons Inc: New York

[30] Edwards JE, Maitra AM (1995) The chemistry of methane reforming with carbon dioxide and its current and potential applications. Fuel Process Technol 42:269-289

[31] Aasberg-Petersen K, Bak Hansen J-H, Christensen TS, Dybkjaer I, Christensen PS, Nielsen CS, Winter Madsen SEL, Rostrup-Nielsen JR (2001) Technologies for large-scale gas conversion. Appl Catal A Gen 221:379–387

[32] Huang A, Xia G, Wang J, Suib SL, Hayashi Y, Matsumoto H (2000) CO_2 Reforming of CH_4 by Atmospheric Pressure ac Discharge Plasmas. J Catal 189:349-359

[33] Gordon CL, Lobban LL, Mallinson RG (2000) The Production of Hydrogen from Methane using Tubular Plasma Reactors In: Advances in Hydrogen Energy. Editors (Padró CEG, Lau F) Kluwer Academic/Plenum Publisher 2000: 57-67

[34] Okumoto M, Mizuno A (2001) Conversion of methane for higher hydrocarbon fuel synthesis using pulsed discharge plasma method. Catal Today 71:211-217

[35] Yao SL, Okumoto M, Nakayama A, Suzuki E (2001) Plasma Reforming and Coupling of Methane with Carbon Dioxide. Energ Fuel 15:1295-1299

[36] Liu C-J, Xue B, Eliasson B, He F, Li Y, Xu G-H (2001) Methane Conversion to Higher Hydrocarbons in the Presence of Carbon Dioxide Using Dielectric-Barrier Discharge Plasmas. Plasma Chem Plasma Process 21:301-310

[37] Yao SL, Suzuki E, Meng N, Nakayama A (2002) A High-Efficiency Reactor for the Pulsed Plasma Conversion of Methane, Plasma Chem Plasma Process 22:225-237

[38] Li Y, Liu C-J, Eliasson B, Wang Y (2002) Synthesis of Oxygenates and Higher Hydrocarbons Directly from Methane and Carbon Dioxide Using Dielectric-Barrier Discharges: Product Distribution. Energ Fuel 16:864-870

[39] Brock SL, Shimojo T, Suib SL, Hayashi Y, Matsumoto H (2002) Application of non-thermal atmospheric pressure ac plasmas to the carbon dioxide reforming of methane. Res Chem Intermediat 28:13-24

[40] Hwang B-B, Yeo Y-K, Na B-K (2003) Conversion of CH_4 and CO_2 to Syngas and Higher Hydrocarbons Using Dielectric Barrier Discharge. Korean J Chem Eng 20:631-634

[41] Kim S-S, Lee H, Na B-K, Song HK (2003) Reaction Pathways of Methane Conversion in Dielectric-Barrier Discharge, Korean J Chem Eng 20:869-872

[42] Zhang Y-P, Li Y, Wang Y, Liu C-J, Eliasson B (2003) Plasma methane conversion in the presence of carbon dioxide using dielectric-barrier discharges. Fuel Process Technol 83:101-109

[43] Zhang J-Q, Zhang J-S, Yang Y-J, Liu Q (2003) Oxidative Coupling and Reforming of Methane with Carbon Dioxide Using a Pulsed Microwave Plasma under Atmospheric Pressure. Energ Fuel 17:54-59

[44] Li M-W, Xu G-H, Tian Y-L, Chen L, Fu HF (2004) Carbon Dioxide Reforming of Methane Using DC Corona Discharge Plasma Reaction. J Phys Chem A 108:1687-1693

[45] Ghorbanzadeh AM, Modarresi H (2007) Carbon dioxide reforming of methane by pulsed glow discharge at atmospheric pressure: The effect of pulse compression. J Appl Phys 101:123303

[46] Matin NS, Savadkoohi HA, Feizabadi SY (2008) Methane Conversion to C_2 Hydrocarbons Using Dielectric-barrier Discharge Reactor: Effects of System Variables. Plasma Chem Plasma Process 28:189-202

[47] Bo Z, Yan J, Li X, Chi Y, Cen K (2008) Plasma assisted dry methane reforming using gliding arc gas discharge: Effect of feed gases proportion. Int J Hydrogen Energy 33:5545-5553

[48] Bromberg L, Cohn DR, Rabinovich A, O'Brien C , Hochgreb S (1998) Plasma Reforming of Methane. Energ Fuel 12:11-18

[49] Kogelschatz U (2004) Atmospheric-pressure plasma technology. Plasma Phys. Control Fusion 46: B63–B75

[50] A Staff Feature (1963) Plasma Fourth State of Matter. Ind Eng Chem 55:16-23

[51] Burm KTAL (2012) Plasma: The Fourth State of Matter. Plasma Chem Plasma Process 32:401-407

[52] Shimizu K, Sugiyama T, Samaratunge MNL (2008) Study of Air Pollution Control by Using Micro Plasma Filter. IEEE Trans Ind Appl 44:506-511

[53] Malik MA (2010) Water Purification by Plasmas: Which Reactors are Most Energy Efficient? Plasma Chem Plasma Process 30:21-31

[54] Heberlein J, Murphy AB (2008) Thermal plasma waste treatment. J Phys D: Appl Phys 41:053001 (20pp)

[55] Dinelli G, Civitano L, Rea M (1990) Industrial experiments on pulse corona simultaneous removal of NO_x AND SO_2 from flue gas. IEEE Trans Ind Appl 26:535-541

[56] Shohet JL (1991) Plasma-Aided Manufacturing. IEEE Trans Plasma Sci 19:725-733

[57] Wolf R, Sparavigna AC (2010) Role of Plasma Surface Treatments on Wetting and Adhesion. Eng 2:397-402

[58] Kobashi K, Nishimura K, Kawate Y, Horiuchi T (1988) Synthesis of diamonds by use of microwave plasma chemical-vapor deposition: Morphology and growth of diamond films. Phys Rev B 38:4067-4084

[59] Bica I (1999) Nanoparticle production by plasma. Mater Sci Eng B68:5–9

[60] Hayashi N, Tsutsui S, Tomari T, Guan W (2008) Sterilization of Medical Equipment Using Oxygen Radicals Produced by Water Vapor RF Plasma. IEEE Trans Plasma Sci 36:1302-1303

[61] Höcker H (2002) Plasma treatment of textile fibers. Pure Appl Chem 74:423–427

[62] Speckhofer G, Schmidt H-P (1996) Experimental and Theoretical Investigation of High-pressure Arcs-Part II: The Magnetically Deflected Arc (Three-Dimensional Modeling). IEEE Trans Plasma Sci 24:1239-1248

[63] Schmidt H-P, Speckhofer G (1996) Experimental and Theoretical Investigation of High-pressure Arcs-Part I: The Cylindrical Arc Column (Two-Dimensional Modeling). IEEE Trans Plasma Sci 24:1229-1238

[64] Tomai T, Ito T, Terashima K (2006) Generation of dielectric barrier discharge in high-pressure N_2 and CO_2 environments up to supercritical conditions. Thin Solid Films 506–507:409-413

[65] Bogomaz AA, Budin AV, Kolikov VA, Pinchuk ME, Pozubenkov AA, Rutberg FG (2002) Influence of the Cathode and Anode Jets on the Properties of a High-Current Electric Arc. Technical Physics 47:26–33. Translated from Zhurnal Tekhnichesko ĭ Fiziki, (2002) 72:28–35

[66] Terashima K, Howald L, Haefke H, Giintherodt H-J (1996) Development of a mesoscale/nanoscale plasma generator. Thin Solid Films 281-28:634-636

[67] Lock EH, Saveliev AV, Kennedy LA (2005) Initiation of Pulsed Corona Discharge Under Supercritical Conditions. IEEE Trans Plasma Sci 33:850-853

[68] Lock EH, Saveliev AV, Kennedy LA (2009) Influence of Electrode Characteristics on DC Point-to-Plane Breakdown in High-Pressure Gaseous and Supercritical Carbon Dioxide. IEEE Trans Plasma Sci 37: 1078-1083

[69] Goto M, Sasaki M, Kiyan T, Fang T, Roy BC, Namihira T, Akiyama H, Hara M (2008) Reaction in Plasma Generated in Supercritical Carbon Dioxide. Joint 21st AIRAPT and 45th EHPRG Int. Conf. on High Pressure Science and Technology, Journal of Physics: Conference Series 121:1-8

[70] Tendero C, Tixier C, Tristant P, Desmaison J, Leprince P (2006) Atmospheric pressure plasmas: A review. Spectrochimica Acta Part B 61:2-30

[71] Lieberman MA, Lichtenberg AJ (1994) Principles of Plasma Discharges and Materials Processing. John Wiley & Sons Inc. New York

[72] Sobolewski MA, Langan JG, Felker BS (1998) Electrical optimization of plasma-enhanced chemical vapor deposition chamber cleaning plasmas. J Vac Sci Technol B 16:173-182

[73] Leroux F, Perwuelz A, Campagne C, Behary N (2006) Atmospheric air plasma treatments of polyester textile structures. J Adhes Sci and Technol 20:939-957

[74] Ouellette RP, Barbier MM, Cheremisinoff PN (1980) Low-Temperature Plasma Technology Applications. Electrotechnology 5, Ann Arbor Science Publishers Inc

[75] Schutze A, Jeong JY, Babayan SE, Park J, Selwyn GS, Hicks RF (1998) The atmospheric-pressure plasma jet: A review and comparison to other plasma sources. IEEE Trans Plasma Sci 26:1685-1694

[76] Schoenbach KH, El-Habachi A, Shi W, Ciocca M (1997) High-pressure hollow cathode discharges. Plasma Sources Sci Technol 6:468-477

[77] Staack D, Farouk B, Gutsol A, Fridman A (2008) DC normal glow discharges in atmospheric pressure atomic and molecular gases. Plasma Sources Sci Technol 17:025011-025013

[78] Kunhardt EE (2000) Generation of Large-Volume Atmospheric-Pressure Nonequilibrium Plasmas. IEEE Trans Plasma Sci 28:189-200

[79] Staack D (2008) Characterization and stabilization of atmospheric pressure dc microplasmas and their application to thin film deposition. Ph.D. Thesis Drexel University, Philadelphia U.S.A

[80] Conrads H, Schmidt M (2000) Plasma generation and plasma sources. Plasma Sources Sci Technol 9 :441-454

[81] Winchester MR, Lazik C, Marcus RK (1991) Characterization of a radio frequency glow discharge emission source. Spectrochim Acta 46B:483-499

[82] Harry J (2010) Introduction to Plasma Technology: Science, Engineering and Applications. Wiley-VCH Verlag GmbH & Co. KGaA, Weinheim

[83] Druyvesteyn MJ, Penning FM (1940) The Mechanism of Electrical Discharges in Gases of Low Pressure. Rev Mod Phys 12: 87-174

[84] Yahya AA, Harry JE (1999) Factors affecting the glow-to-arc transition at the cathode of an electric discharge at atmospheric pressure. Int J Electron 86:755-762

[85] Roth JR (1995) Industrial Plasma Engineering Vol.1 Institute of Physics Publishing, Bristol and Philadelphia as cited by Fulcheri et al.[4]

[86] Brown SC (1959) Basic Data of Plasma Physics: the Fundamental Data on Electric Discharges in Gases. MIT Press, Cambridge MA (reprinted 1997 Classics in Vacuum Sci Technol Springer, New York)

[87] Benilov MS (2008) Understanding and modelling plasma–electrode interaction in high-pressure arc discharges: a review. J Phys D:Appl Phys 41:144001(30pp)

[88] Eliasson B, Kogelschatz U (1991) Nonequilibrium Volume Plasma Chemical Processing. IEEE Trans Plasma Sci 19:1063-1077

[89] Fan HY (1939) The Transition from Glow Discharge to Arc. Physical Review 55:769-775

[90] Staack D, Farouk B, Gutsol A, Fridman A (2009) Stabilization of the ionization overheating thermal instability in atmospheric pressure microplasmas. J Appl Phys 106:013303

[91] Dyuzhev GA (2002) Low-Temperature Plasma and Fullerenes. Plasma Devices Operat 10:63-98

[92] Huska P, Clump CW (1967) Decomposition of Molybdenum Disulfide in an Induction-Coupled Argon Plasma. Ind Eng Chem Proc Design Develop 6:238-244

[93] Kong PC, Lau YC (1990) Plasma synthesis of ceramic powders. Pure Appl Chem, 62:1809-1816

[94] Stokes CS, Cahill JA (1965) Plasma Jet Chemistry. The Research Institute of Temple University, Philadelphia, PA

[95] Grosse AV, Stokes CS (1972) U.S. Patent No. 3,666,408. Germantown Laboratories Inc. Philadelphia, PA

[96] Baddour RF, Bronfin BR (1965) Production of Tetrafluoroethylene by Reaction of Carbon and Carbon Tetrafluoride in an Electric Arc. Ind Eng Chem Proc Design Develop 4:162-166

[97] Nassau K, Shiever JW (1975) Plasma torch preparation of high purity, low OH content fused silica. Ceram Bull 54:1004-1009

[98] Suriyanarayanan N, Kannannithin KV, Bernardo E (2009) Mullite Glass Ceramics Production from Coal Ash and Alumina by High Temperature Plasma. J Non-Oxide Glasses 1:251-264

[99] National Materials Advisory Board, Committee on Plasma Processing of Materials (1985) Plasma processing of materials. Publication NMAB-415, National Academy Press, Washington DC

[100] Ibberson VJ, Thring MW (1969) Plasma Chemical and Process Engineering. Ind Eng Chem 61:48-61

[101] Kizling MB, Järås SG (1996) A review of the use of plasma techniques in catalyst preparation and catalytic reactions. Appl Cata A: General 147:1-21

[102] Midgley T Jr. (1938) Man-Made Molecules. J Ind Eng Chem 30:120-122

[103] Simons JH (1949) Production of Fluorocarbons I. The Generalized Procedure and its Use with Nitrogen Compounds. J Electrochem Soc 95:47-52

[104] Schlosser M (1998) Parametrization of Substituents: Effects of Fluorine and Other Heteroatoms on OH-, NH- and CH-Acidities. Angew Chem Int Ed 37: 1496-1513

[105] Plunkett RJ (1941) Tetrafluoroethylene Polymers. U.S. Patent 2,230,654

[106] Dolbier WR Jr. (2005) Fluorine chemistry at the millennium. J Fluorine Chem 126 157–163

[107] Isanbor C, O'Hagan D (2006) Fluorine in medicinal chemistry: A review of anti-cancer agents. J Fluorine Chem. 127: 303–319

[108] Kirk KL (2006) Fluorine in medicinal chemistry: Recent therapeutic applications of fluorinated small molecules. J Fluorine Chem 127:1013-1029

[109] Baddour RF, Dundas PH (1967) The Application of Plasmas to Chemical Processing. Edited Baddour RF, Timmins RS Pergamon Press New York

[110] Bronfin BR (1967) The Application of Plasmas to Chemical Processing. Edited by Baddour RF, Timmins RS Pergamon Press New York

[111] Timmins RS, Ammann PR (1967) The Application of Plasmas to Chemical Processing. Edited by Baddour RF, Timmins RS Pergamon Press New York

[112] Goldberger WM, Oxley JH (1963) Quenching the Plasma Reaction by Means of the Fluidized Bed. AIChE J 9:778

[113] Grey J, Jacobs PF (1964) Experiments on Turbulent Mixing in a Partially Ionized Gas. AIAA J 2:433

[114] Bronfin BR, Hazlett RN (1966) Synthesis of Nitrogen Fluorides in a Plasma Jet. Ind Eng Chem Fundam 5:472

[115] Dennis PR, Smith CR, Gates DW, Bond JB (1965) Plasma Jet Technology. Technol Survey NASA SP-5033

[116] Ruff O, Menzel W (1933) Neue Sauerstoff Fluoride: O_2F_2 und OF. Z Anorg Allgem Chem 211:20

[117] Bjornson G (1969) Plasma jet conversion of fluoroform. US Pat. 3,471,546

[118] Farlow MW (1955) Process of preparing tetrafluoroethylene. US Pat. 2,709,192

[119] Farlow MW (1961) Method for the preparation of fluorocarbons. US Pat. 2,981,761

[120] Farlow MW (1963) Method for the preparation of tetrafluoroethylene. US Pat. 3,081,245

[121] Malone BS (1990) Preparation of tetrafluoroethylene. US Pat. 4,973,773

[122] Cook NC, Wolfe JK (1957) Transient arc method of preparing fluorocarbons. US Pat.2,785,119

[123] Webster JL (1997) Preparation of tetrafluoroethylene. US Pat. 5,684,218

[124] Webster JL (1998) Process for the preparation of perfluorocarbons. US Pat. 5,744,657

[125] Swanepoel J, Lombaard R (1997) Production of fluorocarbon compounds. US Pat.5,611,896

[126] Fridman A (2008) Plasma Chemistry. Cambridge University Press

[127] Baddour RF, Timmins RS eds. (1967) The Application of Plasmas to Chemical Processing. The MIT Press, Massachusetts Institute of Technology, Cambridge

[128] Truesdale EA, Smolinsky G (1979) The effect of added hydrogen on the rf discharge chemistry of CF_4, CF_3H, and C_2F_6. J Appl Phys 50:6594-6599

[129] Truesdale EA, Smolinsky G, Mayer TM (1980) The effect of added acetylene on the rf discharge chemistry of C_2F_6. A mechanistic model for fluorocarbon plasmas. J Appl Phys 51:2909-2913

[130] Denison JT, Edlin FE, Whipple GH (1958) Preparation of tetrafluoroethylene. US Pat.2,852,574

[131] Von Tress WR (1964) Preparation of tetrafluoroethylene. US Pat. 3,133,871

[132] Petitpas G, Rollier J-D, Darmon A, Gonzalez-Aguilar J, Metkemeijer R, Fulcheri L (2007) A comparative study of non-thermal plasma assisted reforming technologies. Int J Hydrogen Energy 32:2848-2867

[133] Tao X, Bai M, Li X, Long H, Shang S, Yin Y, Dai X (2011) CH_4-CO_2 reforming by plasma - challenges and opportunities. Progress in Energy and Combustion Science 37:113-124

[134] Istadi, Amin NAS (2007) Catalytic-Dielectric Barrier Discharge Plasma Reactor for Methane and Carbon Dioxide Conversion. Bull Chem React Eng Catal 2:37-44

[135] Kraus M, Eliasson B, Kogelschatz U, Wokauna A (2001) CO_2 reforming of methane by the combination of dielectric-barrier discharges and catalysis. Phys Chem Chem Phys 3:294-300

[136] Eliasson B, Liu C-J, Kogelschatz U (2000) Direct Conversion of Methane and Carbon Dioxide to Higher Hydrocarbons Using Catalytic Dielectric-Barrier Discharges with Zeolites. Ind Eng Chem Res 39:1221-1227

[137] Sentek J, Krawczyk K, Mlotek M, Kalczewska M, Kroker T, Kolb T, Schenk A, Gericke K-H, Schmidt-Szalowski K (2010) Plasma-catalytic methane conversion with carbon dioxide in dielectric barrier discharges. Appl Catal B Environ 94:19-26

[138] Pham MH, Goujard V, Tatibouët JM, Batiot-Dupeyrat C (2011) Activation of methane and carbon dioxide in a dielectric-barrier discharge-plasma reactor to produce hydrocarbons-Influence of La_2O_3/γ-Al_2O_3 catalyst. Catal Today 171:67-71

[139] Thanyachotpaiboon K, Chavadej S, Caldwell TA, Lobban LL, Mallinson RG (1998) Conversion of Methane to Higher Hydrocarbons in AC Nonequilibrium Plasmas. AIChE J 44:2252-2257

[140] Czernichowski A (2001) GlidArc Assisted Preparation of the Synthesis Gas from Natural and Waste Hydrocarbons Gases. Oil & Gas Science and Technology – Rev IFP 56:181-198

[141] Rusu I, Cormier J-M (2003) On a possible mechanism of the methane steam reforming in a gliding arc reactor. Chem Eng J 91:23–31

[142] Indarto A, Choi J-W, Lee H, Song HK (2005) Kinetic Modeling of Plasma Methane Conversion Using Gliding Arc. J Natural Gas Chem 14:13-21

[143] Tao X, Bai M, Wu Q, Huang Z, Yin Y, Dai X (2009) CO_2 reforming of CH_4 by binode thermal plasma. Int J Hydrogen Energy 34:9373-9378

[144] Long H, Shang S, Tao X, Yin Y, Dai X (2008) CO_2 reforming of CH_4 by combination of cold plasma jet and Ni/Y-Al2O3 catalyst. Int J Hydrogen Energy 33:5510-5515

[145] Indarto A, Choi JW, Lee H, Song HK (2006) Effect of additive gases on methane conversion using gliding ac discharge. Energy 31:2986-2995

[146] Yan BH, Wang Q, Jin Y, Cheng Y (2010) Dry Reforming of Methane with Carbon Dioxide Using Pulsed DC Arc Plasma at Atmospheric Pressure. Plasma Chem Plasma Process 30:257-266

[147] Farouk TI (2009) Modeling and Simulations of DC and RF Atmospheric Pressure Non-thermal Micro Plasma Discharges: Analysis and Applications. Ph.D. Thesis Drexel University, Philadelphia, U.S.A

[148] Birdsall CK, Langdon AB (2004) Plasma Physics via Computer Simulation. Institute of Physics Publishing, CRC Press, New York

[149] Birdsall CK (1991) Particle-in-cell charged-particle simulations plus Monte Carlo collisions with neutral atoms PIC-MCC. IEEE Trans Plasma Sci 19:65-85

[150] Hutchchinson IH (2002) Principles of Plasma Diagnostics. 2nd edition Cambridge University Press

[151] Nasser E (1971) Fundamentals of Gaseous Ionization and Plasma Electronics. New York: Wiley Interscience

[152] Meyyappan M, Kreskovsky JP (1990) Glow discharge simulation through solutions to the moments of the Boltzmann transport equation. J Appl Phys 68:1506

[153] Ingold J H (1989) Moment method applied to gaseous electronics. Phys Rev E 40:3855-3863

[154] Smirnov BM (2009) Modeling of gas discharge plasma. Phys-Uspekhi 52:559-571

[155] Bogaerts A, De Bie C, Eckert M, Georgieva V, Martens T, Neyts E, Tinck S (2010) Modeling of the plasma chemistry and plasma–surface interactions in reactive plasmas. Pure Appl Chem 82:1283–1299

[156] Graves D, Jensen K (1986) Continuum model of DC and RF discharges. IEEE Trans Plasma Sci 14:78-91

[157] Graves D (1987) Fluid model simulations of a 13.56 MHz RF discharge: time and space dependence of rates of electron impact excitation. J Appl Phys 62:88-94

[158] Meyyappan M (1991) A continuum model for low pressure radio frequency discharges. J Appl Phys 69:8047-8054

[159] Boeuf J (1987) Numerical model of rf glow discharges. Phys Rev A 36:2782-2792

[160] Meyyappan M, Govindan T (1991) Modeling of electronegative radio frequency discharges. IEEE Trans Plasma Sci 19:122-129

[161] Park S, Economou D (1990) Analysis of low pressure glow discharges using a continuum model. J Appl Phys 68:3904-3915

[162] Iza F, Lee SH, Lee JK (2007) Computer modeling of low-temperature plasmas. Gas Discharges - Fundamentals & Applications. Ed: Filho J de A Chapter 1:1-31

[163] Kortshagen U, Pukropski I, Tsendin LD (1995) Experimental investigation and fast two-dimensional self-consistent kinetic modeling of a low-pressure inductively coupled rf discharge. Phys Rev E 51:6063-6078

[164] Kolobov VI, Parker GJ, Hitchon WNG (1996) Modeling of nonlocal electron kinetics in a low-pressure inductively coupled plasma, Phys Rev E 53:1110-1124

[165] Degond P, Lucquin-Desreux B (2007) Mathematical models of electrical discharges in air at atmospheric pressure: a derivation from asymptotic analysis. Int J Computing Sci Math 1:58-97

[166] Surendra M, Graves D (1991) Particle simulations of radio-frequency glow discharges. IEEE Trans Plasma Sci 19:144-157

[167] Nagayama K, Farouk B, Lee YH (1996) Neutral and charged particle simulations of Ar plasma. Plasma Sources Sci Technol 5:685-695

[168] Nagayama K, Farouk B, Lee YH (1998) Modeling of RF plasma discharge of methane for carbon film deposition. IEEE Trans Plasma Sci 26:125-134

[169] Ivanov V, Proshina O, Rakhimova T, Rakhimov A, Herrebout D, Bogaerts A (2002) Comparison of a one-dimensional particle-in-cell - Monte Carlo Model and a one-dimensional fluid model for a CH_4/H_2 capacitively coupled radio frequency discharge. J Appl Phys 91:6296-6302

[170] Iza F, Yang S, Kim H, Lee J (2005) The mechanism of striation formation in plasma display panels. J Appl Phys 98:043302:1-5

[171] Schoenbach K, Chen H, Schaefer G (1990) A model of DC glow discharges with abnormal cathode fall. J Appl Phys 67:154-162

[172] Cartwright KL, Verboncoeur JP, Birdsall CK (2000) Nonlinear hybrid Boltzmann–particle-in-cell acceleration algorithm. Phys Plasma 7:3252-3264

[173] Porteous RK, Graves DB (1991) Modeling and Simulation of Magnetically Confined Low-Pressure Plasmas in Two Dimensions, IEEE Trans Plasma Sci 19:204-213

[174] Sommerer JT, Kushner JM (1992) Numerical investigation of the kinetics and chemistry of RF glow discharge plasmas sustained in He, N_2, O_2, $He/N_2/O_2$, $He/CF_4/O_2$ and SiH_4/NH_3 using a Monte Carlo Fluid hybrid model. J Appl Phys 71:1654-1673

[175] Kolobov V (2003) Fokker-Planck modelling of electron kinetics in plasmas and semiconductors. Comput Mater Sci 28:302-320

[176] Kolobov VI, Arslanbekov RR (2006) Simulation of electron kinetics in gas discharges. IEEE Trans Plasma Sci 34:895-909

[177] Arslanbekov R, Kolobov V (2003) Two-dimensional simulations of the transition from Townsend to glow discharge and subnormal oscillations. J Phys D: Appl Phys 36:1-9

[178] Rohani V, Iwarere S, Fabry F, Mourard D, Izquierdo E, Ramjugernath D, Fulcheri L (2011) Experimental study of hydrocarbon synthesis from syngas by a tip-tip electric discharge at very high pressure. Plasma Chem Plasma Process 31:663-679

[179] Lebouvier A, Delalondre C, Fresnet F, Boch V, Rohani V, Cauneau F and Fulcheri L (2011) Three-dimensional unsteady MHD modeling of a low current - high voltage non-transferred DC plasma torch operating with air. IEEE Trans Plasma Sci 39:1889-99

[180] Bogaerts A (1999) The glow discharge: an exciting plasma! J Anal At Spectrom 14:1375-1384

[181] Fiala A, Pitchford LC, Boeuf JP (1994) Two-dimensional, hybrid model of low-pressure glow discharges. Phys Rev E 49:5607-5622

[182] Boeuf JP, Punset C, Hirech A, Doyeux H (1997) Physics and Modeling of Plasma Display Panels. J Phys IV France 7:C4-3

[183] Lykas B, Amanatides E, Mataras D (2004) 2D Self–Consistent Modeling of Microcrystalline Silicon Deposition Process. 19th European Photovoltaic Solar Energy Conference:1395-1398

[184] Donko Z, Hartmann P, Kutasi K (2006) On the reliability of low-pressure dc glow discharge modelling. Plasma Sources Sci Technol 15:178-186

[185] Petrovic D, Martens T, Dijk Jv, Brok WJM, Bogaerts A (2009) Fluid modelling of an atmospheric pressure dielectric barrier discharge in cylindrical geometry. J Phys D: Appl Phys 42:205206

[186] Donko Z (2011) Particle simulation methods for studies of low-pressure plasma sources, Plasma Sources Sci Technol 20:024001

[187] Benilov MS, Naidis GV (2003) Modelling of low-current discharges in atmospheric-pressure air taking account of non-equilibrium effects. J Phys D: Appl Phys 36:1834-41

[188] Andresen P, Bath A, GrÖger W, Lülf HW, Meijer G, ter Meulen JJ (1988) Laser-induced fluorescence with tunable excimer lasers as a possible method for instantaneous temperature field measurements at high pressures: checks with an atmospheric flame. Appl Opt 27:365-378

[189] Bonitz M, Horing N, Ludwig P eds. (2010) Introduction to Complex Plasmas. Springer Series on Atomic, Optical, and Plasma Physics vol59, Springer

[190] Moreau N, Pasquiers S, Blin-Simiand N, Magne L, Jorand F, Postel C, Vacher J-R (2010) Propane dissociation in a non-thermal high-pressure nitrogen plasma. J Phys D: Appl Phys 43: 285201

[191] Mok YS, Kang H-C, Lee H-J, Koh DJ, Shin DN (2010) Effect of Nonthermal Plasma on the Methanation of Carbon Monoxide over Nickel Catalyst. Plasma Chem Plasma Process 30:437-447

[192] Cruden BA, Rao MVVS, Sharma SP, Meyyappan M (2002) Fourier transform infrared spectroscopy of CF_4 plasmas in the GEC reference cell. Plasma Sources Sci Technol 11:77-90

[193] Olthoff JK, Greenberg KE (1995) The Gaseous Electronics Conference RF Reference Cell-An Introduction. J Res Natl Inst Stand Technol 100:327-339

[194] Barz JP, Oehr C, Lunk A (2011) Analysis and Modeling of Gas-Phase Processes in a CHF_3/Ar Discharge. Plasma Process Polym 8:409-423

[195] Ivanov VV, Klopovski ĭ KS, Lopaev DV, Proshina OV, Rakhimov AT, Rakhimova TV, and Rulev GB (2002) Kinetics of the Reactions Involving CF_2 and CF in a Pure Tetrafluoromethane Plasma: I. Production of CF_2 and CF via Electron-Impact Dissociation. Plasma Phys Rep 28:229-242. Translated from Fizika Plazmy (2002) 28:257-271

[196] Kiss LDB, Sawin HH (1992) Evaluation of CF_4 Plasma Chemistry by Power Modulation. Plasma Chem Plasma Process 12:523-549

[197] Plumb IC, Ryan KR (1986) A Model of the Chemical Processes Occurring in CF_4/O_2 Discharges Used in Plasma Etching. Plasma Chem Plasma Process 6:205-230

[198] Slovestsky DI (1990) Modelling of chemical reactions under nonequilibrium halogenated electrical discharge conditions. Pure Appl Chem 62:1729-1742

[199] Wang W, Wu Y, Rong M, Éhn L, Černušák I (2012) Theoretical computation of thermophysical properties of high-temperature F_2, CF_4, C_2F_2, C_2F_4, C_2F_6, C_3F_6 and C_3F_8 plasmas. J Phys D: Appl Phys 45:285201

[200] Sun J-W, Park D-W (2003) CF_4 Decomposition by Thermal Plasma Processing. Korean J Chem Eng 20:476-481

[201] Kokkoris G, Goodyear A, Cooke M, Gogolides E (2008) A global model for C_4F_8 plasmas coupling gas phase and wall surface reaction kinetics. J Phys D: Appl Phys 41:195211

[202] d'Agostino R, Cramarossa F, De Benedictis S (1982) Diagnostics and Decomposition Mechanism in Radio-Frequency Discharges of Fluorocarbons Utilized for Plasma Etching or Polymerization. Plasma Chem Plasma Process 2:213-231

[203] d'Agostino R, Cramarossa F, De Benedictis S (1984) Chemical Mechanisms in C_3F_8-H_2 Radiofrequency Discharges. Plasma Chem Plasma Process 4:21-31

[204] Hagelaar GJM, Pitchford LC (2005) Solving the Boltzmann equation to obtain electron transport coefficients and rate coefficients for fluid models. Plasma Sources Sci Technol 14:722-733

[205] SIGLO-RF v.1.11(1998) online, www.siglo-kinema.com

[206] Benilov MS, Naidis GV (2006) Modeling of hydrogen-rich gas production by plasma reforming of hydrocarbon fuels. Int J Hydrogen Energy 31:769-774

[207] Smith GP, Golden DM, Frenklach M, Moriarty NW, Eiteneer B, Goldenberg M, et al. (http://me.berkeley.edu/gri_mech/)

[208] Konnov A.A (2000) Development and validation of a detailed reaction mechanism for the combustion of small hydrocarbons. 28th Symposium Int on Combustion, Abstr. Symp. Pap 317

[209] Hughes KJ, Turanyi T, Clague AR, Pilling MJ (2001) Development and testing of a comprehensive chemical mechanism for the oxidation of methane. Int J Chem Kinet 33:513-538 (http://www.chem.leeds.ac.uk/Combustion/methane.htm)

[210] De Bie C, Martens T, Dijk Jv, Paulussen S, Verheyde B, Corthals S, Bogaerts A (2011) Dielectric barrier discharges used for the conversion of greenhouse gases: modeling the plasma chemistry by fluid simulations. Plasma Sources Sci Technol 20:024008

[211] Machrafi H, Cavadias S, Amouroux J (2011) CO_2 valorization by means of Dielectric Barrier Discharge. J Phys: Conf Ser 275: 012016

[212] Izquierdo E (2008) Theoretical and experimental study of a high pressure electric discharge under non-reactive and reactive conditions to hydrocarbon synthesis. PhD thesis at Mines ParisTech

[213] Flinn JE (editor) (1971) Engineering, chemistry, and use of plasma reactors. Chem Eng Progress Symp Ser AIChE 112:67

[214] Parvulescu VI, Magureanu M, Lukes P (2012) Plasma Chemistry and Catalysis in Gases and Liquids. First Edition Wiley-VCH Verlag & Co. KGaA

[215] Pateyron B, Delluc G, Calve N (2005) N Mec Ind 5:651-654

[216] Nakamura Y (1991) Gaseous Electronics and its Applications, eds. Crompton RW, Hayashi M, Boyd DE, Makabe T, KTK Scientific Publishers, Tokyo, Japan

[217] Pedersen T, Brown R (1993) Simulation of electric field effects in premixed methane flames. Combustion and Flame, 94:433–448

[218] Kee RJ, Rupley FM, Miller JA (1989) CHEMKIN-II: a FORTRAN chemical kinetics package for the analysis of gas phase chemical kinetics. Sandia Report SAND89-8009

[219] Delalondre C, Zahrai S, Simonin O (1994) Turbulence modelling in electric arc. Proc Int Symp Heat Transf Under Plasma Conditions

[220] Bauchire J, Gonzalez J, Gleizes A (1997) Modeling of a DC plasma torch in laminar and turbulent flow. Plasma Chem Plasma Process 17:409–432

[221] Lebouvier A, Delalondre C, Fresnet F, Cauneau F, Fulcheri L (2012) 3D MHD modelling of low current–high voltage DC plasma torch under restrike mode. J Phys D: Appl Phys 45:025204

[222] Lebouvier A, Iwarere SA, Ramjugernath D, Fulcheri L (2013) 3D magnetohydrodynamic modelling of a dc low-current plasma arc batch reactor at very high pressure in helium. J Phys D: Appl Phys 46:145203

[223] Freton P, Gonzalez JJ, Escalier G (2009) Prediction of the cathodic arc root behaviour in a hollow cathode thermal plasma torch. J Phys D: Appl Phys 42:195205

[224] Park JM, Kim KS, Hwang TH, Hong SH (2004) Three-dimensional modeling of arc root rotation by external magnetic field in nontransferred thermal plasma torches. IEEE Trans Plasma Sci 32:479–487

[225] Gleizes A, Gonzalez J, Freton P (2005) Thermal plasma modelling. J Phys D: Appl Phys 38: R153–R183

[226] Selvan B, Ramachandran K, Sreekumar KP, Thiyagarajan TK , Ananthapadmanabhan PV (2009) Three-dimensional numerical modeling of an Ar-N_2 plasma arc inside a non-transferred torch. Plasma Sci Technol 11:679–87

Appendix A

CALIBRATION OF THE GAS CHROMATOGRAPHY DETECTOR

A1 Calibration of the GC Detectors with the Hydrocarbons and Elemental Gases

Calibrations of the GC detectors were carried out using the saturated and the unsaturated hydrocarbons (C_1 to C_4) and elemental gases (H_2, CO, CO_2, and N_2) as the calibration gas standards. From the peak area (P_{AREA}) obtained for the known concentration of the gases, the response factor (R_{FACTOR}) was calculated by assuming linearity over the concentration range for each of the gases investigated and then dividing the obtained peak area by the concentration of the reference standard.

Table A.1: GC calibration data for the hydrocarbons and elemental gases used in this project

Gas	R_{TIME} FID	P_{AREA} FID	R_{TIME} TCD	P_{AREA} TCD	Concentration (ppm)	R_{FACTOR} FID	R_{FACTOR} TCD
Hydrogen			2.07	999.800	40000	-	0.025
Hydrogen			2.2	23137.3	999995	-	0.023
Carbon dioxide	4.26	265888	4.16	1136.73	50000	5.318	0.023
Oxygen			11.09	930.915	50000	-	0.019
Nitrogen			11.81	983.925	50000	-	0.020
Carbon Monoxide	14.96	268730.5	14.86	983.700	50000	5.375	0.020
Ethylene	7.27	10815.80	7.28	22.3833	980	11.037	0.023
Acetylene	9.47	10000.03	9.47	19.0167	949	10.537	0.020
Ethane	10.30	10111.78	10.29	22.7375	1034	9.779	0.022
Methane	13.84	5080.248	13.85	16.7900	1030	4.932	0.016
Methane	13.84	212863.5	13.76	662.915	40000	5.322	0.017
Propylene	23.55	15640.07	23.56	36.9867	985	15.878	0.038
Propane	23.86	15011.33	23.88	40.4725	1030	14.574	0.039
Isobutane	27.00	20623.85	27.01	50.5267	1003	20.562	0.050

A2 Calibration of the GC Detector with the Fluorocarbons Gases

Various calibrations were performed for the GC in order to find the response of the FID to the C_1 to C_3 fluorocarbons. The number of moles of the various gases were calculated based on the ideal gas law for small volume of each gas injected (20 to 60 µl) and larger volume (100 to 200 µl) while the concentration of the unknown was then quantified using the GC area ratio method. The calibration curve for the GC with the fluorocarbon gases (CF_4, C_2F_4, C_2F_6, C_3F_6, and C_3F_8) are presented for the small volume range and the large volume range in Figures A1 to A10.

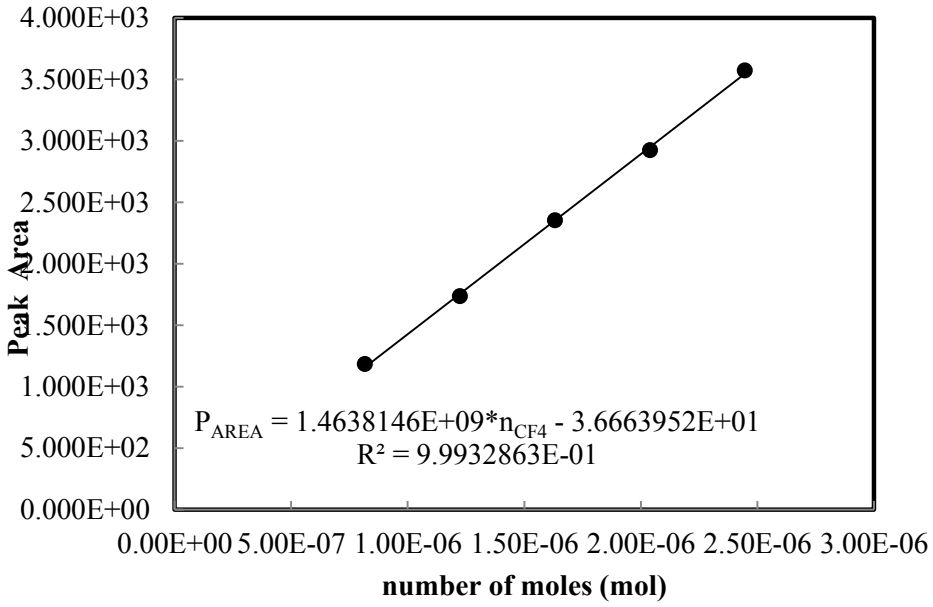

Figure A.1: GC calibration plot with CF_4 gas for injected syringe volumes of 20 to 60 µl

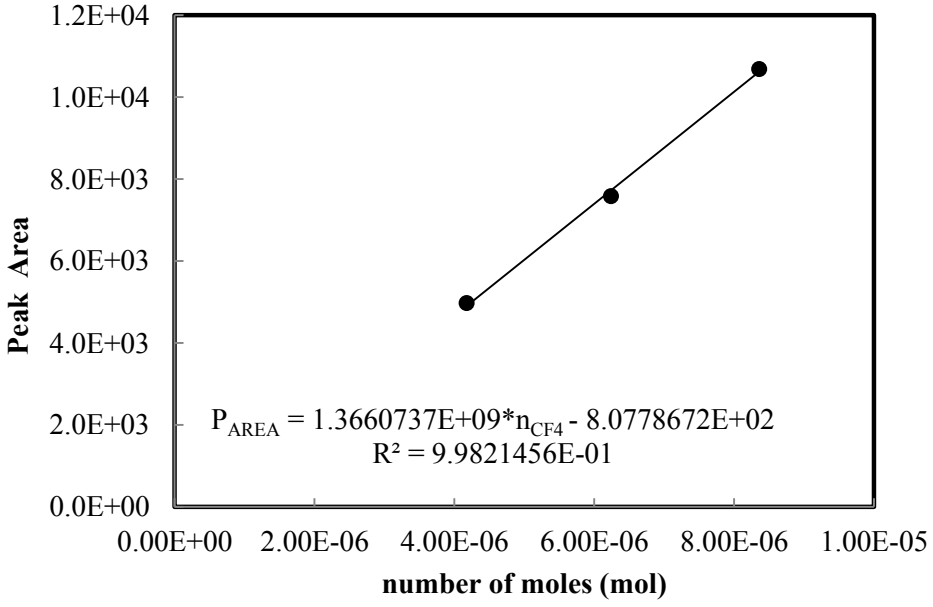

Figure A.2: GC calibration plot with CF_4 gas for injected syringe volumes of 100 to 200 µl

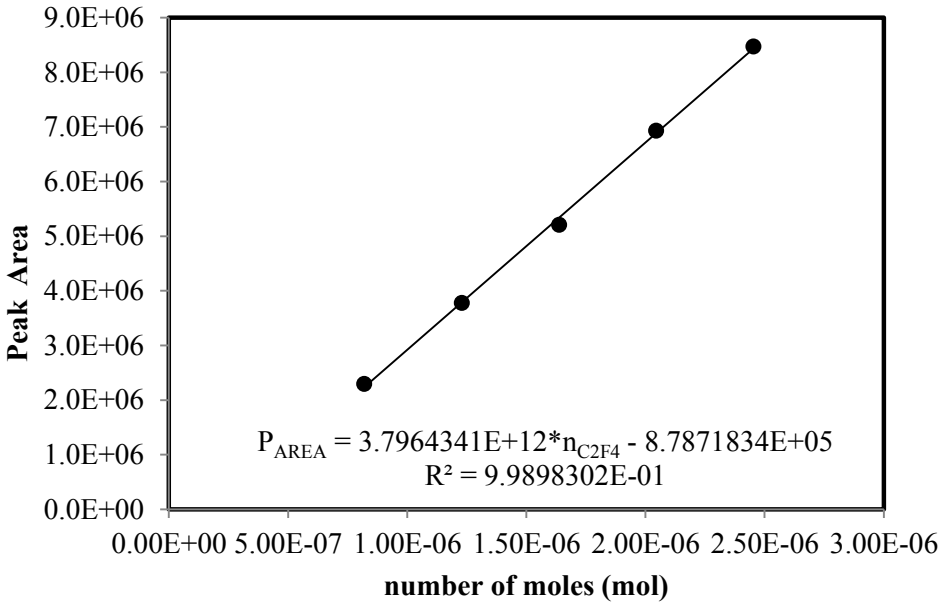

Figure A.3: GC calibration plot with C_2F_4 for injected syringe volumes of 20 to 60 µl

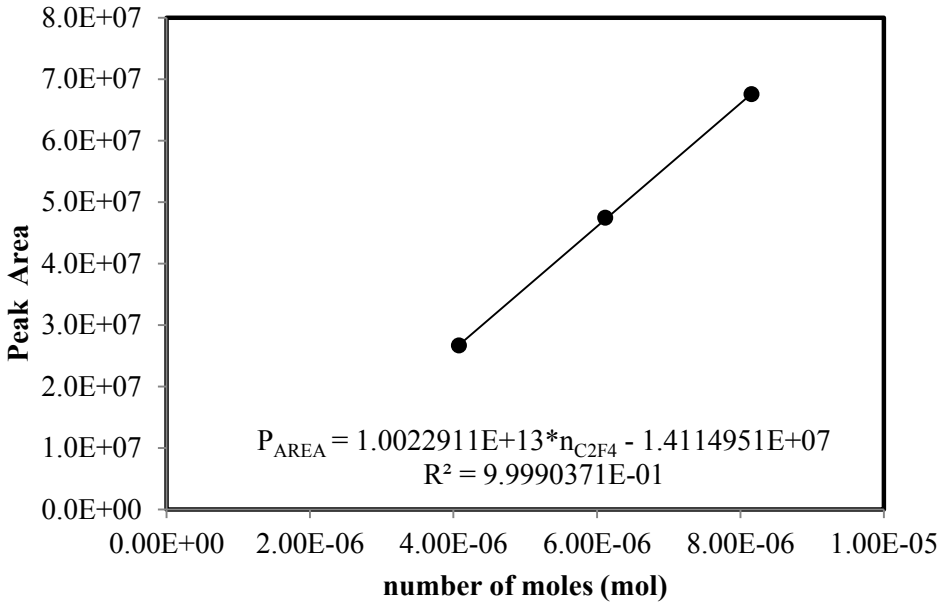

Figure A.4: GC calibration plot with C_2F_4 for injected syringe volumes of 100 to 200 µl

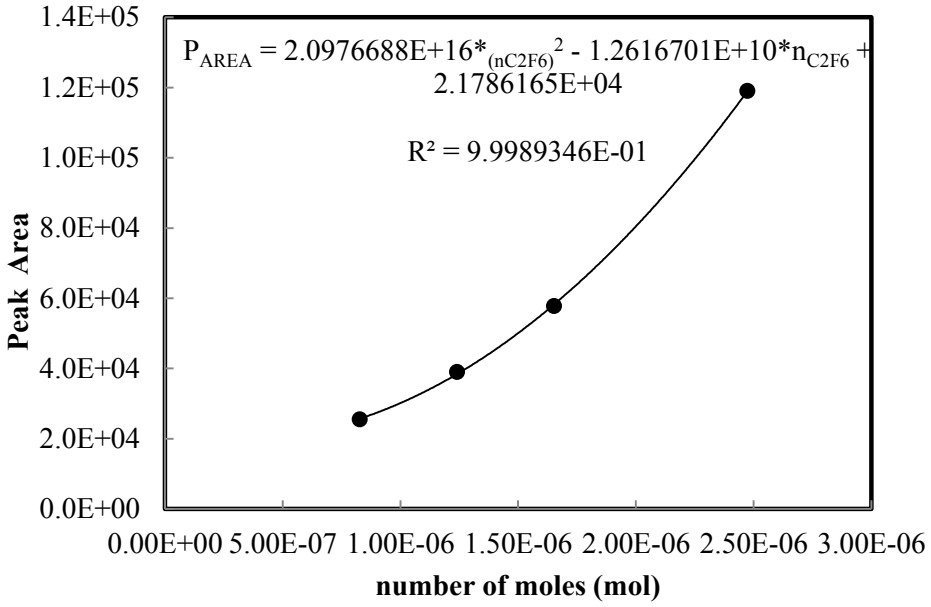

Figure A5: GC calibration plot with C_2F_6 for injected syringe volumes of 20 to 60 µl

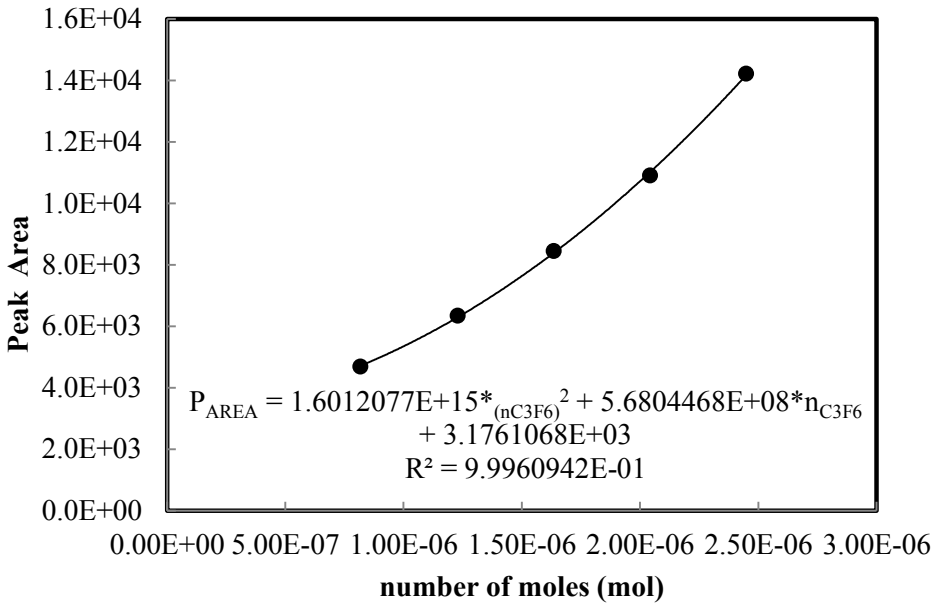

Figure A.6: GC calibration plot with C_3F_6 for injected syringe volumes of 20 to 60 µl

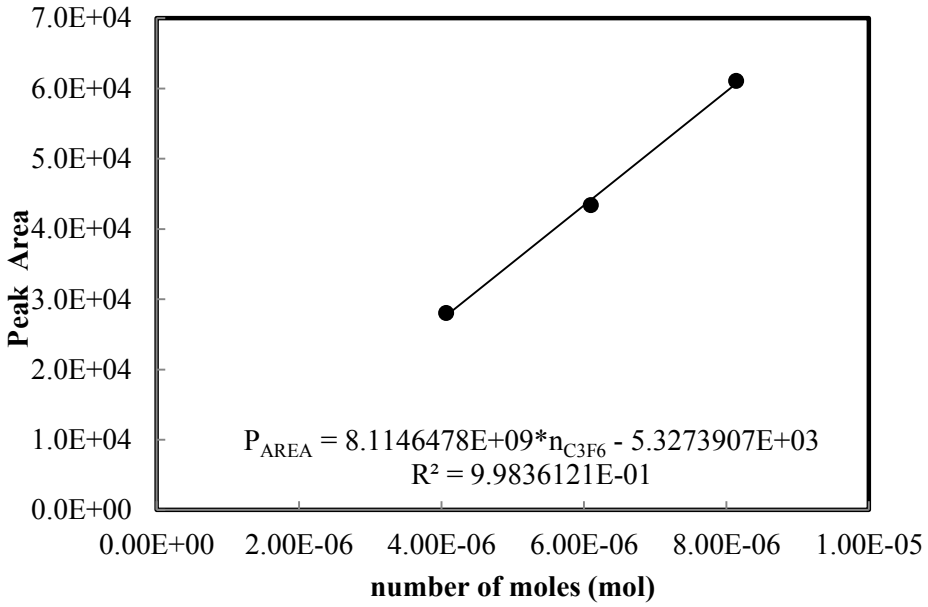

Figure A.7: GC calibration plot with C_3F_6 for injected syringe volumes of 100 to 200 µl

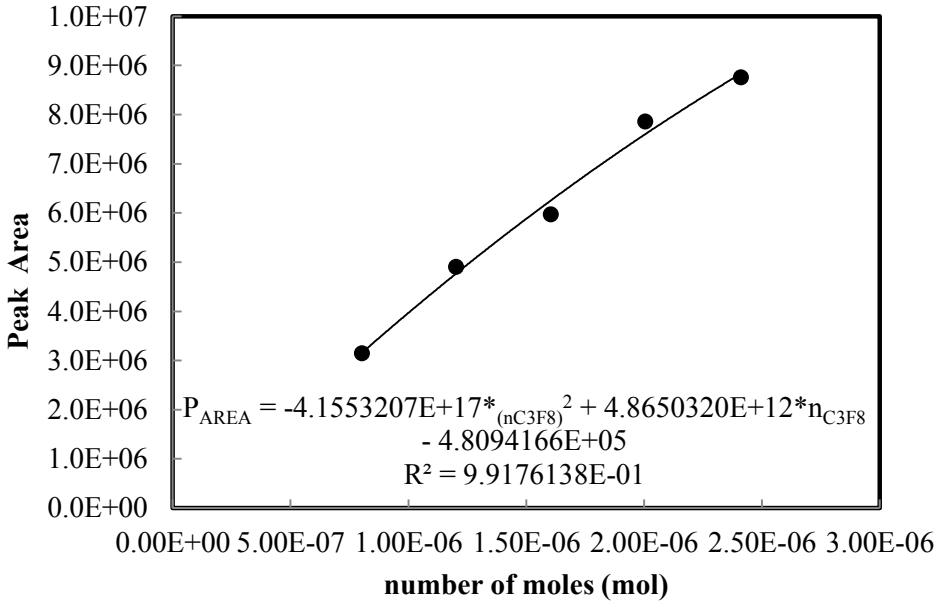

Figure A.8: GC calibration plot with C_3F_8 for injected syringe volumes of 20 to 60 µl

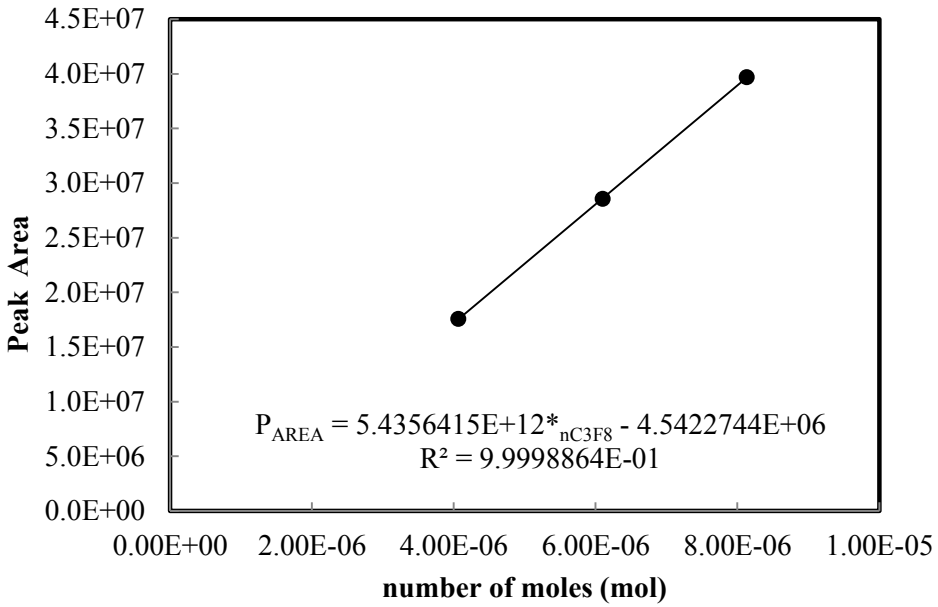

Figure A.9: GC calibration plot with C_3F_8 for injected syringe volumes of 100 to 200 µl

Appendix B

CALIBRATION OF MEASURING DEVICES

B1 Calibration of the Pressure Transmitter

The pressure transmitter used in the experimental setup was calibrated against a standard used as a reference and the uncertainty was estimated for the pressure range from 0 to 200 bar by checking the pressure in an upward direction (lower to high pressure) and downward direction (high to low pressure). Figures B1 and B2 represents the plots of the calibration data, while the residual plots for the calibration data are presented in Figures B3 and B4. The estimated standard error obtained from analysis of the calibration data for Figure B1 and B2 are 0.0614 and 0.0642 respectively. The residual was estimated using the least square fit using the linest function in Microsoft Excel 2010.

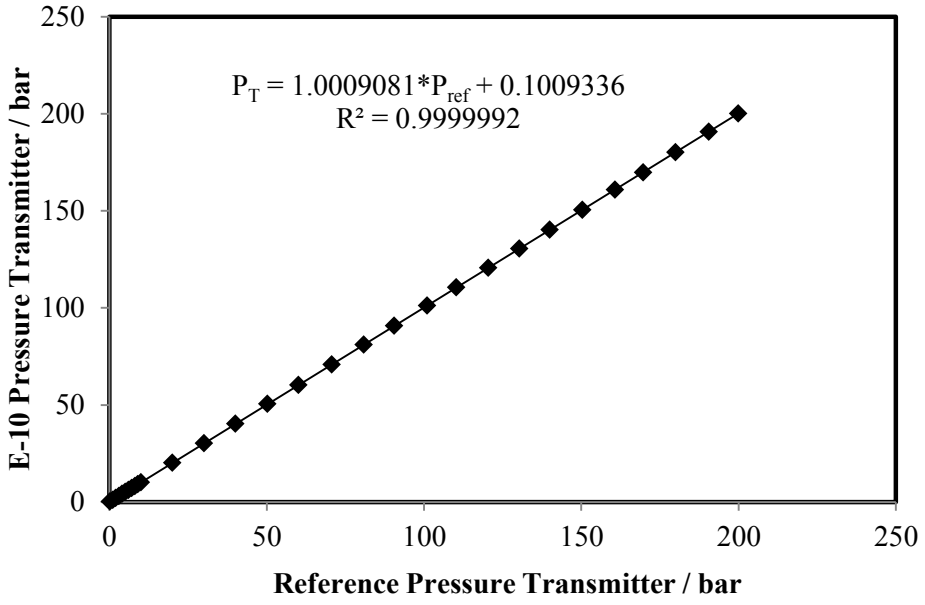

Figure B.1: Pressure calibration plot for the E-10 high pressure transmitter (0 to 200 bar)

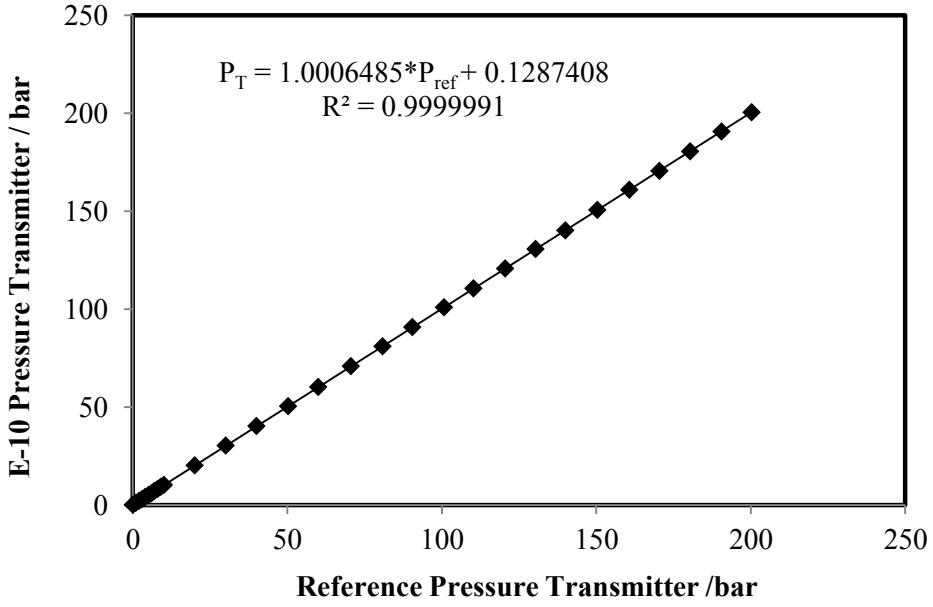

Figure B.2: Pressure calibration plot for the E-10 high pressure transmitter (200-0 bar)

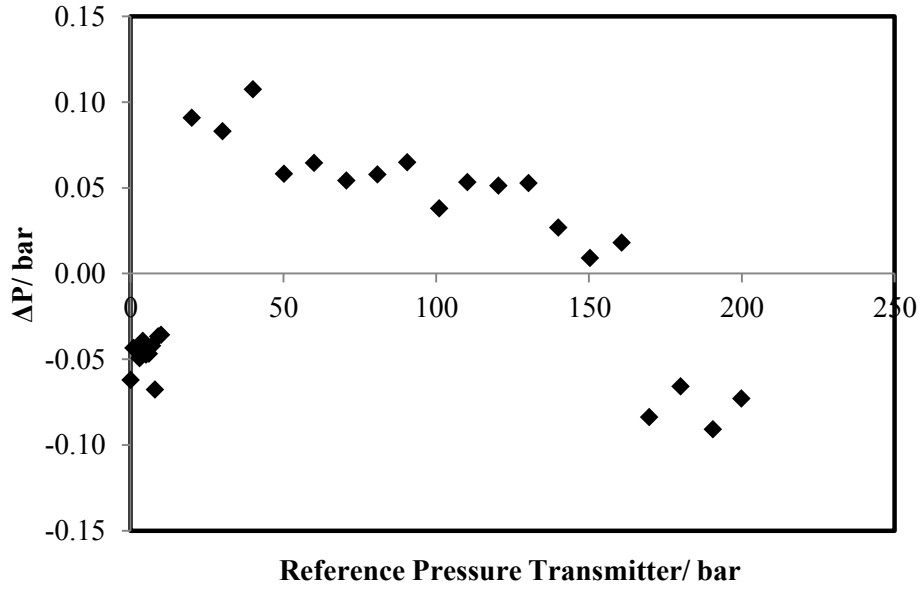

Figure B.3: Pressure deviation plot for the E-10 pressure transmitter from 0 to 200 bar pressure span

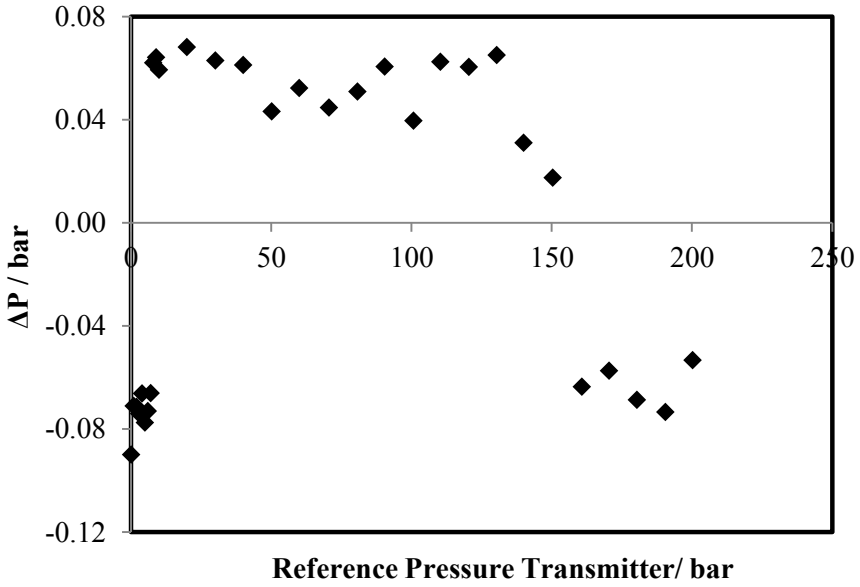

Figure B.4: Pressure deviation plot for the E-10 pressure transmitter from 200 - 0 bar pressure span

Appendix C

CALCULATING REACTOR AND DISCHARGE VOLUME

C1 Calculating the Reactor Volume

In calculating the total volume of the reactor, the following procedure was used:

(1) The dimensions of the reactor chamber was measured and the value taken as constant
(2) The piston for the mobile electrode is a variable which depends on the interelectrode gap used (1 mm was used for as shown in Table C1). Thus, its volume was calculated as a function of the interelectrode gap.
(3) The dimension of the sight window fixed points was measured and multiplied by a factor of 2. The sight window fixed points are cylindrical in form and their volumes were calculated.
(4) The fixed electrode can vary slightly in case the position of the electrode is moved. However, it is taken as constant in this calculation.
(5) The dimension of the mobile electrode cylindrical point was measured and the value was taken to be constant, from which its volume was calculated.
(6) The tip of the electrode can vary slightly in case of erosion of the tip after series of arc discharge. The tip is conical in shape and the volume was calculated.
(7) The dimension for the gas inlet and outlet as well as the thermocouple point was measured and the values are constant.

After calculating the volume of the different parts within the reactor chamber, the following approach was employed to calculate the total volume of the reactor based on step 1 to 7 above. The total volume of reactor is the sum of step 4, 5, and 6 subtracted from the sum of step 1, 2, 3, and 7.

Table C.1: Procedure for calculating the volume of the reactor based on an interelectrode gap of 1 mm

Parts within the reactor chamber	**diameter (mm)**	**height (mm)**	**radius (mm)**	**Volume of parts (mm^3)**
reactor chamber (cylindrical)	12.15	24.45	6.075	2835.16
piston for mobile electrode	8.43	1.00	4.215	55.821
sight window fixed point (cylindrical)	5.00	6.9	2.50	270.998
fixed electrode (cylindrical	4.00	6.9	2.00	86.719
mobile electrode (cylindrical)	4.00	14	2.00	175.95
tip of fixed electrode (cone)	2.00	3.5	1.00	3.6657
gas outlet, inlet and thermocouple point	2.00	12.00	1.00	113.11
pie (π)	3.142			
Total volume of reactor (mm^3)				**3008.8**
Total volume of reactor (cm^3)				**3.0088**

C2 Estimating the Active Discharge Volume

The discharge generated is assumed to be cylindrical in shape and the radius of the discharge is estimated by imaging using a video camera and neutral density four (ND 4) optical filters.

Table C.2: Calculated discharge volume for an interelectrode gap of 1 mm

average discharge radius based on imaging (mm)	0.16
length of arc determined by interelectrode gap (mm)	1.00
Volume of the arc discharge (mm^3)	**0.0804352**
Ratio of discharge arc volume to reactor volume	0.0001069
Minimum reactor volume based on contact (i.e. no gap between the electrodes) (mm^3)	2952.9
Maximum reactor volume based on the maximum possible interelectrode gap of 5 mm (mm^3)	3232.0
Relative variation in volume %	8.64

Appendix D

PUBLICATIONS

Rohani V, Iwarere S, Fabry F, Mourard D, Izquierdo E, Ramjugernath D, Fulcheri L (2011) Experimental study of hydrocarbon synthesis from syngas by a tip-tip electric discharge at very high pressure. Plasma Chem Plasma Process 31:663-679

Abstract

This paper is dedicated to the study of hydrocarbons synthesis from a syngas using a plasma process based on the generation of an electrical discharge at very high pressure. We report experimental results performed using a $He/H_2/CO$ mixture with the ratio 40%/48%/12% at a pressure of 2.2 MPa, through three modes of treatment: one continuous mode and two intermittent modes including a relaxation time between two successive discharges. The study shows that significant quantities of C_1, and saturated and unsaturated C_2 molecules are synthesized at these experimental conditions. It also indicates the better efficiency of the intermittent treatment modes for the C_2 molecules synthesis.

Estimates of the chemical synthesis balance occurring in the reactor during an instantaneous treatment are also presented in the manuscript. In addition, the study indicates a preliminary scan of other synthesized molecules which have been identified by varying the operating pressure in the continuous treatment mode.

Iwarere SA, Rohani V, Fulcheri L , Ramjugernath D (2013) Application of High Pressure Plasma in Hydrocarbon Synthesis from Syngas. “Manusript in preparation”

Abstract

Experimental studies relating to high pressure operation in plasma chemical processes are scare. The influence of very high pressure has not been reported in literature for hydrocarbon synthesis from synthesis gas using plasma technology. This may be attributed to difficulties associated with igniting and sustaining discharge at these pressures. Operating at high pressure is expected to favour chain growth in the Fischer-Tropsch process based on Le Chatelier’s principle. Thus, application of high pressure plasma could provide new routes to hydrocarbon synthesis globally. This paper presents experimental results in a tip-tip arc discharge reactor at very high pressure range of 0.5 to 15 MPa for a H_2/CO mixture ratio of 2.2/1using a high voltage direct current power supply as the plasma source. In addition, results involving the influence of current variation are presented. The results showed that C_1 to C_3 can be synthesized using high pressure with a significant increase in the concentration of the products observed at 12 and 15 MPa. The performance of the reactor was evaluated based on the influence of the specific energy on the Fischer-Tropsch process. The products selectivity and yield for methane, C_2, and C_3 hydrocarbons were calculated based on the conversion of the reactant.

Iwarere, SA, Rohani V, Fabry F, Mourard D, Izquierdo E, Ramjugernath D, Fulcheri L Experimental Study of Hydrocarbons Synthesis from Syngas by a Tip-Tip Electrical Discharge at High Pressure, SAIChE Conference 2012, Champagne Sports Resort, Drakensberg, September 16-19, 2012. (Abstract Peer Reviewed)

Abstract

With the pertinent issues of combating global warming/climate change and reducing gas emissions, plasma processes are valuable technologies that are capable of transforming the energy industry in the 21st century. To this end, a tip-tip electrical discharge reactor has been developed to operate at high pressure (up to 20 MPa) and low current (< 1 A) by generating a nonthermal, nonequilibrium plasma.

Preliminary experiments were performed using this tip-tip electrical discharge reactor at 2.2 MPa and 350 mA for H_2, CO and He gas mixtures of 48, 12 and 40 (mol %) respectively. These experiments further investigated the effect of three different treatment modes (one continuous and two intermittent modes with a relaxation time between successive discharges). This work which is related to the Fischer- Tropsch synthesis of hydrocarbons has shown that significant amount of C_1 and smaller amounts of C_2 hydrocarbons can be synthesized by plasma reaction.

Furthermore, analysis of the results gives a progressive and improved product trends for the intermittent treatment modes with respect to the C_2 molecules synthesized. Analytical estimates were made of the global synthesis reaction equation occurring within the active volume of the reactor during an instantaneous treatment mode and results are presented. This work also indicates that other synthesized molecules were produced in preliminary experiments conducted at various system pressures in the continuous mode. These species were identified on the gas chromatograph mass spectrometer (GCMS).

Lebouvier A, Iwarere SA, Ramjugernath D, Fulcheri L (2013) 3D magnetohydrodynamic modelling of a dc low-current plasma arc batch reactor at very high pressure in helium. J Phys D: Appl Phys 46:145203

Abstract

This paper deals with a three-dimensional (3D) time-dependent magnetohydrodynamic (MHD) model under peculiar conditions of very high pressures (from 2 MPa up to 10 MPa) and low currents (< 1 A). Studies on plasma arc working under these unusual conditions remain almost unexplored because of the technical and technological challenges to develop a reactor able to sustain a plasma at very high pressures. The combined effect of plasma reactivity and high pressure would probably open the way towards new promising applications in various fields: chemistry, lightning, materials, or nanomaterial synthesis.

A MHD model helps one to understand the complex and coupled phenomena surrounding the plasma which cannot be understood by simply experimentation. The model also provides data which are difficult to directly determine experimentally. The model simulates an experimental-based batch reactor working with helium. The particular reactor in question was used to investigate the Fischer-Tropsch application, fluorocarbon production and CO_2 retro-conversion. However, as a first approach in terms of MHD, the model considers the case for helium as a non-reactive working gas.

After a detailed presentation of the model, a reference case has been fully analysed (P = 8 MPa, I = 0.35 A) in terms of physical properties. The results show a bending of the arc and displacement of the anodic arc root towards the top of the reactor, due to the combined effects of convection, gravity and electromagnetic forces. A parametric study on the pressure (2 - 10 MPa) and current (0.25 - 0.4 A) was then investigated. The operating pressure does not show an influence on the contraction of the arc but higher pressures involve a higher natural convection in the reactor, driven by the density gradients between the cold and hot gas.

Appendix E

PROCEDURE FOR CALIBRATION OF THE PR2100 MODEL OF THE PERICHROM GAS CHROMATOGRAPH

E1 Overview of the PR2100 GC

The PR2100 model of the Perichrom GCs has been described to have the best linearity and sensitivity due to the state of the art technology. Hence, it is consider in the analysis of hydrocarbon species.
The PR2100 GC has an automated system for operating the valves via an individual GC events and the process is fully optimised by adjusting the different parameters such as oven temperature, pressure of the gas, flow rate of the carrier gas in order to achieve a good separation of the compounds in the sample mixtures. The configuration for the PR2100 GC and the settings of the acquisition program used are presented in this appendix. Also included is the calibration approach for hydrocarbon gases (saturated C_1 to C_4 and unsaturated C_2 to C_4) as well as the elemental gases.

E2 GC Analysis using Multiple Detectors (TCD and FID) for Hydrocarbon gases

Hydrocarbon gases (C_1 to C_{6+}) generally contain complex mixtures with unavoidable impurities of elemental and inorganic gases such as N_2, O_2, CO, CO_2 .Thus, making it difficult to separate the hydrocarbon gases using a single detector. Moreover, the thermal conductivity of hydrogen (0.168) which is close to that of He (0.142) makes it difficult to get a good response factor on the TCD detector for hydrogen when Helium is used as the carrier gas. Thus, for this analysis, the use of a GC with three detectors (2 TCD with Helium and Nitrogen as the carrier gas, and an FID detector with Helium as the carrier gas) was adopted. This helps to properly calibrate the GC detector for the saturated and unsaturated hydrocarbon gases as well as the elemental and inorganic gases.

E2.1 Calibration Analysis

Step 1: Pure Helium was first injected into the GC for cleaning in order to ensure that no impurities were left behind in the column from the previous experiments. All injection was carried out at a gas flow rate of 30 mL/min, and gas pressure of 0.1 MPa. This flow rate and pressure were kept constant for all the experiment for the purpose of repeatability. Once the cleaning process was completed, the injection of the standards for calibration of the detector response was initiated.

Step 2: A cylinder of acetylene, ethylene, and propylene of known concentration was injected into the GC to obtain their response time as well as calculate the response factor (the ratio by which the detector respond to a given standard of known concentration). The peak obtained was separated by optimising the parameters such as oven temperature. The settings used in this calibration are presented as Table E1.

After the separation of the peaks, the various peaks are then identified (qualitative analysis). Once the peaks are identified and the retention time noted, the peaks may be manually integrated (if necessary). The purpose of manually integrating the peaks is to resolve the peak area of a sample from the neighbouring peaks if the GC program has not satisfactorily done this. Figure E1 is an example of the identified peaks and species for the GC calibration of the hydrocarbon gases.

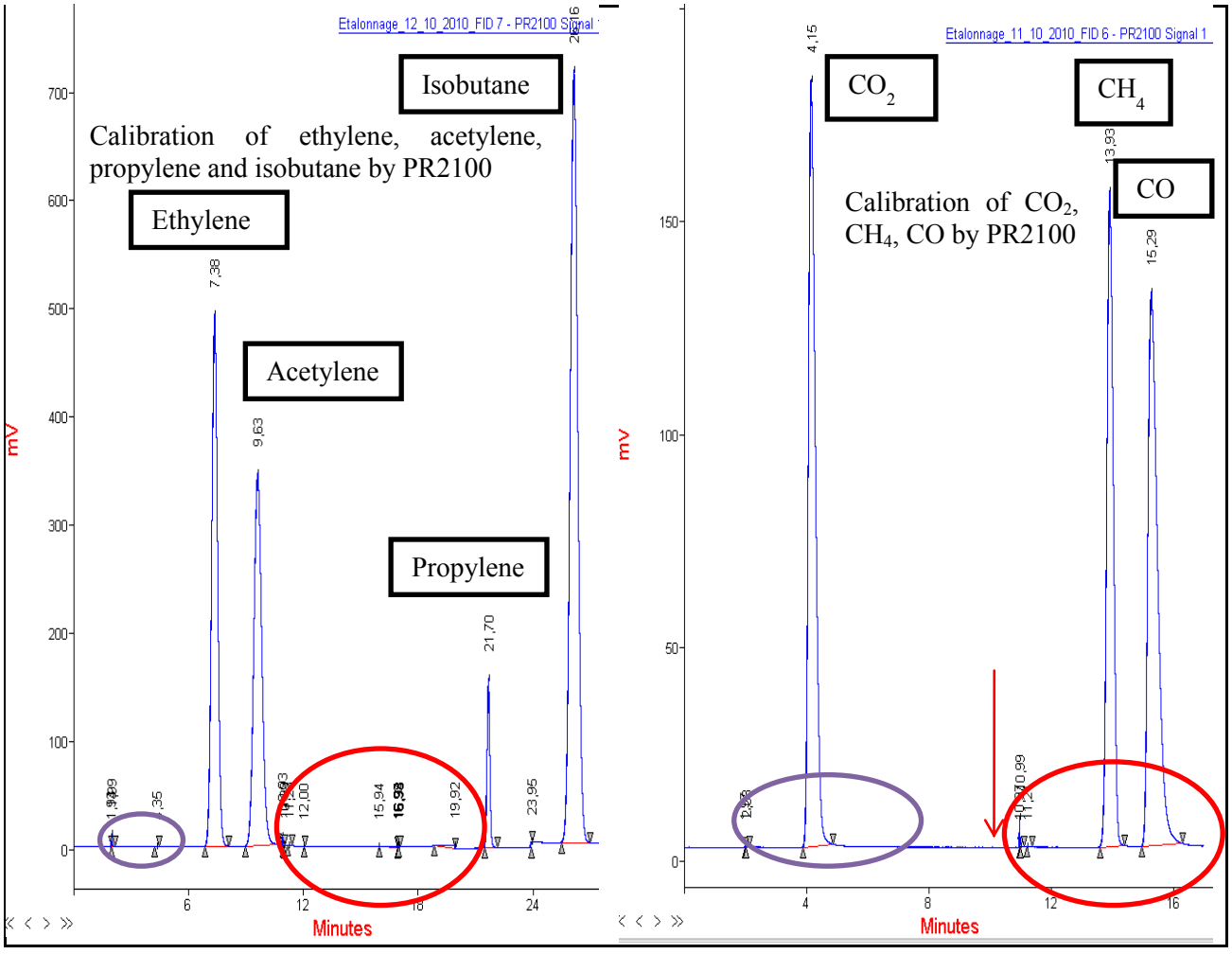

Figure E.1: Example of chromatograms for the PR2100 GC analysis using the hydrocarbon gases

E2.2 Estimating the Response Factor

Step 3: Once the peaks are properly separated and identified as shown in Figure E1 above, the next and final stage in the calibration is in estimating the response factor. The response factor obtained for

the various gas standards injected can then be used in the quantitative analysis of the unknown samples in future experiments.

In estimating the response factors of the gases for the different detectors (TCD and FID), the following procedure is followed:

(a) The properly separated peaks of the standard sample's retention time are recorded against their peak areas;

(b) The known concentrations for the standard sample is tabulated alongside the retention time (R_{TIME}) and the peak area (P_{AREA}).

(c) The ratio of the peak area for each species to its known concentration (in ppm) was used to estimate the response of that detector to the specie (the response factor).
This is given in basic equation form;

$$R_{F_i} = \frac{P_{A_i}}{C_i} \tag{E1}$$

where RF_i, PA_i, and C_i are the response factor, peak area and concentration of specie *i* respectively.

(d) From the response factor (R_{FACTOR}) estimated in equation (E1), the unknown concentration of analytes could be obtained by dividing the peak area obtained for that analyte by its response factor from the standard. The equation is of the form,

$$C_{analyte} = \frac{P_{AREA\,(analyte)}}{R_{FACTOR}} \tag{E2}$$

This calibration method is based on the understanding that the relationship between the peak areas of the sample to the concentration of that sample is linear over a wide range. Thus, the peak area is proportional to the amount of substance in a sample, and therefore, the proportionality constant is the response factor.

Table E.1: Program settings and configuration for PR2100 gas chromatograph

Parameters	**Perichrom PR2100**	
Gas Pressure	0.1 MPa	
Gas Flow rate	30 ml/min	
Column Temperature	Initial = 40 ^{o}C; Final= 200 ^{o}C	
Methanation Oven Temperature	350 ^{o}C	
FID Temperature	255 ^{o}C	
Gain for FID	12	
Pressure entering FID	H_2 = 60 kPa	
	Air = 50 kPa	
	Air Ignition = 37 kPa	
FID Sample Rate	25 Samples/s	
Offset for FID	300 × 10μV	
	Loop #1	Loop #2
Injector Carrier Pressure	200 kPa	300 kPa
Injector Temperature	150 ^{o}C	350 ^{o}C
TCD Carrier Gas Reference Pressure	83 kPa	95 kPa
TCD Temperature	150 ^{o}C	150 ^{o}C
TCD Carrier Gas	N_2	He
TCD Sample Rate	25 Samples/s	25 Samples/s
Gain for TCD	10	10
Temperature Control	From 0 to 2 mins	From 2 mins to 29 mins
Offset for TCD	300 × 10μV	300 × 10μV

Appendix F

REACTION MECHANISM FOR METHANE OXIDATION

F1 Leeds Methane Oxidation Mechanism

The Leeds chemical reaction mechanism for methane oxidation is one of those considered in the kinetic modelling of the dry reforming process. These mechanisms consist of 37 considered species and 175 reactions. The reaction mechanism and species set are presented below.

Table F.1: Chemkin interpreter output for the Leeds methane oxidation

				TEMPERATURE		ELEMENT COUNT				
SPECIES CONSIDERED		PHASE	MOLECULAR WEIGHT	LOW (K)	HIGH (K)	H	O	C	N	Ar
1	H_2	G	2.01594	200	6000	2	0	0	0	0
2	CH_4	G	16.04303	200	6000	4	0	1	0	0
3	C_2H_2	G	26.03824	200	6000	2	0	2	0	0
4	C_2H_4	G	28.05418	300	5000	4	0	2	0	0
5	C_2H_6	G	30.07012	300	5000	6	0	2	0	0
6	C_3H_4	G	40.06533	200	6000	4	0	3	0	0
7	C_3H_6	G	42.08127	300	5000	6	0	3	0	0
8	C_4H_2	G	50.06054	200	6000	2	0	4	0	0
9	O_2	G	31.9988	200	6000	0	2	0	0	0
10	H_2O	G	18.01534	200	6000	2	1	0	0	0
11	H_2O_2	G	34.01474	200	6000	2	2	0	0	0
12	CO	G	28.01055	200	6000	0	1	1	0	0
13	CO_2	G	44.00995	200	6000	0	2	1	0	0
14	CH_2O	G	30.02649	200	6000	2	1	1	0	0
15	CH_2CO	G	42.03764	200	6000	2	1	2	0	0
16	C	G	12.01115	200	6000	0	0	1	0	0
17	H	G	1.00797	200	6000	1	0	0	0	0
18	CH	G	13.01912	200	6000	1	0	1	0	0
19	CH_2	G	14.02709	200	6000	2	0	1	0	0
20	$CH_2(S)$	G	14.02709	300	4000	2	0	1	0	0
21	CH_3	G	15.03506	200	6000	3	0	1	0	0
22	C_2H	G	25.03027	200	6000	1	0	2	0	0
23	C_2H_3	G	27.04621	200	6000	3	0	2	0	0
24	C_2H_5	G	29.06215	200	6000	5	0	2	0	0
25	C_3H_2	G	38.04939	200	6000	2	0	3	0	0

Table F.1 (continued): Chemkin interpreter output for the Leeds methane oxidation

26	H_2CCCH	G	39.05736	200	6000	3	0	3	0	0
27	H_2CCCCH	G	51.06851	298.1	6000	3	0	4	0	0
28	O	G	15.9994	200	6000	0	1	0	0	0
29	OH	G	17.00737	200	6000	1	1	0	0	0
30	HO_2	G	33.00677	200	6000	1	2	0	0	0
31	HCO	G	29.01852	200	6000	1	1	1	0	0
32	CH_3O	G	31.03446	200	6000	3	1	1	0	0
33	CH_2OH	G	31.03446	200	6000	3	1	1	0	0
34	HCCO	G	41.02967	200	6000	1	1	2	0	0
35	CH_2HCO	G	43.04561	300	5000	3	1	2	0	0
36	N_2	G	28.0134	200	6000	0	0	0	2	0
37	Ar	G	39.948	200	6000	0	0	0	0	1

Table F.2: Chemical reaction mechanism for the Leeds methane oxidation (A_i in mol.cm.s.K, E_i in cal.mol^{-1})

REACTIONS CONSIDERED	**A_i**	**β_i**	**E_i**
1. $H_2+CH_2(S)\leftrightarrow CH_3+H$	7.23E+13	0	0
2. $H_2+O\leftrightarrow OH+H$	5.12E+04	2.7	6282
3. $H_2O+H\leftrightarrow H_2+OH$	4.52E+08	1.6	18415
4. $CH_4+O_2\leftrightarrow CH_3+HO_2$	3.97E+13	0	56845
5. $CH_4+C\leftrightarrow CH+CH_3$	5.00E+13	0	24004
6. $CH_4+H\leftrightarrow CH_3+H_2$	1.32E+04	3	8025
7. $CH_4+CH\leftrightarrow C_2H_4+H$	3.01E+13	0	-406
8. $CH_4+CH_2\leftrightarrow CH_3+CH_3$	4.30E+12	0	10032
9. $CH_4+CH_2(S)\leftrightarrow CH_3+CH_3$	7.00E+13	0	0
10. $CH_4+C_2H\leftrightarrow CH_3+C_2H_2$	1.81E+12	0	0
11. $CH_4+O\leftrightarrow CH_3+OH$	7.23E+08	1.6	8479
12. $CH_4+OH\leftrightarrow CH_3+H_2O$	1.57E+07	1.8	2771
13. $CH_4+HO_2\leftrightarrow CH_3+H_2O_2$	9.03E+12	0	24697
14. $C_2H_2+C_2H_2\leftrightarrow H_2CCCCH+H$	2.00E+09	0	57801
15. $C_2H_2+O_2\leftrightarrow C_2H+HO_2$	1.20E+13	0	74520
16. $H_2+C_2H\leftrightarrow C_2H_2+H$	1.08E+13	0	2173
17. $C_2H_2+H(+M)\leftrightarrow C_2H_3(+M)$	8.43E+12	0	2580
Low pressure limit: 0.34300E+19 0.00000E+00 0.61500E+01			
Troe centering: 0.10000E+01 0.10000E+01 0.10000E+01 0.123100E+04			
18. $C_2H_2+CH\leftrightarrow C_2H+CH_2$	2.11E+14	0	-119
19. $C_2H_2+CH_2\leftrightarrow C_3H_4$	1.20E+13	0	6616
20. $C_2H_2+CH_2(S)\leftrightarrow H_2CCCH+H$	1.75E+14	0	0
21. $C_2H_2+C_2H\leftrightarrow C_4H_2+H$	9.03E+13	0	0
22. $C_2H_2+O\leftrightarrow CH_2+CO$	2.17E+06	2.1	1576
23. $C_2H_2+O\leftrightarrow HCCO+H$	5.06E+06	2.1	1576
24. $C_2H_2+OH\leftrightarrow C_2H+H_2O$	6.00E+13	0	12898
25. $C_2H_2+M\leftrightarrow C_2H+H+M$	1.14E+17	0	106764
26. $C_2H_4+H\leftrightarrow C_2H_3+H_2$	5.42E+14	0	14904

Table F.2 (continued): Chemical reaction mechanism for the Leeds methane oxidation (A_i in mol.cm.s.K, E_i in cal.mol^{-1})

REACTIONS CONSIDERED	A_i	β_i	E_i
27. $C_2H_4+H(+M)\leftrightarrow C_2H_5(+M)$	3.97E+09	1.3	1290
Low pressure limit: 0.13500E+20 0.00000E+00 0.31600E+01			
Troe centering: 0.76000E+00 0.40000E+02 0.10250E+04			
28. $C_2H_4+CH\leftrightarrow C_3H_4+H$	1.32E+14	0	-334
29. $C_2H_4+CH_2(S)\leftrightarrow C_3H_6$	9.64E+13	0	0
30. $C_2H_4+CH_3\leftrightarrow CH_4+C_2H_3$	4.16E+12	0	11130
31. $C_2H_4+O\leftrightarrow H+CH_2HCO$	4.74E+06	1.9	191
32. $C_2H_4+O\leftrightarrow CH_3+HCO$	8.13E+06	1.9	191
33. $C_2H_4+O\leftrightarrow CH_2CO+H_2$	6.80E+05	1.9	191
34. $C_2H_4+OH\leftrightarrow C_2H_3+H_2O$	2.05E+13	0	5947
35. $C_2H_4+M\leftrightarrow C_2H_2+H_2+M$	9.97E+16	0	71487
36. $C_2H_4+M\leftrightarrow C_2H_3+H+M$	7.40E+17	0	96518
37. $C_2H_6+H\leftrightarrow C_2H_5+H_2$	1.45E+09	1.5	7404
38. $C_2H_6+CH\leftrightarrow C_2H_4+CH_3$	1.08E+14	0	-263
39. $C_2H_6+CH_2(S)\leftrightarrow CH_3+C_2H_5$	2.40E+14	0	0
40. $C_2H_6+CH_3\leftrightarrow C_2H_5+CH_4$	1.51E-07	6	6043
41. $C_2H_6+O\leftrightarrow C_2H_5+OH$	1.00E+09	1.5	5804
42. $C_2H_6+OH\leftrightarrow C_2H_5+H_2O$	7.23E+06	2	860
43. $C_2H_6+HO_2\leftrightarrow H_2O_2+C_2H_5$	1.32E+13	0	20445
44. $C_4H_2+O\leftrightarrow C_3H_2+CO$	7.89E+12	0	1338
45. $C_4H_2+OH\leftrightarrow C_3H_2+HCO$	6.68E+12	0	-406
46. $O_2+CO\leftrightarrow CO_2+O$	1.26E+13	0	47029
47. $O_2+CH_2O\leftrightarrow HCO+HO_2$	6.02E+13	0	40628
48. $O_2+C\leftrightarrow CO+O$	1.20E+14	0	3989
49. $O_2+H+M\leftrightarrow HO_2+M$	2.10E+18	-0.8	0
50. $O_2+H+H_2O\leftrightarrow HO_2+H_2O$	6.89E+15	0	-2078
51. $O_2+H\leftrightarrow OH+O$	9.76E+13	0	14832
52. $O_2+CH\leftrightarrow CO+OH$	1.66E+13	0	0
53. $O_2+CH\leftrightarrow CO_2+H$	1.66E+13	0	0
54. $O_2+CH_2\leftrightarrow CO_2+H_2$	5.43E+12	0	1481
55. $O_2+CH_2\leftrightarrow CO_2+H+H$	5.43E+12	0	1481
56. $O_2+CH_2\leftrightarrow CO+OH+H$	8.15E+12	0	1481
57. $O_2+CH_2\leftrightarrow CO+H_2O$	1.48E+12	0	1481
58. $O_2+CH_2\leftrightarrow CH_2O+O$	4.20E+12	0	1481
59. $O_2+CH_2(S)\leftrightarrow CO+OH+H$	3.13E+13	0	0
60. $O_2+CH_3\leftrightarrow CH_2O+OH$	3.31E+11	0	8933
61. $O_2+C_2H\leftrightarrow HCCO+O$	9.05E+12	0	0
62. $O_2+C_2H\leftrightarrow CO_2+CH$	9.05E+12	0	0
63. $O_2+C_2H_3\leftrightarrow C_2H_2+HO_2$	5.42E+12	0	0
64. $O_2+C_2H_5\leftrightarrow C_2H_4+HO_2$	1.02E+10	0	-2197
65. $O_2+C_3H_2\leftrightarrow HCO+HCCO$	1.00E+13	0	0
66. $O_2+H_2CCCH\leftrightarrow CH_2CO+HCO$	3.01E+10	0	2866
67. $O_2+HCO\leftrightarrow HO_2+CO$	3.01E+12	0	0

Table F.2 (continued): Chemical reaction mechanism for the Leeds methane oxidation (A_i in mol.cm.s.K, E_i in cal.mol^{-1})

REACTIONS CONSIDERED	A_i	β_i	E_i
68. $O_2+CH_3O\leftrightarrow CH_2O+HO_2$	2.17E+10	0	1744
69. $O_2+CH_2OH\leftrightarrow CH_2O+HO_2$	1.57E+15	-1	0
70. $O_2+CH_2OH\leftrightarrow CH_2O+HO_2$	7.23E+13	0	3583
71. $O_2+HCCO\leftrightarrow CO+CO+OH$	1.63E+12	0	860
72. $H_2O_2+H\leftrightarrow HO_2+H_2$	1.69E+12	0	3750
73. $H_2O_2+H\leftrightarrow OH+H_2O$	1.02E+13	0	3583
74. $H_2O_2+O\leftrightarrow OH+HO_2$	6.62E+11	0	3965
75. $H_2O_2+OH\leftrightarrow H_2O+HO_2$	7.83E+12	0	1338
76. $OH+OH(+M)\leftrightarrow H_2O_2(+M)$	7.23E+13	-0.4	0
Low pressure limit: 0.55300E+20 -0.76000E+00 0.00000E+00			
Troe centering: 0.10000E+01 0.10000E+01 0.10000E+01 0.104000E+04			
77. $CO+O+M\leftrightarrow CO_2+M$	1.54E+15	0	3009
78. $CO+OH\leftrightarrow CO_2+H$	1.66E+07	1.3	-764
79. $CO+HO_2\leftrightarrow CO_2+OH$	1.51E+14	0	23646
80. $CO+CH\leftrightarrow HCCO$	2.77E+11	0	-1720
81. $CO2+CH\leftrightarrow HCO+CO$	3.43E+12	0	693
82. $CO_2+CH_2\leftrightarrow CH_2O+CO$	2.35E+10	0	0
83. $CH_2O+H\leftrightarrow HCO+H_2$	1.26E+08	1.6	2173
84. $CH_2O+CH\leftrightarrow CH_2+HCO$	9.64E+13	0	-525
85. $CH_2O+CH_3\leftrightarrow CH_4+HCO$	7.83E-08	6.1	1959
86. $CH_2O+O\leftrightarrow HCO+OH$	4.16E+11	0.6	2771
87. $CH_2O+OH\leftrightarrow HCO+H_2O$	3.43E+09	1.2	-454
88. $CH_2O+HO_2\leftrightarrow H_2O_2+HCO$	3.01E+12	0	13065
89. $CH_2O+M\leftrightarrow HCO+H+M$	1.40E+36	-5.5	96637
90. $CH_2O+M\leftrightarrow H_2+CO+M$	3.26E+36	-5.5	96637
91. $CH_2CO+H\leftrightarrow CH_3+CO$	1.81E+13	0	3368
92. $CH_2CO+O\leftrightarrow CH_2+CO_2$	1.33E+12	0	1361
93. $CH_2CO+O\leftrightarrow CH_2O+CO$	4.58E+11	0	1361
94. $CH_2CO+O\leftrightarrow HCO+H+CO$	2.52E+11	0	1361
95. $CH_2CO+O\leftrightarrow HCO+HCO$	2.52E+11	0	1361
96. $CH_2CO+OH\leftrightarrow CH_3+CO_2$	2.52E+12	0	0
97. $CH_2CO+OH\leftrightarrow CH_2OH+CO$	4.68E+12	0	0
98. $CH_2CO+M\leftrightarrow CH_2+CO+M$	6.57E+15	0	57562
99. $CH_2CO+M\leftrightarrow HCCO+H+M$	1.14E+09	0	0
100. $C+CH_2\leftrightarrow C_2H+H$	5.00E+13	0	0
101. $C+CH_3\leftrightarrow C_2H_2+H$	5.00E+13	0	0
102. $C+OH\leftrightarrow CO+H$	5.00E+13	0	0
103. $H+H+M\leftrightarrow H_2+M$	1.87E+18	-1	0
104. $H+H+H_2\leftrightarrow H_2+H_2$	9.79E+16	-0.6	0
105. $H+CH\leftrightarrow C+H_2$	8.43E+12	0	0
106. $H+CH_2\leftrightarrow CH+H_2$	6.02E+12	0	-1791
107. $H+CH_2(S)\leftrightarrow CH_2+H$	2.00E+14	0	0
108. $H+CH_3(+M)\leftrightarrow CH_4(+M)$	1.69E+14	0	0

Table F.2 (continued): Chemical reaction mechanism for the Leeds methane oxidation (A_i in mol.cm.s.K, E_i in cal.mol^{-1})

REACTIONS CONSIDERED	A_i	β_i	E_i
Low pressure limit: 0.14080E+25 -0.18000E+01 0.00000E+00			
Troe centering: 0.37000E+00 0.33150E+04 0.61000E+02			
109. $H+C_2H_3 \leftrightarrow C_2H_2+H_2$	1.20E+13	0	0
110. $CH_3+CH_3 \leftrightarrow C_2H_5+H$	3.01E+13	0	13495
111. $H+O+M \leftrightarrow OH+M$	1.18E+19	-1	0
112. $H+OH+M \leftrightarrow H_2O+M$	5.53E+22	-2	0
113. $H+HO_2 \leftrightarrow H_2+O_2$	4.28E+13	0	1409
114. $H+HO_2 \leftrightarrow OH+OH$	1.69E+14	0	884
115. $H+HO_2 \leftrightarrow H_2O+O$	3.01E+13	0	1720
116. $H+HCO \leftrightarrow CO+H_2$	9.03E+13	0	0
117. $H+CH_3O \leftrightarrow CH_2O+H_2$	1.81E+13	0	0
118. $H+CH_2OH \leftrightarrow CH_3+OH$	1.02E+13	0	0
119. $H+CH_2OH \leftrightarrow CH_2O+H_2$	3.08E+13	0	0
120. $H+HCCO \leftrightarrow CH_2+CO$	1.51E+14	0	0
121. $CH+CH_2 \leftrightarrow C_2H_2+H$	4.00E+13	0	0
122. $CH+CH_3 \leftrightarrow C_2H_3+H$	3.00E+13	0	0
123. $CH+C_2H_3 \leftrightarrow CH_2+C_2H_2$	5.00E+13	0	0
124. $CH+O \leftrightarrow CO+H$	3.97E+13	0	0
125. $CH+OH \leftrightarrow HCO+H$	3.00E+13	0	0
126. $CH+HCCO \leftrightarrow C_2H_2+CO$	5.00E+13	0	0
127. $CH_2+CH_2 \leftrightarrow C_2H_2+H_2$	1.20E+13	0	788
128. $CH_2+CH_2 \leftrightarrow C_2H_2+H+H$	1.08E+14	0	788
129. $CH_2+CH_3 \leftrightarrow C_2H_4+H$	4.22E+13	0	0
130. $CH_2+C_2H_3 \leftrightarrow C_2H_2+CH_3$	1.81E+13	0	0
131. $CH_2+O \leftrightarrow CO+H+H$	7.20E+13	0	0
132. $CH_2+O \leftrightarrow CO+H_2$	4.80E+13	0	0
133. $CH_2+OH \leftrightarrow CH_2O+H$	1.81E+13	0	0
134. $CH_2+HCO \leftrightarrow CH_3+CO$	1.81E+13	0	0
135. $CH_2+HCCO \leftrightarrow C_2H_3+CO$	3.00E+13	0	0
136. $CH_2+HCCO \leftrightarrow C_2H+CH_2O$	1.00E+13	0	2006
137. $CH_2(S)+M \leftrightarrow CH_2+M$	1.51E+13	0	0
138. $CH_3+CH_3(+M) \leftrightarrow C_2H_6(+M)$	3.61E+13	0	0
Low pressure limit: 0.36300E+42 -0.70000E+01 0.11560E+02			
Troe centering: 0.62000E+00 0.73000E+02 0.11800E+04			
139. $CH_3+O \leftrightarrow CH_2O+H$	8.43E+13	0	0
140. $CH_3+OH \leftrightarrow CH_2(S)+H_2O$	7.23E+13	0	2771
141. $CH_3+HO_2 \leftrightarrow CH_3O+OH$	1.80E+13	0	0
142. $CH_3+HCO \leftrightarrow CH_4+CO$	1.20E+14	0	0
143. $CH_3+M \leftrightarrow CH_2+H+M$	2.91E+16	0	90547
144. $C_2H+C_2H_3 \leftrightarrow C_2H_2+C_2H_2$	1.90E+13	0	0
145. $C_2H+O \leftrightarrow CH+CO$	1.00E+13	0	0
146. $C_2H+OH \leftrightarrow HCCO+H$	2.00E+13	0	0
147. $C_2H+OH \leftrightarrow CH_2+CO$	1.81E+13	0	0

Table F.2 (continued): Chemical reaction mechanism for the Leeds methane oxidation (A_i in mol.cm.s.K, E_i in cal.mol^{-1})

REACTIONS CONSIDERED	A_i	β_i	E_i
148. $C_2H_3+O \leftrightarrow CO+CH_3$	3.00E+13	0	0
149. $C_2H_3+OH \leftrightarrow C_2H_2+H_2O$	5.00E+12	0	0
150. $C_2H_5+O \leftrightarrow CH_2O+CH_3$	6.62E+13	0	0
151. $H_2CCCH+O \leftrightarrow C_2H_2+CO+H$	1.39E+14	0	0
152. $H_2CCCH+OH \leftrightarrow C_3H_2+H_2O$	2.00E+13	0	0
153. $H_2CCCCH+M \leftrightarrow C_4H_2+H+M$	1.12E+16	0	46479
154. $O+O+M \leftrightarrow O_2+M$	5.40E+13	0	-1791
155. $O+HO_2 \leftrightarrow O_2+OH$	3.19E+13	0	0
156. $O+HCO \leftrightarrow CO+OH$	3.01E+13	0	0
157. $O+HCO \leftrightarrow CO_2+H$	3.01E+13	0	0
158. $O_2+CH_3 \leftrightarrow CH_3O+O$	4.40E+13	0	31384
159. $O+CH_3O \leftrightarrow CH_2O+OH$	1.81E+12	0	0
160. $O+CH_2OH \leftrightarrow CH_2O+OH$	9.03E+13	0	0
161. $O+HCCO \leftrightarrow H+CO+CO$	9.64E+13	0	0
162. $OH+OH \leftrightarrow O+H_2O$	1.51E+09	1.1	96
163. $OH+HO_2 \leftrightarrow H_2O+O_2$	2.89E+13	0	-502
164. $OH+HCO \leftrightarrow H_2O+CO$	1.02E+14	0	0
165. $OH+CH_3O \leftrightarrow CH_2O+H_2O$	1.81E+13	0	0
166. $OH+CH_2OH \leftrightarrow CH_2O+H_2O$	2.41E+13	0	0
167. $OH+HCCO \leftrightarrow HCO+HCO$	1.00E+13	0	0
168. $OH+HCCO \leftrightarrow CH_2O+CO$	1.00E+13	0	0
169. $HO_2+HO_2 \leftrightarrow H_2O_2+O_2$	4.22E+14	0	11966
170. $HO_2+HO_2 \leftrightarrow H_2O_2+O_2$	1.32E+11	0	-1624
171. $HCO+HCO \leftrightarrow CH_2O+CO$	3.01E+13	0	0
172. $HCO+M \leftrightarrow H+CO+M$	4.49E+14	0	15740
173. $CH_3O+M \leftrightarrow CH_2O+H+M$	1.55E+14	0	13495
174. $CH_2OH+M \leftrightarrow CH_2O+H+M$	1.26E+16	0	29999
175. $HCCO+HCCO \leftrightarrow C_2H_2+CO+CO$	1.00E+13	0	0

F2 GRI-Mech Methane Oxidation Mechanism

This chemical mechanism is widely used in the field of combustion. It was compiled from computational and experimental works conducted at Stanford University, University of California at Berkeley, and University of Texas at Austin under the sponsorship of the Gas Research Institute (GRI). The GRI-Mech 3.0 used in this work consists of 53 species and 325 elementary reactions.

The temperatures of each species are presented as low temperature (LT) and high temperature (HT). The molecular weight is represented as MW in Table F.3. The elements considered in the GRI-Mech 3.0 are oxygen (O), hydrogen (H), carbon (C), nitrogen (N), and argon (Ar).

Table F.3: Chemkin interpreter output for the GRI-Mech methane oxidation

No.	SPECIES	PHASE	MW	LT (K)	HT (K)	O	H	C	N	Ar
1	H_2	G	2.01594	200	3500	0	2	0	0	0
2	H	G	1.00797	200	3500	0	1	0	0	0
3	O	G	15.9994	200	3500	1	0	0	0	0
4	O_2	G	31.9988	200	3500	2	0	0	0	0
5	OH	G	17.00737	200	3500	1	1	0	0	0
6	H_2O	G	18.01534	200	3500	1	2	0	0	0
7	HO_2	G	33.00677	200	3500	2	1	0	0	0
8	H_2O_2	G	34.01474	200	3500	2	2	0	0	0
9	C	G	12.01115	200	3500	0	0	1	0	0
10	CH	G	13.01912	200	3500	0	1	1	0	0
11	CH_2	G	14.02709	200	3500	0	2	1	0	0
12	$CH_2(S)$	G	14.02709	200	3500	0	2	1	0	0
13	CH_3	G	15.03506	200	3500	0	3	1	0	0
14	CH_4	G	16.04303	200	3500	0	4	1	0	0
15	CO	G	28.01055	200	3500	1	0	1	0	0
16	CO_2	G	44.00995	200	3500	2	0	1	0	0
17	HCO	G	29.01852	200	3500	1	1	1	0	0
18	CH_2O	G	30.02649	200	3500	1	2	1	0	0
19	CH_2OH	G	31.03446	200	3500	1	3	1	0	0
20	CH_3O	G	31.03446	300	3000	1	3	1	0	0
21	CH_3OH	G	32.04243	200	3500	1	4	1	0	0
22	C_2H	G	25.03027	200	3500	0	1	2	0	0
23	C_2H_2	G	26.03824	200	3500	0	2	2	0	0
24	C_2H_3	G	27.04621	200	3500	0	3	2	0	0
25	C_2H_4	G	28.05418	200	3500	0	4	2	0	0
26	C_2H_5	G	29.06215	200	3500	0	5	2	0	0
27	C_2H_6	G	30.07012	200	3500	0	6	2	0	0
28	HCCO	G	41.02967	300	4000	1	1	2	0	0
29	CH_2CO	G	42.03764	200	3500	1	2	2	0	0
30	HCCOH	G	42.03764	300	5000	1	2	2	0	0
31	N	G	14.0067	200	6000	0	0	0	1	0
32	NH	G	15.01467	200	6000	0	1	0	1	0
33	NH_2	G	16.02264	200	6000	0	2	0	1	0
34	NH_3	G	17.03061	200	6000	0	3	0	1	0
35	NNH	G	29.02137	200	6000	0	1	0	2	0
36	NO	G	30.0061	200	6000	1	0	0	1	0
37	NO_2	G	46.0055	200	6000	2	0	0	1	0
38	N_2O	G	44.0128	200	6000	1	0	0	2	0
39	HNO	G	31.01407	200	6000	1	1	0	1	0
40	CN	G	26.01785	200	6000	0	0	1	1	0
41	HCN	G	27.02582	200	6000	0	1	1	1	0
42	H_2CN	G	28.03379	300	4000	0	2	1	1	0
43	HCNN	G	41.03252	300	5000	0	1	1	2	0
44	HCNO	G	43.02522	300	5000	1	1	1	1	0
45	HOCN	G	43.02522	300	5000	1	1	1	1	0
46	HNCO	G	43.02522	300	5000	1	1	1	1	0
47	NCO	G	42.01725	200	6000	1	0	1	1	0
48	N_2	G	28.0134	300	5000	0	0	0	2	0
49	Ar	G	39.948	300	5000	0	0	0	0	1
50	C_3H_7	G	43.08924	300	5000	0	7	3	0	0
51	C_3H_8	G	44.09721	300	5000	0	8	3	0	0
52	CH_2CHO	G	43.04561	300	5000	1	3	2	0	0
53	CH_3CHO	G	44.05358	200	6000	1	4	2	0	0

Table F.4: Chemical reaction mechanism for the GRI-Mech 3.0 methane oxidation (A_i in mol.cm.s.K, E_i in cal.mol^{-1})

REACTIONS CONSIDERED	$\mathbf{A_i}$	$\boldsymbol{\beta_i}$	$\mathbf{E_i}$
1. $2O+M \leftrightarrow O_2+M$	-1.20E+17	1	0
2. $O+H+M \leftrightarrow OH+M$	-5.00E+17	1	0
3. $O+H_2 \leftrightarrow H+OH$	3.87E+04	2.7	6260
4. $O+HO_2 \leftrightarrow OH+O_2$	2.00E+13	0	0
5. $O+H_2O_2 \leftrightarrow OH+HO_2$	9.63E+06	2	4000
6. $O+CH \leftrightarrow H+CO$	5.70E+13	0	0
7. $O+CH_2 \leftrightarrow H+HCO$	8.00E+13	0	0
8. $O+CH_2(S) \leftrightarrow H_2+CO$	1.50E+13	0	0
9. $O+CH_2(S) \leftrightarrow H+HCO$	1.50E+13	0	0
10. $O+CH_3 \leftrightarrow H+CH_2O$	5.06E+13	0	0
11. $O+CH_4 \leftrightarrow OH+CH_3$	1.02E+09	1.5	8600
12. $O+CO(+M) \leftrightarrow CO_2(+M)$	1.80E+10	0	2385
Low pressure limit: 0.60200E+15 0.00000E+00 3.00E+03			
13. $O+HCO \leftrightarrow OH+CO$	3.00E+13	0	0
14. $O+HCO \leftrightarrow H+CO_2$	3.00E+13	0	0
15. $O+CH_2O \leftrightarrow OH+HCO$	3.90E+13	0	3540
16. $O+CH_2OH \leftrightarrow OH+CH_2O$	1.00E+13	0	0
17. $O+CH_3O \leftrightarrow OH+CH_2O$	1.00E+13	0	0
18. $O+CH_3OH \leftrightarrow OH+CH_2OH$	3.88E+05	2.5	3100
19. $O+CH_3OH \leftrightarrow OH+CH_3O$	1.30E+05	2.5	5000
20. $O+C_2H \leftrightarrow CH+CO$	5.00E+13	0	0
21. $O+C_2H_2 \leftrightarrow H+HCCO$	1.35E+07	2	1900
22. $O+C_2H_2 \leftrightarrow OH+C_2H$	-4.60E+19	1.4	28950
23. $O+C_2H_2 \leftrightarrow CO+CH_2$	6.94E+06	2	1900
24. $O+C_2H_3 \leftrightarrow H+CH_2CO$	3.00E+13	0	0
25. $O+C_2H_4 \leftrightarrow CH_3+HCO$	1.25E+07	1.8	220
26. $O+C_2H_5 \leftrightarrow CH_3+CH_2O$	2.24E+13	0	0
27. $O+C_2H_6 \leftrightarrow OH+C_2H_5$	8.98E+07	1.9	5690
28. $O+HCCO \leftrightarrow H+2CO$	1.00E+14	0	0
29. $O+CH_2CO \leftrightarrow OH+HCCO$	1.00E+13	0	8000
30. $O+CH_2CO \leftrightarrow CH_2+CO_2$	1.75E+12	0	1350
31. $O_2+CO \leftrightarrow O+CO_2$	2.50E+12	0	47800
32. $O_2+CH_2O \leftrightarrow HO_2+HCO$	1.00E+14	0	40000
33. $H+O_2+M \leftrightarrow HO_2+M$	-2.80E+18	0.9	0
34. $H+2O_2 \leftrightarrow HO_2+O_2$	-2.08E+19	1.2	0
35. $H+O_2+H_2O \leftrightarrow HO_2+H_2O$	-1.13E+19	0.8	0
36. $H+O_2+N_2 \leftrightarrow HO_2+N_2$	-2.60E+19	1.2	0
37. $H+O_2+Ar \leftrightarrow HO_2+Ar$	-7.00E+17	0.8	0
38. $H+O_2 \leftrightarrow O+OH$	-2.65E+16	0.7	17041
39. $2H+M \leftrightarrow H_2+M$	-1.00E+18	1	0
40. $2H+H_2 \leftrightarrow 2H_2$	-9.00E+16	0.6	0
41. $2H+H_2O \leftrightarrow H_2+H_2O$	-6.00E+19	1.3	0

Table F.4 (continued): Chemical reaction mechanism for the GRI-Mech 3.0 methane oxidation (A_i in mol.cm.s.K, E_i in cal.mol^{-1})

REACTIONS CONSIDERED	A_i	β_i	E_i
42. $2H+CO_2 \leftrightarrow H_2+CO_2$	-5.50E+20	2	0
43. $H+OH+M \leftrightarrow H_2O+M$	-2.20E+22	2	0
44. $H+HO_2 \leftrightarrow O+H_2O$	3.97E+12	0	671
45. $H+HO_2 \leftrightarrow O_2+H_2$	4.48E+13	0	1068
46. $H+HO_2 \leftrightarrow 2OH$	8.40E+13	0	635
47. $H+H_2O_2 \leftrightarrow HO_2+H_2$	1.21E+07	2	5200
48. $H+H_2O_2 \leftrightarrow OH+H_2O$	1.00E+13	0	3600
49. $H+CH \leftrightarrow C+H_2$	1.65E+14	0	0
50. $H+CH_2(+M) \leftrightarrow CH_3(+M)$	6.00E+14	0	0
Low pressure limit: 0.10400E+27 -0.27600E+01 1.60E+03			
Troe centering: 0.56200E+00 0.91000E+02 5.84E+03 0.855200E+04			
51. $H+CH_2(S) \leftrightarrow CH+H_2$	3.00E+13	0	0
52. $H+CH_3(+M) \leftrightarrow CH_4(+M)$	-1.39E+16	0.5	536
Low pressure limit: 0.26200E+34 -0.47600E+01 2.44E+03			
Troe centering: 0.78300E+00 0.74000E+02 2.94E+03 0.696400E+04			
53. $H+CH_4 \leftrightarrow CH_3+H_2$	6.60E+08	1.6	10840
54. $H+HCO(+M) \leftrightarrow CH_2O(+M)$	1.09E+12	0.5	-260
Low pressure limit: 0.24700E+25 -0.25700E+01 4.25E+02			
Troe centering: 0.78240E+00 0.27100E+03 2.76E+03 0.657000E+04			
55. $H+HCO \leftrightarrow H_2+CO$	7.34E+13	0	0
56. $H+CH_2O(+M) \leftrightarrow CH_2OH(+M)$	5.40E+11	0.5	3600
Low pressure limit: 0.12700E+33 -0.48200E+01 6.53E+03			
Troe centering: 0.71870E+00 0.10300E+03 1.29E+03 0.416000E+04			
57. $H+CH_2O(+M) \leftrightarrow CH_3O(+M)$	5.40E+11	0.5	2600
Low pressure limit: 0.22000E+31 -0.48000E+01 5.56E+03			
Troe centering: 0.75800E+00 0.94000E+02 1.56E+03 0.42000E+04			
58. $H+CH_2O \leftrightarrow HCO+H_2$	5.74E+07	1.9	2742
59. $H+CH_2OH(+M) \leftrightarrow CH_3OH(+M)$	1.06E+12	0.5	86
Low pressure limit: 0.43600E+32 -0.46500E+01 5.08E+03			
Troe centering: 0.60000E+00 0.10000E+03 9.00E+04 0.1000E+05			
60. $H+CH_2OH \leftrightarrow H_2+CH_2O$	2.00E+13	0	0
61. $H+CH_2OH \leftrightarrow OH+CH_3$	1.65E+11	0.7	-284
62. $H+CH_2OH \leftrightarrow CH_2(S)+H_2O$	-3.28E+13	0.1	610
63. $H+CH_3O(+M) \leftrightarrow CH_3OH(+M)$	2.43E+12	0.5	50
Low pressure limit: 0.46600E+42 -0.74400E+01 1.41E+04			
Troe centering: 0.70000E+00 0.10000E+03 9.00E+04 0.1000E+05			
64. $H+CH_3O \leftrightarrow H+CH_2OH$	4.15E+07	1.6	1924
65. $H+CH_3O \leftrightarrow H_2+CH_2O$	2.00E+13	0	0
66. $H+CH_3O \leftrightarrow OH+CH_3$	1.50E+12	0.5	-110
67. $H+CH_3O \leftrightarrow CH_2(S)+H_2O$	-2.62E+14	0.2	1070
68. $H+CH_3OH \leftrightarrow CH_2OH+H_2$	1.70E+07	2.1	4870
69. $H+CH_3OH \leftrightarrow CH_3O+H_2$	4.20E+06	2.1	4870

Table F.4 (continued): Chemical reaction mechanism for the GRI-Mech 3.0 methane oxidation (A_i in mol.cm.s.K, E_i in cal.mol^{-1})

REACTIONS CONSIDERED	**A_i**	**β_i**	**E_i**
70. $H+C_2H(+M)\leftrightarrow C_2H_2(+M)$	-1.00E+17	1	0
Low pressure limit: 0.37500E+34 -0.48000E+01 1.90E+03			
Troe centering: 0.64640E+00 0.13200E+03 1.32E+03 0.556600E+05			
71. $H+C_2H_2(+M)\leftrightarrow C_2H_3(+M)$	5.60E+12	0	2400
Low pressure limit: 0.38000E+41 -0.72700E+01 7.22E+03			
Troe centering: 0.75070E+00 0.98500E+02 1.30E+03 0.416700E+04			
72. $H+C_2H_3(+M)\leftrightarrow C_2H_4(+M)$	6.08E+12	0.3	280
Low pressure limit: 0.14000E+31 -0.38600E+01 3.32E+03			
Troe centering: 0.78200E+00 0.20750E+03 2.66E+03 0.609500E+04			
73. $H+C_2H_3\leftrightarrow H_2+C_2H_2$	3.00E+13	0	0
74. $H+C_2H_4(+M)\leftrightarrow C_2H_5(+M)$	5.40E+11	0.5	1820
Low pressure limit: 0.60000E+42 -0.76200E+01 6.97E+03			
Troe centering: 0.97530E+00 0.21000E+03 9.84E+02 0.437400E+04			
75. $H+C_2H_4\leftrightarrow C_2H_3+H_2$	1.33E+06	2.5	12240
76. $H+C_2H_5(+M)\leftrightarrow C_2H_6(+M)$	-5.21E+17	1	1580
Low pressure limit: 0.19900E+42 -0.70800E+01 6.69E+03			
Troe centering: 0.84220E+00 0.12500E+03 2.22E+03 0.688200E+04			
77. $H+C_2H_5\leftrightarrow H_2+C_2H_4$	2.00E+12	0	0
78. $H+C_2H_6\leftrightarrow C_2H_5+H_2$	1.15E+08	1.9	7530
79. $H+HCCO\leftrightarrow CH_2(S)+CO$	1.00E+14	0	0
80. $H+CH_2CO\leftrightarrow HCCO+H_2$	5.00E+13	0	8000
81. $H+CH_2CO\leftrightarrow CH_3+CO$	1.13E+13	0	3428
82. $H+HCCOH\leftrightarrow H+CH_2CO$	1.00E+13	0	0
83. $H_2+CO(+M)\leftrightarrow CH_2O(+M)$	4.30E+07	1.5	79600
Low pressure limit: 0.50700E+28 -0.34200E+01	8.44E+04		
Troe centering: 0.93200E+00 0.19700E+03	1.54E+03	0.103	0.00E+00
84. $OH+H_2\leftrightarrow H+H_2O$	2.16E+08	1.5	3430
85. $2OH(+M)\leftrightarrow H_2O_2(+M)$	-7.40E+13	0.4	0
Low pressure limit: 0.23000E+19 -0.90000E+00 -1.70E+03			
Troe centering: 0.73460E+00 0.94000E+02 1.76E+03 0.518200E+04			
86. $2OH\leftrightarrow O+H_2O$	3.57E+04	2.4	-2110
87. $OH+HO_2\leftrightarrow O_2+H_2O$	1.45E+13	0	-500
88. $OH+H_2O_2\leftrightarrow HO_2+H_2O$	2.00E+12	0	427
89. $OH+H_2O_2\leftrightarrow HO_2+H_2O$	1.70E+18	0	29410
90. $OH+C\leftrightarrow H+CO$	5.00E+13	0	0
91. $OH+CH\leftrightarrow H+HCO$	3.00E+13	0	0
92. $OH+CH_2\leftrightarrow H+CH_2O$	2.00E+13	0	0
93. $OH+CH_2\leftrightarrow CH+H_2O$	1.13E+07	2	3000
94. $OH+CH_2(S)\leftrightarrow H+CH_2O$	3.00E+13	0	0
95. $OH+CH_3(+M)\leftrightarrow CH_3OH(+M)$	-2.79E+18	1.4	1330
Low pressure limit: 0.40000E+37 -0.59200E+01 3.14E+03			
Troe centering: 0.41200E+00 0.19500E+03 5.90E+03 0.639400E+04			
96. $OH+CH_3\leftrightarrow CH_2+H_2O$	5.60E+07	1.6	5420

Table F.4 (continued): Chemical reaction mechanism for the GRI-Mech 3.0 methane oxidation (A_i in mol.cm.s.K, E_i in cal.mol^{-1})

REACTIONS CONSIDERED	A_i	β_i	E_i
97. $OH+CH_3 \leftrightarrow CH_2(S)+H_2O$	-6.44E+17	1.3	1417
98. $OH+CH_4 \leftrightarrow CH_3+H_2O$	1.00E+08	1.6	3120
99. $OH+CO \leftrightarrow H+CO_2$	4.76E+07	1.2	70
100. $OH+HCO \leftrightarrow H_2O+CO$	5.00E+13	0	0
101. $OH+CH_2O \leftrightarrow HCO+H_2O$	3.43E+09	1.2	-447
102. $OH+CH_2OH \leftrightarrow H_2O+CH_2O$	5.00E+12	0	0
103. $OH+CH_3O \leftrightarrow H_2O+CH_2O$	5.00E+12	0	0
104. $OH+CH_3OH \leftrightarrow CH_2OH+H_2O$	1.44E+06	2	-840
105. $OH+CH_3OH \leftrightarrow CH_3O+H_2O$	6.30E+06	2	1500
106. $OH+C_2H \leftrightarrow H+HCCO$	2.00E+13	0	0
107. $OH+C_2H_2 \leftrightarrow H+CH_2CO$	2.18E-04	4.5	-1000
108. $OH+C_2H_2 \leftrightarrow H+HCCOH$	5.04E+05	2.3	13500
109. $OH+C_2H_2 \leftrightarrow C_2H+H_2O$	3.37E+07	2	14000
110. $OH+C_2H_2 \leftrightarrow CH_3+CO$	4.83E-04	4	-2000
111. $OH+C_2H_3 \leftrightarrow H_2O+C_2H_2$	5.00E+12	0	0
112. $OH+C_2H_4 \leftrightarrow C_2H_3+H_2O$	3.60E+06	2	2500
113. $OH+C_2H_6 \leftrightarrow C_2H_5+H_2O$	3.54E+06	2.1	870
114. $OH+CH_2CO \leftrightarrow HCCO+H_2O$	7.50E+12	0	2000
115. $2HO_2 \leftrightarrow O_2+H_2O_2$	1.30E+11	0	-1630
116. $2HO_2 \leftrightarrow O_2+H_2O_2$	4.20E+14	0	12000
117. $HO_2+CH_2 \leftrightarrow OH+CH_2O$	2.00E+13	0	0
118. $HO_2+CH_3 \leftrightarrow O_2+CH_4$	1.00E+12	0	0
119. $HO_2+CH_3 \leftrightarrow OH+CH_3O$	3.78E+13	0	0
120. $HO_2+CO \leftrightarrow OH+CO_2$	1.50E+14	0	23600
121. $HO_2+CH_2O \leftrightarrow HCO+H_2O_2$	5.60E+06	2	12000
122. $C+O_2 \leftrightarrow O+CO$	5.80E+13	0	576
123. $C+CH_2 \leftrightarrow H+C_2H$	5.00E+13	0	0
124. $C+CH_3 \leftrightarrow H+C_2H_2$	5.00E+13	0	0
125. $CH+O_2 \leftrightarrow O+HCO$	6.71E+13	0	0
126. $CH+H_2 \leftrightarrow H+CH_2$	1.08E+14	0	3110
127. $CH+H_2O \leftrightarrow H+CH_2O$	5.71E+12	0	-755
128. $CH+CH_2 \leftrightarrow H+C_2H_2$	4.00E+13	0	0
129. $CH+CH_3 \leftrightarrow H+C_2H_3$	3.00E+13	0	0
130. $CH+CH_4 \leftrightarrow H+C_2H_4$	6.00E+13	0	0
131. $CH+CO(+M) \leftrightarrow HCCO(+M)$	5.00E+13	0	0
Low pressure limit: 0.26900E+29 -0.37400E+01 1.94E+03			
Troe centering: 0.57570E+00 0.23700E+03 1.65E+03 0.506900E+04			
132. $CH+CO_2 \leftrightarrow HCO+CO$	1.90E+14	0	15792
133. $CH+CH_2O \leftrightarrow H+CH_2CO$	9.46E+13	0	-515
134. $CH+HCCO \leftrightarrow CO+C_2H_2$	5.00E+13	0	0
135. $CH_2+O_2 \rightarrow OH+H+CO$	5.00E+12	0	1500
136. $CH_2+H_2 \leftrightarrow H+CH_3$	5.00E+05	2	7230
137. $2CH_2 \leftrightarrow H_2+C_2H_2$	1.60E+15	0	11944

Table F.4 (continued): Chemical reaction mechanism for the GRI-Mech 3.0 methane oxidation (A_i in mol.cm.s.K, E_i in cal.mol^{-1})

REACTIONS CONSIDERED	A_i	β_i	E_i
138. $CH_2+CH_3 \leftrightarrow H+C_2H_4$	4.00E+13	0	0
139. $CH_2+CH_4 \leftrightarrow 2CH_3$	2.46E+06	2	8270
140. $CH_2+CO(+M) \leftrightarrow CH_2CO(+M)$	8.10E+11	0.5	4510
Low pressure limit: 0.26900E+34 -0.51100E+01 7.10E+03			
Troe centering: 0.59070E+00 0.27500E+03 1.23E+03 0.518500E+04			
141. $CH_2+HCCO \leftrightarrow C_2H_3+CO$	3.00E+13	0	0
142. $CH_2(S)+N_2 \leftrightarrow CH_2+N_2$	1.50E+13	0	600
143. $CH_2(S)+Ar \leftrightarrow CH_2+Ar$	9.00E+12	0	600
144. $CH_2(S)+O_2 \leftrightarrow H+OH+CO$	2.80E+13	0	0
145. $CH_2(S)+O_2 \leftrightarrow CO+H_2O$	1.20E+13	0	0
146. $CH_2(S)+H_2 \leftrightarrow CH_3+H$	7.00E+13	0	0
147. $CH_2(S)+H_2O(+M) \leftrightarrow CH_3OH(+M)$	-4.82E+17	1.2	1145
Low pressure limit: 0.18800E+39 -0.63600E+01 5.04E+03			
Troe centering: 0.60270E+00 0.20800E+03 3.92E+03 0.101800E+04			
148. $CH_2(S)+H_2O \leftrightarrow CH_2+H_2O$	3.00E+13	0	0
149. $CH_2(S)+CH_3 \leftrightarrow H+C_2H_4$	1.20E+13	0	-570
150. $CH_2(S)+CH_4 \leftrightarrow 2CH_3$	1.60E+13	0	-570
151. $CH_2(S)+CO \leftrightarrow CH_2+CO$	9.00E+12	0	0
152. $CH_2(S)+CO_2 \leftrightarrow CH_2+CO_2$	7.00E+12	0	0
153. $CH_2(S)+CO_2 \leftrightarrow CO+CH_2O$	1.40E+13	0	0
154. $CH_2(S)+C_2H_6 \leftrightarrow CH_3+C_2H_5$	4.00E+13	0	-550
155. $CH_3+O_2 \leftrightarrow O+CH_3O$	3.56E+13	0	30480
156. $CH_3+O_2 \leftrightarrow OH+CH_2O$	2.31E+12	0	20315
157. $CH_3+H_2O_2 \leftrightarrow HO_2+CH_4$	2.45E+04	2.5	5180
158. $2CH_3(+M) \leftrightarrow C_2H_6(+M)$	-6.77E+16	1.2	654
Low pressure limit: 0.34000E+42 -0.70300E+01 2.76E+03			
Troe centering: 0.61900E+00 0.73200E+02 1.18E+03 0.999900E+04			
159. $2CH_3 \leftrightarrow H+C_2H_5$	6.84E+12	0.1	10600
160. $CH_3+HCO \leftrightarrow CH_4+CO$	2.65E+13	0	0
161. $CH_3+CH_2O \leftrightarrow HCO+CH_4$	3.32E+03	2.8	5860
162. $CH_3+CH_3OH \leftrightarrow CH_2OH+CH_4$	3.00E+07	1.5	9940
163. $CH_3+CH_3OH \leftrightarrow CH_3O+CH_4$	1.00E+07	1.5	9940
164. $CH_3+C_2H_4 \leftrightarrow C_2H_3+CH_4$	2.27E+05	2	9200
165. $CH_3+C_2H_6 \leftrightarrow C_2H_5+CH_4$	6.14E+06	1.7	10450
166. $HCO+H_2O \leftrightarrow H+CO+H_2O$	-1.50E+18	1	17000
167. $HCO+M \leftrightarrow H+CO+M$	-1.87E+17	1	17000
168. $HCO+O_2 \leftrightarrow HO_2+CO$	1.35E+13	0	400
169. $CH_2OH+O_2 \leftrightarrow HO_2+CH_2O$	1.80E+13	0	900
170. $CH_3O+O_2 \leftrightarrow HO_2+CH_2O$	4.28E-13	7.6	-3530
171. $C_2H+O_2 \leftrightarrow HCO+CO$	1.00E+13	0	-755
172. $C_2H+H_2 \leftrightarrow H+C_2H_2$	5.68E+10	0.9	1993
173. $C_2H_3+O_2 \leftrightarrow HCO+CH_2O$	-4.58E+16	1.4	1015
174. $C_2H_4(+M) \leftrightarrow H_2+C2H_2(+M)$	8.00E+12	0.4	86770

Table F.4 (continued): Chemical reaction mechanism for the GRI-Mech 3.0 methane oxidation (A_i in mol.cm.s.K, E_i in cal.mol^{-1})

REACTIONS CONSIDERED	**Ai**	**β_i**	**E_i**
Low pressure limit: 0.15800E+52 -0.93000E+01 9.78E+04			
Troe centering: 0.73450E+00 0.18000E+03 1.04E+03 0.541700E+04			
175. $C_2H_5+O_2\leftrightarrow HO_2+C_2H_4$	8.40E+11	0	3875
176. $HCCO+O_2\leftrightarrow OH+2CO$	3.20E+12	0	854
177. $2HCCO\leftrightarrow 2CO+C_2H_2$	1.00E+13	0	0
178. $N+NO\leftrightarrow N_2+O$	2.70E+13	0	355
179. $N+O_2\leftrightarrow NO+O$	9.00E+09	1	6500
180. $N+OH\leftrightarrow NO+H$	3.36E+13	0	385
181. $N_2O+O\leftrightarrow N_2+O_2$	1.40E+12	0	10810
182. $N_2O+O\leftrightarrow 2NO$	2.90E+13	0	23150
183. $N_2O+H\leftrightarrow N_2+OH$	3.87E+14	0	18880
184. $N_2O+OH\leftrightarrow N_2+HO_2$	2.00E+12	0	21060
185. $N_2O(+M)\leftrightarrow N_2+O(+M)$	7.91E+10	0	56020
Low pressure limit: 0.63700E+15 0.00000E+00 5.66E+04			
186. $HO_2+NO\leftrightarrow NO_2+OH$	2.11E+12	0	-480
187. $NO+O+M\leftrightarrow NO_2+M$	-1.06E+20	1.4	0
188. $NO_2+O\leftrightarrow NO+O_2$	3.90E+12	0	-240
189. $NO_2+H\leftrightarrow NO+OH$	1.32E+14	0	360
190. $NH+O\leftrightarrow NO+H$	4.00E+13	0	0
191. $NH+H\leftrightarrow N+H_2$	3.20E+13	0	330
192. $NH+OH\leftrightarrow HNO+H$	2.00E+13	0	0
193. $NH+OH\leftrightarrow N+H_2O$	2.00E+09	1.2	0
194. $NH+O_2\leftrightarrow HNO+O$	4.61E+05	2	6500
195. $NH+O_2\leftrightarrow NO+OH$	1.28E+06	1.5	100
196. $NH+N\leftrightarrow N_2+H$	1.50E+13	0	0
197. $NH+H_2O\leftrightarrow HNO+H_2$	2.00E+13	0	13850
198. $NH+NO\leftrightarrow N_2+OH$	-2.16E+13	0.2	0
199. $NH+NO\leftrightarrow N_2O+H$	-3.65E+14	0.5	0
200. $NH_2+O\leftrightarrow OH+NH$	3.00E+12	0	0
201. $NH_2+O\leftrightarrow H+HNO$	3.90E+13	0	0
202. $NH_2+H\leftrightarrow NH+H_2$	4.00E+13	0	3650
203. $NH_2+OH\leftrightarrow NH+H_2O$	9.00E+07	1.5	-460
204. $NNH\leftrightarrow N_2+H$	3.30E+08	0	0
205. $NNH+M\leftrightarrow N_2+H+M$	-1.30E+14	0.1	4980
206. $NNH+O_2\leftrightarrow HO_2+N_2$	5.00E+12	0	0
207. $NNH+O\leftrightarrow OH+N_2$	2.50E+13	0	0
208. $NNH+O\leftrightarrow NH+NO$	7.00E+13	0	0
209. $NNH+H\leftrightarrow H_2+N_2$	5.00E+13	0	0
210. $NNH+OH\leftrightarrow H_2O+N_2$	2.00E+13	0	0
211. $NNH+CH_3\leftrightarrow CH_4+N_2$	2.50E+13	0	0
212. $H+NO+M\leftrightarrow HNO+M$	-4.48E+19	1.3	740
213. $HNO+O\leftrightarrow NO+OH$	2.50E+13	0	0
214. $HNO+H\leftrightarrow H_2+NO$	9.00E+11	0.7	660

Table F.4 (continued): Chemical reaction mechanism for the GRI-Mech 3.0 methane oxidation (A_i in mol.cm.s.K, E_i in cal.mol^{-1})

REACTIONS CONSIDERED	A_i	β_i	E_i
215. HNO+OH↔NO+H_2O	1.30E+07	1.9	-950
216. HNO+O_2↔HO_2+NO	1.00E+13	0	13000
217. CN+O↔CO+N	7.70E+13	0	0
218. CN+OH↔NCO+H	4.00E+13	0	0
219. CN+H_2O↔HCN+OH	8.00E+12	0	7460
220. CN+O_2↔NCO+O	6.14E+12	0	-440
221. CN+H_2↔HCN+H	2.95E+05	2.5	2240
222. NCO+O↔NO+CO	2.35E+13	0	0
223. NCO+H↔NH+CO	5.40E+13	0	0
224. NCO+OH↔NO+H+CO	2.50E+12	0	0
225. NCO+N↔N_2+CO	2.00E+13	0	0
226. NCO+O_2↔NO+CO_2	2.00E+12	0	20000
227. NCO+M↔N+CO+M	3.10E+14	0	54050
228. NCO+NO↔N_2O+CO	-1.90E+17	1.5	740
229. NCO+NO↔N_2+CO_2	-3.80E+18	2	800
230. HCN+M↔H+CN+M	-1.04E+29	3.3	126600
231. HCN+O↔NCO+H	2.03E+04	2.6	4980
232. HCN+O↔NH+CO	5.07E+03	2.6	4980
233. HCN+O↔CN+OH	3.91E+09	1.6	26600
234. HCN+OH↔HOCN+H	1.10E+06	2	13370
235. HCN+OH↔HNCO+H	4.40E+03	2.3	6400
236. HCN+OH↔NH_2+CO	1.60E+02	2.6	9000
237. H+HCN(+M)↔H_2CN(+M)	3.30E+13	0	0
Low pressure limit: 0.14000E+27 -0.34000E+01 1.90E+03			
238. H_2CN+N↔N_2+CH_2	6.00E+13	0	400
239. C+N_2↔CN+N	6.30E+13	0	46020
240. CH+N_2↔HCN+N	3.12E+09	0.9	20130
241. CH+N_2(+M)↔HCNN(+M)	3.10E+12	0.1	0
Low pressure limit: 0.13000E+26 -0.31600E+01 7.40E+02			
Troe centering: 0.66700E+00 0.23500E+03 2.12E+03 0.453600E+04			
242. CH_2+N_2↔HCN+NH	1.00E+13	0	74000
243. CH_2(S)+N_2↔NH+HCN	1.00E+11	0	65000
244. C+NO↔CN+O	1.90E+13	0	0
245. C+NO↔CO+N	2.90E+13	0	0
246. CH+NO↔HCN+O	4.10E+13	0	0
247. CH+NO↔H+NCO	1.62E+13	0	0
248. CH+NO↔N+HCO	2.46E+13	0	0
249. CH_2+NO↔H+HNCO	-3.10E+17	1.4	1270
250. CH_2+NO↔OH+HCN	-2.90E+14	0.7	760
251. CH_2+NO↔H+HCNO	-3.80E+13	0.4	580
252. CH_2(S)+NO↔H+HNCO	-3.10E+17	1.4	1270
253. CH_2(S)+NO↔OH+HCN	-2.90E+14	0.7	760
254. CH_2(S)+NO↔H+HCNO	-3.80E+13	0.4	580

Table F.4 (continued): Chemical reaction mechanism for the GRI-Mech 3.0 methane oxidation (A_i in mol.cm.s.K, E_i in cal.mol^{-1})

REACTIONS CONSIDERED	A_i	β_i	E_i
255. $CH_3+NO \leftrightarrow HCN+H_2O$	9.60E+13	0	28800
256. $CH_3+NO \leftrightarrow H_2CN+OH$	1.00E+12	0	21750
257. $HCNN+O \leftrightarrow CO+H+N_2$	2.20E+13	0	0
258. $HCNN+O \leftrightarrow HCN+NO$	2.00E+12	0	0
259. $HCNN+O_2 \leftrightarrow O+HCO+N_2$	1.20E+13	0	0
260. $HCNN+OH \leftrightarrow H+HCO+N_2$	1.20E+13	0	0
261. $HCNN+H \leftrightarrow CH_2+N_2$	1.00E+14	0	0
262. $HNCO+O \leftrightarrow NH+CO_2$	9.80E+07	1.4	8500
263. $HNCO+O \leftrightarrow HNO+CO$	1.50E+08	1.6	44000
264. $HNCO+O \leftrightarrow NCO+OH$	2.20E+06	2.1	11400
265. $HNCO+H \leftrightarrow NH_2+CO$	2.25E+07	1.7	3800
266. $HNCO+H \leftrightarrow H_2+NCO$	1.05E+05	2.5	13300
267. $HNCO+OH \leftrightarrow NCO+H_2O$	3.30E+07	1.5	3600
268. $HNCO+OH \leftrightarrow NH_2+CO_2$	3.30E+06	1.5	3600
269. $HNCO+M \leftrightarrow NH+CO+M$	1.18E+16	0	84720
270. $HCNO+H \leftrightarrow H+HNCO$	-2.10E+15	0.7	2850
271. $HCNO+H \leftrightarrow OH+HCN$	2.70E+11	0.2	2120
272. $HCNO+H \leftrightarrow NH_2+CO$	-1.70E+14	0.8	2890
273. $HOCN+H \leftrightarrow H+HNCO$	2.00E+07	2	2000
274. $HCCO+NO \leftrightarrow HCNO+CO$	9.00E+12	0	0
275. $CH_3+N \leftrightarrow H_2CN+H$	-6.10E+14	0.3	290
276. $CH_3+N \leftrightarrow HCN+H_2$	3.70E+12	0.1	-90
277. $NH_3+H \leftrightarrow NH_2+H_2$	5.40E+05	2.4	9915
278. $NH_3+OH \leftrightarrow NH_2+H_2O$	5.00E+07	1.6	955
279. $NH_3+O \leftrightarrow NH_2+OH$	9.40E+06	1.9	6460
280. $NH+CO_2 \leftrightarrow HNO+CO$	1.00E+13	0	14350
281. $CN+NO_2 \leftrightarrow NCO+NO$	-6.16E+15	0.8	345
282. $NCO+NO_2 \leftrightarrow N_2O+CO_2$	3.25E+12	0	-705
283. $N+CO_2 \leftrightarrow NO+CO$	3.00E+12	0	11300
284. $O+CH_3 \rightarrow H+H_2+CO$	3.37E+13	0	0
285. $O+C_2H_4 \leftrightarrow H+CH_2CHO$	6.70E+06	1.8	220
286. $O+C_2H_5 \leftrightarrow H+CH_3CHO$	1.10E+14	0	0
287. $OH+HO_2 \leftrightarrow O_2+H_2O$	5.00E+15	0	17330
288. $OH+CH_3 \rightarrow H_2+CH_2O$	8.00E+09	0.5	-1755
289. $CH+H_2(+M) \leftrightarrow CH_3(+M)$	1.97E+12	0.4	-370
Low pressure limit: 0.48200E+26 -0.28000E+01 5.90E+02			
Troe centering: 0.57800E+00 0.12200E+03 2.54E+03 0.936500E+04			
290. $CH_2+O_2 \rightarrow 2H+CO_2$	5.80E+12	0	1500
291. $CH_2+O_2 \leftrightarrow O+CH_2O$	2.40E+12	0	1500
292. $CH_2+CH_2 \rightarrow 2H+C_2H_2$	2.00E+14	0	10989
293. $CH_2(S)+H_2O \rightarrow H_2+CH_2O$	6.82E+10	0.3	-935
294. $C_2H_3+O_2 \leftrightarrow O+CH_2CHO$	3.03E+11	0.3	11
295. $C_2H_3+O_2 \leftrightarrow HO_2+C_2H_2$	1.34E+06	1.6	-384

Table F.4 (continued): Chemical reaction mechanism for the GRI-Mech 3.0 methane oxidation (A_i in mol.cm.s.K, E_i in cal.mol^{-1})

REACTIONS CONSIDERED	A_i	β_i	E_i
296. $O+CH_3CHO \leftrightarrow OH+CH_2CHO$	2.92E+12	0	1808
297. $O+CH_3CHO \rightarrow OH+CH_3+CO$	2.92E+12	0	1808
298. $O_2+CH_3CHO \rightarrow HO_2+CH_3+CO$	3.01E+13	0	39150
299. $H+CH_3CHO \leftrightarrow CH_2CHO+H_2$	2.05E+09	1.2	2405
300. $H+CH_3CHO \rightarrow CH_3+H_2+CO$	2.05E+09	1.2	2405
301. $OH+CH_3CHO \rightarrow CH_3+H_2O+CO$	2.34E+10	0.7	-1113
302. $HO_2+CH_3CHO \rightarrow CH_3+H_2O_2+CO$	3.01E+12	0	11923
303. $CH_3+CH_3CHO \rightarrow CH_3+CH_4+CO$	2.72E+06	1.8	5920
304. $H+CH_2CO(+M) \leftrightarrow CH_2CHO(+M)$	4.87E+11	0.4	-1755
Low pressure limit: 0.10120E+43 -0.76300E+01 3.85E+03			
Troe centering: 0.46500E+00 0.20100E+03 1.77E+03 0.533300E+04			
305. $O+CH_2CHO \rightarrow H+CH_2+CO_2$	1.50E+14	0	0
306. $O_2+CH_2CHO \rightarrow OH+CO+CH_2O$	1.81E+10	0	0
307. $O_2+CH_2CHO \rightarrow OH+2HCO$	2.35E+10	0	0
308. $H+CH_2CHO \leftrightarrow CH_3+HCO$	2.20E+13	0	0
309. $H+CH_2CHO \leftrightarrow CH_2CO+H_2$	1.10E+13	0	0
310. $OH+CH_2CHO \leftrightarrow H_2O+CH_2CO$	1.20E+13	0	0
311. $OH+CH_2CHO \leftrightarrow HCO+CH_2OH$	3.01E+13	0	0
312. $CH_3+C_2H_5(+M) \leftrightarrow C_3H_8(+M)$	9.43E+12	0	0
Low pressure limit: 0.27100E+75 -0.16820E+02 1.31E+04			
Troe centering: 0.15270E+00 0.29100E+03 2.74E+03 0.774800E+04			
313. $O+C_3H_8 \leftrightarrow OH+C_3H_7$	1.93E+05	2.7	3716
314. $H+C_3H_8 \leftrightarrow C_3H_7+H_2$	1.32E+06	2.5	6756
315. $OH+C_3H_8 \leftrightarrow C_3H_7+H_2O$	3.16E+07	1.8	934
316. $C_3H_7+H_2O_2 \leftrightarrow HO_2+C_3H_8$	3.78E+02	2.7	1500
317. $CH_3+C_3H_8 \leftrightarrow C_3H_7+CH_4$	9.03E-01	3.6	7154
318. $CH_3+C_2H_4(+M) \leftrightarrow C_3H_7(+M)$	2.55E+06	1.6	5700
Low pressure limit: 0.30000E+64 -0.14600E+02 1.82E+04			
Troe centering: 0.18940E+00 0.27700E+03 8.75E+03 0.789100E+04			
319. $O+C_3H_7 \leftrightarrow C_2H_5+CH_2O$	9.64E+13	0	0
320. $H+C_3H_7(+M) \leftrightarrow C_3H_8(+M)$	3.61E+13	0	0
Low pressure limit: 0.44200E+62 -0.13545E+02 1.14E+04			
Troe centering: 0.31500E+00 0.36900E+03 3.29E+03 0.666700E+04			
321. $H+C_3H_7 \leftrightarrow CH_3+C_2H_5$	4.06E+06	2.2	890
322. $OH+C_3H_7 \leftrightarrow C_2H_5+CH_2OH$	2.41E+13	0	0
323. $HO_2+C_3H_7 \leftrightarrow O_2+C_3H_8$	2.55E+10	0.3	-943
324. $HO_2+C_3H_7 \rightarrow OH+C_2H_5+CH_2O$	2.41E+13	0	0
325. $CH_3+C_3H_7 \leftrightarrow 2C_2H_5$	-1.93E+13	0.3	0

F3 Konnov's Detailed Methane Oxidation Mechanism

A detailed elementary reaction mechanism for combustion processes was developed and validated by Konnov [208]. This mechanism consists of 127 considered species and 1207 elementary reactions. Below is a list of all the considered species and reactions.

Table F.5: Chemkin interpreter output for the Konnov's chemical reaction mechanism for combustion

				TEMPERATURE		ELEMENT COUNT				
SPECIES CONSIDERED		PHASE	MOLECULAR WEIGHT	LOW (K)	HIGH (K)	H	C	O	N	Ar
1	H	G	1.00797	300	5000	1	0	0	0	0
2	H_2	G	2.01594	300	5000	2	0	0	0	0
3	O	G	15.9994	300	5000	0	0	1	0	0
4	O_2	G	31.9988	300	5000	0	0	2	0	0
5	OH	G	17.00737	300	5000	1	0	1	0	0
6	HO_2	G	33.00677	300	5000	1	0	2	0	0
7	H_2O	G	18.01534	300	5000	2	0	1	0	0
8	H_2O_2	G	34.01474	300	5000	2	0	2	0	0
9	CO	G	28.01055	300	5000	0	1	1	0	0
10	CO_2	G	44.00995	300	5000	0	1	2	0	0
11	HCO	G	29.01852	300	5000	1	1	1	0	0
12	CH_3	G	15.03506	300	5000	3	1	0	0	0
13	CH_4	G	16.04303	300	5000	4	1	0	0	0
14	C_2H_6	G	30.07012	300	4000	6	2	0	0	0
15	CH_2O	G	30.02649	300	5000	2	1	1	0	0
16	C_2H_5	G	29.06215	300	5000	5	2	0	0	0
17	CH_2	G	14.02709	250	4000	2	1	0	0	0
18	CH_3O	G	31.03446	300	3000	3	1	1	0	0
19	CH_2OH	G	31.03446	250	4000	3	1	1	0	0
20	CH	G	13.01912	300	5000	1	1	0	0	0
21	C_2H_2	G	26.03824	300	5000	2	2	0	0	0
22	C_2H_4	G	28.05418	300	5000	4	2	0	0	0
23	C_2H_3	G	27.04621	300	5000	3	2	0	0	0
24	CH_3OH	G	32.04243	300	5000	4	1	1	0	0
25	CH_3HCO	G	44.05358	300	5000	4	2	1	0	0
26	C_2H	G	25.03027	300	4000	1	2	0	0	0
27	CH_2CO	G	42.03764	300	5000	2	2	1	0	0
28	HCCO	G	41.02967	300	4000	1	2	1	0	0
29	C_2H_4O	G	44.05358	200	6000	4	2	1	0	0
30	SCH_2	G	14.02709	300	4000	2	1	0	0	0
31	C_2	G	24.0223	300	5000	0	2	0	0	0
32	C_2O	G	40.0217	300	5000	0	2	1	0	0
33	CH_3CO	G	43.04561	300	5000	3	2	1	0	0
34	C	G	12.01115	300	5000	0	1	0	0	0

Table F.5 (continued): Chemkin interpreter output for the Konnov's chemical reaction mechanism for combustion

No.	SPECIES	PHASE	MW	LT (K)	HT (K)	O	H	C	N	Ar
35	CH_3CO_3	G	75.04441	300	5000	3	2	3	0	0
36	CH_3CO_3H	G	76.05238	300	5000	4	2	3	0	0
37	CH_3O_2	G	47.03386	300	5000	3	1	2	0	0
38	CH_3O_2H	G	48.04183	200	6000	4	1	2	0	0
39	$C_2H_5O_2H$	G	62.06892	200	6000	6	2	2	0	0
40	$C_2H_5O_2$	G	61.06095	300	5000	5	2	2	0	0
41	CH_3CO_2	G	59.04501	300	5000	3	2	2	0	0
42	CH_3CO_2H	G	60.05298	300	5000	4	2	2	0	0
43	C_2H_5OH	G	46.06952	200	6000	6	2	1	0	0
44	C_2H_5O	G	45.06155	300	5000	5	2	1	0	0
45	SC_2H_5O	G	45.06155	300	5000	5	2	1	0	0
46	PC_2H_5O	G	45.06155	300	5000	5	2	1	0	0
47	CH_2HCO	G	43.04561	300	5000	3	2	1	0	0
48	CN	G	26.01785	300	5000	0	1	0	1	0
49	H_2CN	G	28.03379	300	4000	2	1	0	1	0
50	N	G	14.0067	300	5000	0	0	0	1	0
51	NH	G	15.01467	300	5000	1	0	0	1	0
52	HCN	G	27.02582	300	4000	1	1	0	1	0
53	NO	G	30.0061	300	5000	0	0	1	1	0
54	HCNO	G	43.02522	250	4000	1	1	1	1	0
55	HOCN	G	43.02522	300	4000	1	1	1	1	0
56	HNCO	G	43.02522	300	4000	1	1	1	1	0
57	NCO	G	42.01725	300	4000	0	1	1	1	0
58	N_2O	G	44.0128	300	5000	0	0	1	2	0
59	NH_2	G	16.02264	300	5000	2	0	0	1	0
60	N_2O_3	G	76.0116	200	6000	0	0	3	2	0
61	HNO	G	31.01407	300	5000	1	0	1	1	0
62	NO_2	G	46.0055	300	5000	0	0	2	1	0
63	C_2N_2	G	52.0357	300	5000	0	2	0	2	0
64	NNH	G	29.02137	250	4000	1	0	0	2	0
65	NH_3	G	17.03061	300	5000	3	0	0	1	0
66	N_2H_2	G	30.02934	300	5000	2	0	0	2	0
67	HONO	G	47.01347	300	5000	1	0	2	1	0
68	NO_3	G	62.0049	300	5000	0	0	3	1	0
69	HNO_3	G	63.01287	300	5000	1	0	3	1	0
70	N_2H_3	G	31.03731	300	5000	3	0	0	2	0
71	N_2H_4	G	32.04528	300	5000	4	0	0	2	0
72	CNN	G	40.02455	300	5000	0	1	0	2	0
73	HCNN	G	41.03252	300	5000	1	1	0	2	0
74	N_2O_4	G	92.011	300	5000	0	0	4	2	0
75	NH_2OH	G	33.03001	200	6000	3	0	1	1	0
76	HNOH	G	32.02204	300	4000	2	0	1	1	0
77	H_2NO	G	32.02204	300	4000	2	0	1	1	0

Table F.5 (continued): Chemkin interpreter output for the Konnov's chemical reaction mechanism for combustion

No.	SPECIES	PHASE	MW	LT (K)	HT (K)	O	H	C	N	Ar
78	HNNO	G	45.02077	300	4000	1	0	1	2	0
79	HCNH	G	28.03379	300	4000	2	1	0	1	0
80	H_2CNO	G	44.03319	300	4000	2	1	1	1	0
81	CH_3NO	G	45.04116	300	4000	3	1	1	1	0
82	CH_2CHOW	G	43.04561	300	5000	3	2	1	0	0
83	C_2H3O	G	43.04561	298.1	3000	3	2	1	0	0
84	CH_3HCOW	G	44.05358	300	5000	4	2	1	0	0
85	C_3H_6OH	G	59.08864	300	5000	7	3	1	0	0
86	$O_2C_3H_6OH$	G	91.08744	300	5000	7	3	3	0	0
87	$C_3H_5O_2$	G	73.0721	300	5000	5	3	2	0	0
88	$C_3H_5O_2H$	G	74.08007	300	5000	6	3	2	0	0
89	C_3H_5O	G	57.0727	300	5000	5	3	1	0	0
90	$NC_3H_7O_2$	G	75.08804	300	5000	7	3	2	0	0
91	$NC_3H_7O_2H$	G	76.09601	300	5000	8	3	2	0	0
92	$IC_3H_7O_2$	G	75.08804	300	5000	7	3	2	0	0
93	$IC_3H_7O_2H$	G	76.09601	300	5000	8	3	2	0	0
94	IC_3H_7O	G	59.08864	300	5000	7	3	1	0	0
95	NC_3H_7O	G	59.08864	298.1	5000	7	3	1	0	0
96	C_3H_6	G	42.08127	300	5000	6	3	0	0	0
97	C_3H_8	G	44.09721	300	5000	8	3	0	0	0
98	IC_3H_7	G	43.08924	300	5000	7	3	0	0	0
99	NC_3H_7	G	43.08924	300	5000	7	3	0	0	0
100	C_3H_2	G	38.04939	150	4000	2	3	0	0	0
101	C_3H_3	G	39.05736	200	6000	3	3	0	0	0
102	SC_3H_5	G	41.0733	298.1	5000	5	3	0	0	0
103	PC_3H_4	G	40.06533	200	6000	4	3	0	0	0
104	TC_3H_5	G	41.0733	200	6000	5	3	0	0	0
105	C_3H_6O	G	58.08067	300	5000	6	3	1	0	0
106	C_2H_5CHO	G	58.08067	273.1	5000	6	3	1	0	0
107	C_2H_5CO	G	57.0727	298.1	5000	5	3	1	0	0
108	C_3H_5	G	41.0733	200	6000	5	3	0	0	0
109	C_3H_4	G	40.06533	300	4000	4	3	0	0	0
110	IC_4H_7	G	55.10039	300	3000	7	4	0	0	0
111	C_4H_2	G	50.06054	300	5000	2	4	0	0	0
112	C_4H	G	49.05257	300	5000	1	4	0	0	0
113	C_4H_6	G	54.09242	300	5000	6	4	0	0	0
114	H_2C_4O	G	66.05994	300	4000	2	4	1	0	0
115	C_4H_4	G	52.07648	200	6000	4	4	0	0	0
116	IC_4H_5	G	53.08445	300	3000	5	4	0	0	0
117	NC_4H_5	G	53.08445	300	3000	5	4	0	0	0
118	C_4H_8	G	56.10836	300	5000	8	4	0	0	0
119	$T_2C_4H_8$	G	56.10836	300	5000	8	4	0	0	0
120	$C_2C_4H_8$	G	56.10836	300	5000	8	4	0	0	0

Table F.5 (continued): Chemkin interpreter output for the Konnov's chemical reaction mechanism for combustion

No.	SPECIES	PHASE	MW	LT (K)	HT (K)	O	H	C	N	Ar
121	IC_4H_3	G	51.06851	300	5000	3	4	0	0	0
122	NC_4H_3	G	51.06851	300	5000	3	4	0	0	0
123	C_6H_6	G	78.11472	300	5000	6	6	0	0	0
124	C_6H_5O	G	93.10615	300	4000	5	6	1	0	0
125	C_6H_5	G	77.10675	300	4000	5	6	0	0	0
126	Ar	G	39.948	300	5000	0	0	0	0	1
127	N_2	G	28.0134	300	5000	0	0	0	2	0

Table F.6: Chemical reaction mechanism for Konnov's methane oxidation (A_i in mol.cm.s.K, E_i in cal.mol^{-1})

REACTIONS CONSIDERED	A_i	β_i	E_i
1. $H+H+M \leftrightarrow H_2+M$	7.00E+17	-1	0
2. $H+H+H_2 \leftrightarrow H_2+H_2$	1.00E+17	-0.6	0
3. $H+H+N_2 \leftrightarrow H_2+N_2$	5.40E+18	-1.3	0
4. $H+H+H \leftrightarrow H_2+H$	3.20E+15	0	0
5. $O+O+M \leftrightarrow O_2+M$	1.00E+17	-1	0
6. $O+H+M \leftrightarrow OH+M$	6.20E+16	-0.6	0
7. $H_2+O_2 \leftrightarrow OH+OH$	2.50E+12	0	39000
8. $O+H_2 \leftrightarrow OH+H$	5.06E+04	2.7	6290
9. $H+O_2 \leftrightarrow OH+O$	9.75E+13	0	14850
10. $H+O_2(+M) \leftrightarrow HO_2(+M)$	1.48E+12	0.6	0
Low pressure limit: 0.35000E+17 -0.41000E+00 -1.12E+03			
Troe centering: 0.50000E+00 0.10000E+06 1.00E+01			
11. $H+O_2(+Ar) \leftrightarrow HO_2(+Ar)$	1.48E+12	0.6	0
Low pressure limit: 0.70000E+18 -0.80000E+00 0.00E+00			
Troe centering: 0.45000E+00 0.10000E+02 1.00E+05			
12. $H+OH+M \leftrightarrow H_2O+M$	2.20E+22	-2	0
13. $H_2+OH \leftrightarrow H_2O+H$	1.00E+08	1.6	3300
14. $OH+OH \leftrightarrow H_2O+O$	1.50E+09	1.1	100
15. $HO_2+OH \leftrightarrow H_2O+O_2$	2.89E+13	0	-500
16. $HO_2+O \leftrightarrow OH+O_2$	1.63E+13	0	-445
17. $H+HO_2 \leftrightarrow H_2+O_2$	4.28E+13	0	1411
18. $H+HO_2 \leftrightarrow OH+OH$	1.70E+14	0	875
19. $H+HO_2 \leftrightarrow H_2O+O$	3.00E+13	0	1720
20. $HO_2+HO_2 \leftrightarrow H_2O_2+O_2$	4.20E+14	0	12000
21. $HO_2+HO_2 \leftrightarrow H_2O_2+O_2$	1.30E+11	0	-1640
22. $OH+OH(+M) \leftrightarrow H_2O_2(+M)$	7.20E+13	-0.4	0
Low pressure limit: 0.22000E+20 -0.76000E+00 0.00E+00			
Troe centering: 0.50000E+00 0.10000E+06 1.00E+01			
23. $OH+OH(+H_2O) \leftrightarrow H_2O_2(+H_2O)$	7.20E+13	-0.4	0
Low pressure limit: 0.14500E+19 0.00000E+00 0.00E+00			

Table F.6 (continued): Chemical reaction mechanism for Konnov's methane oxidation (A_i in mol.cm.s.K, E_i in cal.mol^{-1})

REACTIONS CONSIDERED	A_i	β_i	E_i
24. $H_2O_2+OH\leftrightarrow HO_2+H_2O$	1.00E+12	0	0
25. $H_2O_2+OH\leftrightarrow HO_2+H_2O$	5.80E+14	0	9560
26. $H_2O_2+H\leftrightarrow HO_2+H_2$	1.70E+12	0	3755
27. $H_2O_2+H\leftrightarrow H_2O+OH$	1.00E+13	0	3575
28. $H_2O_2+O\leftrightarrow HO_2+OH$	2.80E+13	0	6400
29. $N_2+O\leftrightarrow NO+N$	1.80E+14	0	76100
30. $N+O_2\leftrightarrow NO+O$	9.00E+09	1	6500
31. $NO+M\leftrightarrow N+O+M$	9.64E+14	0.0	148300
32. $NO+NO\leftrightarrow N_2+O_2$	3.00E+11	0	65000
33. $N_2O(+M)\leftrightarrow N_2+O(+M)$	1.26E+12	0	62620
Low pressure limit: 0.40000E+15 0.00000E+00 5.66E+04			
34. $N_2O+O\leftrightarrow N_2+O_2$	1.00E+14	0	28200
35. $N_2O+O\leftrightarrow NO+NO$	6.92E+13	0	26630
36. $N_2O+N\leftrightarrow N_2+NO$	1.00E+13	0	20000
37. $N_2O+NO\leftrightarrow N_2+NO_2$	2.75E+14	0	50000
38. $NO+O(+M)\leftrightarrow NO_2(+M)$	1.30E+15	-0.8	0
Low pressure limit: 0.47200E+25 -0.28700E+01 1.55E+03			
Troe centering: 0.96200E+00 0.10000E+02 7.96E+03			
39. $NO+O(+CO_2)\leftrightarrow NO_2(+CO_2)$	1.30E+15	-0.8	0
Low pressure limit: 0.40000E+23 -0.21600E+01 1.05E+03			
Troe centering: 0.96200E+00 0.10000E+02 7.96E+03			
40. $NO_2+O\leftrightarrow NO+O_2$	3.91E+12	0	-238
41. $NO_2+N\leftrightarrow N_2O+O$	8.40E+11	0	0
42. $NO_2+N\leftrightarrow NO+NO$	1.00E+12	0	0
43. $NO_2+NO\leftrightarrow N_2O+O_2$	1.00E+12	0	60000
44. $NO_2+NO_2\leftrightarrow NO+NO+O_2$	3.95E+12	0	27590
45. $NO_2+NO_2\leftrightarrow NO_3+NO$	1.13E+04	2.6	22720
46. $NO_2+O(+M)\leftrightarrow NO_3(+M)$	1.33E+13	0	0
Low pressure limit: 0.14900E+29 -0.40800E+01 2.47E+03			
Troe centering: 0.86000E+00 0.10000E+02 2.80E+03			
47. $NO_2+O(+CO_2)\leftrightarrow NO_3(+CO_2)$	1.33E+13	0	0
Low pressure limit: 0.13400E+29 -0.39400E+01 2.28E+03			
Troe centering: 0.86000E+00 0.10000E+02 2.80E+03			
48. $NO_3\leftrightarrow NO+O_2$	2.50E+06	0	12120
49. $NO_3+NO_2\leftrightarrow NO+NO_2+O_2$	1.20E+11	0	3200
50. $NO_3+O\leftrightarrow NO_2+O_2$	1.02E+13	0	0
51. $NO_3+NO_3\leftrightarrow NO_2+NO_2+O_2$	5.12E+11	0	4870
52. $N_2O_4(+M)\leftrightarrow NO_2+NO_2(+M)$	4.05E+18	-1.1	12840
Low pressure limit: 0.19600E+29 -0.38000E+01 1.28E+04			
53. $N_2O_4+O\leftrightarrow N_2O_3+O_2$	1.21E+12	0	0
54. $NO_2+NO(+M)\leftrightarrow N_2O_3(+M)$	1.60E+09	1.4	0
Low pressure limit: 0.10000E+34 -0.77000E+01 0.00E+00			

Table F.6 (continued): Chemical reaction mechanism for Konnov's methane oxidation (A_i in mol.cm.s.K, E_i in cal.mol^{-1})

REACTIONS CONSIDERED	A_i	β_i	E_i
55. $N_2O_3+O \leftrightarrow NO_2+NO_2$	2.71E+11	0	0
56. $N_2+M \leftrightarrow N+N+M$	1.00E+28	-3.3	225000
57. $NH+M \leftrightarrow N+H+M$	2.65E+14	0	75500
58. $NH+H \leftrightarrow N+H_2$	3.20E+13	0	325
59. $NH+N \leftrightarrow N_2+H$	9.00E+11	0.5	0
60. $NH+NH \leftrightarrow NNH+H$	5.10E+13	0	0
61. $NH+NH \leftrightarrow NH_2+N$	5.95E+02	2.9	-2030
62. $NH+NH \leftrightarrow N_2+H_2$	1.00E+08	1	0
63. $NH_2+M \leftrightarrow NH+H+M$	3.16E+23	-2	91400
64. $NH+H_2 \leftrightarrow NH_2+H$	1.00E+14	0	20070
65. $NH_2+N \leftrightarrow N_2+H+H$	6.90E+13	0	0
66. $NH_2+NH \leftrightarrow N_2H_2+H$	1.50E+15	-0.5	0
67. $NH_2+NH \leftrightarrow NH_3+N$	1.00E+13	0	2000
68. $NH_3+NH \leftrightarrow NH_2+NH_2$	3.16E+14	0	26770
69. $NH_2+NH_2 \leftrightarrow N_2H_2+H_2$	1.00E+13	0	1500
70. $N_2H_3+H \leftrightarrow NH_2+NH_2$	5.00E+13	0	2000
71. $NH_3+M \leftrightarrow NH_2+H+M$	2.20E+16	0	93470
72. $NH_3+M \leftrightarrow NH+H_2+M$	6.30E+14	0	93390
73. $NH_3+H \leftrightarrow NH_2+H_2$	5.42E+05	2.4	9920
74. $NH_3+NH_2 \leftrightarrow N_2H_3+H_2$	1.00E+11	0.5	21600
75. $NNH \leftrightarrow N_2+H$	3.00E+08	0	0
76. $NNH+M \leftrightarrow N_2+H+M$	1.00E+13	0.5	3060
77. $NNH+H \leftrightarrow N_2+H_2$	1.00E+14	0	0
78. $NNH+N \leftrightarrow NH+N_2$	3.00E+13	0	2000
79. $NNH+NH \leftrightarrow N_2+NH_2$	2.00E+11	0.5	2000
80. $NNH+NH_2 \leftrightarrow N_2+NH_3$	1.00E+13	0	0
81. $NNH+NNH \leftrightarrow N_2H_2+N_2$	1.00E+13	0	4000
82. $N_2H_2+M \leftrightarrow NNH+H+M$	5.00E+16	0	50000
83. $N_2H_2+M \leftrightarrow NH+NH+M$	3.16E+16	0	99400
84. $N_2H_2+H \leftrightarrow NNH+H_2$	8.50E+04	2.6	-230
85. $N_2H_2+N \leftrightarrow NNH+NH$	1.00E+06	2	0
86. $N_2H_2+NH \leftrightarrow NNH+NH_2$	1.00E+13	0	6000
87. $N_2H_2+NH_2 \leftrightarrow NH_3+NNH$	8.80E-02	4	-1610
88. $N_2H_3+NH \leftrightarrow N_2H_2+NH_2$	2.00E+13	0	0
89. $N_2H_3+NNH \leftrightarrow N_2H_2+N_2H_2$	1.00E+13	0	4000
90. $N_2H_3+M \leftrightarrow NH_2+NH+M$	5.00E+16	0	60000
91. $N_2H_3+M \leftrightarrow N_2H_2+H+M$	1.00E+16	0	37000
92. $N_2H_3+H \leftrightarrow N_2H_2+H_2$	1.00E+13	0	0
93. $N_2H_3+H \leftrightarrow NH+NH_3$	1.00E+11	0	0
94. $N_2H_3+N \leftrightarrow N_2H_2+NH$	1.00E+06	2	0
95. $N_2H_3+NH_2 \leftrightarrow NH_3+N_2H_2$	1.00E+11	0.5	0
96. $N_2H_3+N_2H_2 \leftrightarrow N_2H_4+NNH$	1.00E+13	0	6000
97. $N_2H_3+N_2H_3 \leftrightarrow NH_3+NH_3+N_2$	3.00E+12	0	0

Table F.6 (continued): Chemical reaction mechanism for Konnov's methane oxidation (A_i in mol.cm.s.K, E_i in cal.mol^{-1})

REACTIONS CONSIDERED	A_i	β_i	E_i
98. $N_2H_3+N_2H_3 \leftrightarrow N_2H_4+N_2H_2$	1.20E+13	0	0
99. $N_2H_4(+M) \leftrightarrow NH_2+NH_2(+M)$	5.00E+14	0	60000
Low pressure limit: 0.15000E+16 0.00000E+00 3.90E+04			
100. $N_2H_4+M \leftrightarrow N_2H_3+H+M$	1.00E+15	0	63600
101. $N_2H_4+H \leftrightarrow N_2H_3+H_2$	7.00E+12	0	2500
102. $N_2H_4+H \leftrightarrow NH_2+NH_3$	2.40E+09	0	3100
103. $N_2H_4+N \leftrightarrow N_2H_3+NH$	1.00E+10	1	2000
104. $N_2H_4+NH \leftrightarrow NH_2+N_2H_3$	1.00E+09	1.5	2000
105. $N_2H_4+NH_2 \leftrightarrow N_2H_3+NH_3$	1.80E+06	1.7	-1380
106. $N+OH \leftrightarrow NO+H$	2.80E+13	0	0
107. $N_2O+H \leftrightarrow N_2+OH$	2.20E+14	0	16750
108. $N_2O+H \leftrightarrow NH+NO$	6.70E+22	-2.2	37155
109. $N_2O+H \leftrightarrow NNH+O$	5.50E+18	-1.1	47290
110. $N_2O+H \leftrightarrow HNNO$	8.00E+24	-4.4	10530
111. $N_2O+OH \leftrightarrow N_2+HO_2$	1.00E+14	0	30000
112. $HNO+NO \leftrightarrow N_2O+OH$	8.50E+12	0	29580
113. $HNO+NO+NO \leftrightarrow HNNO+NO_2$	1.60E+11	0	2090
114. $NH+NO+M \leftrightarrow HNNO+M$	1.63E+23	-2.6	1820
115. $HNNO+H \leftrightarrow N_2O+H_2$	2.00E+13	0	0
116. $HNNO+H \leftrightarrow NH2+NO$	1.00E+12	0	0
117. $HNNO+O \leftrightarrow N_2O+OH$	2.00E+13	0	0
118. $HNNO+OH \leftrightarrow H_2O+N_2O$	2.00E+13	0	0
119. $HNNO+OH \leftrightarrow HNOH+NO$	1.00E+12	0	0
120. $HNNO+NO \leftrightarrow N_2+HONO$	2.60E+11	0	1610
121. $HNNO+NO \leftrightarrow NNH+NO_2$	3.20E+12	0	540
122. $HNNO+NO \leftrightarrow N_2O+HNO$	1.00E+12	0	0
123. $HNNO+NO_2 \leftrightarrow N_2O+HONO$	1.00E+12	0	0
124. $HNNO+NO_2 \leftrightarrow NNH+NO_3$	1.00E+13	0	17000
125. $NO_2+H \leftrightarrow NO+OH$	1.32E+14	0	362
126. $NO_2+OH \leftrightarrow HO_2+NO$	1.81E+13	0	6676
127. $NO_2+HO_2 \leftrightarrow HONO+O_2$	4.64E+11	0	-479
128. $NO_2+H_2 \leftrightarrow HONO+H$	7.33E+11	0	28800
129. $NO_2+NH \leftrightarrow N_2O+OH$	8.65E+10	0	-2270
130. $NO_2+NH \leftrightarrow NO+HNO$	1.25E+11	0	-2270
131. $NO_3+H \leftrightarrow NO_2+OH$	6.62E+13	0	0
132. $NO_3+OH \leftrightarrow NO_2+HO_2$	1.21E+13	0	0
133. $NO_3+HO_2 \leftrightarrow HNO_3+O_2$	5.55E+11	0	0
134. $NO_3+HO_2 \leftrightarrow NO_2+OH+O_2$	1.51E+12	0	0
135. $N_2O_4+H_2O \leftrightarrow HONO+HNO_3$	2.52E+14	0	11590
136. $N_2O_3+H_2O \leftrightarrow HONO+HONO$	3.79E+13	0	8880
137. $H+NO(+M) \leftrightarrow HNO(+M)$	1.52E+15	-0.4	0
Low pressure limit: 0.40000E+21 -0.17500E+01 0.00E+00			
138. $HNO+H \leftrightarrow NO+H_2$	4.46E+11	0.7	655

Table F.6 (continued): Chemical reaction mechanism for Konnov's methane oxidation (A_i in mol.cm.s.K, E_i in cal.mol^{-1})

REACTIONS CONSIDERED	A_i	β_i	E_i
139. HNO+OH↔NO+H_2O	1.30E+07	1.9	-956
140. HNO+O↔OH+NO	5.00E+11	0.5	2000
141. HNO+O↔NO_2+H	5.00E+10	0	2000
142. HNO+O_2↔NO+HO_2	2.20E+10	0	9140
143. HNO+N↔NO+NH	1.00E+11	0.5	2000
144. HNO+N↔H+N_2O	5.00E+10	0.5	3000
145. HNO+NH↔NH_2+NO	5.00E+11	0.5	0
146. HNO+NH_2↔NH_3+NO	2.00E+13	0	1000
147. HNO+HNO↔N_2O+H_2O	3.63E-03	4	1190
148. HNO+HNO↔HNOH+NO	2.00E+08	0	4170
149. HNO+NO_2↔HONO+NO	6.02E+11	0	2000
150. NO+OH(+M)↔HONO(+M)	2.00E+12	-0.1	-721
Low pressure limit: 0.50800E+24 -0.25100E+01 -6.76E+01			
Troe centering: 0.62000E+00 0.10000E+02 1.00E+05			
151. NO+OH(+CO_2)↔HONO(+CO_2)	2.00E+12	-0.1	-721
Low pressure limit: 0.17000E+24 -0.23000E+01 -2.46E+02			
Troe centering: 0.62000E+00 0.10000E+02 1.00E+05			
152. NO_2+H+M↔HONO+M	1.40E+18	-1.5	900
153. HONO+H↔HNO+OH	5.64E+10	0.9	4970
154. HONO+H↔NO+H_2O	8.12E+06	1.9	3840
155. HONO+O↔OH+NO_2	1.20E+13	0	5960
156. HONO+OH↔H_2O+NO_2	1.69E+12	0	-517
157. HONO+NH↔NH_2+NO_2	1.00E+13	0	0
158. HONO+HONO↔H_2O+NO_2+NO	1.00E+13	0	8540
159. HONO+NH_2↔NO_2+NH_3	5.00E+12	0	0
160. NO_2+OH(+M)↔HNO_3(+M)	2.41E+13	0	0
Low pressure limit: 0.64200E+33 -0.54900E+01 2.35E+03			
Troe centering: 0.10000E+01 0.10000E+02 1.17E+03			
161. NO_2+OH(+CO_2)↔HNO_3(+CO_2)	2.41E+13	0	0
Low pressure limit: 0.58000E+33 -0.54000E+01 2.19E+03			
Troe centering: 0.10000E+01 0.10000E+02 1.17E+03			
162. NO+HO_2+M↔HNO_3+M	1.50E+24	-3.5	2200
163. HNO_3+H↔H_2+NO_3	5.56E+08	1.5	16400
164. HNO_3+H↔H_2O+NO_2	6.08E+01	3.3	6290
165. HNO_3+H↔OH+HONO	3.82E+05	2.3	6980
166. HNO_3+OH↔NO_3+H_2O	1.03E+10	0	-1240
167. NH_3+O↔NH_2+OH	1.10E+06	2.1	5210
168. NH_3+OH↔NH_2+H_2O	5.00E+07	1.6	950
169. NH_3+HO_2↔NH_2+H_2O_2	3.00E+11	0	22000
170. NH_2+HO_2↔NH_3+O_2	1.65E+04	1.6	2027
171. NH_2+O↔H_2+NO	5.00E+12	0	0
172. NH_2+O↔HNO+H	4.50E+13	0	0
173. NH_2+O↔NH+OH	7.00E+12	0	0

Table F.6 (continued): Chemical reaction mechanism for Konnov's methane oxidation (A_i in mol.cm.s.K, E_i in cal.mol^{-1})

REACTIONS CONSIDERED	A_i	β_i	E_i
174. $NH_2+OH\leftrightarrow NH+H_2O$	9.00E+07	1.5	-460
175. $NH_2+OH\leftrightarrow NH_2OH$	1.79E+13	0.2	0
176. $NH_2+HO_2\leftrightarrow HNO+H_2O$	5.68E+15	-1.1	707
177. $NH_2+HO_2\leftrightarrow H_2NO+OH$	2.91E+17	-1.3	1248
178. $NH_2+O_2\leftrightarrow HNO+OH$	1.00E+13	0	26290
179. $NH_2+O_2\leftrightarrow H_2NO+O$	6.00E+13	0	29880
180. $NH_2+NO\leftrightarrow NNH+OH$	2.29E+10	0.4	-814
181. $NH_2+NO\leftrightarrow N_2+H_2O$	2.77E+20	-2.6	1258
182. $NH_2+NO\leftrightarrow H_2+N_2O$	1.00E+13	0	33700
183. $NH_2+NO_2\leftrightarrow N_2O+H_2O$	1.62E+16	-1.4	270
184. $NH_2+NO_2\leftrightarrow H_2NO+NO$	6.48E+16	-1.4	270
185. $NH+O\leftrightarrow NO+H$	7.00E+13	0	0
186. $NH+O\leftrightarrow N+OH$	7.00E+12	0	0
187. $NH+OH\leftrightarrow HNO+H$	2.00E+13	0	0
188. $NH+OH\leftrightarrow N+H_2O$	2.00E+09	1.2	0
189. $NH+OH\leftrightarrow NO+H_2$	2.00E+13	0	0
190. $NH+HO_2\leftrightarrow HNO+OH$	1.00E+13	0	2000
191. $NH+O_2\leftrightarrow HNO+O$	4.00E+13	0	17880
192. $NH+O_2\leftrightarrow NO+OH$	4.50E+08	0.8	1190
193. $NH+H_2O\leftrightarrow HNO+H_2$	2.00E+13	0	13850
194. $NH+N_2O\leftrightarrow N_2+HNO$	2.00E+12	0	6000
195. $NNH+O\leftrightarrow NH+NO$	2.00E+14	0	4000
196. $NH+NO\leftrightarrow N_2+OH$	6.10E+13	-0.5	120
197. $N_2H_4+O\leftrightarrow N_2H_2+H_2O$	8.50E+13	0	1200
198. $N_2H_4+O\leftrightarrow N_2H_3+OH$	2.50E+12	0	1200
199. $N_2H_4+OH\leftrightarrow N_2H_3+H_2O$	3.00E+10	0.7	1290
200. $N_2H_4+OH\leftrightarrow NH_3+H_2NO$	3.67E+13	0	0
201. $N_2H_4+HO_2\leftrightarrow N_2H_3+H_2O_2$	4.00E+13	0	2000
202. $N_2H_3+O\leftrightarrow N_2H_2+OH$	2.00E+13	0	1000
203. $N_2H_3+O\leftrightarrow NNH+H_2O$	3.16E+11	0.5	0
204. $N_2H_3+O\leftrightarrow NH_2+HNO$	1.00E+13	0	0
205. $N_2H_3+OH\leftrightarrow N_2H_2+H_2O$	3.00E+10	0.7	1290
206. $N_2H_3+OH\leftrightarrow NH_3+HNO$	1.00E+12	0	15000
207. $N_2H_3+O_2\leftrightarrow N_2H_2+HO_2$	3.00E+12	0	0
208. $N_2H_3+HO_2\leftrightarrow N_2H_2+H_2O_2$	1.00E+13	0	2000
209. $N_2H_3+HO_2\leftrightarrow N_2H_4+O_2$	8.00E+12	0	0
210. $N_2H_3+NO\leftrightarrow HNO+N_2H_2$	1.00E+12	0	0
211. $N_2H_2+O\leftrightarrow NH_2+NO$	1.00E+13	0	0
212. $N_2H_2+O\leftrightarrow NNH+OH$	2.00E+13	0	1000
213. $N_2H_2+OH\leftrightarrow NNH+H_2O$	5.92E+01	3.4	-1360
214. $N_2H_2+HO_2\leftrightarrow NNH+H_2O_2$	1.00E+13	0	2000
215. $N_2H_2+NO\leftrightarrow N_2O+NH_2$	3.00E+10	0	0
216. $NNH+O\leftrightarrow N_2+OH$	1.70E+16	-1.2	500

Table F.6 (continued): Chemical reaction mechanism for Konnov's methane oxidation (A_i in mol.cm.s.K, E_i in cal.mol^{-1})

REACTIONS CONSIDERED	A_i	β_i	E_i
217. $NNH+OH \leftrightarrow N_2+H_2O$	2.40E+22	-2.9	2444
218. $NNH+O_2 \leftrightarrow N_2+HO_2$	1.20E+12	-0.3	150
219. $NNH+O_2 \leftrightarrow N_2O+OH$	2.90E+11	-0.3	150
220. $NNH+HO_2 \leftrightarrow N_2+H_2O_2$	1.00E+13	0	2000
221. $NNH+NO \leftrightarrow N_2+HNO$	5.00E+13	0	0
222. $NH_2OH+OH \leftrightarrow HNOH+H_2O$	2.50E+13	0	4250
223. $H_2NO+M \leftrightarrow H_2+NO+M$	7.83E+27	-4.3	60300
224. $H_2NO+M \leftrightarrow HNO+H+M$	2.80E+24	-2.8	64915
225. $H_2NO+M \leftrightarrow HNOH+M$	1.10E+29	-4	43980
226. $H_2NO+H \leftrightarrow HNO+H_2$	3.00E+07	2	2000
227. $H_2NO+H \leftrightarrow NH_2+OH$	5.00E+13	0	0
228. $H_2NO+O \leftrightarrow HNO+OH$	3.00E+07	2	2000
229. $H_2NO+OH \leftrightarrow HNO+H_2O$	2.00E+07	2	1000
230. $H_2NO+HO_2 \leftrightarrow HNO+H_2O_2$	2.90E+04	2.7	-1600
231. $H_2NO+NH_2 \leftrightarrow HNO+NH_3$	3.00E+12	0	1000
232. $H_2NO+O_2 \leftrightarrow HNO+HO_2$	3.00E+12	0	25000
233. $H_2NO+NO \leftrightarrow HNO+HNO$	2.00E+07	2	13000
234. $H_2NO+NO_2 \leftrightarrow HONO+HNO$	6.00E+11	0	2000
235. $HNOH+M \leftrightarrow HNO+H+M$	2.00E+24	-2.8	58935
236. $HNOH+H \leftrightarrow HNO+H_2$	4.80E+08	1.5	380
237. $HNOH+H \leftrightarrow NH_2+OH$	4.00E+13	0	0
238. $HNOH+O \leftrightarrow HNO+OH$	7.00E+13	0	0
239. $HNOH+O \leftrightarrow HNO+OH$	3.30E+08	1.5	-360
240. $HNOH+OH \leftrightarrow HNO+H_2O$	2.40E+06	2	-1190
241. $HNOH+HO_2 \leftrightarrow HNO+H_2O_2$	2.90E+04	2.7	-1600
242. $HNOH+NH_2 \leftrightarrow HNO+NH_3$	1.80E+06	1.9	-1150
243. $HNOH+NO_2 \leftrightarrow HONO+HNO$	6.00E+11	0	2000
244. $HNOH+O_2 \leftrightarrow HNO+HO_2$	3.00E+12	0	25000
245. $HNOH+HNO \leftrightarrow NH_2OH+NO$	1.00E+12	0	3000
246. $CO+HO_2 \leftrightarrow CO_2+OH$	1.50E+14	0	23650
247. $CO+OH \leftrightarrow CO_2+H$	1.17E+07	1.4	-725
248. $CO+O+M \leftrightarrow CO_2+M$	6.16E+14	0	3000
249. $CO+O_2 \leftrightarrow CO_2+O$	2.50E+12	0	47800
250. $HCO+M \leftrightarrow H+CO+M$	1.56E+14	0	15760
251. $HCO+OH \leftrightarrow CO+H_2O$	1.00E+14	0	0
252. $HCO+O \leftrightarrow CO+OH$	3.00E+13	0	0
253. $HCO+O \leftrightarrow CO_2+H$	3.00E+13	0	0
254. $HCO+H \leftrightarrow CO+H_2$	9.00E+13	0	0
255. $HCO+O_2 \leftrightarrow CO+HO_2$	2.70E+13	0	1190
256. $HCO+CH_3 \leftrightarrow CO+CH_4$	1.20E+14	0	0
257. $HCO+HO_2 \leftrightarrow CO_2+OH+H$	3.00E+13	0	0
258. $HCO+HCO \leftrightarrow CH_2O+CO$	3.00E+13	0	0
259. $HCO+HCO \leftrightarrow H_2+CO+CO$	2.20E+13	0	0

Table F.6 (continued): Chemical reaction mechanism for Konnov's methane oxidation (A_i in mol.cm.s.K, E_i in cal.mol^{-1})

REACTIONS CONSIDERED	A_i	β_i	E_i
260. $CH_4(+M)\leftrightarrow CH_3+H(+M)$	2.40E+16	0.0	14913
Low pressure limit: 0.45000E+18 0.00000E+00 9.08E+04			
Troe centering: 0.10000E+01 0.10000E+02 1.35E+03 0.783			
261. $CH_4(+CH_4)\leftrightarrow CH_3+H(+CH_4)$	2.40E+16	0.0	14913
Low pressure limit: 0.84000E+19 0.00000E+00 9.08E+04			
Troe centering: 0.31000E+00 0.22100E+04 9.00E+01			
262. $CH_4+HO_2\leftrightarrow CH_3+H_2O_2$	9.00E+12	0	24641
263. $CH_4+OH\leftrightarrow CH_3+H_2O$	1.55E+07	1.8	2774
264. $CH_4+O\leftrightarrow CH_3+OH$	7.20E+08	1.6	8485
265. $CH_4+H\leftrightarrow CH_3+H_2$	1.30E+04	3	8050
266. $CH_4+CH_2\leftrightarrow CH_3+CH_3$	4.30E+12	0	10038
267. $CH_4+O_2\leftrightarrow CH_3+HO_2$	4.00E+13	0	56900
268. $CH_3+M\leftrightarrow CH_2+H+M$	2.72E+36	-5.3	117100
269. $CH_3+M\leftrightarrow CH+H_2+M$	1.00E+16	0	85240
270. $CH_3+HO_2\leftrightarrow CH_3O+OH$	1.80E+13	0	0
271. $CH_3+OH\leftrightarrow CH_2OH+H$	2.64E+19	-1.8	8068
272. $CH_3+OH\leftrightarrow CH_3O+H$	5.74E+12	-0.2	13931
273. $CH_3+OH\leftrightarrow CH_2+H_2O$	8.90E+18	-1.8	8067
274. $CH_3+OH\leftrightarrow CH_2O+H_2$	3.19E+12	-0.5	10810
275. $CH_3+O\leftrightarrow H+CH_2O$	8.43E+13	0	0
276. $CH_3+O_2\leftrightarrow CH_2O+OH$	3.40E+11	0	8940
277. $CH_3+O_2\leftrightarrow CH_3O+O$	1.32E+14	0	31400
278. $CH_3+CH_3\leftrightarrow C_2H_5+H$	5.00E+12	0.1	10600
279. $CH_3+CH_3(+M)\leftrightarrow C_2H_6(+M)$	9.21E+16	-1.2	636
Low pressure limit: 0.11300E+37 -0.52460E+01 1.71E+03			
Troe centering: 0.40500E+00 0.11200E+04 6.96E+01			
280. $CH_3+CH_3O\leftrightarrow CH_4+CH_2O$	2.41E+13	0	0
281. $CH_3+CH_2OH\leftrightarrow CH_4+CH_2O$	8.50E+13	0	0
282. $CH_3+H\leftrightarrow SCH_2+H_2$	6.00E+13	0	15100
283. $CH_3+O_2(+M)\leftrightarrow CH_3O_2(+M)$	7.80E+08	1.2	0
Low pressure limit: 0.58000E+26 -0.33000E+01 0.00E+00			
Troe centering: 0.49500E+00 0.23255E+04 1.00E+01			
284. $CH_3+CH_3\leftrightarrow C_2H_4+H_2$	1.00E+14	0	32000
285. $CH_3+OH\leftrightarrow SCH_2+H_2O$	7.20E+13	0	2780
286. $CH_2+OH\leftrightarrow CH_2O+H$	2.50E+13	0	0
287. $CH_2+O\leftrightarrow CO+H_2$	4.80E+13	0	0
288. $CH_2+O\leftrightarrow CO+H+H$	7.20E+13	0	0
289. $CH_2+O\leftrightarrow CH+OH$	3.00E+14	0	11920
290. $CH_2+O\leftrightarrow HCO+H$	3.00E+13	0	0
291. $CH_2+H\leftrightarrow CH+H_2$	3.12E+13	0	-1340
292. $CH_2+O_2\leftrightarrow HCO+OH$	4.30E+10	0	-500
293. $CH_2+O_2\leftrightarrow CO_2+H_2$	6.90E+11	0	500
294. $CH_2+O_2\leftrightarrow CO_2+H+H$	1.60E+12	0	1000

Table F.6 (continued): Chemical reaction mechanism for Konnov's methane oxidation (A_i in mol.cm.s.K, E_i in cal.mol^{-1})

REACTIONS CONSIDERED	A_i	β_i	E_i
295. $CH_2+O_2\leftrightarrow CO+H_2O$	1.90E+10	0	-1000
296. $CH_2+O_2\leftrightarrow CO+OH+H$	8.60E+10	0	-500
297. $CH_2+O_2\leftrightarrow CH_2O+O$	5.00E+13	0	9000
298. $CH_2+CO_2\leftrightarrow CH_2O+CO$	1.10E+11	0	1000
299. $CH_2+CH_2\leftrightarrow C_2H_2+H_2$	1.58E+15	0	11950
300. $CH_2+CH_2\leftrightarrow C_2H_2+H+H$	2.00E+14	0	11000
301. $CH_2+CH_2\leftrightarrow CH_3+CH$	2.40E+14	0	9940
302. $CH_2+CH_2\leftrightarrow C_2H_3+H$	2.00E+13	0	0
303. $CH_2+CH_3\leftrightarrow C_2H_4+H$	4.20E+13	0	0
304. $CH_2+CH\leftrightarrow C_2H_2+H$	4.00E+13	0	0
305. $CH_2+C\leftrightarrow CH+CH$	1.62E+12	0.7	46800
306. $CH_2+M\leftrightarrow C+H_2+M$	1.60E+14	0	64000
307. $CH_2+M\leftrightarrow CH+H+M$	5.60E+15	0	89600
308. $SCH_2+M\leftrightarrow CH_2+M$	6.00E+12	0	0
309. $SCH_2+O_2\leftrightarrow CO+OH+H$	3.00E+13	0	0
310. $SCH_2+H\leftrightarrow CH+H_2$	3.00E+13	0	0
311. $SCH_2+O\leftrightarrow CO+H+H$	1.50E+13	0	0
312. $SCH_2+O\leftrightarrow CO+H_2$	1.50E+13	0	0
313. $SCH_2+OH\leftrightarrow CH_2O+H$	3.00E+13	0	0
314. $SCH_2+HO_2\leftrightarrow CH_2O+OH$	3.00E+13	0	0
315. $SCH_2+H_2O_2\leftrightarrow CH_3O+OH$	3.00E+13	0	0
316. $SCH_2+H_2O\rightarrow CH_3OH$	1.80E+13	0	0
317. $SCH_2+CH_2O\leftrightarrow CH_3+HCO$	1.20E+12	0	0
318. $SCH_2+HCO\leftrightarrow CH_3+CO$	1.80E+13	0	0
319. $SCH_2+CH_3\leftrightarrow C_2H_4+H$	1.80E+13	0	0
320. $SCH_2+CH_4\leftrightarrow CH_3+CH_3$	4.00E+13	0	0
321. $SCH_2+C_2H_6\leftrightarrow CH_3+C_2H_5$	1.20E+14	0	0
322. $SCH_2+CO_2\leftrightarrow CH_2O+CO$	3.00E+12	0	0
323. $SCH_2+CH_2CO\leftrightarrow C_2H_4+CO$	1.60E+14	0	0
324. $CH+OH\leftrightarrow HCO+H$	3.00E+13	0	0
325. $CH+O\leftrightarrow CO+H$	4.00E+13	0	0
326. $CH+O\leftrightarrow C+OH$	1.52E+13	0	4730
327. $H_2O+C\leftrightarrow CH+OH$	7.80E+11	0.7	39300
328. $CH+O_2\leftrightarrow HCO+O$	4.90E+13	0	0
329. $CH+O_2\leftrightarrow CO+OH$	4.90E+13	0	0
330. $CH+CO_2\leftrightarrow HCO+CO$	3.22E-02	4.4	-3530
331. $CH+CH_4\leftrightarrow C_2H_4+H$	3.90E+14	-0.4	0
332. $CH+CH_3\leftrightarrow C_2H_3+H$	3.00E+13	0	0
333. $CH_2+OH\leftrightarrow CH+H_2O$	1.13E+07	2	3000
334. $CH+H\leftrightarrow C+H_2$	7.90E+13	0	160
335. $CH+H_2O\leftrightarrow CH_2O+H$	1.17E+15	-0.8	0
336. $CH+H_2O\leftrightarrow CH_2OH$	5.70E+12	0	-760
337. $CH+CH_2O\leftrightarrow CH_2CO+H$	1.00E+14	0	-515

Table F.6 (continued): Chemical reaction mechanism for Konnov's methane oxidation (A_i in mol.cm.s.K, E_i in cal.mol^{-1})

REACTIONS CONSIDERED	A_i	β_i	E_i
338. $CH_3O+M \leftrightarrow CH_2O+H+M$	5.40E+13	0	13500
339. $CH_3O+HO_2 \leftrightarrow CH_2O+H_2O_2$	3.00E+11	0	0
340. $CH_3O+OH \leftrightarrow CH_2O+H_2O$	1.80E+13	0	0
341. $CH_3O+O \leftrightarrow CH_2O+OH$	1.80E+12	0	0
342. $CH_3O+H \leftrightarrow CH_2O+H_2$	1.80E+13	0	0
343. $CH_3O+O_2 \leftrightarrow CH_2O+HO_2$	2.20E+10	0	1750
344. $CH_3O+CH_2O \leftrightarrow CH_3OH+HCO$	1.00E+11	0	2980
345. $CH_3O+CO \leftrightarrow CH_3+CO_2$	6.81E-18	9.2	-2850
346. $CH_3O+HCO \leftrightarrow CH_3OH+CO$	9.00E+13	0	0
347. $CH_3O+C_2H_5 \leftrightarrow CH_2O+C_2H_6$	2.41E+13	0	0
348. $CH_3O+C_2H_3 \leftrightarrow CH_2O+C_2H_4$	2.41E+13	0	0
349. $CH_3O+C_2H_4 \leftrightarrow CH_2O+C_2H_5$	1.20E+11	0	6750
350. $CH_3O+H \leftrightarrow CH_2OH+H$	3.40E+06	1.6	0
351. $CH_3O+H \leftrightarrow SCH_2+H_2O$	1.00E+12	0	0
352. $CH_2O+M \leftrightarrow HCO+H+M$	5.00E+35	-5.5	96680
353. $CH_2O+M \leftrightarrow CO+H_2+M$	1.10E+36	-5.5	96680
354. $CH_2O+HO_2 \leftrightarrow HCO+H_2O_2$	4.11E+04	2.5	10210
355. $CH_2O+OH \leftrightarrow HCO+H_2O$	3.43E+09	1.2	-447
356. $CH_2O+O \leftrightarrow HCO+OH$	4.10E+11	0.6	2760
357. $CH_2O+H \leftrightarrow HCO+H_2$	1.26E+08	1.6	2166
358. $CH_2O+O_2 \leftrightarrow HCO+HO_2$	6.00E+13	0	40650
359. $CH_2O+CH_3 \leftrightarrow HCO+CH_4$	7.80E-08	6.1	1970
360. $C_2H_6(+M) \leftrightarrow C_2H_5+H(+M)$	8.85E+20	-1.2	12210
Low pressure limit: 0.69000E+43 -0.64310E+01 1.07E+05			
SRI centering: 0.47610E+02 0.16182E+05 3.37E+03			
361. $C_2H_6+HO_2 \leftrightarrow C_2H_5+H_2O_2$	1.33E+13	0	20535
362. $C_2H_6+OH \leftrightarrow C_2H_5+H_2O$	7.20E+06	2	870
363. $C_2H_6+O \leftrightarrow C_2H_5+OH$	1.00E+09	1.5	5800
364. $C_2H_6+H \leftrightarrow C_2H_5+H_2$	1.40E+09	1.5	7400
365. $C_2H_6+H \leftrightarrow CH_3+CH_4$	5.40E+04	0	11630
366. $C_2H_6+O_2 \leftrightarrow C_2H_5+HO_2$	6.00E+13	0	52000
367. $C_2H_6+CH_3 \leftrightarrow C_2H_5+CH_4$	1.47E-07	6	6060
368. $C_2H_6+CH_2 \leftrightarrow CH_3+C_2H_5$	6.50E+12	0	7911
369. $C_2H_6+C_2H_3 \leftrightarrow C_2H_4+C_2H_5$	8.57E-02	4.1	2543
370. $C_2H_6+HCO \leftrightarrow CH_2O+C_2H_5$	4.70E+04	2.7	18235
371. $C_2H_5(+M) \leftrightarrow C_2H_4+H(+M)$	1.11E+10	1	36767
Low pressure limit: 0.40000E+34 -0.49900E+01 4.00E+04			
Troe centering: 0.83200E+00 0.10000E+02 1.20E+03			
372. $C_2H_5(+C_2H_6) \leftrightarrow C_2H_4+H(+C_2H_6)$	8.20E+13	0	39880
Low pressure limit: 0.10000E+19 0.00000E+00 3.34E+04			
Troe centering: 0.75000E+00 0.97000E+02 1.38E+03			
373. $C_2H_5+HO_2 \leftrightarrow C_2H_4+H_2O_2$	1.80E+12	0	0
374. $C_2H_5+OH \leftrightarrow C_2H_4+H_2O$	2.41E+13	0	0

Table F.6 (continued): Chemical reaction mechanism for Konnov's methane oxidation (A_i in mol.cm.s.K, E_i in cal.mol^{-1})

REACTIONS CONSIDERED	A_i	β_i	E_i
375. $C_2H_5+OH\rightarrow CH_3+CH_2O+H$	2.41E+13	0	0
376. $C_2H_5+O\leftrightarrow CH_2O+CH_3$	4.24E+13	0	0
377. $C_2H_5+O\leftrightarrow CH_3HCO+H$	5.30E+13	0	0
378. $C_2H_5+O\leftrightarrow C_2H_4+OH$	3.46E+13	0	0
379. $C_2H_5+H\leftrightarrow C_2H_4+H_2$	1.70E+12	0	0
380. $C_2H_5+O_2\leftrightarrow C_2H_4+HO_2$	2.56E+19	-2.8	1980
381. $C_2H_5+CH_3\leftrightarrow C_2H_4+CH_4$	1.10E+12	0	0
382. $C_2H_5+C_2H_5\leftrightarrow C_2H_4+C_2H_6$	1.40E+12	0	0
383. $C_2H_5+HO_2\leftrightarrow C_2H_5O+OH$	3.00E+13	0	0
384. $C_2H_4+M\leftrightarrow C_2H_2+H_2+M$	3.50E+16	0	71530
385. $C_2H_4+M\leftrightarrow C_2H_3+H+M$	2.60E+17	0	96570
386. $C_2H_4+OH\leftrightarrow C_2H_3+H_2O$	5.53E+05	2.3	2900
387. $C_2H_4+O\leftrightarrow CH_3+HCO$	8.10E+06	1.9	180
388. $C_2H_4+H\leftrightarrow C_2H_3+H_2$	4.49E+07	2.1	13366
389. $C_2H_4+O_2\leftrightarrow C_2H_3+HO_2$	4.00E+13	0	61500
390. $C_2H_4+C_2H_4\leftrightarrow C_2H_5+C_2H_3$	1.86E+14	0	64200
391. $C_2H_4+CH_3\leftrightarrow C_2H_3+CH_4$	4.20E+12	0	11100
392. $C_2H_4+O\leftrightarrow CH_2HCO+H$	4.70E+06	1.9	180
393. $C_2H_4+O\leftrightarrow CH_2O+CH_2$	3.00E+04	1.9	180
394. $C_2H_4+O\leftrightarrow CH_2CO+H_2$	6.70E+05	1.9	180
395. $C_2H_4+O\leftrightarrow C_2H_3+OH$	1.51E+07	1.9	3790
396. $C_2H_4+OH\leftrightarrow CH_2O+CH_3$	2.00E+12	0	960
397. $C_2H_4+OH(+M)\leftrightarrow PC_2H_5O(+M)$	5.42E+12	0	0
Low pressure limit: 0.11900E+28 -0.31000E+01 0.00E+00			
398. $C_2H_4+HO_2\leftrightarrow C_2H_3+H_2O_2$	1.12E+13	0	30400
399. $C_2H_4+CH_3O\leftrightarrow C_2H_3+CH_3OH$	1.00E+11	0	10000
400. $C_2H_3(+M)\leftrightarrow C_2H_2+H(+M)$	2.10E+14	0	39740
Low pressure limit: 0.41500E+42 -0.75000E+01 4.55E+04			
Troe centering: 0.65000E+00 0.10000E+06 1.00E+01			
401. $C_2H_3+HO_2\rightarrow CH_3+CO+OH$	3.00E+13	0	0
402. $C_2H_3+OH\leftrightarrow C_2H_2+H_2O$	3.00E+13	0	0
403. $C_2H_3+H\leftrightarrow C_2H_2+H_2$	1.20E+13	0	0
404. $C_2H_3+O\leftrightarrow CH_3+CO$	1.00E+13	0	0
405. $C_2H_3+O_2\leftrightarrow CH_2O+HCO$	1.70E+29	-5.3	6500
406. $C_2H_3+CH\leftrightarrow CH_2+C_2H_2$	5.00E+13	0	0
407. $C_2H_3+CH_3\leftrightarrow C_2H_2+CH_4$	2.05E+13	0	0
408. $C_2H_3+C_2H\leftrightarrow C_2H_2+C_2H_2$	3.00E+13	0	0
409. $C_2H_3+HCO\leftrightarrow C_2H_4+CO$	9.03E+13	0	0
410. $C_2H_3+CH_2O\leftrightarrow C_2H_4+HCO$	5.42E+03	2.8	5862
411. $C_2H_3+C_2H_3\leftrightarrow C_2H_2+C_2H_4$	1.45E+13	0	0
412. $C_2H_3+O\leftrightarrow C_2H_2+OH$	1.00E+13	0	0
413. $C_2H_3+O\leftrightarrow CH_2+HCO$	1.00E+13	0	0
414. $C_2H_3+O\leftrightarrow CH_2CO+H$	1.00E+13	0	0

Table F.6 (continued): Chemical reaction mechanism for Konnov's methane oxidation (A_i in mol.cm.s.K, E_i in cal.mol^{-1})

REACTIONS CONSIDERED	A_i	β_i	E_i
415. $C_2H_3+OH\leftrightarrow CH_3HCO$	3.00E+13	0	0
416. $C_2H_3+O_2\leftrightarrow C_2H_2+HO_2$	5.19E+15	-1.3	3310
417. $C_2H_3+O_2\leftrightarrow C_2H_2+HO_2$	2.12E-06	6	9484
418. $C_2H_3+O_2\leftrightarrow CH_2HCO+O$	3.50E+14	-0.6	5260
419. $C_2H_3+CH_2\leftrightarrow C_2H_2+CH_3$	3.00E+13	0	0
420. $C_2H_2\leftrightarrow C_2H+H$	2.37E+32	-5.3	130688
421. $C_2H_2+O_2\leftrightarrow HCCO+OH$	2.00E+08	1.5	30100
422. $C_2H_2+O_2\leftrightarrow C_2H+HO_2$	1.20E+13	0	74520
423. $C_2H_2+OH\leftrightarrow C_2H+H_2O$	3.39E+07	2	14000
424. $C_2H_2+OH\leftrightarrow CH_2CO+H$	1.10E+13	0	7170
425. $C_2H_2+O\leftrightarrow CH_2+CO$	1.20E+06	2.1	1570
426. $C_2H_2+O\leftrightarrow HCCO+H$	5.00E+06	2.1	1570
427. $C_2H_2+CH_3\leftrightarrow C_2H+CH_4$	1.80E+11	0	17290
428. $C_2H_2+O\leftrightarrow C_2H+OH$	3.00E+14	0	25000
429. $C_2H_2+OH\leftrightarrow CH_3+CO$	4.83E-04	4	-2000
430. $C_2H_2+HO_2\leftrightarrow CH_2CO+OH$	6.10E+09	0	7950
431. $C_2H_2+O_2\leftrightarrow HCO+HCO$	4.00E+12	0	28000
432. $C_2H+OH\leftrightarrow HCCO+H$	2.00E+13	0	0
433. $C_2H+OH\leftrightarrow C_2+H_2O$	4.00E+07	2	8000
434. $C_2H+O\leftrightarrow CO+CH$	1.45E+13	0	460
435. $C_2H+O_2\leftrightarrow HCO+CO$	9.00E+12	0	0
436. $C_2H+H_2\leftrightarrow C_2H_2+H$	7.88E+05	2.4	346
437. $C_2H+O_2\leftrightarrow CO+CO+H$	9.00E+12	0	0
438. $C_2H+O_2\leftrightarrow HCCO+O$	6.00E+11	0	0
439. $CH_2CO(+M)\leftrightarrow CH_2+CO(+M)$	3.00E+14	0	71000
Low pressure limit: 0.23000E+16 0.00000E+00 5.76E+04			
440. $CH_2CO+O_2\leftrightarrow CH_2O+CO_2$	2.00E+13	0	61500
441. $CH_2CO+HO_2\rightarrow CH_2O+CO+OH$	6.00E+11	0	12738
442. $CH_2CO+O\leftrightarrow HCCO+OH$	1.00E+13	0	8000
443. $CH_2CO+OH\leftrightarrow CH_2OH+CO$	1.00E+13	0	0
444. $CH_2CO+H\leftrightarrow CH_3+CO$	3.28E+10	0.9	2840
445. $CH_2CO+CH_3\leftrightarrow C_2H_5+CO$	2.40E+12	0	8000
446. $CH_2CO+CH_2\leftrightarrow C_2H_4+CO$	2.90E+12	0	3800
447. $CH_2CO+CH_2\leftrightarrow HCCO+CH_3$	3.60E+13	0	11000
448. $CH_2CO+CH_3\leftrightarrow HCCO+CH_4$	7.50E+12	0	13000
449. $CH_2CO+OH\leftrightarrow CH_2O+HCO$	2.80E+13	0	0
450. $CH_2CO+H\leftrightarrow HCCO+H_2$	1.80E+14	0	8600
451. $CH_2CO+O\leftrightarrow HCO+HCO$	7.50E+11	0	1350
452. $CH_2CO+O\leftrightarrow HCO+CO+H$	7.50E+11	0	1350
453. $CH_2CO+O\leftrightarrow CH_2O+CO$	7.50E+11	0	1350
454. $CH_2CO+OH\leftrightarrow HCCO+H_2O$	7.50E+12	0	2000
455. $HCCO+M\leftrightarrow CH+CO+M$	6.00E+15	0	58821
456. $HCCO+OH\leftrightarrow HCO+CO+H$	1.00E+13	0	0

Table F.6 (continued): Chemical reaction mechanism for Konnov's methane oxidation (A_i in mol.cm.s.K, E_i in cal.mol^{-1})

REACTIONS CONSIDERED	A_i	β_i	E_i
457. HCCO+OH↔C_2O+H_2O	3.00E+13	0	0
458. HCCO+O↔CO+CO+H	1.00E+14	0	0
459. HCCO+O↔CH+CO_2	2.95E+13	0	1110
460. HCCO+H↔CH_2+CO	1.50E+14	0	0
461. HCCO+O_2↔CO_2+CO+H	5.40E+11	0	850
462. HCCO+CH_2↔C_2H+CH_2O	1.00E+13	0	2000
463. HCCO+CH_2↔C_2H_3+CO	3.00E+13	0	0
464. HCCO+CH_3↔C_2H_4+CO	2.00E+12	0	0
465. HCCO+CH↔CO+C_2H_2	5.00E+13	0	0
466. HCCO+HCCO↔CO+C_2H_2+CO	1.00E+13	0	0
467. HCCO+OH↔HCO+HCO	1.00E+13	0	0
468. HCCO+O_2↔CO+CO+OH	5.40E+11	0	850
469. HCCO+O_2↔CO_2+HCO	5.40E+11	0	850
470. CH_3OH(+M)↔CH_3+OH(+M)	1.70E+16	0	90885
Low pressure limit: 0.66000E+17 0.00000E+00 6.57E+04			
Troe centering: 0.82000E+00 0.20000E+03 1.44E+03			
471. CH_3OH+HO_2↔CH_2OH+H_2O_2	9.64E+10	0	12580
472. CH_3OH+OH↔CH_2OH+H_2O	1.44E+06	2	-840
473. CH_3OH+OH↔CH_3O+H_2O	1.00E+13	0	1700
474. CH_3OH+O↔CH_2OH+OH	1.63E+13	0	5030
475. CH_3OH+H↔CH_2OH+H_2	1.64E+07	2	4520
476. CH_3OH+CH_3↔CH_2OH+CH_4	3.19E+01	3.2	7172
477. CH_3OH+CH_3↔CH_3O+CH_4	1.45E+01	3.1	6935
478. CH_3OH+C_2H_5↔C_2H_6+CH_3O	1.44E+01	3.1	8942
479. CH_3OH+H↔CH_3+H_2O	2.00E+14	0	5300
480. CH_3OH+O↔CH_3O+OH	1.00E+13	0	4680
481. CH_3OH+CH_3↔C_2H_6+OH	2.00E+12	0	15000
482. CH_3OH+CH_3O↔CH_2OH+CH_3OH	3.00E+11	0	4070
483. CH_3OH(+M)↔CH_2OH+H(+M)	1.38E+16	0	95950
Low pressure limit: 0.53500E+17 0.00000E+00 7.08E+04			
Troe centering: 0.82000E+00 0.20000E+03 1.44E+03			
484. CH_3OH+H↔H_2+CH_3O	4.00E+13	0	6095
485. CH_3OH+O_2↔CH_2OH+HO_2	2.05E+13	0	44900
486. CH_3OH+C_2H_5↔C_2H_6+CH_2OH	3.19E+01	3.2	9161
487. CH_2OH+M↔CH_2O+H+M	1.14E+43	-8	43000
488. CH_2OH+H↔CH_2O+H_2	1.00E+13	0	0
489. CH_2OH+O_2↔CH_2O+HO_2	1.50E+15	-1	0
490. CH_2OH+O_2↔CH_2O+HO_2	7.20E+13	0	3570
491. H+CH_2OH↔SCH_2+H_2O	1.00E+12	0	0
492. CH_2OH+O↔CH_2O+OH	9.00E+13	0	0
493. CH_2OH+OH↔CH_2O+H_2O	1.00E+13	0	0
494. CH_2OH+HO_2↔CH_2O+H_2O_2	1.21E+13	0	0
495. CH_2OH+CH_2OH↔CH_3OH+CH_2O	4.82E+12	0	0

Table F.6 (continued): Chemical reaction mechanism for Konnov's methane oxidation (A_i in mol.cm.s.K, E_i in cal.mol^{-1})

REACTIONS CONSIDERED	A_i	β_i	E_i
496. $CH_2OH+CH_2OH \leftrightarrow CH_2O+CH_2O+H_2$	1.00E+15	-0.7	0
497. $CH_2OH+HCO \leftrightarrow CH_3OH+CO$	1.21E+14	0	0
498. $CH_2OH+CH_2O \leftrightarrow CH_3OH+HCO$	5.49E+03	2.8	5900
499. $CH_2OH+CH_3O \leftrightarrow CH_3OH+CH_2O$	2.40E+13	0	0
500. $CH_3O+CH_3O \leftrightarrow CH_3OH+CH_2O$	2.32E+13	0	0
501. $CH_3HCO \leftrightarrow CH_3+HCO$	7.10E+15	0	81790
502. $CH_3HCO+HO_2 \leftrightarrow CH_3CO+H_2O_2$	3.00E+12	0	12000
503. $CH_3HCO+OH \leftrightarrow CH_3CO+H_2O$	2.30E+10	0.7	-1100
504. $CH_3HCO+O \leftrightarrow CH_3CO+OH$	5.80E+12	0	1800
505. $CH_3HCO+H \leftrightarrow CH_3CO+H_2$	4.10E+09	1.2	2400
506. $CH_3HCO+O_2 \leftrightarrow CH_3CO+HO_2$	3.00E+13	0	39200
507. $CH_3HCO+CH_3 \leftrightarrow CH_3CO+CH_4$	7.60E+00	3.4	3740
508. $CH_3HCO+H \leftrightarrow CH_2HCO+H_2$	7.00E+08	1.5	7400
509. $CH_3HCO+O \leftrightarrow CH_2HCO+OH$	5.00E+08	1.5	5800
510. $CH_3HCO+OH \leftrightarrow CH_2HCO+H_2O$	2.00E+14	0	6000
511. $CH_3HCO+HO_2 \leftrightarrow CH_2HCO+H_2O_2$	3.00E+13	0	15000
512. $CH_3HCO+CH_2 \leftrightarrow CH_3CO+CH_3$	1.66E+12	0	3510
513. $CH_3HCO+CH_3 \leftrightarrow CH_2HCO+CH_4$	1.58E+00	4	7720
514. $CH_3HCO+CH_3O \leftrightarrow CH_3CO+CH_3OH$	5.00E+12	0	0
515. $CH_3HCO+C_2H_5 \leftrightarrow CH_3CO+C_2H_6$	1.26E+12	0	8500
516. $CH_3HCO+C_2H_3 \leftrightarrow CH_3CO+C_2H_4$	8.13E+10	0	3680
517. $CH_2HCO \leftrightarrow CH_3CO$	1.60E+11	0	21600
518. $CH_3HCO+CH_2HCO \leftrightarrow CH_3CO+CH_3HCO$	3.00E+12	0	11200
519. $CH_3CO(+M) \leftrightarrow CH_3+CO(+M)$	2.80E+13	0	17150
Low pressure limit: 0.60000E+16 0.00000E+00 1.41E+04			
Troe centering: 0.50000E+00 0.10000E+06 1.00E+01			
520. $CH_3CO+H \leftrightarrow CH_2CO+H_2$	1.15E+13	0	0
521. $CH_3CO+H \leftrightarrow CH_3+HCO$	2.15E+13	0	0
522. $CH_3CO+O \leftrightarrow CH_2CO+OH$	4.00E+13	0	0
523. $CH_3CO+O \leftrightarrow CH_3+CO_2$	1.50E+14	0	0
524. $CH_3CO+CH_3 \leftrightarrow C_2H_6+CO$	3.30E+13	0	0
525. $CH_3CO+CH_3 \leftrightarrow CH_4+CH_2CO$	6.10E+12	0	0
526. $CH_2HCO+H \leftrightarrow CH_2CO+H_2$	2.00E+13	0	0
527. $CH_2HCO+O_2 \leftrightarrow CH_2O+OH+CO$	1.80E+10	0	0
528. $CH_2HCO+O_2 \leftrightarrow CH_2CO+HO_2$	1.50E+11	0	0
529. $CH_2HCO \leftrightarrow CH_2CO+H$	1.58E+13	0	35200
530. $C_2H_5O \leftrightarrow CH_3+CH_2O$	1.00E+15	0	21600
531. $C_2H_5O+O_2 \leftrightarrow CH_3HCO+HO_2$	3.60E+10	0	1090
532. $C_2H_5O \leftrightarrow CH_3HCO+H$	2.00E+14	0	23300
533. $C_2H_5O+OH \leftrightarrow CH_3HCO+H_2O$	1.00E+14	0	0
534. $C_2H_5O+H \leftrightarrow CH_3HCO+H_2$	1.00E+14	0	0
535. $C_2H_5O+O \leftrightarrow CH_3HCO+OH$	1.21E+14	0	0
536. $C_2H_5O+HO_2 \leftrightarrow CH_3HCO+H_2O_2$	1.00E+14	0	0

Table F.6 (continued): Chemical reaction mechanism for Konnov's methane oxidation (A_i in mol.cm.s.K, E_i in cal.mol^{-1})

REACTIONS CONSIDERED	A_i	β_i	E_i
537. $C_2H_5O+C_2H_5O\leftrightarrow C_2H_5OH+CH_3HCO$	5.00E+13	0	0
538. $C_2H_5O+PC_2H_5O\leftrightarrow C_2H_5OH+CH_3HCO$	5.00E+13	0	0
539. $C_2H_5O+SC_2H_5O\leftrightarrow C_2H_5OH+CH_3HCO$	5.00E+13	0	0
540. $SC_2H_5O+M\leftrightarrow CH_3HCO+H+M$	5.00E+13	0	21860
541. $SC_2H_5O+H\leftrightarrow CH_3HCO+H_2$	2.00E+13	0	0
542. $SC_2H_5O+OH\leftrightarrow CH_3HCO+H_2O$	1.50E+13	0	0
543. $SC_2H_5O+O\leftrightarrow CH_3HCO+OH$	9.04E+13	0	0
544. $SC_2H_5O+O_2\leftrightarrow CH_3HCO+HO_2$	8.40E+15	-1.2	0
545. $SC_2H_5O+O_2\leftrightarrow CH_3HCO+HO_2$	4.80E+14	0	5000
546. $SC_2H_5O+HO_2\leftrightarrow CH_3HCO+H_2O_2$	1.00E+13	0	0
547. $SC_2H_5O+SC_2H_5O\leftrightarrow C_2H_5OH+CH_3HCO$	3.50E+13	0	0
548. $SC_2H_5O+PC_2H_5O\leftrightarrow C_2H_5OH+CH_3HCO$	5.00E+13	0	0
549. $PC_2H_5O\leftrightarrow SC_2H_5O$	1.00E+11	0	27000
550. $PC_2H_5O+PC_2H_5O\leftrightarrow C_2H_5OH+CH_3HCO$	3.40E+13	0	0
551. $C_2H_5OH\leftrightarrow CH_2OH+CH_3$	3.10E+15	0	80600
552. $C_2H_5OH+OH\leftrightarrow SC_2H_5O+H_2O$	3.00E+13	0	5960
553. $C_2H_5OH+OH\leftrightarrow C_2H_5O+H_2O$	1.14E+06	2	914
554. $C_2H_5OH+OH\leftrightarrow PC_2H_5O+H_2O$	2.56E+06	2.1	860
555. $C_2H_5OH+O\leftrightarrow SC_2H_5O+OH$	6.00E+05	2.5	1850
556. $C_2H_5OH+O\leftrightarrow C_2H_5O+OH$	4.82E+13	0	6856
557. $C_2H_5OH+O\leftrightarrow PC_2H_5O+OH$	5.00E+12	0	4411
558. $C_2H_5OH+H\leftrightarrow C_2H_5+H_2O$	5.90E+11	0	3450
559. $C_2H_5OH+H\leftrightarrow SC_2H_5O+H_2$	4.40E+12	0	4570
560. $C_2H_5OH+HO_2\leftrightarrow SC_2H_5O+H_2O_2$	2.00E+13	0	17000
561. $C_2H_5OH+CH_3\leftrightarrow SC_2H_5O+CH_4$	4.00E+11	0	9700
562. $C_2H_5OH+CH_3\leftrightarrow PC_2H_5O+CH_4$	3.00E+00	4	10480
563. $C_2H_5OH+CH_3\leftrightarrow C_2H_5O+CH_4$	8.00E+10	0	9400
564. $C_2H_5OH+CH_3O\leftrightarrow SC_2H_5O+CH_3OH$	2.00E+11	0	7000
565. $C_2H_5OH+CH_2O\leftrightarrow C_2H_5O+CH_3O$	1.50E+12	0	79500
566. $C_2H_5OH+C_2H_5O\leftrightarrow C_2H_5OH+SC_2H_5O$	2.00E+11	0	7000
567. $C_2H_5OH\leftrightarrow C_2H_5+OH$	5.00E+16	0	91212
568. $C_2H_5OH\leftrightarrow C_2H_4+H_2O$	1.00E+14	0	76706
569. $C_2H_5OH+O_2\leftrightarrow PC_2H_5O+HO_2$	4.00E+13	0	50900
570. $C_2H_5OH+O_2\leftrightarrow SC_2H_5O+HO_2$	4.00E+13	0	51200
571. $C_2H_5OH+O_2\leftrightarrow C_2H_5O+HO_2$	2.00E+13	0	56000
572. $C_2H_5OH+H\leftrightarrow PC_2H_5O+H_2$	2.00E+12	0	9500
573. $C_2H_5OH+H\leftrightarrow C_2H_5O+H_2$	1.76E+12	0	4570
574. $C_2H_5OH+HO_2\leftrightarrow H_2O_2+C_2H_5O$	1.00E+11	0	15500
575. $C_2H_5OH+HO_2\leftrightarrow H_2O_2+PC_2H_5O$	1.00E+11	0	12500
576. $C_2H_5OH+C_2H_5\leftrightarrow PC_2H_5O+C_2H_6$	1.50E+12	0	11700
577. $C_2H_5OH+C_2H_5\leftrightarrow SC_2H_5O+C_2H_6$	4.00E+13	0	10000
578. $C_2H_5OH+CH_2OH\leftrightarrow SC_2H_5O+CH_3OH$	4.00E+11	0	9700
579. $C+OH\leftrightarrow CO+H$	5.00E+13	0	0

Table F.6 (continued): Chemical reaction mechanism for Konnov's methane oxidation (A_i in mol.cm.s.K, E_i in cal.mol^{-1})

REACTIONS CONSIDERED	A_i	β_i	E_i
580. $C+O_2 \leftrightarrow CO+O$	1.20E+14	0	4000
581. $C+CH_3 \leftrightarrow C_2H_2+H$	5.00E+13	0	0
582. $C+CH_2 \leftrightarrow C_2H+H$	5.00E+13	0	0
583. $CH_2O+CH_3O_2 \leftrightarrow HCO+CH_3O_2H$	2.00E+12	0	11660
584. $CH_3O_2+H \leftrightarrow CH_3O+OH$	9.60E+13	0	0
585. $CH_3O_2+OH \leftrightarrow CH_3OH+O_2$	6.00E+13	0	0
586. $CH_3O_2+CH_3 \leftrightarrow CH_3O+CH_3O$	2.40E+13	0	0
587. $CH_3O_2+CH_3O_2 \rightarrow CH_2O+CH_3OH+O_2$	2.70E+10	0	-780
588. $CH_3O_2+CH_3O_2 \rightarrow CH_3O+CH_3O+O_2$	2.80E+10	0	-780
589. $CH_3O_2+H_2O_2 \leftrightarrow CH_3O_2H+HO_2$	2.40E+12	0	10000
590. $CH_3O_2H \leftrightarrow CH_3O+OH$	6.00E+14	0	42300
591. $CH_3O_2+HO_2 \leftrightarrow CH_3O_2H+O_2$	2.29E+11	0	-1550
592. $CH_3O_2H+OH \leftrightarrow CH_3O_2+H_2O$	1.15E+12	0	-380
593. $CH_4+CH_3O_2 \leftrightarrow CH_3+CH_3O_2H$	1.81E+11	0	18600
594. $C_2H_6+CH_3O_2 \leftrightarrow C_2H_5+CH_3O_2H$	2.95E+11	0	14940
595. $CH_3OH+CH_3O_2 \leftrightarrow CH_2OH+CH_3O_2H$	1.81E+12	0	13800
596. $CH_3O_2H+O \leftrightarrow OH+CH_3O_2$	2.00E+13	0	4750
597. $CH_3CO+O_2 \leftrightarrow CH_3CO_3$	1.00E+10	0	-2700
598.$CH_3HCO+CH_3CO_3 \leftrightarrow CH_3CO+CH_3CO_3H$	1.20E+11	0	4900
599. $CH_3HCO+C_2H_5O_2 \leftrightarrow CH_3CO+C_2H_5O_2H$	1.15E+11	0	10000
600. $C_2H_5+O_2(+M) \leftrightarrow C_2H_5O_2(+M)$	2.20E+10	0.8	-570
Low pressure limit: 0.71000E+43 -0.82400E+01 4.27E+03			
601. $C_2H_5O_2 \leftrightarrow C_2H_4+HO_2$	5.62E+11	0	28900
602. $C_2H_5O_2+HO_2 \leftrightarrow C_2H_5O_2H+O_2$	3.40E+11	0	-1300
603. $C_2H_5O_2H \leftrightarrow C_2H_5O+OH$	4.00E+15	0	43000
604. $C_2H_5O_2H+O \leftrightarrow OH+C_2H_5O_2$	2.00E+13	0	4750
605. $C_2H_5O_2H+OH \leftrightarrow C_2H_5O_2+H_2O$	2.00E+12	0	-370
606. $CH_4+C_2H_5O_2 \leftrightarrow CH_3+C_2H_5O_2H$	1.14E+13	0	20460
607. $CH_4+CH_3CO_3 \leftrightarrow CH_3+CH_3CO_3H$	1.14E+13	0	20460
608. $C_2H_4+C_2H_5O_2 \leftrightarrow C_2H_3+C_2H_5O_2H$	1.00E+12	0	25000
609. $C_2H_4+CH_3CO_3 \leftrightarrow C_2H_3+CH_3CO_3H$	3.00E+12	0	29000
610. $CH_3CO_3+HO_2 \leftrightarrow CH_3CO_3H+O_2$	1.00E+12	0	0
611. $CH_3CO_3H \rightarrow CH_3CO_2+OH$	1.15E+13	0	32550
612. $CH_3CO_3H \rightarrow CH_3+CO_2+OH$	2.00E+14	0	40150
613. $CH_3CO_3+CH_3O_2 \rightarrow CH_3CO_2+CH_3O+O_2$	1.08E+15	0	3600
614. $CH_3CO_3+CH_3O_2 \rightarrow CH_3CO_2H+CH_2O+O_2$	2.47E+09	0	-4200
615. $CH_3CO_3+HO_2 \rightarrow CH_3CO_2+OH+O_2$	2.59E+11	0	-2080
616. $CH_3CO_3+CH_3CO_3 \rightarrow CH_3CO_2+CH_3CO_2+O_2$	1.69E+12	0	-1060
617. $CH_3CO_2+M \rightarrow CH_3+CO_2+M$	8.70E+15	0	14400
618. $CH_3CO_2H \leftrightarrow CH_4+CO_2$	7.08E+13	0	74600
619. $CH_3CO_2H \leftrightarrow CH_2CO+H_2O$	4.47E+14	0	79800
620. $CH_3CO_2H+OH \leftrightarrow CH_3CO_2+H_2O$	2.40E+11	0	-400
621. $CH_3OH+C_2H_5O_2 \leftrightarrow CH_2OH+C_2H_5O_2H$	6.30E+12	0	19360

Table F.6 (continued): Chemical reaction mechanism for Konnov's methane oxidation (A_i in mol.cm.s.K, E_i in cal.mol^{-1})

REACTIONS CONSIDERED	A_i	β_i	E_i
622. $CH_3OH+CH_3CO_3 \leftrightarrow CH_2OH+CH_3CO_3H$	6.30E+12	0	19360
623. $CH_2O+C_2H_5O_2 \leftrightarrow HCO+C_2H_5O_2H$	1.30E+11	0	9000
624. $CH_2O+CH_3CO_3 \leftrightarrow HCO+CH_3CO_3H$	1.00E+12	0	10560
625. $C_2H_4+CH_3O_2 \leftrightarrow C_2H_3+CH_3O_2H$	1.00E+13	0	25000
626. $CH_3HCO+CH_3O_2 \leftrightarrow CH_3CO+CH_3O_2H$	1.15E+11	0	10000
627. $C_2H_5OH+CH_3O_2 \leftrightarrow SC_2H_5O+CH_3O_2H$	1.00E+13	0	10000
628. $C_2H_5+CH_3O_2 \leftrightarrow C_2H_5O+CH_3O$	2.41E+13	0	0
629. $C_2H_4+HO_2 \leftrightarrow C_2H_4O+OH$	2.20E+12	0	17200
630. $C_2H_4+CH_3O \leftrightarrow C_2H_4O+CH_3$	1.00E+11	0	14500
631. $C_2H_4+CH_3O_2 \leftrightarrow C_2H_4O+CH_3O$	7.00E+11	0	14500
632. $C_2H_4O \rightarrow CH_3HCOW$	1.60E+13	0	54300
633. $CH_3HCOW+M \rightarrow CH_3HCO+M$	1.00E+14	0	0
634. $CH_3HCOW \rightarrow CH_3+HCO$	5.00E+08	0	0
635. $C_2H_4O+H \leftrightarrow H_2+C_2H_3O$	8.00E+13	0	9740
636. $C_2H_4O+H \leftrightarrow H_2O+C_2H_3$	5.00E+09	0	5030
637. $C_2H_4O+H \leftrightarrow C_2H_4+OH$	9.51E+10	0	5030
638. $C_2H_4O+CH_2HCO \leftrightarrow CH_3HCO+C_2H_3O$	1.00E+11	0	14000
639. $C_2H_4O+CH_3 \leftrightarrow CH_4+C_2H_3O$	1.07E+12	0	11900
640. $C_2H_4O+O \leftrightarrow OH+C_2H_3O$	1.91E+12	0	5300
641. $C_2H_4O+OH \leftrightarrow H_2O+C_2H_3O$	1.78E+13	0	3600
642. $C_2H_3O \rightarrow CH_2CHOW$	1.00E+11	0	10000
643. $C_2H_3O \rightarrow CH_3+CO$	8.00E+11	0	10000
644. $C_2H_3O+H+M \rightarrow C_2H_4O+M$	4.00E+15	0	0
645. $CH_2CHOW+M \rightarrow CH_2HCO+M$	1.00E+14	0	0
646. $CH_2CHOW \rightarrow CH_3+CO$	1.00E+08	0	0
647. $CH_2CHOW \rightarrow OH+C_2H_2$	1.00E+11	0	17000
648. $CH_2CHOW \rightarrow CH_2CO+H$	1.00E+08	0	0
649. $C_2H_4O+O_2 \rightarrow HO_2+C_2H_3O$	1.00E+14	0	52000
650. $C_2H_4O+HO_2 \leftrightarrow H_2O_2+C_2H_3O$	5.00E+13	0	18000
651. $CH_3HCOW+O_2 \rightarrow HO_2+CH_3CO$	1.00E+14	0	0
652. $CH_2CHOW+O_2 \rightarrow HO_2+CH_2CO$	1.00E+14	0	0
653. $CH_2+C_2H_2 \leftrightarrow H+C_3H_3$	1.20E+13	0	6620
654. $CH_2+C_2H_4 \leftrightarrow C_3H_6$	3.16E+12	0	5280
655. $SCH_2+C_2H_4 \rightarrow C_3H_6$	1.00E+14	0	0
656. $CH_2+C_3H_8 \leftrightarrow CH_3+IC_3H_7$	1.50E+00	3.5	7470
657. $CH_2+C_3H_8 \leftrightarrow CH_3+NC_3H_7$	9.00E-01	3.6	7150
658. $SCH_2+C_2H_2 \leftrightarrow C_3H_3+H$	1.80E+14	0	0
659. $C_2H_3+CH_2 \leftrightarrow C_3H_4+H$	3.00E+13	0	0
660. $C_2H_3+C_2H_2 \leftrightarrow C_4H_4+H$	1.93E+12	0	6000
661. $C_2H_3+C2H_3 \leftrightarrow C_4H_6$	7.23E+13	0	0
662. $C_2H_2+CH_3 \leftrightarrow SC_3H_5$	1.61E+40	-8.6	20331
663. $C_2H_2+CH_3 \leftrightarrow C_3H_5$	2.61E+46	-9.8	36951
664. $C_2H_2+CH_3 \leftrightarrow C_3H_4+H$	6.74E+19	-2.1	31591

Table F.6 (continued): Chemical reaction mechanism for Konnov's methane oxidation (A_i in mol.cm.s.K, E_i in cal.mol^{-1})

REACTIONS CONSIDERED	A_i	β_i	E_i
665. $CH_2CO+C_2H_3\leftrightarrow C_3H_5+CO$	1.00E+12	0	3000
666. $HCCO+C_2H_2\leftrightarrow C_3H_3+CO$	1.00E+11	0	3000
667. $C_3H_8(+M)\leftrightarrow C_2H_5+CH_3(+M)$	1.10E+17	0	84400
Low pressure limit: 0.78300E+19 0.00000E+00 6.50E+04			
668. $C_3H_8+O_2\leftrightarrow NC_3H_7+HO_2$	4.00E+13	0	50870
669. $C_3H_8+O_2\leftrightarrow IC_3H_7+HO_2$	4.00E+13	0	47690
670. $C_3H_8+HO_2\leftrightarrow NC_3H_7+H_2O_2$	4.76E+04	2.5	16490
671. $C_3H_8+HO_2\leftrightarrow IC_3H_7+H_2O_2$	9.64E+03	2.6	13910
672. $C_3H_8+OH\leftrightarrow NC_3H_7+H_2O$	3.16E+07	1.8	934
673. $C_3H_8+OH\leftrightarrow IC_3H_7+H_2O$	7.06E+06	1.9	-159
674. $C_3H_8+O\leftrightarrow NC_3H_7+OH$	3.72E+06	2.4	5505
675. $C_3H_8+O\leftrightarrow IC_3H_7+OH$	5.50E+05	2.5	3140
676. $C_3H_8+H\leftrightarrow NC_3H_7+H_2$	1.34E+06	2.5	6756
677. $C_3H_8+H\leftrightarrow IC_3H_7+H_2$	1.30E+06	2.4	4470
678. $C_3H_8+CH_3\leftrightarrow NC_3H_7+CH_4$	9.00E-01	3.6	7150
679. $C_3H_8+CH_3\leftrightarrow IC_3H_7+CH_4$	1.50E+00	3.5	5480
680. $C_3H_8+C_2H_5\leftrightarrow NC_3H_7+C_2H_6$	9.00E-01	3.6	9140
681. $C_3H_8+C_2H_5\leftrightarrow IC_3H_7+C_2H_6$	1.20E+00	3.5	7470
682. $C_3H_8+C_2H_3\leftrightarrow NC_3H_7+C_2H_4$	6.00E+02	3.3	10502
683. $C_3H_8+C_2H_3\leftrightarrow IC_3H_7+C_2H_4$	1.00E+03	3.1	8829
684. $C_3H_8+IC_3H_7\leftrightarrow NC_3H_7+C_3H_8$	8.44E-03	4.2	8720
685. $C_3H_8+C_3H_5\leftrightarrow NC_3H_7+C_3H_6$	2.35E+02	3.3	19800
686. $C_3H_8+C_3H_5\leftrightarrow IC_3H_7+C_3H_6$	7.84E+01	3.3	18200
687. $C_3H_8+CH_3O\leftrightarrow NC_3H_7+CH_3OH$	4.34E+11	0	6460
688. $C_3H_8+CH_3O\leftrightarrow IC_3H_7+CH_3OH$	1.45E+11	0	4570
689. $NC_3H_7\leftrightarrow C_2H_4+CH_3$	1.26E+13	0	30404
690. $NC_3H_7+O_2\leftrightarrow C_3H_6+HO_2$	1.00E+12	0	5000
691. $IC_3H_7\leftrightarrow C_2H_4+CH_3$	1.00E+12	0	34500
692. $IC_3H_7+O_2\leftrightarrow C_3H_6+HO_2$	2.75E+10	0	-2151
693. $C_3H_6\leftrightarrow C_3H_5+H$	4.57E+14	0	88900
694. $C_3H_6\leftrightarrow SC_3H_5+H$	7.59E+14	0	101300
695. $C_3H_6\leftrightarrow TC_3H_5+H$	1.45E+15	0	98060
696. $C_3H_6\leftrightarrow C_2H_3+CH_3$	1.10E+21	-1.2	97720
697. $C_3H_6+HO_2\leftrightarrow C_3H_6O+OH$	1.05E+12	0	14210
698. $C_3H_6+HO_2\leftrightarrow C_3H_5+H_2O_2$	9.64E+03	2.6	13910
699. $C_3H_6+HO_2\leftrightarrow SC_3H_5+H_2O_2$	7.50E+09	0	12570
700. $C_3H_6+HO_2\leftrightarrow TC_3H_5+H_2O_2$	3.00E+09	0	9930
701. $C_3H_6+OH\leftrightarrow C_3H_5+H_2O$	3.12E+06	2	-300
702. $C_3H_6+OH\leftrightarrow SC_3H_5+H_2O$	2.14E+06	2	2780
703. $C_3H_6+OH\leftrightarrow TC_3H_5+H_2O$	1.11E+06	2	1450
704. $C_3H_6+O\leftrightarrow C_2H_5+HCO$	6.83E+06	1.6	-628
705. $C_3H_6+O\leftrightarrow CH_3+CH_3CO$	9.11E+06	1.6	-628
706. $C_3H_6+O\leftrightarrow C_2H_4+CH_2O$	4.56E+06	1.6	-628

Table F.6 (continued): Chemical reaction mechanism for Konnov's methane oxidation (A_i in mol.cm.s.K, E_i in cal.mol^{-1})

REACTIONS CONSIDERED	A_i	β_i	E_i
707. $NC_3H_7 \leftrightarrow C_3H_6+H$	1.00E+14	0	37286
708. $C_3H_6+H \leftrightarrow IC_3H_7$	5.70E+09	1.2	874
709. $C_3H_6+H \leftrightarrow C_3H_5+H_2$	6.46E+12	0	4445
710. $C_3H_6+H \leftrightarrow SC_3H_5+H_2$	7.81E+05	2.5	12280
711. $C_3H_6+O_2 \leftrightarrow SC_3H_5+HO_2$	1.95E+12	0	39000
712. $C_3H_6+O_2 \leftrightarrow TC_3H_5+HO_2$	1.95E+12	0	39000
713. $C_3H_6+O_2 \leftrightarrow C_3H_5+HO_2$	1.95E+12	0	39000
714. $C_3H_6+CH_3 \leftrightarrow C_3H_5+CH_4$	2.21E+00	3.5	5680
715. $C_3H_6+CH_3 \leftrightarrow SC_3H_5+CH_4$	1.35E+00	3.5	12850
716. $C_3H_6+CH_3 \leftrightarrow TC_3H_5+CH_4$	8.40E-01	3.5	11660
717. $C_3H_6+C_2H_5 \leftrightarrow C_3H_5+C_2H_6$	2.23E+00	3.5	6640
718. $C_3H_6O \leftrightarrow C_2H_5+HCO$	2.45E+13	0	58500
719. $C_3H_6O \leftrightarrow C_2H_5CHO$	1.82E+14	0	58500
720. $C_3H_6O \leftrightarrow CH_3+CH_3CO$	4.54E+13	0	59900
721. $C_3H_6O \leftrightarrow CH_3+CH_2HCO$	2.45E+13	0	58820
722. $C_3H_6O \leftrightarrow CH_3+C_2H_3O$	8.00E+15	0	92010
723. $C_2H_5CHO \leftrightarrow C_2H_5+HCO$	2.45E+16	0	73000
724. $C_2H_5CHO+O \leftrightarrow C_2H_5CO+OH$	5.68E+12	0	1540
725. $C_2H_5CHO+OH \leftrightarrow C_2H_5CO+H_2O$	1.21E+13	0	0
726. $C_2H_5CHO+HO_2 \leftrightarrow C_2H_5CO+H_2O_2$	1.52E+09	0	0
727. $C_2H_5CHO+C_2H_5 \leftrightarrow C_2H_5CO+C_2H_6$	5.00E+10	0	6290
728. $C_2H_5CO \leftrightarrow C_2H_5+CO$	5.89E+12	0	14400
729. $C_3H_5+O_2 \rightarrow CH_2O+CH_2HCO$	5.00E+12	0	19190
730. $C_3H_5+H \leftrightarrow C_3H_4+H_2$	1.80E+13	0	0
731. $C_3H_5+O \rightarrow C_2H_4+CO+H$	1.81E+14	0	0
732. $C_3H_5+CH_3 \leftrightarrow C_3H_4+CH_4$	3.00E+12	-0.3	-130
733. $C_3H_5+C_2H_5 \leftrightarrow C_3H_4+C_2H_6$	9.64E+11	0	-130
734. $C_3H_5+C_2H_3 \leftrightarrow C_3H_4+C_2H_4$	2.40E+12	0	0
735. $C_3H_5+C_2H_3 \leftrightarrow C_3H_6+C_2H_2$	4.80E+12	0	0
736. $SC_3H_5+O_2 \leftrightarrow CH_3HCO+HCO$	4.34E+12	0	0
737. $SC_3H_5+HO_2 \rightarrow CH_2CO+CH_3+OH$	4.50E+12	0	0
738. $SC_3H_5+H \leftrightarrow C_3H_4+H_2$	3.33E+12	0	0
739. $SC_3H_5+O \rightarrow CH_2CO+CH_3$	1.81E+14	0	0
740. $SC_3H_5+CH_3 \leftrightarrow C_3H_4+CH_4$	1.00E+11	0	0
741. $SC_3H_5+C_2H_5 \leftrightarrow C_3H_4+C_2H_6$	1.00E+11	0	0
742. $SC_3H_5+C_2H_3 \leftrightarrow C_3H_4+C_2H_4$	1.00E+11	0	0
743. $TC_3H_5+O_2 \leftrightarrow CH_3CO+CH_2O$	4.34E+11	0	0
744. $TC_3H_5+HO_2 \rightarrow CH_2CO+CH_3+OH$	4.50E+12	0	0
745. $TC_3H_5+H \leftrightarrow C_3H_4+H_2$	3.33E+12	0	0
746. $TC_3H_5+O \rightarrow HCCO+CH_3+H$	1.81E+14	0	0
747. $TC_3H_5+CH_3 \leftrightarrow C_3H_4+CH_4$	1.00E+11	0	0
748. $TC_3H_5+C_2H_5 \leftrightarrow C_3H_4+C_2H_6$	1.00E+11	0	0
749. $TC_3H_5+C_2H_3 \leftrightarrow C_3H_4+C_2H_4$	1.00E+11	0	0

Table F.6 (continued): Chemical reaction mechanism for Konnov's methane oxidation (A_i in mol.cm.s.K, E_i in cal.mol^{-1})

REACTIONS CONSIDERED	A_i	β_i	E_i
750. $C_3H_4+M\leftrightarrow C_3H_3+H+M$	2.00E+18	0	80000
751. $C_3H_4(+M)\leftrightarrow PC_3H_4(+M)$	1.07E+14	0	64300
Low pressure limit: 0.34800E+18 0.00000E+00 4.84E+04			
752. $C_3H_4+O_2\leftrightarrow C_3H_3+HO_2$	4.00E+13	0	61500
753. $C_3H_4+HO_2\rightarrow CH_2CO+CH_2+OH$	8.00E+12	0	19000
754. $C_3H_4+OH\leftrightarrow CH_2CO+CH_3$	3.12E+12	0	-397
755. $C_3H_4+OH\leftrightarrow C_3H_3+H_2O$	2.00E+07	2	1000
756. $C_3H_4+O\leftrightarrow C_2H_3+HCO$	1.10E-02	4.6	-4243
757. $C_3H_4+H\leftrightarrow C_3H_5$	1.20E+11	0.7	3000
758. $C_3H_4+H\leftrightarrow TC_3H_5$	8.50E+12	0	2000
759. $C_3H_4+H\leftrightarrow C_3H_3+H_2$	2.00E+07	2	5000
760. $C_3H_4+CH_3\leftrightarrow C_3H_3+CH_4$	2.00E+11	0	7700
761. $PC_3H_4+M\leftrightarrow C_3H_3+H+M$	4.70E+18	0	80000
762. $PC_3H_4+O_2\rightarrow HCCO+OH+CH_2$	2.00E+08	1.5	30100
763. $PC_3H_4+O_2\leftrightarrow C_3H_3+HO_2$	5.00E+12	0	51000
764. $PC_3H_4+HO_2\rightarrow C_2H_4+CO+OH$	3.00E+12	0	19000
765. $PC_3H_4+OH\leftrightarrow C_3H_3+H_2O$	2.00E+07	2	1000
766. $PC_3H_4+OH\leftrightarrow CH_2CO+CH_3$	5.00E-04	4.5	-1000
767. $PC_3H_4+O\leftrightarrow CH_2CO+CH_2$	6.40E+12	0	2010
768. $PC_3H_4+O\leftrightarrow C_2H_3+HCO$	3.20E+12	0	2010
769. $PC_3H_4+O\leftrightarrow HCCO+CH_3$	6.30E+12	0	2010
770. $PC_3H_4+O\rightarrow HCCO+CH_2+H$	3.20E+11	0	2010
771. $PC_3H_4+H\leftrightarrow TC_3H_5$	6.50E+12	0	2000
772. $PC_3H_4+H\leftrightarrow C_3H_3+H_2$	2.00E+07	2	5000
773. $PC_3H_4+H\leftrightarrow C_2H_2+CH_3$	1.30E+05	2.5	1000
774. $PC_3H_4+CH_3\leftrightarrow C_3H_3+CH_4$	1.50E+00	3.5	5600
775. $PC_3H_4+C_2H_3\leftrightarrow C_3H_3+C_2H_4$	1.00E+12	0	7700
776. $PC_3H_4+C_3H_5\leftrightarrow C_3H_3+C_3H_6$	1.00E+12	0	7700
777. $C_3H_3+H\leftrightarrow C_3H_2+H_2$	5.00E+13	0	3000
778. $C_3H_3+O\rightarrow C_2H+HCO+H$	7.00E+13	0	0
779. $C_3H_3+O\rightarrow C_2H_2+CO+H$	7.00E+13	0	0
780. $C_3H_3+OH\leftrightarrow C_3H_2+H_2O$	1.00E+13	0	0
781. $C_3H_3+O_2\leftrightarrow CH_2CO+HCO$	3.01E+10	0	2870
782. $C_3H_3+CH\leftrightarrow IC_4H_3+H$	7.00E+13	0	0
783. $C_3H_3+CH\leftrightarrow NC_4H_3+H$	7.00E+13	0	0
784. $C3H_3+CH_2\leftrightarrow C_4H_4+H$	4.00E+13	0	0
785. $C_3H_3+C_3H_3\leftrightarrow C_6H_5+H$	2.00E+12	0	0
786. $CH+C_2H_2\leftrightarrow C_3H_2+H$	1.00E+14	0	0
787. $C_3H_2+O_2\leftrightarrow HCCO+CO+H$	1.00E+14	0	3000
788. $C_3H_2+OH\leftrightarrow C_2H_2+HCO$	5.00E+13	0	0
789. $C_3H_2+CH_2\leftrightarrow IC_4H_3+H$	3.00E+13	0	0
790. $C_4H_8\leftrightarrow IC_4H_7+H$	4.08E+18	-1	97350
791. $C_4H_8\leftrightarrow C_2C_4H_8$	4.00E+11	0	60000

Table F.6 (continued): Chemical reaction mechanism for Konnov's methane oxidation (A_i in mol.cm.s.K, E_i in cal.mol^{-1})

REACTIONS CONSIDERED	A_i	β_i	E_i
792. $C_4H_8 \leftrightarrow T_2C_4H_8$	4.00E+11	0	60000
793. $C_4H_8 \leftrightarrow C_3H_5+CH_3$	1.00E+16	0	73000
794. $C_4H_8 \leftrightarrow C_2H_3+C_2H_5$	1.00E+19	-1	96770
795. $C_4H_8+O_2 \leftrightarrow IC_4H_7+HO_2$	4.00E+12	0	33200
796. $C_4H_8+HO_2 \leftrightarrow IC_4H_7+H_2O_2$	1.00E+11	0	17060
797. $C_4H_8+OH \leftrightarrow NC_3H_7+CH_2O$	6.50E+12	0	0
798. $C_4H_8+OH \leftrightarrow CH_3HCO+C_2H_5$	1.00E+11	0	0
799. $C_4H_8+OH \leftrightarrow C_2H_6+CH_3CO$	1.00E+10	0	0
800. $C_4H_8+OH \leftrightarrow IC_4H_7+H_2O$	2.25E+13	0	2217
801. $C_4H_8+O \leftrightarrow C_3H_6+CH_2O$	2.51E+12	0	0
802. $C_4H_8+O \leftrightarrow CH_3HCO+C_2H_4$	1.25E+12	0	850
803. $C_4H_8+O \leftrightarrow C_2H_5+CH_3CO$	1.63E+13	0	850
804. $C_4H_8+O \leftrightarrow IC_4H_7+OH$	9.60E+12	0	1970
805. $C_4H_8+O \leftrightarrow NC_3H_7+HCO$	1.80E+05	2.5	-1029
806. $C_4H_8+H \leftrightarrow IC_4H_7+H_2$	5.00E+13	0	3900
807. $C_4H_8+CH_3 \leftrightarrow IC_4H_7+CH_4$	1.00E+11	0	7300
808. $C_4H_8+C_2H_5 \leftrightarrow IC_4H_7+C_2H_6$	1.00E+11	0	8000
809. $C_4H_8+C_3H_5 \leftrightarrow IC_4H_7+C_3H_6$	7.90E+10	0	12400
810. $C_4H_8+SC_3H_5 \leftrightarrow IC_4H_7+C_3H_6$	8.00E+10	0	12400
811. $C_4H_8+TC_3H_5 \leftrightarrow IC_4H_7+C_3H_6$	8.00E+10	0	12400
812. $C_2C_4H_8 \leftrightarrow T_2C_4H_8$	4.00E+13	0	62000
813. $C_2C_4H_8 \leftrightarrow C_4H_6+H_2$	1.00E+13	0	65500
814. $C_2C_4H_8 \leftrightarrow IC_4H_7+H$	4.07E+18	-1	97350
815. $C_2C_4H_8 \leftrightarrow SC_3H_5+CH_3$	2.00E+16	0	95000
816. $C_2C_4H_8+OH \leftrightarrow IC_4H_7+H_2O$	1.25E+14	0	3060
817. $C_2C_4H_8+OH \leftrightarrow CH_3HCO+C_2H_5$	1.40E+13	0	0
818. $C_2C_4H_8+O \leftrightarrow IC_3H_7+HCO$	6.03E+12	0	0
819. $C_2C_4H_8+O \leftrightarrow CH_3HCO+C_2H_4$	1.00E+12	0	0
820. $C_2C_4H_8+H \leftrightarrow IC_4H_7+H_2$	1.00E+13	0	3500
821. $C_2C_4H_8+CH_3 \leftrightarrow IC_4H_7+CH_4$	1.00E+11	0	8200
822. $T_2C_4H_8 \leftrightarrow IC_4H_7+H$	4.07E+18	-1	97350
823. $T_2C_4H_8 \leftrightarrow SC_3H_5+CH_3$	2.00E+16	0	96000
824. $T_2C_4H_8+OH \leftrightarrow IC_4H_7+H_2O$	1.00E+14	0	3060
825. $T_2C_4H_8+OH \leftrightarrow CH_3HCO+C_2H_5$	1.50E+13	0	0
826. $T_2C_4H_8+O \leftrightarrow IC_3H_7+HCO$	6.03E+12	0	0
827. $T_2C_4H_8+O \leftrightarrow CH_3HCO+C_2H_4$	1.00E+12	0	0
828. $T_2C_4H_8+H \leftrightarrow IC_4H_7+H_2$	5.00E+12	0	3500
829. $T_2C_4H_8+CH_3 \leftrightarrow IC_4H_7+CH_4$	1.00E+11	0	8200
830. $IC_4H_7 \leftrightarrow C_4H_6+H$	1.20E+14	0	49300
831. $IC_4H_7 \leftrightarrow C_2H_4+C_2H_3$	1.00E+14	0	49000
832. $IC_4H_7+H \leftrightarrow C_4H_6+H_2$	3.16E+12	0	0
833. $IC_4H_7+O_2 \leftrightarrow C_4H_6+HO_2$	1.00E+11	0	0
834. $IC_4H_7+CH_3 \leftrightarrow C_4H_6+CH_4$	1.00E+13	0	0

Table F.6 (continued): Chemical reaction mechanism for Konnov's methane oxidation (A_i in mol.cm.s.K, E_i in cal.mol^{-1})

REACTIONS CONSIDERED	A_i	β_i	E_i
835. $IC_4H_7+C_2H_3\leftrightarrow C_4H_6+C_2H_4$	4.00E+12	0	0
836. $IC_4H_7+C_2H_5\leftrightarrow C_4H_6+C_2H_6$	4.00E+12	0	0
837. $IC_4H_7+C_2H_5\leftrightarrow C_4H_8+C_2H_4$	5.00E+11	0	0
838. $IC_4H_7+C_2H_5\leftrightarrow T_2C_4H_8+C_2H_4$	5.00E+11	0	0
839. $IC_4H_7+C_2H_5\leftrightarrow C_2C_4H_8+C_2H_4$	5.00E+11	0	0
840. $IC_4H_7+C_3H_5\leftrightarrow C_4H_6+C_3H_6$	4.00E+13	0	0
841. $IC_4H_7+IC_4H_7\leftrightarrow C_4H_6+C_4H_8$	3.16E+12	0	0
842. $C_2H_3+C_2H_4\leftrightarrow C_4H_6+H$	3.00E+12	0	1000
843. $C_4H_6+H\leftrightarrow NC_4H_5+H_2$	3.00E+07	2	13000
844. $C_4H_6+H\leftrightarrow IC_4H_5+H_2$	3.00E+07	2	6000
845. $C_4H_6+OH\leftrightarrow NC_4H_5+H_2O$	2.00E+07	2	5000
846. $C_4H_6+OH\leftrightarrow IC_4H_5+H_2O$	2.00E+07	2	2000
847. $C_4H_6+O\leftrightarrow C_2H_4+CH_2CO$	1.00E+12	0	0
848. $C_4H_6+O\leftrightarrow PC_3H_4+CH_2O$	1.00E+12	0	0
849. $C_2H_2+NC_4H_5\leftrightarrow C_6H_6+H$	2.80E+03	2.9	1400
850. $NC_4H_5+OH\leftrightarrow C_4H_4+H_2O$	2.00E+07	2	1000
851. $NC_4H_5+H\leftrightarrow C_4H_4+H_2$	3.00E+07	2	1000
852. $NC_4H_5+H\leftrightarrow IC_4H_5+H$	1.00E+14	0	0
853. $IC_4H_5\leftrightarrow C_4H_4+H$	2.00E+15	0	45000
854. $NC_4H_5\leftrightarrow C_4H_4+H$	1.60E+14	0	41400
855. $C_4H_4+OH\leftrightarrow IC_4H_3+H_2O$	1.00E+07	2	2000
856. $C_4H_4+OH\leftrightarrow NC_4H_3+H_2O$	7.50E+06	2	5000
857. $C_4H_4+H\leftrightarrow NC_4H_3+H_2$	2.00E+07	2	15000
858. $NC_4H_3+H\leftrightarrow IC_4H_3+H$	1.00E+14	0	0
859. $IC_4H_3+CH_2\leftrightarrow C_3H_4+C_2H$	2.00E+13	0	0
860. $IC_4H_3+O_2\leftrightarrow CH_2CO+HCCO$	1.00E+12	0	0
861. $IC_4H_3+OH\leftrightarrow C_4H_2+H_2O$	3.00E+13	0	0
862. $IC_4H_3+O\leftrightarrow CH_2CO+C_2H$	2.00E+13	0	0
863. $IC_4H_3+H\leftrightarrow C_4H_2+H_2$	5.00E+13	0	0
864. $NC_4H_3+C_2H_2\leftrightarrow C_6H_5$	2.80E+03	2.9	1400
865. $NC_4H_3+M\leftrightarrow C_4H_2+H+M$	1.00E+16	0	59700
866. $IC_4H_3+M\leftrightarrow C_4H_2+H+M$	4.46E+15	0	46516
867. $IC_4H_3+O\leftrightarrow H_2C_4O+H$	2.00E+13	0	0
868. $H_2C_4O+H\leftrightarrow C_2H_2+HCCO$	5.00E+13	0	3000
869. $H_2C_4O+OH\leftrightarrow CH_2CO+HCCO$	1.00E+07	2	2000
870. $C_4H_2+OH\leftrightarrow H_2C_4O+H$	6.66E+12	0	-410
871. $C_2H_2+C_2H_2\leftrightarrow IC_4H_3+H$	2.20E+12	0	64060
872. $C_2H_2+C_2H_2\leftrightarrow NC_4H_3+H$	1.00E+12	0	66000
873. $C_2H_2+C_2H_2\leftrightarrow C_4H_4$	5.50E+12	0	37000
874. $C_4H_2(+M)\leftrightarrow C_4H+H(+M)$	2.20E+14	0.0	116740
Low pressure limit: 0.35000E+18 0.00000E+00 8.01E+04			
875. $C_4H_2+O\leftrightarrow C_3H_2+CO$	2.70E+13	0	1720
876. $C_2H_2+C_2H\leftrightarrow C_4H_2+H$	1.82E+14	0	467

Table F.6 (continued): Chemical reaction mechanism for Konnov's methane oxidation (A_i in mol.cm.s.K, E_i in cal.mol^{-1})

REACTIONS CONSIDERED	A_i	β_i	E_i
877. $C_2H_2+C_2H\leftrightarrow NC_4H_3$	1.00E+13	0	0
878. $C_4H+O_2\leftrightarrow C_2H+CO+CO$	1.00E+14	0	0
879. $C_2O+H\leftrightarrow CH+CO$	1.32E+13	0	0
880. $C_2O+O\leftrightarrow CO+CO$	5.20E+13	0	0
881. $C_2O+OH\leftrightarrow CO+CO+H$	2.00E+13	0	0
882. $C_2O+O_2\leftrightarrow CO+CO+O$	2.00E+13	0	0
883. $C_2O+O_2\leftrightarrow CO+CO_2$	2.00E+13	0	0
884. $C_2+H_2\leftrightarrow C_2H+H$	6.60E+13	0	7950
885. $C_2+O\leftrightarrow C+CO$	3.60E+14	0	0
886. $C_2+O_2\leftrightarrow CO+CO$	9.00E+12	0	980
887. $C_2+OH\leftrightarrow C_2O+H$	5.00E+13	0	0
888. $C_6H_5+OH\leftrightarrow C_6H_5O+H$	5.00E+13	0	0
889. $C_6H_5+O_2\leftrightarrow C_6H_5O+O$	2.60E+13	0	6120
890. $C_6H_5+HO_2\leftrightarrow C_6H_5O+OH$	5.00E+13	0	1000
891. $C_6H_6+H\leftrightarrow C_6H_5+H_2$	3.00E+12	0	8100
892. $C_6H_6+OH\leftrightarrow C_6H_5+H_2O$	1.68E+08	1.4	1450
893. $C_6H_6+O\leftrightarrow C_6H_5O+H$	2.78E+13	0	4910
894. $C_6H_6+O_2\leftrightarrow C_6H_5O+OH$	4.00E+13	0	34000
895. $H+C_6H_5\leftrightarrow C_6H_6$	7.80E+13	0	0
896. $C_3H_3+O\rightarrow C_2H_3+CO$	3.80E+13	0	0
897. $C_3H_3+O\leftrightarrow CH_2O+C_2H$	2.00E+13	0	0
898. $C_3H_3+O_2\rightarrow HCCO+CH_2O$	6.00E+12	0	0
899. $C_3H_3+CH_3\leftrightarrow C_2H_5+C_2H$	1.00E+13	0	37500
900. $C_3H_3+CH_3\leftrightarrow C_4H_6$	5.00E+12	0	0
901. $C_3H_6+C_2H_3\leftrightarrow C_3H_5+C_2H_4$	2.21E+00	3.5	4680
902. $C_3H_6+C_2H_3\leftrightarrow SC_3H_5+C_2H_4$	1.35E+00	3.5	10860
903. $C_3H_6+C_2H_3\leftrightarrow TC_3H_5+C_2H_4$	8.40E-01	3.5	9670
904. $C_3H_6+CH_3O\leftrightarrow C_3H_5+CH_3OH$	9.00E+01	3	12000
905. $CH_2+C_2H_2\leftrightarrow C_3H_4$	1.20E+13	0	6620
906. $C_3H_4+C_3H_4\leftrightarrow C_3H_5+C_3H_3$	5.00E+14	0	64700
907. $C_3H_4+OH\leftrightarrow CH_2O+C_2H_3$	1.70E+12	0	-300
908. $C_3H_4+OH\leftrightarrow HCO+C_2H_4$	1.70E+12	0	-300
909. $C_3H_4+O\leftrightarrow CH_2O+C_2H_2$	1.00E+12	0	0
910. $C_3H_4+O\rightarrow CO+C_2H_4$	7.80E+12	0	1600
911. $C_3H_4+C_3H_5\leftrightarrow C_3H_3+C_3H_6$	2.00E+12	0	7700
912. $C_3H_4+C_2H\leftrightarrow C_3H_3+C_2H_2$	1.00E+13	0	0
913. $PC_3H_4\leftrightarrow C_2H+CH_3$	4.20E+16	0.0	10
914. $PC_3H_4+C_2H\leftrightarrow C_3H_3+C_2H_2$	1.00E+13	0	0
915. $C_3H_2+O_2\leftrightarrow HCO+HCCO$	1.00E+13	0	0
916. $C_2H_2+C_2H_3\leftrightarrow NC_4H_5$	2.51E+05	1.9	2100
917. $C_2H_3+C_2H_3\leftrightarrow IC_4H_5+H$	4.00E+13	0	0
918. $IC_4H_5+H\leftrightarrow C_4H_4+H_2$	3.00E+07	2	1000
919. $C_4H_2+H\leftrightarrow C_4H+H_2$	1.00E+14	0	35000

Table F.6 (continued): Chemical reaction mechanism for Konnov's methane oxidation (A_i in mol.cm.s.K, E_i in cal.mol^{-1})

REACTIONS CONSIDERED	A_i	β_i	E_i
920. $C_4H_6+OH\leftrightarrow C_3H_5+CH_2O$	7.23E+12	0	-994
921. $C_4H_8+IC_4H_7\leftrightarrow IC_4H_7+C_2C_4H_8$	3.98E+10	0	12400
922. $C_4H_8+IC_4H_7\leftrightarrow IC_4H_7+T_2C_4H_8$	3.98E+10	0	12400
923. $C_3H_3+C_3H_3\leftrightarrow C_6H_6$	3.00E+11	0	0
924. $C_3H_3+C_3H_4\leftrightarrow C_6H_6+H$	1.40E+12	0	10000
925. $C_3H_5+C_2H_5\leftrightarrow C_3H_6+C_2H_4$	2.60E+12	0	-130
926. $C_3H_6+OH\leftrightarrow C_2H_5+CH_2O$	8.00E+12	0	0
927. $C_3H_6+OH\leftrightarrow CH_3+CH_3HCO$	3.40E+11	0	0
928. $C_3H_5+O_2\leftrightarrow C_3H_4+HO_2$	1.20E+12	0	13550
929. $CH_2O+C_3H_5\leftrightarrow HCO+C_3H_6$	8.00E+10	0	12400
930. $CH_3HCO+C_3H_5\leftrightarrow CH_3CO+C_3H_6$	3.80E+11	0	7200
931. $C_3H_8+CH_3O_2\leftrightarrow NC_3H_7+CH_3O_2H$	6.03E+12	0	19380
932. $C_3H_8+CH_3O_2\leftrightarrow IC_3H_7+CH_3O_2H$	1.99E+12	0	17050
933. $C_3H_8+C_2H_5O_2\leftrightarrow NC_3H_7+C_2H_5O_2H$	6.03E+12	0	19380
934. $C_3H_8+C_2H_5O_2\leftrightarrow IC_3H_7+C_2H_5O_2H$	1.99E+12	0	17050
935. $C_3H_8+IC_3H_7O_2\leftrightarrow NC_3H_7+IC_3H_7O_2H$	6.03E+12	0	19380
936. $C_3H_8+IC_3H_7O_2\leftrightarrow IC_3H_7+IC_3H_7O_2H$	1.99E+12	0	17050
937. $C_3H_8+NC_3H_7O_2\leftrightarrow NC_3H_7+NC_3H_7O_2H$	6.03E+12	0	19380
938. $C_3H_8+NC_3H_7O_2\leftrightarrow IC_3H_7+NC_3H_7O_2H$	1.99E+12	0	17050
939. $NC_3H_7+O_2\leftrightarrow NC_3H_7O_2$	4.82E+12	0	0
940. $IC_3H_7+O_2\leftrightarrow IC_3H_7O_2$	6.62E+12	0	0
941. $NC_3H_7+HO_2\leftrightarrow NC_3H_7O+OH$	3.20E+13	0	0
942. $IC_3H_7+HO_2\leftrightarrow IC_3H_7O+OH$	3.20E+13	0	0
943. $NC_3H_7+CH_3O_2\leftrightarrow NC_3H_7O+CH_3O$	3.80E+12	0	-1200
944. $IC_3H_7+CH_3O_2\leftrightarrow IC_3H_7O+CH_3O$	3.80E+12	0	-1200
945. $NC_3H_7+NC_3H_7O_2\leftrightarrow NC_3H_7O+NC_3H_7O$	3.80E+12	0	-1200
946. $IC_3H_7+NC_3H_7O_2\leftrightarrow IC_3H_7O+NC_3H_7O$	3.80E+12	0	-1200
947. $NC_3H_7+IC_3H_7O_2\leftrightarrow NC_3H_7O+IC_3H_7O$	3.80E+12	0	-1200
948. $IC_3H_7+IC_3H_7O_2\leftrightarrow IC_3H_7O+IC_3H_7O$	3.80E+12	0	-1200
949. $NC_3H_7O_2+HO_2\leftrightarrow NC_3H_7O_2H+O_2$	4.60E+10	0	-2600
950. $IC_3H_7O_2+HO_2\leftrightarrow IC_3H_7O_2H+O_2$	4.60E+10	0	-2600
951. $CH_3+NC_3H_7O_2\leftrightarrow CH_3O+NC_3H_7O$	3.80E+12	0	-1200
952. $CH_3+IC_3H_7O_2\leftrightarrow CH_3O+IC_3H_7O$	3.80E+12	0	-1200
953. $NC_3H_7O_2H\leftrightarrow NC_3H_7O+OH$	4.00E+15	0	43000
954. $IC_3H_7O_2H\leftrightarrow IC_3H_7O+OH$	4.00E+15	0	43000
955. $NC_3H_7O\leftrightarrow C_2H_5+CH_2O$	5.00E+13	0	15700
956. $IC_3H_7O\leftrightarrow CH_3+CH_3HCO$	4.00E+14	0	17200
957. $C_3H_6+OH(+M)\leftrightarrow C_3H_6OH(+M)$	1.81E+13	0	0
Low pressure limit: 0.13300E+31 -0.35000E+01 0.00E+00			
958. $C_3H_6OH\rightarrow C_2H_5+CH_2O$	1.40E+09	0	17200
959. $C_3H_6OH\rightarrow CH_3+CH_3HCO$	1.00E+09	0	17200
960. $C_3H_6OH+O_2\leftrightarrow O_2C_3H_6OH$	1.00E+12	0	-1100
961. $O_2C_3H_6OH\rightarrow CH_3HCO+CH_2O+OH$	1.00E+16	0	25000

Table F.6 (continued): Chemical reaction mechanism for Konnov's methane oxidation (A_i in mol.cm.s.K, E_i in cal.mol^{-1})

REACTIONS CONSIDERED	A_i	β_i	E_i
962. $C_3H_6+CH_3O_2\leftrightarrow C_3H_5+CH_3O_2H$	2.00E+12	0	17000
963. $C_3H_6+CH_3O_2\leftrightarrow C_3H_6O+CH_3O$	4.00E+11	0	11720
964. $C_3H_6+C_2H_5O_2\leftrightarrow C_3H_5+C_2H_5O_2H$	3.20E+11	0	14900
965. $C_3H_6+C_3H_5O_2\leftrightarrow C_3H_5+C_3H_5O_2H$	3.20E+11	0	14900
966. $C_3H_6+C_3H_5O_2\leftrightarrow C_3H_6O+C_3H_5O$	1.05E+11	0	14200
967. $C_3H_6+CH_3CO_3\leftrightarrow C_3H_5+CH_3CO_3H$	3.20E+11	0	14900
968. $C_3H_6+NC_3H_7O_2\leftrightarrow C_3H_5+NC_3H_7O_2H$	3.20E+11	0	14900
969. $C_3H_6+IC_3H_7O_2\leftrightarrow C_3H_5+IC_3H_7O_2H$	3.20E+11	0	14900
970. $C_3H_6+NC_3H_7O_2\leftrightarrow C_3H_6O+NC_3H_7O$	1.70E+07	0	0
971. $C_3H_5+O_2\leftrightarrow C_3H_5O_2$	1.20E+10	0	-2300
972. $C_3H_5+HO_2\leftrightarrow C_3H_5O+OH$	9.00E+12	0	0
973. $C_3H_5+CH_3O_2\leftrightarrow C_3H_5O+CH_3O$	3.80E+11	0	-1200
974. $C_3H_5O_2+CH_3\leftrightarrow C_3H_5O+CH_3O$	3.80E+11	0	-1200
975. $C_3H_5O_2+C_3H_5\leftrightarrow C_3H_5O+C_3H_5O$	3.80E+11	0	-1200
976. $C_3H_5O_2+HO_2\leftrightarrow C_3H_5O_2H+O_2$	4.60E+10	0	-2600
977. $C_3H_5O_2+HO_2\rightarrow C_3H_5O+OH+O_2$	1.00E+12	0	0
978. $C_3H_5O_2+CH_3O_2\rightarrow C_3H_5O+CH_3O+O_2$	1.70E+11	0	-1000
979. $C_3H_5O_2+C_3H_5O_2\rightarrow C_3H_5O+C_3H_5O+O_2$	3.70E+12	0	2200
980. $C_3H_5O\leftrightarrow CH_2O+C_2H_3$	1.00E+14	0	21600
981. $C_3H_5O_2H\leftrightarrow C_3H_5O+OH$	4.00E+15	0	43000
982. $CH_2O+C_3H_5O_2\leftrightarrow HCO+C_3H_5O_2H$	1.30E+11	0	10500
983. $CH_2O+NC_3H_7O_2\leftrightarrow HCO+NC_3H_7O_2H$	1.30E+11	0	9000
984. $CH_2O+IC_3H_7O_2\leftrightarrow HCO+IC_3H_7O_2H$	1.30E+11	0	9000
985. $C_2H_4+NC_3H_7O_2\leftrightarrow C_2H_3+NC_3H_7O_2H$	7.10E+11	0	25000
986. $C_2H_4+IC_3H_7O_2\leftrightarrow C_2H_3+IC_3H_7O_2H$	7.10E+11	0	25000
987. $CH_4+C_3H_5O_2\leftrightarrow CH_3+C_3H_5O_2H$	1.14E+13	0	20460
988. $CH_4+NC_3H_7O_2\leftrightarrow CH_3+NC_3H_7O_2H$	1.14E+13	0	20460
989. $CH_4+IC_3H_7O_2\leftrightarrow CH3+IC_3H_7O_2H$	1.14E+13	0	20460
990. $CH_3OH+NC_3H_7O_2\leftrightarrow CH_2OH+NC_3H_7O_2H$	6.30E+12	0	19360
991. $CH_3OH+IC_3H_7O_2\leftrightarrow CH_2OH+IC_3H_7O_2H$	6.30E+12	0	19360
992. $CH_3HCO+C_3H_5O_2\leftrightarrow CH_3CO+C_3H_5O_2H$	1.15E+11	0	10000
993. $CH_3HCO+NC_3H_7O_2\leftrightarrow CH_3CO+NC_3H_7O_2H$	1.15E+11	0	10000
994. $CH_3HCO+IC_3H_7O_2\leftrightarrow CH_3CO+IC_3H_7O_2H$	1.15E+11	0	10000
995. $C+N_2+M\leftrightarrow CNN+M$	1.12E+15	0	0
996. $C_2H+NO\leftrightarrow HCN+CO$	6.00E+13	0	570
997. $C_2H+HCN\leftrightarrow CN+C_2H_2$	3.20E+12	0	1530
998. $CH_2+NO\leftrightarrow HCN+OH$	5.00E+11	0	2870
999. $HCN+M\leftrightarrow H+CN+M$	3.57E+26	-2.6	124900
1000. $C_2N_2+M\leftrightarrow CN+CN+M$	3.20E+16	0	94400
1001. $CN+N_2O\leftrightarrow CNN+NO$	6.00E+13	0	15360
1002. $CN+N_2O\leftrightarrow CNN+NO$	1.80E+10	0	1450
1003. $CH+N_2(+M)\leftrightarrow HCNN(+M)$	3.10E+12	0.1	0

Table F.6 (continued): Chemical reaction mechanism for Konnov's methane oxidation (A_i in mol.cm.s.K, E_i in cal.mol^{-1})

REACTIONS CONSIDERED	A_i	β_i	E_i
Low pressure limit: 0.13000E+26 -0.31600E+01 7.40E+02			
Troe centering: 0.66700E+00 0.23500E+03 2.12E+03 4.54E+03			
1004. HCNN+H↔H_2+CNN	5.00E+13	0	0
1005. HCNN+H→CH_2+N_2	2.00E+13	0	3000
1006. HCNN+O↔OH+CNN	2.00E+13	0	20000
1007. HCNN+O↔CO+H+N_2	5.00E+13	0	15000
1008. HCNN+O↔HCN+NO	5.00E+13	0	15000
1009. HCNN+OH↔H_2O+CNN	1.00E+13	0	8000
1010. HCNN+OH↔H+HCO+N_2	1.00E+13	0	16000
1011. HCNN+O_2↔HO_2+CNN	1.00E+12	0	4000
1012. HCNN+O_2→H+CO_2+N_2	4.00E+12	0	0
1013. HCNN+O_2↔HCO+N_2O	4.00E+12	0	0
1014. CNN+O↔CO+N_2	1.00E+13	0	0
1015. CNN+O↔CN+NO	1.00E+14	0	20000
1016. CNN+OH↔H+CO+N_2	1.00E+13	0	1000
1017. CNN+H↔NH+CN	5.00E+14	0	40000
1018. CNN+OH↔HCN+NO	1.00E+12	0	1000
1019. CNN+H↔HCN+N	5.00E+13	0	25000
1020. CNN+O_2↔NO+NCO	1.00E+13	0	5000
1021. HNO+CH_3↔NO+CH_4	8.20E+05	1.9	954
1022. HONO+CH_3↔NO_2+CH_4	8.10E+05	1.9	5504
1023. H_2NO+CH_3↔CH_3O+NH_2	2.00E+13	0	0
1024. H_2NO+CH_3↔HNO+CH_4	1.60E+06	1.9	2960
1025. HNOH+CH_3↔HNO+CH_4	1.60E+06	1.9	2096
1026. NH_2OH+CH_3↔HNOH+CH_4	1.60E+06	1.9	6350
1027. NH_2OH+CH_3↔H_2NO+CH_4	8.20E+05	1.9	5500
1028. N_2H_2+CH_3↔NNH+CH_4	1.60E+06	1.9	2970
1029. N_2H_3+CH_3↔N_2H_2+CH_4	8.20E+05	1.9	1818
1030. N_2H_4+CH_3↔N_2H_3+CH_4	3.30E+06	1.9	5325
1031. CH_4+NH↔CH_3+NH_2	9.00E+13	0	20080
1032. CH_4+NH_2↔CH_3+NH_3	1.20E+13	0	15150
1033. CH_3+NH_2↔CH_2+NH_3	1.60E+06	1.9	7570
1034. C_2H_6+NH↔C_2H_5+NH_2	7.00E+13	0	16700
1035. C_2H_6+NH_2↔C_2H_5+NH_3	9.70E+12	0	11470
1036. C_3H_8+NH_2↔NC_3H_7+NH_3	1.70E+13	0	10660
1037. C_3H_8+NH_2↔IC_3H_7+NH_3	4.50E+11	0	6150
1038. CH_3+NO(+M)↔CH_3NO(+M)	1.00E+13	0	0
Low pressure limit: 0.19000E+19 0.00000E+00 0.00E+00			
SRI centering: 0.30000E-01 -0.79000E+03 1.00E+00			
1039. CH_3NO+H↔H_2CNO+H_2	4.40E+08	1.5	377
1040. CH_3NO+H↔CH_3+HNO	1.80E+13	0	2800
1041. CH_3NO+O↔H_2CNO+OH	3.30E+08	1.5	3615
1042. CH_3NO+O↔CH_3+NO_2	1.70E+06	2.1	0

Table F.6 (continued): Chemical reaction mechanism for Konnov's methane oxidation (A_i in mol.cm.s.K, E_i in cal.mol^{-1})

REACTIONS CONSIDERED	A_i	β_i	E_i
1043. $CH_3NO+OH\leftrightarrow H_2CNO+H_2O$	3.60E+06	2	-1192
1044. $CH_3NO+OH\leftrightarrow CH_3+HONO$	2.50E+12	0	1000
1045. $CH_3NO+CH_3\leftrightarrow H_2CNO+CH_4$	7.90E+05	1.9	5415
1046. $CH_3NO+NH_2\leftrightarrow H_2CNO+NH_3$	2.80E+06	1.9	1073
1047. $H_2CNO\leftrightarrow HNCO+H$	2.30E+42	-9.1	53840
1048. $H2CNO+O_2\leftrightarrow CH_2O+NO_2$	2.90E+12	-0.3	17700
1049. $H_2CNO+H\leftrightarrow CH_3+NO$	4.00E+13	0	0
1050. $H_2CNO+H\leftrightarrow HCNO+H_2$	4.80E+08	1.5	-894
1051. $H_2CNO+O\leftrightarrow HCNO+OH$	3.30E+08	1.5	-894
1052. $H_2CNO+O\leftrightarrow CH_2O+NO$	7.00E+13	0	0
1053. $H_2CNO+OH\leftrightarrow CH_2OH+NO$	4.00E+13	0	0
1054. $H_2CNO+OH\leftrightarrow HCNO+H_2O$	2.40E+06	2	-1192
1055. $H_2CNO+CH_3\leftrightarrow C_2H_5+NO$	3.00E+13	0	0
1056. $H_2CNO+CH_3\leftrightarrow HCNO+CH_4$	1.60E+06	1.9	-1113
1057. $H_2CNO+NH_2\leftrightarrow HCNO+NH_3$	1.80E+06	1.9	-1152
1058. $CH_3+NO_2\leftrightarrow CH_3O+NO$	1.40E+13	0	0
1059. $CH+NO_2\leftrightarrow HCO+NO$	1.20E+14	0	0
1060. $CH_2+NO_2\leftrightarrow CH_2O+NO$	4.20E+13	0	0
1061. $CN+NO\leftrightarrow N_2+CO$	1.00E+11	0	0
1062. $HNCO+M\leftrightarrow H+NCO+M$	5.00E+15	0	120000
1063. $HNCO+N\leftrightarrow NH+NCO$	4.00E+13	0	36000
1064. $CH_3O+HNO\leftrightarrow CH_3OH+NO$	3.16E+13	0	0
1065. $NCO+HO_2\leftrightarrow HNCO+O_2$	2.00E+13	0	0
1066. $N_2O+CO\leftrightarrow CO_2+N_2$	2.51E+14	0	46000
1067. $N_2O+CH_2\leftrightarrow CH_2O+N_2$	1.00E+12	0	0
1068. $N_2O+CH_3\leftrightarrow CH_3O+N_2$	9.00E+09	0	0
1069. $N_2O+HCO\leftrightarrow CO_2+H+N_2$	1.70E+14	0	20000
1070. $N_2O+HCCO\leftrightarrow CO+HCO+N_2$	1.70E+14	0	25500
1071. $N_2O+C_2H_2\leftrightarrow HCCO+H+N_2$	6.59E+16	0	61200
1072. $N_2O+C_2H_3\leftrightarrow CH_2HCO+N_2$	1.00E+11	0	0
1073. $HOCN+O\leftrightarrow NCO+OH$	1.50E+04	2.6	4000
1074. $HOCN+H\leftrightarrow NCO+H_2$	2.00E+07	2	2000
1075. $HOCN+H\leftrightarrow NH_2+CO$	1.20E+08	0.6	2080
1076. $HOCN+OH\leftrightarrow NCO+H_2O$	6.38E+05	2	2560
1077. $HOCN+CH_3\leftrightarrow NCO+CH_4$	8.20E+05	1.9	6620
1078. $HOCN+NH_2\leftrightarrow NCO+NH_3$	9.20E+05	1.9	3645
1079. $CN+NO_2\leftrightarrow CO+N_2O$	4.93E+14	-0.8	344
1080. $CN+NO_2\leftrightarrow CO_2+N_2$	3.70E+14	-0.8	344
1081. $CN+CO_2\leftrightarrow NCO+CO$	3.67E+06	2.2	26900
1082. $CN+NH_3\leftrightarrow HCN+NH_2$	9.20E+12	0	-357
1083. $HNCO+CN\leftrightarrow HCN+NCO$	1.50E+13	0	0
1084. $NCO+CN\leftrightarrow CNN+CO$	1.80E+13	0	0
1085. $HONO+NCO\leftrightarrow HNCO+NO_2$	3.60E+12	0	0

Table F.6 (continued): Chemical reaction mechanism for Konnov's methane oxidation (A_i in mol.cm.s.K, E_i in cal.mol^{-1})

REACTIONS CONSIDERED	A_i	β_i	E_i
1086. $NCO+CH_2O \leftrightarrow HNCO+HCO$	6.00E+12	0	0
1087. $CH+N_2 \leftrightarrow HCN+N$	3.68E+07	1.4	20723
1088. $NH_2+C \leftrightarrow CH+NH$	5.80E+11	0.7	20900
1089. $C+N_2 \leftrightarrow CN+N$	5.20E+13	0	44700
1090. $CH_2+N_2 \leftrightarrow HCN+NH$	4.80E+12	0	35850
1091. $C2+N_2 \leftrightarrow CN+CN$	1.50E+13	0	41700
1092. $H_2CN+N \leftrightarrow N_2+CH_2$	6.00E+13	0	400
1093. $H_2CN+H \leftrightarrow HCN+H_2$	2.40E+08	1.5	-894
1094. $H_2CN+O \leftrightarrow HCN+OH$	1.70E+08	1.5	-894
1095. $H_2CN+O \leftrightarrow HNCO+H$	6.00E+13	0	0
1096. $H_2CN+O \leftrightarrow HCNO+H$	2.00E+13	0	0
1097. $H_2CN+M \leftrightarrow HCN+H+M$	3.00E+14	0	22000
1098. $H_2CN+HO_2 \leftrightarrow HCN+H_2O_2$	1.40E+04	2.7	-1610
1099. $H_2CN+O_2 \leftrightarrow CH_2O+NO$	3.00E+12	0	6000
1100. $H_2CN+CH_3 \leftrightarrow HCN+CH_4$	8.10E+05	1.9	-1113
1101. $H_2CN+OH \leftrightarrow HCN+H_2O$	1.20E+06	2	-1192
1102. $H_2CN+NH_2 \leftrightarrow HCN+NH_3$	9.20E+05	1.9	-1152
1103. $C+NO \leftrightarrow CN+O$	2.00E+13	0	0
1104. $CH+NO \leftrightarrow HCN+O$	8.69E+13	0	0
1105. $CH+NO \leftrightarrow CN+OH$	1.68E+12	0	0
1106. $CH+NO \leftrightarrow CO+NH$	9.84E+12	0	0
1107. $CH+NO \leftrightarrow NCO+H$	1.67E+13	0	0
1108. $CH_2+NO \leftrightarrow HNCO+H$	2.50E+12	0	5970
1109. $CH_2+NO \leftrightarrow HCNO+H$	3.80E+13	-0.4	576
1110. $CH_2+NO \leftrightarrow NH_2+CO$	2.30E+16	-1.4	1331
1111. $CH_2+NO \leftrightarrow H_2CN+O$	8.10E+07	1.4	4110
1112. $CH_3+NO \leftrightarrow HCN+H_2O$	2.40E+12	0	15700
1113. $CH_3+NO \leftrightarrow H_2CN+OH$	5.20E+12	0	24240
1114. $HCCO+NO \leftrightarrow HCNO+CO$	4.64E+13	0	700
1115. $HCCO+NO \leftrightarrow HCN+CO_2$	1.39E+13	0	700
1116. $SCH_2+NO \leftrightarrow HCN+OH$	1.00E+14	0	0
1117. $HCNO \leftrightarrow HCN+O$	4.20E+31	-6.1	61210
1118. $HCNO+H \leftrightarrow HCN+OH$	1.00E+14	0	12000
1119. $HCNO+H \leftrightarrow HNCO+H$	2.10E+15	-0.7	2850
1120. $HCNO+H \leftrightarrow HOCN+H$	1.40E+11	-0.2	2484
1121. $HCNO+H \leftrightarrow NH_2+CO$	1.70E+14	-0.8	2890
1122. $HCNO+O \leftrightarrow HCO+NO$	7.00E+13	0	0
1123. $CH_2+N \leftrightarrow HCN+H$	5.00E+13	0	0
1124. $CH_2+N \leftrightarrow NH+CH$	6.00E+11	0.7	40500
1125. $CH+N \leftrightarrow CN+H$	1.67E+14	-0.1	0
1126. $CH+N \leftrightarrow C+NH$	4.50E+11	0.7	2400
1127. $N+CO_2 \leftrightarrow NO+CO$	1.90E+11	0	3400
1128. $N+HCCO \leftrightarrow HCN+CO$	5.00E+13	0	0

Table F.6 (continued): Chemical reaction mechanism for Konnov's methane oxidation (A_i in mol.cm.s.K, E_i in cal.mol^{-1})

REACTIONS CONSIDERED	A_i	β_i	E_i
1129. $CH_3+N\leftrightarrow H_2CN+H$	7.10E+13	0	0
1130. $CH_3+N\leftrightarrow HCNH+H$	1.20E+11	0.5	367.6
1131. $HCNH\leftrightarrow HCN+H$	6.10E+28	-5.7	24270
1132. $HCNH+H\leftrightarrow H_2CN+H$	2.00E+13	0	0
1133. $HCNH+H\leftrightarrow HCN+H_2$	2.40E+08	1.5	-894
1134. $HCNH+O\leftrightarrow HNCO+H$	7.00E+13	0	0
1135. $HCNH+O\leftrightarrow HCN+OH$	1.70E+08	1.5	-894
1136. $HCNH+OH\leftrightarrow HCN+H_2O$	1.20E+06	2	-1192
1137. $HCNH+CH_3\leftrightarrow HCN+CH_4$	8.20E+05	1.9	-1113
1138. $C_2H_3+N\leftrightarrow HCN+CH_2$	2.00E+13	0	0
1139. $CN+H_2O\leftrightarrow HCN+OH$	4.00E+12	0	7400
1140. $CN+H_2O\leftrightarrow HOCN+H$	4.00E+12	0	7400
1141. $OH+HCN\leftrightarrow HOCN+H$	3.20E+04	2.5	12120
1142. $OH+HCN\leftrightarrow HNCO+H$	5.60E-06	4.7	-490
1143. $OH+HCN\leftrightarrow NH_2+CO$	6.44E+10	0	11700
1144. $HOCN+H\leftrightarrow HNCO+H$	1.00E+13	0	0
1145. $HCN+O\leftrightarrow NCO+H$	1.38E+04	2.6	4980
1146. $HCN+O\leftrightarrow NH+CO$	3.45E+03	2.6	4980
1147. $HCN+O\leftrightarrow CN+OH$	2.70E+09	1.6	26600
1148. $CN+H_2\leftrightarrow HCN+H$	2.00E+04	2.9	1600
1149. $CN+O\leftrightarrow CO+N$	1.90E+12	0.5	720
1150. $CN+O_2\leftrightarrow NCO+O$	7.20E+12	0	-400
1151. $CN+OH\leftrightarrow NCO+H$	4.00E+13	0	0
1152. $CN+HCN\leftrightarrow C_2N_2+H$	1.51E+07	1.7	1530
1153. $CN+NO_2\leftrightarrow NCO+NO$	5.32E+15	-0.8	344
1154. $CN+N_2O\leftrightarrow NCO+N_2$	6.00E+12	0	15360
1155. $C_2N_2+O\leftrightarrow NCO+CN$	4.57E+12	0	8880
1156. $C_2N_2+OH\leftrightarrow HNCO+CN$	1.86E+11	0	2900
1157. $C_2N_2+OH\leftrightarrow HOCN+CN$	2.00E+12	0	19000
1158. $HNCO+H\leftrightarrow H_2+NCO$	1.76E+05	2.4	12300
1159. $HNCO+H\leftrightarrow NH_2+CO$	3.60E+04	2.5	2340
1160. $HNCO+M\leftrightarrow NH+CO+M$	1.10E+16	0	86000
1161. $HNCO+O\leftrightarrow NCO+OH$	2.20E+06	2.1	11430
1162. $HNCO+O\leftrightarrow NH+CO_2$	9.80E+07	1.4	8530
1163. $HNCO+O\leftrightarrow HNO+CO$	1.50E+08	1.6	44012
1164. $HNCO+OH\leftrightarrow NCO+H_2O$	3.45E+07	1.5	3600
1165. $HNCO+OH\leftrightarrow NH_2+CO_2$	6.30E+10	-0.1	11645
1166. $HNCO+HO_2\leftrightarrow NCO+H_2O_2$	3.00E+11	0	29000
1167. $HNCO+O_2\leftrightarrow HNO+CO_2$	1.00E+12	0	35000
1168. $HNCO+NH_2\leftrightarrow NCO+NH_3$	5.00E+12	0	6200
1169. $HNCO+NH\leftrightarrow NCO+NH_2$	1.04E+15	0	39390
1170. $NCO+H\leftrightarrow NH+CO$	5.36E+13	0	0
1171. $NCO+O\leftrightarrow NO+CO$	4.20E+13	0	0

Table F.6 (continued): Chemical reaction mechanism for Konnov's methane oxidation (A_i in mol.cm.s.K, E_i in cal.mol^{-1})

REACTIONS CONSIDERED	A_i	β_i	E_i
1172. NCO+O↔N+CO_2	8.00E+12	0	2500
1173. NCO+N↔N_2+CO	2.00E+13	0	0
1174. NCO+OH↔NO+HCO	5.00E+12	0	15000
1175. NCO+M↔N+CO+M	2.20E+14	0	54050
1176. NCO+NO↔N_2O+CO	4.60E+18	-2	934
1177. NCO+NO↔N_2+CO_2	5.80E+18	-2	934
1178. NCO+O_2↔NO+CO_2	2.00E+12	0	20000
1179. NCO+HCO↔HNCO+CO	3.60E+13	0	0
1180. NCO+NO_2↔CO+NO+NO	2.83E+13	-0.6	-326
1181. NCO+NO_2↔CO_2+N_2O	3.57E+14	-0.6	-326
1182. NCO+HNO↔HNCO+NO	1.80E+13	0	0
1183. NCO+NCO↔CO+CO+N_2	3.00E+12	0	0
1184. NO+HCO↔CO+HNO	7.24E+13	-0.4	0
1185. NO_2+CO↔CO_2+NO	9.00E+13	0	33800
1186. NO_2+HCO↔H+CO_2+NO	8.40E+15	-0.8	1930
1187. CH_3O+NO_2↔HONO+CH_2O	3.00E+12	0	0
1188. CH_3O+NO↔CH_2O+HNO	1.30E+14	-0.7	0
1189. NO_2+CH_2O↔HONO+HCO	1.00E+10	0	15100
1190. NO+CH_2O↔HNO+HCO	1.00E+13	0	40820
1191. NO_2+HCO↔HONO+CO	1.00E+13	0	0
1192. NO_2+HCO↔OH+NO+CO	1.00E+14	0	0
1193. NCO+N↔NO+CN	2.70E+18	-1	17200
1194. CN+CH_4↔HCN+CH_3	9.00E+04	2.6	-300
1195. C+NO↔CO+N	2.80E+13	0	0
1196. NH+CO_2↔HNO+CO	1.00E+13	0	14350
1197. NCO+CH_4↔HNCO+CH_3	1.00E+13	0	8130
1198. C+N_2O↔CN+NO	4.80E+12	0	0
1199. CH+NH_2↔HCN+H+H	3.00E+13	0	0
1200. CH+NH↔HCN+H	5.00E+13	0	0
1201. CH_2+NH↔HCN+H+H	3.00E+13	0	0
1202. CH_3+N↔HCN+H+H	2.00E+11	0	0
1203. CH_3+N↔HCN+H_2	7.10E+12	0	0
1204. CH_4+N↔NH+CH_3	1.00E+13	0	24000
1205. C_3H_3+N↔HCN+C_2H_2	1.00E+13	0	0
1206. CH+N_2O↔HCN+NO	1.34E+13	0	-510
1207. CH+N_2O↔CO+H+N_2	5.20E+12	0	-510